Nd'ordre 2010-ISAL–0023 Année 2010

THÈSE

Nonlinear dynamics of M&NEMS resonant sensors: design strategies for performance enhancement

Présentée devant
l'Institut National des Sciences Appliquées de Lyon

pour obtenir
le GRADE DE DOCTEUR

École doctorale :
Mécanique, Énergétique, Génie Civil, Acoustique

Spécialité :
MÉCANIQUE - GÉNIE MÉCANIQUE

par
NAJIB KACEM
Ingénieur Arts et Métiers

Thèse soutenue le 12 Mars 2010 devant la Commission d'examen

Jury

Claude Henri Lamarque	Président
Liviu Nicu	Rapporteur
Bruno Cochelin	Rapporteur
Ron Lifshitz	Examinateur
Régis Dufour	Directeur de thèse
Sébastien Hentz	Examinateur
Sébastien Baguet	Examinateur

Réalisé à l'université de Lyon-CNRS INSA-Lyon, LaMCoS UMR 5259
18-20, rue des Sciences F 69621 Villeurbanne Cedex (FRANCE)
et au CEA/LETI-MINATEC
17 rue des Martyrs F38054 Grenoble Cedex 9 (FRANCE)

INSA Direction de la Recherche - Ecoles Doctorales – Quadriennal 2007-2010

SIGLE	ECOLE DOCTORALE	NOM ET COORDONNEES DU RESPONSABLE
CHIMIE	**CHIMIE DE LYON** **http://sakura.cpe.fr/ED206** M. Jean Marc LANCELIN Insa : R. GOURDON	M. Jean Marc LANCELIN Université Claude Bernard Lyon 1 Bât CPE 43 bd du 11 novembre 1918 69622 VILLEURBANNE Cedex Tél : 04.72.43 13 95 Fax : lancelin@hikari.cpe.fr
E.E.A.	**ELECTRONIQUE, ELECTROTECHNIQUE, AUTOMATIQUE** **http://www.insa-lyon.fr/eea** M. Alain NICOLAS Insa : D. BARBIER ede2a@insa-lyon.fr Secrétariat : M. LABOUNE AM. 64.43 – Fax : 64.54	M. Alain NICOLAS Ecole Centrale de Lyon Bâtiment H9 36 avenue Guy de Collongue 69134 ECULLY Tél : 04.72.18 60 97 Fax : 04 78 43 37 17 eea@ec-lyon.fr Secrétariat : M.C. HAVGOUDOUKIAN
E2M2	**EVOLUTION, ECOSYSTEME, MICROBIOLOGIE, MODELISATION** **http://biomserv.univ-lyon1.fr/E2M2** M. Jean-Pierre FLANDROIS Insa : H. CHARLES	M. Jean-Pierre FLANDROIS CNRS UMR 5558 Université Claude Bernard Lyon 1 Bât G. Mendel 43 bd du 11 novembre 1918 69622 VILLEURBANNE Cédex Tél : 04.26 23 59 50 Fax 04 26 23 59 49 06 07 53 89 13 e2m2@biomserv.univ-lyon1.fr
EDIIS	**INFORMATIQUE ET INFORMATION POUR LA SOCIETE** http://ediis.univ-lyon1.fr M. Alain MILLE Secrétariat : I. BUISSON	M. Alain MILLE Université Claude Bernard Lyon 1 LIRIS - EDIIS Bâtiment Nautibus 43 bd du 11 novembre 1918 69622 VILLEURBANNE Cedex Tél : 04.72. 44 82 94 Fax 04 72 44 80 53 ediis@liris.cnrs.fr - alain.mille@liris.cnrs.fr
EDISS	**INTERDISCIPLINAIRE SCIENCES-SANTE** Sec : Safia Boudjema M. Didier REVEL Insa : M. LAGARDE	M. Didier REVEL Hôpital Cardiologique de Lyon Bâtiment Central 28 Avenue Doyen Lépine 69500 BRON Tél : 04.72.68 49 09 Fax :04 72 35 49 16 Didier.revel@creatis.uni-lyon1.fr
Matériaux	**MATERIAUX DE LYON** M. Jean Marc PELLETIER Secrétariat : C. BERNAVON 83.85	M. Jean Marc PELLETIER INSA de Lyon MATEIS Bâtiment Blaise Pascal 7 avenue Jean Capelle 69621 VILLEURBANNE Cédex Tél : 04.72.43 83 18 Fax 04 72 43 85 28 Jean-marc.Pelletier@insa-lyon.fr
Math IF	**MATHEMATIQUES ET INFORMATIQUE FONDAMENTALE** M. Pascal KOIRAN Insa : G. BAYADA	M.Pascal KOIRAN Ecole Normale Supérieure de Lyon 46 allée d'Italie 69364 LYON Cédex 07 Tél : 04.72.72 84 81 Fax : 04 72 72 89 69 Pascal.koiran@ens-lyon.fr Secrétariat : Fatine Latif - latif@math.univ-lyon1.fr
MEGA	**MECANIQUE, ENERGETIQUE, GENIE CIVIL, ACOUSTIQUE** M. Jean Louis GUYADER Secrétariat : M. LABOUNE PM : 71.70 –Fax : 87.12	M. Jean Louis GUYADER INSA de Lyon Laboratoire de Vibrations et Acoustique Bâtiment Antoine de Saint Exupéry 25 bis avenue Jean Capelle 69621 VILLEURBANNE Cedex Tél :04.72.18.71.70 Fax : 04 72 18 87 12 mega@lva.insa-lyon.fr
ScSo	**ScSo*** M. BRAVARD Jean Paul Insa : J.Y. TOUSSAINT	M. BRAVARD Jean Paul Université Lyon 2 86 rue Pasteur 69365 LYON Cedex 07 Tél : 04.78.69.72.76 Fax : 04.37.28.04.48 Jean-paul.bravard@univ-lyon2.fr

*ScSo : Histoire, Geographie, Aménagement, Urbanisme, Archéologie, Science politique, Sociologie, Anthropologie

Acknowledgments

Mes travaux de thèse effectués au sein de l'équipe DIHS/LCMS du laboratoire LETI du CEA de Grenoble et en collaboration avec le LaMCoS de l'Insa de Lyon ont étés menés à terme grâce à un travail d'équipe et un soutient permanant de mes encadrants et responsables hiérarchiques. Je tiens donc à remercier tous ceux qui ont participé directement ou indirectement dans mes recherches de thèse.

Tout d'abord, je remercie mon encadrant CEA Sébastien Hentz pour ses choix pertinents concernant les orientations de ma thèse dont la richesse en résultats est due principalement au développement de l'aspect dynamique nonlinéaire dans le domaine des micro et nano capteurs. Je remercie également mon directeur de thèse Régis Dufour et mon encadrant Sébastien Baguet du coté LaMCoS pour leurs suivis et conseils.

Je voudrais témoigner ma gratitude envers les membres du jury qui ont bien voulu examiner ce mémoire, et dont la participation à fourni un éclairage supplémentaire:

- M Bruno Cochelin du LMA
- M Liviu Nicu du LAAS
- M Claude Henri Lamarque de l'ENTPE
- M Ron Lifshitz de l'université de Tel Aviv
- M Régis Dufour du LaMCoS
- M Sébastien Baguet du LaMCoS
- M Sébastien Hentz du CEA-LETI

Je remercie également Philippe Robert, le directeur du LCMS, Valérie Nguyen, chef des projets MNT et M&NEMS ainsi que le chef du projet Carnot NEMS, Philippe Andreucci. C'est grâce à ces projets, que j'ai pu confronter les résultats théoriques aux caractérisations expérimentales sur de nombreux résonateurs et capteurs MEMS, NEMS et M&NEMS.

Merci à Julien Arcamone du LCMS qui m'a fourni les résultats expérimentaux de sa thèse effectué au CNM-IMB à Barcelone sur les cantilevers résonants. Ceci m'a permis d'avoir une première validation du modèle nonlinéaire sur les poutres encastrée-libre à actionnement électrostatique avant de le généraliser à d'autres capteurs de gaz /masse fabriqués dans le cadre du projet Carnot NEMS.

Merci à Hervé Fontaine, Bruno Reig et Delphine Pinto pour leurs participations dans la caractérisation électrique des accéléromètres MNT en régime nonlinéaire. Sans oublier de remercier Marc Sworowski pour son aide sur la mise en place de bancs de caractérisation hétérodyne pour les capteurs M&NEMS résonants.

Je remercie également Samuel Harrison et Mylène Savoie qui ont suivi successivement la filière du projet M&NEMS pour la fabrication des capteurs que j'ai dimensionné durant ma thèse.

Toute ma gratitude va aux secrétaires Beatrice et Christine, qui étaient toujours présentes pour toutes les démarches administratifs.

Merci aux membres du LCMS que j'ai côtoyés pendant toute ma thèse, et avec qui j'ai toujours apprécié les discussions et les échanges d'idées: Carine, Laurent, Stephan, JS, JPP, Cecilia, Stephane, Emerick, Samuel, Eric, Arnaud, Henri, Hubert, Patrice, Kamal, Julien et Paul.

Je remercie aussi les thésards du LCMS : Thomas, Hoang Trang, Lise, Ervin, Sébastien, Paul, Dirk et Antoine. Merci a toutes les personnes du LCMS et du LCRF pour l'ambiance sympathique dans la salle café au cours des trois années.

Enfin, je termine ces lignes en remerciant toute ma famille pour son soutien non seulement durant cette thèse, mais aussi tout au long de mon parcours d'études en Tunisie et puis en France.

Abstract

Nanoelectromechanical systems (NEMS) have been the focus of recent applied and fundamental research. With critical dimensions down to a few tens of nm, most NEMS are used working in resonance. In this size regime, they display high fundamental resonance frequencies, diminished active masses, tolerable force constants and relatively high quality factors in the range of $10^2 - 10^4$. These attributes collectively make NEMS suitable for a multitude of technological applications such as ultrasensitive force and mass sensing, narrow band filtering, and time keeping. So as to fulfill their full promises, that is, to begin to come out of industrial foundries, a certain number of challenges are yet to be addressed: in particular, their frequency stability, *i.e.* their output carrier power has to be improved. Mechanical transduction gain of the devices has been thoroughly studied, but the drive power has always been a priori limited to the onset of nonlinearities. Besides, the smaller the structures, the sooner nonlinearities occur, reducing their dynamic range and even making extremely difficult to detect their oscillation, as the abundant literature about characterization techniques proves.

In this thesis, this limitation is reconsidered, *i.e.* the behavior of NEMS at large amplitude through the nonlinear dynamics of NEMS-based resonant sensors is investigated. A review of inertial, mass and gas sensors is carried out. Particularly, the design issues of resonant sensors are addressed and the sources of nonlinearities in clamped-clamped resonators and cantilevers are exposed. A review of nonlinear methods is also presented in order to define a modeling strategy for the dynamics of resonant accelerometers, gyroscopes and mass/gas sensors. Close-form solutions of the critical amplitudes were provided for several devices and the importance of the fifth order nonlinearities has been demonstrated through the mixed behavior identification. Several analytical design rules are provided in order to enhance the dynamic range of NEMS resonators and the detection limit of NEMS-based resonant sensors. These rules essentially include hysteresis suppression by nonlinearity cancellation as well as mixed behavior and pull-in retarding under superharmonic resonance and simultaneous resonances leading to the possibility of driving the resonator linearly at high oscillations compared to the critical amplitude. The experimental validation of the model has been performed in the case of resonant capacitive ($4\,\mu m$ SOI) MEMS and ($2\,\mu m$ MEMS level/$500\,nm$ NEMS level) SOI M&NEMS accelerometers and gyroscopes as well as capacitive (fabricated using nanostencil lithography) and piezoresistive ($160\,nm$ SOI NEMS) gas/mass sensors.

Keywords

Nonlinear dynamics, resonator, MEMS and NEMS, dynamics range, detection limit, resonant sensors, accelerometer, gyroscope, gas and mass sensors, design rules, superharmonic resonance, simultaneous resonances, mixed behavior, pull-in, critical amplitude

Résumé

Les systèmes nano-électromécaniques (NEMS) sont au centre de la recherche appliquée et fondamentale. Avec des dimensions critiques de quelques dizaines de nanomètres, la plupart des NEMS fonctionnent en mode résonant. A cette échelle, leur fréquence fondamentale est rejetée à plusieurs MHz, et ils bénéficient d'une masse faible, d'une raideur active et de facteurs de qualité dans la gamme de 100 à 10000. Ces attributs rendent collectivement les NEMS appropriés à une multitude d'applications technologiques telles que les capteurs ultrasensibles d'accélération, de force et de masse, les filtres et les oscillateurs pour base de temps. Afin que les résonateurs NEMS tiennent leurs promesses et répondent aux attentes sociétales, un certain nombre de défis et verrous technologiques restent à lever. En particulier, la stabilité en fréquence, cest à dire la puissance de porteuse, doit être améliorée. Le gain mécanique de transduction des NEMS a été analysé avec grand intérêt mais la sensibilité a toujours été a priori limitée par lapparition des non-linéarités. En outre, la miniaturisation des structures descend les seuils d'apparition des non-linéarités, réduit donc la gamme dynamique et complique la détection de leur oscillation.

La thèse reconsidère la limitation de détection des NEMS. Le comportement de NEMS résonants en grands déplacements est analysé en déployant les techniques de la dynamique non linéaire et validé grâce à des méthodes de caractérisation électrique du domaine des NEMS. Tout d'abord il est établi un état de lart de certaines catégories de capteurs. Suit une présentation des problèmes de conception des capteurs résonants puis des sources de non linéarités. L'état de lart des méthodes non linéaires permet de dégager une stratégie de modélisation des capteurs résonants M&NEMS, inertiels, de gaz et de masse. Les expressions analytiques des amplitudes critiques sont données pour plusieurs dispositifs et l'importance des non-linéarités d'ordre cinq a été démontrée par l'identification analytique et l'analyse expérimentale du comportement non linéaire mixte, combinant raidissement et assouplissement, indiquée par la réponse harmonique. Enfin la thèse préconise plusieurs règles de conception analytique afin doptimiser la gamme dynamique des résonateurs NEMS et la limite de détection des capteurs résonant M&NEMS. Pour cela il s'agit de supprimer tout phénomène d'hystérésis par l'annulation des non-linéarités dordre trois, de retarder le comportement mixte et le pull-in (collage du résonateur sur l'électrode) en déclenchant des résonances super harmoniques et des résonances simultanées garantissant le comportement linéaire du résonateur au delà de l'amplitude critique. La validation expérimentale des modèles a été effectuée sur des capteurs inertiels MEMS et M&NEMS à transduction capacitive résonante ainsi que sur des nano capteurs de gaz et de masse à transduction capacitive avec cointégration CMOS et piézorésistive.

Mots-clés

Dynamique non-linéaire, résonateur, MEMS et NEMS, gamme dynamique, limite de détection, capteurs résonnants, accéléromètres, gyromètres, capteurs de gaz et de masse, règles de conception, résonance superharmonique, résonances simultanées, comportement non-linéaire mixte, pull-in, amplitude critique

Contents

1 Introduction **1**
1.1 Motivations . . . 1
1.2 Overview . . . 2

I M&NEMS resonant sensors capabilities and nonlinear dynamics limitations **5**

2 MEMS and NEMS sensors **7**
2.1 Introduction . . . 7
2.1.1 What is MEMS? . . . 8
2.1.2 Materials for MEMS manufacturing . . . 8
2.1.3 MEMS basic processes . . . 9
2.1.4 MEMS applications and market . . . 10
2.1.5 From MEMS to NEMS . . . 10
2.2 Inertial sensors . . . 11
2.2.1 Introduction . . . 11
2.2.2 Accelerometers . . . 13
2.2.3 Gyroscopes . . . 19
2.2.4 Conclusion . . . 24
2.3 Gas and Mass Sensors . . . 25
2.3.1 Gas Sensors . . . 25
2.3.2 Mass Sensors . . . 30
2.4 Resonant sensors . . . 32
2.4.1 Frequency measurement . . . 33
2.4.2 Mechanical analysis . . . 35
2.4.3 Quality factor . . . 37
2.4.4 Noise analysis . . . 40
2.4.5 Resolution . . . 41
2.4.6 Linearity and Dynamic Range . . . 43
2.4.7 Physical Nonlinearities . . . 44
2.4.8 Nonlinearities and noise mixing . . . 45
2.5 Summary . . . 45

3 Nonlinear dynamics and nonlinear methods **47**
3.1 Introduction . . . 47
3.2 Sources of nonlinearities . . . 47
3.2.1 Beams . . . 47
3.2.2 Cantilevers . . . 49
3.3 Nonlinear methods . . . 51
3.3.1 Perturbation techniques . . . 51
3.3.2 Numerical methods for periodic solutions . . . 69
3.4 Summary . . . 77

II Strategies for performance enhancement of resonant accelerometers 79

4 Nonlinear dynamics modeling of resonant accelerometers 81
4.1 Introduction . . . 82
4.2 Choices and motivations . . . 82
4.2.1 Studied resonant accelerometer structure . . . 83
4.2.2 MEMS accelerometer . . . 84
4.2.3 M&NEMS accelerometer . . . 85
4.2.4 Path towards the nonlinear dynamic modeling of NEMS resonators . . . 87
4.3 Model of a nonlinear 1-port resonator . . . 88
4.3.1 Equation of motion . . . 89
4.3.2 Normalization . . . 89
4.3.3 Solving . . . 89
4.3.4 Numerical solutions . . . 93
4.3.5 Simplified analytical model . . . 94
4.4 Confrontation and reduced order model validation . . . 96
4.4.1 Shooting/HBM . . . 96
4.4.2 HBM/Analytical model . . . 97
4.5 Model of a nonlinear 2-port resonator . . . 101
4.5.1 Equation of motion . . . 101
4.5.2 Normalization . . . 102
4.5.3 Solving . . . 102
4.6 Experimental validation . . . 103
4.6.1 Resonance frequency localization . . . 103
4.6.2 Lock-in modes . . . 104
4.6.3 Experimental characterization . . . 105
4.6.4 Linear case ($A < A_c$) . . . 108
4.6.5 Nonlinear case ($A > A_c$) . . . 108
4.7 Summary . . . 110

5 Design rules and performance enhancement 111
5.1 Introduction . . . 112
5.2 Nonlinear phenomena: behavior and physical limitations . . . 112
5.2.1 Hardening behavior . . . 112
5.2.2 Mechanical critical amplitude . . . 112
5.2.3 Bifurcation points . . . 115
5.2.4 Softening behavior . . . 115
5.2.5 Global critical amplitude . . . 116
5.2.6 Mixed behavior . . . 116
5.2.7 Pull-in . . . 116
5.3 Hysteresis suppression by nonlinearity cancellation . . . 119
5.4 Mixed behavior retarding by design optimization . . . 119
5.4.1 Introduction . . . 119
5.4.2 Experimental identification of the mixed behavior . . . 120
5.4.3 Bifurcation topology tuning . . . 121
5.4.4 Conclusion . . . 123
5.5 Pull-in retarding by superharmonic resonance . . . 123

5.5.1 Introduction . . . 123
5.5.2 Model . . . 124
5.5.3 Critical amplitude . . . 125
5.5.4 pull-in . . . 126
5.5.5 Conclusion . . . 127
5.6 Mixed behavior retarding by simultaneous resonances . . . 129
5.6.1 Introduction . . . 129
5.6.2 Model . . . 130
5.6.3 Analytical results . . . 132
5.6.4 Experimental validation . . . 133
5.7 Summary . . . 135

6 Experimental investigations **137**
6.1 Designs and motivations . . . 137
6.2 Experimental set-up . . . 137
6.2.1 Capacitive down-mixing principle . . . 137
6.2.2 Capacitive down-mixing configurations . . . 140
6.2.3 Nonlinear down-mixing model . . . 143
6.3 Experimental validation . . . 144
6.3.1 High capabilities set-up . . . 144
6.3.2 First validation (design for hardening behavior) . . . 145
6.3.3 Design for nonlinearities compensation . . . 146
6.3.4 Strange attraction and transition to the softening behavior . . . 150
6.4 Summary . . . 151

III Extension to other resonant sensors: gyroscopes and mass/gas sensors **153**

7 Resonant gyroscope **155**
7.1 Introduction . . . 156
7.2 The Resonant Gyroscope . . . 157
7.3 Device Analysis . . . 158
7.3.1 Actuation part . . . 160
7.3.2 Lever mechanism . . . 161
7.3.3 Sensing part . . . 163
7.4 Model . . . 163
7.4.1 Normalization . . . 165
7.4.2 Solving . . . 165
7.5 Analytical results and device specifications . . . 167
7.5.1 Proof mass frequency effect . . . 167
7.5.2 Resonant gyroscope scale factor . . . 170
7.5.3 Resonant gyroscope resolution . . . 172
7.5.4 Scale factor sensitivity to environmental variables . . . 174
7.5.5 Quadrature error . . . 174
7.5.6 Bias stability . . . 174
7.5.7 Common mode acceleration . . . 174
7.5.8 Decoupled resonant gyroscope . . . 175

7.6 Electronics and Signal Processing . . . 176
7.7 Designs . . . 177
7.8 Fabrication . . . 180
7.9 Experimental validation . . . 180
7.9.1 Low axial load frequency . . . 180
7.9.2 High axial load frequency . . . 183
7.10 Summary . . . 185

8 Resonant gas and mass sensors **187**
8.1 Introduction . . . 187
8.2 Resonant nanocantilever based on electrostatic detection . . . 188
8.2.1 Equation of motion . . . 189
8.2.2 Normalization . . . 190
8.2.3 Solving . . . 190
8.2.4 Critical amplitude . . . 192
8.2.5 Fabrication: Monolithic integration of nanocantilevers with CMOS . . . 195
8.2.6 Electrical characterization of nanocantilever beams . . . 197
8.3 Resonant nanocantilever based on piezoresistive detection . . . 201
8.3.1 Device description . . . 201
8.3.2 Transduction . . . 202
8.3.3 Equation of motion . . . 203
8.3.4 Normalization . . . 203
8.3.5 Solving . . . 204
8.3.6 The critical amplitude . . . 208
8.3.7 Fabrication . . . 209
8.3.8 Electrical characterization . . . 210
8.3.9 Mass resolution enhancement . . . 217
8.4 Summary . . . 219

9 Conclusions **221**
9.1 Summary . . . 221
9.2 Future work . . . 223

A Appendices **225**
A.1 The fringing field effect . . . 225
A.2 The integration parameters of Equation (4.62) . . . 226
A.3 Approximate integrals . . . 227

Bibliography **229**

List of Figures

2.1 Micro-sized Multiple gear speed reduction. 8
2.2 The principal steps in surface micromachining. 10
2.3 Market overview and forecast for MEMS by device type (Source: Yole Développement-2008-). 11
2.4 Three axis linear accelerometer from ST 12
2.5 Lumped parameter model of an accelerometer consisting of a proof (or seismic) mass, a spring, and a damping element. 15
2.6 Open loop accelerometer. 15
2.7 Examples of simple capacitance displacement sensors. 16
2.8 High-performance capacitive accelerometer using a combination of surface and bulk-micromachining techniques [Yazdi 2000]. 16
2.9 A pieozoresistor generates a voltage when deformed (the output voltage is proportional to the resistivity change). 17
2.10 Cross-sectional view of the piezoresistive accelerometer [Seidel 1995]. 17
2.11 Tunneling current accelerometer [Rockstad 1996]. 18
2.12 Schematic of a resonant accelerometer [Roessig 1997b]. 19
2.13 A complete family of single-axis (yaw) and two-axis (pitch-and-roll, pitch-and-yaw) MEMS gyroscope from ST. (b): Lumped parameter model of a vibratory gyroscope. . 20
2.14 A decoupled translational gyroscope from Bosch [Geiger 2002]. 22
2.15 Surface-micromachined gyroscope with decoupled drive and sense mode. The drive mode is excited by an electrostatic comb drive and is rotational about the z-axis (out-of-plane) [Geiger 2000]. 22
2.16 (a): Operational principle of a ring gyroscope. (b): Delphi metal ring gyroscope [Sparks 1999]. 23
2.17 (a): Schematic design concept for Berkeley dual-axis gyroscope. (b): Polysilicon surface-micromachined dual-axis gyroscopes designed at the Berkeley Sensors and Actuators Center [Juneau 1997]. 24
2.18 Schematic of the mechanical structure of the resonant output gyroscope [Seshia 2002a]. 25
2.19 Acoustic wave devices configurations 28
2.20 An array of microcantilevers with their lower surfaces passivated and their upper surfaces functionalized for recognition of target molecules. 29
2.21 The Caltech cantilevers are just 400 nm wide by 80 nm thick (M Roukes) 30
2.22 Three simple implementations of resonant sensors: a cantilever beam (a), a clamped-clamped beam (b) and a double-ended tuning fork (c) 33
2.23 A schematic of a resonator subject to different inputs. These inputs could be direct or coupled through a secondary transducer that responds to the measurand. The micromechanical structure itself might take on a number of different forms. 33
2.24 Schematic of a simple zero crossing counting scheme for frequency (or period) measurement. 34
2.25 Diagram showing the problem of phase synchronization for indirect counting. Note that the quantization error is some fraction of the period of the higher frequency reference signal. 35

2.26 Block Diagram of a phase-locked loop. 35
2.27 Schematic representation of noise aliasing in micro-oscillator. A linear resonator would filter out the amplifier low-frequency $\frac{1}{f}$ noise present at the resonator input, but nonlinear filtering element will result in noise aliasing [Kaajakari 2005a]. 46

3.1 A schematic of an electrostatically actuated beam 48
3.2 (a): A schematic of an electrostatically actuated cantilever beam. (b): Flexural-flexural motions of a fixed-free beam. 50
3.3 (a): Long time integration. (b): Phase plane portrait. (c): Periodic solution. (d): Phase plane portrait of the periodic solution. 70
3.4 a): time integration over a period T. (b): Forced nonlinear frequency response. 71
3.5 Consecutive iterations of the shooting method in the phase plane 72
3.6 Algorithm of the shooting method with natural parameter continuation. 73
3.7 Pseudo-arclength Continuation Technique 73

4.1 (a): Studied resonant accelerometer structure. (b): Model of the resonant accelerometer. 83
4.2 (a): Interferometric image showing the topography of the fabricated MEMS accelerometer. (b): SEM image of the micromachined resonant accelerometer (after mass release). 84
4.3 Process flow of a MEMS resonant accelerometer 85
4.4 M&NEMS accelerometer process flow 86
4.5 (a): SEM view of an in-plane M&NEMS accelerometer. (b): A focus on the gauge lets clearly appear the MEMS inertial mass of $2\,\mu m$ thick, and the sub-μm resonator that has a section of $0.25 \times 0.5\,\mu m^2$. 86
4.6 Schema of an electrostatically actuated clamped-clamped microbeam 88
4.7 the first four linear undamped mode shapes of a clamped-clamped microbeam. 91
4.8 Confrontation Shooting/HBM+ANM on a slightly nonlinear behavior (Design $1/V_{dc} = 5V/V_{ac} = 0.5V$). Ω is the normalized drive frequency. W_{max} is the displacement of the beam normalized by the gap g at its middle point $\frac{l}{2}$. 97
4.9 First confrontation Shooting/HBM+ANM on a strongly nonlinear behavior (Design $1/V_{dc} = 8V/V_{ac} = 0.8V$). Ω is the normalized drive frequency and W_{max} is the displacement of the beam normalized by the gap g at its middle point $\frac{l}{2}$. 97
4.10 Second confrontation Shooting/HBM+ANM on a strongly nonlinear behavior (Design $1/V_{dc} = 9V/V_{ac} = 0.9V$). Ω is the normalized drive frequency and W_{max} is the displacement of the beam normalized by the gap g at its middle point $\frac{l}{2}$. 98
4.11 Confrontation HBM+ANM/Analytical model on a slightly nonlinear behavior (Design $1/V_{dc} = 5V/V_{ac} = 0.5V$). Ω is the normalized drive frequency and W_{max} is the displacement of the beam normalized by the gap g at its middle point $\frac{l}{2}$. 99
4.12 First confrontation HBM+ANM/Analytical model on a strongly nonlinear behavior (Design $1/V_{dc} = 8V/V_{ac} = 0.8V$). Ω is the normalized drive frequency and W_{max} is the displacement of the beam normalized by the gap g at its middle point $\frac{l}{2}$. 99
4.13 Second confrontation HBM+ANM/Analytical model on a strongly nonlinear behavior (Design 1 $/V_{dc} = 9V/V_{ac} = 0.9V$). Ω is the normalized drive frequency and W_{max} is the displacement of the beam normalized by the gap g at its middle point $\frac{l}{2}$. 100
4.14 Confrontation HBM+ANM/Analytical model on a strongly nonlinear behavior (Design $2/V_{dc} = 5V/V_{ac} = 0.5V$). Ω is the normalized drive frequency and W_{max} is the displacement of the beam normalized by the gap g at its middle point $\frac{l}{2}$. 100
4.15 Schema of a 2-port resonator. 101

4.16 (a): SEM image of the resonator resonance. (b): SEM image of the resonator at rest. Dimensions: $200\mu m \times 2\mu m \times 4\mu m$. The gap: around $750\,nm$. 104
4.17 Connection layout for the electrical characterization. 105
4.18 Lock-In Schematic / 1f Mode 106
4.19 Lock-In Schematic / 2f Mode 106
4.20 The raw signal given by the lock-in amplifier. 107
4.21 Equivalent electric circuit. 107
4.22 Dimensions of a typical fabricated resonator. 108
4.23 Measured and predicted frequency responses. 109
4.24 Measured and predicted frequency responses. 109

5.1 (a): Dimensions of a typical fabricated resonator. (b): Predicted forced frequency responses. W_{max} is the displacement of the beam normalized by the gap g_d at its middle point $\frac{l}{2}$, σ_r is the axial residual stress on the beam material, A_c is the critical amplitude above which bistability occurs, $\{1,2,3,4,5,6,7,P\}$ are the different bifurcation points, A_p is the pull-in domain initiation amplitude and P is the third bifurcation point characterizing the initiation of the mixed behavior. 113
5.2 Forced frequency responses of the typical resonator described in Figure 4.6. f_a is the dimensionless frequency and W_{max} is the displacement of the beam normalized by the gap g at its middle point $\frac{l}{2}$. A_c is the mechanical critical amplitude and $\{B_1, B_2\}$ are the two bifurcation points of a typical hardening behavior. 114
5.3 Predicted forced frequency responses. W_{max} is the displacement of the beam normalized by the gap g_d at its middle point $\frac{l}{2}$, σ_r is the axial residual stress on the beam material, A_c is the critical amplitude above which bistability occurs, $\{1,2,3,4,5,6,7,P\}$ are the different bifurcation points, A_p is the pull-in domain initiation amplitude and P is the third bifurcation point characterizing the initiation of the mixed behavior. 119
5.4 Analytical and experimental frequency curves showing a mixed behavior and the followed paths respectively in a sweep up frequency $f_0 - P - d_1 - 2 - d_2 - f_1$ and a sweep down frequency $f_1 - 1 - d_3 - 3 - d_4 - f_0$. $\{J_1, J_2, J_3, J_4\}$ are the four jumps cauterizing a typical mixed behavior of MEMS and NEMS resonators, $\{1,2,3,P\}$ are the different bifurcation points and $\{d_1, d_2, d_3, d_4\}$ are the destination points after jumps. The two branches $[3,P]$ and $[1,2]$ in dashed lines are unstable. 121
5.5 Analytical frequency responses showing mixed behaviors, the location of the different bifurcation points and the effect of the DC voltage on the stability of the different branches and the P point location. 122
5.6 Resonance frequency responses showing measured mixed behaviors, the location of the bifurcation points, the effect of the DC voltage on the stability of the different branches and the P point vertical position. HD and SD are respectively the hardening and the softening domains. The point 3 is the highest bifurcation point in the softening domain. 123
5.7 Competition between hardening and softening behaviors for several values of the ratio $\frac{h}{g_d}$ (W_{max} is the normalized displacement at the middle of the beam) 126
5.8 (a): Dependency of the critical amplitude on the quality factor (Here A_c is the peak of W_{max}). (b): Critical quality factor determination for several DC voltage. (c): Dependency of the critical amplitude on the vibrating width. (d): Critical vibrating width determination for several DC voltage 127
5.9 Predicted frequency curves for several DC voltage 128

5.10 (a): Predicted frequency curves (up to pull-in) for several AC and DC polarizations. (b): Dependency of the pull-in amplitude on the AC voltage . . . 128
5.11 (a) Dimensions of a typical fabricated resonator. (b): SEM image of the device. (c): Resonance frequency responses showing mixed behaviors analytically Predicted under combined primary and superharmonic excitations, the location of the different bifurcation points and the effect of the AC voltage on the P point vertical position. P is the mixed behavior domain initiation point and the point 3 is the highest bifurcation point in the softening domain. . . . 133
5.12 Resonance frequency responses showing measured mixed behaviors under primary resonance as well as under simultaneous primary and superharmonic excitations, the location of the different bifurcation points and the effect of the DC voltage on the P point vertical position. . . . 134

6.1 (a): M&NEMS mask showing the structure of a typical designed resonator, the disposition of the pads and their polarization. (b): A SEM image of a designed resonator. . 138
6.2 A working principle schematic of a downmixing setup. . . . 139
6.3 ω configuration of a capacitive downmixing technique. . . . 141
6.4 2ω configuration of a capacitive downmixing technique. . . . 142
6.5 $V_a.V_b$ configuration of a capacitive downmixing technique. . . . 143
6.6 Measured linear resonance peaks of resonator RN_4 using the $V_a.V_b$ capacitive downmixing technique. . . . 144
6.7 SEM images of the resonator RN4. . . . 144
6.8 Measured hardening resonance peaks of resonator RN_4 using the $V_a.V_b$ capacitive downmixing technique. . . . 145
6.9 SEM images of the resonator RM2. . . . 146
6.10 Measured softening resonance peaks of resonator RM_2 using 2ω direct characterization. 147
6.11 Measured critical hardening resonance peak of resonator RM_2 using ω direct characterization. . . . 148
6.12 Measured strange hardening and mixed resonance peaks of resonator RM_2 using ω direct characterization. P is the mixed behavior initiation point and the third bifurcation is the highest bifurcation in the hardening domain. . . . 149
6.13 Measured linear compensated resonance peak of resonator RM_2 using 2ω direct characterization. . . . 150
6.14 Measured mixed and softening resonance peaks of resonator RM_2 using ω direct characterization. The mixed behavior displays a strange mechanical attraction. . . . 151

7.1 Lumped parameter model of a vibratory gyroscope. . . . 156
7.2 Schema of a simple mass resonant gyroscope. . . . 159
7.3 Proof mass and spring designs for a resonant gyroscope. . . . 160
7.4 Lever mechanism. . . . 161
7.5 Model used to predict leverage force magnification. . . . 162
7.6 Schema of a 2-port Mathieu resonator. . . . 163
7.7 Transition curves in a linear autonomous Mathieu equation. S denotes stable quasiperiodic domains and U denotes the unstable domains. . . . 164

7.8 Predicted forced frequency responses displaying a hardening behavior for $\Delta = 0.1$. W_{max} is the displacement of the beam normalized by the gap g at its middle point $\frac{l}{2}$, $\{1, 2\}$ are the bifurcation points. The frequency shift is due to the variation of the external angular rate θ. 168
7.9 Predicted forced frequency responses displaying a softening behavior for $\Delta = 0.1$. W_{max} is the displacement of the beam normalized by the gap g at its middle point $\frac{l}{2}$, $\{1, 2\}$ are the bifurcation points. The frequency shift is due to the variation of the external angular rate θ. 168
7.10 Predicted forced frequency responses displaying a hardening behavior for $\Delta = 0.25$. W_{max} is the displacement of the beam normalized by the gap g at its middle point $\frac{l}{2}$, $\{1, 2, 3, 4\}$ are the bifurcation points. The frequency shift is due to the variation of the external angular rate θ. 169
7.11 Predicted forced frequency responses displaying a softening behavior for $\Delta = 0.25$. W_{max} is the displacement of the beam normalized by the gap g at its middle point $\frac{l}{2}$, $\{1, 2, 3, 4\}$ are the bifurcation points. The frequency shift is due to the variation of the external angular rate θ. 170
7.12 Variation of the Mathieu resonator displacement at its middle point and at resonance when the phase $\beta = \frac{\pi}{2}$ for several values of angular rates θ. 171
7.13 Scale factor variation with respect to the proof mass frequency in the resonator linear regime and inside the dynamic range of the resonant gyroscope. SR and PR are superharmonic and parametric resonances. 172
7.14 Scale factor variation curves with respect to the proof mass frequency for a nonlinear resonator and several rotation rates. 173
7.15 Fully symmetric dual mass resonant gyroscope. 175
7.16 Decoupled z-axis resonant gyroscope. 176
7.17 Functional block diagram schematic of the resonant gyroscope electronics. 177
7.18 M&NEMS mask showing the MEMS ($2\mu m$) and NEMS ($500nm$) levels on a dual-mass resonant gyroscope structure. On the right a zoom on the NEMS protected zone. . . . 178
7.19 Design and specifications of a dual mass resonant gyroscope. 179
7.20 SEM images of a M&NEMS simple mass resonant gyroscope. In (a), the lever mechanism and self-test comb drive actuators to simulate a Coriolis force which can be used also for electrostatic trimming in order to control the frequency matching between the drive and the sense mode. In (b) MEMS level: actuation part (proof mass + flexures). (c): Flexural pivot of the lever mechanism. (d) NEMS level: resonator. (e). Self-test comb drive actuators. 181
7.21 SEM images of a M&NEMS dual mass resonant gyroscope. (a): The dual mass fully symmetric structure (the flexural pivot is located at the center of the gyroscope in order to reduce the sensor bias). The two masses are actuated anti-phase to each others for the cancellation of the common mode acceleration. (b): Zoom on the actuation part (proof mass + flexures). (c): Zoom on the sensing part (the resonator). (d): Comb drive actuators for the proof mass actuation. (e): Zoom on the comb drive actuators showing a $0.5\mu m$ gap between the fingers. 182
7.22 Schematic of a downmixing setup. 183
7.23 Measured hardening nonlinear resonance peaks of resonator RN_5 using 2ω downmixing characterization for several actuation voltages. 184

8.1 Schema of an electrostatically actuated nanocantilever 189

8.2 Analytical forced frequency responses for $Q = 10^4$ and several values of g and V_{ac}. W_{max} is the beam displacement at its free end normalized by the gap g, A_c is the critical amplitude above which bistability occurs, the different bifurcation points are $\{1, 2, 3, 4, 5, 6, 7, P\}$, the P point characterizes the initiation of the mixed behavior. . . 193
8.3 Optical picture of the [NEMS resonator / CMOS readout circuit] system. The scanning electron micrograph zooms the cantilever beam itself and its driving electrode. 196
8.4 Electrical scheme of the monolithic NEMS/CMOS system. 197
8.5 (a): Raw electrical response R_{NA} around the mechanical resonance of a nanocantilever. This is the response as measured by the NA of the full NEMS-CMOS system. (b): Motional admittance frequency response extracted from the data of Figure 8.5(a) according to Equation (8.33) 199
8.6 Analytical and measured motional admittance frequency curves (in air) of cantilever A. W_{max} is the cantilever displacement at the its free end normalized by the gap. 200
8.7 Analytical and measured motional admittance frequency curves (in vacuum) of cantilever B. W_{max} is the cantilever displacement at the its free end normalized by the gap. 201
8.8 Resonant nanocantilever based on piezoresistive detection. 202
8.9 The first four linear undamped mode shapes of the device described in Figure 8.8. . . . 206
8.10 Analytical forced frequency responses of the resonant piezoresistive device presented in Figures 8.8 and 8.11 for a quality factor $Q = 10^4$. W_{max} is the displacement of the beam normalized by the gap g at its free end. 208
8.11 SEM image of the in-plane piezoresistive structure. 210
8.12 In-plane piezoresistive structure process flow 211
8.13 Test-bench for motion detection of piezoresistive resonant NEMS based on an ω down-mixing technique. PS, LPF are power splitter and phase shifter, respectively. 212
8.14 Linear resonance frequency responses measured using an ω down-mixing technique. The effect of the DC voltage on the resonance frequency is presented. 212
8.15 Nonlinear resonance frequency responses measured using an ω down-mixing technique and showing the location of the different bifurcation points $\{B_1$, B_2 and $B_3\}$. W_{max} is the cantilever displacement at the its free end normalized by the gap. 214
8.16 Test-bench for motion detection of piezoresistive resonant NEMS based on a 2ω down-mixing technique. PS, LPF are power splitter and phase shifter, respectively. W_{max} is the cantilever displacement at the its free end normalized by the gap. 215
8.17 Linear resonance frequency responses measured using a 2ω down-mixing technique. The effect of the DC voltage on the resonance frequency is negligeable. W_{max} is the cantilever displacement at its free end normalized by the gap. 216
8.18 Slightly softening resonance frequency response measured using a 2ω down-mixing technique at the optimal DC voltage. The peak is close to the critical amplitude. W_{max} is the cantilever displacement at the its free end normalized by the gap. 216
8.19 Softening frequency response measured using a 2ω down-mixing technique at $V_{dc} = 2V$. The maximal stress on the piezoresistive gauges is reached for the pull-in amplitude. W_{max} is the cantilever displacement at the its free end normalized by the gap. 217
8.20 The next generation of NEMS resonant mass/gas sensor currently in fabrication in the clean rooms of LETI. 218

A.1 Fringing field effect: distribution of the electric potential in a cross section of the resonator in the plane (W, Z) under $5V$ of DC voltage. 225

List of Tables

2.1 Mechanical properties of silicon ($1\,dyn = 10\,\mu N$). 9
2.2 Typical Applications for Micromachined Accelerometers 14
2.3 Typical Applications for Micromachined Gyroscopes 20
2.4 Application for gas sensors and electronic noses. 26
2.5 Incomplete list of solid state gas sensors 27
2.6 Coefficients for the first four eigenfrequencies of cantilevers and clamped-clamped beams. 36

4.1 Geometrical parameters of the accelerometer 87
4.2 Performances computed for the accelerometer presented in Table 4.1 87
4.3 Approximate solutions of $\cos(\lambda_k)\cosh(\lambda_k) = 1$ 91
4.4 Design parameters of investigated resonators. 96

5.1 Lock-in amplifier configurations with respect to the actuation and references frequencies (SIR=simultaneous resonances, PR= primary resonance, SR= superharmonic resonance, PaR=parametric resonance). f_0 is the natural frequency of the resonator. . . . 129

6.1 Physical parameters of MEMS resonators. C_{0a} and C_{0d} are actuation and detection static capacitances. f_0 is the resonance frequency of the first in-plane bending mode. . 138
6.2 Physical parameters of NEMS resonators. C_{0a} and C_{0d} are actuation and detection static capacitances. f_0 is the resonance frequency of the first in-plane bending mode. . 139
6.3 Predicted dynamic behaviors of the designed MEMS and NEMS resonators. 139

7.1 Primary system parameters required to be simultaneously identified and controlled for a modematched gyroscope. In addition to the above, for defects and error compensation due to fabrication tolerances or other asymmetries, additional variables will require to be identified as described in [Shkel 1999]. 158
7.2 Resolution requirement of gyroscope for typical high performance application [Giessibl 2003].180

8.1 Approximate solutions of $det\,\{S\} = 0$ 205

Chapter 1
Introduction

Contents

1.1 Motivations 1
1.2 Overview 2

1.1 Motivations

Micro and nanoelectromechanical (MEMS/NEMS) devices have been the subject of extensive research for a number of years and have generated much excitement as their use in commercial applications has increased. Indeed, MEMS technology has opened up a wide variety of potential applications not only in the inertial measurement sector, but also spanning areas such as communications (filters, relays, oscillators, LC passives, optical switches), biomedicine (point-of-care medical instrumentation, microarrays for DNA detection and high throughput screening of drug targets, immunoassays, in-vitro characterization of molecular interactions), computer peripherals (memory, new I/O interfaces, read-write heads for magnetic disks) and other miscellaneous areas such as in projection displays, gas detection and mass flow detection.

NEMS are the natural successor to MEMS as the size of the devices is scaled down to the submicron domain. This transition is well adapted with the resonant sensing technique for a large panel of applications. One reason of down scaling resonant sensors to the NEMS size is the ability to detect very small physical quantities by increasing their sensitivity [Ekinci 2005]. In particular, NEMS have been proposed for use in ultrasensitive mass detection [Ekinci 2004a, Jensen 2008], radio frequency (RF) signal processing [Nguyen 1999b, Nguyen 1999a], and as a model system for exploring quantum phenomena in macroscopic systems [Cho 2003, LaHaye 2004].

Unfortunately, the nonlinear regime for nanomechanical resonators is easily reachable, so that the useful linear dynamic range of the smallest NEMS devices is severely limited. In fact, many applications we are hoping for in the near future will involve operation in the nonlinear regime, where the response to the stimulus is suppressed and frequency is pulled away from the original resonant frequency.

Actually, it is a challenge to achieve large-amplitude motion of NEMS resonators without deteriorating their frequency stability [Feng 2007]. The relative frequency noise spectral density [Robins 1984] of a NEMS resonator is given by:

$$S_f = \left(\frac{1}{2Q}\right)^2 \frac{S_x}{P_0} \tag{1.1}$$

where S_x is the displacement spectral density and P_0 is the displacement carrier power, ie the RMS drive amplitude of the resonator $\frac{1}{2}A^2$. Remarkably, driving the resonator at large oscillation amplitude leads to better SNR and, thus, simplifies the design of the electronic feedback loop. However, doing so in the nonlinear regime reduces the sensor performances since the frequency instability of a nonlinear resonator is proportional to its oscillation amplitude. Moreover, even when NEMS resonators are used as oscillators in closed-loop, a large part of noise mixing [Roessig 1997a, Kaajakari 2005a] due to nonlinearities drastically reduces their dynamic range and alters their detection limit.

This thesis is about overcoming such limitations between operating in the nonlinear regime and noise mixing issue [Roessig 1997a, Kaajakari 2005a]. Based on the nonlinear dynamics of nanomechanical resonators, the main idea is to provide simple analytical tools for MEMS and NEMS designers in order to optimize resonant sensors designs and enhance their performances for precision measurement applications.

1.2 Overview

Part I entitled "*M&NEMS resonant sensors capabilities and nonlinear dynamics limitations*" includes two chapters:

- Chapter 2 presents a short state of art of M&NEMS sensors focused on inertial and gas/mass sensors. In order to justify our design choices and within the framework of the transition from MEMS to NEMS, the capabilities of the resonant sensing technique are demonstrated compared to other detection techniques. Indeed, a linear study of the resonant sensing is developed to quantify its specifications, its advantages and its limitations when sensors are scaled down to the NEMS size. In particular, the physical nonlinearities are briefly introduced and the noise mixing issue is explained.

- Chapter 3 starts with a presentation of nonlinearity sources in clamped-clamped beams as well as cantilevers electrostatically actuated. The nonlinear equations of motion of these resonators are introduced. Then, several methods for solving nonlinear differential equations analytically as well as numerically are presented. The goal is to define a strategy to solve the nonlinear equations of NEMS resonators under electrostatic actuation.

Part II entitled "*Strategies for performance enhancement of resonant accelerometers*" includes three chapters:

- Chapter 4 describes two resonant accelerometers (MEMS and M&NEMS) as well as their fabrication process. A complete analytical model for the nonlinear dynamics of MEMS and NEMS resonators including all main sources of nonlinearities is presented and validated numerically as well as experimentally.

- Chapter 5 provides several design rules for M&NEMS resonant sensors, based on the analytical model developed in chapter 4. The model ability to enhance the dynamic range of resonant accelerometer and its detection limit by hysteresis suppression is demonstrated. Also, the possibility to obtain a complex nonlinear behavior strongly unstable is shown and a way to retard it by design or by using the dynamic effect of nonlinear resonances is demonstrated.

- Chapter 6 presents the experimental validation of several nonlinear dynamics effects as well as the design rules provided in chapter 5. An original capacitive down-mixing set up is described and its high measurement performances are presented on designed high frequency M&NEMS resonators. The potential of the hysteresis suppression by nonlinearity cancellation is demonstrated under simultaneous resonances.

Part III entitled "*Extension to other resonant sensors: gyroscopes and mass/gas sensors*" is the extension of part II to more complicated sensors such as gyroscopes and gass/mass sensors. It includes two chapters:

- Chapter 7 deals with the nonlinear dynamics of resonant M&NEMS gyroscopes. A complete analytical model is developed NEMS Mathieu-Duffing resonators. The model concerns only periodic motions and permits the identification of some rules of resonant angular rate sensors. The partial validation of the model was achieved thanks to the design and fabrication of M&NEMS gyroscope.

- Chapter 8 concerns the nonlinear dynamics of NEMS cantilevers. The nonlinear problem is solved analytically by including main sources of nonlinearity. A first experimental validation is demonstrated on nanocantilevers electrostatically actuated in plane, fabricated by nanostencil lithography and electrically characterized at CNM-IMB in Barcelona. Then, the model is adapted for a NEMS piezoresistive mass sensor. Several design rules are provided and experimentally validated demonstrating a large potential of performance enhancement for resonant gass/mass nanosensors.

Part I

M&NEMS resonant sensors capabilities and nonlinear dynamics limitations

Chapter 2

MEMS and NEMS sensors

Contents

2.1 Introduction **7**
2.1.1 What is MEMS? 8
2.1.2 Materials for MEMS manufacturing 8
2.1.3 MEMS basic processes 9
2.1.4 MEMS applications and market 10
2.1.5 From MEMS to NEMS 10
2.2 Inertial sensors **11**
2.2.1 Introduction 11
2.2.2 Accelerometers 13
2.2.3 Gyroscopes 19
2.2.4 Conclusion 24
2.3 Gas and Mass Sensors **25**
2.3.1 Gas Sensors 25
2.3.2 Mass Sensors 30
2.4 Resonant sensors **32**
2.4.1 Frequency measurement 33
2.4.2 Mechanical analysis 35
2.4.3 Quality factor 37
2.4.4 Noise analysis 40
2.4.5 Resolution 41
2.4.6 Linearity and Dynamic Range 43
2.4.7 Physical Nonlinearities 44
2.4.8 Nonlinearities and noise mixing 45
2.5 Summary **45**

2.1 Introduction

MEMS/NEMS (Micro/Nano Electro-Mechanical Systems) is a rapidly growing field building upon the existing silicon processing infrastructure to create micron/nano-scale machines. These devices are widely used in aerospace, automotive, biotechnology, instrumentation, robotics, manufacturing and other applications and our gateway into coming nanotechnology devices and systems. Unlike conventional integrated circuits, these devices can have many functions, including sensing, communication, and actuation. Just like microelectronics, MEMS/NEMS technology will permeate our everyday lives in the coming decades.

2.1.1 What is MEMS?

Micro-Electro-Mechanical Systems (MEMS) is the integration of a number of microcomponents on a single chip which allows the microsystem to both sense and control the environment (see Figure 2.1). The components typically include microelectronic integrated circuits (the "brains"), sensors (the "senses" and "nervous system"), and actuators (the "hands" and "arms").

Figure 2.1: Micro-sized Multiple gear speed reduction.

2.1.2 Materials for MEMS manufacturing

2.1.2.1 Silicon

Silicon is the material used to create most integrated circuits used in consumer electronics in the modern world. The economies of scale, ready availability of cheap high-quality materials and ability to incorporate electronic functionality make silicon attractive for a wide variety of MEMS applications. Silicon also has significant advantages engendered through its material properties. In single crystal form, silicon is an almost perfect Hookean material, meaning that when it is flexed there is virtually no hysteresis and hence almost no energy dissipation. Its mechanical properties (Table 2.1) are anisotropic and hence are dependent on the orientation to the crystal axis. As well as making for highly repeatable motion, this also makes silicon very reliable as it suffers very little fatigue and can have service lifetimes in the range of billions to trillions of cycles without breaking. Silicon itself exists in three forms: crystalline, amorphous, and polycrystalline (polysilicon). High purity, crystalline silicon substrates are readily available as circular wafers with typical diameters of $100\,mm$, $150\,mm$, $200\,mm$, or $300\,mm$ in a variety of thicknesses. The basic techniques for producing all silicon based MEMS devices are deposition of material layers, patterning of these layers by photolithography and then etching to produce the required shapes.

2.1.2.2 Polymers

Even though the electronics industry provides an economy of scale for the silicon industry, crystalline silicon is still a complex and relatively expensive material to produce. Polymers on the other hand can be produced in huge volumes, with a great variety of material characteristics. MEMS devices can

PROPERTY	VALUE
Bulk modulus of elasticity	$9.8 \cdot 10^{11}$ dyn/cm^2
Density (ρ)	2.329 g/cm^3
Hardness	7 (on the Mohs scale)
Surface microhardness (using Knoop's pyramid test)	1150 kg/mm^2
Elastic constants	$C_{11} = 16.60 \cdot 10^{11}$ dyn/cm^2 $C_{12} = 6.40 \cdot 10^{11}$ dyn/cm^2 $C_{44} = 7.96 \cdot 10^{11}$ dyn/cm^2
Young's Modulus (E)	<100> 129.5 GPa <110> 168.0 GPa <111> 186.5 GPa
Shear Modulus	64.1 GPa
Poisson's Ratio	0.22 to 0.28

Table 2.1: Mechanical properties of silicon ($1\,dyn = 10\,\mu N$).

be made from polymers by processes such as injection molding, embossing or stereolithography and are especially well suited to microfluidic applications such as disposable blood testing cartridges.

2.1.2.3 Metals

Metals can also be used to create MEMS elements. While metals do not have some of the advantages displayed by silicon in terms of mechanical properties, when used within their limitations, metals can exhibit very high degrees of reliability. Commonly used metals include gold, nickel, aluminium, chromium, titanium, tungsten, platinum, and silver.

2.1.3 MEMS basic processes

MEMS are fabricated in one of two ways: either through surface micromachining (see Figure 2.2), in which successive layers of material are deposited on a surface and then etched to shape, or through bulk micromachining, where the substrate itself is etched to produce a final product. Surface micromachining is most common because it builds on the advances of integrated circuits. Unique to MEMS, deposition techniques sometimes leave behind "sacrificial layers", layers of material meant to be dissolved and washed away at the end of the fabrication process, leaving a remaining structure. This process allows a MEMS device to have complex structure in 3 dimensions. Various microscale gears, pumps, sensors, pipes, and actuators have been fabricated and some of them are already integrated into everyday commercial products.

Globally, there are three principal steps in surface micromachining:

- Deposition processes: thin films of material are placed on a substrate (Chemical Vapor Deposition (CVD), Electrodeposition, Epitaxy, Thermal oxidation, Physical Vapor Deposition (PVD), Casting).
- Lithography: a patterned mask is applied on top of the films.
- Etching processes: the films are etched selectively to provide relief following the mask outlines (Wet etching, dry etching).

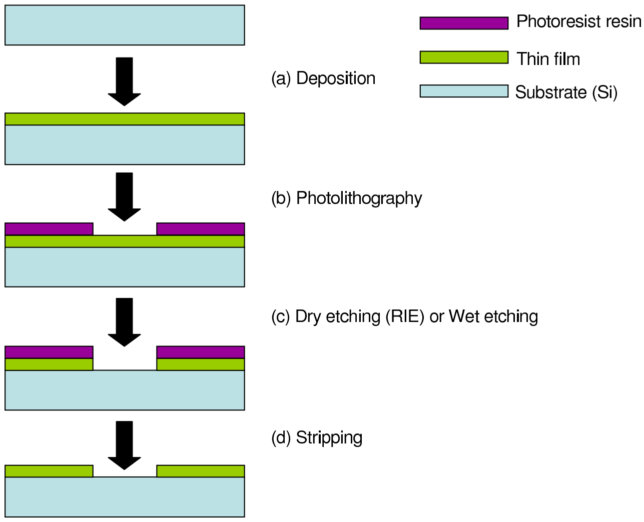

Figure 2.2: The principal steps in surface micromachining.

2.1.4 MEMS applications and market

From one viewpoint MEMS application is categorized by type of use (sensor, actuator and structure). Examples of modern-day MEMS use include inkjet printers, accelerometers in automobiles, pressure sensors, high-precision optics, microfluidics, monitoring of individual neurons, control systems, and microscopy. There is currently no such thing as a productive microscale machine system on the order of productive macroscale assembly lines, but it seems that the invention of such a device is only a matter of time. The prospect of manufacturing with MEMS is exciting because arrays of such systems working in tangent could be substantially more productive than macroscale systems occupying the same volume and consuming the same amount of energy. One prominent limitation, however, would be that macroscale products built by microscale machine systems would need to be composed primarily of prefabricated microscale building blocks.

The MEMS technology is growing very rapidly as shown in Figure 2.3. While estimates for MEMS markets vary considerably, they all show significant present and future growth, reaching total volumes in the many billions of dollars by 2012. The expected growth stems from technical innovations and acceptance of the technology by an increasing number of end users and customers and especially after taking into the consideration that MEMS technology emphasis in the next few years on the "systems" not only the components and subsystems.

2.1.5 From MEMS to NEMS

NanoElectroMechanical Systems (NEMS) have critical structural elements at or below 100 nm. This distinguishes them from MicroElectroMechancial Systems (MEMS), where the critical structural elements are on the micrometer length scale. Compared to MEMS, NEMS combine smaller mass with higher surface area to volume ratio and are therefore most interesting for applications regarding high frequency resonators and ultrasensitive sensors. Because of the scale on which they can function, NEMS are expected to significantly impact many areas of technology and science and eventually replace MEMS.

As noted by Richard Feynman in his famous talk in the 60s, There's Plenty of Room at the Bottom, there are a lot of potential applications of machines at smaller and smaller sizes; by building

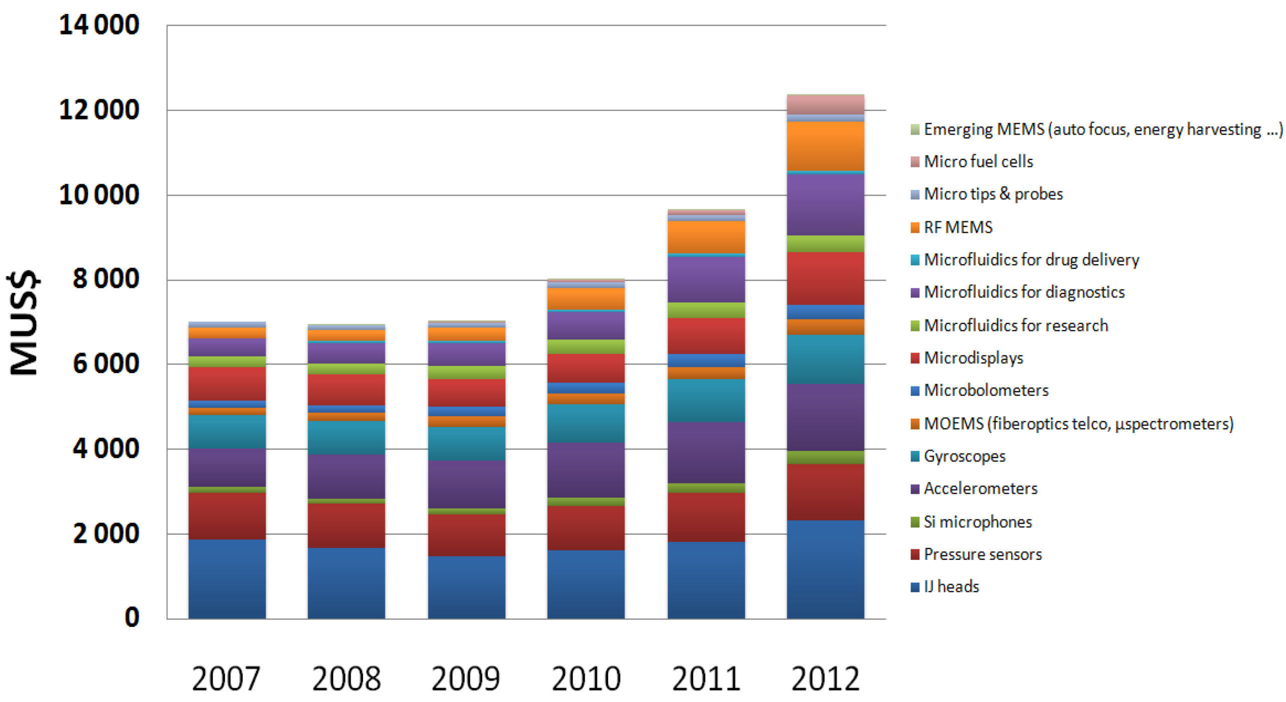

Figure 2.3: Market overview and forecast for MEMS by device type (Source: Yole Développement-2008-).

and controlling devices at smaller scales, all technology benefits. Among the expected benefits include greater efficiencies and reduced size, decreased power consumption and lower costs of production in electromechanical systems.

In 2000, the first Very Large Scale Integration (VLSI) NEMS device was demonstrated by researchers from IBM [Despont 2000]. Its premise was an array of AFM tips which can heat/sense a deformable substrate in order to function as a memory device. In 2007, the International Technical Roadmap for Semiconductors (ITRS) contains NEMS Memory as a new entry for the Emerging Research Devices section.

In this chapter, an overview of MEMS inertial sensors and NEMS gas and mass sensors is presented. These applications are well adapted for resonant sensing technique which offers the opportunity to combine NEMS and MEMS in a single structure for inertial sensors. The area of this thesis is resonant MEMS and NEMS sensors and the motivation of this choice comes from the recent tendency of scaling sensors down to NEMS which brings the classical displacement sensing techniques to their limits.

2.2 Inertial sensors

2.2.1 Introduction

A sensor is a device, which responds to an input quantity by generating a functionally related output usually in the form of an electrical or optical signal. Motion sensing devices are not new. They have been used since the 1950s in the aerospace and defense fields to perform navigation functions. MEMS versions of accelerometers and gyroscopes have been developed more recently, bringing the key advantages of cost and size reduction. While not as accurate as the devices used for military applications, MEMS-type accelerometers and gyroscopes are well adapted to be integrated into cars and many consumer electronic products. Most commonly, MEMS accelerometers have been used extensively since the 1990s in light vehicle airbags as crash sensors. Since then, many other devices have benefited from the use of motion sensors. The latest and most striking examples are their use in Nintendo Wii game controllers and Apple iPhone and iPod devices.

MEMS inertial sensors, consisting of accelerometers and gyroscopes, are one of the most important types of silicon-based sensors and represent a significant business: 859 million MEMS accelerometers (Figure 2.4) and gyroscopes were produced worldwide in 2008, corresponding to a 1.85 B$ market. The majority of this market still comes from automotive applications; however, consumer applications should overtake automotive by 2012. This is not only due to the current downturn that is impacting the automotive world, but massive use of these sensors is likely to remain limited to established applications such as airbag, brake pressure (ESC) and tire-pressure monitoring systems (TPMS).

Figure 2.4: Three axis linear accelerometer from ST

Inertial sensors have seen a steady improvement in their performance and their fabrication technology, and today, microaccelerometers are among the highest volume MEMS sensors for the automotive. While the performance of gyroscopes has improved by a factor of 10 every two years, their costs have not dropped as was originally predicted. The initial drive for lower cost, greater functionality, higher levels of integration, and higher volume had slowed down during the optical bubble, when the sensor market was over taken with high potential returns promised by the telecom market. Although the telecom boom had slowed the wide spread development in gyroscopes, it poured billions of dollars into development of next generation MEMS technologies, equipment, modeling tools, foundries, and micromachine experts.

The medical and industrial fields increasingly use inertial sensors, but in a more fragmented way. Seismic detection, the major application for motion sensors, is suffering greatly because of low oil prices. However, plenty of other applications will benefit from MEMS inertial sensors in coming years. Defense and aerospace applications are likely to remain a minor market for MEMS sensors because of the low volumes involved. But the increasing performance of MEMS accelerometers and gyroscopes is leading to a revolution in selected applications such as rockets, munitions and soldier equipment.

There are a large number of relevant operational parameters for a micromechanical inertial sensor, especially a gyroscope. We will describe a partial set of the more important parameters. A complete list of gyroscope parameters can be found in the published IEEE standard for inertial sensor terminology [IEE 2001]. Some of the key parameters for consideration in inertial sensor design are listed overleaf:

- Sensitivity (Scale Factor): The sensitivity of the device is the constant of proportionality relating the input and output, assuming a linear response. In general terms, it is the sensitivity of the output to the input.

- Noise floor/resolution: Random energy dissipation in the sensor results in noise. This limits the minimum detectable signal of the sensor.

- Sensitivity to extrinsic parameters: $\frac{\partial O}{\partial X}$ where O is the output and X is the variable of interest. When X is the input this is usually the same as the scale factor for a linear relationship between input and output. However, what is also of importance is the gyroscope sensitivity to parameters other than angular motion. These parameters include temperature, pressure and external accelerations (including shock and environmental vibrations). The sensitivity of the sensor to these other variables should be low.

- Bias stability: This variable provides a measure of the drift of the output offset value over time. The drift can be measured in several ways (one method is to measure the root allan variance of the output over fixed time intervals).

- Bandwidth: The range of input frequencies for which the output-input relation is preserved. Traditionally, a $3 - dB$ variation in the scale is tolerated at the edge of the bandwidth.

- Response time: The time the output takes to settle to within a certain range of the expected value for a step function input.

- Startup time: The time between turning on the power supply to the sensor to the time when a reliable output can be obtained from the device.

- Linearity: For an ideally linear relation between output and input, this parameter measures the extent of deviation from the norm.

- Dynamic Range: The range of input values over which the output is detectable and the input-output relation is preserved.

- Maximum input rate: The maximum input rate that can be detected under operational conditions preserving linearity and bandwidth considerations for the device.

- Shock limit: The maximum shock that the device can tolerate while operating.

2.2.2 Accelerometers

The application of micro-accelerometers (Table 2.2) covers a wide range of fields due to their small size, high performance and low cost. This clearly confirms its second largest sensor market share after pressure sensors. Microaccelerometers are commonly used tools in automotive, biomedical, industrial, military and numerous consumer applications since it is crucial for safety, measurement and control. Many types of micromachined accelerometers have been developed and are reported in the literature; however, the vast majority has in common that their mechanical sensing element consists of a proof mass that is attached by a mechanical suspension system to a reference frame, as shown in Figure 2.5. Any inertial force due to acceleration will deflect the proof mass according to Newtons second law. Ideally, such a system can be described mathematically in the Laplace domain by

$$\frac{x(s)}{a(s)} = \frac{1}{s^2 + \frac{b}{m}s + \frac{k}{m}} = \frac{1}{s^2 + \frac{\omega_n}{Q}s + \omega_n^2} \tag{2.1}$$

Application	Bandwidth	Resolution	Dynamic Range
Automotive			
Airbag release	0-0.5kHz	$< 500mG$	$\pm 100G$
Stability and active	0-0.5kHz	$< 10mG$	$\pm 2G$
control systems	dc-1kHz	$< 10mG$	100G
Active suspension			
Inertial navigation	0-100Hz	$<5\mu G$	$\pm 1G$
Seismic activity			
Shipping of fragile goods	0-1kHz	$< 100mG$	$\pm 1kG$
Space microgravity	0-10Hz	$<1\mu G$	$\pm 1G$
measurements			
Medical applications	0-100Hz	$<10mG$	$\pm 100G$
Vibration monitoring	1-100kHz	$<100mG$	$\pm 10kG$
Virtual reality	0-100Hz	$<1mG$	$\pm 10G$
Smart ammunition	10Hz to 100kHz	1G	$\pm 100kG$

Table 2.2: Typical Applications for Micromachined Accelerometers

where x is the displacement of the proof mass from its rest position with respect to a reference frame, a is the acceleration to be measured, b is the damping coefficient, m is the mass of the proof mass, k is the mechanical spring constant of the suspension system, s is the Laplace operator, $Q = \frac{\omega_n m}{b}$ is the quality factor and $\omega_n = \sqrt{\frac{k}{m}}$ is the natural resonant frequency of the undamped system. As an accelerometer can typically be used at a frequency below its resonant frequency, an important design trade-off becomes apparent here since sensitivity and resonant frequency increase and decrease with m/k, respectively. This trade-off can be partly overcome by including the sensing element in a closed loop, force-feedback control system. A common factor for all micromachined accelerometers is that the displacement of the proof mass has to be measured by a position-measuring interface circuit, and it is then converted into an electrical signal. Many types of sensing mechanisms have been reported, such as capacitive, piezoresistive, piezoelectric, optical, tunneling current, and resonant. The characteristic and performance of any accelerometer is greatly influenced by the position measurement interface, and the main requirements are low noise, high linearity, good dynamic response, and low power consumption. Ideally, the interface circuit should be represented by an ideal gain block, relating the displacement of the proof mass to an electrical signal (see Figure 2.6).

2.2.2.1 Capacitive Accelerometers

The physical structures of capacitive sensors are relatively simple. The technique nevertheless provides a precise way of sensing the movement of an object. Essentially the devices comprise a set of one (or more) fixed electrode and one (or more) moving electrode. They are generally characterized by the inherent nonlinearity and temperature cross-sensitivity, but the ability to integrate signal conditioning circuitry close to the sensor allows highly sensitive, compensated devices to be produced. Figure 2.7 illustrates three configurations for a simple parallel plate capacitor structure. Measuring the displacement of the proof mass capacitively has some inherent advantages. It provides a large output signal, good steady-state response, and better sensitivity due to low noise performance. The main drawback is that capacitive sensors are susceptible to electromagnetic fields from their surroundings; hence, they have to be shielded carefully. It is also unavoidable that parasitic capacitances at the

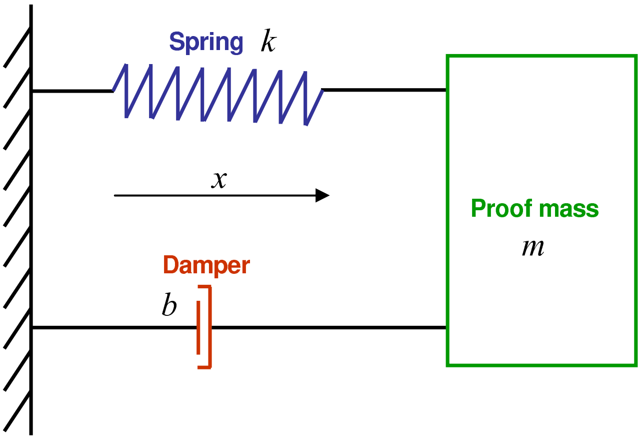

Figure 2.5: Lumped parameter model of an accelerometer consisting of a proof (or seismic) mass, a spring, and a damping element.

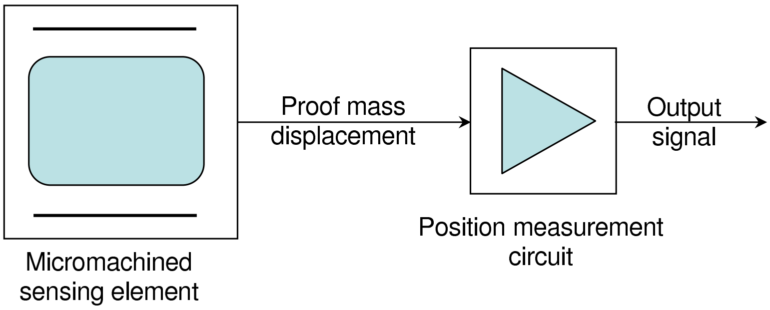

Figure 2.6: Open loop accelerometer.

input to the interface amplifiers will degrade the signal. Usually, a differential change in capacitance is detected. As the proof mass moves away from an electrode, the capacitance decreases, and as it moves towards the electrodes, the capacitance increases. Neglecting the fringing field effects, the change in capacitance is given by

$$\Delta C = \varepsilon_0 \varepsilon_r A \left(\frac{1}{d_0 - x} - \frac{1}{d_0 + x} \right) = 2\varepsilon_0 \varepsilon_r A \frac{x}{d_0^2} + O(x^2) \tag{2.2}$$

where ε_0 is the permittivity of free space, ε_r is the relative permittivity of the separation material. A and d_0 are respectively, the area of overlap and the gap between the proof mass and the electrode.

ΔC is proportional to the deflection caused by the input acceleration only if the assumption of small deflections is made ($x << d_0$). For precision accelerometers this assumption may be not justifiable, and hence, closed loop control can be used to keep the proof mass deflections small.

One of the highest performance capacitive accelerometers created was developed by Yazdi and Najafi [Yazdi 2000]. It uses a combination of bulk and surface micromachining that allows the fabrication of the sensing element on a single wafer, thereby avoiding the need to bond several wafers together, but nevertheless having the advantage of a wafer-thick proof mass. The latter is compliant to acceleration in the z-direction and moves between electrodes fabricated from polysilicon, which was deposited on a thin sacrificial silicon dioxide layer on the top and bottom wafer surface. Low cross-axis sensitivity of the sensor was achieved by a fully symmetrical suspension system consisting

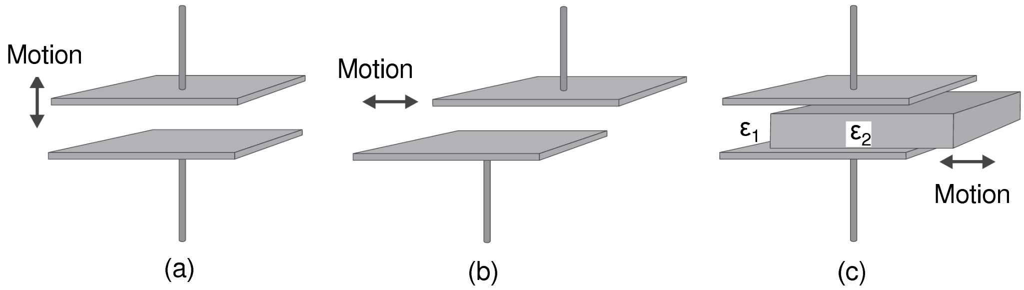

Figure 2.7: Examples of simple capacitance displacement sensors.

of eight beams, two on each side of the proof mass. The sensing element is shown in Figure 2.8. This results in a high-precision accelerometer with a measured sensitivity of $219.4\,pF/G$ for a proof mass area of $2 \times 1\,mm$ and $4 \times 1\,mm$, respectively. The reported noise floor was around $0.2\,\mu G/\sqrt{Hz}$. Parasitic capacitance between the structural layer to the substrate can be around $50\,pF$ for a typical

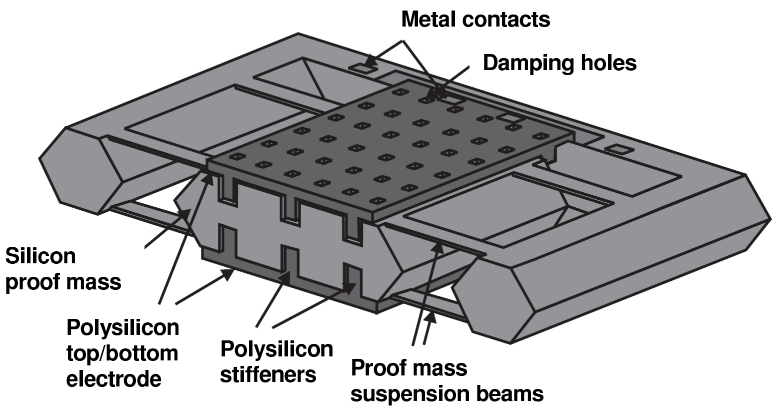

Figure 2.8: High-performance capacitive accelerometer using a combination of surface and bulk-micromachining techniques [Yazdi 2000].

capacitive accelerometer. Interconnection between microstructures and electronics is implemented by the polysilicon layer or by diffusion with large resistance and parasitic capacitance to substrate, which result in large wiring noise and signal attenuation. Extra micromachining process steps usually involve performance and yield compromises, and are in compatible with standard IC technology.

2.2.2.2 Piezoresistive Accelerometers

The piezoresistive effect describes the changing electrical resistance of a material due to applied mechanical stress. The piezoresistive effect differs from the piezoelectric effect. In contrast to the piezoelectric effect, the piezoresistive effect only causes a change in resistance; it does not produce an electric potential. The change of resistance of metal devices due to an applied mechanical load was first discovered in 1856 by Lord Kelvin. With single crystal silicon becoming the material of choice for the design of analog and digital circuits, the large piezoresistive effect in silicon and germanium was first discovered in 1954 (Smith 1954). The sensitivity of piezoresistive devices is characterized by the gauge factor:

$$K = \frac{\frac{dR}{R}}{\varepsilon_L} \tag{2.3}$$

where dR is the change in resistance due to deformation ε_L, R is the undeformed resistance and is the strain.

A silicon piezoresistor (see Figure 2.9) is generally placed at the edge of the rim and proof mass where stress variation is maximum. This causes change in the resistivity as the beam changes its mechanical state. The first micromachined, batch-fabricated accelerometer was reported by Roylance

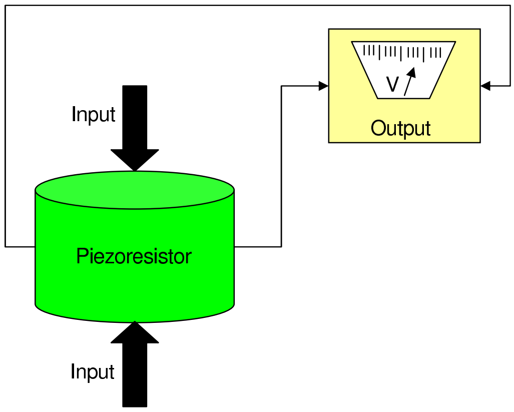

Figure 2.9: A pieozoresistor generates a voltage when deformed (the output voltage is proportional to the resistivity change).

and Angell [Roylance 1979] at Stanford University in 1979. Examples of early devices are described in [Barth 1988, Allen 1989a]. They typically consist of a multiwafer assembly with the central wafer comprising the bulk-micromachined proof mass and suspension system and either silicon or Pyrex glass wafers on top and bottom to provide over-range protection and near critical damping due to squeeze film effects. The disadvantages of piezoresistive signal pick-off can be partially overcome by integrating the read-out electronics on the same chip. A good example is the accelerometer presented by Seidel et al. [Seidel 1995]. The sensing element consists of a bulkmicromachined proof mass, which is attached to the substrate by three cantilever beams. On the main cantilever four piezoresistors are implanted and form a full Wheatstone bridge. A cross-section of the sensor is shown in Figure 2.10. The sensing element is encapsulated by top and bottom wafers, which are bonded to the middle

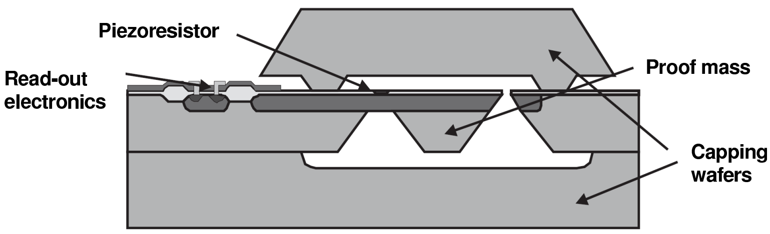

Figure 2.10: Cross-sectional view of the piezoresistive accelerometer [Seidel 1995].

layer at wafer level. The reported performance of this device was a full-scale measurement range up to $\pm 20\,G$, a resonance frequency of 1.2 KHz, a sensitivity of $0.4\,mV/V/G$ with a sensitivity drift of $1.8\,{}^{0}/_{00}/K$ and an offset drift of $8\,/V/K$.

The structure, fabrication process and circuitry of these devices are simple. However, a serious drawback, is that the output signal tends to have a strong temperature dependency because the piezoresistors inherently produce thermal noise and the output signal is relatively small [Allen 1989b].

2.2.2.3 Tunneling Accelerometers

The tunneling current from a sharp tip to an electrode is an exponential function of the tip-electrode distance and hence can be used for position measurement of a proof mass. The tunneling current is given by

$$I = I_0 \exp\left(-\beta\sqrt{\phi z}\right) \tag{2.4}$$

where I_0 is a scaling current dependent on material and tip shape (a typical value is $1.410^{-6}\,A$), β is a conversion factor with a typical value of $10.25\,eV^{-\frac{1}{2}}/nm$, ϕ is the tunnel barrier height with a typical value of $0.5\,eV$, and z is the tip/electrode distance. The distance between the tunneling tip and the electrode has to be precisely controlled; hence, these sensors have to be used in closed loop operation. Electrostatic force-feedback is employed for the majority of research devices and this keeps the separation distance approximately constant. The acceleration can then be inferred from the voltage required to produce the necessary electrostatic force.

Micromachined tunneling accelerometers (Figure 2.11) were first introduced by researchers with the Jet Propulsion Laboratory (JPL), Pasadena, CA [Kenny 1992, Rockstad 1996]. One of their devices provided a bandwidth of several kilohertz, with a noise floor of less than $10\,g/Hz$ in the 10200 Hz frequency range [Rockstad 1996]. However, a high supply voltage (tens to hundreds of volts) is required for these devices, thus limiting their application. Theoretically, this is the most sensitive

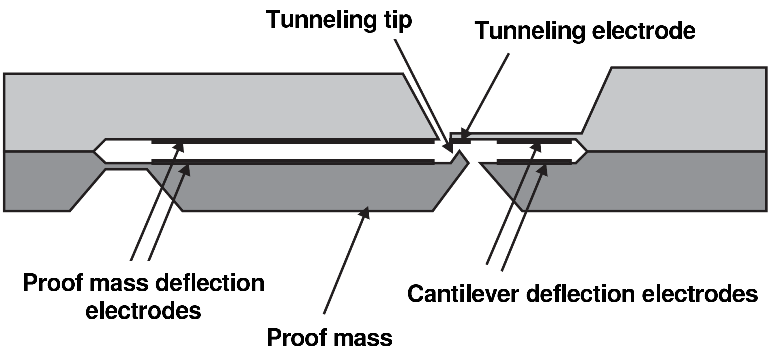

Figure 2.11: Tunneling current accelerometer [Rockstad 1996].

detection mechanism. Several other accelerometers based on this principle have been reported, but no commercial device has been developed. One unresolved problem is the long-term drift of the tunneling current as material from the tip is removed by the high electric fields.

2.2.2.4 Resonant Accelerometers

The main advantage of resonant sensors is their direct digital output. As shown in Figure 2.12, silicon resonant accelerometers are generally based on transferring the proof-mass inertial force to axial force on the resonant beams and hence shifting their frequency. To cancel device thermal mismatches and nonlinearities, a differential matched resonator configuration can be used. A fully integrated, surface-micromachined resonant accelerometer was reported by Roessig et al. [Roessig 1997b]. The device consists of a proof mass attached to two double-ended tuning fork (DETF) resonators via a force amplifier such as a mechanical lever. Resonance is sustained by embedding each DETF in the feedback loop of an oscillator circuit. An external acceleration that is applied to the proof mass along the sensitive axis of the device, results in a force communicated axially onto the double-ended tuning fork sensors. The applied axial force results in a shift in the resonant frequency of the DETF resonant sensors due to a change in the nominal stored potential energy of the system. This effect is identical to that of tuning a guitar string to resonate at different frequencies by varying the tension in the string. The output of the device is the difference in the output frequency of the two oscillators. The nominal frequency of the double-ended tuning fork resonator was 68 KHz, and the scale factor of the sensor was measured to be 45 Hz/G. The resonator beams had comb drives attached to sense their motion via a capacitance change and to excite them into resonance using electrostatic forces. This is achieved by incorporating them into an oscillation loop. The coupling of the mechanical force caused by motion of the proof mass into the resonators was achieved by a novel mechanical leverage system that amplifies the force. A range of other resonant devices has been reported in the literature [Roszhart 1995, Burrer 1995].

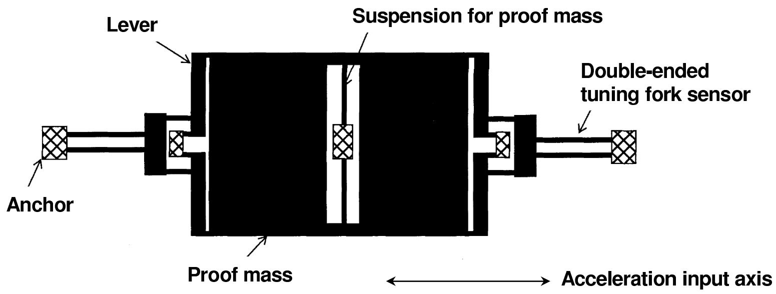

Figure 2.12: Schematic of a resonant accelerometer [Roessig 1997b].

2.2.2.5 Other Accelerometers

In addition to the above mentioned accelerometers types, there are other devices based on optical [Uttamchandani 1992], electromagnetic [Abbaspour-Sani 1994], thermal [Leung 1998] and piezoelectric [DeVoe 1997] principles. The reason behind is to use advantages of both micro-machined and physical principle like optics which are immune to noise and linear.

2.2.3 Gyroscopes

Micromachined gyroscopes (Figure 2.13a) for measuring rate or angle of rotation have also attracted a lot of attention during the past few years for several applications. They can be used either as a low-cost miniature companion with micromachined accelerometers to provide heading information for inertial navigation purposes or in other areas (Table 2.3), including automotive applications for ride stabilization and rollover detection; some consumer electronic applications, such as video-camera stabilization, virtual reality, and inertial mouse for computers; robotics applications; and a wide range of military applications.

Micromachined gyroscopes typically rely on the coupling of an excited vibration mode into a secondary mode due to the Coriolis acceleration (see Figure 2.13b). The magnitude of oscillation in the sense mode provides a measure of the input angular velocity. These devices require no rotational parts which would need bearings and hence can be relatively easily miniaturized. Gyroscopes are much

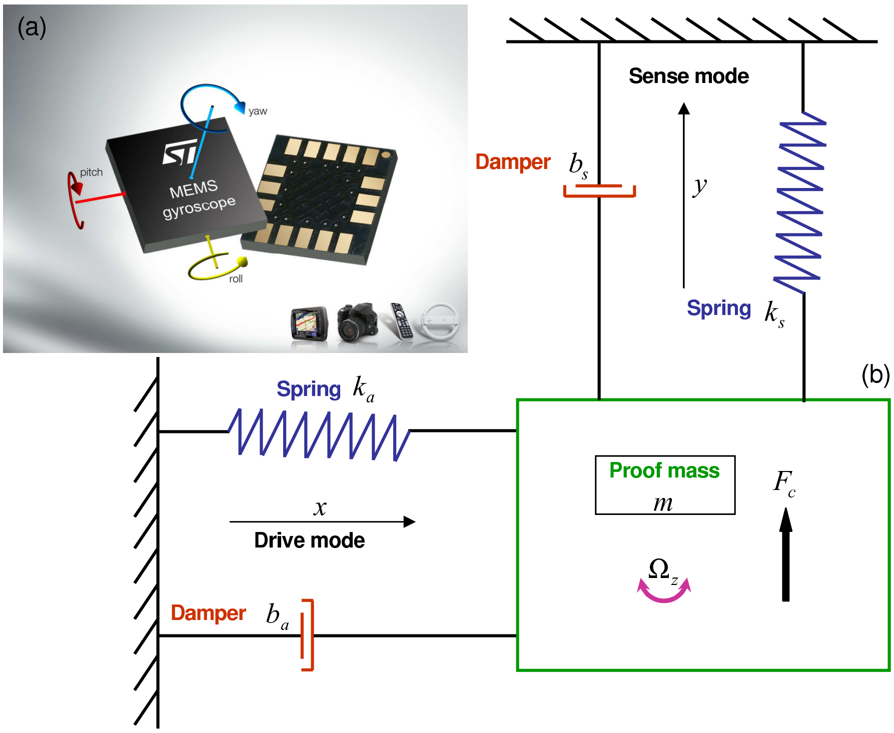

Figure 2.13: A complete family of single-axis (yaw) and two-axis (pitch-and-roll, pitch-and-yaw) MEMS gyroscope from ST. (b): Lumped parameter model of a vibratory gyroscope.

Application	Bandwidth	Resolution	Dynamic Range
Automotive			
Rollover protection	0-100Hz	$< 1°/sec$	$\pm 100°/sec$
Stability and active control systems	0-100Hz	$< 0.1°/sec$	$\pm 100°/sec$
Inertial navigation	0-10Hz	$<< 10^{4}°/sec$	$\pm 10°/sec$
Platform stabilization (video camera))	0-100Hz	$\pm 100°/sec$	
Virtual reality	dc-10Hz	$<< 0.1°/sec$	$\pm 100°/sec$
Pointing devices for computer control	dc–10Hz	$< 0.1°/sec$	$\pm 100°/sec$
Robotics	dc–100Hz	$< 0.01°/sec$	$\pm 10°/sec$

Table 2.3: Typical Applications for Micromachined Gyroscopes

more challenging devices and most of them are still under development. Currently, it is not clear which approach will be dominant for future commercial devices. One difficulty is that the sensing element must be able to move and hence be controlled in two degrees of freedom, one for the excited or driven mode, the other for the sense mode. One way of describing a micromachined gyroscope is that it acts as a resonator in the drive direction and as an accelerometer in the sense direction. Since the Coriolis acceleration is proportional to the velocity of the driven mode, it is desirable to make the amplitude and the frequency of the drive oscillation as large as possible. At the same time it has to be ensured that the frequency and amplitude remain constant since even very small variations can swamp the Coriolis acceleration. For amplitude control typically an automatic gain control loop is used, frequency stability can be ensured by a phase locked loop.

As already mentioned the coupling from the sense to the drive mode by the Coriolis force is very weak, therefore often mechanical amplification is employed. Both the drive and sense mode can be described by a second order transfer function (mass-damper-spring system). The dominating damping mechanism is due to the proof mass moving in air. If the proof mass is operated in vacuum, systems with very high Q (several 10000) can be realized. If the resonant frequencies of the drive and sense mode are matched, the coupling is effectively amplified by Q. The difficulty is to design the two resonance frequencies to match precisely (better than 1 Hz) over the operating temperature range and other environmental influences. The tolerances in the mechanical fabrication process are far too high hence active tuning is normally used. This relies on applying electrostatic forces on the proof mass which effectively act as a negative spring constant, hence can be used to lower the overall spring constant of either the drive or sense mode. Even with this active tuning method it is still challenging to maintain precise tuning over the operating range of a gyroscope and considerable research effort is made to solve this problem. Another problem is so-called quadrature error which originates from an unavoidable misalignment of the drive mode from the ideal direction. This produces a signal in the sense mode which can be orders of magnitudes larger than the Coriolis signal. It can be shown that these two signals are usually 90° out of phase and consequently can be distinguished by further signal processing. This assumes that all building blocks operate in linear region, however, even for small misalignments quadrature error can cause the sense electronics to saturate. Consequently, it is desirable to suppress quadrature error at its origin which can be achieved by applying electrostatic forces to the proof mass [Clark 1996].

2.2.3.1 Single-Axis Gyroscopes

Choice of topology is a critical step in gyroscope design. Vibrating gyroscopes may be categorized into single or dual spring mass or gimbaled mass. A single mass-spring system shares the same flexure for both the drive and sense modes, and thus suppressing mode coupling is a design issue. Dual mass structures can be arranged to form tuning fork resonators to reject translational vibration. Single-gimbaled structures have an advantage of decoupling the drive and sense modes, but may have poor linear acceleration rejection and temperature performance. The dual-gimbaled structure can be employed in order to improve the linear acceleration rejection and stability at the price of increased structural complexity.

Translational Vibration:

Most vibrating microgyroscopes use translational actuation. HSG-IMIT reported in 2002 a gyroscope with excellent structural decoupling of drive and sense modes. The gyroscope [Geiger 2002] is shown in Figure 2.14. It was fabricated in the standard Bosch fabrication process. The device demonstrated a resolution of $0.005°/s$ in a bandwidth of 50 Hz, a scale-factor of $10\,mV/°/s$ in a dynamic range of $\pm 100\,°/s$ and a nonlinearity $< 0.1\%$.

Rotational Vibration:

Rotational vibration around the z-axis makes it possible to detect lateral-axis angular rate with out-of-plane Coriolis acceleration sensing. Geiger et al. [Geiger 1999, Geiger 2000] presented a rotational surface-micromachined gyroscope manufactured using the Bosch foundry process, which features a polycrystalline structural layer with a thickness of $10.3\,\mu m$. This relatively large thickness for a surface-micromachined process is achieved by epitaxial deposition of silicon. Under the freestanding structures a second thinner layer of polycrystalline silicon is used for electrodes and as interconnects. The sensing element, shown in Figure 2.15, has two decoupled rotary oscillation modes. The primary driven mode

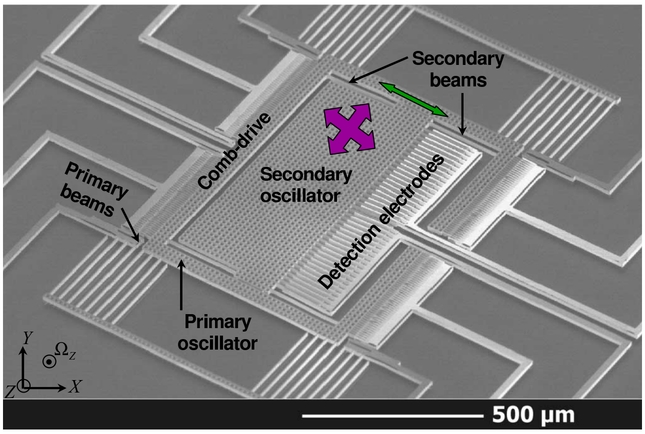

Figure 2.14: A decoupled translational gyroscope from Bosch [Geiger 2002].

is around the z-axis and is excited with electrostatic forces using the inner spoke electrodes of the inner wheel. Attached to the inner wheel, by torsional springs, is a rectangular structure, which, in response to rotation about the sensitive axis (x-axis), will exhibit a secondary rotary oscillation about the y-axis. Owing to the high stiffness of the suspension beam in this direction, the oscillation of the inner wheel is suppressed and only the rectangular structure can move due to a Coriolis force. With this approach the primary and secondary modes are mechanically decoupled, which suppresses mechanical cross-coupling effects such as quadrature error. The oscillation of the secondary mode is detected capacitively by electrodes on the substrate. The sensor reported a dynamic range of $200\,°/sec$, a scale factor of $10\,mV/(°/sec)$, and a RMS noise of $0.05\,°/sec$ in a 50 Hz bandwidth, which makes it suitable for most automotive applications.

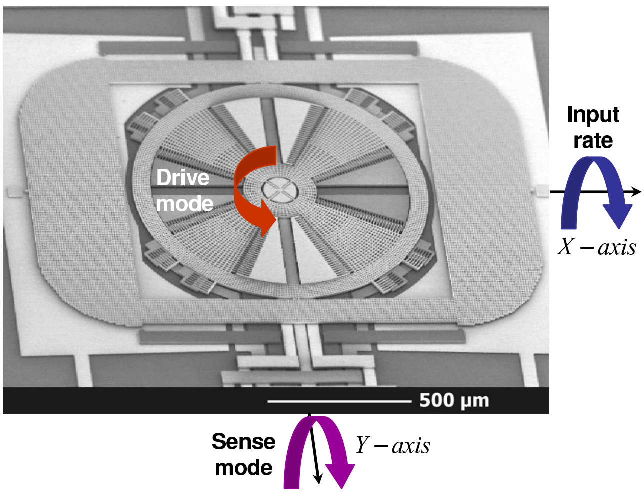

Figure 2.15: Surface-micromachined gyroscope with decoupled drive and sense mode. The drive mode is excited by an electrostatic comb drive and is rotational about the z-axis (out-of-plane) [Geiger 2000].

Vibrating Ring Gyroscope:

In a vibrating ring gyroscope [Putty 1994, Sparks 1999], the ring structure is driven into resonance in the plane of the chip. The vibration of the ring forms an elliptically shaped pattern. In the absence of an external rotation, the four nodal points at ±45° from the drive axis on the ring remain stationary (Figure 2.16a). An external rotation about the z-axis generates a Coriolis force that excites the resonant mode along the 45° axes. The resulting displacement is sensed capacitively by a series of electrodes around the ring. The symmetry of the structure provides identical drive and sense resonance if manufacturing is perfect. Delphi reported a vibratory ring gyroscope using electroplated metal to

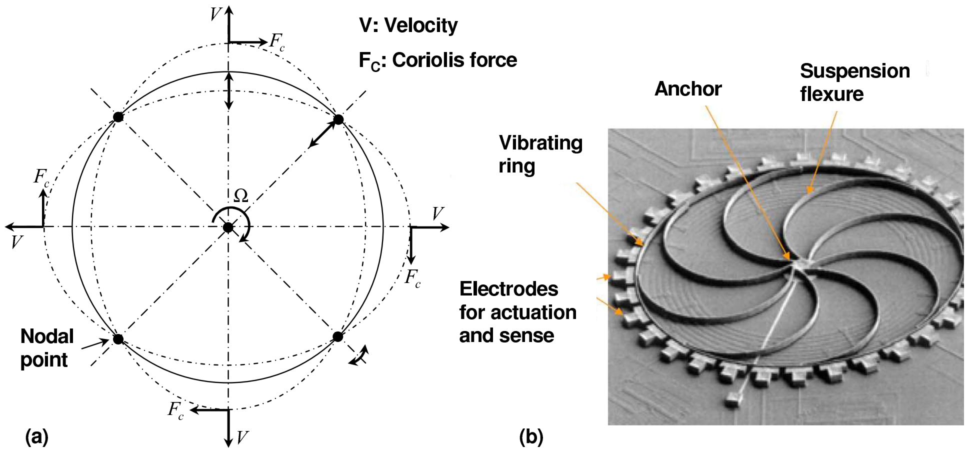

Figure 2.16: (a): Operational principle of a ring gyroscope. (b): Delphi metal ring gyroscope [Sparks 1999].

form a ring structure on top of CMOS chips [Sparks 1999]. As shown in Figure 2.16b, semicircular springs support the ring and store the vibration energy. The springs are attached to the substrate with a symmetric post. The post/spring design greatly reduces the effect of packaging stresses on the sensor. Electrodes with a small gap to the ring are placed along the circumference of the ring with equal intervals. These electrodes, forming capacitors with the ring, are used to drive, sense, balance, and control the ring vibration. During operation, an *ac* voltage signal is applied to the drive electrodes to excite the ring electrostatically into resonant oscillation. A *dc* bias voltage is applied to the ring. The sense electrodes are 45° apart from the corresponding drive electrodes and are connected to on-chip lowinput-capacitance CMOS buffer amplifiers. Another ASIC chip that includes four independent control loops is used to maintain the ring in resonance at a constant amplitude, to obtain the rate signal, and to correct for mechanical imbalance in the ring. The sensor has a measured noise floor of $0.1\,°/s/\sqrt{Hz}$ and a bandwidth of 25 Hz.

2.2.3.2 Dual-Axis Gyroscopes

It is also possible to design micromachined gyroscopes that are capable of sensing angular motion about two axes simultaneously. These devices are based on a rotorlike structure that is driven into a rotary oscillation by electrostatic comb-drives. Angular motion about the x-axis causes a Coriolis acceleration about the y-axis, which, in turn, results in a tilting oscillation of the rotor. Similarly, any rotation of the sensor about the y-axis causes the rotor to tilt about the x-axis. Conceptually, this is shown in Figure 2.17(a).

An implementation of such a dual-axis gyroscope was reported by Junneau et al. [Juneau 1997]. This gyroscope shown in Figure 2.17(b) was designed at the Berkeley Sensors and Actuators Center and manufactured in a surface-micromachining process with a $2\,\mu m$ thick proof mass. The interface

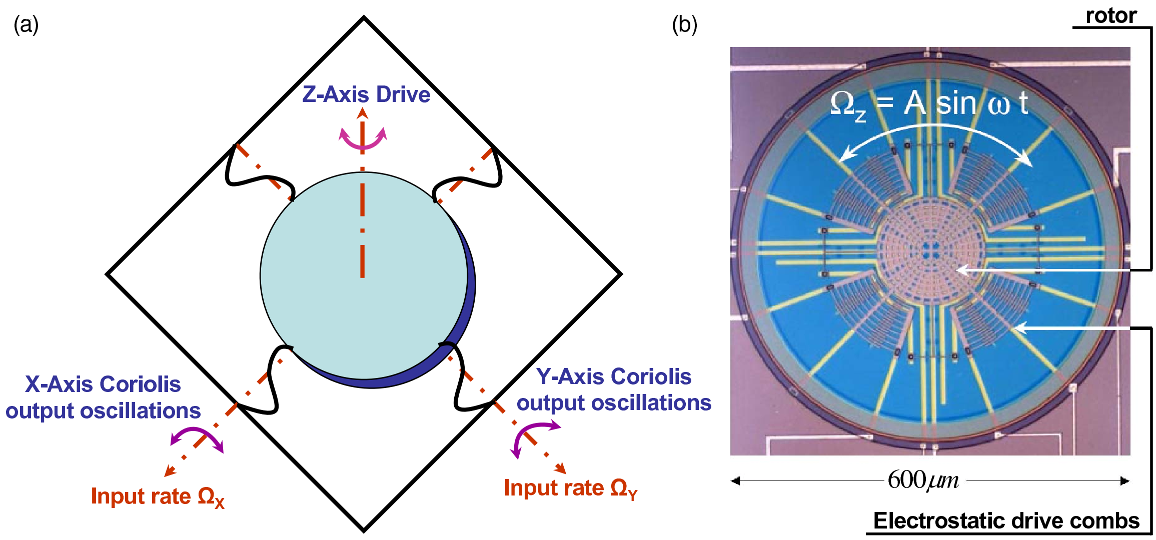

Figure 2.17: (a): Schematic design concept for Berkeley dual-axis gyroscope. (b): Polysilicon surface-micromachined dual-axis gyroscopes designed at the Berkeley Sensors and Actuators Center [Juneau 1997].

and control electronics were integrated on the same chip. Underlying pie-shaped electrodes capacitively detect the tilting motion. To distinguish the two different output modes, a different voltage modulation frequency (200 and 300 KHz) is used for each sense electrode pair. The reported performance was $1\,^{\circ}/sec$ in a 25 Hz bandwidth. The natural driving frequency of the rotor is about 25 KHz. Electrostatic tuning of the different resonant frequencies can be used. Cross-coupling between the two output modes is a major problem and was measured to be as high as 15%. This implies that for a commercially viable version more research has to be done for such a dual-axis gyroscope.

2.2.3.3 Resonant Gyroscopes

Seshia et al. [Seshia 2002a] reported an integrated MEMS gyroscope based on resonant sensing. A schematic of this gyroscope design is shown in Figure 2.18. The polysilicon sensor is about $1.2\,mm$ by $1.2\,mm$ in size and $2.25\,\mu m$ thick. The device consists of a proof mass suspended by flexures attached to a rigid frame. The proof mass is driven relative to the outer frame in the x direction using embedded lateral comb drive actuators. When there is an external rotation along the z axis, a Coriolis force induced by the vibration of the center proof mass acts in the y direction on one end of a lever mechanism. The force is amplified by the lever and transmitted to a double-ended tuning fork (DETF) along the axial direction of the DETF. The resonant frequency of the DETF is sensitive to axial stress. Therefore, the DETF self-oscillation frequency is a measure of the external rotation rate. There is one DETF on each side of the structure to form a differential output. The output of the gyroscope is a frequency-modulated signal that can be easily converted to a digital signal. The measured noise floor is $0.3\,^{\circ}/s/\sqrt{Hz}$, limited by electronic noise of the oscillator circuit.

2.2.4 Conclusion

The recent transition from MEMS to NEMS makes the resonant sensing one of the best alternatives for inertial sensors in order to overcome the physical limitations of classical detection techniques such

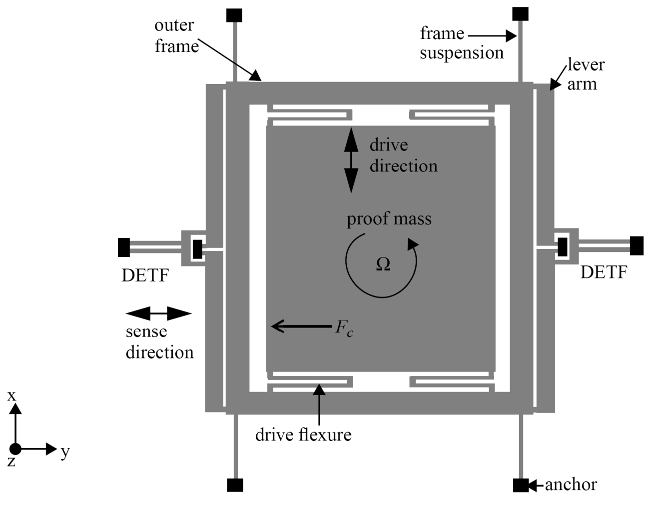

Figure 2.18: Schematic of the mechanical structure of the resonant output gyroscope [Seshia 2002a].

as the capacitive sensing. Moreover, the resonant sensing technique is known to be highly sensitive and well adapted for M&NEMS inertial sensors (device including MEMS and NEMS parts). It can also overcome several of the problems associated with displacement sensing gyroscopes and simplifies the control implementation as well (see chapter 7). For all these reasons, we made the choice to use the resonant sensing technique for small MEMS and M&NEMS inertial sensors applications.

2.3 Gas and Mass Sensors

2.3.1 Gas Sensors

Gas sensors are increasingly used in the growing markets of automotive [Moos 2002, McGeehin 2000], aerospace [Moos 2002, McGeehin 2000, Kallergis 2001, Kohl 2001], and logistic [Abad 2007] applications. Within these domains, gas sensors play important roles in providing comfort and safety or in enabling process control or smart maintenance functionalities. Future important markets are likely to emerge in the fields of safety and security [Gardner 2004]. Two important groups of applications are the detection of single gases (as NOx, NH3, O3, CO, CH4, H2, SO2, etc.) and the discrimination of odours or generally the monitoring of changes in the ambient. Single gas sensors can, for examples, be used as fire detectors, leakage detectors, controllers of ventilation in cars and planes, alarm devices warning the overcoming of threshold concentration values of hazardous gases in the work places. The detection of volatile organic compounds (VOCs) or smells generated from food or household products has also become increasingly important in food industry and in indoor air quality, and multisensor systems (often referred to as electronic noses) are the modern gas sensing devices designed to analyse such complex environmental mixtures [Gardner 2004, Gardner 1999, Mielle 2000]. Examples of application for gas sensors and electronic noses are reported in Table 2.4.

Solid state gas sensors, based on a variety of principles and materials, are the best candidates to the development of commercial gas sensors for a wide range of such applications [Moseley 1987, Madou 1989, Mandelis 1993, Moseley 1997, Lundström 1996]. The great interest of industrial and scientific world on solid state gas sensors comes from their numerous advantages, like small sizes, high sensitivities in detecting very low concentrations (at level of ppm or even ppb) of a wide range of gaseous chemical compounds, possibility of on-line operation and, due to possible bench production,

Gas sensors and electronic noses applications	
Automobiles Car ventilation control Filter control Gasoline vapour detection Alcohol breath tests	**Automobiles** Car ventilation control Filter control Gasoline vapour detection Alcohol breath tests
Indoor air quality Air purifiers Ventilation control Cooking control	**Food** Food quality control Process control Packaging quality control (off-odours)
Environmental control Weather stations Pollution monitoring	**Industrial production** Fermentation control Process control
Medicine Breath analysis Disease detection	

Table 2.4: Application for gas sensors and electronic noses.

low cost. On the contrary, traditional analytical instruments such as mass spectrometer, NMR, and chromatography are expensive, complex, and large in size. In addition, most analysis requires sample preparation, so that on-line, real-time analysis is difficult. However, recent advances in nanotechnology, *i.e.* in the cluster of technologies related to the synthesis of materials with new properties by means of the controlled manipulation of their microstructure on a nanometer scale, produce novel classes of nanostructured materials with enhanced gas sensing properties providing in such a way the opportunity to dramatically increase the performances of solid state gas sensors.

Several physical effects are used to achieve the detection of gases in solid state gas sensors. A characteristic of such devices is the reversible interaction of the gas with the surface of a solid-state material. In addition to the conductivity change of gas-sensing material, the detection of this reaction can be performed by measuring the change of capacitance, work function, mass, optical characteristics or reaction energy released by the gas/solid interaction. Organic (as conducting polymers [Harsányi 2000], porphyrins and phtalocyanines [Hu 1999]) or inorganic (as semiconducting metal oxides [Meixner 1996]) materials, deposited in the form of thick or thin films, are used as active layers in such gas sensing devices. The read-out of the measured value is performed via electrodes, diode arrangements, transistors, surface wave components, thickness-mode transducers or optical arrangements. Indeed, although the basic principles behind solid state gas sensors are similar for all the devices, a multitude of different technologies have been developed. An incomplete list of solid state gas sensors is reported in Table 2.5.

Since we are just interested on resonant sensors, only the last line of Table 2.5 based on mass changes is detailed in the following sections.

2.3.1.1 Acoustic wave devices

Acoustic wave devices are based on high-frequency mechanical vibrations. Originally developed for precision radio frequency (rf) signal-processing applications, they are widely utilized in mobile and wireless communications, and are routinely found in most modern day electronics [Campbell 1998].

	Type of devices	Physical change
1	❑ **Semiconductor gas sensors**	Electrical conductivity
2	❑ **Field effect gas sensors** diodes, transistors, capacitors	Work function (electrical polarisation)
3	❑ **Optical sensors** (fibre optic or thin film)	Optical parameters: SPR, reflection, interferometry, absorption, fluorescence, refractive index or optical path length
4	❑ **Catalytic gas sensors** Seebeck effect, pellistors, semistors	Heat or temperature
5	❑ **Electrochemical gas sensors** (Potentiometric or amperometric)	Electromotive force or electrical current in a solid state electrochemical cell
6	❑ **Resonant sensors** Acoustic wave devices MEMS and NEMS cantilevers	Mass

Table 2.5: Incomplete list of solid state gas sensors

As pointed out by Ballantine and Wohltjen [Ballantine 1989], their inherent sensitivity to ambient environmental effects, which requires hermetic shielding or isolation in signal processing applications, has ironically become a windfall in the field of chemical and physical sensing.

Acoustic-wave based sensors offer a simple, direct and sensitive method for probing the chemical and physical properties of materials. The term acoustic is commonly used in the literature, even when referring to frequencies which are well above the audible range. Acoustic waves cover a frequency range of 14 orders of magnitude from $10^{-2}\,Hz$ (seismic waves) and extending to $10^{12}\,Hz$ (thermo-elastic excited phonons) [Janshoff 2000]. Acoustic wave devices such as those mentioned in this chapter operate in a narrow frequency range between 10^{6}-$10^{9}\,Hz$. In this chapter the discussion is concentrated on acoustic wave devices employed for measuring concentrations of gas- or vapor-phase analytes. The utilization of acoustic wave devices for gas-phase sensing applications relies on their sensitivity towards small changes (perturbations) occurring at the active surface. In order to monitor a specific gas or vapor, a sensitive layer is generally employed. In the presence of an analyte species, the waves properties become perturbed in a measurable way that can be correlated to the analyte concentration.

Virtually all acoustic-wave-based devices use a piezoelectric material to generate the acoustic wave which propagates along the surface or throughout the bulk of the structure. Piezoelectricity is the ability of certain crystals to couple mechanical strain to electrical polarization, and will only occur in crystals that lack a center of inversion symmetry [Ballantine 1996]. By applying a time-varying electrical field, a synchronous mechanical deformation of the piezoelectric material will arise, resulting in the coincident generation of an acoustic wave in the material, and vice versa [Wohltjen 1979]. Acoustic wave devices come in a number of configurations (Figure 2.19), each with their own distinct acoustic and electrical characteristics.

Two different groups of acoustic wave devices that are commonly employed for gas sensing will be discussed herein. The first are bulk acoustic wave (BAW) devices, which concern acoustic wave propagation through the bulk of the structure. This category of devices includes the quartz crystal microbalance (QCM) and thin-film resonators (TFRs), the latter encapsulating thin-film bulk acoustic resonator (TFBAR) and solidly mounted resonator (SMR) structures. The second type utilize acoustic waves confined to the surface of the piezoelectric material, and are known as surface acoustic wave

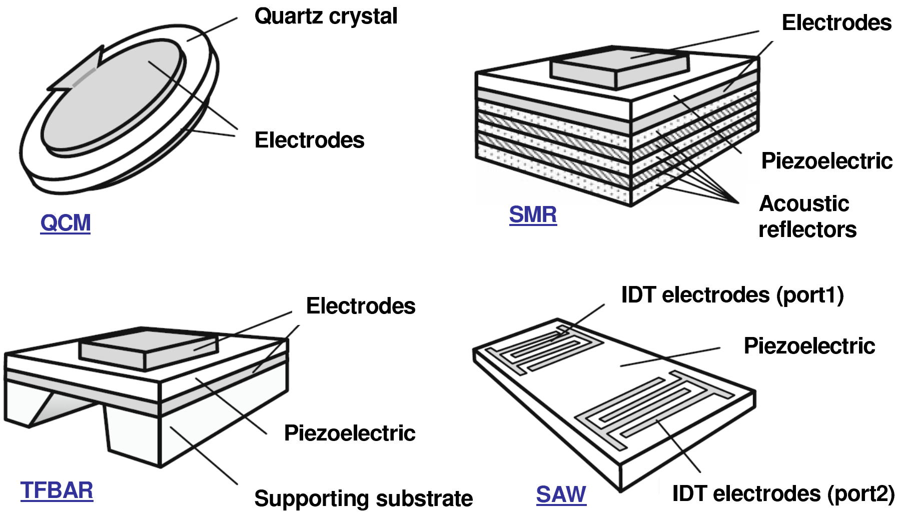

Figure 2.19: Acoustic wave devices configurations

(SAW) devices. Unlike the electrode structures found on QCM, TFBAR and SMR structures, SAW devices use patterned thin-film interdigital transducers (IDTs) to generate and detect the acoustic waves. Both QCM and TFRs are single port devices, whereas SAW devices can be configured as two-port delay line or as one-port resonator structures. All of these devices are mass sensitive, while SAW devices can be specifically designed to be highly sensitive towards sheet conductivity deviations at the active surface of the device. It should be noted that there are other members of the acoustic wave device family, such as thin-film flexural-plate-wave (FPW) delay lines and shear horizontal acoustic plate mode (SH-APM) devices [Ballantine 1996], however they are not commonly used for gas or vapor-sensing applications.

The interactions between an analyte gas and the active surface of the device perturb the phase velocity of the propagating wave. The most commonly measured properties of acoustic modes are resonant frequency, phase shift or attenuation [Powell 2006]. However, for single port devices such as QCMs and TFRs, direct measurements of impedance can be made. In any case, the measured change serves to quantify the analyte concentration. The perturbations affecting acoustic phase velocity can be attributed to by many factors, each of which represents a potential sensor response [Ricco 1991].

2.3.1.2 Resonant Cantilevers

Micromachined cantilevers commonly employed in atomic force microscopy (AFM) constitute a promising type of gas-sensitive transducer for chemical sensors [Thundat 1995a, Maute 1999, Jensenius 2000, Fritz 2000, Berger 1997]. The microcantilever surfaces represent the platform to sense adsorption of molecules. Such processes involve generation of surface stress, resulting in bending of the microcantilever, provided adsorption preferentially occurs on one cantilever surface. Selective adsorption on one surface only is controlled by coating typically the upper surface with a thin layer showing affinity to the molecules in the environment to be detected. This surface will be called sensor surface or functionalized surface of the microcantilever (see Figure 2.20). The other surface, typically the lower surface, may be left uncoated or be coated with a passivation layer being inert or not exhibiting substantial affinity to the molecules that are to be detected. To establish functionalized surfaces, often a metal layer is evaporated onto the surface designed as sensor surface. Metal surfaces, such as gold, are frequently used to covalently bind a monolayer representing the actual detection layer, *e.g.*, a thiol monolayer with defined surface chemistry. The molecules to be detected bind then to the thiol layer. The underlying gold coating also serves as reflection layer for optical readout of the cantilever.

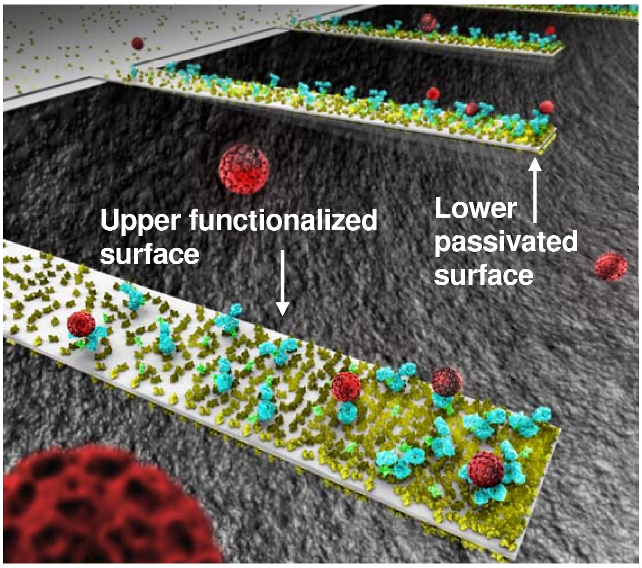

Figure 2.20: An array of microcantilevers with their lower surfaces passivated and their upper surfaces functionalized for recognition of target molecules.

By oscillating a microcantilever at its eigenfrequency, information on the amount of molecules adsorbed can be obtained. However, the surface coverage is basically not known. Furthermore, molecules on the surface might be exchanged with molecules from the environment in a dynamic equilibrium. In contrast, mass changes can be determined accurately by tracking the eigenfrequency of the microcantilever during mass adsorption or desorption. The eigenfrequency equals the resonance frequency of an oscillating rectangular microcantilever of length l, thickness t, and width w, if its elastic properties remain unchanged during the molecule adsorption/desorption process and damping effects are negligible. This operation mode is called the dynamic mode. The cantilever is used as a resonator. A shift of the resonant frequency induced by mass adsorbate is read out as the sensing signal [Thundat 1995b, Ilic 2001a, Gupta 2004, Ono 2003, Ekinci 2004a]. This shift in resonance frequency, Δf_{res}, for a homogeneously distributed adsorbed mass is given by the following equation:

$$\Delta f_{res} \approx -f_0 \frac{\Delta m}{2m_0} \tag{2.5}$$

where Δm is the mass of the adsorbents and m_0 is the initial mass of the cantilever. The pioneer investigation by Thundat et al demonstrated the mass-sensing capability of micromechanical resonant cantilevers [Thundat 1995b]. With precise optical detection of an AFM (atomic force microscopy) mode, a single cell or a virus has been sensed in an air environment [Ilic 2001a, Gupta 2004]. In an ultrahigh vacuum, the resonant cantilevers even showed the mass resolution as high as an attogram level [Ono 2003, Ekinci 2004a]. Indeed, MEMS and NEMS resonant cantilevers offer sensitivities more than two orders of magnitude better than quartz crystal microbalances [Janata 1989], flexural plate wave oscillators [Cunningham 2001], and surface acoustic wave devices [Bodenhöfer 1996]. This increase in sensitivity can be attributed largely to the extremely small size of the sensing element.

Recently, a 100 zeptogram resolution has been demonstrated using a resonant nanoelectromechanical cantilever [Mo 2007].

2.3.2 Mass Sensors

A biosensing approach in which MEMS technologies are now playing an increasingly important role is mass sensing. A key strength of mass-based biosensing is its "label-free" character, *i.e.*, the inertial mass of the analyte molecules provides the detector response, hence no fluorophore or electroactive tag need to be attached. Mass detection does not, however, obviate specific interfacial biochemical recognition; analyte molecules must be selectively recognized and bound in preference to all other species. Herein lies a key limitation of label-free detection: nonspecific adsorption. This problem can be avoided by precoating the surface with a material that is resistant to protein adsorption. Polymers such as poly(vinyl alcohol), poly(acrylamide), dextran, and poly(ethylene glycol) (PEG) have been used as coating materials to prevent nonspecific adsorption [Amanda 2001, Park 2000, Holland 1998, Masson 2005]. Mass-sensitive micro- and nanodevices can be divided into two broad categories:

- 1. piezoelectric crystal-based devices, those utilizing a small "slab" or film of piezoelectric material (quartz, zinc oxide, lithium tantalate, lithium niobate, gallium arsenide) to generate, by application of the appropriate time and spatially varying electrical signal, traveling or standing acoustic waves whose propagation characteristics are perturbed by changes in the mass or mechanical properties of matter on the moving device surface [Ballantine 1997]
- 2. silicon MEMS-based devices, those relying on thermal, electromagnetic, or direct mechanical means to periodically or statically deflect a micro(nano)fabricated beam, cantilever, or membrane from some nonpiezoelectric material, most often silicon [Yang 2003, Subramanian 2002, Tamayo 2003, Liu 2003, Su 2003, Cleland 2002, Arntz 2003], with the oscillation characteristics or extent of bending being a measure of the mass of sorbed analytes.

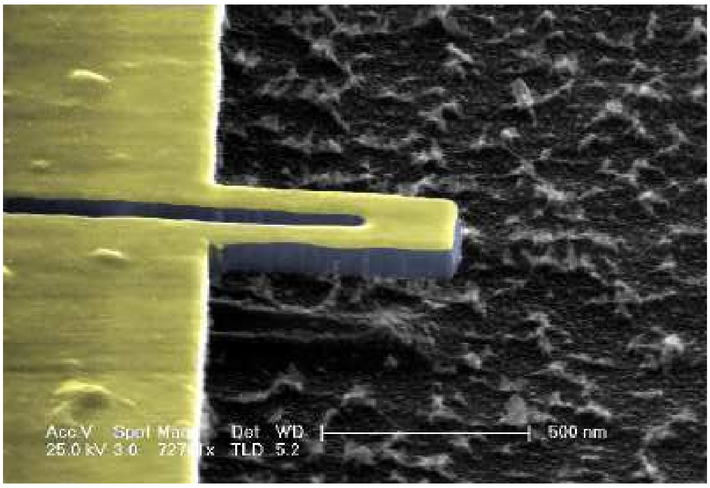

Figure 2.21: The Caltech cantilevers are just 400 nm wide by 80 nm thick (M Roukes)

2.3.2.1 Piezoelectric Crystal-Based Devices

The best known of the piezoelectric devices are those that utilize surface acoustic waves (SAWs) or thickness-shear modes (TSMs); resonators based on the latter mode are popularly known as "quartz (crystal) microbalances" (QCMs or QMBs). A principal limitation of both types of oscillating mechanical device when used in biosensing is the potential for intolerable levels of damping of the acoustic wave by the liquid. A "classic" SAW (a Rayleigh wave), while an excellent basis for a gas sensor, is ill-suited to liquid-phase detection applications, as the surface-normal component of its motion leads to excessive damping by the contacting liquid. Close relatives of the SAW, including the shear-horizontal acoustic plate mode (SH-APM), the Love wave, the surface transverse wave (STW) and the leaky SAW (LSAW) carry much or all of their energy (as do TSM resonators) in modes that cause in-plane motion of the device surface, leading to manageable attenuation of the wave. The flexural plate wave (FPW) has significant surface-normal displacement, but unlike the other modes described above, its velocity is slower than that of sound in water, so that energy transfer from wave to liquid is relatively inefficient, and damping is therefore quite manageable. One important trend noted by the WTEC team in TSM resonators and other acoustic wave biosensing devices is operation at ever-higher frequencies, leading to enhanced sensitivity and, in some cases, lower limits of detection provided the associated circuitry is carefully designed so as not introduce additional noise, which can offset the gains in sensitivity as frequencies go higher. Where TSM resonators running at 5 and 9 MHz were the rule a number of years ago, devices over the $5 - 30$ MHz range are now commercially available and widely in use (for example, at International Crystal Manufacturing Co., Inc.), and devices up to 100 MHz are being evaluated in research labs. Note, however, that the thickness of the crystal is inversely proportional to the fundamental frequency and, in practice, quartz TSM devices above about 30 MHz are quite fragile. Improving the stability of the oscillator circuitry and sample temperature control system to provide, for example, 0.1 Hz short-term stability rather than the more typical 1 Hz is often a more effective means to improve the limit of detection. MEMS methods have also been used to provide a localized thin, "energy trapping" region within a quartz substrate that is thick elsewhere to maintain mechanical robustness [Smith 1995b]. Notably, many of the other acoustic modes, though less widely used than TSMs, are either independent of substrate thickness or depend in a way that allows realization of higher sensitivities without unreasonably thin substrates. A second general finding of the WTEC team with regard to piezoelectric crystal-based devices is the relatively mature state of the technology. For these transducers, the fundamental biosensing advances are predominantly in the interfacial chemistry, while the basic platform is static, save for a gradual increase in operating frequencies. A growing number of commercial operations supply complete TSM resonator-based systems, in some cases including oscillator circuitry, temperature control apparatus (critical for highsensitivity measurements), and integral flow cells [Handley 2001, Gizeli 2002].

2.3.2.2 Silicon MEMS-Based Devices

Among academic and national laboratory researchers, silicon MEMS-based micro/nano cantilevers and beams are receiving an increasing share of the visibility formerly focused on piezoelectric devices (cantilever review). Being silicon themselves, the new MEMS mass-sensitive devices are simpler to integrate with control and measurement electronics. These devices operate in two principal modes:

- 1. by vibrating, where the drive can be electrothermal (*e.g.*, using resistors incorporated in the silicon chip as heaters), electromagnetic (using the force of an external magnetic field acting upon a current passing along the structure) [Hagleitner 2001], or even piezoelectric, using an added-on transduction material.

- 2. by bending, where a biomechanical transduction layer deposited on one side of the cantilever creates a mechanical bimorph that bends in response to binding of the target species.

In the case of the vibrating structures, changes in the mass on the cantilever tip lead to changes in resonant frequency that are readily measured with integrated circuitry, typically resistive or capacitive. Smaller cantilever effective mass leads to better sensitivity and, noise and background issues being appropriately addressed, to improved limits of detection. The fact that GHz frequencies are now routinely achieved in microprocessors and other silicon microelectronics means that high frequencies no longer preclude complete integration of drive and measurement electronics. For bimorph measurements, readout can be optical, using angular or interferometric changes of light reflected from the cantilever tip; or capacitive, if a plate-to-plate gap varies with bio-target-induced mechanical stress; or based upon integrated resistive measurement of variation in the strain over some portion of the cantilever. Though it is not piezoelectric, silicon is piezoresistive, and therefore provides the opportunity to include a convenient means of direct electrical readout. The manufacturing advantages described above for MEMS device types makes it much simpler to fabricate arrays of mass sensing devices that include diverse sets of sensing materials in addition to redundant, control, and reference devices. Such integration of multiple sensors and controls has yet to be fully exploited, offering an important opportunity for chip-level integrated design to positively impact system performance. While the record for the lowest limits of detection on a mass-per-area basis is arguably still held by highfrequency piezoelectric SAW resonators, which are pushing from the hundreds of MHz into the GHz regime (in synchrony with wireless communications of various types, for which they are used as filtering and frequency-control elements), the limit-of-detection gap is closing quickly between the piezoelectric and the MEMS technology families. The power of integrated control electronics combined with sophisticated temperature-control strategies is beginning to be developed for integrated silicon mass-sensing systems; this area is ripe for further advances.

Progress has been made on another front that offers unique challenges to micro/nano mechanical biosensing devices: the tasks of reproducibly depositing selective, fully viable biointerface materials onto one surface or the tip of a cantilever whose dimensions are measured in micrometers or nanometers. Advances in ink-jet, pin-based, and similar dispensing technologies are being driven by the needs of the burgeoning DNA microarray industry, as well as the nascent field of protein microarrays. The needs of such spot-based biomaterial arrays have provided impetus for improved hardware as well as solution matrices specifically designed to place a micrometer or smaller "spot" of material in a precise location. Funding is significant for such technologies; in many cases, they should be directly applicable to the needs of micro/nanomechanical biosensors.

2.4 Resonant sensors

Resonant sensing technique has been implemented in numerous devices for the measurement of pressure [Esashi 1996], humidity [Boltshauser 1992], temperature [Burns 1996b], acceleration [Burns 1996a, Seshia 2002b], mass flow [Enoksson 1997], specific gas [Hagleitner 2002], biological detection (immunosensors [Florin 1995], cytometers [Ilic 2001b]), force (AFM cantilevers [Albrecht 1991]) and magnetic field [Kádár 1998], and angular rate (vibratory gyroscopes [Seshia 2002a]). The resonator sensor element is often built into a larger device that transmits the effect of the parameter to be measured as a variation in either the mass or spring constant or some other parameter of the resonant sensor element. As shown in Figure 2.22, the resonant sensor element can take a number of forms such as a cantilever (mass and gas sensors), a double-ended tuning fork or a singly clamped-clamped beam (inertial sensors).

There are various ways in which the resonant characteristics of this system can be changed. However, the most common technique is to modulate either the spring constant (resonant inertial sensors) or

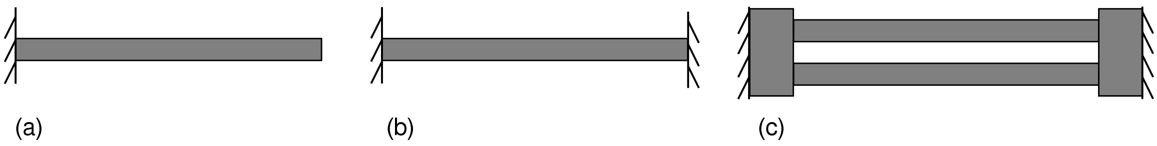

Figure 2.22: Three simple implementations of resonant sensors: a cantilever beam (a), a clamped-clamped beam (b) and a double-ended tuning fork (c)

the mass (resonant gas and mass sensors) of the resonating element (see Figure 2.23). The change in either of these quantities can be monitored as a shift in the resonant frequency of the system. While changing the damping coefficient results in a change in the amplitude of the displacement, changing the proof mass or spring constant changes the frequency of the system.

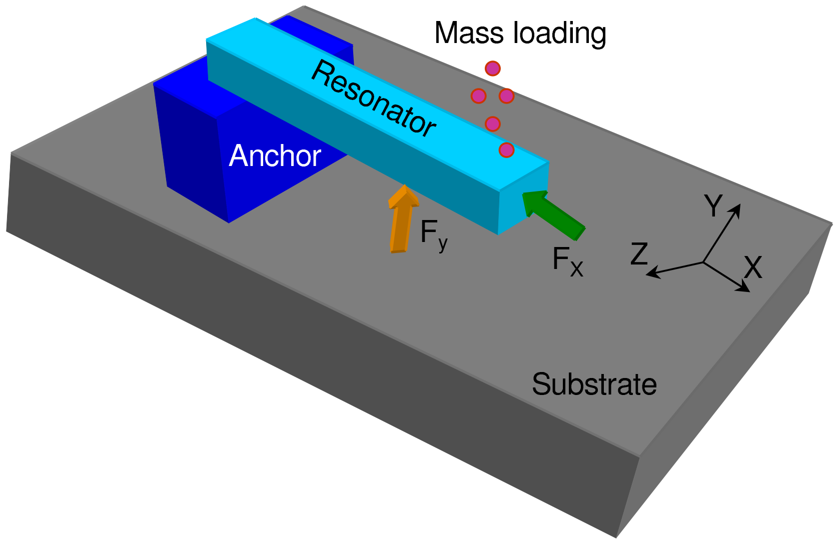

Figure 2.23: A schematic of a resonator subject to different inputs. These inputs could be direct or coupled through a secondary transducer that responds to the measurand. The micromechanical structure itself might take on a number of different forms.

Detection of frequency shift is more advantageous as compared to detecting changes in amplitude, as it is less sensitive to effects such as feedthrough coupling from undesired sources and parasitic passive elements. Other mechanisms of varying the resonant characteristics include variation of rigidity [Tabata 1999], material parameters, changes in the drive forces and applied torques. A comparison of resonant sensing with other sensing mechanisms can be found in several sources in literature [Brand 1998, Prak 1993].

2.4.1 Frequency measurement

2.4.1.1 Direct counting

The simplest way to measure frequency of a periodic signal is to count zero crossings of the amplitude of the signal to be measured. A precise (low frequency) reference oscillator is used to gate the counting scheme as shown in Figure 2.24.

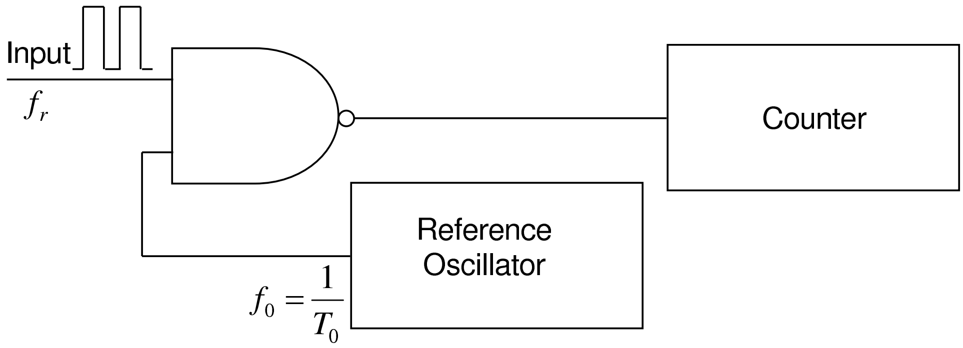

Figure 2.24: Schematic of a simple zero crossing counting scheme for frequency (or period) measurement.

If T_0 is the period of the reference oscillator, the frequency of the input signal can be calculated in terms of the number of zero crossings (N_x) and the period of the reference oscillator (T_0):

$$f_x = \frac{N_x}{T_0} \tag{2.6}$$

The quantization error introduced by the counting scheme can be written as:

$$\Delta_q = \pm\frac{1}{f_x T_0} \tag{2.7}$$

In other words, it is clear that the longer the interval for which the counting scheme is continued, the better is the resolution. However, there is a trade-off in terms of the bandwidth (BW) of the counting scheme.

$$BW \cong \frac{1}{2T_0} \tag{2.8}$$

Indirectly, this imposes a limitation on the drive frequency of the proof mass for resonant gyroscopes.

2.4.1.2 Indirect counting

The other common method for frequency measurement is to measure the frequency of the input signal in terms of a precise high frequency reference signal. In this case, the bandwidth of the measurement is again based on the averaging time. The frequency of the input signal can be calculated as:

$$f_x = n\frac{f_r}{N_x} \tag{2.9}$$

The quantization error is given as [Kirianaki 2002]:

$$\Delta_q = \pm\frac{1}{\sqrt{3}nN_x f_r} \tag{2.10}$$

As shown in Figure 2.25, this error has its roots in phase synchronization between the reference and input signals.

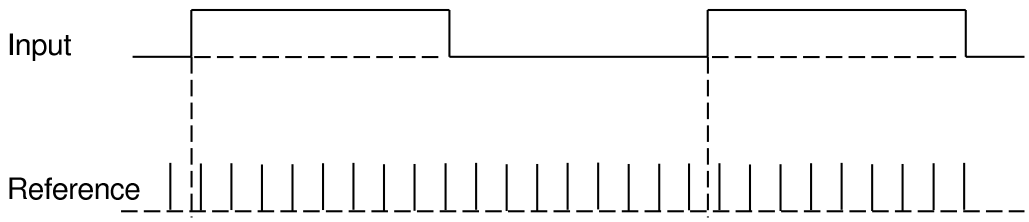

Figure 2.25: Diagram showing the problem of phase synchronization for indirect counting. Note that the quantization error is some fraction of the period of the higher frequency reference signal.

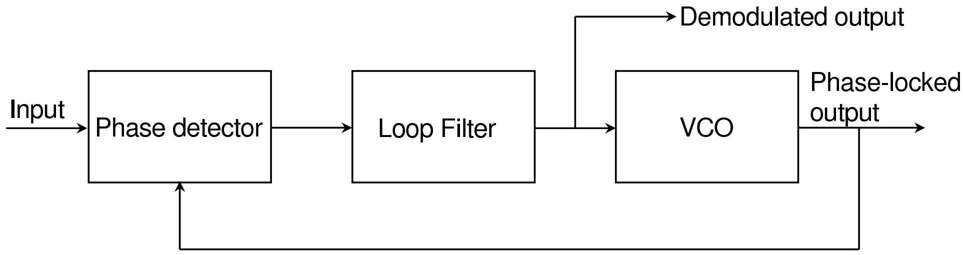

Figure 2.26: Block Diagram of a phase-locked loop.

2.4.1.3 Phase-Locked Loop (PLL)

A phase-locked loop can be used for several applications ranging from frequency and phase demodulation and frequency synthesis. A block diagram of a PLL is shown in Figure 2.26.

The Linear PLL consists of three components: a phase detector, a VCO and a Loop Filter. The phase of the input and output signals is compared and the difference is converted to a voltage input to a voltage-controlled oscillator whose output frequency tracks the input voltage. An analog multiplier may be used as a phase detector for instance. A Loop Filter is added for bandwidth selection. The loop filter is a low-pass (active or passive) implementation. The PLL may also comprise of a frequency divider and/or a phase-shifter. A complete analysis of the PLL is beyond the scope of this dissertation and the reader is referred to several excellent sources [Wolaver 1991, Stephens 2002].

2.4.2 Mechanical analysis

Here, we investigate the mechanics of the resonator (the sensitive part of a resonant sensor). This is an important step towards the determination of the resonance frequency and the sensitivity expressions. Moreover, through the resonator dynamic response, the transfer function is deduced which will be used later for the noise analysis.

2.4.2.1 Resonance frequency

Assuming that the nonlinear terms are negligible, the equation of motion of a beam in bending (the resonator) subjected to an axial tensile force (F) can be written as:

$$EI\frac{\partial^4 \tilde{w}}{\partial \tilde{x}^4} + \xi\frac{\partial \tilde{w}}{\partial \tilde{t}} - F\frac{\partial^2 \tilde{w}}{\partial \tilde{x}^2} + \rho A\frac{\partial^2 \tilde{w}}{\partial \tilde{t}^2} = 0 \tag{2.11}$$

where E is the Young's modulus, I is the bending moment of inertia, ξ is the viscous damping coefficient, ρ is the material density and A is the beam section. The solution $\tilde{w}(\tilde{x}, \tilde{t})$ can be solved by the method of speration of variables where:

$$\tilde{w}(\tilde{x},\tilde{t}) = \phi(\tilde{x}).a(\tilde{t}) \tag{2.12}$$

The equation for the modes shape of the beam as a function of position coordinate can be written as:

$$\phi(\tilde{x}) = C_1 \cos\left(\frac{\lambda\tilde{x}}{L}\right) + C_2 \sin\left(\frac{\lambda\tilde{x}}{L}\right) + C_3 \cosh\left(\frac{\lambda\tilde{x}}{L}\right) + C_4 \sinh\left(\frac{\lambda\tilde{x}}{L}\right) \tag{2.13}$$

Constants C_1-C_4 can be evaluated depending on the boundary conditions of the resonator. λ is a dimensionless parameter related to the wavelength. λ depends on the mode shape and the resonator boundary conditions. It can be evaluated numerically as listed in Table 2.6 for several bending modes of cantilevers as well as clamped-clamped beams resonators. Using the Galerkin method, the time

mode/λ	cantilever beam	clamped-clamped beam
mode1	1.875	4.730
mode2	4.694	7.854
mode3	7.855	11.00
mode4	10.995	14.14

Table 2.6: Coefficients for the first four eigenfrequencies of cantilevers and clamped-clamped beams.

dependence can be cast in the form of a mass-spring-damper equation:

$$M_{eff}\ddot{a} + B_{eff}\dot{a} + K_{eff}a = 0 \tag{2.14}$$

where expressions for M_{eff} and K_{eff} can be written as [Roessig 1998]:

$$M_{eff} = \int_0^L \rho A\phi^2(\tilde{x})d\tilde{x} \tag{2.15}$$

$$K_{eff} = \frac{EI}{L^3}\int_0^L \left(\frac{\partial^2\phi}{\partial\tilde{x}^2}\right)^2 d\tilde{x} + \frac{F}{L}\int_0^L \left(\frac{\partial\phi}{\partial\tilde{x}}\right)^2 d\tilde{x} \tag{2.16}$$

Thus, for a null axial force, the natural frequency of the mechanical resonator is:

$$f_0 = \frac{1}{2\pi}\sqrt{\frac{K_{eff}(F=0)}{M_{eff}}} \tag{2.17}$$

2.4.2.2 Sensitivity

For a resonator vibrating in its fundamental mode, the natural frequency for a constant axial force (F) along the length of the beam can be written in terms of the nominal resonant frequency by evaluating the integrals in Equations (2.15) and (2.16).

$$f = f_0\sqrt{1+F.S} \tag{2.18}$$

$$S = \frac{\rho AL^2 \int_0^L \phi^2(\tilde{x})d\tilde{x} \int_0^L \left(\frac{\partial\phi}{\partial\tilde{x}}\right)^2 d\tilde{x}}{EI\int_0^L \left(\frac{\partial^2\phi}{\partial\tilde{x}^2}\right)^2 d\tilde{x}} \tag{2.19}$$

Thus the resonator sensitivity to axial loads (mechanical scale factor) can be written as

$$SF_f = \frac{S}{2} f_0 \tag{2.20}$$

In the same way, the resonator mechanical mass sensitivity can be deduced as

$$SF_m = \frac{1}{2M_{eff}} f_0 \tag{2.21}$$

2.4.2.3 Dynamic response

The starting point for the simplest dynamic analysis is once again the characteristic differential equation describing the evolution of the displacement of the resonating element subjected to a linear time-varying drive force F_d.

$$M_{eff}\ddot{a} + B_{eff}\dot{a} + K_{eff}a = F_d \cos\left(\Omega\tilde{t}\right) \tag{2.22}$$

where Ω is the drive frequency. Equation (2.22) can be written in its canonical form as

$$\ddot{a} + \frac{\omega_0}{Q}\dot{a} + \omega_0^2 a = \frac{F_d}{M_{eff}} \cos\left(\Omega\tilde{t}\right) \tag{2.23}$$

where $\omega_0 = 2\pi f_0$ and Q is the resonator quality factor that can be estimated by evaluating the different system losses. Using the Fourier transform, the resonator transfer function can be deduced as follow

$$H(\Omega) = \frac{\frac{1}{Meff}}{\Omega^2 - \omega_0^2 + j\frac{\Omega\omega_0}{Q}} \tag{2.24}$$

The previous analysis is not valid for a nonlinear differential equation when the nonlinearities are not negligible (Duffing resonator) or in the case of resonant gyroscopes for Coriolis acceleration sensing with time-varying axial load (Mathieu resonator).

For MEMS and NEMS resonant sensors designers, the quality factor is an important parameter, since it defines the sensor bandwidth. Also, as we can see in Equation (2.24), the resonator transfer function depends in Q. Hence, the importance of estimating the quality factor which is detailed below.

2.4.3 Quality factor

The mechanical quality factor Q is a measure for the energy losses of a resonator or in other words, a measure for the mechanical damping. The Q-factor is defined as the ratio between the total energy stored in the vibration and the energy loss per cycle:

$$Q \approx 2\pi \frac{total\, energy\, stored\, in\, vibration}{dissipated\, energy\, per\, period} \tag{2.25}$$

Low energy losses imply a high Q-factor. The Q-factor cannot be determined directly, but instead can be deduced from the response characteristics of the resonator. One common method of determining Q is from the steady-state frequency plot of a resonator excited by a harmonic force with constant amplitude:

$$Q \approx \frac{\omega_{res}}{\Delta\omega_{-3db}} \tag{2.26}$$

where ω_{res} is the frequency with maximum frequency response and $\Delta\omega_{-3db}$ is the half-power bandwidth of the frequency response. Equation (2.26) indicates that Q is a measure of the sharpness of the frequency selectivity of the resonator. A high Q-factor means a sharp resonance peak and has several advantages:

- The energy required to maintain the vibration is low.
- Minimal effect of the electronic circuitry on the oscillation frequency.
- Low sensitivity to mechanical disturbances.

In nanomechanical resonators, there are numerous possible sources of dissipation which may broadly be classified as either intrinsic or extrinsic. Intrinsic sources of dissipation, such as phonon-phonon and phonon-electron interactions, result from properties of the resonating material, whereas extrinsic sources, such as gas friction, clamping loss, and surface loss, result from interactions with the environment. Obviously, little can be done to control dissipation from intrinsic sources other than careful choice of resonator material. Theoretical calculations have shown that these intrinsic sources of dissipation are small compared to the dissipation currently exhibited by nanomechanical resonators.

There are many extrinsic mechanisms of dissipation in naomechanical resonators. They can be listed by their origin as follow:

2.4.3.1 Gas friction

At pressures above approximately $1\,torr$, viscous damping of a resonator by the surrounding gas is the dominant form of dissipation [Ekinci 2005]. Here the energy is radiated as sound. Fortunately, it is easy to achieve lower pressures where viscous damping no longer dominates. At these lower pressures, where the mean free path of the gas molecules is much larger than the relevant sound wavelength, energy may still be dissipated through momentum transfer to individual molecules. In this case the dissipation is calculated to be:

$$Q_{gas}^{-1} = \frac{pA}{m_{eff}\omega_r \nu} \tag{2.27}$$

where p is the pressure, A is the surface area, M_{eff} is the effective mass of the resonator, ω_r is the resonator angular frequency, and ν is the thermal velocity of the gas. According to Equation (2.27) and multiple experiments, gas friction is not a significant source of dissipation below $10\,mTorr$.

2.4.3.2 Surface losses

Surface losses are caused by adsorbed molecules, dangling or broken bonds, an amorphous oxide layer, or other metastable systems that occur at a resonator's surface. These systems absorb energy from the fundamental resonant mode and irreversibly transfer it other modes and thermal energy. For resonating beams, the energy of a resonator is stored in the elastic strain throughout its volume and thus is proportional to its volume, V. If we assume that energy is predominately dissipated at the surface, then we would expect that the energy lost per cycle would be proportional to the surface area S, and thus:

$$Q_{surface}^{-1} \propto \frac{S}{V} \propto L^{-1} \tag{2.28}$$

Fortunately, it may be possible to control surface losses [Jensen 2006] in NEMS resonators, through careful experimental techniques and the proper choice of resonator material.

2.4.3.3 Clamping loss

Clamping loss refers to mechanical energy dissipated through a resonators supports. Typically, this is theoretically modeled as elastic radiation of energy through the supports. There is still some contention as to the appropriate description of elastic clamping loss; though the most recent theoretical calculations predict a loss for a rectangular beam of:

$$Q^{-1}_{clamping} \propto \frac{wt^4}{l^5} \tag{2.29}$$

where w is the beam width in the direction of vibration, t is the beam thickness, l is the beam length, and the proportionality constant is dependent upon material properties [Geller 2005]. Clearly, to reduce clamping loss, a beam with a high aspect ratio is desirable. However, according to Equation (2.29), clamping loss should be negligible for current resonator designs, including nanotube resonators with their extremely high aspect ratio.

Despite these model-based constraints, researchers have had some success increasing quality factors through creative clamping geometries [Wang 2000]. Thus, it is clear that the theory behind clamping loss is not fully developed, and that this may still prove to have been a significant form of dissipation for existing NEMS resonators.

2.4.3.4 Thermoelastic loss

Thermoelastic damping is the result of the transformation of elastic energy into thermal energy via thermal currents flowing between compressed and expanded regions of a deformed resonator. Zener [Zener 1938] first studied the phenomenon for a beam in flexure, giving the damping as :

$$Q^{-1}_{Zener} = \frac{E\alpha^2 T}{C_P}\frac{\omega\tau_0}{1+\omega^2\tau_0^2} \tag{2.30}$$

where E is Youngs modulus, α is the thermal expansion coefficient, C_p is the constant-stress heat capacity, ω is the angular frequency of vibration, T is temperature, and $\tau_0 = \frac{h^2 C_p}{\pi^2 K}$ is the thermal relaxation time, with K the thermal conductivity and h the beam thickness. More realistically, for nanomechanical resonators the quality factors will likely be limited by thermoelastic dissipation. In this mode of dissipation, strain in the resonator generates local temperature differences via the materials thermal-expansion coefficient. Heat then flows irreversibly along local temperature gradients leading to dissipation. However, even in this case, quality factors on the order of 10^4 are still obtainable at low temperatures [Lifshitz 2000].

2.4.3.5 Ohmic loss

Another type of dissipation associated with electrostatic actuation is ohmic losses from the electrons moving on and off the resonator due to capacitive coupling to a nearby gate. Following Sazonova [Sazonova 2006], the system can be represented as a variable capacitor in series with a resistor to which a voltage V is applied. If the time scales for the electrons to flow on the resonator and the time for one oscillation are matched perfectly, all of the charge flows through a resistor, dissipating energy through Joule heating. Thus, the ohmic losses are given by:

$$Q^{-1}_{ohmic} = \frac{1}{\pi\omega}\frac{R(C'V)^2}{m_{eff}} \tag{2.31}$$

where ω is the angular frequency of vibration, C' is the gradient of the capacitance, R is the output resistor and m_{eff} is the effective mass of the considered mode. The smaller the resonator, the smaller the mass, the higher this contribution, hence NEMS are very sensitive to this effect.

2.4.3.6 Loss due to dislocations

Internal friction due to intrinsic dislocations [Seeger 1981] present in the resonators induce losses. This mechanism of dissipation is related to the density of defects of the micro/nanostructure. These defects are dislocations or impurities like the doping agents used in micro-electronics. At nanoscale, dislocation-induced internal friction is extremely low and the structure is rather pure. Thus, these losses are negligible in NEMS resonators.

In nanomechanical resonators, there are other extrinsic loss mechanisms such as anharmonic mode coupling and extrinsic noise [Mohanty 2002] which can be neglected compared to the other sources of dissipation already cited.

2.4.4 Noise analysis

In resonant sensors, the dominating noise sources originate from the sensing part (the resonator). Therefore, the following noise analysis concerns only MEMS and NEMS resonators.

2.4.4.1 Thermomechanical noise

Thanks to the fluctuation-dissipation theorem, it can be written that the force noise spectral density due to thermomechanical fluctuations of the mass is [Postma 2005].

$$S_f(\omega) = \frac{2}{\pi} K_B T \frac{M_{eff}\omega_0}{Q} \tag{2.32}$$

where M_{eff} is the effective mass of the resonator, ω_0 is the angular frequency of vibration, Q is the quality factor, k_B is Boltzmanns constant and T is the resonator temperature.

It may be assumed without loss of generality that the bandwidth BW used by the phase locked loop (PLL) readout is very narrow compared with the -3dB bandwidth of the resonator. Then, following Equation (2.24), the transfer function of the resonator at resonance giving the displacement versus a constant force per unit length is

$$H_{fx}(\omega) = \frac{Q}{K_{eff}} = \frac{Q}{m_{eff}\omega_0^2} \tag{2.33}$$

The displacement spectral density is then

$$S_x(\omega_0) = ||H_{fx}(\omega)||^2 S_f(\omega) = \frac{2}{\pi} K_B T \frac{Q}{M_{eff}\omega_0^3} \tag{2.34}$$

Following Robins [Robins 1984], for a PLL-based readout technique, the frequency noise spectral density is

$$S_\omega(\omega) = \left(\frac{\omega_0}{2Q}\right)^2 \frac{S_x(\omega_0)}{P_0} \tag{2.35}$$

where P_0 is the displacement carrier power, ie the RMS drive amplitude of the resonator $P_0 = \frac{1}{2}a_d^2$. The latter should be driven below the hysteretic limit due to the mechanical non-linearity. Even though this one will be higher when using a PLL based technique, the open loop value may be used to stay on the safe side. It is assumed here that the resonator (clamped-clamped beam) is driven at its open-loop stability limit [Cleland 2002]:

$$a_d \propto w.Q^{-\frac{1}{2}} \tag{2.36}$$

2.4.4.2 Temperature fluctuations

Given its small heat capacity, a nanomechanical resonator can be subject to rather large temperature fluctuations. Its susceptibility to such fluctuations depends upon the strength of its thermal contact to the environment. Since the resonators dimensions and material parameters are both temperature dependent, temperature fluctuations will generate frequency fluctuations. Cleland and Roukes [Cleland 2002] have evaluated the spectral density of frequency fluctuations arising from temperature fluctuations of a NEMS clamped-clamped resonator. They find that:

$$S_\omega(\omega) = \left(-\frac{22.4C_s^2}{\omega_0^2 l^2}\alpha_T + \frac{2}{C_s}\frac{\partial C_s}{\partial T}\right)^2 \frac{\omega_0^2 k_B T^2}{\pi g\left(1+(\omega-\omega_0)^2\tau_T^2\right)} \tag{2.37}$$

where $C_s = \sqrt{\frac{E}{\rho}}$ is the temperature dependent speed of sound, l is the beam length $\alpha_T = \frac{1}{l}\frac{\partial l}{\partial T}$ is the linear thermal expansion coefficient, and g and τ_T are the thermal conductance and the thermal time constant for the nanostructure, respectively.

2.4.4.3 Adsorption-desorption noise

This noise could be critical for resonant gas sensors applications, operating in air. Gas molecules in the vicinity of a resonator can adsorb upon the resonators surface, mass load the device, and thereby change its resonant frequency. Random, thermally driven adsorption and desorption of molecules will therefore induce fluctuations in the resonance frequency.

This so-called adsorption-desorption noise has been discussed in detail by Yong and Vig [Yong 1989, Yong 1990] and Cleland and Roukes [Cleland 2002]. Adsorption-desorption noise becomes most significant in the temperature regime where the adsorption and desorption rates are comparable; hence, for a given device configuration, it can be minimized by judicious choice of operating temperature. Surface passivation to reduce the binding energy between the molecule and the surface should also be effective in this regard.

2.4.4.4 Momentum exchange noise

For mass and gas sensing applications, the resonator can undergo gas damping due to impingement and momentum exchange of gas molecules on its surface [Cleland 2003, Ekinci 2004b].

Palasantzas [Palasantzas 2008] investigated the simultaneous influence of thermomechanical and momentum exchange noise on the limit to mass sensitivity for nanoresonators. He found With increasing surface roughness, the limit to mass sensitivity increases significantly if the quality factor due to gas collisions is comparable to or smaller than the intrinsic quality factor associated with thermomechanical noise.

2.4.5 Resolution

The resolution is the lower limit of the dynamic range. It is set by the incoherent sum of all stochastic processes driving the resonator [Cleland 2002], such as thermomechanical fluctuations, quantum noise, noise from adsorption and desorption of gaseous species [Ekinci 2004b], and extrinsic sources such as vibrational and instrumental (read-out) noise. For simplicity, we solely consider thermomechanical noise in the case of a clamped-clamped resonator driven at its critical amplitude (open-loop stability limit).

2.4.5.1 Inertial resonant sensors

The resonator sensitivity to axial loads (Equation (2.20)) is computed by evaluating the integrals in Equations (2.15) and (2.16).

$$SF_f = \frac{S}{2} f_0 \propto w^{-2}.t^{-1} \tag{2.38}$$

For a resonant accelerometer, since the axial load is proportional to the seismic mass M_S and to the acceleration γ, the sensitivity to acceleration is:

$$SF_\gamma \propto M_S.w^{-2}.t^{-1} \tag{2.39}$$

For a resonant gyroscope, since the axial load is proportional to the seismic mass M_S, its velocity V_S and to the angular rate Ω_R, the sensitivity to angular rate is:

$$SF_{\Omega_R} \propto F_S.Q_S.\omega_S^{-1}.w^{-2}.t^{-1} \tag{2.40}$$

where F_S is the seismic mass actuation force, ω_S is its angular resonance frequency and Q_S is its quality factor.
The frequency variance is computed as

$$\sigma_\omega = \sqrt{\int_0^{BW} S_\omega(\omega) d\omega} \tag{2.41}$$

Performing this integration for the case where $Q >> 1$ and $BW << \frac{\omega_0}{Q}$, we obtain

$$\sigma_\omega = \sqrt{S_\omega(\omega).BW} \propto w^{-2}.l^{\frac{1}{2}}.t^{-\frac{1}{2}} \tag{2.42}$$

Thus, the accelerometer and gyroscope resolutions are respectively:

$$\delta\gamma = \frac{\sigma_\omega}{SF_\gamma} \propto M_S^{-1}.l^{\frac{1}{2}}.t^{\frac{1}{2}} \tag{2.43}$$

$$\delta\Omega_R = \frac{\sigma_\omega}{SF_{\Omega_R}} \propto F_S^{-1}.Q_S^{-1}.\omega_S.l^{\frac{1}{2}}.t^{\frac{1}{2}} \tag{2.44}$$

2.4.5.2 Gas and mass resonant sensors

The resonator mass sensitivity (Equation (2.21)) is

$$SF_m = \frac{1}{2M_{eff}} f_0 \propto l^{-3}.t^{-1} \tag{2.45}$$

Thus, the mass sensor resolution is given by:

$$\delta m = \frac{\sigma_\omega}{SF_m} \propto w^{-2}.l^{\frac{7}{2}}.t^{\frac{1}{2}} \tag{2.46}$$

At equilibrium, the concentration resolution for gas sensors is given by:

$$\delta C = \frac{\delta m}{K_P V_P \rho_g} \propto w^{-3}.l^{\frac{5}{2}}.t^{\frac{1}{2}} \tag{2.47}$$

where K_P is the partition coefficient depending on the couple polymer-gas combination, V_P is the polymer layer volume and ρ_g is the density of the gas analyte.
Equations (2.43), (2.44), (2.46) and (2.47) demand some important comments:

- One surprising thing here is that the minimum detectable acceleration and angular rate are independent on the quality factor. This, of course is true if the PLL does not induce any error in the readout, ie if it can ideally lock in phase with the signal, and also if the resonator is driven at a quality factor-dependent amplitude, like the open loop stability limit, which sets the dynamic range of the resonator. But in terms of noise, the quality factor does not influence the result.

- The second surprising result concerning resonant accelerometers and gyroscopes is that the resolution is independent on the width of the resonator w. This is again not trivial, as one would think that the smaller the cross-section area, the more sensitive the resonator, which is true as the sensitivity scales like w^{-2}. But one would have also thought that the narrower the resonator, the more resolved the measure, which proves wrong as the frequency noise also scales like w^{-2}.

- In the case of resonant accelerometers and gyroscopes and for a fixed seismic mass design, if the resonator dimensions are proportionally scaled down with respect to a given scale factor $N_{sf} << 1$, the resolution is proportionally improved with respect to N_{sf}. Therefore, for resonant inertial sensors, M&NEMS design that involves MEMS parts (seismic Mass, anchors) and NEMS parts (resonators) is a great alternative to improve the performances of such sensors.

$$\frac{\delta\gamma(M\&NEMS)}{\delta\gamma(MEMS)} = \frac{\delta\Omega_R(M\&NEMS)}{\delta\Omega_R(MEMS)} = N_{sf} \tag{2.48}$$

- In the case of resonant mass sensors, if the resonator dimensions are proportionally scaled down with respect to a given scale factor $N_{sf} << 1$, the resolution is proportionally improved with respect to N_{sf}^2. It proves that nanomechanical resonators, with their high fundamental resonance frequencies, diminished active masses and tolerable force constants, are extremely sensitive to mass changes. Therefore, for resonant mass sensors, NEMS resonators are a great alternative to improve the performances of such sensors.

$$\frac{\delta m(NEMS)}{\delta m(MEMS)} = N_{sf}^2 \tag{2.49}$$

- For resonant gas sensors, for a constant resonator width, if the resonator length and thickness are proportionally scaled down with respect to a given scale factor $N_{sf} << 1$ while keeping an acceptable slenderness ratio for Euler-Bernoulli beam model validity, the concentration resolution is proportionally improved with respect to N_{sf}^3. It proves that nanomechanical resonators are a great alternative for ultimate gas measurements.

2.4.6 Linearity and Dynamic Range

Tables 2.2 and 2.3 show the importance of the dynamic range accelerometers and gyroscopes for several applications. Here, only resonant inertial sensors are considered (similar analysis can be done for resonant mass and gas sensors).

The limiting factor on the resonator full scale is the output nonlinearity. The latter, for a single resonant sensor, can be analyzed in several ways. Since this nonlinearity is due to the natural frequency behavior of the resonator (Equation (2.18)), let us examine the case when the higher order terms in the output-input expression become important. To do so, Equation (2.18) can be analyzed by taking a Taylors series expansion about the point F.S=0:

$$F = f_0 \left(1 + \frac{1}{2}FS - \frac{1}{8}F^2S^2 + \frac{1}{16}F^3S^3 + \dots\right) \tag{2.50}$$

A full scale linearity condition can be placed on the output such that the square term remains within a certain fraction of the linear term. If this fraction is denoted α, the condition can be written as:

$$\frac{F.S}{4} \leq \alpha \tag{2.51}$$

Which means that for a given nonlinearity α, the sensor full scale is given by:

$$F_{max} = \frac{4\alpha}{S} l^{-2}.w^3.t \tag{2.52}$$

In order to enhance the dynamic range, a differential resonant sensing topology can be used. It consists of two resonators with common-mode effects and respectively strained in tension and compression. This topology permits the cancellation of the quadratic nonlinearities in the output-input expression as well as the temperature variations in frequency. Therefore, the dynamic range becomes limited by the cubic term.

$$F_{max} = \frac{2\sqrt{2\alpha}}{S} \propto l^{-2}.w^3.t \tag{2.53}$$

The ratio between the dynamic ranges of both topologies is then:

$$\frac{F_{max}^{Diff}}{F_{max}^{1R}} = \frac{1}{\sqrt{2\alpha}} \tag{2.54}$$

In inertial sensors specifications, the nonlinearity α is typically $\leq 1\%$. Thus:

$$\frac{F_{max}^{Diff}}{F_{max}^{1R}} \geq 5\sqrt{2} \tag{2.55}$$

2.4.7 Physical Nonlinearities

The validity of Equation (2.11) is limited by the resonator physical nonlinearities. The mechanical nonlinearities are considered as a fundamental limit of the linear lower bound of the resonant sensor dynamic range [Cleland 2002]. Furthermore, the actuation force can bring additional nonlinearities into the resonator dynamics. Electrostatic actuation is a good example for spring softening nonlinearities (see chapter 3 for details).

Nanoscale mechanical resonant sensors offer a greatly enhanced performance that is unattainable with microscale devices. However, scaling down resonators from MEMS to NEMS makes nonlinearities quickly reachable [Cleland 2002] and drastically restrict the sensor resolution.

To underline this fact, let us write Equations (2.43), (2.44), (2.46) and (2.47) without restrictions on the displacement carrier power.

$$\delta\gamma = \frac{\sigma_\omega}{SF_\gamma} \propto M_S^{-1}.l^{\frac{1}{2}}.t^{\frac{1}{2}}.w.a_d^{-1}.Q^{-\frac{1}{2}} \tag{2.56}$$

$$\delta\Omega_R = \frac{\sigma_\omega}{SF_{\Omega_R}} \propto F_S^{-1}.Q_S^{-1}.\omega_S.l^{\frac{1}{2}}.t^{\frac{1}{2}}.w.a_d^{-1}.Q^{-\frac{1}{2}} \tag{2.57}$$

$$\delta m = \frac{\sigma_\omega}{SF_m} \propto w^{-1}.l^{\frac{7}{2}}.t^{\frac{1}{2}}.a_d^{-1}.Q^{-\frac{1}{2}} \tag{2.58}$$

$$\delta C = \frac{\delta m}{K_P V_P \rho_g} \propto w^{-2}.l^{\frac{5}{2}}.t^{\frac{1}{2}}.a_d^{-1}.Q^{-\frac{1}{2}} \tag{2.59}$$

To simplify the analysis of Equations (2.56), (2.57), (2.58) and (2.59) when the resonator dimensions are scaled down, we suppose that the quality factor Q is constant. Then, it is clear that nanomechanical resonators resolution depends on the drive oscillation. The latter is limited by the mechanical nonlinearity for thin clamped-clamped resonators.

Under this limit, Equations (2.43) and (2.44) show that proportionally scaling down the resonator improves the inertial sensor resolution. As the latter does not depend on the beam width for in-plane actuation, one can reduce only the beam length l and thickness t while keeping an acceptable slenderness ratio for the validity of the Euler-Bernoulli model.

For inertial, mass and gas resonant sensors, using this design rule permits the enhancement of the resolution device as explained in the section 2.4.5. Ultimate optimization depends on the drive amplitude of the resonator. Ideally, the resonator should be actuated to oscillate at the highest possible amplitude (below the pull-in for an electrostatic actuation). In open loop, the resonator is classically driven below its critical amplitude in order to ensure the stability of its dynamic response. This fundamental limit is set by the nonlinear dynamics of the resonator (details are in chapters 5 and 7).

However, when used as a practical sensor, the resonator is most of the time used as an oscillator, embedded in a feedback loop, or a PLL. In such closed loop operation, the phase is the control parameter of the system (the frequency is now an output) and hence stabilizes its dynamics: even in the non-linear regime, the frequency is a single valued function of the phase [Yurke 1995, Juillard 2008]. In other words, the steady state solution in the closed loop case is always stable.

Now, the question is: what is the most important issue when the resonator is driven beyond its critical amplitude in either open or closed loop? The answer is detailed below.

2.4.8 Nonlinearities and noise mixing

In a capacitive resonator, mechanical and electrostatic nonlinearities are analytically combined to show that low-frequency voltage drift in the sustaining amplifier is directly converted into a frequency shift in the oscillator output. Experimental evidence of this effect is presented in [Roessig 1997a], and it is shown that this is the dominant source of near-carrier frequency instability in tuning fork oscillators.

Besides, a significant near-carrier noise source is the aliasing of $\frac{1}{f}$-noise to carrier side-bands due to the mixing of low-frequency noise and carrier signal in the active circuit elements. Kaajakari et al [Kaajakari 2005a] showed that, in addition to amplifier nonlinearities, the electrostatic transduction commonly used for coupling to silicon resonators is inherently nonlinear and leads to aliasing of noise. This process is illustrated in Figure 2.27 that shows a schematic representation of an oscillator comprised of a resonator and sustaining amplifier. In addition to amplifying oscillation signal u_{ac}, the amplifier output may present a significant amount of low-frequency $\frac{1}{f}$-noise to the resonator input. A linear resonator element would effectively filter out this low-frequency noise, but nonlinearities in the resonator will lead to unwanted aliasing of the low-frequency noise to carrier side-bands. Thus, the capacitive coupling is expected to be intrinsically more prone to noise aliasing. A detailed analysis of the noise-mixing mechanisms can be found in [Kaajakari 2005a] where the capacitive force nonlinearity was found to be the dominant up-mixing mechanism in electrostatic transduction.

Since the capacitive transduction will be used in our devices, any source of frequency instability in the oscillator is detrimental to the noise behavior of the transducer, so it is important that these sources be understood and minimized or cancelled.

Practically, in order to avoid most of noise which reduces the resonant sensor performances, the resonator should be driven linearly beyond its fundamental critical amplitude. Therefore, for ultimate optimizations, one should investigate the open loop nonlinear dynamics of the resonator.

2.5 Summary

In this chapter, a short review of MEMS/NEMS inertial sensors as well as gas and mass sensors was presented. It has been shown that the resonant sensing technique benefits from being highly sensitive,

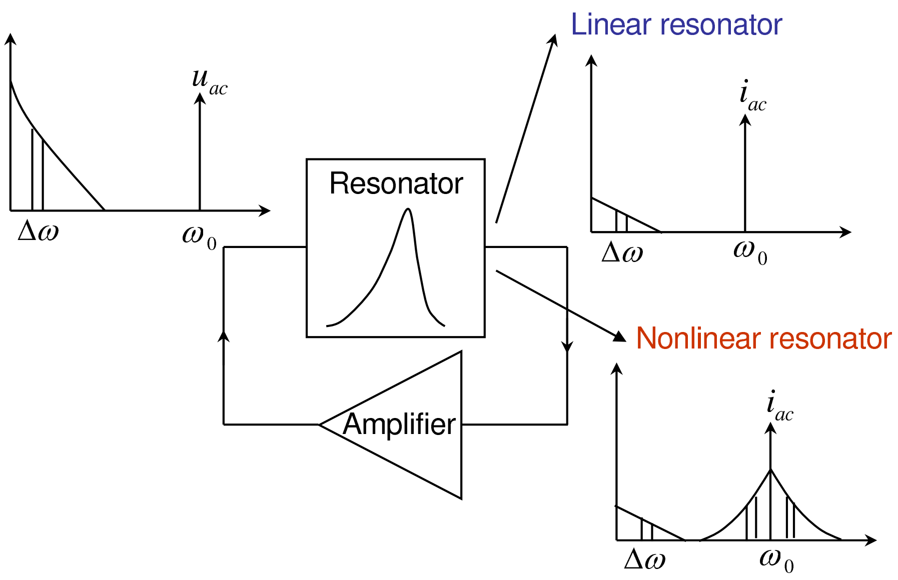

Figure 2.27: Schematic representation of noise aliasing in micro-oscillator. A linear resonator would filter out the amplifier low-frequency $\frac{1}{f}$ noise present at the resonator input, but nonlinear filtering element will result in noise aliasing [Kaajakari 2005a].

has the potential for large dynamic range, good linearity, low noise and potentially low power.

Particularly, for resonant gyroscopes, it simplifies the control implementation. For these reasons as well as to overcome the limitations of some detection techniques (such as the capacitive sensing) when sensors are scaled down from MEMS to NEMS, the resonant sensing technique was chosen among many other detection techniques.

A detailed analysis of resonant sensors has been presented in order to investigate the variation of the sensor performances when the resonator dimensions are scaled down from MEMS to NEMS. A discussion on resonant sensors resolution, showed the importance of adopting M&NEMS designs for resonant inertial sensors and the use of nanomechanical resonators for resonant gas and mass sensors. The case of clamped-clamped resonator was considered in order to give some design rules based on the analysis of the sensor resolution when the resonator is driven at its open loop stability limit. At this amplitude (few nanometres for NEMS resonators), it proves difficult to detect the output signal. Moreover, if the resonator is driven beyond its critical amplitude its frequency stability proportional to its oscillation amplitude in the nonlinear regime is significantly deteriorated.

Furthermore, for ultimate resonant measurements (mass spectrometry), we showed the importance of highly driving the resonator beyond its critical amplitude. However, when the resonator is used in the nonlinear regime in either open-loop or closed-loop, the physical nonlinearities mix the low-frequency noise and the carrier signal in the active circuit and lead to a significant near-carrier noise source called the aliasing of $\frac{1}{f}$-noise to carrier side-bands [Kaajakari 2005a]. Consequently, the resonant sensor performances are drastically reduced.

Being easily reachable for NEMS resonators, the nonlinear regime limits the performances of resonant sensors due to the noise mixing issue and alters the frequency stability of the sensor. Therefore, for ultimate sensing applications, the nonlinear dynamics of nanomechnical resonators [Lifshitz 2008] should be modelled using nonlinear methods which are the subject of chapter 3.

CHAPTER 3

Nonlinear dynamics and nonlinear methods

Contents

3.1 Introduction **47**

3.2 Sources of nonlinearities **47**

3.2.1 Beams 47

3.2.2 Cantilevers 49

3.3 Nonlinear methods **51**

3.3.1 Perturbation techniques 51

3.3.2 Numerical methods for periodic solutions 69

3.4 Summary **77**

3.1 Introduction

Nonlinearities in NEMS silicon resonators are caused by different effects. Depending on the resonator layout, different nonlinearities may be dominant in the resonator response. The nonlinearities can be of either mechanical or electrical origin. In this chapter, the sources of nonlinearities in NEMS resonators are sorted in cantilevers as well as clamped-clamped beams. These nonlinearities add complexity in the dynamic analysis of resonant sensors. Thus, the equations of motion become nonlinear and traditional methods are no more useful for such problems. The second part of this chapter is a review of quasianalytical methods (perturbation techniques) and numerical methods for nonlinear differential equations which are important for nonlinear modelling of resonant sensors.

3.2 Sources of nonlinearities

3.2.1 Beams

We consider the clamped-clamped Bernoulli beam shown in Figure 3.1 subjected to a viscous damping and actuated by an electric load $V(t) = V_{dc} + V_{ac}\cos(\Omega t)$, where V_{dc} is the DC polarization voltage, V_{ac} is the amplitude of the applied AC voltage, and Ω is the excitation frequency.

3.2.1.1 Mechanical nonlinearity

The mechanical nonlinearity in the resonator can be illustrated using a simple clamped-clamped beam resonator. As shown in Figure 3.1, the beam is forced to extend under the large vibration amplitude.

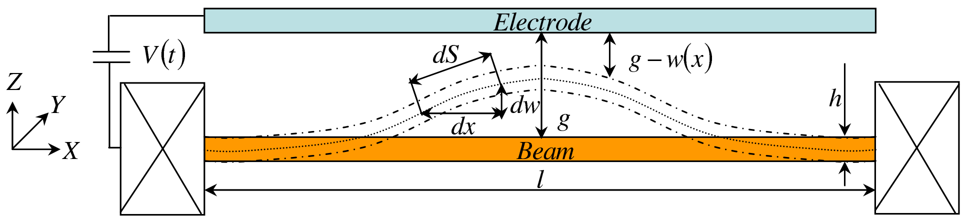

Figure 3.1: A schematic of an electrostatically actuated beam

The axial extension $T(w)$ depends on the transverse displacement w. It introduces additional stress to the beam, adding to the effective stiffness in the structure. As the vibration amplitude grows, the response peak moves up in the frequency due to the spring hardening effect [Mestrom 2008, Michon 2008]. $T(w)$ can be written as:

$$T(w) = Ebh\frac{\Delta l}{l} \tag{3.1}$$

where E is the silicon Young modulus, b, h and l are the beam thickness, width and length respectively. Moreover, after extension, the beam length becomes:

$$S = l + \Delta l = \int_0^l \sqrt{1 + \left[\frac{\partial w(x,t)}{\partial x}\right]^2} dx \tag{3.2}$$

Hence:

$$T(w) = \frac{Ebh}{l}\left\{\int_0^l \sqrt{1 + \left[\frac{\partial w(x,t)}{\partial x}\right]^2} dx - l\right\} \tag{3.3}$$

3.2.1.2 Electrostatic nonlinearity

By contrary with the mechanical hardening effect, the electrostatic nonlinearity usually makes the effective stiffness of the device smaller under the large vibration amplitude (it adds a negative electrostatic stiffness), leading to a frequency response that bends toward the lower frequency side as the driving force is increased.

Considering the clamped-clamped beam resonator shown in Figure 3.1, the net electrostatic force on the resonator is given by:

$$f_e = \frac{1}{2}\varepsilon_0 \frac{bV(t)^2}{(g - w(x,t))^2} \tag{3.4}$$

where ε_0 is the dielectric constant of the capacitor gap medium, b is the beam thickness and g is the gap thickness.

3.2.1.3 Equation of motion

We consider the following variables:

- The transverse displacement: $w(x,t)$
- The cross section rotation : $\theta(x,t) = \frac{\partial w}{\partial x}$
- the curvature : $\chi_f = \frac{\partial \theta}{\partial x}$
- The bending moment $M_b = EI\frac{\partial \chi_f}{\partial x}$

- The shear force T_s
- The viscous damping force $f_d = -\tilde{c}\frac{\partial w}{\partial t}$
- The mechanical nonlinear force $f_m = (\tilde{N} + T(w))\frac{\partial^2 w}{\partial x^2}$
- The electrostatic nonlinear force $f_e = \frac{1}{2}\varepsilon_0 \frac{bV^2}{(g-w)^2}$

The equations of local equilibrium are:

$$\left\{ \begin{array}{c} \rho bh\frac{\partial^2 w}{\partial t^2} = \frac{\partial T_s}{\partial x} + f_d + f_m + f_e \\ \\ \frac{\partial M_b}{\partial x} + T_s = 0 \end{array} \right\} \tag{3.5}$$

where ρ is the material density. Substituting the shear force expression into the first local equilibrium equation, we obtain the nonlinear Euler-Bernoulli equation, which is the commonly used approximate equation of motion for a thin beam [Landau 1986]:

$$EI\frac{\partial^4 w(x,t)}{\partial x^4} + \rho bh\frac{\partial^2 w(x,t)}{\partial t^2} + \tilde{c}\frac{\partial w(x,t)}{\partial t} - \left\{\tilde{N} + T(w(x,t))\right\}\frac{\partial^2 w(x,t)}{\partial x^2} = \frac{1}{2}\varepsilon_0\frac{bV(t)^2}{(g-w(x,t))^2} \tag{3.6}$$

where $V(t) = V_{dc} + V_{ac}\cos(\tilde{\Omega}t)$ and the boudary conditions are:

$$w(0,t) = w(l,t) = \frac{\partial w}{\partial x}(0,t) = \frac{\partial w}{\partial x}(l,t) = 0 \tag{3.7}$$

3.2.2 Cantilevers

We consider a cantilever beam (Figure 3.2) subjected to viscous dampings c_w and c_v and actuated by an electric load $V(t) = V_{dc} + V_{ac}\cos(\Omega t)$, where V_{dc} is the DC polarization voltage, V_{ac} is the amplitude of the applied AC voltage, and Ω is the excitation frequency.

3.2.2.1 Electrostatic nonlinearity

The electrostatic force is nonlinear with respect to the gap thickness which depends on two variables (the time t and the position along the cantilever beam s). In other words, the electrostatic nonlinearity in the case of the cantilever has the same origins as the clamped-clamped beam case [Shao 2008b]. Considering the cantilever beam resonator shown in Figure 3.2, the net electrostatic force on the resonator is given by:

$$f_e = \frac{1}{2}\varepsilon_0\frac{bV(t)^2}{(g-w(s,t))^2} \tag{3.8}$$

where s is the arclength and $w(s,t)$ is the transverse displacement of the cantilever.

3.2.2.2 Mechanical nonlinearity

A large deformation of a structure does not necessarily mean the presence of large strains. Under large rigid-body rotations, structures like cantilever beams undergo large deformations but small strains. Even when the rigid-body rotations are small, deformations will still be large for long structures. With respect to a coordinate system co-rotated with the rigid-body movement, the relative displacements are small and the problem becomes linearly elastic. But the large deformations give rise to geometric nonlinearities due to nonlinear curvature and/or midplane stretching, leading to nonlinear strain-displacement relations. In other words, for cantilever beams, nonlinearity results from a geometric effect: as the cantilever deflects its local stiffness and effective mass increase.

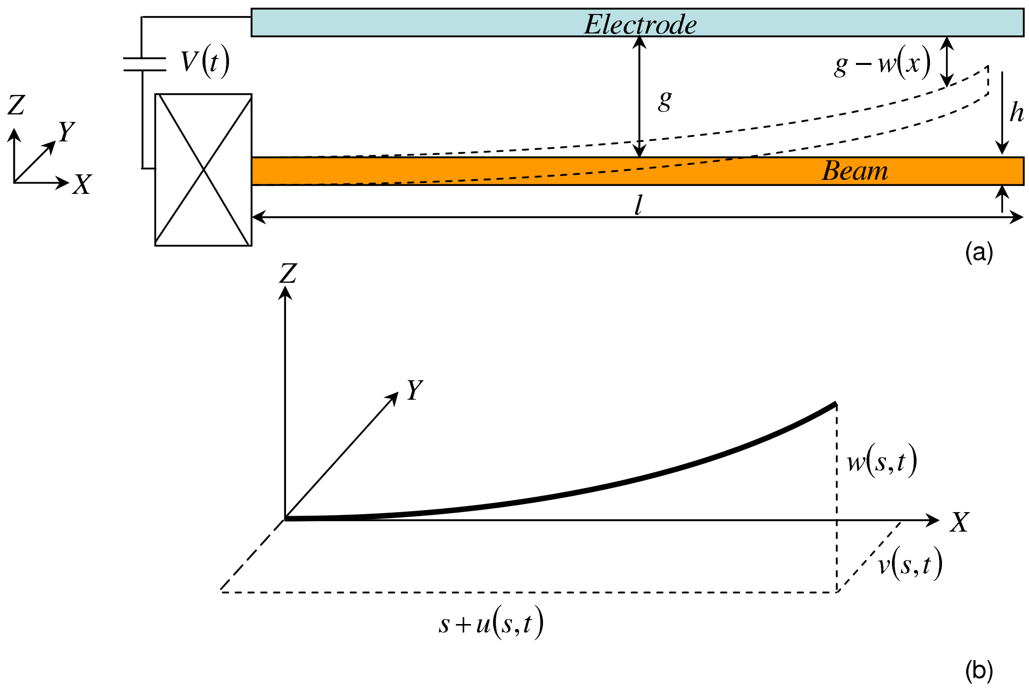

Figure 3.2: (a): A schematic of an electrostatically actuated cantilever beam. (b): Flexural-flexural motions of a fixed-free beam.

3.2.2.3 Equation of motion

In order to develop a model for the microcantilever beam, a slender uniform flexible beam is considered as shown in Figure 3.2. The beam is initially straight and it is clamped at one end and free at the other end. In addition, the beam follows the Euler-Bernoulli beam theory, where shear deformation and rotary inertia terms are negligible.

We follow a variational approach, based on the extended Hamilton principle. This approach has been used by Crespo da Silva and Glynn [Silva 1978a, Silva 1978b] and Crespo da Silva [Silva 1988a, Silva 1988b] in order to derive the nonlinear equations of motion describing the flexural-flexural vibrations of a cantilever beam as follow:

$$\begin{aligned} m\ddot{w} + c_w\dot{w} + D_\zeta w'''' &= (D_\nu - D_\zeta)\left[v''\int_1^s w''v''ds - v'''\int_0^s w"v'ds\right]' \\ &-\frac{(D_\nu - D_\zeta)^2}{D_\xi}\left(v''\int_0^s\int_l^s w''v''dsds\right)'' - D_\zeta\left\{w'\left(w'w''+v'v''\right)'\right\}' \\ &-\frac{1}{2}m\left\{w'\int_l^s\frac{\partial^2}{\partial t^2}\left[\int_0^s\left(w'^2+v'^2\right)ds\right]ds\right\}' + \frac{1}{2}\varepsilon_0\frac{bV(t)^2}{(g-w(s,t))^2} \end{aligned} \tag{3.9}$$

$$\begin{aligned} m\ddot{v} + c_v\dot{v} + D_\nu v'''' &= -(D_\nu - D_\zeta)\left[w''\int_l^s v''w''ds - w'''\int_0^s v"w'ds\right]' \\ &+\frac{(D_\nu - D_\zeta)^2}{D_\xi}\left(w''\int_0^s\int_l^s v''w''dsds\right)'' - D_\nu\left\{v'\left(v'v''+w'w''\right)'\right\}' \\ &-\frac{1}{2}m\left\{v'\int_l^s\frac{\partial^2}{\partial t^2}\left[\int_0^s\left(v'^2+w'^2\right)ds\right]ds\right\}' \end{aligned} \tag{3.10}$$

where D_ξ, D_ν and D_ζ are the principal stiffnesses of the beam (D_ξ is the torsional stiffness, while D_ζ and D_ν are the flexural stiffnesses). Primes and dots denote respectively the partial differentiation with respect to the arclength s and to the time t. The first three terms in the right-hand side of each equation are due to nonlinear expressions for the curvatures of the beam including the nonlinear coupling between the lateral displacements and torsion, while the fourth term, which involves a double time derivative, is the nonlinear inertial term.

The boundary conditions are given as

$$w(0,t) = v(0,t) = w'(0,t) = v'(0,t) = 0 \tag{3.11}$$

$$w''(l,t) = v''(l,t) = w'''(l,t) = v'''(l,t) = 0 \tag{3.12}$$

3.3 Nonlinear methods

As shown in section 3.2, the equation of motion of a resonator electrostatically actuated involves several nonlinear terms in both cases (clamped-clamped beams or cantilevers) due to the mechanical as well as electrostatic nonlinearities. The obtained PDE is highly nonlinear and in order to solve it, one possible method is the modal decomposition for which the linear undamped mode shapes are identified. These functions are used as a basis on which the nonlinear PDE is projected using the so called "Galerkin method" (details are in section 4.3). It permits the transformation of a nonlinear PDE into a system of coupled nonlinear ODE. Depending on the strength of the nonlinearities, the obtained nonlinear equations can be solved using analytical methods such as perturbation techniques or numerical methods such as shooting and continuation techniques.

3.3.1 Perturbation techniques

3.3.1.1 Introduction

Perturbation theory [Murdock 1991] comprises mathematical methods that are used to find an approximate solution to a problem which cannot be solved exactly, by starting from the exact solution of a related problem. Perturbation theory is applicable if the problem at hand can be formulated by adding a "small" term to the mathematical description of the exactly solvable problem.

Perturbation theory leads to an expression for the desired solution in terms of a power series in some "small" parameter that quantifies the deviation from the exactly solvable problem. The leading term in this power series is the analytical solution of the exactly solvable problem, while further terms describe the deviation of the solution from the linear problem. Formally, we have for the approximation to the full solution A, a series in the small parameter (here called ε), like the following:

$$A = \varepsilon^0 A_0 + \varepsilon^1 A_1 + \varepsilon^2 A_2 + \cdots \tag{3.13}$$

In this example, A_0 would be the known solution to the exactly solvable initial problem and $A_1, A_2, \cdots$ represent the "higher orders" which are found iteratively by some systematic procedure. For small ε these higher orders are presumed to become successively less important. An approximate "perturbation solution" is obtained by truncating the series, usually by keeping only the first two terms, $A_0 + \varepsilon A_1$, the initial solution and the "first order" perturbation correction.

3.3.1.2 Direct method

Formalism:

The asymptotic solution of the weakly-nonlinear scalar second-order differential equation

$$\frac{d^2y(t)}{dt^2}+y(t)+\varepsilon f\left\{y(t),\frac{dy(t)}{dt}\right\}=0 \tag{3.14}$$

for f smooth and ε small and positive is a classical problem of nonlinear oscillations [Minorsky 1947]. Using the initial conditions : $y(0)=1$ and $\frac{dy(0)}{dt}=0$

It is natural to seek an approximate solution as a truncation of the unique formal power series

$$y_\varepsilon(t)=\sum_{i=0}^{n}\varepsilon^i y_i(t) \tag{3.15}$$

The expansion for $y(t)$ directly implies those for $\frac{dy(t)}{dt}$ and $\frac{d^2y(t)}{dt^2}$, while the implied Maclaurin expansion for $f\{y(t),\frac{dy(t)}{dt}\}$ has the form :

$$\begin{aligned}f\left\{y_\varepsilon(t),\frac{dy_\varepsilon(t)}{dt}\right\}&=f\left\{y_0(t),\frac{dy_0(t)}{dt}\right\}+\varepsilon\frac{\partial f}{\partial y}\left\{y_0(t),\frac{dy_0(t)}{dt}\right\}y_1(t)\\&+\varepsilon\frac{\partial f}{\partial\frac{dy}{dt}}\left\{y_0(t),\frac{dy_0(t)}{dt}\right\}\frac{dy_1(t)}{dt}+\varepsilon^2(\cdots)\end{aligned} \tag{3.16}$$

From the coefficients of ε^i for $i=0$, 1 and 2, we thereby obtain the linear initial value problems

$$\frac{d^2y_0(t)}{dt^2}+y_0(t)=0,y_0(0)=1,\frac{dy_0(0)}{dt}=0 \tag{3.17}$$

$$\frac{d^2y_1(t)}{dt^2}+y_1(t)+f\{y_0(t),\frac{dy_0(t)}{dt}\}=0,y_1(0)=0,\frac{dy_1(0)}{dt}=0 \tag{3.18}$$

$$\frac{d^2y_2(t)}{dt^2}+y_2(t)+f_y\left\{y_0(t),\frac{dy_0(t)}{dt}\right\}y_1(t)+f_{\frac{dy}{dt}}\left\{y_0(t),\frac{dy_0(t)}{dt}\right\}\frac{dy_1(t)}{dt}=0,y_2(0)=0,\frac{dy_2(0)}{dt}=0 \tag{3.19}$$

More generally, the coefficient $y_i(t)$ for each $i\geq 1$ will satisfy an initial value problem of the form $\frac{d^2y_i(t)}{dt^2}+y_i(t)=g_{i-1}\left\{y_0(t),\frac{dy_0(t)}{dt},...,y_{i-1}(t),\frac{dy_{i-1}(t)}{dt}\right\}$ with trivial initial conditions at $t=0$ and with the forcing g_{i-1} being known successively. Variation of parameters immediately implies the unique coefficients :

$$y_i(t)=\int_0^t\sin(t-s)g_{i-1}\left\{y_0(s),\frac{dy_0(s)}{ds},...,y_{i-1}(s),\frac{dy_{i-1}(s)}{ds}\right\}ds \tag{3.20}$$

Thus

$$y_0(t)=\cos(t) \tag{3.21}$$

$$y_1(t)=-\int_0^t\sin(t-s)f\left(\cos(s),-\sin(s)\right)ds \tag{3.22}$$

$$y_2(t)=-\int_0^t\sin(t-s)\left\{\begin{array}{c}f_y\left(\cos(s),-\sin(s)\right)\int_0^s\sin(t-r)f\left(\cos(r),-\sin(r)\right)\\+f_{\frac{dy}{dt}}\left(\cos(s),-\sin(s)\right)\int_0^s\cos(t-r)f\left(\cos(r),-\sin(r)\right)\end{array}\right\}ds \tag{3.23}$$

Using Gronwall inequality estimates, it is quite simple to show that the series obtained (as well as those for its derivatives) converges on any finite t interval for ε sufficiently small [Murdock 1991, Smith 1985]. The stated conclusions also apply, without significant change, for nonautonomous equations :

$$\frac{d^2y(t)}{dt^2} + y(t) + \varepsilon f\left\{t, y(t), \frac{dy(t)}{dt}, \varepsilon\right\} = 0 \tag{3.24}$$

Limitations:

- The linear example
$$\frac{d^2y(t)}{dt^2} + y(t) - \varepsilon\sin(t) = 0 \tag{3.25}$$
has the exact two-term solution
$$y_\varepsilon(t) = \cos(t) + \frac{\varepsilon}{2}\left(\sin(t) - t\cos(t)\right) \tag{3.26}$$
It is well-defined for all bounded values of t, but the solution obviously becomes unbounded when $\varepsilon t \to \infty$. One says a singular perturbation problem arises when the regular perturbation method is no longer uniformly valid. The technique might, for example, break down (as in equation) for large t values or in the presence of boundary or interior layers [OMalley 1991]. One generally solves such problems using asymptotic series [Hardy 1949, Copson 1965, Ramis 1991] for which one typically uses only a few terms of the series and insists that the successive approximations so defined improve in the $\varepsilon \to 0$ limit. For equation , we would readily conclude that asymptotic convergence no longer holds when t becomes unbounded, since the second term dominates the first when $t >> O(\frac{1}{\varepsilon})$: One calls the second term secular, intending no negative connotation since it accurately reflects the needed correction to $\cos t$ and the limited time interval of the solution existence. More often in what follows, encountering secular terms will indicate the inappropriateness of a regular power series expansion when t becomes large.

- The Duffing equation
$$\frac{d^2y(t)}{dt^2} + y(t) + 2\varepsilon y(t)^3 = 0 \tag{3.27}$$
The Duffing equation [Struble 1964] describes the motion of a slightly nonlinear spring. It can be solved in terms of elliptic integrals, or more simply, one can integrate once to get a conserved energy and then separate variables to get the bounded implicit solution. Using the first order direct method, the solution of the Duffing equation can be written as
$$y_\varepsilon(t) = \cos(t) - \frac{\varepsilon}{8}\sin(t)\left(6t - t\sin(2t)\right) \tag{3.28}$$
For the Duffing equation, the regular perturbation method breaks down when $\varepsilon t \to \infty$, due to the appearance of false or spurious (i.e., misleading) secular terms. Because the exact solution is bounded, one must find a way of exorcising them from the regular perturbation series (if it is to retain its value as an asymptotic expansion as t increases without bound).

3.3.1.3 Poincaré-Lindstedt method

Correction of the direct technique:

To break the limitations of the direct technique, when the resolution reveals secular terms which restrict the existence of the solution to finished time intervals T, Lindstedt proposed in 1882 a method, which for certain differential equations, allows the elimination of these secular terms.

It is called Lindstedt-Poincaré method, Poincaré had demonstrated that Lindstedt series should be interpreted as asymptotic expressions. Lindstedt (1882) cleverly introduced the natural strained co-ordinate $\tau = \omega t$ and expanded ω in asymptotic series of ε.

$$\omega(\varepsilon) = \sum_{i=0}^{n} \varepsilon^i \omega_i \tag{3.29}$$

To highlight the performance of this method, it is used to solve the Duffing equation (3.27).
By applying the method of Lindstedt-Poincaré [Hu 2004] up to the third order, one obtains the following differential system:

$$y_0(\tau) + \omega_0^2 \frac{d^2 y_0(\tau)}{d\tau^2} = 0, y_0(0) = 1, \frac{dy_0(0)}{d\tau} = 0 \tag{3.30}$$

$$2y_0(\tau)^3 + y_1(\tau) + 2\omega_0\omega_1 \frac{d^2 y_0(\tau)}{d\tau^2} + \omega_0^2 \frac{d^2 y_1(\tau)}{d\tau^2} = 0, y_1(0) = 0, \frac{dy_1(0)}{d\tau} = 0 \tag{3.31}$$

$$\left\{ \begin{array}{c} 6y_0(\tau)^2 y_1(\tau) + y_2(\tau) + (\omega_1^2 + 2\omega_0\omega_2)\frac{d^2 y_0(\tau)}{d\tau^2} \\ \\ +2\omega_0\omega_1 \frac{d^2 y_1(\tau)}{d\tau^2} + \omega_0^2 \frac{d^2 y_2(\tau)}{d\tau^2} = 0, y_2(0) = \frac{dy_2(0)}{d\tau} = 0 \end{array} \right\} \tag{3.32}$$

$$\left\{ \begin{array}{c} 6y_0(\tau)\left\{y_1(\tau)^2 + y_0(\tau)y_2(\tau)\right\} + y_3(\tau) + 2(\omega_1\omega_2 + \omega_0\omega_3)\frac{d^2 y_0(\tau)}{d\tau^2} \\ \\ +(\omega_1^2 + 2\omega_0\omega_2)\frac{d^2 y_1(\tau)}{d\tau^2} + 2\omega_0\omega_1\frac{d^2 y_2(\tau)}{d\tau^2} + \omega_0^2\frac{d^2 y_3(\tau)}{d\tau^2}) = 0, y_3(0) = \frac{dy_3(0)}{d\tau} = 0 \end{array} \right\} \tag{3.33}$$

The solution of this system can be built in a recursive way. For each order $i\,(i \geq 1)$, the elimination of the secular terms permits the identification of the component ω_i of the series $\omega(\varepsilon)$.

Order 0 (solution of Equation (3.30)):

$$y_0(\tau) = \cos(\frac{\tau}{\omega_0}) \tag{3.34}$$

$y_0(\tau)$ and its second derivative are substituted into the differential equation of the first order expansion. After linearization of the trigonometric functions, Equation (3.31) becomes:

$$(\frac{3}{2} - \frac{2\omega_1}{\omega_0})\cos(\frac{\tau}{\omega_0}) + \frac{1}{2}\cos(\frac{3\tau}{\omega_0}) + y_1(\tau) + \omega_0^2\frac{d^2 y_1(\tau)}{d\tau^2} = 0 \tag{3.35}$$

Equation (3.35) contains secular terms that should be eliminated, which corresponds to conditioning the component ω_1 of the frequency asymptotic series.

$$(\frac{3}{2} - \frac{2\omega_1}{\omega_0})\cos(\frac{\tau}{\omega_0}) = 0 \Longrightarrow \omega_1 = \frac{3\omega_0}{4} \tag{3.36}$$

First order (solution of Equation (3.35)):

$$y_1(\tau) = \frac{1}{16}\left\{\cos(\frac{3\tau}{\omega_0}) - \cos(\frac{\tau}{\omega_0})\right\} \tag{3.37}$$

Then, $y_0(\tau), y_1(\tau)$, their second derivative as well as ω_1 are substituted into the differential equation of the second order expansion. After linearization of the trigonometric functions, Equation (3.32) becomes:

$$-(\frac{21}{32}+\frac{2\omega_2}{\omega_0})\cos(\frac{\tau}{\omega_0})-\frac{3}{4}\cos(\frac{3\tau}{\omega_0})+\frac{3}{32}\cos(\frac{5\tau}{\omega_0})+y_2(\tau)+\omega_0^2\frac{d^2y_2(\tau)}{d\tau^2}=0 \tag{3.38}$$

The elimination of the secular terms, permits the identification of ω_2

$$(\frac{21}{32}+\frac{2\omega_2}{\omega_0})\cos(\frac{\tau}{\omega_0})=0 \Longrightarrow \omega_2=\frac{-21\omega_0}{64} \tag{3.39}$$

Second order (solution of Equation (3.38)):

$$y_2(\tau)=\frac{1}{256}\left\{23\cos(\frac{\tau}{\omega_0})-24\cos(\frac{3\tau}{\omega_0})+\cos(\frac{5\tau}{\omega_0})\right\} \tag{3.40}$$

$y_0(\tau), y_1(\tau), y_2(\tau)$, their second derivative as well as ω_1 and ω_2 are substituted into the differential equation of the third order expansion. After linearization of the trigonometric functions, Equation (3.33) becomes:

$$(\frac{81}{128}+\frac{2\omega_3}{\omega_0})\cos(\frac{\tau}{\omega_0})+\frac{549}{512}\cos(\frac{3\tau}{\omega_0})-\frac{69}{256}\cos(\frac{5\tau}{\omega_0})+\frac{3}{256}\cos(\frac{7\tau}{\omega_0})+y_3(\tau)+\omega_0^2\frac{d^2y_3(\tau)}{d\tau^2}=0 \tag{3.41}$$

The elimination of the secular terms, permits the identification of ω_3

$$(\frac{81}{128}+\frac{2\omega_3}{\omega_0})\cos(\frac{\tau}{\omega_0})=0 \Longrightarrow \omega_3=\frac{81\omega_0}{256} \tag{3.42}$$

Third order (solution of Equation (3.41)):

$$y_3(\tau)=\frac{1}{4096}\left\{549\cos(\frac{3\tau}{\omega_0})-504\cos(\frac{\tau}{\omega_0})-46\cos(\frac{5\tau}{\omega_0})+\cos(\frac{7\tau}{\omega_0})\right\} \tag{3.43}$$

ω_0 is the frequency of the dynamic system modeled by the differential Equation (3.27) when $\varepsilon=0$. In our case : $\omega_0=1$. The Lindstedt-Poincaré method gives a third order general solution of Equation (3.27) in the form:

$$\left\{\begin{array}{c} y_\varepsilon(t)=y_0(\tau)+\varepsilon y_1(\tau)+\varepsilon^2y_2(\tau)+\varepsilon^3y_3(\tau)+O(\varepsilon^4) \\ \\ \tau=(1+\frac{3\varepsilon}{4}-\frac{21\varepsilon^2}{64}+\frac{81\varepsilon^3}{256})t+O(\varepsilon^4t) \end{array}\right\} \tag{3.44}$$

Inspecting Equation (3.44), the error is $O(1)$ when $t=O(\varepsilon^{-4})$ which is the same order than the first term. Thus, Equation (3.44) is not valid for $t\geq(\varepsilon^{-4})$. Moreover, if $t=O(\varepsilon^{-3})$, the error is $O(\varepsilon)$, and hence, the order of the second term.
Indeed, to determine an asymptotic expansion of the solution of Equation (3.27) up to the n^{th} order by using Lindstedt-Poincaré method, there is no need for the particular solution of the n^{th} differential equation. However, one should eliminate the secular terms up to the n^{th} order.

$$y_\varepsilon=\sum_{i=0}^{n-1}\varepsilon^iy_i\left\{t\sum_{i=0}^{n}\varepsilon^i\omega_i\right\}+O(\varepsilon^n) \tag{3.45}$$

Then, a valid asymptotic expansion for $t \leq O(\varepsilon^{-3})$ is :

$$y_\varepsilon = \left\{ \begin{array}{c} \cos[\left\{1 + \frac{3}{4}\varepsilon - \frac{15\varepsilon^2}{64} + \frac{123\varepsilon^3}{1024}\right\} t] \\ + \frac{\varepsilon}{16}\cos[3\left\{1 + \frac{3}{4}\varepsilon - \frac{15\varepsilon^2}{64} + \frac{123\varepsilon^3}{1024}\right\} t] \\ + \frac{\varepsilon^2}{256}\left\{ \begin{array}{c} \cos[5\left\{1 + \frac{3}{4}\varepsilon - \frac{15\varepsilon^2}{64} + \frac{123\varepsilon^3}{1024}\right\} t] \\ -21\cos[3\left\{1 + \frac{3}{4}\varepsilon - \frac{15\varepsilon^2}{64} + \frac{123\varepsilon^3}{1024}\right\} t] \end{array} \right\} + O(\varepsilon^3) \end{array} \right\} \tag{3.46}$$

Damped systems:

To illustrate the validity limits of Lindstedt-Poincaré method, a slightly damped linear oscillator described by the following equation is considered:

$$\frac{d^2y(t)}{dt^2} + y(t) + 2\varepsilon\frac{dy(t)}{dt} = 0 \tag{3.47}$$

The second order differential system obtained is:

$$y_0(\tau) + \omega_0^2\frac{d^2y_0(\tau)}{d\tau^2} = 0, y_0(0) = 1, \frac{dy_0(0)}{d\tau} = 0 \tag{3.48}$$

$$y_1(\tau) + 2\omega_0\frac{dy_0(\tau)}{d\tau} + 2\omega_0\omega_1\frac{d^2y_0(\tau)}{d\tau^2} + \omega_0^2\frac{d^2y_1(\tau)}{d\tau^2} = 0, y_1(0) = 0, \frac{dy_1(0)}{d\tau} = 0 \tag{3.49}$$

$$\left\{ \begin{array}{c} y_2(\tau) + 2\omega_1\frac{dy_0(\tau)}{d\tau} + \left[2\omega_0\omega_2 + \omega_1^2\right]\frac{d^2y_0(\tau)}{d\tau^2} \\ +\omega_0\left[2\frac{dy_1(\tau)}{d\tau} + 2\omega_1\frac{d^2y_1(\tau)}{d\tau^2} + \omega_0\frac{dy_2(0)}{d\tau}\right] = 0, y_2(0) = 0, \frac{dy_2(0)}{d\tau} = 0 \end{array} \right\} \tag{3.50}$$

$y_0(\tau)$ is the solution of Equation (3.48):

$$y_0(\tau) = \cos(\frac{\tau}{\omega_0}) \tag{3.51}$$

$\frac{dy_0(\tau)}{d\tau}, \frac{d^2y_0(\tau)}{d\tau^2}$ are substituted into the differential equation of the first order expansion. Equation 3.49 becomes :

$$-2\left[\sin(\frac{\tau}{\omega_0}) + \frac{\cos(\frac{\tau}{\omega_0})\omega_1}{\omega_0}\right] + y_1(\tau) + \omega_0^2\frac{d^2y_1(\tau)}{d\tau^2} = 0 \tag{3.52}$$

One obtains an equation which presents secular terms. A priori, it is impossible to conditionate the frequency components in order to cancel out the two resonating terms $\sin(\frac{\tau}{\omega_0})$ and $\cos(\frac{\tau}{\omega_0})$ knowing that $\omega_0 = 1$ as well as ω_1 are independent of t. Thus, the Lindstedt-Poincaré method validity is limited to conservative systems because secular terms cannot be eliminated due to damping.

3.3.1.4 Multiple time scales

Time scales dependency:

The solution of Equation (3.27) given by the Lindstedt-Poincaré method up to the third order can be written as:

$$y_\varepsilon = \left\{ \begin{array}{c} \cos[t + \frac{3}{4}\varepsilon t - \frac{15\varepsilon^2 t}{64} + \frac{123\varepsilon^3 t}{1024}] \\ + \frac{\varepsilon}{16}\cos[3t + \frac{9}{4}\varepsilon t - \frac{45\varepsilon^2 t}{64} + \frac{369\varepsilon^3 t}{1024}] \\ + \frac{\varepsilon^2}{256} \left\{ \begin{array}{c} \cos[5t + \frac{15}{4}\varepsilon t - \frac{75\varepsilon^2 t}{64} + \frac{615\varepsilon^3 t}{1024}] \\ -21\cos[3t + \frac{9}{4}\varepsilon t - \frac{45\varepsilon^2 t}{64} + \frac{369\varepsilon^3 t}{1024}] \end{array} \right\} + O(\varepsilon^3) \end{array} \right\} \tag{3.53}$$

Thus $y_\varepsilon(t) = y(t, \varepsilon) = y(t, \varepsilon t, \varepsilon^2 t, \varepsilon)$
By carrying out the expansion to higher order, we find that $y(t)$, besides the individual ε and t, depends on the combinations εt,$\varepsilon^2 t$,$\varepsilon^3 t$,$\varepsilon^4 t$,. Hence:

$$y_\varepsilon(t) = \tilde{y}(t, \varepsilon t, \varepsilon^2 t, \varepsilon^3 t, \varepsilon^4 t, ..., \varepsilon) = \tilde{y}(T_0, T_1, T_2, T_3, T_4, ..., \varepsilon) \tag{3.54}$$

The T_n are defined as: $\quad T_0 = t \quad T_1 = \varepsilon t \quad ... \quad T_n = \varepsilon^n t$
We note that the T_n represents different time scales because ε is a small parameter. For illustration, the watch example is considered: if $\varepsilon = \frac{1}{60}$, variations on the scale T_0 can be observed on the second arm, variations on the scale T_1 can be observed on the minute arm, and T_2 can be observed on the hour arm. Thus, T_0 represents a fast scale, T_1 represents a slower scale, T_2 represents an even slower scale and so on.
Now, instead of determining $y_\varepsilon(t)$ as a function of t, we determine $y_\varepsilon(t)$ as a function of $T_0, T_1, T_2, ...$. To this end, we change the independent variable in the original equation from t to $T_0, T_1, T_2, ...$. Using the chain rule, we have:

$$\frac{d}{dt} = \frac{\partial}{\partial T_0} + \varepsilon\frac{\partial}{\partial T_1} + \varepsilon^2\frac{\partial}{\partial T_2} + ... \tag{3.55}$$

$$\frac{d^2}{dt^2} = \frac{\partial^2}{\partial T_0^2} + 2\varepsilon\frac{\partial^2}{\partial T_0 \partial T_1} + \varepsilon^2\left[2\frac{\partial^2}{\partial T_0 \partial T_2} + \frac{\partial^2}{\partial T_1^2}\right] + ... \tag{3.56}$$

Damped nonlinear system:
We considerer the equation of a slightly damped Duffing oscillator:

$$\frac{d^2 y(t)}{dt^2} + y(t) + \varepsilon\left\{\alpha y(t)^3 + 2\mu\frac{dy(t)}{dt}\right\} = 0 \tag{3.57}$$

For convenience and equations simplicity, we use the following notation:

$y_i(T_0, T_1, T_2, \ldots, T_n) = y_i$

$\frac{\partial^k y_i(T_0,T_1,T_2,...,T_j,...,T_n)}{\partial T_j^k} = {y_i}^{(0,0,0,...,k,...,0)}$ where k is located at the place $j \in [0, n] \cap \mathbb{N}$

$\frac{\partial^k y_i(T_0,T_1,T_2,...,T_j,...,T_n)}{\partial T_0 \partial T_1 ... \partial T_k} = {y_i}^{(1,1,1,...,1,0,...,0)}$ where k is the length of the colored part.

$\frac{\partial^k y_i(T_0,T_1,T_2,...,T_j,...,T_n)}{\partial T_0^{p_0} \partial T_1^{p_1} \partial T_2^{p_2} ... \partial T_j^{p_j} ... \partial T_n^{p_n}} = {y_i}^{(p_0,p_1,p_2,...,p_j,...,p_n)}$ where $\sum p_i = k$

If we use the multiple time scales method [Sanchez 1996] and expand the asymptotic series up to the nth order ($y_\varepsilon(t) = \sum_{i=0}^n \varepsilon^i y_i(T_0, T_1, T_2, ...)$), the ordinary differential Equation (3.57) can be transformed into a system of n partial differential equations. Up to the third order, the obtained system

$$y_0 + {y_0}^{(2,0,0,0)} = 0 \tag{3.58}$$

$$\alpha {u_0}^3 + y_1 + 2\mu {y_0}^{(1,0,0,0)} + 2{y_0}^{(1,1,0,0)} + {y_1}^{(2,0,0,0)} = 0 \tag{3.59}$$

$$\begin{aligned} &3\alpha {y_0}^2 y_1 + y_2 + 2\mu {y_0}^{(0,1,0,0)} + {y_0}^{(0,2,0,0)} + 2\mu {y_1}^{(1,0,0,0)} \\ &\quad + 2{y_0}^{(1,0,1,0)} + 2{y_1}^{(1,1,0,0)} + {y_2}^{(2,0,0,0)} = 0 \end{aligned} \tag{3.60}$$

$$\begin{aligned} &3\alpha y_0 {y_1}^2 + 3\alpha {y_0}^2 y_2 + y_3 + 2\mu {y_0}^{(0,0,1,0)} + 2\mu {y_1}^{(0,1,0,0)} + 2{y_0}^{(0,1,1,0)} + {y_1}^{(0,2,0,0)} \\ &\quad + 2\mu {y_2}^{(1,0,0,0)} + 2{y_0}^{(1,0,0,1)} + 2{y_1}^{(1,0,1,0)} + 2{y_2}^{(1,1,0,0)} + {y_3}^{(2,0,0,0)} = 0 \end{aligned} \tag{3.61}$$

is solved in a recursive manner by substituting the solution of the i^{th} order equation into the $i+1^{th}$ order equation. The secular terms elimination at each order conditionates the phase and the amplitude of the system.

Order ε^0:

The solution of the first Equation (3.58) can be written as:

$$y_0 = A\cos(\Theta) \quad avec \;\; A = A[T_1, T_2, T_3] \;\; et \;\; \Theta = \Theta[T_0, T_1, T_2, T_3] \tag{3.62}$$

The expression of y_0 is substituted into Equation (3.58) in order to determinate the forms of A et Θ. Thus, we obtain:

$$\cos[\Theta]\left\{A\left(1 - \left[\Theta^{(1,0,0,0)}\right]^2\right) + A^{(2,0,0,0)}\right\} - \sin[\Theta]\left\{2A^{(1,0,0,0)}\Theta^{(1,0,0,0)} + A\Theta^{(2,0,0,0)}\right\} = 0 \tag{3.63}$$

$A^{(1,0,0,0)} = 0$ and $\Theta^{(1,0,0,0)} = \pm 1$. we chose $\Theta^{(1,0,0,0)} = 1$.Up to this order, y_0 can be written as :

$$y_0 = A\cos(\Theta) \quad avec \;\; A = A[T_1, T_2, T_3] \;\; et \;\; \Theta = T_0 + \Phi[T_1, T_2, T_3] \tag{3.64}$$

Order ε^1:

Now, knowing y_0, we substitute it into the differential Equation (3.59). Then, we linearize the trigonometric functions in order to identify the secular terms and obtain:

$$\frac{\cos[\Theta]}{4}\left\{3\alpha A^3 - 8A\Phi^{(1,0,0)}\right\} - 2\sin[\Theta]\left\{\mu A + A^{(1,0,0)}\right\} + \frac{1}{4}\alpha A^3\cos[3\Theta] + y_1 + y_1^{(2,0,0,0)} = 0 \tag{3.65}$$

In order to keep a bounded solution, the two first secular terms are eliminated, which conditionates the amplitude A and the phase Φ as follow:

$$\left(\begin{array}{c} 3\alpha A^3 - 8A\Phi^{(1,0,0)} = 0 \Rightarrow \Phi^{(1,0,0)} = \frac{3}{8}\alpha A^2 \\ \\ \mu A + A^{(1,0,0)} = 0 \Rightarrow A^{(1,0,0)} = -\mu A \end{array}\right) \tag{3.66}$$

Then, a particular solution of Equation (3.59) without secular terms is determinated as:

$$y_1 = \frac{1}{32}\alpha A^3\cos[3\Theta] \tag{3.67}$$

Ordre ε^2:

Following the same algorithm, the differential Equation (3.60) becomes:

$$\left(\begin{array}{c} \cos[\Theta]\left\{\frac{3}{128}A^5\alpha^2 + 2\mu A^{(1,0,0)} - A\left(2\Phi^{(0,1,0)} + \left[\Phi^{(1,0,0)}\right]^2\right) + A^{(2,0,0)}\right\} \\ \\ -2\sin[\Theta]\left\{A^{(0,1,0)} + A\left(\mu\Phi^{(1,0,0)} + \frac{1}{2}\Phi^{(2,0,0)}\right) + A^{(1,0,0)}\Phi^{(1,0,0)}\right\} \\ \\ +\frac{3}{64}A^3\alpha\cos[3\Theta]\left\{A^2\alpha - 12\Phi^{(1,0,0)}\right\} - \frac{3}{16}A^2\alpha\sin[3\Theta]\left\{A\mu + 3A^{(1,0,0)}\right\} \\ \\ +\frac{3}{128}A^5\alpha^2\cos[5\Theta] + y_2 + {y_2}^{(2,0,0,0)} = 0 \end{array}\right) \tag{3.68}$$

The partial derivatives of the amplitude A and the phase Φ with respect to the time scale T_1 are used in order to simplify Equation (3.68). Up to the order ε^1, the first derivative of A and Φ with respect to T_1(Equations (3.66)) have already been determinated. The second derivatives are deduced as follow:

$$\left\{ \begin{array}{c} \Phi^{(1,0,0)} = \frac{3}{8}\alpha A^2 \\ \\ A^{(1,0,0)} = -\mu A \end{array} \right\} \Longrightarrow \left\{ \begin{array}{c} \Phi^{(2,0,0)} = \frac{3}{4}\alpha A A^{(1,0,0)} \\ \\ A^{(2,0,0)} = -\mu A^{(1,0,0)} \end{array} \right\} \Longrightarrow \left\{ \begin{array}{c} \Phi^{(2,0,0)} = -\frac{3}{4}\alpha\mu A^2 \\ \\ A^{(2,0,0)} = \mu^2 A \end{array} \right\} \tag{3.69}$$

Equation (3.68) is simplified as follow:

$$\left(\begin{array}{c} 2\sin[\Theta]\left(\frac{3}{8}A^3\alpha\mu - A^{(0,1,0)}\right) - \cos[\Theta]\left(A\left[\frac{15}{128}A^4\alpha^2 + \mu^2 + 2\Phi^{(0,1,0)}\right]\right) \\ \\ -\frac{21}{128}A^5\alpha^2\cos[3\Theta] + \frac{3}{8}A^3\alpha\mu\sin[3\Theta] + \frac{3}{128}A^5\alpha^2\cos[5\Theta] \\ \\ +y_2 + y_2{}^{(2,0,0,0)} = 0 \end{array} \right) \tag{3.70}$$

The elimination of the secular terms conditionate the partial derivatives of A and ϕ with respect to T_2 in order to keep a bounded solution.

$$\left\{ \begin{array}{c} A^{(0,1,0)} = \frac{3}{8}\alpha\mu A^3 \\ \\ \Phi^{(0,1,0)} = -\frac{1}{2}\mu^2 - \frac{15}{256}\alpha^2 A^4 \end{array} \right\} \tag{3.71}$$

Then, a particular solution of Equation (3.70) is determinated.

$$y_2 = \frac{1}{1024}\alpha^2 A^5 \left\{\cos[5\Theta] - 21\cos[3\Theta]\right\} + \frac{3}{64}\alpha\mu A^3 \sin[3\Theta] \tag{3.72}$$

Ordre ε^3:
Knowing y_0, y_1, y_2 and their derivatives, the differential Equation (3.61) becomes:

$$\left(\begin{array}{c} \cos[\Theta]\left\{2A^{(1,1,0)} - \frac{57}{4096}A^7\alpha^3 - 2A\Phi^{(0,0,1)} + 2\mu A^{(0,1,0)} - 2A\Phi^{(0,1,0)}\Phi^{(1,0,0)}\right\} \\ \\ +\sin[\Theta]\left\{ \begin{array}{c} \frac{9}{256}A^5\alpha^2\mu - 2\left(A^{(0,0,1)} + A\mu\Phi^{(0,1,0)}\right) \\ \\ -2\left(\Phi^{(0,1,0)}A^{(1,0,0)} + A^{(0,1,0)}\Phi^{(1,0,0)} + A\Phi^{(1,1,0)}\right) \end{array} \right\} \\ \\ +\cos[3\Theta]\left\{ \begin{array}{c} \frac{3}{32}A\alpha A^{(1,0,0)}\left(11A\mu + 2A^{(1,0,0)}\right) + \frac{9}{512}A^3\alpha\Phi^{(1,0,0)}\left(21A^2\alpha - 16\Phi^{(1,0,0)}\right) \\ \\ -\frac{3}{4096}A^2\alpha\left(41A^5\alpha^2 - 384A\mu^2 + 768A\Phi^{(0,1,0)} - 128A^{(2,0,0)}\right) \end{array} \right\} \\ \\ +\sin[3\Theta]\left\{ \begin{array}{c} \frac{99}{512}A^5\alpha^2\mu - \frac{9}{16}A^2\alpha A^{(0,1,0)} + \frac{315}{512}A^4\alpha^2 A^{(1,0,0)} \\ \\ -\frac{3}{32}A^2\alpha\Phi^{(1,0,0)}\left(11A\mu + 6A^{(1,0,0)}\right) - \frac{3}{32}A^3\alpha\Phi^{(2,0,0)} \end{array} \right\} \\ \\ -\frac{A^5\alpha^2}{2048}\cos[5\Theta]\left\{27A^2\alpha + 100\Phi^{(1,0,0)}\right\} + \frac{1}{512}A^4\alpha^2\sin[5\Theta]\left\{13A\mu - 25A^{(1,0,0)}\right\} \\ \\ +\frac{3}{2048}A^7\alpha^3\cos[7\Theta] + y_3 + y_3{}^{(2,0,0,0)} = 0 \end{array} \right) \tag{3.73}$$

In order to simplify Equation (3.73), we need the partial derivatives of the amplitude A and the phase Φ with respect to the time scales T_1 and T_2. The previous expansions of order ε^1 and ε^2 gave the partial derivatives of A and Φ with respect to T_1 and T_2(Equations (3.66) and (3.71)). The mixed derivatives are deduced as follow:

$$\left\{ \left\{ \begin{array}{c} A^{(1,0,0)} = -\mu A \\ \Phi^{(1,0,0)} = \frac{3}{8}\alpha A^2 \\ A^{(0,1,0)} = \frac{3}{8}\alpha\mu A^3 \\ \Phi^{(0,1,0)} = -\frac{1}{2}\mu^2 - \frac{15}{256}\alpha^2 A^4 \end{array} \right\} \Rightarrow \left\{ \begin{array}{c} A^{(1,1,0)} = \left[A^{(1,0,0)}\right]^{(0,1,0)} = [-\mu A]^{(0,1,0)} \\ A^{(1,1,0)} = -\frac{3}{8}\alpha\mu^2 A^3 \\ \Phi^{(1,1,0)} = \left[\Phi^{(1,0,0)}\right]^{(0,1,0)} = \left[\frac{3}{8}\alpha A^2\right]^{(0,1,0)} \\ \Phi^{(1,1,0)} = \frac{9}{32}\alpha^2\mu A^4 \end{array} \right\} \right\} \tag{3.74}$$

Then, Equation (3.73) is simplified:

$$\left(\begin{array}{c} \cos[\Theta]\left\{A[\frac{123}{4096}A^6\alpha^3 + \frac{3}{8}A^2\alpha\mu^2 - 2\Phi^{(0,0,1)}]\right\} - \sin[\Theta]\left\{\frac{207}{256}A^5\alpha^2\mu + 2A^{(0,0,1)}\right\} \\ +\left\{\frac{417}{4096}A^7\alpha^3 - \frac{3}{16}A^3\alpha\mu^2\right\}\cos[3\Theta] - \frac{189}{256}A^5\alpha^2\mu\sin[3\Theta] \\ -\frac{129}{4096}A^7\alpha^3\cos[5\Theta] + \frac{19}{256}A^5\alpha^2\mu\sin[5\Theta] \\ +\frac{3}{2048}A^7\alpha^3\cos[7\Theta] + y_2 + y_2{}^{(2,0,0,0)} = 0 \end{array} \right) \tag{3.75}$$

The elimination of the secular terms permits the identification of the partial derivatives of A and Φ with respect to T_3 as follow:

$$\left\{ \begin{array}{c} A^{(0,0,1)} = -\frac{207}{512}\alpha^2\mu A^5 \\ \Phi^{(0,0,1)} = \frac{123}{8192}A^6\alpha^3 + \frac{3}{16}A^2\alpha\mu^2 \end{array} \right\} \tag{3.76}$$

After secular term elimination, a particular solution of Equation (3.75) is:

$$y_3 = \frac{\alpha A^3}{98304}\left\{ \begin{array}{c} \left(1251A^4\alpha^2 - 2304\mu^2\right)\cos[3\Theta] - 129A^4\alpha^2\cos[5\Theta] \\ +3A^4\alpha^2\cos[7\Theta] - 9072A^2\alpha\mu\sin[3\Theta] + 304A^2\alpha\mu\sin[5\Theta] \end{array} \right\} \tag{3.77}$$

Using the multiple time scales method, the complete solution of (3.57) up to the third order can be written as:

$$y_\varepsilon = y_0 + \varepsilon y_1 + \varepsilon^2 y_2 + \varepsilon^3 y_3 + +O\left(\varepsilon^4\right) \tag{3.78}$$

Hence:

$$y_\varepsilon = \left\{ \begin{array}{c} A\cos(\Theta) + \frac{\varepsilon}{32}\alpha A^3\cos[3\Theta] + \\ \varepsilon^2\left\{\frac{1}{1024}\alpha^2 A^5\left\{\cos[5\Theta] - 21\cos[3\Theta]\right\} + \frac{3}{64}\alpha\mu A^3\sin[3\Theta]\right\} \\ +\frac{\varepsilon^3}{98304}\alpha A^3\left\{ \begin{array}{c} \left(1251A^4\alpha^2 - 2304\mu^2\right)\cos[3\Theta] - 129A^4\alpha^2\cos[5\Theta] \\ +3A^4\alpha^2\cos[7\Theta] - 9072A^2\alpha\mu\sin[3\Theta] + 304A^2\alpha\mu\sin[5\Theta] \end{array} \right\} + O\left(\varepsilon^4\right) \end{array} \right. \tag{3.79}$$

where:

$$\begin{Bmatrix} \frac{\mathrm{dA}}{\mathrm{dt}} = \varepsilon A^{(1,0,0)} + \varepsilon^2 A^{(0,1,0)} + \varepsilon^3 A^{(0,0,1)} + O\left(\varepsilon^4\right) \\ \frac{\mathrm{d}\Theta}{\mathrm{dt}} = 1 + \varepsilon \Phi^{(1,0,0)} + \varepsilon^2 \Phi^{(0,1,0)} + \varepsilon^3 \Phi^{(0,0,1)} + O\left(\varepsilon^4\right) \end{Bmatrix}$$

$$\Downarrow \tag{3.80}$$

$$\begin{Bmatrix} \frac{\mathrm{dA}}{\mathrm{dt}} = -\varepsilon \mu A + \frac{3}{8}\varepsilon^2 \alpha \mu A^3 - \frac{207}{512}\varepsilon^3 \alpha^2 \ \mu A^5 + O\left(\varepsilon^4\right) \\ \frac{\mathrm{d}\Theta}{\mathrm{dt}} = 1 + \frac{3}{8}\varepsilon \alpha \ A^2 + \frac{\varepsilon^2}{256}\left(-128\mu^2 - 15\alpha^2 A^4\right) + \frac{3\varepsilon^3}{8192}\left(512\alpha\mu^2 A^2 + 41\alpha^3 A^6\right) + O\left(\varepsilon^4\right) \end{Bmatrix}$$

In the case $\mu = 0$ (conservative system) and $\alpha = 2$ (the Equation (3.57) becomes the same as Equation (3.27) already solved using second order Lindstedt-Poincaré method), the solution of Equation (3.57) up to the third order of the multiple time scales method is:

$$y_\varepsilon = \begin{Bmatrix} A\cos(\Theta) + \frac{\varepsilon}{16}A^3\cos[3\Theta] + \frac{\varepsilon^2}{256}A^5\left\{\cos[5\Theta] - 21\cos[3\Theta]\right\} \\ +\frac{\varepsilon^3}{12288}A^7\left\{1251\cos[3\Theta] - 129\cos[5\Theta] + 3\cos[7\Theta]\right\} + O\left(\varepsilon^4\right) \end{Bmatrix} \tag{3.81}$$

where:

$$\begin{Bmatrix} \frac{\mathrm{dA}}{\mathrm{dt}} = O\left(\varepsilon^4\right) \\ \frac{\mathrm{d}\Theta}{\mathrm{dt}} = 1 + \frac{3}{4}\varepsilon \ A^2 - \frac{15\varepsilon^2}{64}A^4 + \frac{123\varepsilon^3}{1024}A^6 + O\left(\varepsilon^4\right) \end{Bmatrix} \tag{3.82}$$

Using the initial conditions $A(0) = 1$ and $\Theta(0) = 0$, the solution of Equation (3.57) can be written as:

$$y_\varepsilon = \begin{Bmatrix} \cos[\left\{1 + \frac{3}{4}\varepsilon - \frac{15\varepsilon^2}{64} + \frac{123\varepsilon^3}{1024}\right\}t] \\ +\frac{\varepsilon}{16}\cos[3\left\{1 + \frac{3}{4}\varepsilon - \frac{15\varepsilon^2}{64} + \frac{123\varepsilon^3}{1024}\right\}t] \\ +\frac{\varepsilon^2}{256}\begin{Bmatrix} \cos[5\left\{1 + \frac{3}{4}\varepsilon - \frac{15\varepsilon^2}{64} + \frac{123\varepsilon^3}{1024}\right\}t] \\ -21\cos[3\left\{1 + \frac{3}{4}\varepsilon - \frac{15\varepsilon^2}{64} + \frac{123\varepsilon^3}{1024}\right\}t] \end{Bmatrix} \\ +\frac{\varepsilon^3}{12288}\begin{Bmatrix} 1251\cos[3\left\{1 + \frac{3}{4}\varepsilon - \frac{15\varepsilon^2}{64} + \frac{123\varepsilon^3}{1024}\right\}t] \\ -129\cos[5\left\{1 + \frac{3}{4}\varepsilon - \frac{15\varepsilon^2}{64} + \frac{123\varepsilon^3}{1024}\right\}t] \\ +3\cos[7\left\{1 + \frac{3}{4}\varepsilon - \frac{15\varepsilon^2}{64} + \frac{123\varepsilon^3}{1024}\right\}t] \end{Bmatrix} + O\left(\varepsilon^4 t\right) \end{Bmatrix} \tag{3.83}$$

The same error analysis already done for Lindstedt-Poincaré method, permits the elimination of the last term to get exactly the same asymptotic expansion of the solution as in Equation (3.46).

$$y_\varepsilon = \left\{ \begin{array}{c} \cos[\left\{1+\frac{3}{4}\varepsilon-\frac{15\varepsilon^2}{64}+\frac{123\varepsilon^3}{1024}\right\}t] \\ +\frac{\varepsilon}{16}\cos[3\left\{1+\frac{3}{4}\varepsilon-\frac{15\varepsilon^2}{64}+\frac{123\varepsilon^3}{1024}\right\}t] \\ +\frac{\varepsilon^2}{256}\left\{ \begin{array}{c} \cos[5\left\{1+\frac{3}{4}\varepsilon-\frac{15\varepsilon^2}{64}+\frac{123\varepsilon^3}{1024}\right\}t] \\ -21\cos[3\left\{1+\frac{3}{4}\varepsilon-\frac{15\varepsilon^2}{64}+\frac{123\varepsilon^3}{1024}\right\}t] \end{array} \right\} + O(\varepsilon^3) \end{array} \right\} \tag{3.84}$$

3.3.1.5 The averaging method

It is supposed here that the fast effects are oscillating. A long time ago, the averaging method was used in celestial mechanics in order to determine the evolution of the planetary orbits under the influence of the mutual disturbances between planets and to study the stability of the solar system.

The parameter variation method:

Let us consider again the slightly damped nonlinear Duffing oscillator described in Equation (3.57). When $\varepsilon = 0$, the solution of Equation (3.57) is:

$$y(t) = A\cos(t+\beta) \tag{3.85}$$

A and β are integration constants that could be considered as parameters. The derivative of $y(t)$ with respect to the time t is immediately deduced.

$$\frac{dy(t)}{dt} = -A\sin(t+\beta) \tag{3.86}$$

When $\varepsilon \neq 0$, we assume that the solution of Equation (3.57) keeps the same form given by Equation (3.85), where the amplitude A and the phase β are time-varying functions. In other words, we consider Equation (3.85) as a transformation from $y(t)$ to $A(t)$ and $\beta(t)$. This is why this approach is called the method of variation of parameters. Using this approach, we note that we have two Equations (3.57) et (3.85) for the three unknowns $y(t)$, $A(t)$ and $\beta(t)$. Hence, we have the freedom to impose a third condition that must be independent of Equations (3.57) and (3.85). This arbitrariness can be used to advantage, namely to produce a simple and convenient transformation. Out of all possible conditions, we choose to impose the Equation (3.86), thereby assuming that $y(t)$ as well as $\frac{dy(t)}{dt}$ have the same form as the linear case. This condition leads to a convenient transformation because it gives two sets of first-order differential equations for A and β.

Differentiating Equation (3.85) with respect to t and recalling that A and β are functions of t, we obtain:

$$\frac{dy(t)}{dt} = -A(t)\sin(t+\beta(t)) + \frac{dA(t)}{dt}\cos(t+\beta(t)) - A(t)\frac{d\beta(t)}{dt}\sin(t+\beta(t)) \tag{3.87}$$

Comparing Equations (3.87) and (3.86), we conclude that:

$$\frac{dA(t)}{dt}\cos(t+\beta(t)) - A(t)\frac{d\beta(t)}{dt}\sin(t+\beta(t)) = 0 \tag{3.88}$$

Differentiating Equation (3.86) with respect to t, we have:

$$\frac{d^2y(t)}{dt^2} = -A(t)\cos(t+\beta(t)) - \frac{dA(t)}{dt}\sin(t+\beta(t)) - A(t)\frac{d\beta(t)}{dt}\cos(t+\beta(t)) \tag{3.89}$$

Substituting $y(t)$ and $\frac{d^2y(t)}{dt^2}$ from Equations (3.85) and (3.89) into Equation (3.57), we obtain:

$$\frac{dA(t)}{dt}\sin(t+\beta(t))+A(t)\frac{d\beta(t)}{dt}\cos(t+\beta(t))=\varepsilon\left\{\alpha A^3\cos^3(t+\beta(t))-2\mu A\sin(t+\beta(t))\right\} \tag{3.90}$$

We note that Equations (3.88) and (3.90) constitute a system of two first order differential equations for $\frac{dA(t)}{dt}$ and $\frac{d\beta}{dt}$. They can be simplified if we multiply Equation (3.88) by $\cos(t+\beta(t))$ and equation(3.90) by $\sin(t+\beta(t))$, then, add the results in order to determine $\frac{dA(t)}{dt}$ as follow:

$$\frac{dA(t)}{dt}=\varepsilon\sin(t+\beta(t))\left\{\alpha A^3\cos^3(t+\beta(t))-2\mu A\sin(t+\beta(t))\right\} \tag{3.91}$$

Substituting $\frac{dA(t)}{dt}$ into Equation (3.88) and solving, we determine $\frac{d\beta}{dt}$.

$$\frac{d\beta(t)}{dt}=\varepsilon\cos(t+\beta(t))\left\{\alpha A^2\cos^3(t+\beta(t))-2\mu\sin(t+\beta(t))\right\} \tag{3.92}$$

If $A\neq 0$. Thus, the original second order Equation (3.57) for $y(t)$ has been replaced by two first order Equations (3.91) and (3.92) for $A(t)$ and $\beta(t)$. It is notable that no approximations have been made in deriving Equations (3.91) and (3.92). The latter are more nonlinear than the original Equation (3.57). Nevertheless, if ε is small, the major parts of $A(t)$ and $\beta(t)$ vary more slowly than $y(t)$ with respect to t. Thus, the analytical advantage of the variation of parameters approach can be used in a perturbation method such as the averaging method.

The first order averaging:

Using the following trigonometric identities,

$$\sin\phi\cos\phi=\frac{1}{2}\sin 2\phi \tag{3.93}$$

$$\sin^2\phi=\frac{1}{2}-\frac{1}{2}\cos 2\phi \tag{3.94}$$

$$\sin\phi\cos^3\phi=\frac{1}{4}\sin 2\phi+\frac{1}{8}\sin 4\phi \tag{3.95}$$

$$\cos^4\phi=\frac{3}{8}+\frac{1}{2}\cos 2\phi+\frac{1}{8}\cos 4\phi \tag{3.96}$$

Equations (3.91) and (3.92) become:

$$\frac{dA(t)}{dt}=\frac{1}{8}\varepsilon A\left\{-8\mu+8\mu\cos 2\phi+2\alpha A^2\sin 2\phi+\alpha A^2\sin 4\phi\right\} \tag{3.97}$$

$$\frac{d\beta(t)}{dt}=\frac{1}{8}\varepsilon\left\{3\alpha A^2+4\alpha A^2\cos 2\phi-8\mu\sin 2\phi+\alpha A^2\cos 4\phi\right\} \tag{3.98}$$

where $\phi=t+\beta$. Since $-1\leq\sin n\phi\leq 1$ and $-1\leq\cos n\phi\leq 1$, $\frac{dA(t)}{dt}=O(\varepsilon)$ and $\frac{d\beta(t)}{dt}=O(\varepsilon)$ if the amplitude A is bounded. Thus, the major parts of A and β are slowly time-varying functions if ε is small. Then, the amplitude A and the phase β change very little during the time interval $[0,\pi]$ and,

as a first approximation, they can be considered constant in the interval $[0, \pi]$.
We average the right-hand sides of Equations (3.97) and (3.98) over the interval $[0, \pi]$ and obtain:

$$\frac{dA(t)}{dt} = \frac{1}{\pi}\int_0^{\pi}\left[\frac{1}{8}\varepsilon A\left\{-8\mu + 8\mu\cos 2\phi + 2\alpha A^2\sin 2\phi + \alpha A^2 \sin 4\phi\right\}\right]d\phi \tag{3.99}$$

$$\frac{d\beta(t)}{dt} = \frac{1}{\pi}\int_0^{\pi}\left[\frac{1}{8}\varepsilon\left\{3\alpha A^2 + 4\alpha A^2\cos 2\phi - 8\mu\sin 2\phi + \alpha A^2 \cos 4\phi\right\}\right]d\phi \tag{3.100}$$

Hence:

$$\frac{dA(t)}{dt} = -\varepsilon\mu A \tag{3.101}$$

$$\frac{d\beta(t)}{dt} = \frac{3}{8}\varepsilon\alpha A^2 \tag{3.102}$$

Since $\phi = t + \beta$, then

$$\frac{dA(t)}{dt} = -\varepsilon\mu A \tag{3.103}$$

$$\frac{d\phi(t)}{dt} = 1 + \frac{d\beta(t)}{dt} = 1 + \frac{3}{8}\varepsilon\alpha A^2 \tag{3.104}$$

We found exactly the same results as those obtained with the method of multiple time scales up to order ε^1(see Equation (3.66)).

Assuming the initial conditions $\left\{\begin{array}{c} A(0) = 1 \\ \\ \phi(0) = 0 \end{array}\right\}$, we obtain : $\left\{\begin{array}{c} A(t) = e^{-\varepsilon\mu t} \\ \\ \phi(t) = t + \frac{3\alpha}{16\mu}\left\{1 - e^{-2\varepsilon\mu t}\right\} \end{array}\right\}$

The amplitude A decreases exponentially with respect to the damping μ, while the phase ϕ grows quasi-linearly. The averaging method is a fast and simple perturbation technique, commonly used in nonlinear dynamics when a first order approximate solution is sought. This method assumes that the damping, the excitation in the case of a nonautonomous system as well as all the nonlinearities are synchronized (they occur at the same and unique time scale). If the nonlinearities of the system appear on different time scales, some terms which come from the interactions between the different scales will not be taken into account by the first order averaging method. For this type of system, one can use a generalized method of averaging [Nayfeh 2005a] which takes into account the multiscale aspect of the nonlinearities in the same way as the multiple time scales method.

The generalized averaging method:

Let the solutions of Equations (3.97) and (3.98) have the following forms:

$$A(t) = A_0(t) + \sum_{i=1}^{n}\varepsilon^i A_i(A_0, \phi_0) + O(\varepsilon^n) \tag{3.105}$$

$$\phi(t) = \phi_0(t) + \sum_{i=1}^{n}\varepsilon^i \phi_i(A_0, \phi_0) + O(\varepsilon^n) \tag{3.106}$$

$$\dot{A}_0 = \sum_{i=1}^{n}\varepsilon^i \Delta_i(A_0) + O(\varepsilon^n) \tag{3.107}$$

$$\dot{\phi}_0 = 1 + \sum_{i=1}^{n}\varepsilon^i \Psi i(A_0) + O(\varepsilon^n) \tag{3.108}$$

The functions A_i and ϕ_i are fast time-varying functions of ϕ_0, while it follows from Equations (3.107) and (3.108), A_0 as well as Δ_i and Ψ_i are slowly time-varying functions.
The use of the chain rule leads to the first derivative of Equations (3.105) and (3.106) as follow:

$$\frac{dA(t)}{dt} = \dot{A}_0 + \sum_{i=1}^{n} \varepsilon^i \left\{ \frac{\partial A_i}{\partial A_0}\dot{A}_0 + \frac{\partial A_i}{\partial \phi_0}\dot{\phi}_0 \right\} + O(\varepsilon^n) \tag{3.109}$$

$$\frac{d\phi(t)}{dt} = \dot{\phi}_0 + \sum_{i=1}^{n} \varepsilon^i \left\{ \frac{\partial \phi_i}{\partial A_0}\dot{A}_0 + \frac{\partial \phi_i}{\partial \phi_0}\dot{\phi}_0 \right\} + O(\varepsilon^n) \tag{3.110}$$

Substituting Equations (3.107) and (3.108), into Equations (3.109) and (3.110) and keeping terms up to $O(\varepsilon^2)$, yield:

$$\frac{dA(t)}{dt} = \varepsilon \left\{ \Delta_1 + \frac{\partial A_1}{\partial \phi_0} \right\} + \varepsilon^2 \left\{ \Delta_2 + \frac{\partial A_2}{\partial \phi_0} + \Delta_1 \frac{\partial A_1}{\partial A_0} + \Psi_1 \frac{\partial A_1}{\partial \phi_0} \right\} + O(\varepsilon^2) \tag{3.111}$$

$$\frac{d\phi(t)}{dt} = 1 + \varepsilon \left\{ \Psi_1 + \frac{\partial \phi_1}{\partial \phi_0} \right\} + \varepsilon^2 \left\{ \Psi_2 + \frac{\partial \phi_2}{\partial \phi_0} + \Delta_1 \frac{\partial \phi_1}{\partial A_0} + \Psi_1 \frac{\partial \phi_1}{\partial \phi_0} \right\} + O(\varepsilon^2) \tag{3.112}$$

Next, we substitute Equations (3.105) and (3.106) into Equations (3.97) and (3.98). We expand the right-hand sides for small ε keeping terms up to $O(\varepsilon^2)$.

$$\frac{dA(t)}{dt} = \left\{ \begin{array}{c} \varepsilon \left[-\mu A_0 + \mu A_0 \cos 2\phi_0 + \frac{1}{4}\alpha {A_0}^3 \sin 2\phi_0 + \frac{1}{8}\alpha {A_0}^3 \sin 4\phi_0 \right] \\ +\varepsilon^2 \left[\begin{array}{c} -\mu A_1 + \mu A_1 \cos 2\phi_0 + \frac{3}{4}\alpha {A_0}^2 A_1 \sin 2\phi_0 + \frac{3}{8}\alpha {A_0}^2 A_1 \sin 4\phi_0 \\ +\frac{1}{2}\alpha A_0^3 \phi_1 \cos 2\phi_0 + \frac{1}{2}\alpha A_0^3 \phi_1 \cos 4\phi_0 - 2\mu \phi_1 A_0 \sin 2\phi_0 \end{array} \right] \end{array} \right\} + O(\varepsilon^2) \tag{3.113}$$

$$\frac{d\phi(t)}{dt} = \left\{ \begin{array}{c} 1 + \varepsilon \left[\frac{3}{8}\alpha {A_0}^2 - \mu \sin 2\phi_0 + \frac{1}{2}\alpha {A_0}^2 \cos 2\phi_0 + \frac{1}{8}\alpha {A_0}^2 \cos 4\phi_0 \right] \\ +\varepsilon^2 \left[\begin{array}{c} \frac{3}{4}\alpha A_0 A_1 + \alpha A_0 A_1 \cos 2\phi_0 + \frac{1}{4}\alpha A_0 A_1 \cos 4\phi_0 \\ -2\mu \phi_1 \cos 2\phi_0 - \alpha A_0^2 \phi_1 \sin 2\phi_0 - \frac{1}{2}\alpha A_0^2 \phi_1 \sin 4\phi_0 \end{array} \right] \end{array} \right\} + O(\varepsilon^2) \tag{3.114}$$

The use of Equations (3.113) and (3.111) as well as Equations (3.114) and (3.112) leads to the identification of the terms of order ε^1 and ε^2. It permits to write the four following equations:

$$\Delta_1 + \frac{\partial A_1}{\partial \phi_0} = -\mu A_0 + \mu A_0 \cos 2\phi_0 + \frac{1}{4}\alpha {A_0}^3 \sin 2\phi_0 + \frac{1}{8}\alpha {A_0}^3 \sin 4\phi_0 \tag{3.115}$$

$$\Delta_2 + \frac{\partial A_2}{\partial \phi_0} + \Delta_1 \frac{\partial A_1}{\partial A_0} + \Psi_1 \frac{\partial A_1}{\partial \phi_0} = \left\{ \begin{array}{c} -\mu A_1 + \mu A_1 \cos 2\phi_0 + \frac{3}{4}\alpha {A_0}^2 A_1 \sin 2\phi_0 + \frac{3}{8}\alpha {A_0}^2 A_1 \sin 4\phi_0 \\ +\frac{1}{2}\alpha A_0^3 \phi_1 \cos 2\phi_0 + \frac{1}{2}\alpha A_0^3 \phi_1 \cos 4\phi_0 - 2\mu \phi_1 A_0 \sin 2\phi_0 \end{array} \right\} \tag{3.116}$$

$$\Psi_1 + \frac{\partial \phi_1}{\partial \phi_0} = \frac{3}{8}\alpha {A_0}^2 - \mu \sin 2\phi_0 + \frac{1}{2}\alpha {A_0}^2 \cos 2\phi_0 + \frac{1}{8}\alpha {A_0}^2 \cos 4\phi_0 \tag{3.117}$$

$$\Psi_2 + \frac{\partial \phi_2}{\partial \phi_0} + \Delta_1 \frac{\partial \phi_1}{\partial A_0} + \Psi_1 \frac{\partial \phi_1}{\partial \phi_0} = \left\{ \begin{array}{c} \frac{3}{4}\alpha A_0 A_1 + \alpha A_0 A_1 \cos 2\phi_0 + \frac{1}{4}\alpha A_0 A_1 \cos 4\phi_0 \\ -2\mu \phi_1 \cos 2\phi_0 - \alpha A_0^2 \phi_1 \sin 2\phi_0 - \frac{1}{2}\alpha A_0^2 \phi_1 \sin 4\phi_0 \end{array} \right\} \tag{3.118}$$

Then, we use the method of separation of variables to separate the fast and slowly varying terms of Equations (3.115), (3.116), (3.117) and (3.118). The slowly varying parts of Equations (3.115) and (3.117) yield:

$$\left\{ \begin{array}{c} \Delta_1 = -\mu A_0 \\ \\ \Psi_1 = \frac{3}{8}\alpha {A_0}^2 \end{array} \right\} \tag{3.119}$$

We find exactly the same relation as those obtained by the method of first order averaging (Equations (3.101) and (3.102)). The fast varying parts of Equations (3.115) and (3.117) yield:

$$\frac{\partial A_1}{\partial \phi_0} = \mu A_0 \cos 2\phi_0 + \frac{1}{4}\alpha {A_0}^3 \sin 2\phi_0 + \frac{1}{8}\alpha {A_0}^3 \sin 4\phi_0 \tag{3.120}$$

$$\frac{\partial \phi_1}{\partial \phi_0} = -\mu \sin 2\phi_0 + \frac{1}{2}\alpha {A_0}^2 \cos 2\phi_0 + \frac{1}{8}\alpha {A_0}^2 \cos 4\phi_0 \tag{3.121}$$

Particular solutions for Equations (3.120) and (3.121) have the following expressions:

$$A_1 = \frac{1}{2}\mu A_0 \sin 2\phi_0 - \frac{1}{8}\alpha {A_0}^3 \cos 2\phi_0 - \frac{1}{32}\alpha {A_0}^3 \cos 4\phi_0 \tag{3.122}$$

$$\phi_1 = \frac{1}{2}\mu \cos 2\phi_0 + \frac{1}{4}\alpha {A_0}^2 \sin 2\phi_0 + \frac{1}{32}\alpha {A_0}^2 \sin 4\phi_0 \tag{3.123}$$

Then, Equations (3.119), (3.122) and (3.123) are replaced into Equations (3.116) and (3.118).

$$\Delta_2 + \frac{\partial A_2}{\partial \phi_0} = \left\{ \begin{array}{c} -\frac{1}{4}\mu^2 A_0 \sin 4\phi_0 - \frac{29}{64}\alpha\mu A_0^3 \cos 2\phi_0 + \frac{1}{16}\alpha\mu A_0^3 \cos 4\phi_0 + \frac{3}{64}\alpha\mu A_0^3 \cos 6\phi_0 \\ \\ -\frac{41}{256}\alpha^2 A_0^5 \sin 2\phi_0 - \frac{1}{32}\alpha^2 A_0^5 \sin 4\phi_0 + \frac{9}{256}\alpha^2 A_0^5 \sin 6\phi_0 + \frac{1}{512}\alpha^2 A_0^5 \sin 8\phi_0 \end{array} \right\} \tag{3.124}$$

$$\Psi_2 + \frac{\partial \phi_2}{\partial \phi_0} = \left\{ \begin{array}{c} -\frac{1}{2}\mu^2 - \frac{51}{256}\alpha^2 A_0^4 \\ \\ -\frac{1}{2}\mu^2 \cos 4\phi_0 + \frac{33}{32}\alpha\mu A_0^2 \sin 2\phi_0 - \frac{3}{16}\alpha\mu A_0^2 \sin 4\phi_0 - \frac{3}{32}\alpha\mu A_0^2 \sin 6\phi_0 \\ \\ -\frac{25}{64}\alpha^2 A_0^4 \cos 2\phi_0 - \frac{1}{128}\alpha^2 A_0^4 \cos 4\phi_0 + \frac{3}{64}\alpha^2 A_0^4 \cos 6\phi_0 + \frac{1}{256}\alpha^2 A_0^4 \cos 8\phi_0 \end{array} \right\} \tag{3.125}$$

An approximate solution up to order $O(\varepsilon^2)$, does not require A_2 and ϕ_2. Indeed, only the slowly varying terms Δ_2 and Ψ_2 have to be identified.

$$\left\{ \begin{array}{c} \Delta_2 = 0 \\ \\ \Psi_2 = -\frac{1}{2}\mu^2 - \frac{51}{256}\alpha^2 A_0^4 \end{array} \right\} \tag{3.126}$$

Substituting Equations (3.122-3.123) into Equations (3.105-3.106) as well as Equations (3.119) and (3.126) into Equations (3.107-3.108), yield:

$$A(t) = A_0 + \varepsilon \left[\frac{1}{2}\mu A_0 \sin 2\phi_0 - \frac{1}{8}\alpha {A_0}^3 \cos 2\phi_0 - \frac{1}{32}\alpha {A_0}^3 \cos 4\phi_0 \right] \tag{3.127}$$

$$\phi(t) = \phi_0 + \varepsilon \left[\frac{1}{2}\mu \cos 2\phi_0 + \frac{1}{4}\alpha {A_0}^2 \sin 2\phi_0 + \frac{1}{32}\alpha {A_0}^2 \sin 4\phi_0 \right] \tag{3.128}$$

$$\dot{A}_0 = -\varepsilon\mu A_0 \tag{3.129}$$

$$\dot{\phi}_0 = 1 + \frac{3}{8}\varepsilon\alpha {A_0}^2 - \frac{1}{2}\varepsilon^2\mu^2 - \frac{51}{256}\varepsilon^2\alpha^2 A_0^4 \tag{3.130}$$

Equations (3.105) and (3.106) are used in order to obtain the following expansion of Equation (3.85) for small ε.

$$y(t) = A_0 \cos \phi_0 + \varepsilon \left[A_1 \cos \phi_0 - A_0 \phi_1 \sin \phi_0 \right] \tag{3.131}$$

Finally, the expressions of A_1 and ϕ_1 in Equations (3.122) and (3.123) are replaced into Equation (3.131) in order to obtain the following solution:

$$y(t) = A_0 \cos(t+\beta) + \varepsilon \left[\frac{1}{2}\ \mu A_0 \sin(t+\beta) - \frac{3}{16} \alpha A_0^3 \cos(t+\beta) + \frac{1}{32} \alpha A_0^3 \cos(3t+3\beta) \right] \tag{3.132}$$

3.3.1.6 Krylov-Bogoliubov-Mitropolsky technique

Krylov-Bogoliubov-Mitropolsky technique [Yuste 1992] is an asymptotic method considered as a variant of the multiscale averaging method. We consider Equation (3.85) to be the first term in an approximate solution of (3.57) where A and β are slowly varying variables. Moreover, we introduce the fast scale $\phi = t + \beta$ and we use A to represent the slow variations. Thus, we seek an approximate solution in the form:

$$y(t) = A \cos \phi + \sum_{i=1}^{n} \varepsilon^i y_i(A, \phi) \tag{3.133}$$

Since A and β are slowly time-varying variables, their power series expansions of ε in terms of A are:

$$\dot{A} = \sum_{i=1}^{n} \varepsilon^i \Delta_i(A) \tag{3.134}$$

$$\dot{\phi} = 1 + \sum_{i=1}^{n} \varepsilon^i \Psi_i(A) \tag{3.135}$$

Thus, this method can be viewed as a multiscale procedure with A and ϕ being the scales. Using the chain rule, the derivatives with respect to t in terms of the new independent variables A and ϕ are:

$$\frac{d}{dt} = \dot{A} \frac{\partial}{\partial A} + \dot{\phi} \frac{\partial}{\partial \phi} \tag{3.136}$$

$$\frac{d^2}{dt^2} = \dot{A}^2 \frac{\partial^2}{\partial A^2} + \ddot{A} \frac{\partial}{\partial A} + 2 \dot{A} \dot{\phi} \frac{\partial^2}{\partial A \partial \phi} + \dot{\phi}^2 \frac{\partial^2}{\partial \phi^2} + \ddot{\phi} \frac{\partial}{\partial \phi} \tag{3.137}$$

Differentiating (3.134) and (3.135) with respect to t and using the notation $\frac{\partial X_i(A)}{\partial A} = X_i'$, we obtain:

$$\ddot{A} = \dot{A} \sum_{i=1}^{n} \varepsilon^i \Delta_i' \tag{3.138}$$

$$\ddot{\phi} = \dot{A} \sum_{i=1}^{n} \varepsilon^i \Psi_i' \tag{3.139}$$

We substitute Equation (3.134) into Equation (3.138) as well as Equation (3.135) into Equation (3.139) up to the order $O(\varepsilon^2)$.

$$\ddot{A} = \varepsilon^2 \Delta_1 \Delta_1' + O(\varepsilon^2) \tag{3.140}$$

$$\ddot{\phi} = \varepsilon^2 \Delta_1 \Psi_1' + O(\varepsilon^2) \tag{3.141}$$

By using Equations (3.140), (3.141), (3.136) and (3.137), we rewrite Equations (3.134) and (3.135).

$$\frac{d}{dt}=\frac{\partial}{\partial\phi}+\varepsilon\left[\Delta_1\frac{\partial}{\partial A}+\Psi_1\frac{\partial}{\partial\phi}\right]+\varepsilon^2\left[\Delta_2\frac{\partial}{\partial A}+\Psi_2\frac{\partial}{\partial\phi}\right] \tag{3.142}$$

$$\frac{d^2}{dt^2}=\left\{\begin{array}{c}\frac{\partial^2}{\partial\phi^2}+2\varepsilon\left[\Psi_1\frac{\partial^2}{\partial\phi^2}+\Delta_1\frac{\partial^2}{\partial A\partial\phi}\right]\\ +\varepsilon^2\left[\left(\Psi_1^2+2\Psi_2\right)\frac{\partial^2}{\partial\phi^2}+2\left(\Delta_2+\Delta_1\Psi_1\right)\frac{\partial^2}{\partial A\partial\phi}+\Delta_1^2\frac{\partial^2}{\partial A^2}+\Delta_1\Delta_1'\frac{\partial}{\partial A}+\Delta_1\Psi_1'\frac{\partial}{\partial\phi}\right]\end{array}\right\} \tag{3.143}$$

Thus, Equation (3.57) becomes:

$$y+\frac{\partial^2 y}{\partial\phi^2}+\left\{\begin{array}{c}2\varepsilon\left[\Psi_1\frac{\partial^2 y}{\partial\phi^2}+\Delta_1\frac{\partial^2 y}{\partial A\partial\phi}+\mu\frac{\partial y}{\partial\phi}+\frac{1}{2}\alpha y^3\right]\\ +\varepsilon^2\left[\begin{array}{c}\left(\Psi_1^2+2\Psi_2\right)\frac{\partial^2 y}{\partial\phi^2}+2\left(\Delta_2+\Delta_1\Psi_1\right)\frac{\partial^2 y}{\partial A\partial\phi}\\ +\Delta_1^2\frac{\partial^2 y}{\partial A^2}+\left(\Delta_1\Delta_1'+2\mu\Delta_1\right)\frac{\partial y}{\partial A}+\left(\Delta_1\Psi_1'+2\mu\Psi_1\right)\frac{\partial y}{\partial\phi}\end{array}\right]\end{array}\right\}=0 \tag{3.144}$$

The substitution of Equation (3.133) into Equation (3.144) and the trigonometric linearization, up to the order $O(\varepsilon^2)$, yields the following differential system.

$$\left\{\begin{array}{c}\left(\frac{3}{4}\alpha A^3-2A\ \Psi_1\right)\cos\phi-2\left(A\mu+\Delta_1\right)\sin\phi+\frac{1}{4}\alpha A^3\cos 3\phi+y_1+\frac{\partial^2 y_1}{\partial\phi^2}=0\\ \left\{\begin{array}{c}\left(2\mu\Delta_1+\Delta_1\Delta_1'-A\Psi_1^2-2A\Psi_2\right)\cos\phi-\left(2\Delta_2+2A\mu\Psi_1+2\Delta_1\Psi_1+A\Delta_1\Psi_1'\right)\sin\phi\\ +\frac{3}{2}A^2\alpha(1+\cos 2\phi)y_1+2\mu\frac{\partial y_1}{\partial\phi}+2\Psi_1\frac{\partial^2 y_1}{\partial\phi^2}+2\Delta_1\frac{\partial^2 y_1}{\partial A\partial\phi}+y_2+\frac{\partial^2 y_2}{\partial\phi^2}=0\end{array}\right\}\end{array}\right. \tag{3.145}$$

The elimination of the secular terms of the first equation of the differential system (3.145) constraints Δ_1 and Ψ_1 in order to keep the approximate solution bounded.

$$\left\{\begin{array}{l}\Delta_1=-\mu A\\ \Psi_1=\frac{3}{8}\alpha A^2\end{array}\right. \tag{3.146}$$

Let a particular solution of the differential equation for y_1 be:

$$y_1=\frac{1}{32}\alpha A^3\cos 3\phi \tag{3.147}$$

which is introduced into Equation (3.145). Thus, the differential equation for y_2 becomes:

$$\left\{\begin{array}{l}\left[\frac{3}{128}\alpha^2 A^5+(2\mu+\Delta_1')\Delta_1-A(\Psi_1^2+2\Psi_2)\right]\cos\phi-\left[2\Delta_2+2\Psi_1(\mu A+\Delta_1)+A\Delta_1\Psi_1'\right]\sin\phi\\ \quad +\frac{3}{128}\left[\alpha A^3\left(2\alpha A^2\ -24\Psi_1\right)\cos 3\phi-4\alpha A^2\left(2\mu A+6\Delta_1\right)\sin 3\phi+A^5\alpha^2\cos 5\phi\right]=0\end{array}\right. \tag{3.148}$$

The elimination of secular terms of order $O(\varepsilon^2)$ constraints Δ_2 and Ψ_2.

$$\left\{\begin{array}{c}\Delta_2=-A\mu\Psi_1-\Delta_1\Psi_1-\frac{1}{2}A\Delta_1\Psi_1'=\frac{3}{8}\alpha\mu A^3\\ \Psi_2=\frac{1}{2A}\left(2\mu\Delta_1+\Delta_1\Delta_1'+\frac{3}{128}\alpha^2A^5-A\Psi_1^2\right)=-\frac{1}{2}\mu^2-\frac{15}{256}\alpha^2A^4\end{array}\right. \tag{3.149}$$

The results are the same as those already found by the multiple time scales method. The approximate solution of Equation (3.57) up to the order $O(\varepsilon^2)$ can be written as:

$$\begin{cases} y(t) = A\cos\phi + \frac{\varepsilon}{32}\cos 3\phi \\ \frac{dA}{dt} = -\varepsilon\mu A + \frac{3}{8}\varepsilon^2\alpha\mu A^3 \\ \frac{d\phi}{dt} = \frac{3}{8}\varepsilon\alpha A^2 - \frac{1}{2}\varepsilon^2\mu^2 - \frac{15}{256}\varepsilon^2\alpha^2 A^4 \\ \phi = t + \beta \end{cases} \tag{3.150}$$

3.3.1.7 Conclusion

The principal disadvantage of the perturbation theory is the necessity, from the beginning, to have a precise idea about the solution we are looking for: it is convenient to find a small parameter ε and to isolate the fast part of the system. At this level, the physical intuition plays an important role.

To conclude, we clearly showed on examples that the dynamics of nonlinear systems with primarily periodic behavior was accessible by various perturbation methods. The choice of the method will be justified firstly by the conservative aspect of the system and secondly by the reliability of the assumption concerning the synchronization of the system nonlinearities.

Typically, in the case of the resonator which is a dissipative nonlinear system (equations), the multiple time scales, the averaging method or the Krylov-Bogoliubov-Mitropolsky technique are well adapted in order to model the nonlinear dynamics of resonant MEMS and NEMS sensors.

The use of these perturbation methods concerns weakly nonlinear systems ($\varepsilon << 1$ in the case of normalized nonlinearities). Nevertheless, the classical perturbation methods have been modified by several researchers [He 2002, Yang 2004] in order to adapt them to the strongly nonlinear systems.

3.3.2 Numerical methods for periodic solutions

3.3.2.1 Direct integration

The following forced nonlinear Duffing equation is considered.

$$m\frac{d^2x}{dt^2} + c\frac{dx}{dt} + kx + k_{nl}x^3 = \tilde{f}\cos(\Omega t) \tag{3.151}$$

Its normalized form can be written as

$$\frac{d^2x}{dt^2} + 2\mu\frac{dx}{dt} + \omega_0^2 x + \alpha x^3 = f\cos(\Omega t) \tag{3.152}$$

which can be transformed into a system of two first-order-ordinary differential equations as follows:

$$\begin{cases} \frac{dx}{dt} = y \\ \frac{dy}{dt} = -2\mu y - \omega_0^2 x - \alpha x^3 + f\cos(\Omega t) \end{cases} \tag{3.153}$$

which is equivalent to:

$$\frac{dz}{dt} = g(z,t) \tag{3.154}$$

where $z(t) = (x(t), y(t))^t$. The next step consists in finding stationary solutions to Equation (3.154). To do so, it is solved numerically for a set of initial conditions using a time-difference method (Runge-Kutta, Adams, etc...) until until motion settles down onto a steady oscillation (periodic motion). The process is described in Figure 3.3 for the following set of parameters ($\mu = 0.05$, $\omega_0 = 1$, $\alpha = 0.25$, $f = 0.5$, $\Omega = 1$). The periodic solutions are governed by the following equation:

$$z(z_0, t+T) = z(z_0, t) \tag{3.155}$$

where $z_0 = z(t=0)$ defines the initials conditions and T is the period of the solution. It corresponds to a periodic orbit in the phase plane as shown in Figure 3.3.

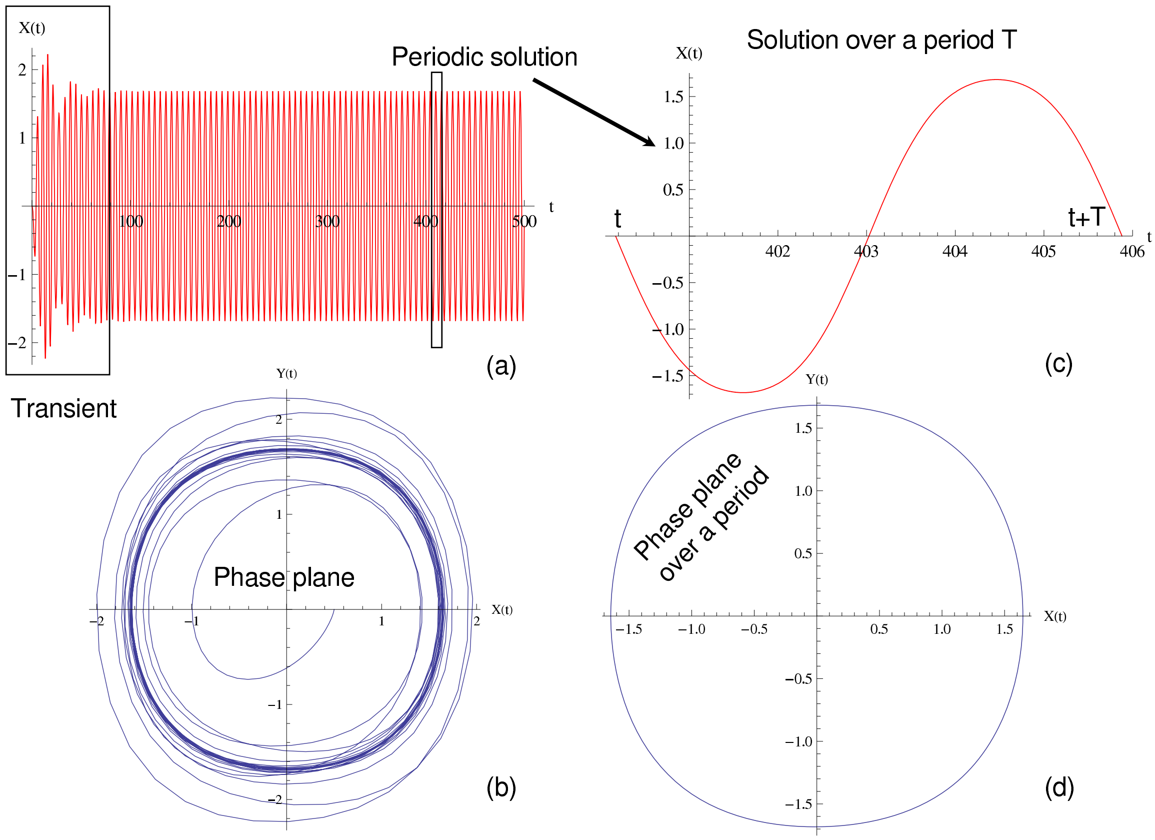

Figure 3.3: (a): Long time integration. (b): Phase plane portrait. (c): Periodic solution. (d): Phase plane portrait of the periodic solution.

For a given period T i.e. for a given forcing frequency Ω, once the motion settles down onto a steady oscillation, the maximal amplitude gives a point (Ω, x_{Max}) in the frequency response curve, as described in Figure 3.4. The process is then repeated several times for different values of Ω in order to describe the complete nonlinear frequency response. However, this is applicable only to stable solutions. Close to the bifurcation points 1 and 2, jump phenomena occur and the unstable branch between points 1 and 2 cannot be obtained using the direct integration.

The main drawback of this method lies in its high computational time since it is extremely long to reach the steady state motion especially for ordinary differential equations which are strongly nonlinear or contain high order nonlinearities.

3.3.2.2 The shooting method

Motivation When periodic solutions are of interest, the shooting method is much more efficient than the direct integration method. With the shooting method, the transient motion preceeding the

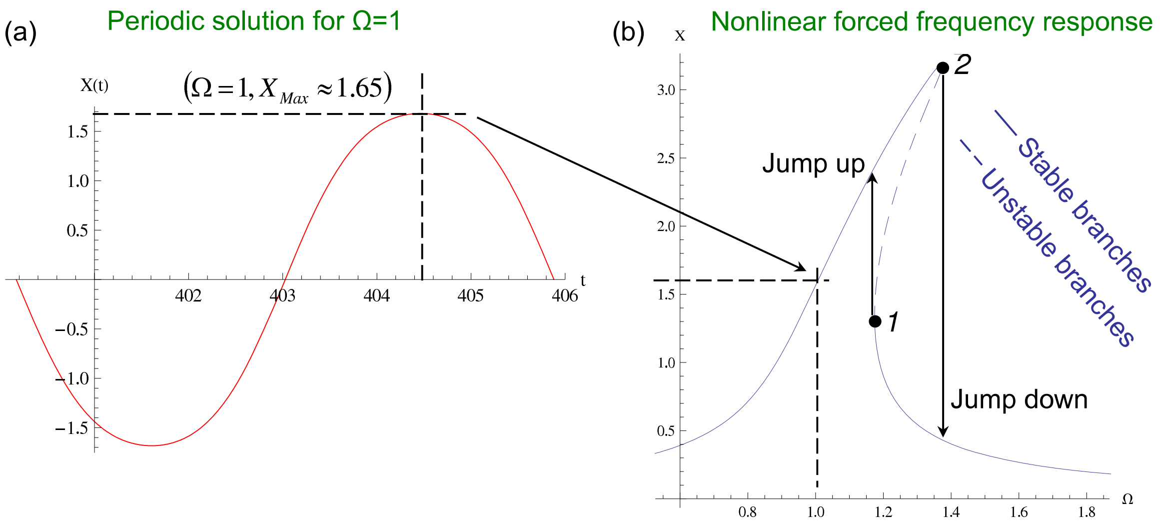

Figure 3.4: a): time integration over a period T. (b): Forced nonlinear frequency response.

steady state is not computed, thus leading to high computational time saving. It consists in directly computing periodic solutions by considering the boundary value problem made of the motion Equations (3.154) and the periodicity condition (3.155)

$$\begin{cases} \frac{dz}{dt} = g(z,t) \\ z(z_0, T) = z_0 \end{cases} \tag{3.156}$$

Compared to the direct integration method, the implementation of the shooting method in computational software is more complex, but it has the advantage of fast convergence since the time integration is only performed over a period T.

Implementation This boundary value problem can be transformed into an initial value problem by considering the periodicity equation

$$H(z_O, T) = z(z_0, T) - z_0 = 0 \tag{3.157}$$

H is not an analytical function. It is evaluated through the time integration of Equation (3.154). For a given period T, let z_0 be an approximate initial solution of Equation (3.157). Since z_0 is not an exact solution, an iterative Newton-Raphson correction procedure is used, i.e. we search Δz such as $z_0 + \Delta z$ is a solution of Equation (3.157). The correction phase at iteration k is

$$z_0^{k+1} = z_0^k + \Delta z \tag{3.158}$$

The increment Δz is solution of the linear system

$$J(z_0^k, T)\, \Delta z = -H(z_0^k, T) \tag{3.159}$$

where J is the Jacobian matrix defined by

$$J(z_0^k, T) = \left.\frac{\partial H}{\partial z_0}\right|_{(z_0^k, T)} \tag{3.160}$$

The iterations are repeated until a user-defined accuracy ε is obtained by the test function

$$\frac{\|\Delta z\|}{\left\|z_0^{k+1}\right\|} \leq \varepsilon \tag{3.161}$$

This method is illustrated in Figure 3.5 for the Duffing equation (3.153) with the same parameters as in section 3.3.2.1 and $\varepsilon = 10^{-5}$. Only five Newton-Raphson iterations are needed to obtain the periodic solution, i.e. a closed loop in the phase plane.

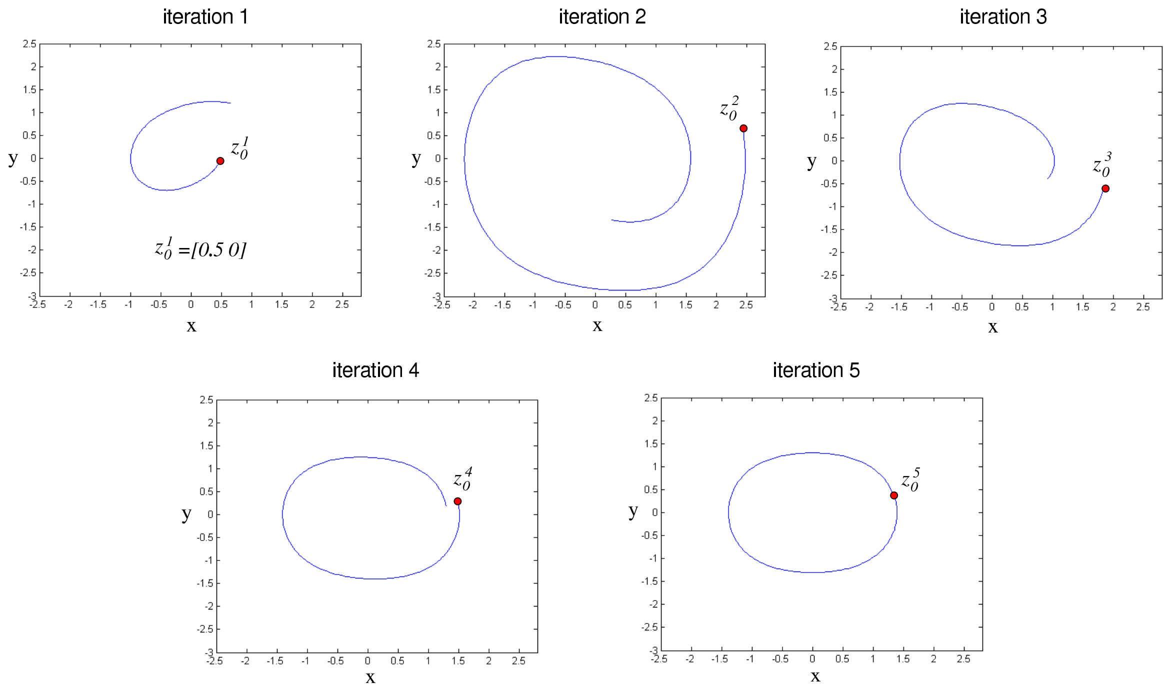

Figure 3.5: Consecutive iterations of the shooting method in the phase plane

Natural parameter continuation Nonlinear dynamical systems can exhibit a very complex behavior within a range of parameters or even become unstable. The evolution of the solution with respect to a system parameter is thus of prime interest. To this end, continuation methods can be used. The simplest of these methods is the natural parameter continuation which is implemented as follows. After convergence, T is incremented such as $T = T + \Delta T$, the solution at T is used as the initial guess for the solution at $T = T+\Delta T$ and the Newton-Raphson procedure is repeated in order to find the corresponding solution z_0. With ΔT sufficiently small the iteration applied to the initial guess should converge. The overall algorithm is given in Figure 3.6. One advantage of natural parameter continuation is that it uses the solution method for the problem as a black box. All that is required is that an initial solution can be given. However, natural parameter continuation fails at turning points [Nayfeh 1995], where the branch of solutions turns round. So for problems with turning points, a more sophisticated method such as pseudo-arclength continuation must be used.

Pseudo-arclength Continuation This method, which was proposed by H.B. Keller [Keller 1977] in the late 1970's, is based on the observation that the "ideal" parameterization of a curve is arclength. Pseudo-arclength is an approximation of the arclength in the tangent space of the curve. With this method, the parameter dependent nonlinear equation $H(z_O, T) = 0$ is solved by introducing a new

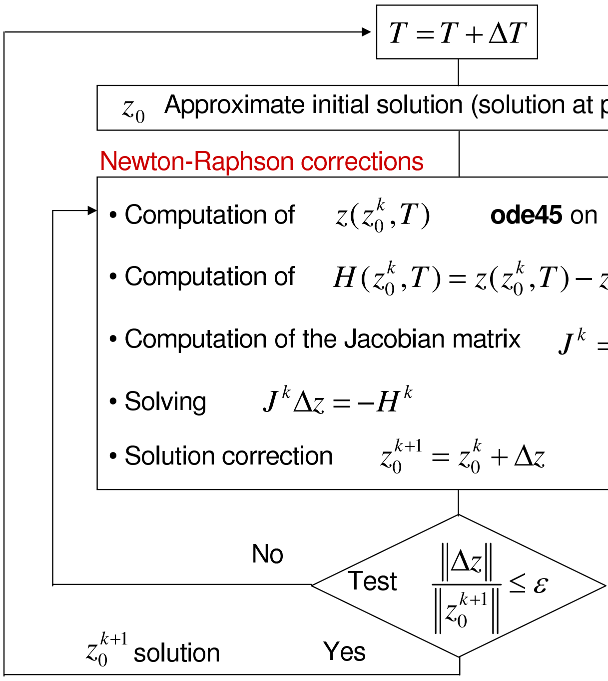

Figure 3.6: Algorithm of the shooting method with natural parameter continuation.

parameter s, which approximates arclength, and viewing the vector $x = (z_O, T)$ as a function of s. The resulting modified natural continuation method makes a step in the new pseudo-arclength parameter s (rather than T). The iterative Newton-Raphson procedure is required to find a point at the given pseudo-arclength, which requires appending an additional constraint (the pseudo-arclength constraint) to the n by $n+1$ Jacobian in order to produce a square Jacobian. The algorithm is a predictor-corrector

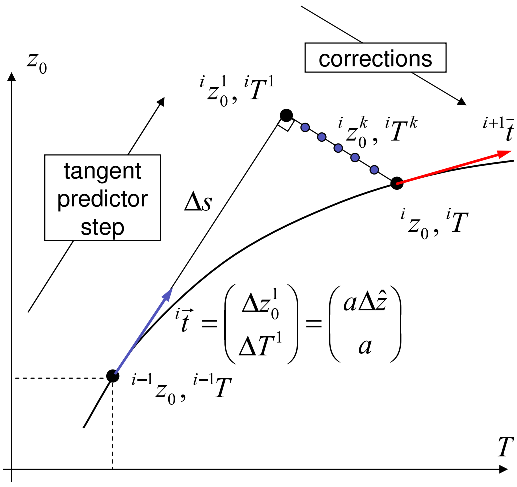

Figure 3.7: Pseudo-arclength Continuation Technique

method. The prediction step finds the point which is a step Δs along the tangent vector at the current pointer and the corrections are usually computed with Newton-Raphson method (Figure 3.7).

Predictor step Let $({}^{i-1}z_0, {}^{i-1}T)$ be the converged solution at the end of the previous step. The tangent vector ${}^{i}\vec{t} = (\Delta z_0^1, \Delta T^1)^t$ is obtained from a first order Taylor development of Equation (3.157) in the neighborhood of this solution, combined with a normalization condition

$$\begin{aligned} \left.\frac{\partial H}{\partial z_0}\right|_{({}^{i-1}z_0, {}^{i-1}T)} \Delta z_0^1 + \left.\frac{\partial H}{\partial T}\right|_{({}^{i-1}z_0, {}^{i-1}T)} \Delta T^1 = 0 \\ \|{}^{i}\vec{t}\|^2 = \Delta z_0^{1^t} \Delta z_0^1 + (\Delta T^1)^2 = 1 \end{aligned} \tag{3.162}$$

The end point $({}^{i}z_0^1, {}^{i}T^1)$ of the predictor step of length Δs is then given by

$$\begin{pmatrix} {}^{i}z_0^1 \\ {}^{i}T^1 \end{pmatrix} = \begin{pmatrix} {}^{i-1}z_0 \\ {}^{i-1}T \end{pmatrix} + \Delta s\, {}^{i}\vec{t} = \begin{pmatrix} {}^{i-1}z_0 \\ {}^{i-1}T \end{pmatrix} + \Delta s \begin{pmatrix} \Delta z_0^1 \\ \Delta T^1 \end{pmatrix} \tag{3.163}$$

The sign of Δs (positive or negative) is chosen such that the direction of continuation is conserved, i.e. such that

$${}^{i-1}\vec{t}^{\,T} \cdot {}^{i}\vec{t} > 0 \tag{3.164}$$

Corrections The corrections are performed in the direction orthogonal to the tangent step by imposing the orthogonality condition

$$\Delta z_0^{1^T} \cdot \Delta z_0^{k+1} + \Delta T^1 \Delta T^{k+1} = 0 \tag{3.165}$$

The correction at iteration k is

$$\begin{pmatrix} {}^{i}z_0^{k+1} \\ {}^{i}T^{k+1} \end{pmatrix} = \begin{pmatrix} {}^{i}z_0^{k} \\ {}^{i}T^{k} \end{pmatrix} + \begin{pmatrix} \Delta z_0^{k+1} \\ \Delta T^{k+1} \end{pmatrix} \tag{3.166}$$

with Δz_0^{k+1} and ΔT^{k+1} solutions of the bordered system

$$\begin{bmatrix} J_z & J_T \\ \Delta z_0^{1^T} & \Delta T^1 \end{bmatrix} \begin{bmatrix} \Delta z_0^{k+1} \\ \Delta T^{k+1} \end{bmatrix} = \begin{bmatrix} -H({}^{i}z_0^k, {}^{i}T^k) \\ 0 \end{bmatrix} \tag{3.167}$$

The iterations are repeated until the user-defined accuracy ε is reached

$$\frac{\left\| \Delta z_0^{k+1} \right\|}{\left\| {}^{i}z_0^{k+1} \right\|} \leq \varepsilon \tag{3.168}$$

The right-hand side term of Equation (3.167) is computed by means of Equation (3.157), in which $z({}^{i}z_0^k, {}^{i}T^k)$ is obtained by time integration of Equation (3.154) with initial condition $({}^{i}z_0^k, {}^{i}T^k)$. The expression of the Jacobian matrix J_z is deduced from Equation (3.157)

$$J_z = \left.\frac{\partial H}{\partial z_0}\right|_{({}^{i}z_0^k, {}^{i}T^k)} = M^k - Id \tag{3.169}$$

where

$$M^k = \left.\frac{\partial z}{\partial z_0}\right|_{({}^{i}z_0^k, {}^{i}T^k)} \tag{3.170}$$

is the so-called Monodromy matrix. M^k can be efficiently computed by integrating

$$\left[\dot{M}^k\right] = \left[\frac{\partial g}{\partial z}\right] \left[M^k\right] \tag{3.171}$$

with $M^k(t=0) = Id$ as initial conditions.
The expression of the Jacobian matrix J_T is deduced from Equation (3.157)

$$J_T = \left.\frac{\partial H}{\partial T}\right|_{({}^i z_0^k, {}^i T^k)} = \left.\frac{\partial z}{\partial T}\right|_{({}^i z_0^k, {}^i T^k)} \tag{3.172}$$

Stability analysis a stability analysis can be conducted at each step of the continuation method by studying the (complex) eigenvalues of the Monodromy matrix (3.170), which are called the Floquet multipliers. The periodic solution is stable if all the multipliers lie inside the complex unit circle. It is unstable otherwise.

The shooting method with arc-length continuation and stability has been programmed under Matlab. In order to use it, the user must program the function g of Equation (3.152).

3.3.2.3 Harmonic Balance Method + Asymptotic Numerical Method

The Harmonic Balance Method (HBM) is commonly used for computing periodic solutions. It consists in assuming a time solution in the form of a Fourier series and comparing/balancing the coefficients of the same harmonic components. In this way, non linear differential equations in the space variables and time are transformed into a nonlinear algebraic system in the space variables and frequency. However, when nonlinearities are complex, the derivation of the algebraic system become very cumbersome. Alternative methods have been proposed to overcome these shortcomings, such as the incremental harmonic balance method (IHBM) [Lau 1981] or the alternating frequency/time domain harmonic balance method (AFT) [Nacivet 2003], but they are very demanding from a computational point of view.

Recently, Cochelin et al. [Cochelin 2009] have proposed another strategy for applying the classical HBM with a large number of harmonics. The basic idea consists in recasting the original system (4.29) into a new system where nonlinearities are at most quadratic polynomials by introducing as many new variables as needed. This leads to an augmented, but quadratic only, nonlinear system for which the application of the HBM is quite straightforward. Furthermore, this quadratic framework makes it possible to use the so-called Asymptotic Numerical Method (ANM) for the continuation of solutions. The ANM consists in computing power series expansions of solution branches and presents several advantages : it provides continuous solutions, the continuation is very robust and the control of the step length is automatic and always optimal [Azrar 1993, Cochelin 1994, Baguet 2003, Cochelin 2007].

This method is detailled in [Cochelin 2009]. Its application to our nonlinear differential system (4.29) is detailled hereafter.

Quadratic recast The key point of this method consists in operating a quadratic recast of Equation (3.154) by introducing auxiliary variables. This transformation leads to the following quadratic system

$$m(\dot{\mathbf{X}}) = c(\Omega) + l(\mathbf{X}) + q(\mathbf{X}, \mathbf{X}) \tag{3.173}$$

where $\mathbf{X}$ is the unknown vector of size N_{eq}, which contains the auxiliary variables, c is a constant vector with respect to $\mathbf{X}$, $l(\cdot)$ and $m(\cdot)$ are linear vector valued operators with respect to $\mathbf{X}$, and $q(\cdot,\cdot)$ is a quadratic vector valued operator. The expressions of the operators c , l, m and q are problem-dependant.

Application of the HBM The HBM consists in decomposing $\mathbf{X}(t)$ into a truncated Fourier series

$$\mathbf{X}(t) = \mathbf{X}_0 + \sum_{k=1}^{H} \mathbf{X}_k^c \cos(k\Omega t) + \sum_{k=1}^{H} \mathbf{X}_k^s \sin(k\Omega t) \tag{3.174}$$

and inserting this expansion in the nonlinear differential system (4.36). By balancing the first $2H+1$ harmonic terms and neglecting higher order harmonics, the following nonlinear algebraic system of size $(2H+1) \times N_{eq}$ is obtained

$$\Omega\, M(\mathbf{U}) = C + L(\mathbf{U}) + Q(\mathbf{U}, \mathbf{U}) \tag{3.175}$$

where $\mathbf{U} = [\mathbf{X}_0, \mathbf{X}_1^{cT}, \mathbf{X}_1^{sT}, \ldots, \mathbf{X}_H^{c\,T}, \mathbf{X}_H^{s\,T}]^T$ contains the components of the Fourier series (3.174). The new operators C, $M(\cdot)$, $L(\cdot)$ and $Q(\cdot,\cdot)$ depend only on the operators c, $m(\cdot)$, $l(\cdot)$ and $q(\cdot,\cdot)$. Their explicit expressions can be found in Cochelin et al. [Cochelin 2009].

Continuation by the ANM In order to apply the Asymptotic Numerical Method (ANM), (3.175) is rewritten as

$$\mathbf{R}(\mathbf{U}, \Omega) = C + L(\mathbf{U}) + Q(\mathbf{U}, \mathbf{U}) - \Omega\, M(\mathbf{U}) = 0 \tag{3.176}$$

Assuming that a regular solution $(\mathbf{U}_0, \Omega_0)$ of (3.175) is known, the branch of solution starting at $(\mathbf{U}_0, \Omega_0)$ is represented as a power series expansion (truncated at order N) with respect to the path-parameter a [Cochelin 2007]

$$\begin{aligned} \mathbf{U}(a) &= \mathbf{U}_0 + a\mathbf{U}_1 + a^2\mathbf{U}_2 + \ldots + a^N\mathbf{U}_N \\ \Omega(a) &= \Omega_0 + a\Omega_1 + a^2\Omega_2 + \ldots + a^N\Omega_N \end{aligned} \tag{3.177}$$

If the pseudo-arclength definition is chosen, the path-parameter a can be expressed as [Cochelin 1994]

$$a = \mathbf{U}_1.(\mathbf{U} - \mathbf{U}_0)^T + \Omega_1(\Omega - \Omega_0) \tag{3.178}$$

where $(\mathbf{U}_1, \Omega_1)$ is the tangent vector at $(\mathbf{U}_0, \Omega_0)$. Introducing the series expansions (3.177) into (3.176) and (3.178) and keeping the power terms up to order N leads to

$$\mathbf{R}(a) = \mathbf{R}_0 + a\mathbf{R}_1 + a^2\mathbf{R}_2 + \ldots + a^N\mathbf{R}_N = 0 \tag{3.179}$$

Equating the terms $\mathbf{R}_{i\ (1 \le i \le N)}$ to zero permits to transform the nonlinear system (3.176) into a succession of N linear systems of N_{eq} equations, that are then solved recursively in order to provide $\mathbf{U}_i$ and Ω_i $(1 \le i \le N)$. This is very efficient from a computational point of view since all the linear systems share the same matrix which corresponds to the Jacobian of $\mathbf{R}$ evaluated at $(\mathbf{U}_0, \Omega_0)$. Only the right-hand side vector changes with the order. Moreover, the range of validity a_{max} of the series can be approximated a-priori by

$$a_{max} = \left(\frac{\varepsilon}{\mathbf{R}_{N+1}} \right)^{\frac{1}{N+1}} \tag{3.180}$$

where ε is a user-defined tolerance parameter. Thus a part of the solution branch is obtained by following (3.177) until $a = a_{max}$. This end point is then used as a new starting point $(\mathbf{U}_0, \Omega_0)$ and the next part of the solution branch is obtained by restarting the continuation process. As a consequence, the step length is naturally adaptative and optimal [Baguet 2003] and the continuation is very robust.

MANlab software This continuation method has been implemented in Matlab by Cochelin et al. [Cochelin 2009], resulting in the interactive software MANlab[1]. In order to use it, the user must program the operators c, $m(\cdot)$, $l(\cdot)$ and $q(\cdot,\cdot)$. The resulting operators C, $M(\cdot)$, $L(\cdot)$ and $Q(\cdot,\cdot)$ are then automatically computed and the continuation procedure is launched.

3.4 Summary

In this chapter, the main sources of nonlinearities in resonators electrostatically actuated have been identified in both clamped-clamped beam and cantilever cases. These nonlinearities are mechanical as well as electrostatic. The equation of motions have been set by extending the Euler-Bernoulli model to the nonlinear case for clamped-clamped beams and by following a variational approach, based on the extended Hamilton principle [Silva 1978a, Silva 1978b] for cantilevers. The next step was the review of some analytical as well as numerical nonlinear methods in order to solve the equation of motions of the considered resonators. These methods have been applied to the nonlinear Duffing equation in order to check their abilities to solve nonlinear problems. Among the perturbation techniques, the averaging method and the multiple time scales are very useful and commonly used in the modern science to solve analytically several nonlinear problems. They have the advantage to be relatively simple and easily implementable in Mathematica. Hence, they can be used as quick nonlinear design methods for MEMS and NEMS designers. Nevertheless, their validity which depends on the strength of the nonlinearities has to be checked via numerical nonlinear methods and particularly, the shooting coupled with a continuation technique as well as the harmonic balance method coupled with the so called "asymptotic numerical method (ANM)".

[1] MANlab can be downloaded at http://manlab.lma.cnrs-mrs.fr/

Part II

Strategies for performance enhancement of resonant accelerometers

Chapter 4

Nonlinear dynamics modeling of resonant accelerometers

Contents

4.1 Introduction **82**

4.2 Choices and motivations **82**

4.2.1 Studied resonant accelerometer structure 83

4.2.2 MEMS accelerometer 84

4.2.3 M&NEMS accelerometer 85

4.2.4 Path towards the nonlinear dynamic modeling of NEMS resonators 87

4.3 Model of a nonlinear 1-port resonator **88**

4.3.1 Equation of motion 89

4.3.2 Normalization 89

4.3.3 Solving 89

4.3.4 Numerical solutions 93

4.3.5 Simplified analytical model 94

4.4 Confrontation and reduced order model validation **96**

4.4.1 Shooting/HBM 96

4.4.2 HBM/Analytical model 97

4.5 Model of a nonlinear 2-port resonator **101**

4.5.1 Equation of motion 101

4.5.2 Normalization 102

4.5.3 Solving 102

4.6 Experimental validation **103**

4.6.1 Resonance frequency localization 103

4.6.2 Lock-in modes 104

4.6.3 Experimental characterization 105

4.6.4 Linear case ($A < A_c$) 108

4.6.5 Nonlinear case ($A > A_c$) 108

4.7 Summary **110**

4.1 Introduction

In this chapter, the motivations behind the choice of resonant sensing for M&NEMS accelerometers are detailed. The general mechanical structure of the resonant accelerometer, the fabricated devices as well as their process flows are presented. The path towards the nonlinear dynamic modeling of NEMS resonator is demonstrated. This leads to the main idea of this chapter which is the development of a simple and robust analytical model for the nonlinear dynamics of NEMS resonators. To do so, a first analytical model is performed on a 1-port resonator and validated thanks to the harmonic balance method coupled with an asymptotic numerical method. This numerical approach (HBM+ANM), fast and robust too, is validated with respect to a reference solution built by a classical shooting method. Finally, the analytical approach is extended to more realistic 2-port resonator and validated experimentally thanks to the electrical characterization of the sensing elements of the fabricated resonant accelerometers.

4.2 Choices and motivations

An accelerometer is a device that measures acceleration forces. These forces may be static, like the constant force of gravity pulling at our feet, or they could be dynamic - caused by moving or vibrating the accelerometer. Accelerometers are used for a variety of motion sensing applications ranging from inertial navigation to vibration monitoring. A wide variety of accelerometers have been designed and implemented based on a number of different techniques (see chapter 2). These techniques can be categorized as force sensing and displacement sensing based on the principle used to detect accelerations. Displacement sensing accelerometers operate by transducing the acceleration to be measured into a displacement of movable mass. This displacement can then be picked up by optical, capacitive, piezoresistive or tunnelling principles.

The first micro machined accelerometer was designed in 1979 at Stanford University, but it took over 15 years before such devices became accepted mainstream products for large volume applications. In the 1990s MEMS accelerometers revolutionised the automotive-airbag system industry. Since then they have enabled unique features and applications ranging from hard-disk protection on laptops to game controllers. More recently, people tried to develop something smaller, that could increase applicability and started searching in the fields of NEMS and nanotechnology. Small "MEMS" accelerometers or more specifically devices which combine MEMS and NEMS parts (M&NEMS) are the best alternative to follow the emerging tendency of scaling down MEMS sensors and the need of compatibility with IC technology. This implies a large reduction in delectability for most devices using displacement sensing. Consequently, the force sensing technique is inescapable.

Accelerometers based on force sensing operate by directly detecting the force applied on a proof mass as a result of the measurand. Resonant sensing of accelerations can be classified under the category of an accelerometer based on force sensing. Here, the input acceleration is detected in terms of a shift in the resonant characteristics of a sensing device coupled to the proof mass. In this chapter, we focus on the application of the resonant sensing technique for detection of accelerations on small devices which combine micro and nanotechnologies. As described in chapter 2, resonant sensing benefits from a direct frequency output, high resolution and large dynamic range. MEMS resonant accelerometers have been previously demonstrated [Burns 1996a, Roessig 1997b]. Single-crystal silicon resonant accelerometers with scale factors of greater than $1\,KHz/g$ [Kim 1997] and noise floors of $2\,\mu g$ have been reported [Roszhart 1995].

Many of the applications for resonant accelerometers have been for sensing accelerations that are slowly time varying. One of the primary reasons for this limitation is related to the main advantage of the resonant sensing principle in lending itself to a quasi-digital output. This allows for the acceleration signal to be easily demodulated by period-measuring techniques based on counting zero crossings.

4.2.1 Studied resonant accelerometer structure

The studied structure is shown in Figure 4.1a. It consists in a mass M, suspended on the substrate by anchors (made of narrow beams), and a resonator placed at a distance d from the intersection of the anchors. The used resonator is a clamped-clamped micro/nanobeam electrostatically driven by electrode 1. Electrode 2 is used for sensing which allows 2 ports measurements. Resonance is sustained by embedding the resonator in the feedback loop of an oscillator circuit. An external acceleration γ that is applied to the proof mass along the sensitive X-axis of the device, results in a force communicated axially onto the resonator. The applied axial force results in a shift in the resonator frequency due to a change in the nominal stored potential energy of the system. Thus, by evaluating the frequency shift, the acceleration applied to the device can be estimated. For the sake of generality, the resonator

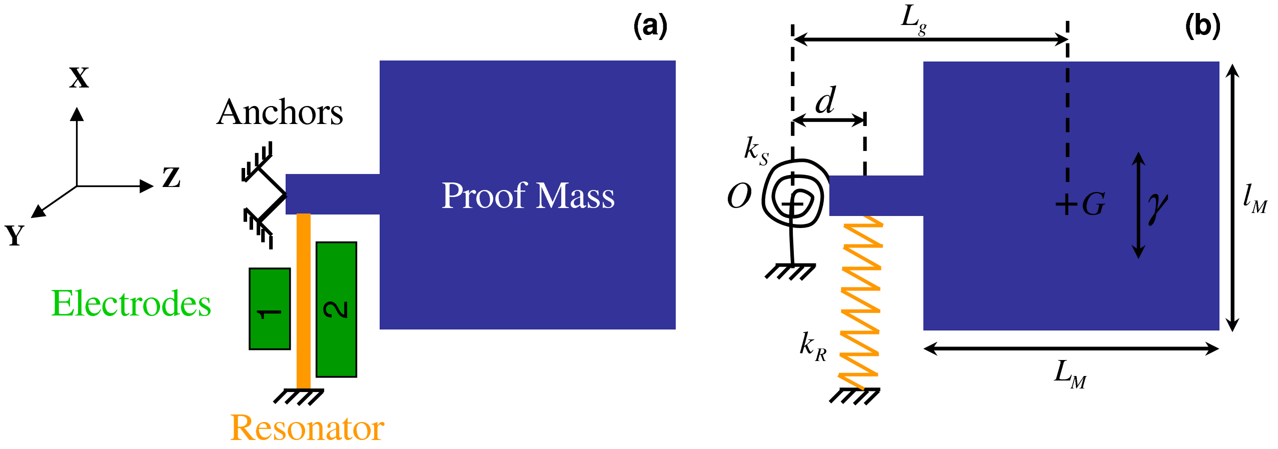

Figure 4.1: (a): Studied resonant accelerometer structure. (b): Model of the resonant accelerometer.

thickness e_R could be different from the mass and anchors thickness e_M in the resonant accelerometer. The proof mass M is assumed to be rigid, the resonator is assumed to work in compression-tension and to undergo no parasitic bending moment. Moreover, the suspension axial stiffness is assumed to be much higher than its bending stiffness. This leads to the model shown Figure 4.1b.

Assuming that under a constant acceleration $\underline{\gamma} = \gamma\underline{x}$, the rotation angle of the mass is θ; one can write the moment equilibrium of the mass at the point O:

$$k_S\theta + k_R d^2\theta = \left(\int_M \underline{OM}\nabla\rho\underline{\gamma}dV\right).\underline{y} \tag{4.1}$$

from where one obtains

$$\theta = \frac{ML_g\gamma}{k_S + d^2k_R} \tag{4.2}$$

The axial force applied on the resonator is then

$$N = k_R d\theta = \frac{ML_g}{d}\frac{1}{1+\frac{k_S}{d^2k_R}}\gamma \tag{4.3}$$

One can also write $k_R = \frac{ES_R}{L_R}$, E being the $< 110 >$ silicon Young's modulus, S_R the cross section area of the resonator and L_R its length, as well as $k_S = \frac{2EI_S}{L_S}$, I_S being the suspension quadratic modulus and L_S their length. Thus we have

$$\frac{k_S}{d^2 k_R} = \frac{1}{6d^2} \frac{L_R}{L_S} \frac{e_M}{e_R} \frac{l_S^3}{l_R} \tag{4.4}$$

Considering that the lengths of the resonator and of the suspensions are of the same order of magnitude, as well as their width l_R and l_S and their thicknesses e_M and e_R, but $l_S << d$, one has

$$\frac{k_S}{d^2 k_R} \propto \left(\frac{l_S}{d}\right)^2 << 1 \tag{4.5}$$

Hence

$$N \approx \frac{M L_g}{d} \gamma \tag{4.6}$$

Let us define $\Gamma = \frac{L_g}{d}$ = the amplification factor. The very basic but specific structure presented here may be seen as a generic structure consisting of a mass undergoing some acceleration and applying an factor Γ-amplified force on a resonator $N = \Gamma M \gamma$.

4.2.2 MEMS accelerometer

Within the framework of the European MNT project (project leader V. Nguyen), small MEMS accelerometers have been designed and fabricated in the clean rooms of LETI using a developed process flow. For this first fabricated accelerometer, all parts are made at the same level $e_M = e_R = 4\mu m$. These MEMS resonant accelerometer (Figure 4.2) have been micromachined as a first step for the transition from MEMS to NEMS. They were not designed to display high inertial performances, but rather is a way to validate process, characterization as well as to test the sensing parts (in plane clamped-clamped resonators electrostatically actuated).

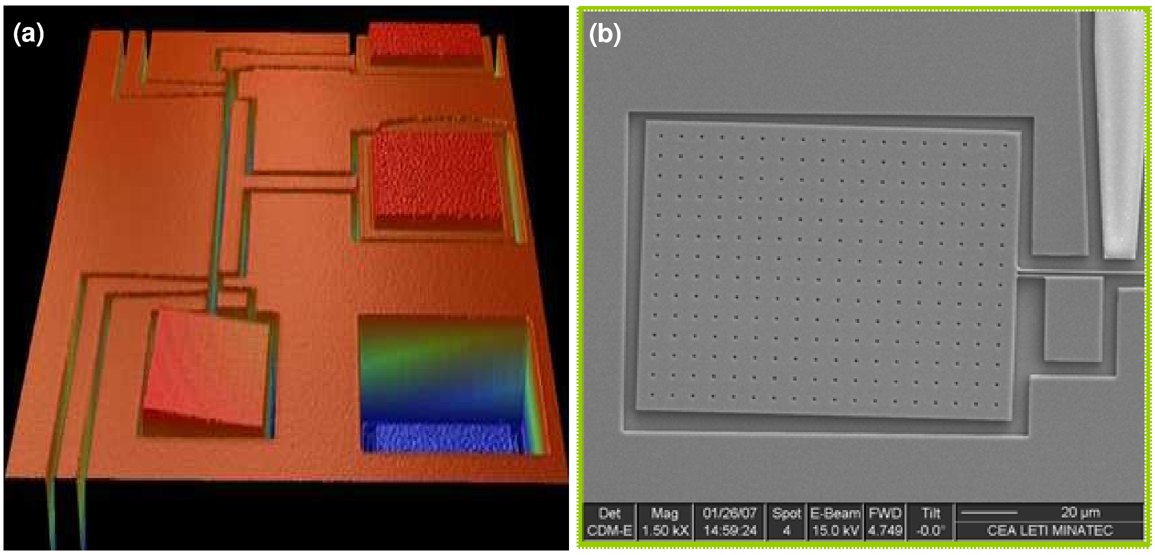

Figure 4.2: (a): Interferometric image showing the topography of the fabricated MEMS accelerometer. (b): SEM image of the micromachined resonant accelerometer (after mass release).

The fabrication starts with 200mm SOI wafers (4μm Si, 1μm $SiO2$). The use of DUV lithography combined with deep RIE process has allowed 500nm wide gaps and lines. Some low stiffness beams have been designed, so HF-vapor technique had to be improved to enable the release and protection against in-plane sticking. The simplified flow is shown in Figure 4.3.

Schema	Description - Equipment
	**<u>Substrate :</u> SOI wafer** **- SOI 4µm P 1-10 mohm.cm** **- Oxide 1000nm** **- Bulk 725 µm P 7-12 ohm.cm**
	**Photolithography ASM300 (MEMS Level)** **Dry etching 4µm of Si (DRIE).**
	**Metal deposition and etching** **HF vapor etching of TEOS** **HF vapor etching of SiO2 (Time control – Lateral release = 5µm)**

Figure 4.3: Process flow of a MEMS resonant accelerometer

4.2.3 M&NEMS accelerometer

Within the framework of the European M&NEMS project (project leader V. Nguyen), resonant accelerometers have been designed and fabricated in the clean rooms of LETI using a developed process flow. As discussed in section 2.4 and in order to improve the performances of micromachined resonant accelerometers, the idea consists in using on the same device MEMS and NEMS technologies. The MEMS part is used for the mass to keep sufficient inertial force, and the NEMS is used as a very sensitive sub-μm suspended resonator. As opposed to MNT MEMS accelerometers, these state-of-art devices were designed in order to display high performances.

The M&NEMS technology is based on SOI substrate, with a silicon top layer thickness equal to the NEMS resonator thickness. The main process steps are summarized on Figure 4.4. It starts with the lithography and etching of the NEMS resonator and of the bulk contact. Then a 0.3 μm thick oxide deposition followed by a lithography and etching of the nanoresonator protection are proceeded. In the same step, an over etching of the oxide is led to open the silicon bulk contact. A few microns thick silicon epitaxial growth (or a polysilicon deposition) is done to realize the MEMS part. Depending on the silicon doping level of the MEMS part, an implantation step can be added for the electrical contact pads. Contacts are defined by a 0.5 μm metal deposition followed by a lithography and etching of pads. A last lithography step and a DRIE of silicon thick layer is proceeded to make the MEMS structure, to isolate the bulk contact, and to open the SiO2 protective layer of the NEMS. The release of the sensor then is achieved by HF-vapor etching. Using the previous process flow, with the 6 mask levels of the M&NEMS technology, a first high-g accelerometer was designed and fabricated in the 8" silicon platform of the LETI. For that proof of concept device, the resonator was limited to $0.25 \times 0.5\,\mu m^2$ section, and the MEMS thickness was reduced to 2 μm thick. The total area of the accelerometer is less than 0.1 mm^2. SEM photograph of an in-plane M&NEMS accelerometer is shown below in Figure 4.5. Table 4.1 shows the geometrical parameters of an accelerometer being fabricated

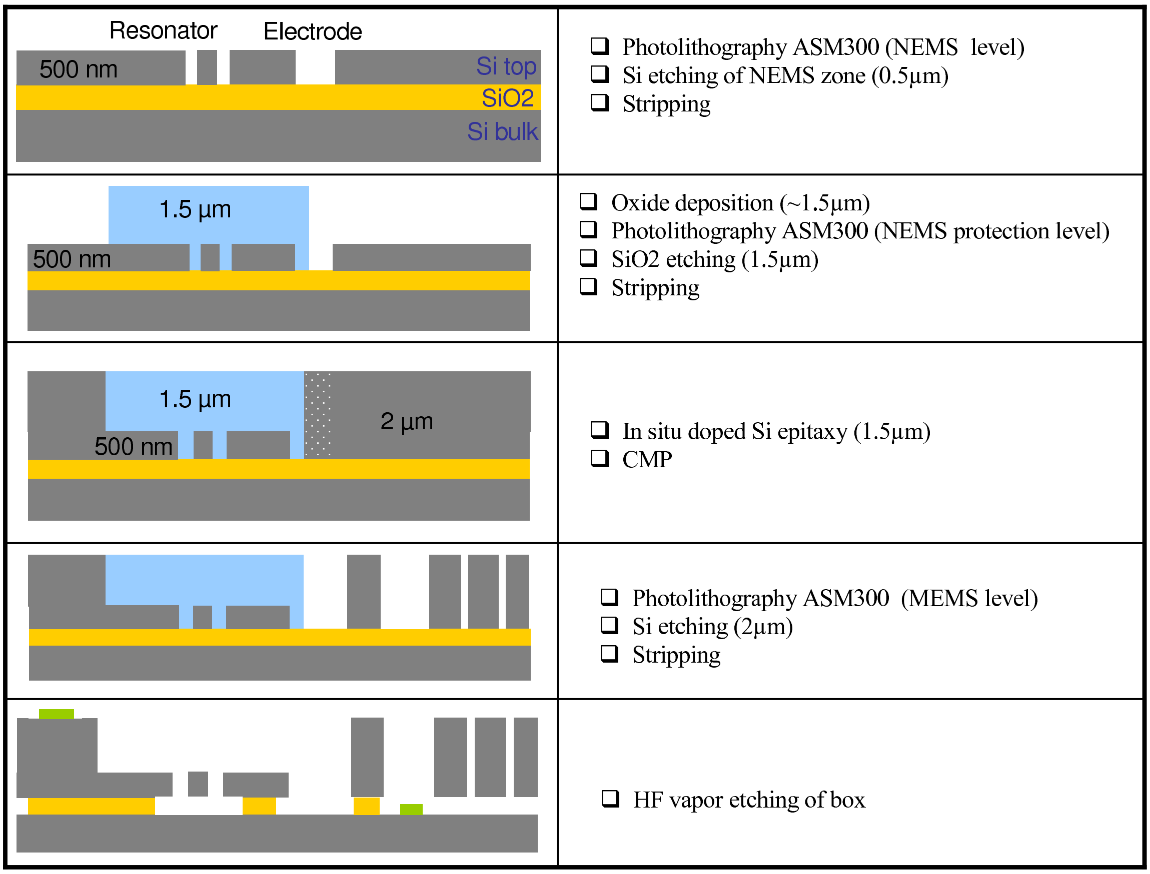

Figure 4.4: M&NEMS accelerometer process flow

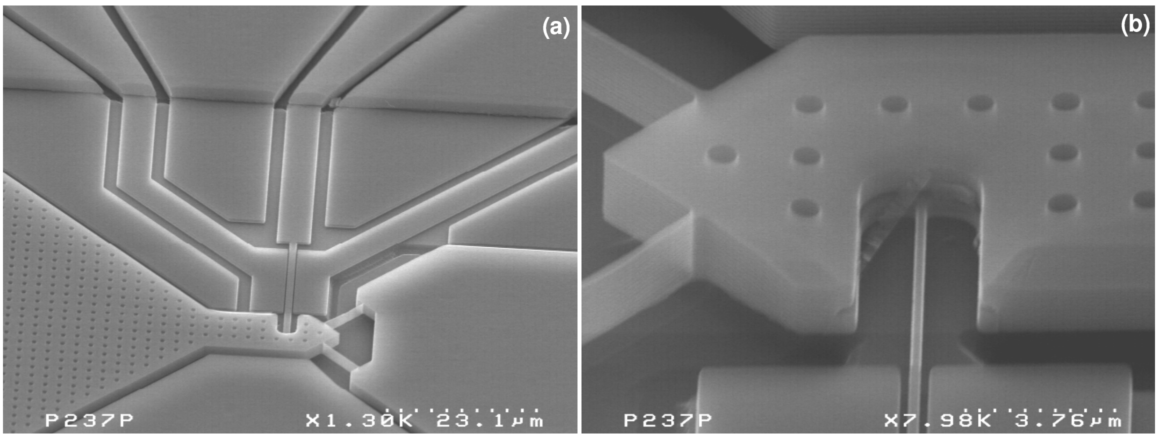

Figure 4.5: (a): SEM view of an in-plane M&NEMS accelerometer. (b): A focus on the gauge lets clearly appear the MEMS inertial mass of 2 μm thick, and the sub-μm resonator that has a section of $0.25 \times 0.5\,\mu m^2$.

in the LETI clean rooms. We have assumed $Q_m = 50000$ from empirical values obtained, $NF = 10$ which is consistent for the typical motional resistances considered here, and we have used a bandwidth $BW = 100Hz$. While the resonator is actuated to oscillate around its critical amplitude (see section 6.23), the M&NEMS accelerometer displays the performances summarized in Table 4.2. As observed, the noise coming from the thermomechanical fluctuations of the mass is negligible compared with the other sources.

$e_M(\mu m)$	$e_R(\mu m)$	$L_M(\mu m)$	$l_M(\mu m)$	$d(\mu m)$	$L_r(\mu m)$	$l_r(\mu m)$
2	0.5	150	120	3	25	0.25

Table 4.1: Geometrical parameters of the accelerometer

$f_0 = \frac{\omega_0}{2\pi}$	S_{lin}	γ_{full}	S_ω^m	S_ω^r	S_ω^a	$\mathcal{R}$	$\frac{\mathcal{R}}{\gamma_{full}}$
$3.5\,Mhz$	$5\,kHz.g^{-1}$	$30\,g$	$6.7 * 10^{-4}\,Hz^2.Hz^{-1}$	$0.23\,Hz^2.Hz^{-1}$	$2\,Hz^2.Hz^{-1}$	$1.4\,mg$	$5 * 10^{-5}$

Table 4.2: Performances computed for the accelerometer presented in Table 4.1

The device is highly sensitive in comparison with the resonant accelerometer designed and fabricated in the Sandia National Laboratories Integrated MEMS process [Smith 1995a]. The latter has a better noise-limited acceleration level is $40\mu g/\sqrt{Hz}$ which gives a resolution of $0.4mg$ in $100Hz$ bandwidth. However, the product resolution per mechanical surface of the M&NEMS accelerometer is far better which demonstrates that such accelerometers are promising low cost candidates for consumer applications, since the price is quasi-proportional to the surface of the device. For inertial navigation-grade performance, further improvements are possible based on the nonlinear dynamics of the sensor's sensitive part (the resonator) which is explained below.

4.2.4 Path towards the nonlinear dynamic modeling of NEMS resonators

The resolution of a resonant accelerometer may be given by its frequency noise spectral density [Robins 1984]:

$$S_\omega(\omega) = \left(\frac{\omega_n}{2Q}\right)^2 \frac{S_x(\omega)}{P_0} \tag{4.7}$$

where $S_x(\omega)$ is the displacement spectral density and P_0 is the displacement carrier power, ie the RMS drive amplitude of the resonator $\frac{1}{2}A^2$. Following Postma & Roukes [Postma 2005], the resonator critical amplitude is $A_c \propto \frac{h}{Q}$ where h is the resonator thickness in the direction of vibration and Q is its quality factor. It corresponds to the hysteretic limit below which the resonator is classically driven due to the mechanical nonlinearity. It is easy to see how drastic the performance degradation may be in the case of a NEMS with small h. It has been shown that closed-loop control allows operation beyond the critical amplitude [Juillard 2008], eventually up to the pull-in amplitude in the case of capacitive transduction. But to do so, it is necessary -first, to precisely know up to which amplitude the resonator may be driven, and -second, to avoid the noise mixing issue [Kaajakari 2005a, Roessig 1997a], so as not to degrade the amplitude noise density. To this end, the nonlinear behavior of resonators remains yet to be explored, and numerous models have been presented. Some of them are purely analytical [Tilmans 1994, Gui 1995, Kozinsky 2006] but they include coarse assumptions concerning nonlinearities. For example, Kozinsky et al. [Kozinsky 2006] use a nonlinear model with a 3rd order Taylor series expansion of the electrostatic forcing applied to a nanoresonator in order to tune the effective Duffing coefficient using an external electrostatic potential. However, this approximation is limited by the beam displacement (no more than 20% of the gap). Moreover, the static displacement is used for tuning, which stays limited for practical designs of resonators with high quality factors because of the very small ratio between the static and the dynamic displacement which makes the nonlinear coupling between both components negligible. Other models are more complicated and use numerical integrations such as differential quadrature method in [Najar 2006] and shooting in [Nayfeh 2007]. These methods are computationally more demanding, which makes them less interesting for M/NEMS designers. Osterberg and Senturia [Osterberg 1997] use the finite difference method to determine the static pull-in parameters and provide approximate empirical formulas. In [Abdel-Rahman 2002], the pull-in instability is studied using the shooting method and in [Younis 2003a], reduced-order models and perturbation techniques are used to analyze the pull-in behavior without giving closed form solution.

In this chapter, we first model the nonlinear dynamics of a 1-port resonator for acceleration sensing. This leads to establish our solving strategy, to justify the analytical reduced model via the modes properties as well as by numerical simulations. The second step is an extension of the analytical model to practical 2-port resonators experimentally validated thanks to the electrical characterization of the sensing elements of the fabricated MEMS resonant accelerometers described in Figure 4.2.

4.3 Model of a nonlinear 1-port resonator

A clamped-clamped microbeam is considered (Figure 4.6) subject to a viscous damping with coefficient $\tilde{c}$ per unit length and actuated by an electric load $v(t) = Vdc + Vac\cos(\tilde{\Omega}\tilde{t})$, where V_{dc} is the DC polarization voltage, V_{ac} is the amplitude of the applied AC voltage, and $\tilde{\Omega}$ is the excitation frequency.

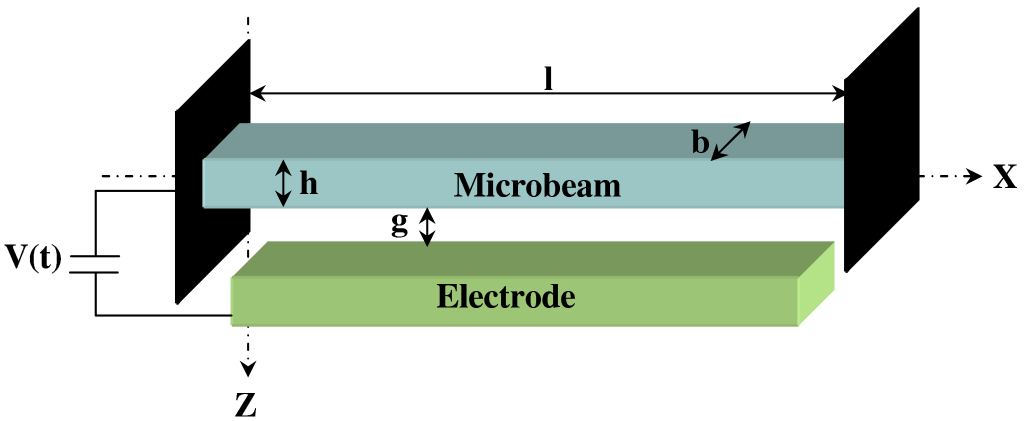

Figure 4.6: Schema of an electrostatically actuated clamped-clamped microbeam

4.3.1 Equation of motion

As previously constructed in section 3.2 (Equation (3.6)), the equation of motion that governs the transverse deflection $w(x,t)$ is written as:

$$EI\frac{\partial^4 \tilde{w}(\tilde{x},\tilde{t})}{\partial \tilde{x}^4} + \rho bh\frac{\partial^2 \tilde{w}(\tilde{x},\tilde{t})}{\partial \tilde{t}^2} + \tilde{c}\frac{\partial \tilde{w}(\tilde{x},\tilde{t})}{\partial \tilde{t}} - \left[\tilde{N} + \frac{Ebh}{2l}\int_0^l \left[\frac{\partial \tilde{w}(\tilde{x},\tilde{t})}{\partial \tilde{x}}\right]^2 d\tilde{x}\right]\frac{\partial^2 \tilde{w}(\tilde{x},\tilde{t})}{\partial \tilde{x}^2} = \frac{1}{2}\varepsilon_0\frac{bC_n\left[Vdc + Vac\cos(\tilde{\Omega}\tilde{t})\right]^2}{(g-\tilde{w}(\tilde{x},\tilde{t}))^2} \tag{4.8}$$

where $\tilde{x}$ is the position along the microbeam length, E and I are the Young's modulus and moment of inertia of the cross section. $\tilde{N}$ is the applied tensile axial force due to the residual stress on the silicon or the effect of the measurand, $\tilde{t}$ is time, ρ is the material density, h is the microbeam thickness, g is the capacitor gap width, and ε_0 is the dielectric constant of the gap medium. The last term in Equation (4.8) represents an approximation of the electric force assuming a complete overlap of the area of the microbeam and the stationary electrode including the fringing field effect through the coefficient C_n computed analytically by using the analytical expressions provided in [Nishiyama 1990] and which has been validated by 3D FE Comsol Multiphysics simulations (details are in Appendix A.1). The boundary conditions of Equation (4.8) are:

$$\tilde{w}(0,\tilde{t}) = \tilde{w}(l,\tilde{t}) = \frac{\partial \tilde{w}}{\partial \tilde{x}}(0,\tilde{t}) = \frac{\partial \tilde{w}}{\partial \tilde{x}}(l,\tilde{t}) = 0 \tag{4.9}$$

4.3.2 Normalization

For convenience and equations simplicity, we introduce the nondimensional variables:

$$w = \frac{\tilde{w}}{g}, \quad x = \frac{\tilde{x}}{l}, \quad t = \frac{\tilde{t}}{\tau} \tag{4.10}$$

where $\tau = \frac{2l^2}{h}\sqrt{\frac{3\rho}{E}}$. The substitution of Equation (4.10) into Equations (4.8) and (4.9) leads to:

$$\frac{\partial^4 w}{\partial x^4} + \frac{\partial^2 w}{\partial t^2} + c\frac{\partial w}{\partial t} - \left[N + \alpha_1\int_0^1 \left[\frac{\partial w}{\partial x}\right]^2 dx\right]\frac{\partial^2 w}{\partial x^2} = \alpha_2\frac{[Vdc + Vac\cos(\Omega t)]^2}{(1-w)^2} \tag{4.11}$$

$$w(0,t) = w(1,t) = \frac{\partial w}{\partial x}(0,t) = \frac{\partial w}{\partial x}(1,t) = 0 \tag{4.12}$$

The parameters appearing in Equation (4.11) are:

$$c = \frac{\tilde{c}l^4}{EI\tau} \quad N = \frac{\tilde{N}l^2}{EI} \quad \alpha_1 = 6\left[\frac{g}{h}\right]^2 \quad \alpha_2 = 6C_n\frac{\varepsilon_0 l^4}{Eh^3g^3} \quad \Omega = \tilde{\Omega}\tau \tag{4.13}$$

4.3.3 Solving

The total beam displacement $w(x,t)$ is a sum of a static dc displacement $w_s(x)$ and a time-varying ac displacement $w_d(x,t)$. However, for our devices, it is easy to check that the static deflexion is negligible. Typically, the measured quality factors Q are in the range of $10^4 - 5.10^4$ and the $Vdc \leq 200Vac$. Thus, the ratio between the static and the dynamic deflection is:

$$\frac{w_s(x)}{w_d(x,t)} \approx \frac{Vdc}{2Q.Vac} \leq 1\% \tag{4.14}$$

4.3.3.1 Modal decomposition

A reduced-order model is generated by modal decomposition transforming Equation (4.11) into a finite-degree-of-freedom system consisting of ordinary differential equations in time. We use the undamped linear mode shapes of the straight microbeam as basis functions in the Galerkin procedure. To this end, we express the deflection as :

$$w(x,t) = \sum_{k=1}^{N_m} a_k(t)\phi_k(x) \tag{4.15}$$

where N_m is the number of modes retained in the solution, $a_k(t)$ is the k^{th} generalized coordinate and $\phi_k(x)$ is the k^{th} linear undamped mode shape (Figure 4.7) of the straight microbeam, normalized such that $\int_0^1 \phi_k\phi_j = \delta_{kj}$ where $\delta_{kj} = 0$ if $k \neq j$ and $\delta_{kj} = 1$ if $k = j$.

4.3.3.2 Modal basis

The modal basis is formed of the eigenmodes of a linear undamped straight microbeam. The latter are the solutions of the following equation:

$$\frac{d^4\phi_k(x)}{dx^4} = \lambda_k^4 \phi_k(x) \tag{4.16}$$

The solutions of Equation (4.16) are:

$$\phi_k(x) = A\cos\lambda_k x + B\sin\lambda_k x + C\cosh\lambda_k x + D\sinh\lambda_k x \tag{4.17}$$

with $\phi_k(x)$ verifying the following boundary conditions,

$$\phi_k(0) = \phi_k(1) = \phi_k'(0) = \phi_k'(1) \tag{4.18}$$

Thus, the 4 constants A, B, C and D are solutions of the following equations :

$$A + C = 0 \tag{4.19}$$
$$B + D = 0 \tag{4.20}$$
$$A\cos\lambda_k + B\sin\lambda_k + C\cosh\lambda_k + D\sinh\lambda_k = 0 \tag{4.21}$$
$$-A\sin\lambda_k + B\cos\lambda_k + C\sinh\lambda_k + D\cosh\lambda_k = 0 \tag{4.22}$$

The non trivial solution of Equations (4.19), (4.20), (4.21) and (4.22) is :

$$det\begin{pmatrix} 1 & 0 & 1 & 0 \\ 0 & 1 & 0 & 1 \\ \cos\lambda_k & \sin\lambda_k & \cosh\lambda_k & \sinh\lambda_k \\ -\sin\lambda_k & \cos\lambda_k & \sinh\lambda_k & \sin\lambda_k \end{pmatrix} = 0 \tag{4.23}$$

$$1 - \cos\lambda_k\cosh\lambda_k = 0 \tag{4.24}$$

The λ_k, solutions of the transcendantal Equation (4.24), are listed in Table 1:
Thus, the mathematical form of the eigenmodes is given by :

$$\phi_k(x) = A_k\left\{\cos\lambda_k x - \cosh\lambda_k x + \left[\frac{\cosh\lambda_k - \cos\lambda_k}{\sin\lambda_k - \sinh\lambda_k}\right][\sin\lambda_k x - \sinh\lambda_k x]\right\} \tag{4.25}$$

Mode k	λ_k
1	4.730
2	7.853
3	10.996
4	14.137

Table 4.3: Approximate solutions of $\cos(\lambda_k)\cosh(\lambda_k) = 1$

These functions are a modal basis for the scalar product :

$$\langle u, v \rangle = \int_0^1 u(x)v(x)dx \tag{4.26}$$

In order to normalize this basis, we chose:

$$A_k = \left[\int_0^1 \left[\frac{\phi_k(x)}{A_k} \right]^2 dx \right]^{-\frac{1}{2}} \tag{4.27}$$

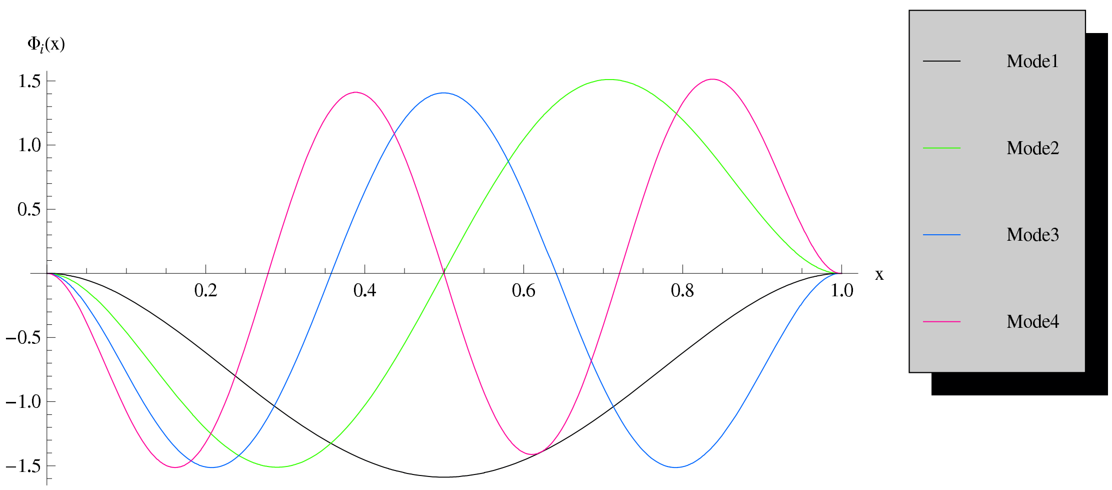

Figure 4.7: the first four linear undamped mode shapes of a clamped-clamped microbeam.

4.3.3.3 Galerkin procedure

In many models in the literature, the electrostatic nonlinear forcing term is approximated by means of a Taylor development in order to simplify the Galerkin procedure [Xie 2003, Younis 2003a]. However, when vibration amplitudes become large, such a development is no longer valid. Here, the complete contribution of the nonlinear electrostatic forces is included in the resonator dynamics without approximation. The modal projection consists in substituting Equation (4.15) in Equation (4.11), multiplying by $\phi_i(x)(1-w)^2$, using Equation (4.16) to eliminate $d^4\phi_k(x)/dx^4$ and integrating the outcome from

$x = 0$ to 1. Doing so, Equation (4.11) becomes

$$\begin{aligned}
&\ddot{a}_i - 2\sum_{j=1}^{N_m}\sum_{k=1}^{N_m}\left(\int_0^1 \phi_k\phi_j\phi_i dx\right)a_k\ddot{a}_j + \sum_{j=1}^{N_m}\sum_{k=1}^{N_m}\sum_{l=1}^{N_m}\left(\int_0^1 \phi_l\phi_k\phi_j\phi_i dx\right)a_l a_k\ddot{a}_j \\
&+c_i\dot{a}_i - 2\sum_{j=1}^{N_m}\sum_{k=1}^{N_m}\left(\int_0^1 \phi_k\phi_j\phi_i dx\right)c_j a_k\dot{a}_j + \sum_{j=1}^{N_m}\sum_{k=1}^{N_m}\sum_{l=1}^{N_m}\left(\int_0^1 \phi_l\phi_k\phi_j\phi_i dx\right)c_j a_l a_k\dot{a}_j \\
&+\lambda_i^4 a_i - 2\sum_{j=1}^{N_m}\sum_{k=1}^{N_m}\left(\int_0^1 \phi_k\phi_j\phi_i dx\right)\lambda_j^4 a_k a_j + \sum_{j=1}^{N_m}\sum_{k=1}^{N_m}\sum_{l=1}^{N_m}\left(\int_0^1 \phi_l\phi_k\phi_j\phi_i dx\right)\lambda_j^4 a_l a_k a_j \\
&-\left[N + \alpha_1\left(\sum_{m=1}^{N_m}\sum_{n=1}^{N_m}\left(\int_0^1 \phi_n'\phi_m' dx\right)a_n a_m\right)\right] \\
&\left[\sum_{j=1}^{N_m}\left(\int_0^1 \phi_j''\phi_i dx\right)a_j - 2\sum_{j=1}^{N_m}\sum_{k=1}^{N_m}\left(\int_0^1 \phi_k\phi_j''\phi_i dx\right)a_k a_j + \sum_{j=1}^{N_m}\sum_{k=1}^{N_m}\sum_{l=1}^{N_m}\left(\int_0^1 \phi_l\phi_k\phi_j''\phi_i dx\right)a_l a_k a_j\right] \\
&= \alpha_2\left(V_{dc} + V_{ac}cos\Omega t\right)^2\left(\int_0^1 \phi_i dx\right) \qquad \text{for } i = 1, 2, \ldots, N_m
\end{aligned} \tag{4.28}$$

Equation (4.28) can be written in matrix-vector form as

$$\begin{aligned}
&\left[\mathbf{M}_0 + \mathbf{M}_1(\mathbf{a}) + \mathbf{M}_2(\mathbf{a})\right]\ddot{\mathbf{a}} + \left[\mathbf{C}_0 + \mathbf{C}_1(\mathbf{a}) + \mathbf{C}_2(\mathbf{a})\right]\dot{\mathbf{a}} + \left[\mathbf{K}_0 + \mathbf{K}_1(\mathbf{a}) + \mathbf{K}_2(\mathbf{a})\right]\mathbf{a} \\
&\qquad - \left[N + \alpha_1 T_2(\mathbf{a})\right]\left[\mathbf{K}_T + \mathbf{K}_{T1}(\mathbf{a}) + \mathbf{K}_{T2}(\mathbf{a})\right]\mathbf{a} = \alpha_2\left(V_{dc} + V_{ac}cos\Omega t\right)^2\mathbf{F}
\end{aligned} \tag{4.29}$$

where $\mathbf{a}(t) = [a_1(t), a_2(t), \ldots, a_{N_m}(t)]^T$. The entries of matrices $\mathbf{M}_0$, $\mathbf{M}_1$,$\mathbf{M}_2$, $\mathbf{C}_0$, $\mathbf{C}_1$,$\mathbf{C}_2$, $\mathbf{K}_0$, $\mathbf{K}_1$,$\mathbf{K}_2$, $\mathbf{K}_T$, $\mathbf{K}_{T1}$ and $\mathbf{K}_{T2}$ are respectively M_{ij}, M_{1ij}, M_{2ij}, C_{ij}, C_{1ij}, C_{2ij}, K_{ij}, K_{1ij}, K_{2ij}, K_{Tij}, K_{T1ij}, K_{T2ij} with

$$\begin{aligned}
&M_{0ij} = \delta_{ij} \\
&M_{1ij} = -2\sum_{k=1}^{N_m}\left(\int_0^1 \phi_k\phi_j\phi_i dx\right)a_k \\
&M_{2ij} = \sum_{k=1}^{N_m}\sum_{l=1}^{N_m}\left(\int_0^1 \phi_l\phi_k\phi_j\phi_i dx\right)a_l a_k \\
&C_{0ij} = c_i\delta_{ij} \qquad C_{1ij} = c_j M_{1ij} \qquad C_{2ij} = c_j M_{2ij} \\
&K_{0ij} = \lambda_i^4\delta_{ij} \qquad K_{1ij} = \lambda_j^4 M_{1ij} \qquad K_{2ij} = \lambda_j^4 M_{2ij} \\
&K_{Tij} = \int_0^1 \phi_j''\phi_i dx \\
&K_{T1ij} = -2\sum_{k=1}^{N_m}\left(\int_0^1 \phi_k\phi_j''\phi_i dx\right)a_k \\
&K_{T2ij} = \sum_{k=1}^{N_m}\sum_{l=1}^{N_m}\left(\int_0^1 \phi_l\phi_k\phi_j''\phi_i dx\right)a_l a_k
\end{aligned} \tag{4.30}$$

The scalar $T_2(\mathbf{a})$ and the entries of vector $\mathbf{F}$ are respectively

$$\begin{aligned} T_2(\mathbf{a}) &= \sum_{m=1}^{N_m}\sum_{n=1}^{N_m}\left(\int_0^1 \phi'_n\phi'_m dx\right) a_n a_m \\ F_i &= \int_0^1 \phi_i dx \end{aligned} \tag{4.31}$$

Indices 1 and 2 for matrices $\mathbf{M}$, $\mathbf{C}$, $\mathbf{K}$, $\mathbf{K}_T$ and for T_2 denote nonlinearities of order 1 and 2 with respect to $\mathbf{a}$.

4.3.4 Numerical solutions

4.3.4.1 Shooting

The shooting method with arc-length continuation is described in section 3.3.2.2. The first step consists in writing Equation (4.29) under the same form as Equation (3.152)

$$\frac{d\mathbf{z}}{dt} = g(\mathbf{z}, t) \tag{4.32}$$

so that the shooting method can be applied. This is done through the introduction of the state variable $\mathbf{y}(t) = \dot{\mathbf{a}}(t)$ and the vector $\mathbf{z}(t) = (\mathbf{a}(t), \mathbf{y}(t))^t$, and (4.29) becomes

$$\begin{cases} \dot{\mathbf{a}} &= \mathbf{y} \\ \dot{\mathbf{y}} &= \left[\tilde{M}\right]^{-1}\Big(-\left[\mathbf{C}_0 + \mathbf{C}_1(\mathbf{a}) + \mathbf{C}_2(\mathbf{a})\right]\dot{\mathbf{a}} - \left[\mathbf{K}_0 + \mathbf{K}_1(\mathbf{a}) + \mathbf{K}_2(\mathbf{a})\right]\mathbf{a} \\ & \qquad + \left[N + \alpha_1 T_2(\mathbf{a})\right]\left[\mathbf{K}_T + \mathbf{K}_{T1}(\mathbf{a}) + \mathbf{K}_{T2}(\mathbf{a})\right]\mathbf{a} + \alpha_2\left(V_{dc} + V_{ac}cos\Omega t\right)^2 \mathbf{F}\Big) \end{cases} \tag{4.33}$$

with $\tilde{M} = \mathbf{M}_0 + \mathbf{M}_1(\mathbf{a}) + \mathbf{M}_2(\mathbf{a})$. The next step consists in programming the function g in the home-made shooting procedure implemented in Matlab, which follows the solution curve automatically.

4.3.4.2 HBM + ANM

This numerical method is described in section 3.3.2.3. Its application to our nonlinear differential system (4.29) is detailed here. After introducing the following set of auxiliary variables,

$$\begin{aligned} \mathbf{y} &= \dot{\mathbf{a}} && \text{(size } N_m\text{)} \\ \mathbf{z} &= \ddot{\mathbf{a}} = \dot{\mathbf{y}} && \text{(size } N_m\text{)} \\ \mathbf{M}_{tot} &= \mathbf{M}_1(\mathbf{a}) + \mathbf{M}_2(\mathbf{a}) && \text{(size } N_m^2\text{)} \\ \mathbf{K}_{Ttot} &= \mathbf{K}_{T1}(\mathbf{a}) + \mathbf{K}_{T2}(\mathbf{a}) && \text{(size } N_m^2\text{)} \\ \mathbf{S} &= \mathbf{K}_{Ttot}\,\mathbf{a} && \text{(size } N_m\text{)} \\ T &= T_2(\mathbf{a}) && \text{(size 1)} \end{aligned} \tag{4.34}$$

system (4.29) can be rewritten as

$$
\begin{array}{cc|c|c|c|c}
 & & & & & \text{Size}\\
\dot{\mathbf{a}} & = & & \mathbf{y} & & N_m\\
\dot{\mathbf{y}} & = & & \mathbf{z} & & N_m\\
\mathbf{0} & = & & \mathbf{M}_{tot}-\mathbf{M}_1(\mathbf{a}) & -\mathbf{M}_2(\mathbf{a}) & N_m^2\\
\mathbf{0} & = & & \mathbf{K}_{Ttot}-\mathbf{K}_{T1}(\mathbf{a}) & -\mathbf{K}_{T2}(\mathbf{a}) & N_m^2\\
\mathbf{0} & = & & \mathbf{S} & -\mathbf{K}_{Ttot}\,\mathbf{a} & N_m\\
0 & = & & T & -T_2(\mathbf{a}) & 1\\
\mathbf{0} & = & -\alpha_2(V_{dc} & +\mathbf{M}_0\,\mathbf{z}+\mathbf{C}_0\,\mathbf{y}+\mathbf{K}_0\,\mathbf{a} & +\mathbf{M}_{tot}\,(\mathbf{z}+\mathbf{C}_0\,\mathbf{y}+\mathbf{K}_0\,\mathbf{a}) & N_m\\
 & & +V_{ac}cos\Omega t)^2\mathbf{F} & -N\,\mathbf{K}_T\,\mathbf{a}-N\,\mathbf{S} & -N\,\mathbf{K}_{Ttot}\mathbf{a}-\alpha_1 T\mathbf{a}-\alpha_1 T\mathbf{S} & N_m
\end{array}
\tag{4.35}
$$

$$
\underbrace{}_{m(\dot{\mathbf{X}})=}\quad \underbrace{}_{c(\Omega)} \quad + \quad \underbrace{}_{l(\mathbf{X})} \quad + \quad \underbrace{}_{q(\mathbf{X},\mathbf{X})}
\tag{4.36}
$$

where $\mathbf{X} = (\mathbf{a}, \mathbf{y}, \mathbf{z}, \mathbf{M}_{tot}, \mathbf{K}_{Ttot}, \mathbf{S}, T)^T$ is the unknown vector of size $N_{eq} = 2N_m^2 + 4N_m + 1$, in which matrices $\mathbf{M}_{tot}$ and $\mathbf{K}_{Ttot}$ are reshaped as vectors. c is a constant vector with respect to $\mathbf{X}$, $l(\cdot)$ and $m(\cdot)$ are linear vector valued operators with respect to $\mathbf{X}$, and $q(\cdot,\cdot)$ is a quadratic vector valued operator. The next step consists in programming these operators in MANlab software (see section 3.3.2.3) which computes the solution by the Harmonic Balance combined with continuation with the Asymptotic Numerical Method.

4.3.5 Simplified analytical model

In view of enhancing the performances of resonant sensing and since an analytical approach is more convenient and simple for MEMS and NEMS designers, the perturbation techniques described in section 3.3 can potentially be used to solve the nonlinear equations of motion that govern the resonator dynamics.

4.3.5.1 Mode properties

Using the change of variable $z = x - \frac{1}{2}$ for all the eigenmodes, it is easy to check that $\Delta : z = 0$ represents an axis of symmetry for all the odd modes and an axis of antisymmetry for all the even modes. Thus, the odd modes are even functions and the even modes are odd functions $\forall\ z \in \left[-\frac{1}{2}, \frac{1}{2}\right]$. Consequently:

$$\forall\ k \in \mathbb{N}^*\ ,\forall\ i \in \mathbb{N}^*\ \ et\ \ \forall\ z \in \left[-\frac{1}{2}, \frac{1}{2}\right]$$

$$\int_0^1 \Phi_{2i} dx = \int_0^1 \Phi_{2i} {\Phi_k}^2 dx = \int_0^1 \Phi_{2i} \Phi_{2k-1}^3 dx = 0 \tag{4.37}$$

$$\int_0^1 \Phi_{2i-1} \Phi_{2k}^3 dx = \int_0^1 \Phi_{2i} \Phi_k \Phi_k'' dx = 0 \tag{4.38}$$

$$\int_0^1 \Phi_{2i}' \Phi_{2k-1}' dx = \int_0^1 \Phi_{2i-1}' \Phi_{2k}' dx = 0 \tag{4.39}$$

$$\int_0^1 \Phi_{2i} \Phi_{2k-1}^2 \Phi_{2k-1}'' dx = \int_0^1 \Phi_{2i-1} \Phi_{2k}^2 \Phi_{2k}'' dx = 0 \tag{4.40}$$

4.3.5.2 Approximate integrals

As a first approximation, the eigenvalues λ_k which are solutions of the transcendental Equation (4.24), can be written as:

$$\forall k \geq 1 \quad \lambda_k \simeq \frac{[2k+1]\pi}{2} \tag{4.41}$$

Consequently:

$$\forall k \geq 1 \quad \left\{ \begin{array}{c} \cos[\lambda_k] \simeq 0 \\ \\ \sin[\lambda_k] \simeq [-1]^k \\ \\ \cos[2\lambda_k] \simeq -1 \\ \\ \sin[2\lambda_k] \simeq 0 \end{array} \right\} \tag{4.42}$$

Moreover, $\cosh[\lambda_k] \sim \sinh[\lambda_k]$ in $[\lambda_1, +\infty]$. One can check that the validity of this equivalence starts from the first mode. In fact, for $k = 1$, $\lambda_k \simeq 4.73$ and $\cosh[\lambda_1] \simeq \sinh[\lambda_1] \simeq 56.65$.
In order to simplify the different integrals in Equation (4.28), Equations (4.41) and (4.42) are used combined with the equivalence $\cosh[\lambda_k] \sim \sinh[\lambda_k]$. Then, these integrals are approximated as equivalent to their limit when the unbounded function $\cosh[\lambda_k] \to +\infty$. Thus, approximate analytical forms of the different integrals are obtained with respect to the mode number. All the analytical close-forms of these integrals are listed in Appendix A.3.

4.3.5.3 Reduced order model

Assuming that the first mode should be the dominant mode of the system and the other modes are neglected (assumption discussed later: see section 4.4), it suffices to consider the case $n = 1$. Equation (4.29) becomes:

$$\begin{aligned} &\ddot{a}_1 + (500.564 + 12.3N)a_1 + (927 + 28N + 151\alpha_1)\,{a_1}^3 + 347\alpha_1 {a_1}^5 \\ &\quad +(1330.9 + 38.3N){a_1}^2 + 471\alpha_1 {a_1}^4 + 2.66c_1 a_1 \dot{a}_1 + 1.85c_1 {a_1}^2 \dot{a}_1 \\ &\quad +c_1\dot{a}_1 + 2.66a_1\ddot{a}_1 + 1.85{a_1}^2\ddot{a}_1 = -\frac{8}{3\pi}\alpha_2\,[Vdc + Vac\cos(\Omega t)]^2 \end{aligned} \tag{4.43}$$

To analyse the equation of motion (4.43), it proves convenient to invoke perturbation techniques which work well with the assumptions of "small" excitation and damping, typically valid in MEMS resonators. Since we are interested on the resonator dynamics around its primary resonance, the first order averaging method is sufficient especially that this method is very simple to implement in computational software compared to the multiple time scales method (see section 3.3.1.5). To facilitate the perturbation approach, in this case the method of averaging [Nayfeh 1981], a standard constrained coordinate transformation is introduced, as given by:

$$a_1 = A(t)\cos[\Omega t + \beta(t)] \tag{4.44}$$

$$\dot{a}_1 = -A(t)\Omega\sin[\Omega t + \beta(t)] \tag{4.45}$$

$$\ddot{a}_1 = -A(t)\Omega^2\cos[\Omega t + \beta(t)] \tag{4.46}$$

In addition, since near-resonant behavior is the principal operating regime of the proposed system, a detuning parameter, σ is introduced, as given by:

$$\Omega = \omega_n + \varepsilon\sigma \tag{4.47}$$

Separating the resulting equations and averaging them over the period $\frac{2\pi}{\Omega}$ in the t-domain results in the system's averaged equations, in terms of amplitude and phase, which are given by:

$$\dot{A} = -\frac{1}{2}\varepsilon\xi_0 A - \frac{1}{8}\varepsilon\xi_2 A^3 + \frac{1}{2}\varepsilon\frac{\kappa}{\omega_n}\sin\beta + O(\varepsilon^2) \tag{4.48}$$

$$A\dot{\beta} = -A\sigma\varepsilon + \frac{3}{8}\varepsilon\frac{\chi_3}{\omega_n}A^3 + \frac{5}{16}\varepsilon\frac{\chi_5}{\omega_n}A^5 - \frac{7}{10}\varepsilon\omega_n A^3 + \frac{1}{2}\varepsilon\frac{\kappa}{\omega_n}\cos\beta + O(\varepsilon^2) \tag{4.49}$$

where $\omega_n = \sqrt{500.564 + 12.3N}$, $\xi_0 = c_1$, $\xi_2 = 1.85c_1$, $\chi_3 = 927 + 28N + 151\alpha_1$, $\chi_5 = 347\alpha_1$ and $\kappa = \frac{16}{3\pi}\alpha_2 VacVdc$.

The steady-state motions occur when $\dot{A} = \dot{\beta} = 0$, which corresponds to the singular points of Equations (4.48) and (4.49). Thus, the frequency-response equation can be written in its implicit form as:

$$\left(\frac{3\chi_3}{4\omega_n}A^2 + \frac{5\chi_5}{8\omega_n}A^4 - \frac{7\omega_n}{5}A^2 - 2\sigma\right)^2 + \left(\xi_0 + \frac{\xi_2}{4}A^2\right)^2 = \left(\frac{\kappa}{A\omega_n}\right)^2 \tag{4.50}$$

The normalized displacement W_{max} with respect to the gap at the middle of the beam and the drive frequency Ω can be expressed in function of the phase β. Thus, the frequency response curve can be plotted parametrically with respect to the phase.

4.4 Confrontation and reduced order model validation

The goal of this section is to check the validity of the analytical model. First, the HBM+ANM is compared to the shooting method on a particular resonator design. Once the HBM+ANM model is validated with respect to a reference solution built by shooting, the analytical model is then compared to the HBM+ANM model. Indeed, the shooting method is computationally time-demanding and except for validation of other models, it is not a convenient tool for MEMS and NEMS designers. The investigated designs are listed in Table 4.4 and the ratio between the AC and DC voltages is set at $V_{ac} = 0.1V_{dc}$.

Resonator	$L(\mu m)$	$b(\mu m)$	$h(\mu m)$	$g(\mu m)$	Q
Design 1	400	10	10	2	10000
Design 2	50	1	1	0.4	1000

Table 4.4: Design parameters of investigated resonators.

4.4.1 Shooting/HBM

The confrontation is shown in Figures 4.8-4.10 on the first design of Table 4.4 using several modes for the shooting method and several configurations for the HBM+ANM (1, 2, 3 and 4 modes combined with 3, 5 and 7 harmonics) without including the antisymmetric modes. Indeed, these modes do not change the global dynamics of the resonator which has been shown analytically (see subsection 4.3.5) as well as numerically. Hence, the only symmetric modes were considered. In other words, when n modes are used, their numbers are the integers $i \in [1, 2n-1]$.

The results on the first mode are in good agreements between both methods. Moreover, 3 harmonics are sufficient to obtain the convergence of the HBM+ANM. A small difference between the curves for 1 mode and 2, 3 or 4 modes is noticeable. It is less than 0.1% with respect to the peak frequency, which is negligible compared to the frequency shifts induced by the fabrication tolerances. The slight difference between the curves obtained by shooting and those obtained by HBM+ANM is due to the numerical precision as well as the error accumulation caused by the time-integration scheme.

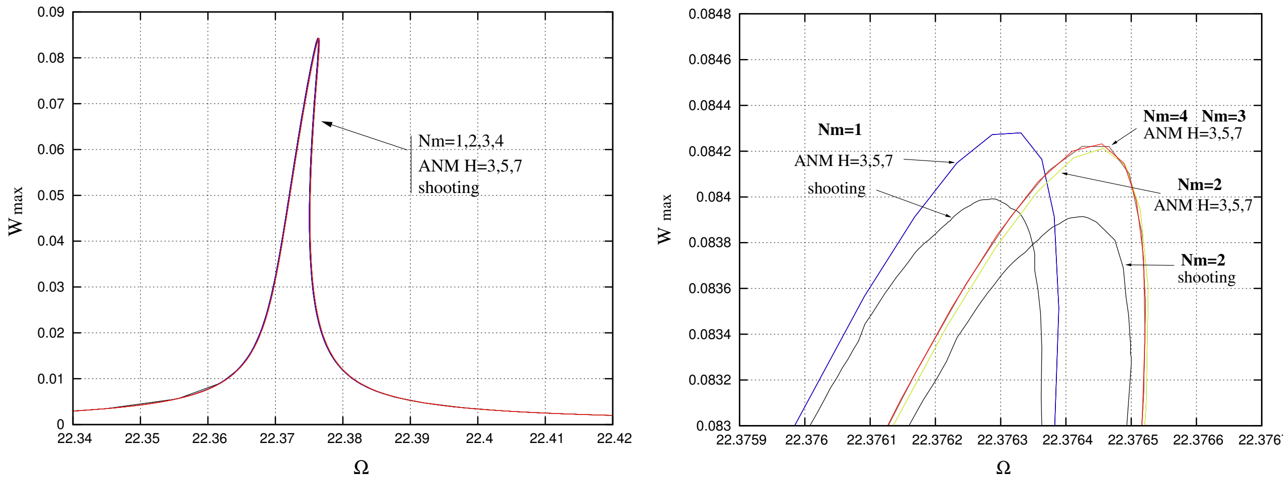

Figure 4.8: Confrontation Shooting/HBM+ANM on a slightly nonlinear behavior (Design $1/V_{dc} = 5V/V_{ac} = 0.5V$). Ω is the normalized drive frequency. W_{max} is the displacement of the beam normalized by the gap g at its middle point $\frac{l}{2}$.

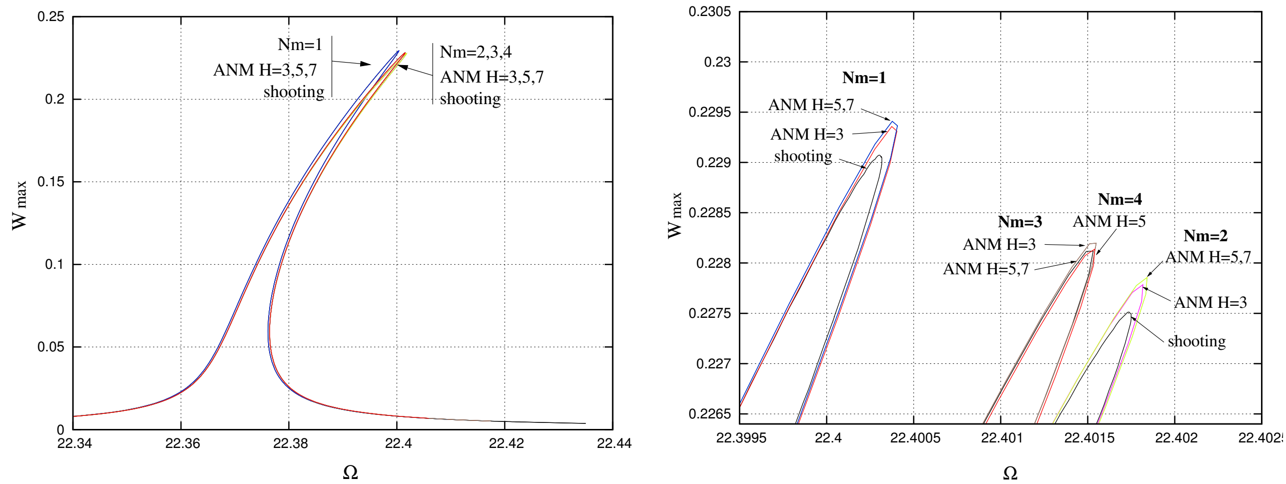

Figure 4.9: First confrontation Shooting/HBM+ANM on a strongly nonlinear behavior (Design $1/V_{dc} = 8V/V_{ac} = 0.8V$). Ω is the normalized drive frequency and W_{max} is the displacement of the beam normalized by the gap g at its middle point $\frac{l}{2}$.

4.4.2 HBM/Analytical model

The HBM+ANM model being validated, one can check easily the analytical model validation. First, as already demonstrated during the confrontation HBM+ANM/Shooting, the error made using only the first mode instead of the first three odd modes is negligible with respect to errors due to others constraints such as fabrication, temperature, pressure.... Consequently, the first mode is sufficient for the precision needed in our applications.

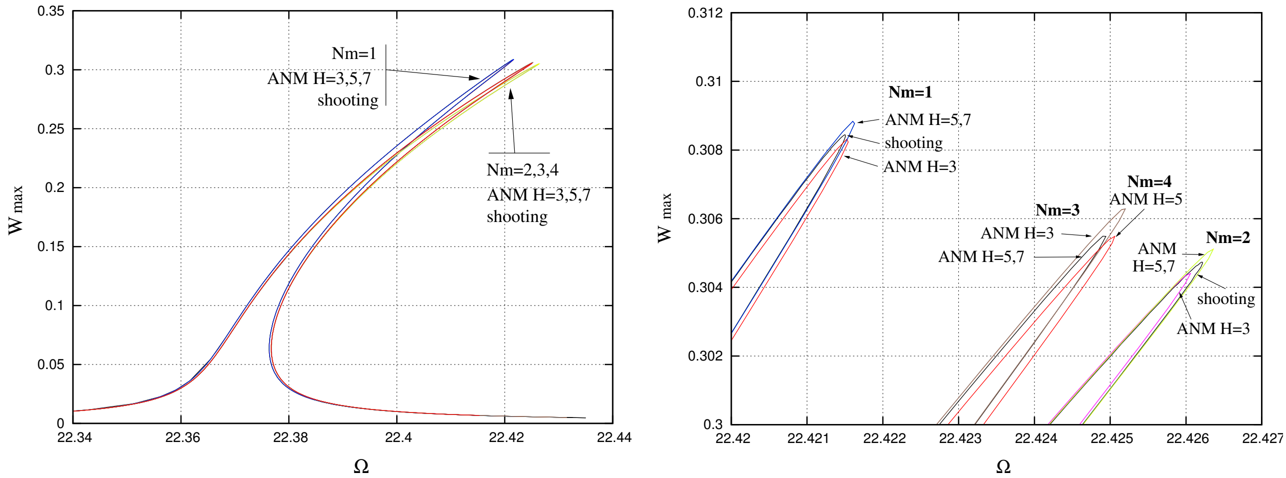

Figure 4.10: Second confrontation Shooting/HBM+ANM on a strongly nonlinear behavior (Design $1/V_{dc} = 9V/V_{ac} = 0.9V$). Ω is the normalized drive frequency and W_{max} is the displacement of the beam normalized by the gap g at its middle point $\frac{l}{2}$.

Figure 4.11 shows first comparisons between both methods on the first design of Table 4.4 at a slight nonlinear regime for a DC voltage $V_{dc} = 5V$. Analytical and numerical results are in good agreement. Particularly, at this nonlinear level, no notable difference exists between using one, two or three modes for the HBM+ANM model. Obviously, the coupling between the different modes is extremely low in this case and the influence of higher modes is negligible.

Then, the polarization voltage is increased up to $8V$ then $9V$. Consequently, the dynamic behavior of the resonator becomes strongly nonlinear as shown in Figures 4.12 and 4.13 for peak amplitudes between 20% and 35% of the gap. In these configurations, the coupling between the modes is strongly amplified. Nevertheless, the error between the analytical model and the HBM/ANM model is still negligible, even with respect to the computational solution with 3 modes (frequency shift$< 0.1\%$).

Finally, for confirmation, the same investigations have been made on a smaller resonator with a different geometry described in Table 4.4 (design 2) . Figure 4.14 displays the confrontation of both models at a high nonlinear regime for a polarization voltage $V_{dc} = 5V$ and a drive voltage $V_{ac} = 0.5V$. The same conclusions as the previous case are reached, which completes the analytical model validation.

It is important to underline that the HBM/ANM model is an interesting computational tool for nonlinear multimodal design. Indeed, it proves to be faster and more robust than the shooting method. However, we focus on the analytical model for the following reasons listed hereafter:

- The analytical model has the advantage to be fast and accurate. In fact, the committed error compared to a multimodal model is negligible with respect to other constraint errors (at least at this level).
- Its ability for performing analytical parametric investigations with respect to the phase of the resonator oscillation. Hence, it is possible to build analytical expressions that can be used as design rules for MEMS and NEMS designers in order to enhance the performances of resonant sensors.

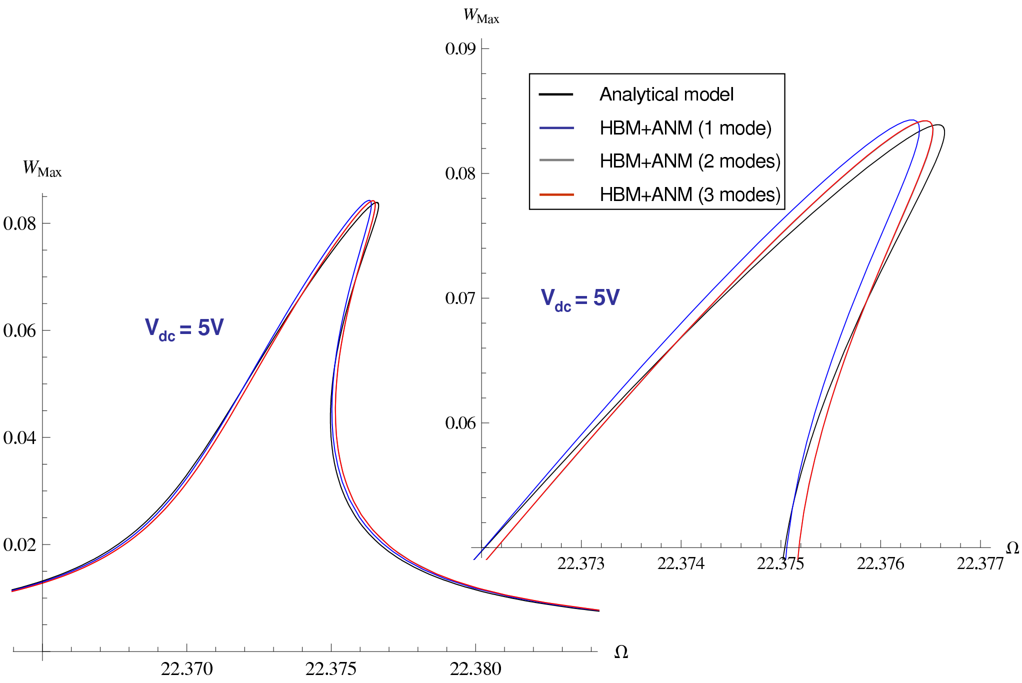

Figure 4.11: Confrontation HBM+ANM/Analytical model on a slightly nonlinear behavior (Design $1/V_{dc} = 5V/V_{ac} = 0.5V$). Ω is the normalized drive frequency and W_{max} is the displacement of the beam normalized by the gap g at its middle point $\frac{l}{2}$.

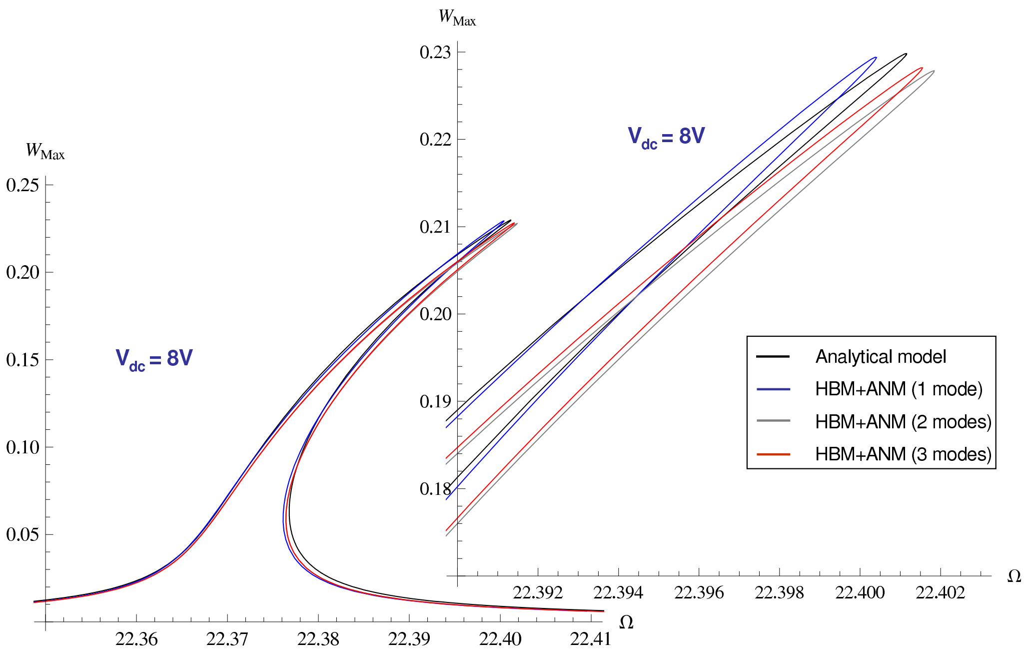

Figure 4.12: First confrontation HBM+ANM/Analytical model on a strongly nonlinear behavior (Design $1/V_{dc} = 8V/V_{ac} = 0.8V$). Ω is the normalized drive frequency and W_{max} is the displacement of the beam normalized by the gap g at its middle point $\frac{l}{2}$.

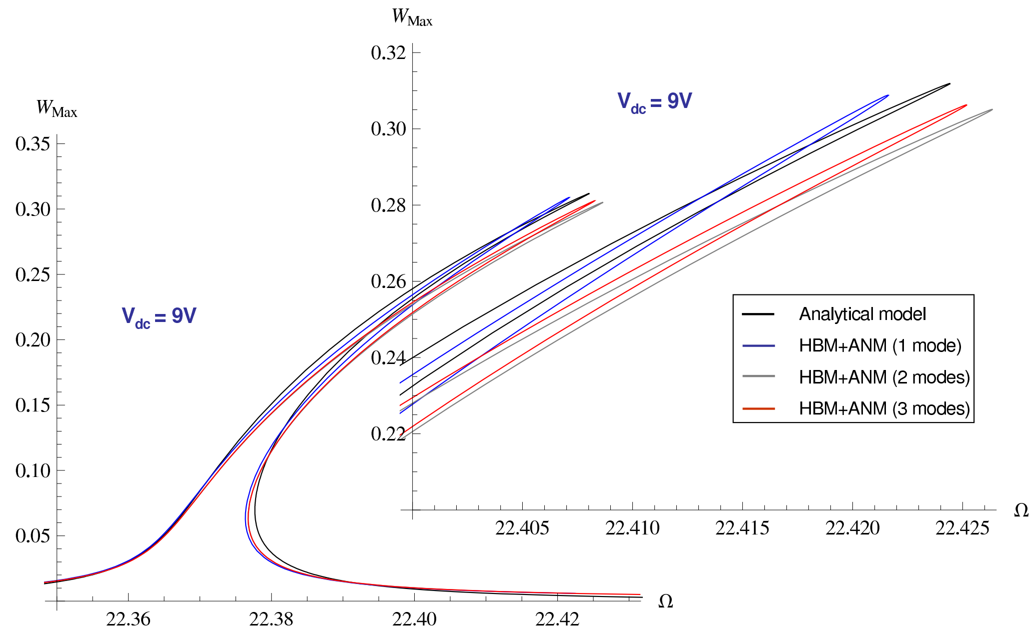

Figure 4.13: Second confrontation HBM+ANM/Analytical model on a strongly nonlinear behavior (Design 1 $/V_{dc} = 9V/V_{ac} = 0.9V$). Ω is the normalized drive frequency and W_{max} is the displacement of the beam normalized by the gap g at its middle point $\frac{l}{2}$.

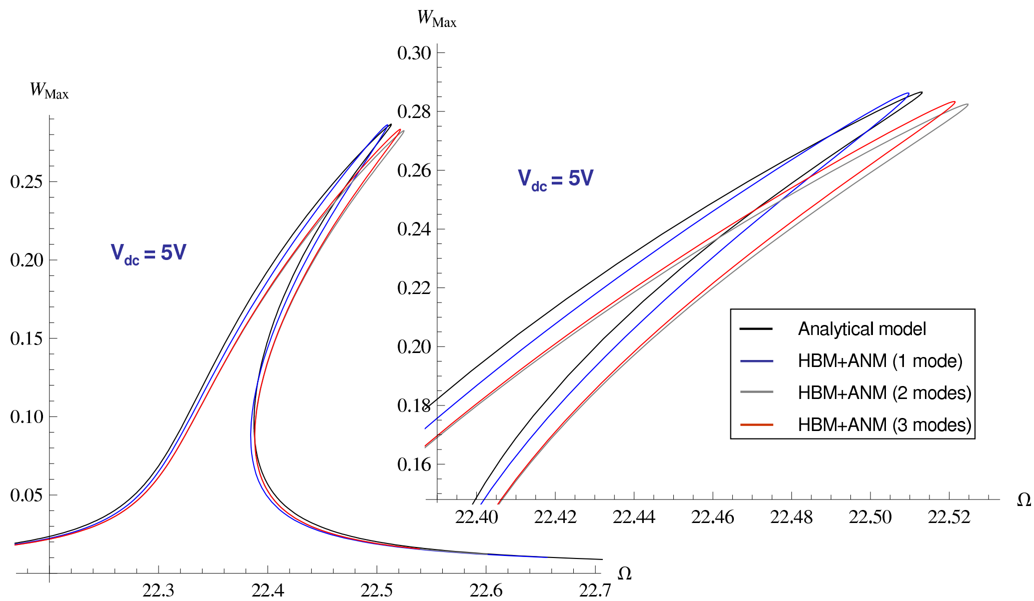

Figure 4.14: Confrontation HBM+ANM/Analytical model on a strongly nonlinear behavior (Design $2/V_{dc} = 5V/V_{ac} = 0.5V$). Ω is the normalized drive frequency and W_{max} is the displacement of the beam normalized by the gap g at its middle point $\frac{l}{2}$.

4.5 Model of a nonlinear 2-port resonator

Existing models [Najar 2006, Nayfeh 2007] for the nonlinear dynamics of MEMS resonators with relatively high capacitive variations concern designs with only one electrode for both actuation and sensing. NEMS resonators though, have low capacitive variations, and it is almost necessary to use a two port measurement, *i.e.* to separate detection and actuation electrodes in order to enhance the signal to background ratio. Moreover, the use of different gaps ($g_d < g_a$) enables the maximization of the detection signal. Below, we detail the equation of motion showing the complexity of the PDE to be solved and this is actually the case of the real designs described in Figure 4.15.

A clamped-clamped microbeam is considered (Figure 4.15) subject to a viscous damping with coefficient $\tilde{c}$ per unit length and actuated by an electric load $v(t) = -V_{dc} + V_{ac}\cos(\tilde{\Omega}\tilde{t})$, where V_{dc} is the DC polarization voltage, V_{ac} is the amplitude of the applied AC voltage, and $\tilde{\Omega}$ is the excitation frequency.

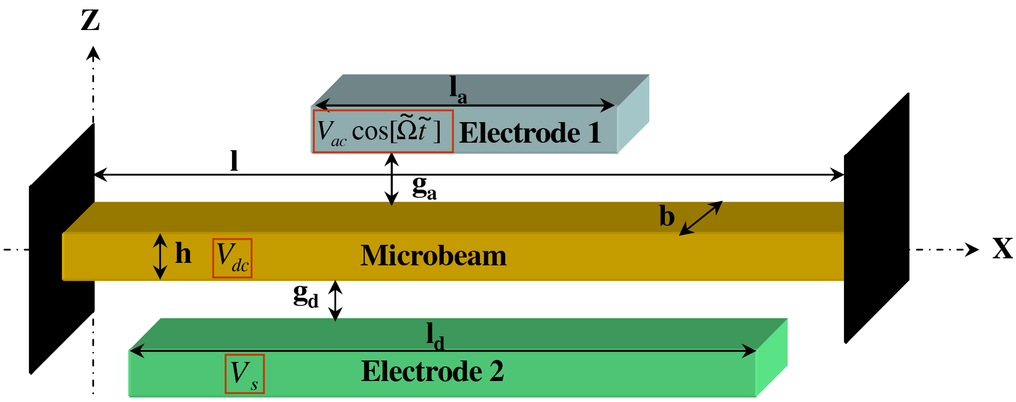

Figure 4.15: Schema of a 2-port resonator.

4.5.1 Equation of motion

The transverse deflection of the microbeam $\tilde{w}(x,t)$ is governed by the following nonlinear Euler-Bernoulli equation

$$EI\frac{\partial^4 \tilde{w}(\tilde{x},\tilde{t})}{\partial \tilde{x}^4} + \rho bh\frac{\partial^2 \tilde{w}(\tilde{x},\tilde{t})}{\partial \tilde{t}^2} + \tilde{c}\frac{\partial \tilde{w}(\tilde{x},\tilde{t})}{\partial \tilde{t}} - \left[\tilde{N} + \frac{Ebh}{2l}\int_0^l \left[\frac{\partial \tilde{w}(\tilde{x},\tilde{t})}{\partial \tilde{x}}\right]^2 d\tilde{x}\right]\frac{\partial^2 \tilde{w}(\tilde{x},\tilde{t})}{\partial \tilde{x}^2}$$

$$= \frac{1}{2}\varepsilon_0\frac{bC_{n1}\left[V_{ac}\cos(\tilde{\Omega}\tilde{t}) - V_{dc}\right]^2}{(g_a - \tilde{w}(\tilde{x},\tilde{t}))^2}H_1(\tilde{x}) - \frac{1}{2}\varepsilon_0\frac{bC_{n2}\left[Vs - V_{dc}\right]^2}{(g_d + \tilde{w}(\tilde{x},\tilde{t}))^2}H_2(\tilde{x}) \tag{4.51}$$

$$H_1(\tilde{x}) = H(\tilde{x} - \frac{l+l_a}{2}) - H(\tilde{x} - \frac{l-l_a}{2}) \tag{4.52}$$

$$H_2(\tilde{x}) = H(\tilde{x} - \frac{l+l_d}{2}) - H(\tilde{x} - \frac{l-l_d}{2}) \tag{4.53}$$

where g_a and g_d are respectively the actuation and the sensing capacitor gap width. The last term in Equation (4.51) represents an approximation of the electric force assuming a resonator design with 2 stationary electrodes : electrode 1 for the actuation and electrode 2 for the sensing including the fringing field effect [Nishiyama 1990] using the coefficients C_{ni} (see Appendix A.1). $H(\tilde{x})$ are Heaviside functions modeling the electrostatic forces distributions. The boundary conditions are:

$$\tilde{w}(0,\tilde{t}) = \tilde{w}(l,\tilde{t}) = \frac{\partial \tilde{w}}{\partial \tilde{x}}(0,\tilde{t}) = \frac{\partial \tilde{w}}{\partial \tilde{x}}(l,\tilde{t}) = 0 \tag{4.54}$$

4.5.2 Normalization

For convenience and equations simplicity, we introduce the nondimensional variables:

$$w = \frac{\tilde{w}}{g_d}, \quad x = \frac{\tilde{x}}{l}, \quad t = \frac{\tilde{t}}{\tau} \tag{4.55}$$

where $\tau = \frac{2l^2}{h}\sqrt{\frac{3\rho}{E}}$. Substituting Equation (4.55) into Equations (4.51), (4.52), (4.53) and (4.54), we obtain:

$$\frac{\partial^4 w}{\partial x^4} + \frac{\partial^2 w}{\partial t^2} + c\frac{\partial w}{\partial t} - \left[N + \alpha_1 \int_0^1 \left[\frac{\partial w}{\partial x}\right]^2 dx\right] \frac{\partial^2 w}{\partial x^2} + \alpha_2 C_{n2} \frac{[Vs - V_{dc}]^2}{(1+w)^2} H_2(x)$$
$$= \alpha_2 C_{n1} \frac{[V_{ac}\cos(\Omega t) - V_{dc}]^2}{(R_g - w)^2} H_1(x) \tag{4.56}$$
$$w(0,t) = w(1,t) = \frac{\partial w}{\partial x}(0,t) = \frac{\partial w}{\partial x}(1,t) = 0 \tag{4.57}$$

The parameters appearing in Equation (4.56) are:

$$H_2(x) = H(x - \frac{l + l_a}{2l}) - H(x - \frac{l - l_a}{2l}) \tag{4.58}$$
$$H_2(x) = H(x - \frac{l + l_d}{2l}) - H(x - \frac{l - l_d}{2l}) \tag{4.59}$$
$$c = \frac{\tilde{c}l^4}{EI\tau}, \quad N = \frac{\tilde{N}l^2}{EI}, \quad \alpha_1 = 6\left[\frac{g_a}{h}\right]^2 \tag{4.60}$$
$$R_g = \frac{g_a}{g_d}, \quad \alpha_2 = 6\frac{\varepsilon_0 l^4}{Eh^3 g_a^3}, \quad \Omega = \tilde{\Omega}\tau \tag{4.61}$$

4.5.3 Solving

Similarly to the one port resonator model (Section 4.3), the static deflection is negligible with respect to the dynamic deflection. Then, a reduced-order model is generated by modal decomposition (Equation (4.15)) transforming Equation (4.56) into a finite-degree-of-freedom system consisting in ordinary differential equations in time. We use the undamped linear mode shapes of the straight microbeam as basis functions in the Galerkin procedure.

We multiply Equation (4.56) by $\phi_k(x)\left[(1+w)(R_g - w)\right]^2$ in order to include the complete contribution of the nonlinear electrostatic forces in the resonator dynamics without approximation. This particular step is similar to what Nayfeh et al. [Nayfeh 2007] used for a one port resonator. It is adapted here for a two ports resonator. This method has some disadvantages like the non orthogonality of the operator $w^4 \frac{\partial^4 w}{\partial x^4}$ with respect to the undamped linear mode shapes of the resonator, the increase of the nonlinearity level in the normalized equation of motion (4.56) as well as the incorporation of new nonlinear terms such as the Vander Pool damping. Nevertheless, the resulting equation contains less parametric terms than if the nonlinear electrostatic forces were expanded in Taylor series and the solution of nonlinear problem is valid for large displacements of the beam up to the sensing gap thickness.

Next, we substitute Equation (4.15) into the resulting equation, use Equation (4.16) to eliminate $\frac{d^4\phi_k(x)}{dx^4}$, integrate the outcome from $x = 0$ to 1, and obtain a system of coupled ordinary differential equations in time.

Since the first mode is the dominant mode of the system and the higher modes are negligible (See section 4.4), it is enough to consider $n = 1$ and obtain:

$$\begin{aligned} &\ddot{a}_1 + c\dot{a}_1 + {\omega_n}^2 a_1 + \mu_1 a_1 \ddot{a}_1 + \mu_2 {a_1}^2 \ddot{a}_1 + \mu_3 {a_1}^3 \ddot{a}_1 + \mu_4 {a_1}^4 \ddot{a}_1 + c\mu_1 a_1 \dot{a}_1 + c\mu_2 {a_1}^2 \dot{a}_1 \\ &+ c\mu_3 {a_1}^3 \dot{a}_1 + c\mu_4 {a_1}^4 \dot{a}_1 + \chi_2 {a_1}^2 + \chi_3 {a_1}^3 + \chi_4 {a_1}^4 + \chi_5 {a_1}^5 + \chi_6 {a_1}^6 + \chi_7 {a_1}^7 + \nu \\ &+ \zeta_0 \cos(\Omega t) + \zeta_1 a_1 \cos(\Omega t) + \zeta_2 {a_1}^2 \cos(\Omega t) + \zeta_3 \cos(2\Omega t) \\ &+ \zeta_4 a_1 \cos(2\Omega t) + \zeta_5 {a_1}^2 \cos(2\Omega t) = 0 \end{aligned} \tag{4.62}$$

We recognize in the Equation (4.62) some canonical nonlinear terms such as the cubic stiffness term (Duffing nonlinearity), the nonlinear Van der Pol damping ($c\mu_2 {a_1}^2 a_1'$) as well as the parametric excitation (Mathieu term). However, the presence of other high-level nonlinearities in Equation (4.62) makes the described system in Figure 4.15 as a forced nonlinear resonator under multifrequency parametric excitation. This kind of equation is not so frequently used in the literature and includes terms coming from the coupling between the mechanical and the electrostatic nonlinearities as well as the nonlinear coupling between both electrostatic forces. In the appendix A.3, we show the expressions of all the integration parameters presented in Equation (4.62) which can be easily computed with any computational software. To analyze this equation of motion, we use perturbation techniques well adapted to "small" excitation and damping ($Q > 10$), typically valid in NEMS resonators [Husain 2003].

Thus, as previously, the averaging method is used in order to obtain the two first order nonlinear ordinary differential equations that modulate the amplitude A and the phase β.

$$\dot{A} = \varepsilon \frac{\sin[\beta]\zeta_0}{2\omega_n} + \varepsilon \frac{A^2 \sin[\beta]\zeta_2}{8\omega_n} - \varepsilon \frac{Ac}{2} - \varepsilon \frac{A^3 c\mu_2}{8} - \varepsilon \frac{A^5 c\mu_4}{16} + O(\varepsilon^2) \tag{4.63}$$

$$\begin{aligned} \dot{\beta} = \varepsilon\sigma - \varepsilon \frac{3A^2\chi_3}{8\omega_n} - \varepsilon \frac{5A^4\chi_5}{16\omega_n} - \varepsilon \frac{35A^6\chi_7}{128\omega_n} - \varepsilon \frac{\cos[\beta]\zeta_0}{2A\omega_n} \\ - \varepsilon \frac{3A\cos[\beta]\zeta_2}{8\omega_n} + \varepsilon \frac{3}{8} A^2 \omega_n \mu_2 + \varepsilon \frac{5}{16} A^4 \omega_n \mu_4 + O(\varepsilon^2) \end{aligned} \tag{4.64}$$

The steady-state motions occur when $\dot{A} = \dot{\beta} = 0$, which corresponds to the singular points of Equations (4.63) and (4.64).Thus, the frequency-response equation can be written in its parametric form $\{A = K_1(\beta),\ \Omega = K_2(\beta)\}$ in function of the phase β as a set of 2 equations easy to introduce in Matlab or Mathematica. This ability makes the model suitable for NEMS designers as a quick tool of resonant sensor performance optimization.

For the sake of clarity, the frequency-response equation can be written in its implicit form as:

$$\frac{A^2 \left\{\Lambda_1(A) - 8\omega_n \left(16\Omega + \Lambda_2(A)\right)\right\}^2}{256 \left(4\zeta_0 + 3A^2\zeta_2\right)^2} + \frac{\left(8cA + 2A^3 c\mu_2 + A^5 c\mu_4\right)^2 \omega_n^2}{4 \left(4\zeta_0 + A^2\zeta_2\right)^2} = 1 \tag{4.65}$$

$$\Lambda_1(A) = 48A^2\chi_3 + 40A^4\chi_5 + 35A^6\chi_7 \tag{4.66}$$

$$\Lambda_2(A) = \left(6A^2\mu_2 + 5A^4\mu_4 - 16\right)\omega_n \tag{4.67}$$

4.6 Experimental validation

4.6.1 Resonance frequency localization

This first step towards the electrical characterization of NEMS resonators at LETI was performed with the help of Herve Fontaine during his internship.

The fabricated resonators are electrostatically actuated in-plane. These resonators are described in Figure 5.1a and Figure 4.16 and their measured quality factors are very high ($10^4 - 5.10^5$). As a consequence, the critical amplitude is around $15nm$ and thus, the capacitance variation is around $2\ aF$. Considering the low capacitance variations and the high motional resistance combined with the important parasitic capacitances, tracking the resonance peak purely electrically is really difficult. Being at the limit of electric direct measurement, a SEM set-up was developed as a first step, coupled with a real-time in-situ electrical measurement using an external low noise lock-in amplifier (Figure 4.17). This set-up allows the simultaneous visualization of the resonance by SEM imaging (Figure

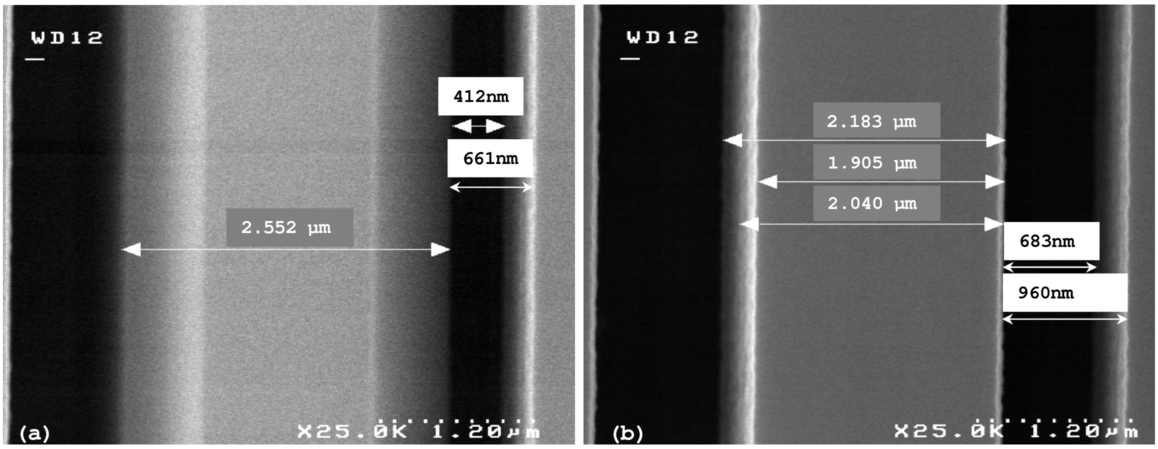

Figure 4.16: (a): SEM image of the resonator resonance. (b): SEM image of the resonator at rest. Dimensions: $200\mu m \times 2\mu m \times 4\mu m$. The gap: around $750\,nm$.

4.16) and the motional current frequency response measurement. However, it is not recommended for NEMS devices, since the SEM changes significantly their electric proprieties.

4.6.2 Lock-in modes

Operation of a lock-in amplifier relies on the orthogonality of sinusoidal functions. Specifically, when a sinusoidal function of frequency f_1 is multiplied by another sinusoidal function of frequency f_2 not equal to f_1 and integrated over a time much longer than the period of the two functions, the result is zero. In the case when f_2 is equal to f_1, and the two functions are in phase, the average value is equal to half of the product of the amplitudes.

In essence, a lock-in amplifier takes the input signal, multiplies it by the reference signal (either provided from the internal oscillator or an external source), and integrates it over a specified time, usually on the order of milliseconds to a few seconds. The resulting signal is an essentially DC signal, where the contribution from any signal that is not at the same frequency as the reference signal is attenuated essentially to zero, as well as the out-of-phase component of the signal that has the same frequency as the reference signal (because sine functions are orthogonal to the cosine functions of the same frequency), and this is also why a lock-in is a phase sensitive detector.

4.6.2.1 $1f$ mode

A schematic of the lock-in amplifier when used in $1f$ mode is show in Figure 4.18. Here the generator signal which serves for the resonator actuation and the reference signal have the same frequency.

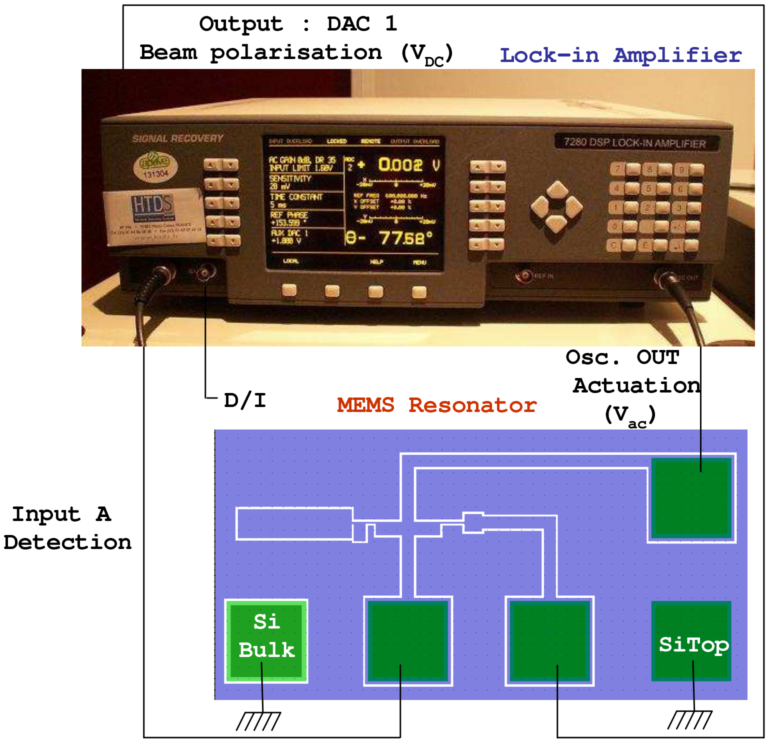

Figure 4.17: Connection layout for the electrical characterization.

4.6.2.2 $2f$ mode

As show in Figure 4.19., the $2f$ reference is generated between the phase shifter and the multiplier input by doubling the output from the Sine Generator. At the output of the frequency doubler, the $2f$ reference is by default set to be "in phase" with the $1f$ signal input and to have the same amplitude. The actuation and detection signals are not at the same frequency which ensures a better decoupling and avoid most of parasitic capacitances.

For a sine reference signal and an input waveform $U_{in}(t)$, the DC output signal $U_{out}(t)$ can be calculated for an analog lock-in amplifier by:

$$U_{out}(t) = \frac{1}{T}\int_{t-T}^{t} \sin[2\pi f_{ref} s + \phi] U_{in}(s) ds \tag{4.68}$$

where ϕ is a phase that can be set on the lock-in (set to zero by default). Practically, many applications of the lock-in only require recovering the signal amplitude rather than relative phase to the reference signal; a lock-in usually measures both in-phase (X) and out-of-phase (Y) components of the signal and can calculate the magnitude (R) from that.

4.6.3 Experimental characterization

As a second step, once the resonance frequency was found, the SEM setup was not used to allow for precise measurements and the device was placed in a vacuum chamber and measurements were performed at room temperature. The residual stress $(\frac{\tilde{N}}{bh})$ calculated knowing the frequency shift between the natural frequency and the measured frequency is around $15MPa$ and the fringing field

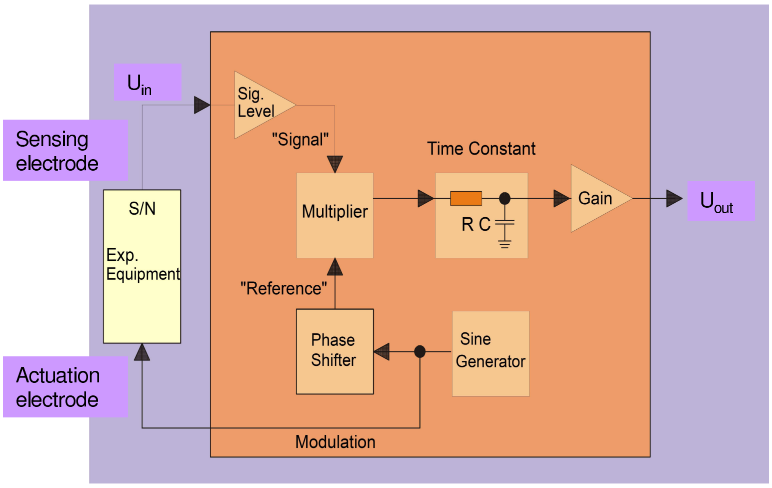

Figure 4.18: Lock-In Schematic / 1f Mode

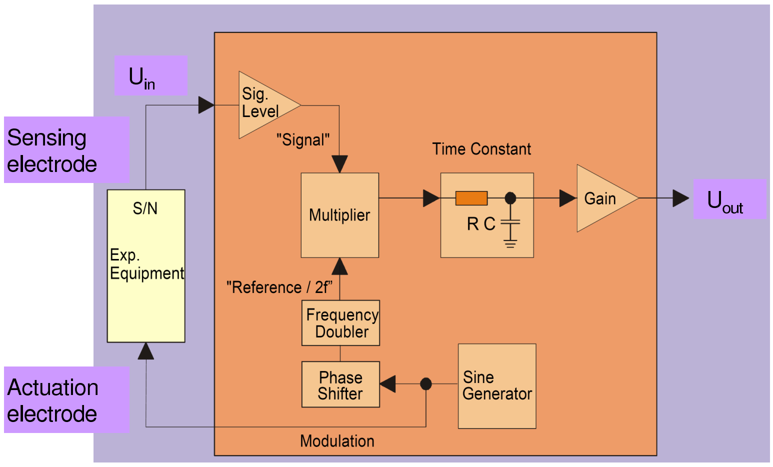

Figure 4.19: Lock-In Schematic / 2f Mode

effect coefficients are $C_{n1} = 1.6$ and $C_{n2} = 1.5$. As shown in Figure 4.20, the raw signal given by the lock-in amplifier shows a weak resonance peak drowned in a large background, followed by an antiresonance, both due to a large feedthrough capacitance. To get rid of this effect, a measurement is carried out with null DC voltage. In this case, the beam does not resonate and thus, no motional signal is measured. The vectorial subtraction of the two signals gives the signal purely due to the motional current which is compared with the model results. Considering the equivalent electrical scheme of the measurement chain (See Figure 4.21), the output voltage generated by this system can be expressed as follows:

$$V_{out}(t) = Z_t \left(V_{dc} - V s\right) \frac{dC_{res}}{dt} \tag{4.69}$$

$$\frac{dC_{res}}{dt} = \int_{\frac{l-l_d}{2l}}^{\frac{l+l_d}{2l}} \frac{bC_{n2}\varepsilon_0\phi_1(x)a_1'(t)}{\left(1 - a_1(t)\phi_1(x)\right)^2}\, dx \tag{4.70}$$

$$Z_t = \frac{Z_{cable} Z_{Lockin}}{Z_{cable} + Z_{Lockin}} \tag{4.71}$$

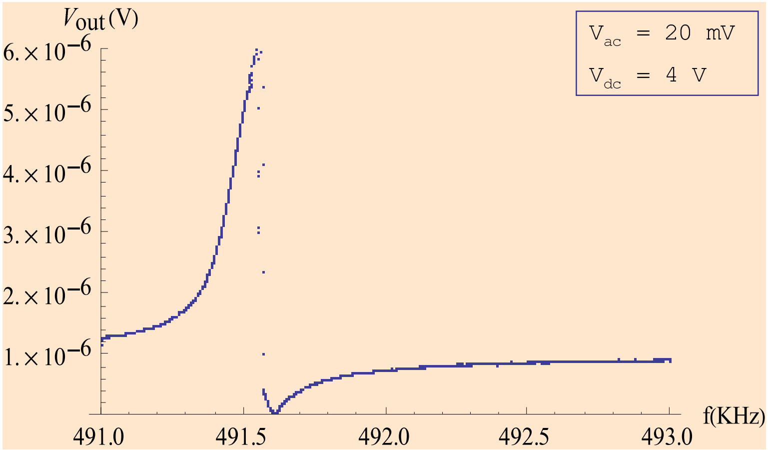

Figure 4.20: The raw signal given by the lock-in amplifier.

where V_s is the DC voltage applied to the sensing electrode, Z_{Lockin} is the internal impedance of the lock-in amplifier and Z_{cable} is the impedance of the parasitic capacitances due to the connection cables. The derivative of the resonator capacitance with respect to the dimensionless time t has been

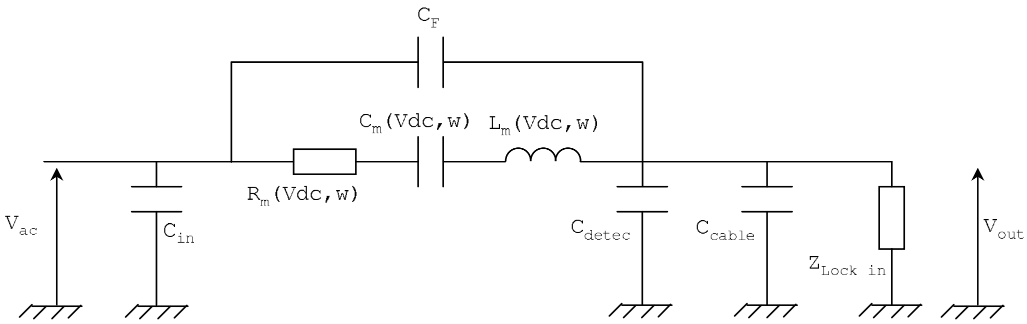

Figure 4.21: Equivalent electric circuit.

expanded in a fifth order Taylor series which enables the analytical computation of the integral in Equation (4.70). Then, Equation (4.44) and (4.45) are substituted into the outcome equation and the trigonometric functions are linearized. Since the electrical measurement filters out all frequency components of the readout signal except which of the drive frequency, the first harmonic of the Fourier transform of Equation (4.70) gives the motional current frequency response including the coupling between the dynamics of the resonator and the read-out voltage (Equation (4.44)). Although this coupling brings extra nonlinear terms, their contribution happens to be negligible and the read-out voltage is proportional to the dynamic deflection.

All results shown below were obtained with the same device described in Figure 4.22 using the same experimental conditions, and in particular at a pressure low enough so that the quality factor has reached saturation. Only the bias and drive voltages may vary as indicated on the graphs.

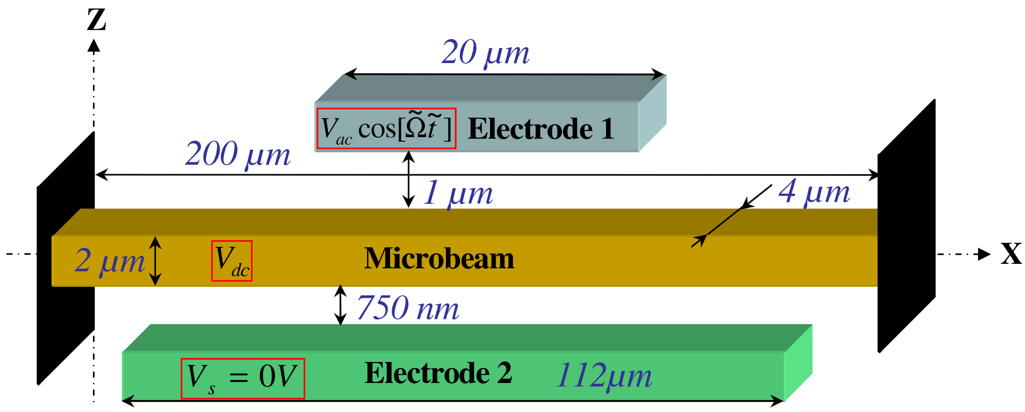

Figure 4.22: Dimensions of a typical fabricated resonator.

4.6.4 Linear case $(A < A_c)$

The vibration amplitude of the resonator is lower than the critical amplitude (A_c is the highest amplitude below bistability). It is paradoxically a difficult condition to obtain, as it demands a low drive, and thus the signals are very weak. A great effort has been needed on the noise and output capacitances reduction to get the peaks out of the background. It is important to underline that all the inputs of the model are known physical parameters including the fringing field coefficients computed using the analytical formulas [Nishiyama 1990], except the quality factor Q measured experimentally. So as to evaluate the model, Q has been fitted using linear curves. But for NEMS design optimization, the quality factor will be computed analytically using existing models taking into account the thermoelastic damping [Lifshitz 2000], the support loss [Hao 2003] and the surface loss [Yang 2002] and which actually give results in good agreement with experimental measurements. Figure 4.23 shows 3 linear peaks obtained for different values of the bias voltage V_{dc} $(1V - 3V - 5V)$ and same drive voltage. The reader will note that the loaded quality factor changes $(5.10^4 - 23.10^3 - 11.10^3)$ accordingly [Sazonova 2006]. The resonance frequency also decreases from $493KHz$ (black curve) down to $490.5KHz$ (green curve) due to the negative stiffness, phenomenon very well displayed by the model. Precisely, the effect of the negative electrostatic stiffness gives frequency shifts of $0.8KHz$ between the green and the red curves and $1.6KHz$ between the red and the black curve. Moreover, the shape of the peaks and their predicted amplitudes using the model are in excellent correlation with the experimental measured points. Both red and black linear peaks are in the same range of oscillation amplitude ($1.8\mu V$ for the red peak and $2.4\mu V$ for the black curve). However, the red peak with high quality factor ($Q = 23000$) is very close to the critical amplitude ($V_{out} = 1.9\mu V$), which is well in agreement with Equations (5.6) and (5.10) (details are in section 5.3).

4.6.5 Nonlinear case $(A > A_c)$

The vibration amplitude of the resonator is higher than the critical amplitude. The actuation voltage V_{ac} is increased from $5mV$ used for linear peaks to $20mV$ here. Figure 4.24 shows 3 nonlinear peaks, again obtained for different values of V_{dc} $(1V - 3V - 5V)$. The use of the same resonator, same vacuum conditions and same bias values as in the linear case allows for the identification of the quality factors from the measurements in Figure 4.23, assuming that no extra damping mechanism takes place. The predicted curves using the model are in very good correlation in shape and frequency shift (negative stiffness) with the measured points, although the model displays slightly higher amplitudes; the un-

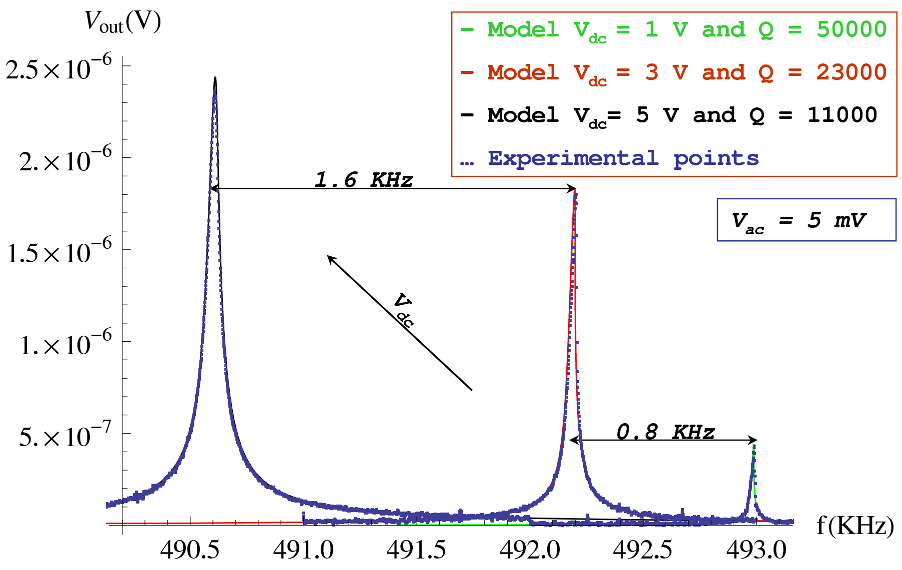

Figure 4.23: Measured and predicted frequency responses.

stable jumps make it awkward to obtain precise comparison of high quality factor peaks. Indeed, it is easy to fit perfectly the experimental curves with slightly different values of width, quality factor and residual stress. This is confirmed by the fact that the ratio between the critical amplitude calculated using the model and the peak amplitude measured experimentally $\frac{V_{out}}{V_c}$ is around 5 for the red curve (for which the discrepancy is highest) and 3 for the green and the black curves. Consequently, the red peak is more nonlinear than the two other peaks which is clearly shown in Figure 4.24 from the curvature of each peak. Also, this validates the close form expression of the critical amplitude (Equation (5.10)) (details are in section 5.3).

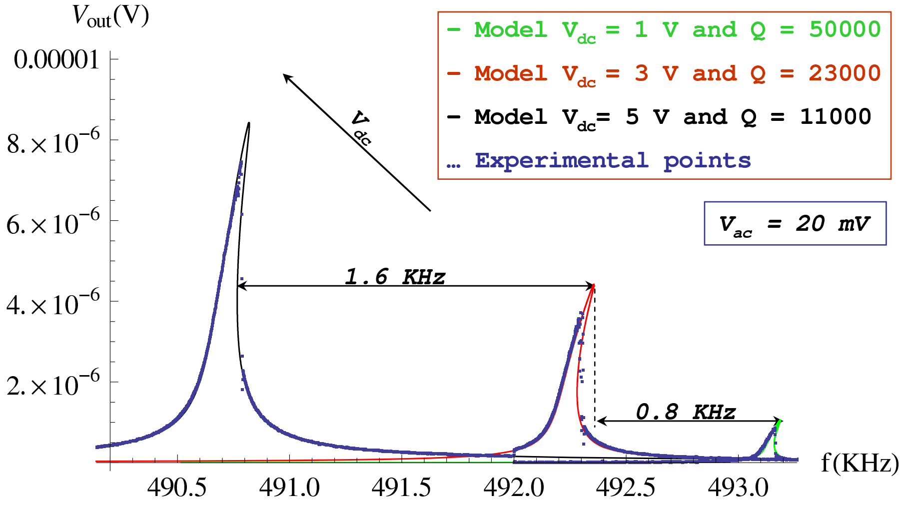

Figure 4.24: Measured and predicted frequency responses.

4.7 Summary

In this chapter, the nonlinear dynamics of MEMS and NEMS clamped-clamped beam resonators electrostatically actuated was modeled including all main sources of nonlinearities as well as the fringing field effects. The modal decomposition method was used in order to transform the nonlinear Euler-Bernoulli PDE that governs the resonator motion into a system of a coupled nonlinear ODE.

First, a multimodal approach was developed by using the harmonic balance method coupled with a continuation technique (asymptotic numerical method (ANM)) on a 1-port resonator. The method was validated with respect to a reference solution built by shooting.

Then, the mode properties were investigated in order to simplify the matrices of the nonlinear system to solve. It has been shown that the effect of the even modes is negligible due to their antisymmetry with respect to the X axis. Also, simplified analytical expressions for the integration constants have been set based on the modes functions and their properties.

The coupling between the odd modes was investigated around the resonator primary resonance of its first linear undamped mode shape. Then, a reduced order model was developed based on the averaging method and validated numerically with respect to the HBM+ANM. Once it was numerically validated, the reduced order model was adapted for a 2-port resonator and validated experimentally on fabricated in-plane resonators (sensing parts of MEMS resonant accelerometers) electrically characterized using a direct synchronic detection via a lock-in amplifier in $1f$ mode.

This model has the advantage to be a simple and fast tool for the prediction of the nonlinear behavior of MEMS and NEMS resonators. Moreover, being purely analytical, the model permits parametric investigations with respect to the phase of the resonator oscillation. Indeed, the principal advantage of the reduced order model consists on its ability to build close-form expressions which can be used as design rules for MEMS and NEMS designers in order to enhance the performances of resonant sensors.

Chapter 5

Design rules and performance enhancement

Contents

5.1 Introduction **112**

5.2 Nonlinear phenomena: behavior and physical limitations **112**

5.2.1 Hardening behavior 112

5.2.2 Mechanical critical amplitude 112

5.2.3 Bifurcation points 115

5.2.4 Softening behavior 115

5.2.5 Global critical amplitude 116

5.2.6 Mixed behavior 116

5.2.7 Pull-in 116

5.3 Hysteresis suppression by nonlinearity cancellation **119**

5.4 Mixed behavior retarding by design optimization **119**

5.4.1 Introduction 119

5.4.2 Experimental identification of the mixed behavior 120

5.4.3 Bifurcation topology tuning 121

5.4.4 Conclusion 123

5.5 Pull-in retarding by superharmonic resonance **123**

5.5.1 Introduction 123

5.5.2 Model 124

5.5.3 Critical amplitude 125

5.5.4 pull-in 126

5.5.5 Conclusion 127

5.6 Mixed behavior retarding by simultaneous resonances **129**

5.6.1 Introduction 129

5.6.2 Model 130

5.6.3 Analytical results 132

5.6.4 Experimental validation 133

5.7 Summary **135**

5.1 Introduction

In the previous chapter, it has been experimentally shown on a 2-port resonator model (more realistic for MEMS and NEMS designers) the low output signal beyond which bistability occurs on a hardening behavior (see section 4.5). This can have important consequences on the resonant accelerometer in term of performance reduction and detection complexity. Therefore, a particular attention is given to this resonator category in term of nonlinear dynamics, potential of performance enhancement based on the analytical model developed in chapter 4, but first several nonlinear phenomena based on the analytical model of a 2-port resonator are identified including bistability in the case of purely hardening or softening behavior as well as multistability in the case of a mixed behavior (details are listed below). The idea is to provide several design rules that can potentially enhance the detection limit of resonant M&NEMS accelerometers.

5.2 Nonlinear phenomena: behavior and physical limitations

As previously shown in chapter 4, the singular points of Equations (4.63) and (4.64) permit the identification of a 2-port resonator frequency response written in its parametric form $\{A = K_1(\beta),\ \Omega = K_2(\beta)\}$ in function of the phase β. Particularly, for one of our devices (Figure 5.1a), the frequency response curve can be plotted parametrically as shown in Figure 5.1b. Figure 5.1 contains most important informations delivered by the analytical model. From these informations, some rules of design can be established in order to enhance the performances of resonant M&NEMS accelerometers.

5.2.1 Hardening behavior

At the micro and nanoscale, the spring hardening is the most classical effect observed in clamped-clamped resonators electrostatically actuated [Gui 1995, Shao 2008a]. Besides, the mechanical nonlinearities due to mid-plane stretching dominate the resonator dynamics and the frequency response peak is hysteretic and shifted to the high frequencies which is the case of the green curve in Figure 5.1b. Furthermore, when the mechanical nonlinearities are preponderant, the dynamics of one and two ports resonators are equivalent.

5.2.2 Mechanical critical amplitude

The critical amplitude is the oscillation amplitude A_c above which bistability occurs. Thus, A_c is the transition amplitude from the linear to the nonlinear behavior (see Figure 5.2). At the critical drive, the resonance curve exhibits a point of infinite slope, called the critical point. Moreover, at the same point, the phase curve also exhibits an infinite slope at the same detuning as the resonance curve itself. Nayfeh studied the stability of an excited Duffing oscillator [Nayfeh 1979] and deduced its critical amplitude. Kaajakari [Kaajakari 2005b] provided close form expression for the critical amplitude using a reduced order model including the crystalline direction of beam resonators. However, they do not incorporate in their models the complete contribution of the electrostatic nonlinearities. In other words, they simply provide the mechanical critical amplitude. For the primary resonance of a clamped-clamped microbeam, A_c is defined as the oscillation amplitude for which the equation $\frac{d\sigma}{d\beta} = 0$ has a unique solution. In order to explain how to deduce the mechanical critical amplitude from Equation (4.50) written in its parametric form, we assume the simplified case of neglected nonlinear electrostatic effects

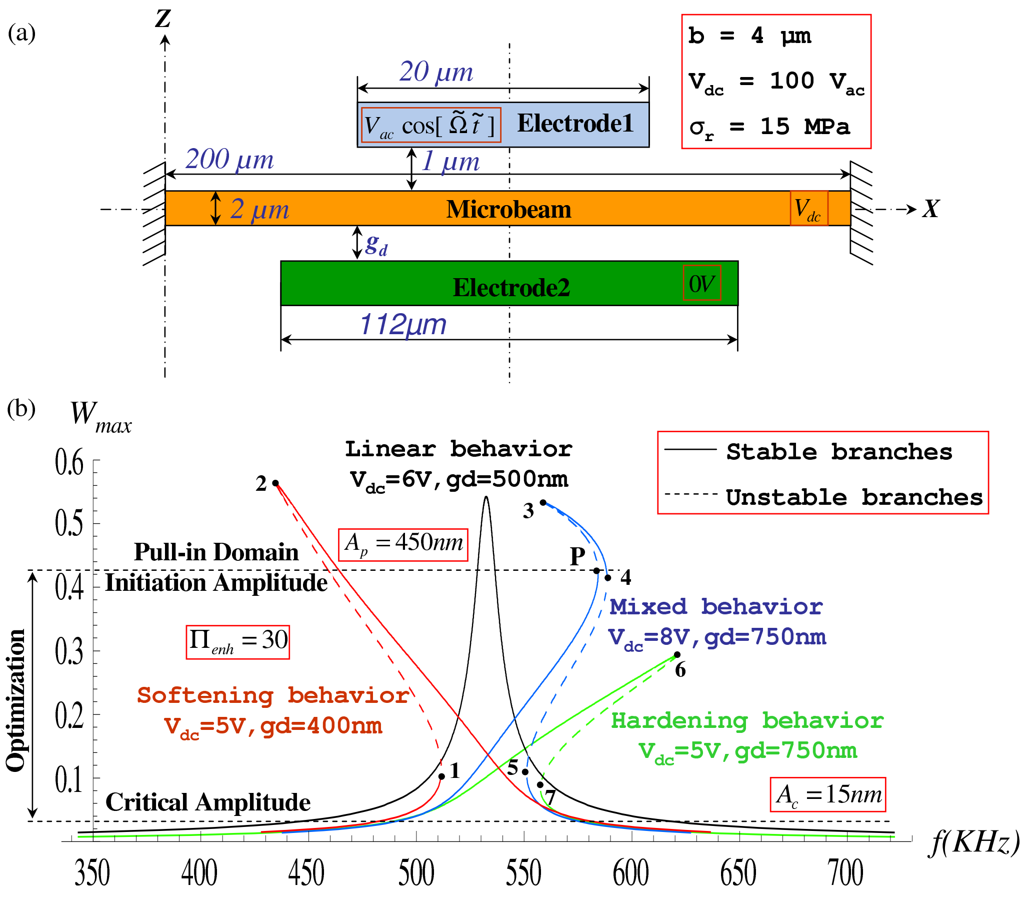

Figure 5.1: (a): Dimensions of a typical fabricated resonator. (b): Predicted forced frequency responses. W_{max} is the displacement of the beam normalized by the gap g_d at its middle point $\frac{l}{2}$, σ_r is the axial residual stress on the beam material, A_c is the critical amplitude above which bistability occurs, $\{1, 2, 3, 4, 5, 6, 7, P\}$ are the different bifurcation points, A_p is the pull-in domain initiation amplitude and P is the third bifurcation point characterizing the initiation of the mixed behavior.

$(\dfrac{h}{g} << 1)$. The parametric form of the frequency response can be written as:

$$\sigma = \frac{1}{8}\left(\frac{3\kappa^2\chi_3}{\xi_0^2\omega_n^3}\sin^2\beta - 4\xi_0\cot\beta\right) \tag{5.1}$$

$$A = \frac{\kappa}{\xi_0\omega_n}\sin\beta \tag{5.2}$$

Using Equation (5.1), the derivative of the detuning parameter σ with respect to the phase β is directly deduced:

$$\frac{d\sigma}{d\beta} = \frac{6\chi_3\kappa^2\sin 2\beta - 3\chi_3\kappa^2\sin 4\beta + 16\xi_0^3\omega_n^3}{32\xi_0^2\omega_n^3\sin^2\beta} \tag{5.3}$$

One can search the condition for which the equation $6\chi_3\kappa^2\sin 2\beta - 3\chi_3\kappa^2\sin 4\beta + 16\xi_0^3\omega_n^3 = 0$ has solutions. This equation can be written as $\Delta(2\sin 2\beta - \sin 4\beta) + 1 = 0$ where $\Delta = \frac{3\kappa^2\chi_3}{16\xi_0^3\omega_n^3}$.
When one solves this equation which can be transformed to a fourth order polynomial equation by

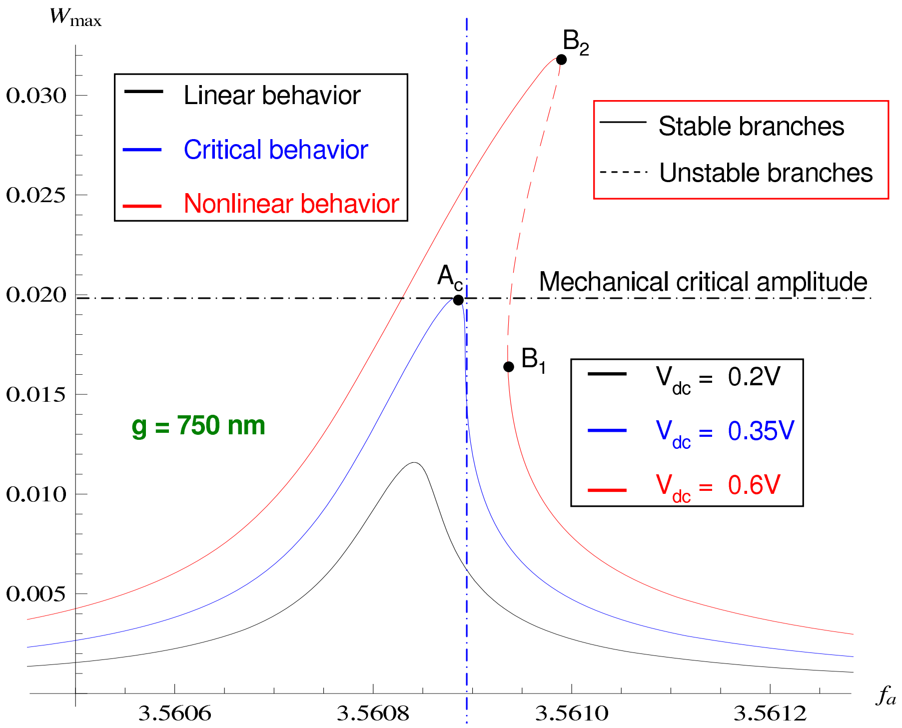

Figure 5.2: Forced frequency responses of the typical resonator described in Figure 4.6. f_a is the dimensionless frequency and W_{max} is the displacement of the beam normalized by the gap g at its middle point $\frac{l}{2}$. A_c is the mechanical critical amplitude and $\{B_1, B_2\}$ are the two bifurcation points of a typical hardening behavior.

using the change of variable $X = \sin 2\beta$, one obtains:

$$\begin{cases} If \quad \Delta < \frac{2}{3\sqrt{3}} & \Longrightarrow \quad No\ solutions \quad\quad Linear\ behavior \\ If \quad \Delta = \frac{2}{3\sqrt{3}} & \Longrightarrow \quad A\ unique\ solution\ \beta_c = \frac{2\pi}{3} \quad Critical\ behavior \\ If \quad \Delta > \frac{2}{3\sqrt{3}} & \Longrightarrow \quad 2\ distinct\ solutions\ \beta_1\ et\ \beta_2 \quad Nonlinear\ behavior \end{cases}$$

The condition $\Delta = \frac{2}{3\sqrt{3}}$ implies the following relation

$$\kappa_c = \frac{4\sqrt{2}\xi_0^{3/2}\omega_n^{3/2}}{3\sqrt[4]{3}\sqrt{\chi_3}} \tag{5.4}$$

The mechanical critical amplitude is the value of Equation (5.2) at the phase $\beta = \frac{\pi}{2}$ (for a critical behavior) multiplied by 1.588 which correspond to the amplification coefficient of the first mode at the middle of the clamped-clamped beam $x = \frac{1}{2}$ (See Figure 4.7). Substituting Equation (5.4) in the resulting equation and mutiplying by the gap g to obtain the dimensional value, yields:

$$A_{c_m} = \frac{2.275 g\sqrt{\xi_0}\sqrt{\omega_n}}{\sqrt{\chi_3}} \tag{5.5}$$

Substituting ω_n, ξ_0 and χ_3 expressions in Equation (5.5), yields:

$$A_{c_m} = 1.685\frac{h}{\sqrt{Q}} \tag{5.6}$$

Q is the quality factor of a resonant clamped-clamped beam under its first bending vibration mode. Using the reduced order model and the first order averaging method, the mechanical critical amplitude was easily deduced and the obtained close-form solution is comparable to those defined in [Kaajakari 2005b, Shao 2008a].

5.2.3 Bifurcation points

In the nonlinear case, the Ferrari method [Martin 1997] can be used in order to determinate the two bifurcations points β_1 and β_2.

$$\beta_1 = \frac{1}{2}\left(\pi - \arcsin\left(\frac{3^{\frac{1}{3}}\left(\Psi_1 + 4\Psi_2\right)}{42^{1/6}\Delta\left(\frac{23^{1/3}\Delta^2+2^{1/3}\Theta^2}{\Delta^2\Theta}\right)^{\frac{1}{2}}}\right)\right) \tag{5.7}$$

$$\beta_1 = \frac{1}{2}\left(\pi - \arcsin\left(\frac{3^{\frac{1}{3}}\left(\Psi_1 - 4\Psi_2\right)}{42^{1/6}\Delta\left(\frac{23^{1/3}\Delta^2+2^{1/3}\Theta^2}{\Delta^2\Theta}\right)^{\frac{1}{2}}}\right)\right) \tag{5.8}$$

where:

$$\Theta = \left(9\Delta^4 + \sqrt{3}\sqrt{-4\Delta^6 + 27\Delta^8}\right)^{\frac{1}{3}}$$

$$\Psi_1 = -\frac{2^{5/6}\left(23^{1/3}\Delta^2 + 2^{1/3}\Theta^2\right)}{3^{2/3}\Delta\Theta}$$

$$\Psi_2 = \left(-\frac{\left(23^{1/3}\Delta^2 + 2^{1/3}\Theta^2\right)^2}{126^{1/3}\Delta^2\Theta^2} + \frac{\Delta\left(\frac{23^{1/3}\Delta^2+2^{1/3}\Theta^2}{\Delta^2\Theta}\right)^{\frac{1}{2}}}{6^{1/3}}\right)^{\frac{1}{2}}$$

Thus, the frequency interval of the unstable branche in the resonator frequency response can be detreminated.

$$I_{instable} = \left[\frac{\omega_n + \sigma(\beta_1)}{2\pi}, \frac{\omega_n + \sigma(\beta_2)}{2\pi}\right] \tag{5.9}$$

One can verify easily that if $\Delta = \frac{3\kappa^2\chi_3}{16\xi_0^3\omega_n^3} = \frac{2}{3\sqrt{3}}$, $\beta_1 = \beta_2 = \frac{2\pi}{3}$.

5.2.4 Softening behavior

In order to increase the softening electrostatic nonlinearities, the resonator designs have to involve very narrow gaps with respect to the beam width which is of great difficulty with Top-Down technology for NEMS. Therefore the softening behavior is difficult to obtain in clamped-clamped NEMS resonators electrostatically actuated. For the considered resonator of Figure 5.1a, the softening behavior is possible for a sensing gap $g_d = 400\,nm$ (red curve). The frequency response curve is hysteretic and shifted to the low frequencies. In this case, the critical amplitude given by Equation (5.6) is no more valid.

5.2.5 Global critical amplitude

The close-form expression of the mechanical critical amplitude A_{c_m} has been provided using the one port nonlinear resonator model (see section 4.3). Equation (5.6) represents the classical form of the critical amplitude for a Duffing resonator (only mechanical nonlinearity) [Osterberg 1997] and still valid for a two port nonlinear resonator. It shows that the critical amplitude is only determined by the beam thickness in the direction of vibration h and the quality factor Q and does not depend on the beam length l. This information has been observed experimentally by Shao et al. [Shao 2008a] for micromechanical clamped-clamped beam resonators using stroboscopic SEM. Our model allows the computation of the critical amplitude when all sources of nonlinearities are included: it can be deduced in the same way as explained in the simplified case above.

$$A_c = \sqrt{\theta_1 h^2 - \theta_2 + \sqrt{\theta_3 - \theta_4 h^2 + \theta_5 h^4 + \frac{\theta_6 h^2}{Q}}} \tag{5.10}$$

$$\theta_1 = 0.003632757220621099 \tag{5.11}$$

$$\theta_2 = \frac{19328 {g_d}^2}{43375} \tag{5.12}$$

$$\theta_3 = 0.19856141464508456 {g_d}^4 \tag{5.13}$$

$$\theta_4 = 0.0032375299854832426 {g_d}^2 \tag{5.14}$$

$$\theta_5 = 0.000013196925023975936 \tag{5.15}$$

$$\theta_6 = 2.56831390855867 {g_d}^2 \tag{5.16}$$

We can easily check that $\lim_{g_d \to \infty} A_c = A_{c_m}$.
For example, the critical amplitude of a resonator having a quality factor of 10^4 designed with $100nm$ of thickness in the direction of vibration and a sensing gap thickness of $200nm$, is about $1.68nm$.
0.84% of the gap thickness is thus the restrictive amplitude in order to stay linear which leads to a very weak signal to noise ratio and thus a low resolution.

5.2.6 Mixed behavior

Both mechanical and electrostatic nonlinearities are always operating into the system. However, in some configurations one kind of nonlinearity is negligible with respect to the second one. Practically, when $\frac{h}{g_d} << 1$, then the dynamics is dominated by the hardening nonlinearities and in the opposite case ($\frac{h}{g_d} >> 1$), the frequency response is nonlinearly softening. Between these two configurations and for the typical fabricated resonator described in Figure 5.1a, a mixed hardening-softening behavior is inescapable except for one the optimal gap $g_d = 500\,nm$ for which both nonlinearities are perfectly equilibrated (black curve of Figure 5.1b). The mixed behavior is characterized by a four-bifurcation points frequency response and up to 5 amplitude for a given frequency. It is highly unstable, dangerous and thus undesirable for MEMS and NEMS designers. Analytical and experimental investigation of this particular behavior are detailed in section 5.4.

5.2.7 Pull-in

As it can be observed in equation 4.8, the electrostatic force is inversely proportional to the gap between the beam and the electrode. As the gap decreases, the generated attractive force increases quadratically. The only opposing force to the electrostatic loading is the mechanical restoring force. If the voltage is increased, the gap decreases generating an incremented force. At some point the mechanical forces defined by the spring cannot balance this force anymore. Once reached this state, the beam snaps against the electrode, and in most cases, the system would be permanently disabled. Consequently, the electrostatic loading has an upper limit beyond which the mechanical force can no longer resist the opposing electrostatic force, thereby leading to the collapse of the structure. This actuation instability phenomenon is known as pull-in, and the associated critical voltage is called the Pull-in Voltage.

5.2.7.1 Static pull-in

To derive the expression for pull-in, let us consider the one port resonator described in Figure 4.6. Neglecting the mechanical nonlinearities, the total potential energy in the system can be written as follows:

$$E_p = -\frac{1}{2}\frac{\varepsilon_0 bl}{g-\tilde{w}}V_{dc}^2 + \frac{1}{2}k\tilde{w}^2 \tag{5.17}$$

where the first term is the electrostatic potential of the deformable capacitor (the resonator) and the second term is due to the mechanical energy stored in the spring (k is the effective spring constant of the resonator). The force acting on the movable beam is obtained by deriving Equation (5.17):

$$F = -\frac{\partial E_p}{\partial \tilde{w}} = \frac{1}{2}\frac{\varepsilon_0 bl}{(g-\tilde{w})^2}V_{dc}^2 - k\tilde{w} \tag{5.18}$$

At equilibrium, the electrostatic force and spring force cancels ($F = 0$) and Equation (5.18) gives:

$$k\tilde{w} = \frac{1}{2}\frac{\varepsilon_0 bl}{(g-\tilde{w})^2}V_{dc}^2 \tag{5.19}$$

Equation (5.19) can be solved for the equilibrium beam position $\tilde{w}$ as a function of applied voltage V_{dc}. Above the pull-in voltage V_P, Equation (5.19) has no solutions. A simple expression for the pull-in point is deduced by deriving Equation (5.18) to obtain the stiffness of the system:

$$\frac{\partial F}{\partial \tilde{w}} = \frac{\varepsilon_0 bl}{(g-\tilde{w})^3}V_{dc}^2 - k \tag{5.20}$$

Substituting Equation (5.19) gives the stiffness around the equilibrium point:

$$\frac{\partial F}{\partial \tilde{w}} = \frac{2k\tilde{w}}{g-\tilde{w}} - k \tag{5.21}$$

With no applied voltage Equation (5.21) is simply $\frac{\partial F}{\partial \tilde{w}} = -k$; a small positive movement $\delta\tilde{w}$ result in negative restoring force $\frac{\partial F}{\partial \tilde{w}}\delta\tilde{w} = -k\delta\tilde{w}$. Increasing the bias voltage V_{dc} makes the stiffness less negative. The unstable point is given by $\frac{\partial F}{\partial \tilde{w}} = 0$ giving

$$\tilde{w} = \frac{1}{3}g \tag{5.22}$$

Beyond this point the stiffness becomes positive and the system is unstable: a small positive movement $\delta\tilde{w}$ result in positive force that increases $\tilde{w}$. Substituting Equation (5.22) into Equation (5.19) gives the pull-in voltage at which the system becomes unstable

$$V_P = \sqrt{\frac{8kg^3}{27\varepsilon_0 bl}} \tag{5.23}$$

5.2.7.2 Dynamic pull-in

The pull-in amplitude is the oscillation amplitude above which the resonator position becomes unstable and collapses. The dynamic pull-in is the collapse of the beam subjected to a time-varying electrostatic force completely different from the static pull-in [Osterberg 1997] where the electrostatic force depends only on the gap. In the general case, pull-in can occur for hardening and softening behavior even at amplitudes lower than A_p [Nayfeh 2007]. Nevertheless, this study here is restricted to practical cases of nanoresonators which are designed with gaps and width in the direction of vibration of the same order of magnitude. In the softening domain, the existence of an inevitable escape band (band where no other possible solution exists except pull-in [Thompson 2001, Ouakad 2008]) is very likely (even for small AC voltage) and consequently it is not wished to work in this domain. Anyway, this would mean being able to fabricate a much smaller gap than the beam width, which is of great difficulty with Top-Down technology for NEMS (small cross-sections). In the other hand, hardening behavior has been easily observed in our experiments like in many others [Gui 1995, Shao 2008a], without pull-in occurrence, although it is theoretically possible in the general case for initial conditions outside the homoclinic manifold associated with the system. This may be explained by two facts: for our typical designs, basins of attraction of upper and lower stable branches are much larger than pull-in attractors at points 5, 6 and 7. Secondly, the ensemble of possible initial conditions in practical cases of electrical characterization is rather limited (small static displacement vs dynamic on section 4.3, slow change of frequency...). Finally, in the mixed regime (See section 5.4 for details), the P point, being highly unstable, can lead to a high sensitivity to initial conditions or the unpredictability of motion [Nayfeh 2007], which is undesirable for NEMS designers. In particular, the pull-in instability may occur at the bifurcation point P, where the effect of the nonlinear electrostatic stiffness becomes significantly important, and where the domain of attraction of stable branches are small, making the jump of the system to these stable branches quite hard physically [Nayfeh 2007]. Consequently, and like other studies [Ouakad 2008], we define the P point as the initiation of an unstability domain and thus an upper bound of possible drive ($V_p = (V_{ac}V_{dc})_p$), beyond which dynamic pull-in (characterized by a Floquet multiplier approaching unity) is likely to occur. Consequently the pull-in domain initiation amplitude is defined as $A_p = A(\frac{\pi}{2}, V_p)$. Using this criterion, we situate the initiation of the dynamic pull-in domain using the model via the transition from two to three bifurcation points as shown in Figure 5.1b. The third bifurcation point is situated at the phase $\beta = \frac{\pi}{2}$ which corresponds to the initiation of the mixed behavior. The latter is characterized by a slope approaching infinity at the point P as shown in Figure 5.1b. Therefore, the pull-in can occur when $\dfrac{d\Omega(\frac{\pi}{2})}{d\beta} = \dfrac{d^2\Omega(\frac{\pi}{2})}{d\beta^2} = 0$ and the V_p voltage is directly deduced.

$$V_p = \left\| \frac{3l\pi c\omega_n \Delta \left(-\chi_3 + \mu_2\omega_n^2\right)^{\frac{1}{2}} \left[\chi_5 - \mu_4\omega_n^2\right]^{-\frac{5}{2}}}{400\sqrt{10}\alpha_2 C_{n1} \left(l^2 \cos\left[\frac{\pi}{l}\right] \sin\left[\frac{\pi l_d}{l^2}\right] - \pi l_d\right)} \right\| \tag{5.24}$$

$$\begin{aligned} \Delta = {} & 200\chi_5^2 + \mu_4\left(-21\mu_2^2 + 200\mu_4\right)\omega_n^4 - 30\mu_2\chi_3\chi_5 \\ & +2\left(6\mu_2\mu_4\chi_3 + 5\left(3\mu_2^2 - 40\mu_4\right)\chi_5\right)\omega_n^2 + 9\mu_4\chi_3^2 \end{aligned} \tag{5.25}$$

In the particular case of $V_s = V_{dc}$, the electrostatic force due to the second electrode is null and the model is similar with a resonator comprising only one electrode. For the resonator described in Figure 5.1a ($l_a = l_d = 200\mu m$), dynamic pull-in voltage has been computed using published formula based on an energetic analysis and validated experimentally [Fargas-Marques 2007] which actually gives results in good agreement with Equation (5.24).

5.3 Hysteresis suppression by nonlinearity cancellation

Up to now, it is the first time that closed-form expressions of the critical amplitude and the pull-in domain initiation amplitude with full mechanical and electrostatic nonlinearities have been deduced thanks to the model (Figure 5.3) in the complicated but typical case of the resonator design described in Figure 4.15. Hence, it constitutes an interesting tool to set the highest drive possible of the resonator

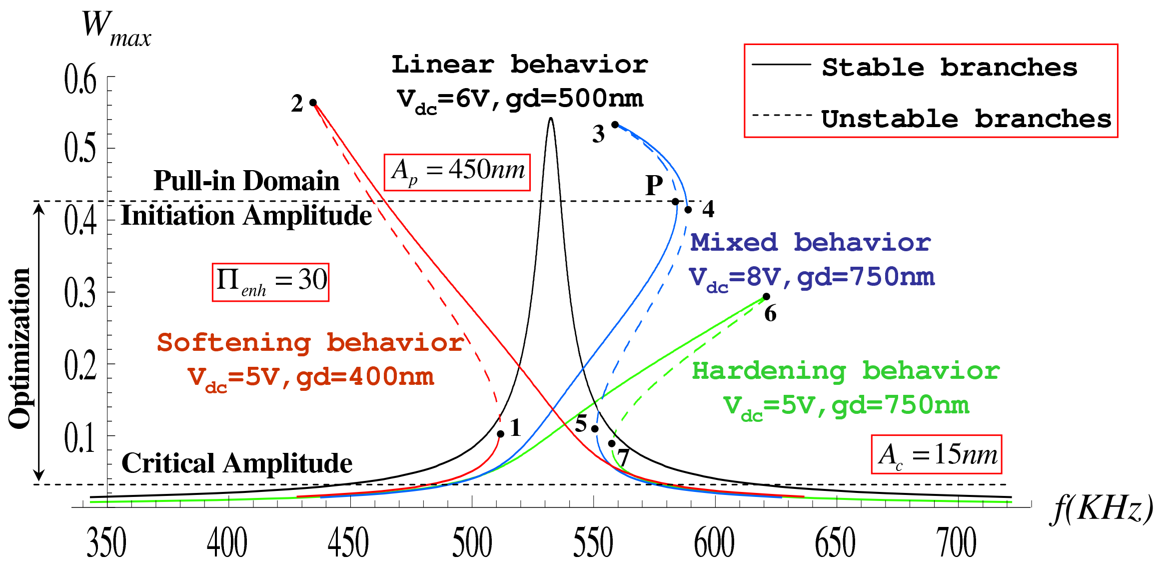

Figure 5.3: Predicted forced frequency responses. W_{max} is the displacement of the beam normalized by the gap g_d at its middle point $\frac{l}{2}$, σ_r is the axial residual stress on the beam material, A_c is the critical amplitude above which bistability occurs, $\{1, 2, 3, 4, 5, 6, 7, P\}$ are the different bifurcation points, A_p is the pull-in domain initiation amplitude and P is the third bifurcation point characterizing the initiation of the mixed behavior.

while keeping its behavior linear. The hysteresis suppression [Kacem 2008] is based on the tuning of the parameter $\frac{h}{g_d}$ which permits the enhancement of resonant sensor resolution. Thus, the rate of enhancement can be written as:

$$\Pi_{enh} = \frac{A_p}{A_c} \tag{5.26}$$

In the particular case of Figure 5.1a, the critical amplitude is $A_c = 0.02g_d = 15nm$. Using the model, the hysteresis suppression is possible for a $\frac{h}{g_d} \approx 4$ and the pull-in domain initiation amplitude is $A_p \approx 0.6g_d$. Therefore, the enhancement rate of the sensor performance Π_{enh} is around 30.

5.4 Mixed behavior retarding by design optimization

5.4.1 Introduction

In the previous section, we theoretically showed the possibility to cancel out the resonator nonlinearities by maximising the global critical amplitude which significantly enhances the resonant accelerometer resolution. Since the hysteresis suppression is based on equilibrating the cubic mechanical and electrostatic nonlinearities, the domain of validity of such operation is limited by an upper amplitude for which the quintic nonlinear terms are no more negligible (the P point). Thus, the compensation of the nonlinearities is limited by the mixed behavior initiation. In other words, the hysteresis suppression is potentially sensitive to the mixed behavior and ideally the initiation of this behavior must be retarded as far as possible. Therefore, the analytical and experimental investigation of the mixed behavior as well as its bifurcation topology is an important step towards the control of the resonator and the optimization of its performances.

5.4.2 Experimental identification of the mixed behavior

The device was placed in a vacuum chamber (down to 1 mTorr), and the 2-port electrical measurements were performed at room temperature using a low noise lock-in amplifier (Signal Recovery 7280). The drive voltage is $V_{ac} = 0.5V$ and the beam is polarized with $V_{dc} = 10V$. Figure 5.4 shows the frequency response of the device, with up- and down- sweeps. The quality factor obtained with this polarization voltage and in a linear regime is 4000. The critical amplitude is then $A_c = 53nm$, *i.e.* $V_c = 25\mu V$. The peak obtained is then far beyond A_c, up to 75% of the gap. The frequency response shows 4 bifurcation points noted P, 1, 2 and 3, at which jumps J_i occur to destination points di on stable branches, according to the direction of the sweep : as the frequency is swept up from f_0, the output voltage follows the path labelled $f_0 - P - d_1 - 2 - d_2 - f_1$, and as it is swept down from f_1, the path $f_1 - 1 - d_3 - 3 - d_4 - f_0$ is followed. When in the presence of the 3 other bifurcation points, the P point may be called the mixed behavior initiation point. It is highly unstable [Kacem 2009b], as will be seen later: it is located at relatively high amplitude (*i.e.* in a state of high potential energy) as opposed to point 1 or as opposed to a typical softening behavior, and the state variables have to jump to a destination stable branch at even higher amplitude. The parametric analytical frequency response is superposed to the experimental points in Figure 5.4. As it takes into account the electrostatic fringing field and the measured parasitic capacitances, the only fitting parameter is the quality factor, measured in the linear regime. The model shows an excellent agreement: the 4 bifurcation points exist and are well located, and the stable branches coincide very well with the measurement. This confirms the performance and the accuracy of the model at high amplitude in the nonlinear regime. The mixed behavior takes its roots from the competition between hardening and softening behaviors all along the covered amplitude range. One can think of tuning its bifurcation topology by changing the relative proportions of the softening versus hardening behavior for a given design. One way to achieve this is to make the DC polarization applied to the beam vary. This has several effects: firstly, the initial static deflection changes, but we keep it in the regime where it is negligible compared to the displacement on resonance. Secondly, the electrostatic spring softening produces a resonance frequency shift proportional to V_{dc}^2. Thirdly, the displacement on resonance, proportional to the product $V_{dc}V_{ac}$, increases, which slightly enlarge the softening domain. The fourth effect is that the overall quality factor decreases when V_{dc} increases because of the ohmic losses from the electrons moving on and off the resonator due to capacitive coupling to a nearby electrode [Sazonova 2006]. This ohmic contribution adds up to the other sources of dissipation (thermomechanical, anchor losses, adsorption/desorption[Lifshitz 2000], . . .) like $Q_{total}^{-1} = Q_{thermo}^{-1} + Q_{anchor}^{-1} + ... + Q_{ohmic}^{-1}$ and may be expressed as $\left(Q_{ohmic}^{-1} = \frac{1}{\pi\omega}\frac{R(C'V_{dc})^2}{m_{eff}}\right)$ [Sazonova 2006] where C' is the gradient of the capacitance, R is the output resistor and m_{eff} is the effective mass of the considered mode. The smaller the resonator, the smaller the mass, the higher this contribution, hence NEMS are very sensitive to this effect. The critical amplitude being $\left(A_c = 1.68\frac{h}{\sqrt{Q}}\right)$[Kacem 2009b], it varies then with V_{dc}, which makes the hardening regime to appear sooner or later in amplitude compared with the softening behavior.

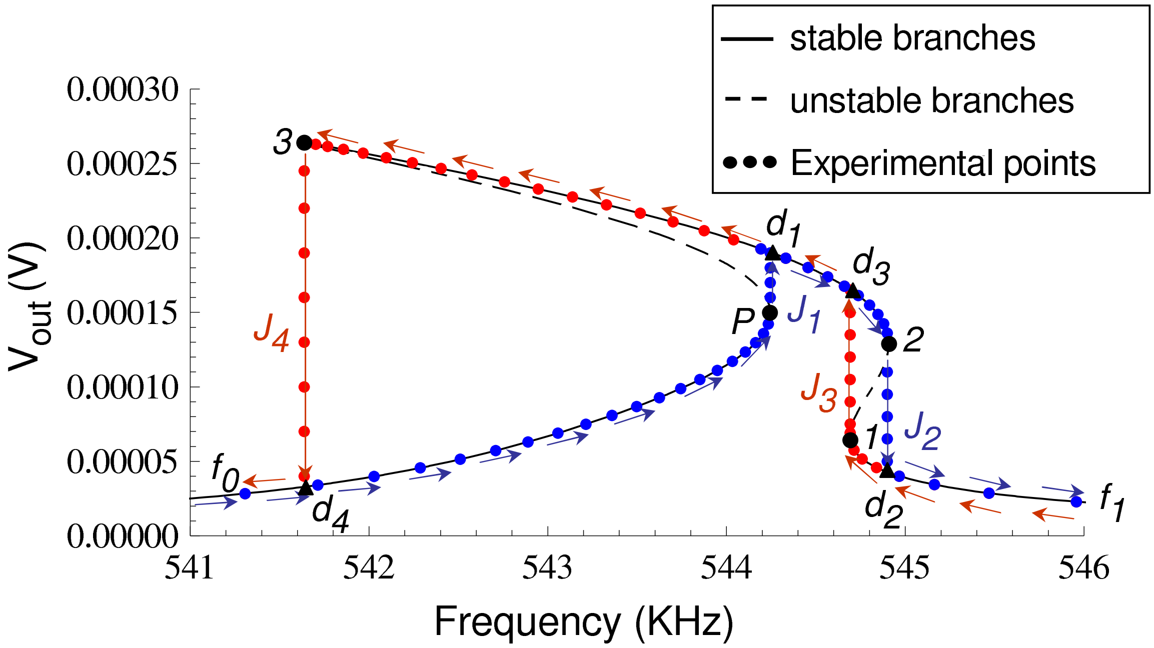

Figure 5.4: Analytical and experimental frequency curves showing a mixed behavior and the followed paths respectively in a sweep up frequency $f_0 - P - d_1 - 2 - d_2 - f_1$ and a sweep down frequency $f_1 - 1 - d_3 - 3 - d_4 - f_0$. $\{J_1, J_2, J_3, J_4\}$ are the four jumps cauterizing a typical mixed behavior of MEMS and NEMS resonators, $\{1, 2, 3, P\}$ are the different bifurcation points and $\{d_1, d_2, d_3, d_4\}$ are the destination points after jumps. The two branches $[3, P]$ and $[1, 2]$ in dashed lines are unstable.

5.4.3 Bifurcation topology tuning

The bifurcation topology is the number and location of the bifurcation points defining the stability of the device (stable and unstable branches of the force response) and how it evolves with respect to design parameters.

5.4.3.1 Analytical results

The various effects are illustrated in Figure 5.5, showing analytical frequency responses for $Vac = 0.6V$, three different polarization voltages from 6.5 to 10V, and then three different quality factors computed from the ohmic contribution above, from 9500 to 4500. It is interesting to note in particular that the relative frequencies of the bifurcation points 1 and P can be tuned by varying the polarization voltage, and how the bifurcation topology evolves while doing so. The first case is that of Figure 5.4, where the frequency of P is lower than that of point 1: the polarization voltage is high, the quality factor is low, the hardening domain is reduced, the branch $[d_1, 3]$ is stable and accessible when sweeping down. The critical case is that of the extreme left curve of Figure 5.5: points 1 and P have the same frequency, d_1 and d_3 have the same location. When V_{dc} is still decreased (two right curves of Figure 5.5), the hardening regime is dominant, the frequency of point 1 is lowest and d_3 is on the branch below P. The branch $[d_1, 3]$ loses stability and the bifurcation point 3 cannot be reached anymore.

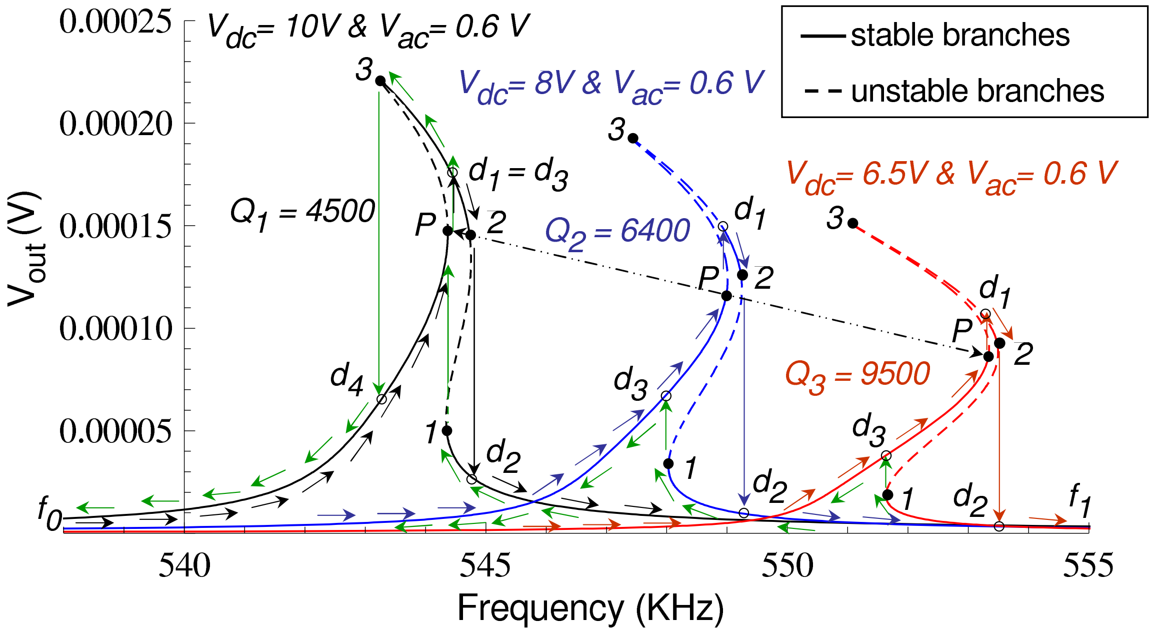

Figure 5.5: Analytical frequency responses showing mixed behaviors, the location of the different bifurcation points and the effect of the DC voltage on the stability of the different branches and the P point location.

5.4.3.2 Experimental results

This bifurcation tuning mechanism is experimentally demonstrated in Figure 5.6: we show three primary resonance response curves (1f mode) for a constant drive voltage $V_{ac} = 0.5V$ and different polarization voltages. At the P point, the first jump to the upper branch is preceded by some oscillations down and up as shown in Figure 5.6 which confirms the instability of this point where the basins of attractions of the stable upper branch are not sufficiently large. The quality factor decreases as explained from 10000 at $V_{dc} = 6V$ to 5600 at $V_{dc} = 9V$. This decrease also reduces the hardening domain (HD) measured between the bifurcation point 1 and the P point. Consequently, the softening domain which is measured between the bifurcation point 2 and the bifurcation point 3 is highly extended. Unlike the other two curves, the extreme left curve shows the critical case, and as expected, the bifurcation point 3 exists, and the branch 2-3 is stable while sweeping down. This provides for a dramatic enlargement of the possible drive amplitude (factor of 3), and hence of the output carrier power despite the decrease in Q. On the other hand, and depending on the particular design, this point 3 amplitude may be close or beyond the dynamic pull-in, and the noise may increase because of mixing. Further work is required to investigate this point. The output signal in Figure 5.6 is expressed in the dimensionless quantity $\tilde{V} = \frac{V_{out}}{V_{dc}}$. The output voltage being proportional to V_{dc} at a given mechanical displacement, $\tilde{V}$ is also proportional to this displacement. As can be seen on the different curves, the P point vertical location is invariant with respect to the drive amplitude, the polarization voltage and the quality factor. This is also a feature displayed by the model when the curves of Figure 5.5 are plotted vs $\tilde{V}$. This is an interesting result when it comes to designing, as the P point amplitude is set only by the geometry of the device (ratio gap/width of the beam). The polarization voltage allows for the tuning of the relative proportion of the hardening and softening domains and the bifurcation topology around this P point.

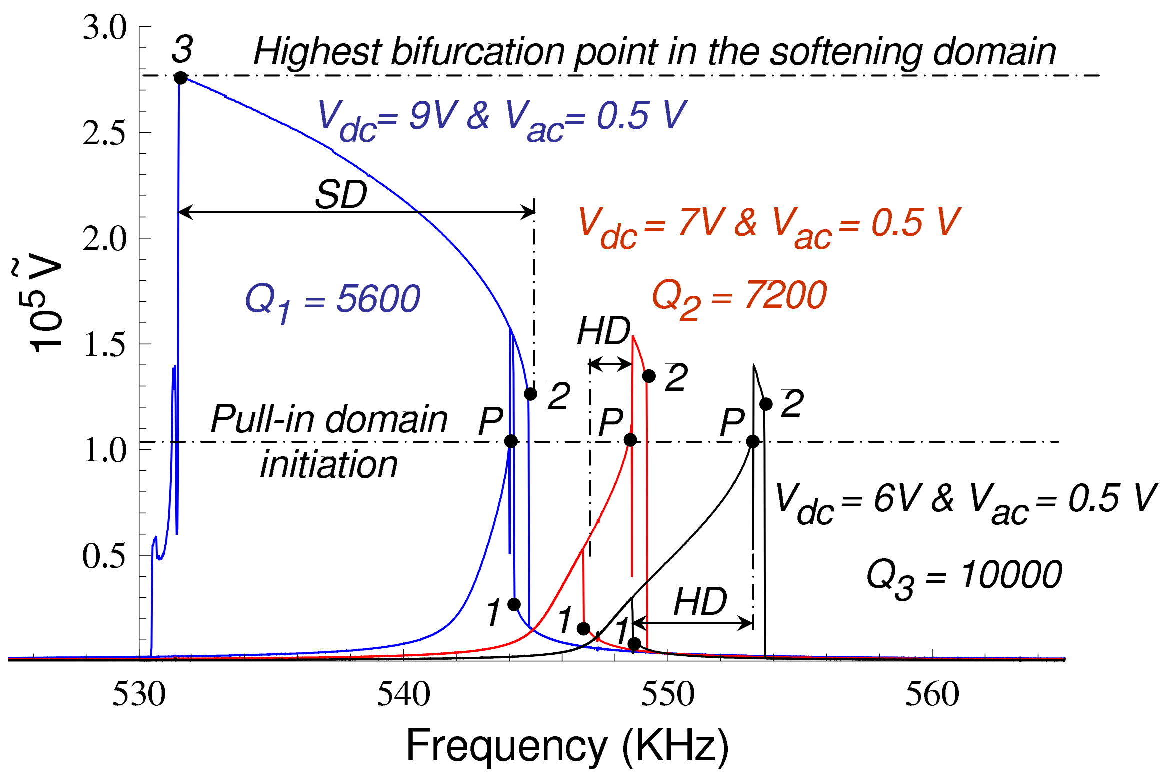

Figure 5.6: Resonance frequency responses showing measured mixed behaviors, the location of the bifurcation points, the effect of the DC voltage on the stability of the different branches and the P point vertical position. HD and SD are respectively the hardening and the softening domains. The point 3 is the highest bifurcation point in the softening domain.

5.4.4 Conclusion

An experimental observation of the mixed behavior in NEMS resonators, its bifurcation points and branch stability were presented. We also demonstrate an electrostatic mechanism to tune the bifurcation topology with the polarization voltage, whereas, we show that the onset of the mixed behavior is set by the geometry of the device. These mechanisms and their analysis provided here are helpful for any applications requiring adjustable stable branches, frequency, bandwidth, or dynamic range. Bifurcation tuning will allow applications of small and sensitive devices by either suppressing the undesired branch in the softening domain, or obtaining a very large amplitude with a given design by decreasing the quality factor, which is counterintuitive.

5.5 Pull-in retarding by superharmonic resonance

5.5.1 Introduction

Nonlinear resonators do not oscillate sinusoidal. Their oscillation is a sum of harmonic (*i.e.*, sinusoidal) oscillations with frequencies which are integer multiples of the fundamental frequency (*i.e.*, the inverse of the period of the nonlinear oscillation). This is the well-known theorem of Jean Baptiste Joseph Fourier (1768-1830) which says that periodic functions can be written as (infinite) sums (so-called Fourier series) of sinus and cosinus functions. Superharmonic resonance is simply the resonance with one of this higher harmonics of a nonlinear oscillation. In a plot of oscillation amplitude versus driving frequency, you can, therefore, expect additional resonance peaks. In general, they appear at driving frequencies which are integer fractions of the fundamental frequency.

Jin and Wang [Jin 1998] showed that driving a microbeam of a resonant microsensor by a superharmonic excitation of order one-half increases the signal-to-crosstalk ratio as compared to driving it at primary resonance.

The dynamic behavior of MEMS resonators under secondary resonances has been investigated by many authors. Turner et al [Turner 1998] studied the response of a comb-drive device to a parametric excitation that offers interesting behavior, and a possibility for novel applications such as parametric amplification [Rugar 1991, Carr 2000, Carr 1999] and noise squeezing [Rugar 1991]. Kenig et al [Kenig 2009a, Kenig 2009b] and Lifshitz and Cross [Lifshitz 2003] investigated the dynamics of parametrically driven coupled NEMS resonators. Younis and Nayfeh [Younis 2003b] and Abdel-Rahman and Nayfeh [Abdel-Rahman 2003] used the method of multiple scales to study the response of an electrostatically deflected microbeam based resonator to a primary-resonance excitation, a superharmonic-resonance excitation of order two, and a subharmonic-resonance excitation of order one-half. Younis et al [Younis 2004] and Nayfeh and Younis [Nayfeh 2005b] studied the global dynamics of MEMS resonators under superharmonic excitation and showed that the dynamic pull-in phenomenon can occur for a superharmonic excitation at an electric load much lower than that predicted by a static analysis.

This section is an extension to the previous sections of chapter 4 which dealt with primary resonance excitation of an electrostatically actuated micro/nanoresonator. Here, secondary resonance excitations are considered. The dynamics of microbeams excited near half their fundamental natural frequencies (superharmonic excitation) is simulated and it is shown that the dynamic pull-in phenomenon can be retarded by decreasing the ratio of the AC voltage with respect to the DC polarization.

5.5.2 Model

Let us consider the resonator of Figure 4.15. After Galerkin projection on the first linear undamped mode shape, the obtained reduced order model is described in equation 4.62. The second harmonic terms are neglected and the method of multiple scales [Nayfeh 1981] is used to attack the resulting equation in order to determine a uniformly valid approximate solution. To this end, we seek a first-order uniform solution in the form

$$a_1(t,\varepsilon) = a_{10}(T_0,T_1) + \varepsilon a_{11}(T_0,T_1) + \cdots \tag{5.27}$$

where ε is the small nondimensional bookkeeping parameter, $T_0 = t$ and $T_1 = \varepsilon t$. Since we analyze the non linear response to a superharmonic resonance excitation of order two, we express the nearness of Ω to $\frac{\omega_n}{2}$ by introducing the detuning parameter σ according to

$$2\Omega = \omega_n + \varepsilon\sigma \tag{5.28}$$

Substituting Equation (5.27) into Equation (4.62) and equating coefficients of like powers of ε yields
Order ε^0

$$\cos\left(\sigma T_1 + \frac{T_0\omega_n}{2}\right)\zeta_0 + \omega_n^2 a_{10} + a_{10}{}^{(2,0)} = 0 \tag{5.29}$$

Order ε^1

$$\begin{aligned}\cos\left(\sigma T_1+\frac{T_0\omega_n}{2}\right)a_{10}\zeta_1+\cos\left(\sigma T_1+\frac{T_0\omega_n}{2}\right)a_{10}^2\zeta_2+\cos\left(\sigma T_1+T_0\omega_n\right)\zeta_3\\ +\cos\left(\sigma T_1+T_0\omega_n\right)a_{10}\zeta_4+\cos\left(\sigma T_1+T_0\omega_n\right)a_{10}^2\zeta_5+a_{10}^2\chi_2+a_{10}^3\chi_3+a_{10}^4\chi_4\\ +a_{10}^5\chi_5+a_{10}^6\chi_6+a_{10}^7\chi_7+a_{11}\omega_n^2+ca_{10}{}^{(1,0)}+a_{10}c\mu_1a_{10}{}^{(1,0)}\\ +a_{10}^2c\mu_2a_{10}{}^{(1,0)}+a_{10}^3c\mu_3a_{10}{}^{(1,0)}+a_{10}^4c\mu_4a_{10}{}^{(1,0)}\\ +a_{10}\mu_1a_{10}{}^{(2,0)}+a_{10}^2\mu_2a_{10}{}^{(2,0)}+a_{10}^3\mu_3a_{10}{}^{(2,0)}\\ +2a_{10}{}^{(1,1)}+a_{10}^4\mu_4a_{10}{}^{(2,0)}+a_{11}{}^{(2,0)}=0\end{aligned} \tag{5.30}$$

where $a_i^{(j,k)}=\dfrac{\partial^k}{\partial T_1^k}\left(\dfrac{\partial^j}{\partial T_0^j}\right)$.

The general solution of Equation (5.29) can be written as

$$a_{01}=A\cos\left(\omega_nT_0+\Phi\right)-\frac{4\zeta_0}{3\omega_n^2}\cos\left(\frac{\omega_nT_0}{2}+\sigma T_1\right) \tag{5.31}$$

Equation (5.31) is then substituted in Equation (5.30) and the trigonometric functions are expanded. The elimination of the secular terms yields two first order non-linear ordinary-differential equations which describe the amplitude and phase modulation of the response and permit a stability analysis

$$\begin{cases}\dot{A}=f_1(\varepsilon,A,\beta)+O(\varepsilon^2)\\ \\ \dot{\beta}=f_2(\varepsilon,A,\beta)+O(\varepsilon^2)\end{cases} \tag{5.32}$$

where $\beta=2\sigma T_1-\Phi$. The steady-state motions occur when $\dot{A}=\dot{\beta}=0$, which corresponds to the singular points of Equation (5.32).Thus, the frequency-response equation can be written in its parametric form with respect to the phase β as a set of two equations

$$\begin{cases}A=K_1(\beta)\\ \Omega=K_2(\beta)\end{cases} \tag{5.33}$$

This analytic expression makes the model suitable for MEMS and NEMS designers as a fast and efficient tool for resonant sensor performances optimisation. All the analytical computations were carried out with the following set of parameters : $l=50\mu m$, $b=0.5\mu m$, $l_a=40\mu m$, $g_a=500nm$, $l_d=48\mu m$, $g_d=300nm$, $V_s=0V$. h, V_{ac} and V_{dc} were used for parametric studies.

As shown in Figure 5.7, the analytical model enables the capture of the competition between the hardening and the softening behaviors. Remarkably, when the resonator is under superharmonic excitation of order half its primary resonance, the analytical model did not capture any mixed behavior. It is due to the contribution of the nonlinearities into the secular terms completely different from the primary resonance case. Consequently, this ensures the cancellation of the nonlinearities ($\frac{h}{g_d}=1$) without any sensitivity to the mixed behavior. Nevertheless, the upper bound limit of the obtained linear peak is set by the pull-in. Then, to enlarge the validity domain of the hysteresis suppression, it is important to control the dynamic pull-in which is demonstrated below.

5.5.3 Critical amplitude

Under primary resonance, the mechanical critical amplitude of a nanoresonator is only determined by the beam vibrating thickness h and the quality factor Q (see section 4.3).

$$A_c=1.65\frac{h}{\sqrt{Q}} \tag{5.34}$$

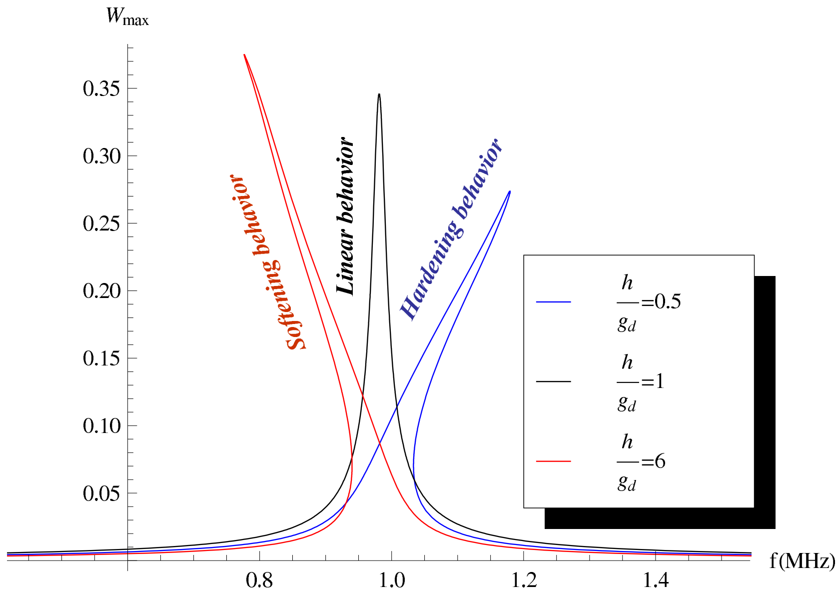

Figure 5.7: Competition between hardening and softening behaviors for several values of the ratio $\frac{h}{g_d}$ (W_{max} is the normalized displacement at the middle of the beam)

In order to check the validity of Equation (5.34) for NEMS resonator under superharmonic resonance, the AC voltage and the beam vibrating width are respectively fixed at $V_{ac} = 0.6V$ and $h = 1\mu m$. Then, for 3 values of DC voltage, $\frac{d\Omega}{d\beta}$ is calculated at the phase $\beta_c = \frac{2\pi}{3}$ and plotted with respect to the quality factor Q as shown in Figure 5.8(b). The critical quality factor Q_c is determinated graphically as the intersection between the curve $\frac{d\Omega(\frac{2\pi}{3})}{d\beta}[Q]$ and the Q-axis.
For the sake of clarity, these values are reported above each corresponding curve in Figure 5.8(a). This permits to conclude that the critical amplitude A_c decreases when the quality factor increases. Moreover, Equation (5.34) gives the same critical amplitudes as those deduced graphically.
Figure 5.8(c) shows the variation of the critical vibrating width h_c for different DC polarizations V_{dc}. The fixed values of the AC voltage and the quality factor Q are $V_{ac} = 0.6V$ and $Q = 4900$. h_c is determinated graphically in the same way as Q_c. Then, these values are reported in Figure 5.8(d) which clearly indicates the linear dependence of the critical amplitude A_c on the vibrating width of the resonator. Again, Equation (5.34) gives the same critical amplitudes as those deduced graphically.
In the same way, using the model and assuming that the mechanical nonlinearities are preponderant, we can show that the critical amplitude A_c has no dependencies on any other physical parameter.

5.5.4 pull-in

The pull-in amplitude is the oscillation amplitude A_p above which the resonator position becomes unstable and collapses. Mathematically, for a doubly clamped NEMS resonator under superharmonic resonance, it can be shown that the pull-in occurs when the amplitude reaches an infinite slope at the phase $\beta_p = \frac{\pi}{2}$.

Figure 5.9 shows some predicted frequency curves. For $V_{dc} = 20V$, the resonator becomes instable and goes to pull-in (Red curve) at the amplitude of the point PI. At this level of oscillation, the resonator dynamics reaches a saturation similar to the separation of branches reported in [Nayfeh 2005b]. Unlike the primary resonance case for which the dynamic-pull-in was defined by a domain starting at

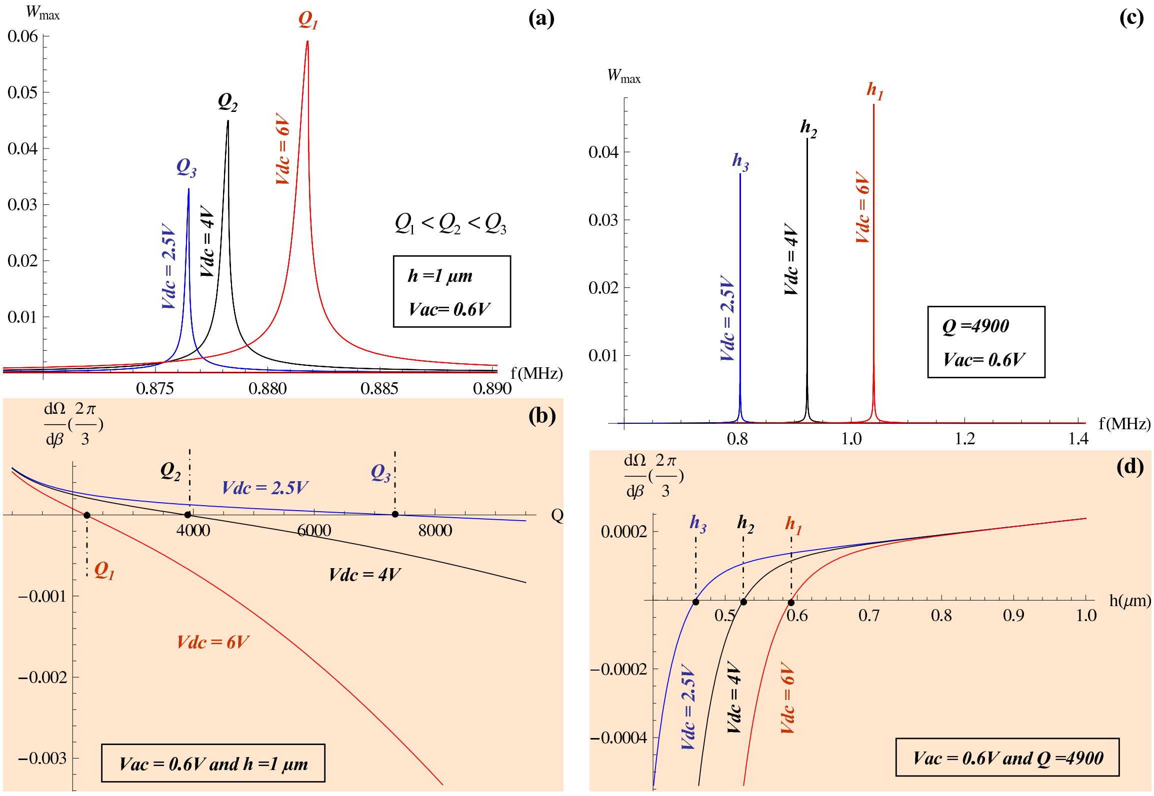

Figure 5.8: (a): Dependency of the critical amplitude on the quality factor (Here A_c is the peak of W_{max}). (b): Critical quality factor determination for several DC voltage. (c): Dependency of the critical amplitude on the vibrating width. (d): Critical vibrating width determination for several DC voltage

the initiation of the mixed behavior (point P), the solution under superharmonic resonance follows a pull-in attractor at the point PI. Figure 5.10 shows the variation of the pull-in amplitude with respect to AC voltage V_{ac}. For NEMS resonators under superharmonic resonance, it is possible to shift up the pull-in amplitude by applying a low AC voltage. It is important to underline that this ability to control the pull-in amplitude with only two physical parameters which are the driving AC and the DC polarization voltages is not possible under primary resonance. However, in order to compensate the loss of performance, the resonator must be actuated with higher DC polarizations.

5.5.5 Conclusion

A global approach to model and simulate the nonlinear dynamics of NEMS resonators under superharmonic excitation of order-two was presented. Compared to the primary resonance, the results show that the critical amplitude of the resonator does not change and keep the same dependencies on the quality factor Q and the vibrating width h. We demonstrated the existence and mechanism of the dynamic pull-in phenomenon under superharmonic excitation. Moreover, close-form expressions for the pull-in amplitude and the pull-in voltage can be provided using the model which constitutes a quick tool for NEMS designers to choose the appropriate DC voltage and the amplitude and frequency of the AC load to shift up or retard pull-in.

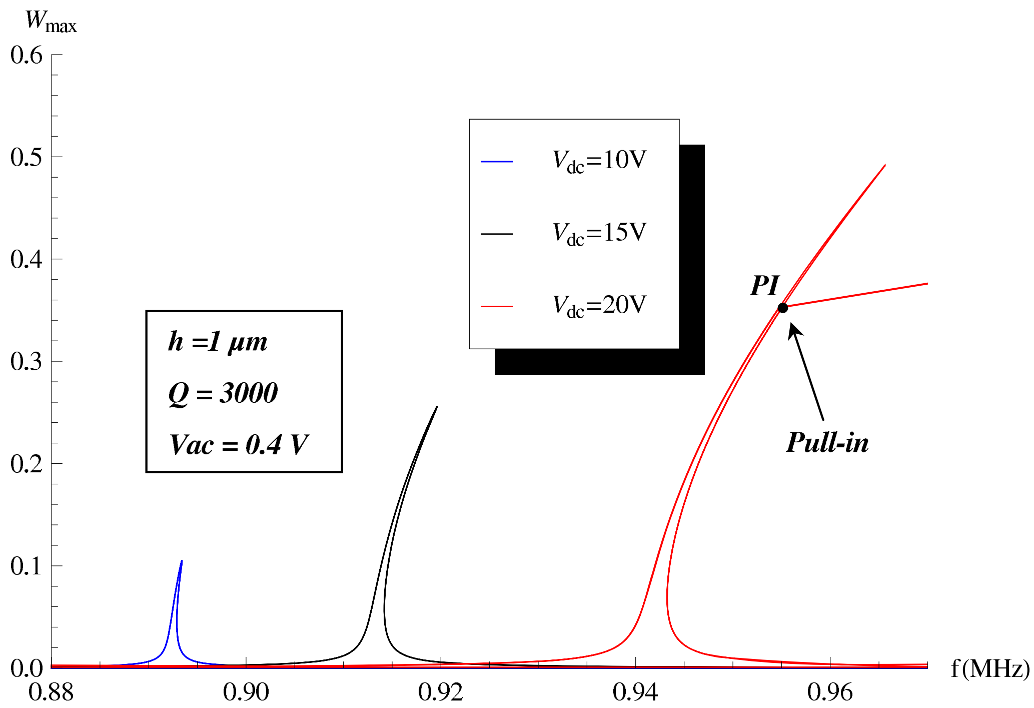

Figure 5.9: Predicted frequency curves for several DC voltage

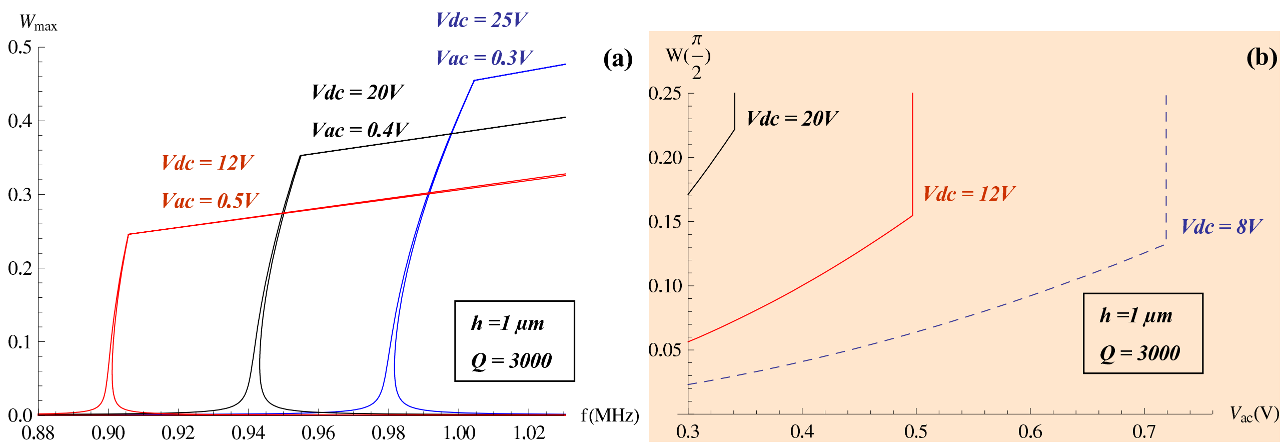

Figure 5.10: (a): Predicted frequency curves (up to pull-in) for several AC and DC polarizations. (b): Dependency of the pull-in amplitude on the AC voltage

5.6 Mixed behavior retarding by simultaneous resonances

5.6.1 Introduction

Although it is possible to retard the pull-in phenomena under superharmonic resonance, it demands extremely high DC voltage which is sometimes unrealistic. Nevertheless, the superharmonic resonance seems to be with a great benefit for the bifurcation topology control of the resonator dynamics. The question is: what if we combine both dynamics (primary and superharmonic resonances)? In other words, what is the effect of the superharmonic resonance on the primary one in the case of simultaneous resonances?

Obviously, if we are asking such questions, we know exactly how we can simply excite the resonator simultaneously under primary and superharmonic resonance using a lock-in amplifier. In fact, since the electrostatic force is proportional to the square of the drive voltage (DC polarization+AC voltage), two harmonics excite the system: the first one proportional to $V_{ac}V_{dc}$ at the frequency Ω and the second one proportional to V_{ac}^2 at the frequency 2Ω. Consequently, the simultaneous resonance is intrinsic to the electrostatic excitation for a nonlinear resonator. Several configurations are presented in table 5.1 with respect to the actuation and references frequencies as well as the lock-in mode.

Excitation/Reference	$f_0/2$	f_0
$f_0/2$	❑ mode 1f. ❑ SIR (Primary+Superharmonic). ❑ Effect of the PR on the SR.	❑ mode 2f. ❑ SIR (Primary+Superharmonic). ❑ Effect of the SR on the PR.
f_0		❑ mode 1f. ❑ SIR (Primary+Parametric). ❑ Effect of the PaR on the PR.
Excitation/Reference	**f_0**	**$2f_0$**
f_0	❑ mode 1f. ❑ SIR (Primary+Parametric). ❑ Effect of the PaR on the PR.	❑ mode 2f. ❑ SIR (Primary+Parametric). ❑ Effect of the PR on the PaR.
$2f_0$		❑ mode 1f. ❑ Parametric Resonance.

Table 5.1: Lock-in amplifier configurations with respect to the actuation and references frequencies (SIR=simultaneous resonances, PR= primary resonance, SR= superharmonic resonance, PaR=parametric resonance). f_0 is the natural frequency of the resonator.

Remarkably, even when the $1f$ mode of the lock-in amplifier is used in the third configuration of the first part in Table 5.1, simultaneous primary and parametric resonances occur. However, since the AC voltage is very low with respect to the DC polarization (see sections 4.3 and 4.5), the effect of the parametric resonance on the primary one is negligible.

Our previous investigations of the mixed behavior in nonlinear micromechanical resonators (see sections 4.5 and 5.4) have led to the discovery of an invariant bifurcation point (see section 5.4) corresponding to the initiation of the mixed behavior which can typically be set by design. Nevertheless, since the hysteresis suppression is set for a given design by the gap and the width in the direction of vibration h (see section 5.3) and furthermore, the length and the thickness are set to optimize the sensitivity of the resonator (see section 2.4), the design is completely determined and the P point location is consequently set. In other words, when it comes to design, the hysteresis suppression and the resonator sensitivity are privileged and thus we can not retard anymore the initiation of the mixed behavior for a primary resonance excitation.

In this section, unlike previous schemes under primary resonance excitation, the resonator is excited simultaneously under primary and superharmonic resonances. We investigate experimentally the energy transfer in a single nonlinear system (the resonator) through simultaneous resonances. The superharmonic dynamics, twice as slow as the primary one, pumps energy from the system and modifies the bifurcation topology highly sensitive with respect to the secondary excitation. Experimentally, the $2f$ mode driven via a lock-in amplifier, has been used to excite simultaneously the primary resonance and the superharmonic resonance of order half the resonator natural frequency. For this first illustration of energy pumping through a simultaneous resonances in a micromechanical resonator, high drive voltages have been applied in order to reach the mixed behavior and then the amplitude of the superhamonic excitation has been increased gradually, indicating a significant modification on the bifurcation topology, and precisely providing a practical tool for mixed behaviour retarding in nonlinear MEMS and NEMS resonators.

5.6.2 Model

To understand simultaneous resonance, consider a single generic resonator - in our case a micromechanical clamped-clamped beam electrostatically actuated and vibrating in its fundamental transverse mode - and assume it undergoes weak damping and possesses quadratic, cubic and quintic nonlinearities. The electrostatic force proportional to the square of the drive voltage -basically involves a static DC voltage and a time varying AC voltage- possesses two harmonics, the first one twice as slow as the second one. To be quantitative, this generic resonator can be described approximately by the equation of motion

$$\begin{aligned} &\ddot{x} + \mu\dot{x} + \omega_n x + \alpha_2 x^2 + \alpha_3 x^3 \\ &+\alpha_5 x^5 = \zeta_1 \cos\Omega + \zeta_2 \cos(2\Omega) \end{aligned} \tag{5.35}$$

where x represents the deviation of the resonator from its equilibrium. The normal frequency of the resonator is ω_n. α_2, α_3 and α_5 are respectively the nonlinear quadratic, cubic and quintic spring constants and μ is the linear damping rate. ζ_1 and ζ_2 are respectively the drive amplitudes of the first and the second harmonic. Ω is the drive frequency.

One can immediately see that when the frequency drive Ω is tuned around the resonator normal frequency ω_n, only the primary resonance given by the first harmonic is excited. Experimentally, it corresponds to the "1f mode" classically used via a lock-in amplifier in NEMS and MEMS electrical characterizations. For this case, the bifurcation topology of a mixed behavior has been investigated experimentally in nonlinear micromechanical resonators (see section 5.4) and we showed the invariance of the mixed behavior initiation domain for a fixed resonator design.

Now, when using the "2f mode" for the electrical characterization of the primary resonance using the second harmonic, simultaneously, the first harmonic excites the system at its superharmonic resonance of order half its natural frequency. In this configuration and in order to analyse the nonlinear equation of motion (5.35) which involves simultaneous resonances, the method of multiple scales was used in order to take into account the contribution of each dynamics in the resonator frequency response. To this end, we seek a first-order uniform solution in the form

$$x(t,\varepsilon) = x_0(T_0,T_1) + \varepsilon x_1(T_0,T_1) + \cdots \tag{5.36}$$

where ε is the small nondimensional bookkeeping parameter, $T_0 = t$ and $T_1 = \varepsilon t$.

Since both harmonics are linked by the drive frequency Ω, in order to analyze the nonlinear response under simultaneous primary and superharmonic resonances, we express the nearness of Ω to $\frac{\omega_n}{2}$ by introducing the detuning parameter σ according to

$$2\Omega = \omega_n + \varepsilon\sigma \tag{5.37}$$

Substituting Equation (5.36) into Equation (5.35) and equating coefficients of like powers of ε yields

Order ε^0

$$\zeta_1 \cos\left(\sigma T_1 + \frac{T_0\omega_n}{2}\right) + \omega_n^2 x_0 + {x_0}^{(2,0)} = 0 \tag{5.38}$$

Order ε^1

$$\begin{aligned} &\zeta_2 \cos(\sigma T_1 + T_0\omega_n) + x_0^2\alpha_2 + x_0^3\alpha_3 + x_0^5\alpha_5 \\ &+x_1\omega_n^2 + \ c{x_0}^{(1,0)} + 2{x_0}^{(1,1)} + {x_1}^{(2,0)} = 0 \end{aligned} \tag{5.39}$$

where $x_i^{(j,k)} = \dfrac{\partial^k}{\partial T_1^k}\left(\dfrac{\partial^j x_i}{\partial T_0^j}\right)$.

The general solution of Equation (5.38) can be written as

$$x_0 = X\cos(\omega_n T_0 + \Phi) - \frac{4\zeta_1}{3\omega_n^2}\cos\left(\frac{\omega_n T_0}{2} + \sigma T_1\right) \tag{5.40}$$

Equation (5.40) is then substituted into Equation (5.39) and the trigonometric functions are expanded. The elimination of the secular terms yields two first order non-linear ordinary-differential equations which describe the amplitude and phase modulation of the response and permit a stability analysis

$$\begin{aligned} \dot{A} = &-\frac{4\varepsilon\zeta_1^2 \sin\beta\left(20X\alpha_5\zeta_1^2\cos\beta + 9\alpha_2\omega_n^4\right)}{81\omega_n^9} \\ &-\frac{\varepsilon\mu X}{2} + O(\varepsilon^2) \end{aligned} \tag{5.41}$$

$$\begin{aligned} \dot{\beta} = 2\sigma &- \frac{40\varepsilon\alpha_5\zeta_1^4\{6+\cos(2\beta)\}}{81\omega_n^9} - \frac{6\varepsilon\alpha_3X^2 + 5\varepsilon\alpha_5X^4}{16\omega_n} \\ &-\frac{2\varepsilon\zeta_1^2\left(2\alpha_2\cos\beta + 6\alpha_3X + 15\alpha_5X^3\right)}{9\omega_n^5X} + O(\varepsilon^2) \end{aligned} \tag{5.42}$$

where $\beta = 2\sigma T_1 - \Phi$. The steady-state motions occur when $\dot{X} = \dot{\beta} = 0$, which corresponds to the singular points of Equations (5.41) and (5.42).Thus, the frequency-response equation can be written in its parametric form with respect to the phase β as a set of two equations

$$\begin{cases} X = K_1(\beta) \\ \Omega = K_2(\beta) \end{cases} \tag{5.43}$$

The parametric form of the system frequency response under simultaneous primary and superharmonic excitation (Equation (5.43)) is a practical tool for the parametric plot of the resonance curves with

respect to the phase β.
More generally, this approach has been applied to the projected nonlinear Euler-Bernoulli partial differential equation on the first bending undamped linear mode shape of clamped-clamped microbeam. This ensures that all nonlinear terms are included in the studied equation of motion even if Equation (5.35) contains most significant non linear terms for a clamped-clamped resonator under simultaneous resonances. Thus, qualitative explanations of physical phenomena can be based on the solution of Equation (5.35).

5.6.3 Analytical results

5.6.3.1 Critical amplitude

The critical amplitude has been calculated analytically for the response of a clamped-clamped resonator to simultaneous primary and superharmonic excitations. The same close form expressions has been obtained as those determinated in sections 4.3 and 4.5 for the case of primary resonance. Indeed, the superharmonic contribution in the resonator dynamics has no effect on the critical bifurcation point at the transition from the linear to the nonlinear behavior. Around this limit, some parametric studies have been performed using the model. They showed that the nonlinear terms are negligible and the coupling between the slow dynamics due to the superharmonic resonance and the fast dynamics due to the primary resonance is very low. Consequently, the critical amplitude is invariant.

5.6.3.2 Bifurcation topology tuning and mixed behavior retarding

The resonator design considered for analytical simulations is described in Figures 5.11(a) and 5.11(b). Figure 5.11(c) shows 3 nonlinear resonance peaks predicted analytically using the model of the resonator under combined primary and superharmonic excitations. The applied DC voltage is $10V$, combined with high V_{ac} which ensures a mixed behavior. Then, the P bifurcation point is tracked analytically while keeping a mixed behavior and increasing the AC voltage from $0.6V$ to $1V$.

As opposed to the actuation under primary resonance where the dynamic position of the P point is vertically fixed (see section 5.4), here, the contribution of the superharmonic resonance on the vertical location of the P point is very interesting. As shown in Figure 5.11, the increase of the AC voltage permits to shift up the P point which retards the apparition of the mixed behavior and then the pull-in domain is reduced.

If we take a look at Equations (5.41) and (5.42) that modulate the amplitude X and the phase β of the system, we can identify that their modulations depend on the fast the fast dynamic proportional to the quintic nonlinear stiffness term α_5 enabling the capture of the mixed behavior and coming from the primary resonance (terms proportional to $\cos 2\beta$ or $\sin 2\beta$), as well as the slow dynamics proportional to the quadratic nonlinear stiffness term α_2 enabling the capture the superharmonic resonance effect (terms proportional to $\cos \beta$ or $\sin \beta$).

Obviously, the increase of the AC voltage corresponds simultaneously to the amplification of both primary and superharmonic excitations. Nevertheless, knowing that the primary excitation has no effects on the mixed behavior initiation domain which has been also demonstrated using Equations (5.41) and (5.42), the alteration of the bifurcation topology in this configuration (simultaneous resonances) is due to the increase of the superharmonic excitation.

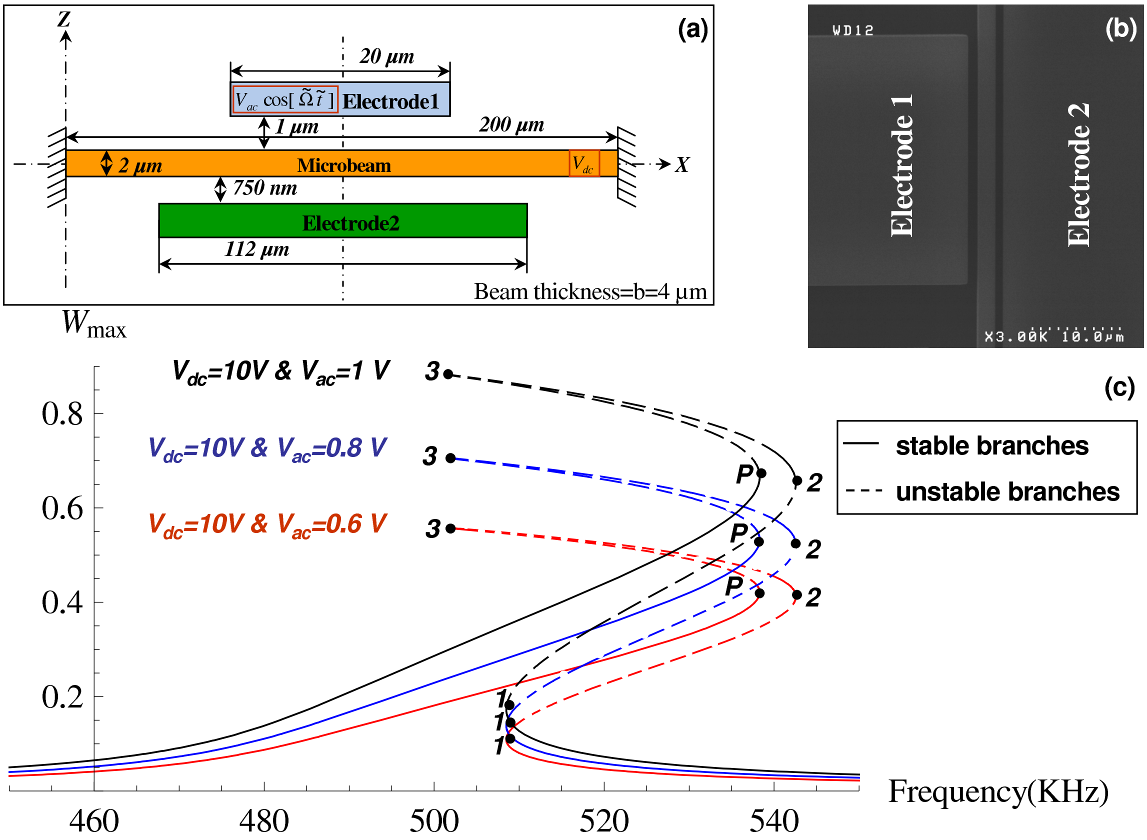

Figure 5.11: (a) Dimensions of a typical fabricated resonator. (b): SEM image of the device. (c): Resonance frequency responses showing mixed behaviors analytically Predicted under combined primary and superharmonic excitations, the location of the different bifurcation points and the effect of the AC voltage on the P point vertical position. P is the mixed behavior domain initiation point and the point 3 is the highest bifurcation point in the softening domain.

5.6.4 Experimental validation

The device was placed in a vacuum chamber and measurements were performed at room temperature. The residual stress calculated by knowing the frequency shift between the natural frequency and the measured frequency is around $15MPa$ and the fringing field effect coefficients calculated using an analytical model [Nishiyama 1990] are $C_{n1} = 1.6$ and $C_{n2} = 1.5$. As shown in Figure 4.17, a lock-in amplifier has been used to track experimentally the resonance peak. Moreover, for combined primary and superhamonic excitation, the $2f$ mode has been used which allows the direct measurement of the output voltage due to the motional capacitance and thus no vectorial substraction with measurement at a null DC is required as the case of the $1f$ mode.

Figure 5.12 shows 6 nonlinear mixed behavior peaks: the 3 dashed curves obtained using the $1f$ mode and the 3 others were obtained under primary and superharmonic excitations ($2f$ mode). The output signal in Figure 5.12 is expressed in the dimensionless quantity $\tilde{V} = \frac{V_{out}}{V_{dc}}$. The output voltage being proportional to V_{dc} at a given mechanical displacement, $\tilde{V}$ is also proportional to this displacement. As it can be seen on the different dashed curves where the AC voltage has been fixed around $0.5V$, the P point vertical location is invariant with respect to the drive amplitude, the bias voltage and the quality factor (which vary due to the ohmic losses [Sazonova 2006] increase). In this

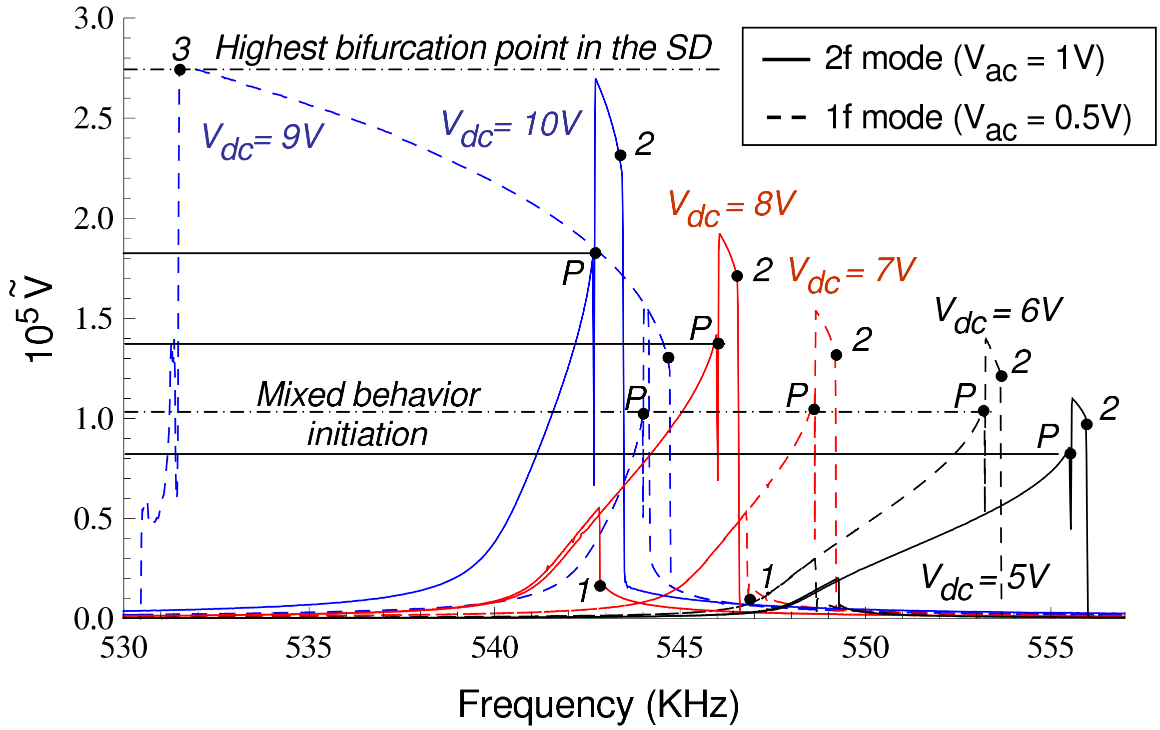

Figure 5.12: Resonance frequency responses showing measured mixed behaviors under primary resonance as well as under simultaneous primary and superharmonic excitations, the location of the different bifurcation points and the effect of the DC voltage on the P point vertical position.

configuration (resonator under primary resonance: $1f$ mode), the P point amplitude is set only by the geometry of the device (ratio gap/width of the beam). This interesting result will add an other criterion for MEMS and NEMS designers in order to retard the onset of the mixed behavior. This criterion, not usually compatible with the resonator sensitivity enhancement and the hysteresis suppression, could not be satisfied.

For the 3 other peaks, the 2 f mode has been used and the applied AC voltage has been fixed around $1V$. The DC voltage has been increased from 6 to 10 and consequently the amplitude of the superhamonic excitation has been amplified.

This increases significantly the quadratic stiffness α_2 proportional to $V_{dc}^2 + \frac{V_{ac}^2}{2}$. Since α_2 is the term that produces internal resonance into the system (precisely superharmonic resonance of order half the system natural frequency), the slow dynamics involved into the phase modulation (Equation (5.42)) pumps energy from the global dynamic due to the nonlinear interaction between the two harmonics (the phase of the system depends on both dynamics). Thus, the bifurcation topology is modified, and particularly the initiation of the mixed behavior can be retarded as shown in Figure 5.12 and can be tuned using a superharmonic excitation. Unlike the first configuration, where no superharmonic resonance exists, the simultaneous resonance shows the fast effect of a slow nonlinear resonance on the resonator bifurcation topology around the mixed behavior and broke the invariance of the P point vertical location with respect to the drive voltages which offers a better alternative for MEMS and NEMS designers to avoid the onset of the mixed behavior and reduce the domain of possible pull-in.

5.7 Summary

In this chapter the nonlinear model developed in chapter 4 was used to provide several design rules for the performance enhancement of NEMS resonators for resonant accelerometers applications. In particular, it has been shown how it is possible to tune some design parameters (like the ratio between the beam thickness in the direction of vibration h and the detection gap thickness g_d) in order to keep a linear behavior up to the pull-in domain initiation. The consequence of this may be a great gain in sensors' resolution, as the resonator's carrier power is largely increased while keeping linear may prevent most of noise aliasing [Roessig 1997a, Kaajakari 2005a].

Since the hysteresis suppression is potentially limited by the mixed behavior initiation amplitude (the fifth order nonlinear terms become no more negligible), the next step was the analytical and experimental investigations of the mixed behavior in NEMS resonators. We essentially demonstrate an electrostatic mechanism to tune the bifurcation topology with the polarization voltage, whereas we show that the onset of the mixed behavior is set by the geometry of the device. Consequently, such undesirable behavior can be retarded by design. Nevertheless, we showed that the resonator geometry is fully set to enhance the device sensitivity (small length and small thickness) as well as to enable the hysteresis suppression depending on the width h and the gap g. This makes quite difficult to satisfy the cancellation of nonlinearities and the mixed behavior retarding only by design.

That is why the next step consisted of using nonlinear resonances such as the superharmonic resonance of order half the fundamental frequency of the resonator in order to retard the pull-in and furthermore the use of simultaneous resonances (primary+superharmonic) for mixed behavior retarding while keeping possible the compensation of the nonlinearities by design.

Chapter 6

Experimental investigations

Contents

6.1 Designs and motivations **137**

6.2 Experimental set-up **137**

6.2.1 Capacitive down-mixing principle 137

6.2.2 Capacitive down-mixing configurations 140

6.2.3 Nonlinear down-mixing model 143

6.3 Experimental validation **144**

6.3.1 High capabilities set-up 144

6.3.2 First validation (design for hardening behavior) 145

6.3.3 Design for nonlinearities compensation 146

6.3.4 Strange attraction and transition to the softening behavior 150

6.4 Summary **151**

6.1 Designs and motivations

Within the framework of the European M&NEMS project, several resonators electrostatically actuated in plane have been designed and fabricated in order to complete the validation of the nonlinear model described in section 4.5 as well as the design rules provided in chapter 5. They have been designed with two electrodes allowing 2 ports electric measurements (See Figure 6.1).
These devices were fabricated using the M&NEMS process flow (See Figure 4.4) enabling designers to obtain both MEMS ($2\,\mu m$ thick) and NEMS ($500\,nm$ thick) resonators. Tables 6.1 and 6.2 present the geometry parameters and some characteristics of each resonator. The predicted dynamic behaviors beyond the critical amplitude of these resonators are described in Table 6.3. Besides, these devices were designed in order to cover all possible linear and nonlinear behaviors described by the model in Figure 5.1 as well as to display a high acceleration sensitivity when they are used as sensitive parts in resonant accelerometers.

6.2 Experimental set-up

6.2.1 Capacitive down-mixing principle

Among the devices listed in Tabless 6.1 and 6.2, many resonators were designed with high frequencies (in the MHz range) which makes the direct synchronic detection via a lock-in amplifier quite difficult. Indeed, the electrical read-out at high frequency is complicated by parasitic capacitances which changes

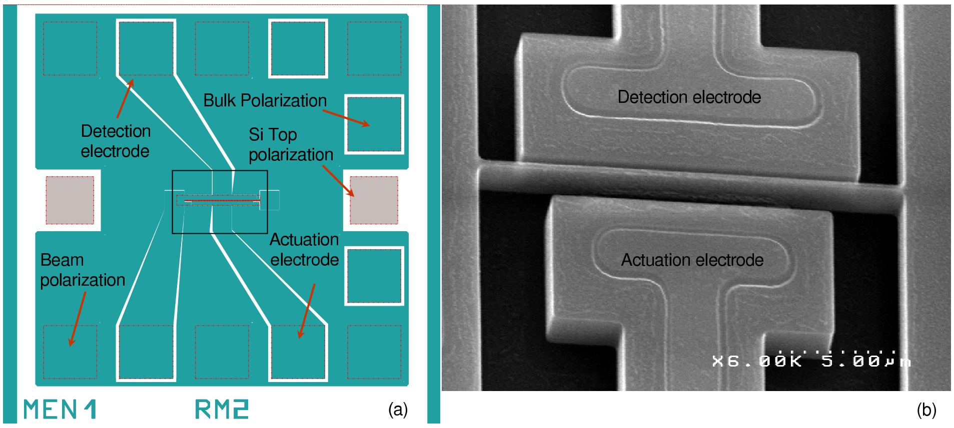

Figure 6.1: (a): M&NEMS mask showing the structure of a typical designed resonator, the disposition of the pads and their polarization. (b): A SEM image of a designed resonator.

	RM_1	RM_2	RM_3	RM_4	RM_5	RM_6	RM_7
l	$100\,\mu m$	$200\,\mu m$	$200\,\mu m$	$15\,\mu m$	$30\,\mu m$	$50\,\mu m$	$75\,\mu m$
h	$5\,\mu m$	$5\,\mu m$	$10\,\mu m$	$250\,nm$	$500\,nm$	$300\,nm$	$500\,nm$
l_a	$80\,\mu m$	$160\,\mu m$	$160\,\mu m$	$10\,\mu m$	$25\,\mu m$	$45\,\mu m$	$70\,\mu m$
l_d	$90\,\mu m$	$180\,\mu m$	$180\,\mu m$	$12\,\mu m$	$28\,\mu m$	$48\,\mu m$	$72\,\mu m$
g_a	$1\,\mu m$	$1\,\mu m$	$1\,\mu m$	$1\,\mu m$	$2\,\mu m$	$4\,\mu m$	$2\,\mu m$
g_d	$300\,nm$	$300\,nm$	$300\,nm$	$250\,nm$	$500\,nm$	$500\,nm$	$750\,nm$
C_{0a}	$1.42\,fF$	$2.83\,fF$	$2.83\,fF$	$0.18\,fF$	$0.22\,fF$	$0.2\,fF$	$0.62\,fF$
C_{0d}	$5.31\,fF$	$10.62\,fF$	$10.62\,fF$	$0.85\,fF$	$0.99\,fF$	$1.7\,fF$	$1.7\,fF$
f_0	$4.37\,MHz$	$1.09\,MHz$	$2.18\,MHz$	$9.7\,MHz$	$4.86\,MHz$	$1.05\,MHz$	$0.77\,MHz$

Table 6.1: Physical parameters of MEMS resonators. C_{0a} and C_{0d} are actuation and detection static capacitances. f_0 is the resonance frequency of the first in-plane bending mode.

the expected behavior of the electrical circuit. In order to avoid parasitic impedances and cross-talk problem, the down-mixing technique has been used in several configurations to read-out the capacitance variation at a lower frequency $\Delta\omega$ [Bargatin 2005]. A working principle schematic is shown in Figure 6.2. The down-mixing technique has been widely used in NEMS read-out to avoid high frequency problems by making measurements at a lower frequency through synchronous lock-in methods [Bargatin 2005, Sazonova 2006]. Important investigations concerning the capacitive down-mixing possibilities were done in LETI with the help of Marc Sworowski during his postdoctoral period. The capacitive down-mixing principle is explained below.

A periodic electrostatic force is generated between the actuation electrode and the clamped-clamped beam in order to enable the oscillation of the resonator at its first bending mode shape which corresponds to the first harmonic (the primary resonance at the frequency ω). Moreover, the beam is polarized using a periodic voltage which corresponds to the second harmonic at the frequency $\omega + \Delta\omega$. Consequently and due to the NEMS mixing, a capacitance variation is generated between the beam and the detection electrode at a low frequency harmonic $\Delta\omega$. Thus, the created low motional current at the frequency $\Delta\omega$ is detected using a lock-in amplifier (LIA). The latter needs a reference signal, which is created thanks to an RF mixer as shown in Figure 6.2 in order to track the resonance

	RN_1	RN_2	RN_3	RN_4	RN_5	RN_6	RN_7
l	$100\,\mu m$	$200\,\mu m$	$150\,\mu m$	$15\,\mu m$	$30\,\mu m$	$50\,\mu m$	$75\,\mu m$
h	$250\,nm$	$500\,nm$	$400\,nm$	$400\,nm$	$750\,nm$	$250\,nm$	$300\,nm$
l_a	$80\,\mu m$	$160\,\mu m$	$140\,\mu m$	$10\,\mu m$	$25\,\mu m$	$45\,\mu m$	$70\,\mu m$
l_d	$90\,\mu m$	$180\,\mu m$	$145\,\mu m$	$12\,\mu m$	$28\,\mu m$	$48\,\mu m$	$72\,\mu m$
g_a	$1\,\mu m$	$1\,\mu m$	$1\,\mu m$	$1\,\mu m$	$2\,\mu m$	$4\,\mu m$	$2\,\mu m$
g_d	$300\,nm$	$300\,nm$	$300\,nm$	$250\,nm$	$500\,nm$	$500\,nm$	$750\,nm$
C_{0a}	$0.35\,fF$	$0.71\,fF$	$0.71\,fF$	$0.04\,fF$	$0.06\,fF$	$0.05\,fF$	$0.15\,fF$
C_{0d}	$1.33\,fF$	$2.66\,fF$	$2.66\,fF$	$0.21\,fF$	$0.25\,fF$	$0.42\,fF$	$0.42\,fF$
f_0	$0.22\,MHz$	$0.11\,MHz$	$0.16\,MHz$	$15.6\,MHz$	$7.3\,MHz$	$0.88\,MHz$	$0.47\,KHz$

Table 6.2: Physical parameters of NEMS resonators. C_{0a} and C_{0d} are actuation and detection static capacitances. f_0 is the resonance frequency of the first in-plane bending mode.

Hardening behavior	Sofetening behavior	Mixed and linear compensated behavior
$RM_i/RN_i \quad i \in \{4,5,6,7\}$	RM_3/RN_3	$RM_1/RN_1/RM_2/RN_2$

Table 6.3: Predicted dynamic behaviors of the designed MEMS and NEMS resonators.

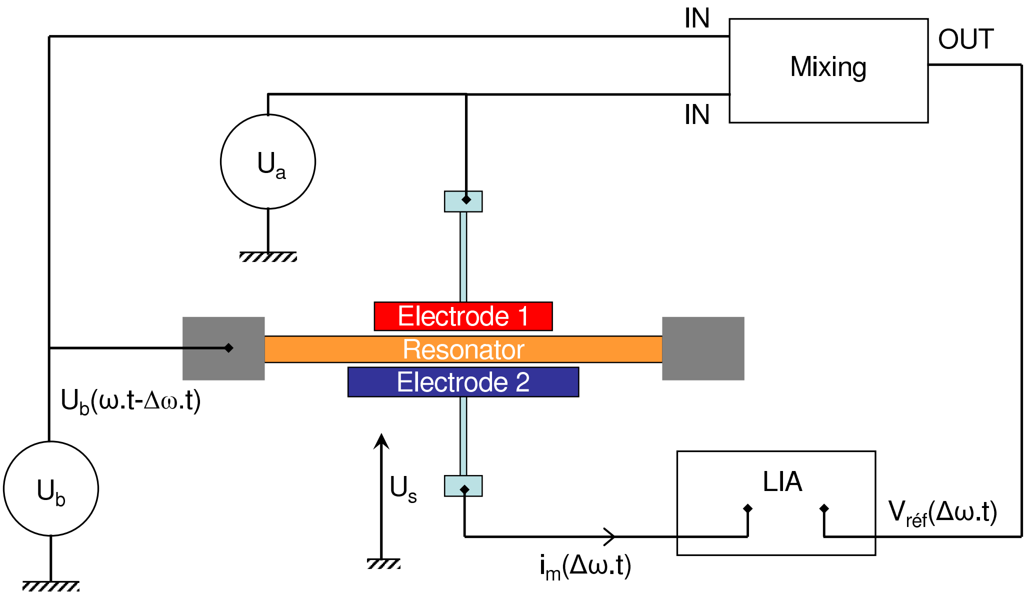

Figure 6.2: A working principle schematic of a downmixing setup.

peak at the low frequency $\Delta\omega$.

The current I_{out} between the resonator and the detection electrode is converted into the tension V_{out} due to an equivalent impedance that corresponds to the cable capacitance ($\approx 100pF$) in parallel with the lock-in input impedance (a capacitance of $25pF$ // a resistance of $10M\Omega$). For a frequency $> 1KHz$, the equivalent impedance is reduced to the capacitance due to the cables and the lock-in input $Z_{load} \approx C_{load} \approx 125pF$. Under the effect of the electrostatic forces applied to the beam, we consider that the resonator vibrates on its first mode at the frequency ω close to its primary resonance

ω_0. We consider also the phase φ which can exist between the vibration of the beam and the harmonic ω of the force of actuation. At resonance, the beam displacement is $w(t)$ and the capacitance between the beam and the detection electrode is assumed to be:

$$C_d(\omega t) \approx C_{0d}\left(1 + w(t).\cos(\omega t + \varphi)\right) \tag{6.1}$$

The current I_{out} is then:

$$I_{out} = \frac{dQ}{dt} = (U_b - U_s)\frac{dC_d}{dt} + C_d\frac{d(U_b - U_s)}{dt} \tag{6.2}$$

We admit that $V_b >> V_s$, hence:

$$\begin{aligned} I_{out}(t) = U_b\frac{dC_d}{dt} + C_d\frac{dU_b}{dt} = \frac{\Delta\omega}{2}C_{0d}.w(t).V_b\sin(\Delta\omega t + \varphi) \\ + (\omega - \Delta\omega).C_{0d}.V_b\sin(\omega t - \Delta\omega t) + \left(\omega - \frac{\Delta\omega}{2}\right).C_{0d}.w(t).V_b\sin(2\omega t - \Delta\omega t + \varphi) \end{aligned} \tag{6.3}$$

The measured voltage via the LIA is then:

$$U_{out} = Z_{load}.I_{out} = \frac{R_{load}.Iout}{1 + jR_{load}C_{load}\omega} \tag{6.4}$$

$$For\,\omega >> \omega_{load} = \frac{1}{R_{load}C_{load}},\ \ U_{out} \approx \frac{I_{out}}{jC_{load}\omega} \tag{6.5}$$

$$U_{out}^{\Delta\omega} \approx \frac{I_{out}^{\Delta\omega}}{jC_{load}\Delta\omega} \approx \frac{\frac{\Delta\omega}{2}C_{0d}.w.V_b\sin(\Delta\omega t + \varphi)}{jC_{load}\Delta\omega} \approx j\frac{C_{0d}}{2C_{load}}.w(t).V_b.\,sin\,(\Delta\omega t + \varphi) \tag{6.6}$$

$$||U_{out}^{\Delta\omega}|| \approx j\frac{C_{0d}}{2C_{load}}.w.V_b = V_{out} \tag{6.7}$$

6.2.2 Capacitive down-mixing configurations

The beam displacement w depends on the electrostatic forces (in actuation and detection). In order to simplify the following analysis, only the actuation forces are considered. Then, the electrostatic force can be written as:

$$||F_{elec}||_{\omega} = \frac{C_n}{2}\varepsilon_0.b.l\left|\left|\frac{(U_a - U_b)^2}{(g_a - w)^2}\right|\right| \tag{6.8}$$

This electrostatic force depends on the actuation voltage. Therefore, three different configurations can be distinguished.

6.2.2.1 ω configuration

In this configuration, as shown in Figure 6.3:

$$U_a = V_{dc} + V_a\cos(\omega t) \tag{6.9}$$

$$U_b = V_b\cos(\omega t - \Delta\omega t) \tag{6.10}$$

Hence:

$$(U_a - U_b)^2 = 2V_a.V_{dc}\cos(\omega t) + V_{dc}^2 - V_a.V_b\cos(\Delta\omega t) - 2V_b.V_{dc}\cos(\omega t - \Delta\omega t)$$
$$+\frac{1}{2}V_a^2 + \frac{1}{2}V_b^2 + \frac{1}{2}V_a^2\cos(2\omega t) + \frac{1}{2}V_b^2\cos(2\omega t - 2\Delta\omega t) - V_a.V_b\cos(2\omega t - \Delta\omega t) \quad (6.11)$$

The first term on the right hand side of Equation (6.11) is the excitatory harmonic. Then:

$$||(U_a - U_b)^2||_\omega = 2V_a.V_{dc} \quad (6.12)$$

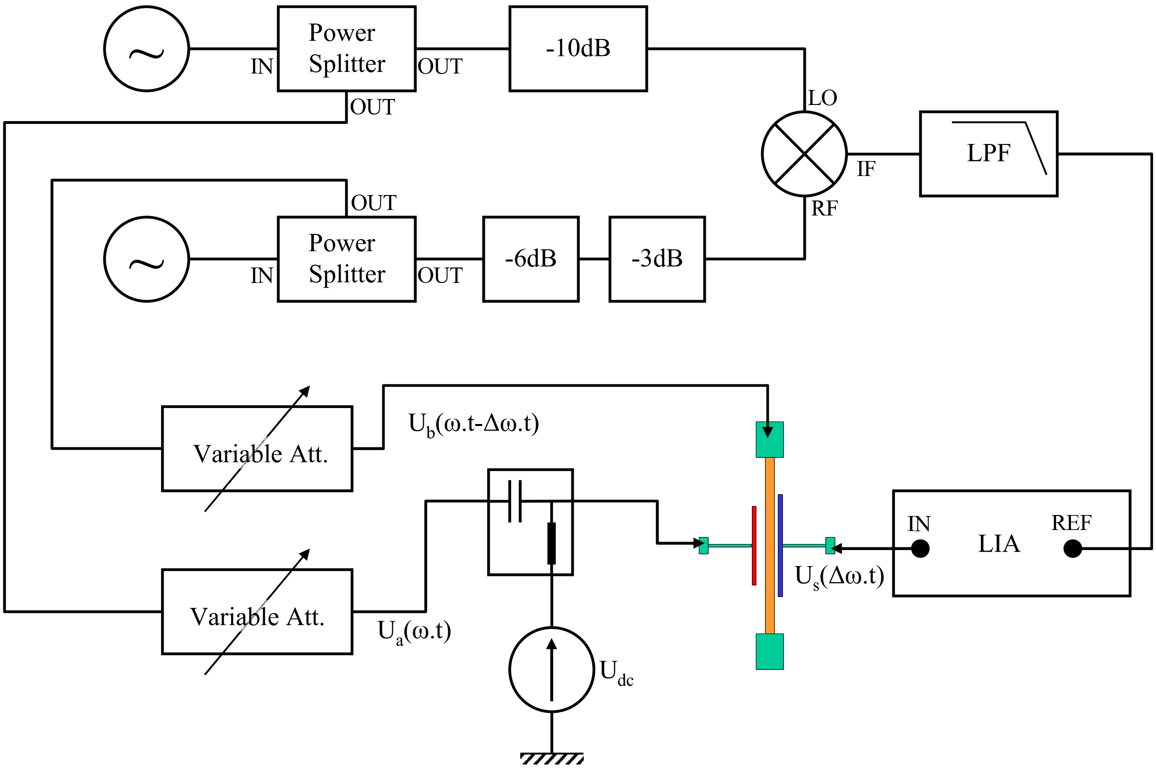

Figure 6.3: ω configuration of a capacitive downmixing technique.

6.2.2.2 2ω configuration

In this configuration, as shown in Figure 6.4:

$$U_a = V_a\cos(\frac{\omega}{2}t) \quad (6.13)$$
$$U_b = V_b\cos(\omega t - \Delta\omega t) \quad (6.14)$$

Hence:

$$(U_a - U_b)^2 = \frac{1}{2}V_a^2\cos(\omega t) + \frac{1}{2}V_a^2 + \frac{1}{2}V_b^2 - V_a.V_b\cos(\frac{\omega}{2}t - \Delta\omega t)$$
$$-V_a.V_b\cos(\frac{3\omega}{2}t - \Delta\omega t) + \frac{1}{2}V_b^2\cos(2\omega t - 2\delta\omega t) \quad (6.15)$$

The first term on the right hand side of Equation (6.15) is the excitatory harmonic. Then:

$$||(U_a - U_b)^2||_\omega = \frac{1}{2}V_a^2 \tag{6.16}$$

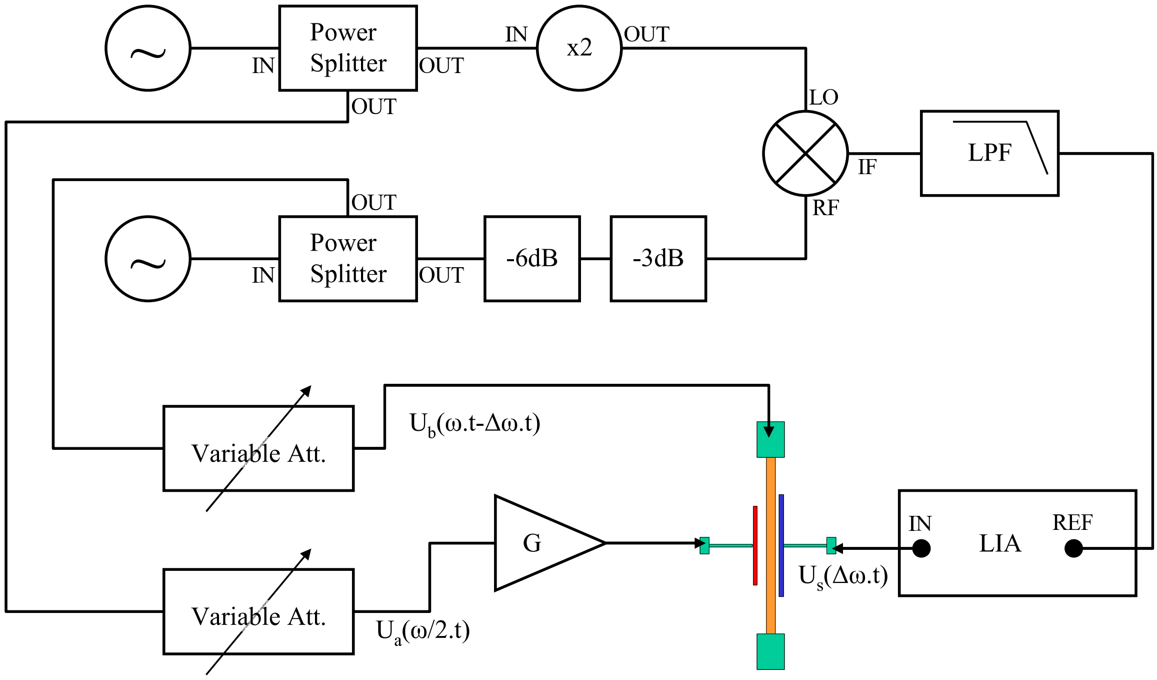

Figure 6.4: 2ω configuration of a capacitive downmixing technique.

6.2.2.3 $V_a.V_b$ configuration

In this configuration, as shown in Figure 6.5:

$$U_a = V_a \cos(2\omega t - \Delta\omega t) \tag{6.17}$$

$$U_b = V_b \cos(\omega t - \Delta\omega t) \tag{6.18}$$

Hence:

$$\begin{aligned}(U_a - U_b)^2 = &-V_a.V_b\cos(\omega t) + \frac{1}{2}V_a^2 + \frac{1}{2}V_b^2 - V_a.V_b\cos(3\omega t - 2\Delta\omega t)\\ &+\frac{1}{2}V_a^2\cos(\frac{4\omega}{2}t - 2\Delta\omega t) + \frac{1}{2}V_b^2\cos(2\omega t - 2\delta\omega t)\end{aligned} \tag{6.19}$$

The first term on the right hand side of Equation (6.19) is the excitatory harmonic. Then:

$$||(U_a - U_b)^2||_\omega = V_a.V_b \tag{6.20}$$

After some experimental investigations, the last configuration ($V_a.V_b$) has been chosen for the electrical characterization of the high frequency MEMS and NEMS resonators. Compared to ω and 2ω configurations, the last capacitive downmixing configuration gives the highest background to signal ratio (SBR) (low V_a and high V_b) while it keeps a low noise level ($20 - 30nV$).

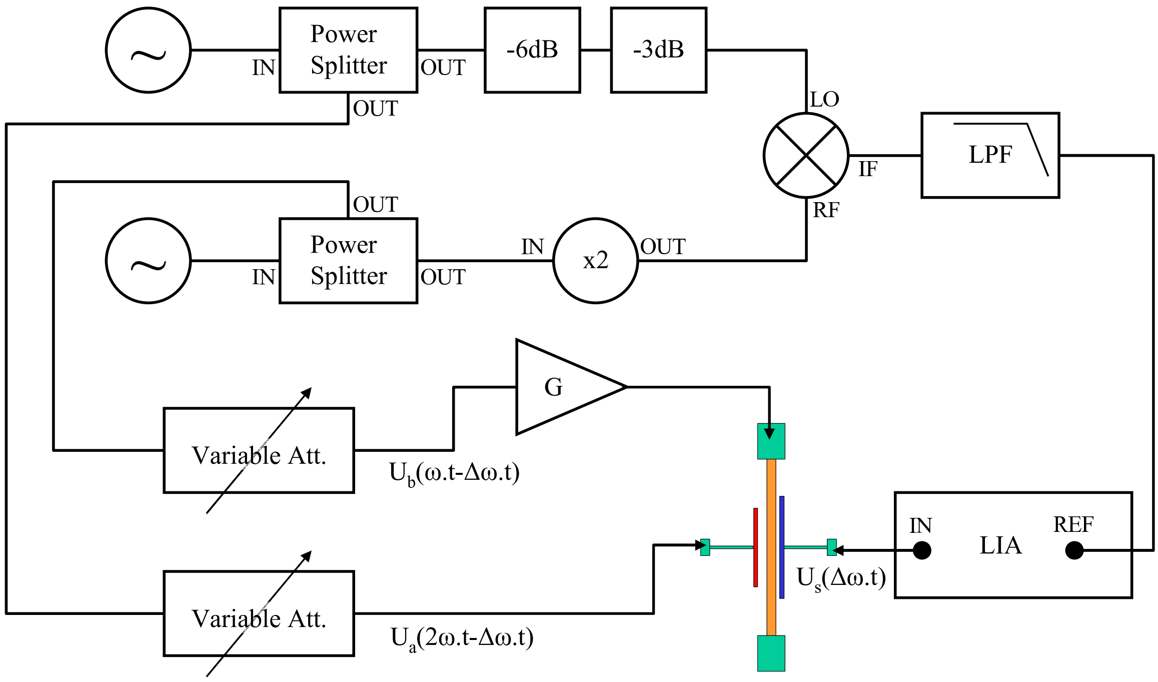

Figure 6.5: $V_a.V_b$ configuration of a capacitive downmixing technique.

6.2.3 Nonlinear down-mixing model

Following section 4.5, the transverse deflection of the resonator $\tilde{w}(x,t)$ is governed by the nonlinear Euler-Bernoulli equation.

$$EI\frac{\partial^4 \tilde{w}(\tilde{x},\tilde{t})}{\partial \tilde{x}^4} + \rho bh \frac{\partial^2 \tilde{w}(\tilde{x},\tilde{t})}{\partial \tilde{t}^2} + \tilde{c}\frac{\partial \tilde{w}(\tilde{x},\tilde{t})}{\partial \tilde{t}} - \left[\tilde{N} + \frac{Ebh}{2l}\int_0^l \left[\frac{\partial \tilde{w}(\tilde{x},\tilde{t})}{\partial \tilde{x}}\right]^2 d\tilde{x}\right]\frac{\partial^2 \tilde{w}(\tilde{x},\tilde{t})}{\partial \tilde{x}^2}$$
$$= \frac{1}{2}\varepsilon_0 \frac{bC_{n1}\left[V_a \cos(2\tilde{\omega}\tilde{t} - \tilde{\Delta\omega}\tilde{t}) - V_b\cos(\tilde{\omega}\tilde{t} - \tilde{\Delta\omega}\tilde{t})\right]^2}{(g_a - \tilde{w}(\tilde{x},\tilde{t}))^2} H_1(\tilde{x})$$
$$-\frac{1}{2}\varepsilon_0 \frac{bC_{n2}V_b^2\cos(\tilde{\omega}\tilde{t} - \tilde{\Delta\omega}\tilde{t})^2}{(g_d + \tilde{w}(\tilde{x},\tilde{t}))^2} H_2(\tilde{x}) \tag{6.21}$$

$$H_1(\tilde{x}) = H(\tilde{x} - \frac{l+l_a}{2}) - H(\tilde{x} - \frac{l-l_a}{2}) \tag{6.22}$$

$$H_2(\tilde{x}) = H(\tilde{x} - \frac{l+l_d}{2}) - H(\tilde{x} - \frac{l-l_d}{2}) \tag{6.23}$$

The nonlinear partial differential equation is then solved in the same way as section 4.5 using the Galerkin method coupled with a perturbation technique. Then, the steady-state motion equations are used in order to write the frequency response around the primary resonance in its parametric form in function of the phase φ.

6.3 Experimental validation

6.3.1 High capabilities set-up

Figure 6.6 shows two linear resonance peaks obtained by down-mixing ($V_a.V_b$ configuration) for the smallest NEMS resonator RN_4 (see Figure 6.7) at an actuation voltage of $50mv$. The experimental resonance frequency is around $13.5MHz$.

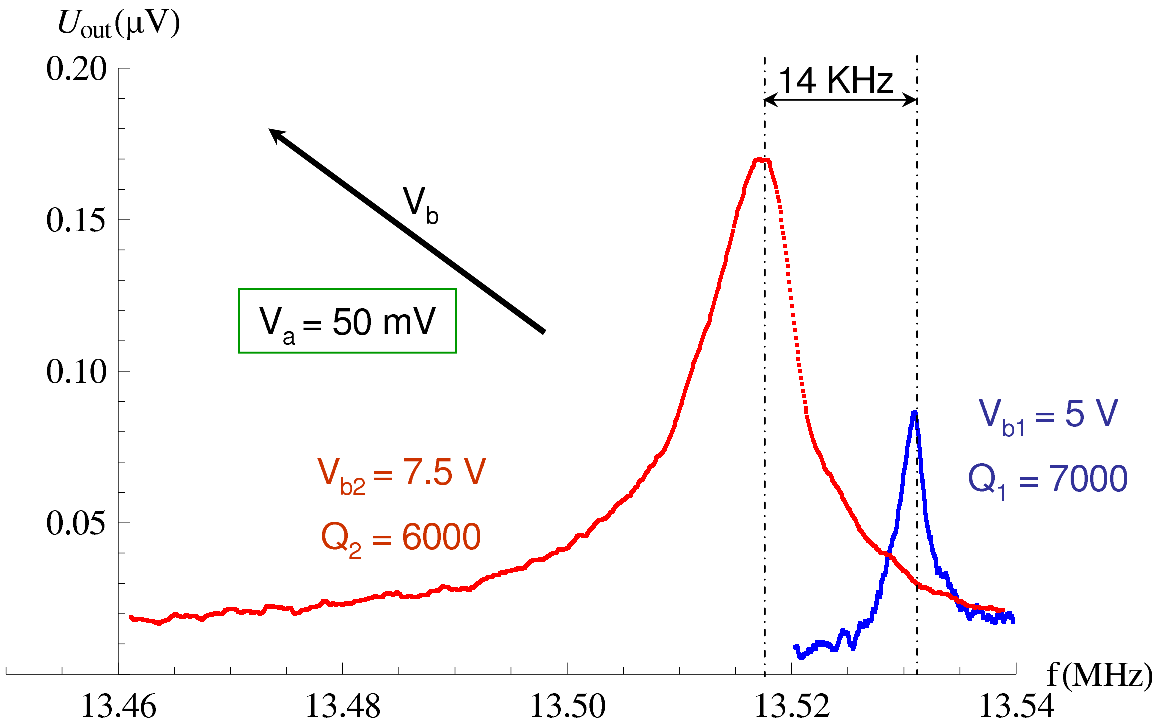

Figure 6.6: Measured linear resonance peaks of resonator RN_4 using the $V_a.V_b$ capacitive down-mixing technique.

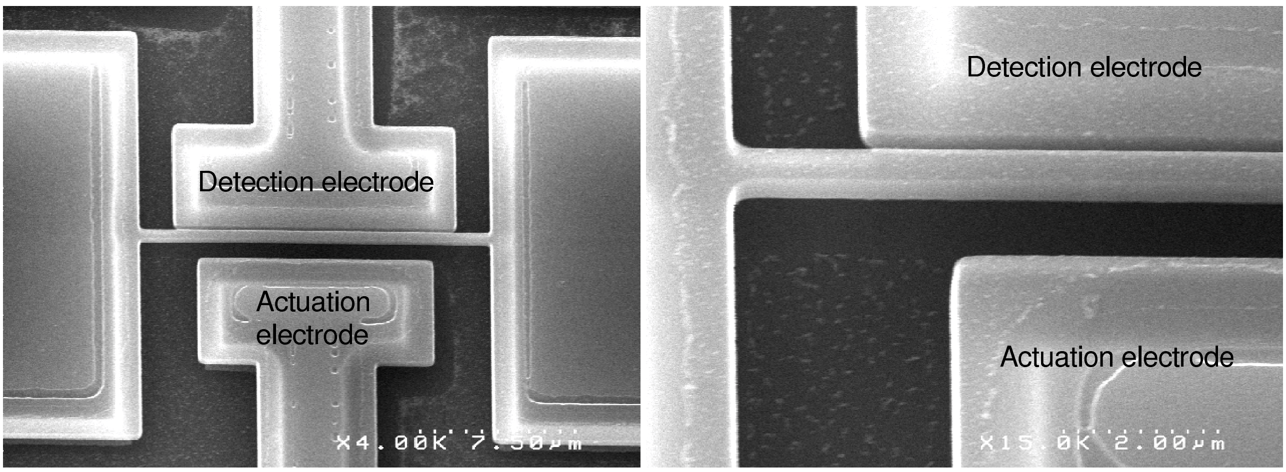

Figure 6.7: SEM images of the resonator RN4.

This negative frequency shift with respect to the theoretical frequency ($15.6MHz$) is due to the compression residual stress combined with the fabrication defects and the variation of the Young modulus for silicon nanostructure. Moreover, the computed fringing field coefficients for this resonator design are $C_{n1} = 4.5$ and $C_{n2} = 2.1$. Remarkably, The experimental setup enables the detection of very low capacitance variations ($C_{0a} = 40aF$ and $C_{0d} = 210aF$) as demonstrated by the right blue curve where the output voltage is below $100nV$ for a bias voltage $V_b = 5V$ and the measured quality factor is around 7.10^3. When the bias voltage is increased from $5V$ to $7.5V$, the frequency is shifted by $14KHz$ due to the negative electrostatic stiffness proportional to V_b^2 (for $V_a << V_b$). The dynamic bending deflection of the beam $w(x,t)$ is proportional to V_b, V_a as well as the quality factor. Moreover, the output voltage V_{out} is proportional to V_b and $w(x,t)$. Therefore, for a given drive voltage, the output voltage is proportional to the product $Q.V_b^2$. Obviously, for a bias voltage of $7.5V$, the ohmic losses significantly increase and consequently, the quality factor decreases from to 7.10^3 to 6.10^3. The ratio between the two peaks amplitudes is around 1.9 which is approximately equal to $\frac{Q_2.V_{b2}^2}{Q_1.V_{b1}^2}$. It shows the accuracy of the model concerning the proportionality of the output voltage to the product $Q.V_b^2$.

6.3.2 First validation (design for hardening behavior)

Figure 6.8 shows two nonlinear hardening resonance peaks for the NEMS resonator RN_4 at an actuation voltage of $100mv$. The right curve (in blue) is close to the critical amplitude A_c, even if the output voltage is about $200nV$ which is close to the amplitude of the left linear peak (in red) of Figure 6.6. Actually, since the dynamic bending deflection of the beam $w(x,t)$ is proportional to, V_a and

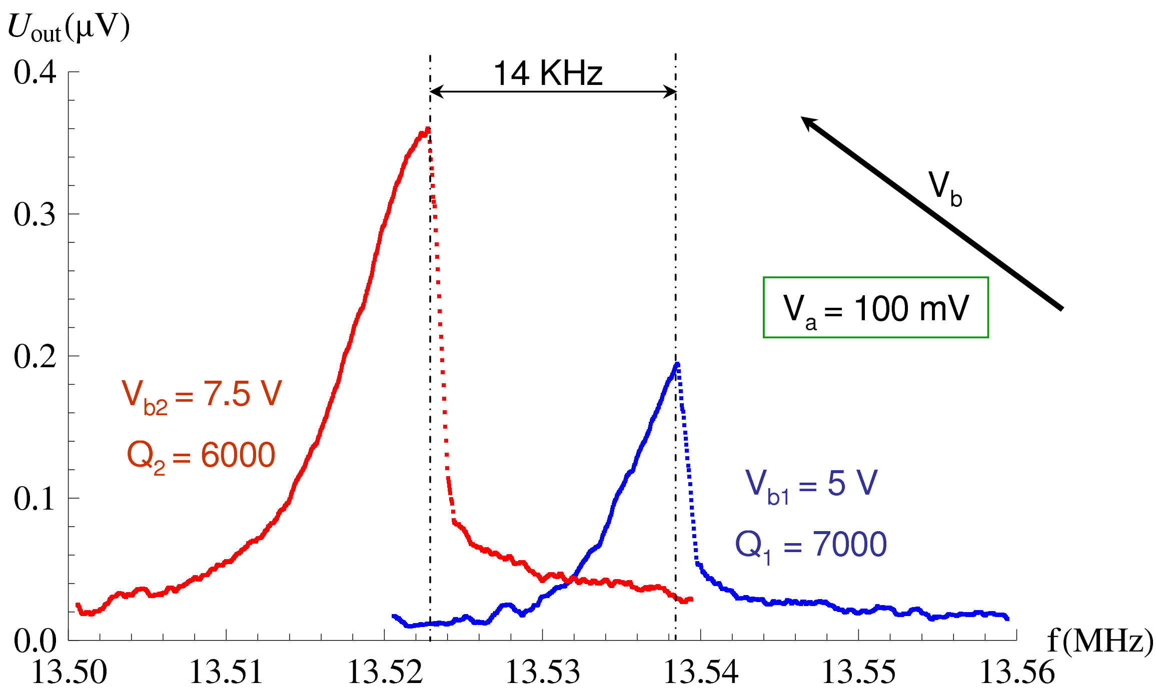

Figure 6.8: Measured hardening resonance peaks of resonator RN_4 using the $V_a.V_b$ capacitive down-mixing technique.

the quality factor, the increase of the drive voltage (for a given bias voltage), amplify proportionally purely mechanically the output voltage V_{out}. However, for a given drive voltage, the increase of the bias voltage amplify mechanically and electrically the output signal. Hence, in order to maximise the output voltage while keeping a linear behavior, the use of very high bias voltage with respect to the drive voltage is recommended. The analytical critical amplitude for RN_4 is around $10nm$ which corresponds approximately to the oscillation amplitude of the beam in the right curve of Figure 6.8. Consequently, the resonator oscillation is below $5nm$ for the measured blue peak of Figure 6.6 which confirms the high sensitivity of the experimental setup for the capacitive detection of few nanometres of motion. As predicted using the nonlinear down-mixing model, the red curve of Figure 6.8 displays a hardening behavior beyond the critical mechanical amplitude of the resonator for a bias voltage of $7.5V$. The frequency shift of $14KHz$ due to the negative stiffness is maintained like in the linear case.

6.3.3 Design for nonlinearities compensation

6.3.3.1 Softening behavior

The MEMS resonator RM_2 (see Figure 6.9) has been designed with a high ratio $\frac{h}{g_d}$ (> 16) which should enable the compensation of the mechanical and the electrostatic nonlinearities. The theoretical resonance frequency of RM_2 is around $1.09MHz$ which is below the cutoff frequency of the available lock-in amplifier. Figure 6.10 presents two nonlinear softening resonance peaks obtained by direct

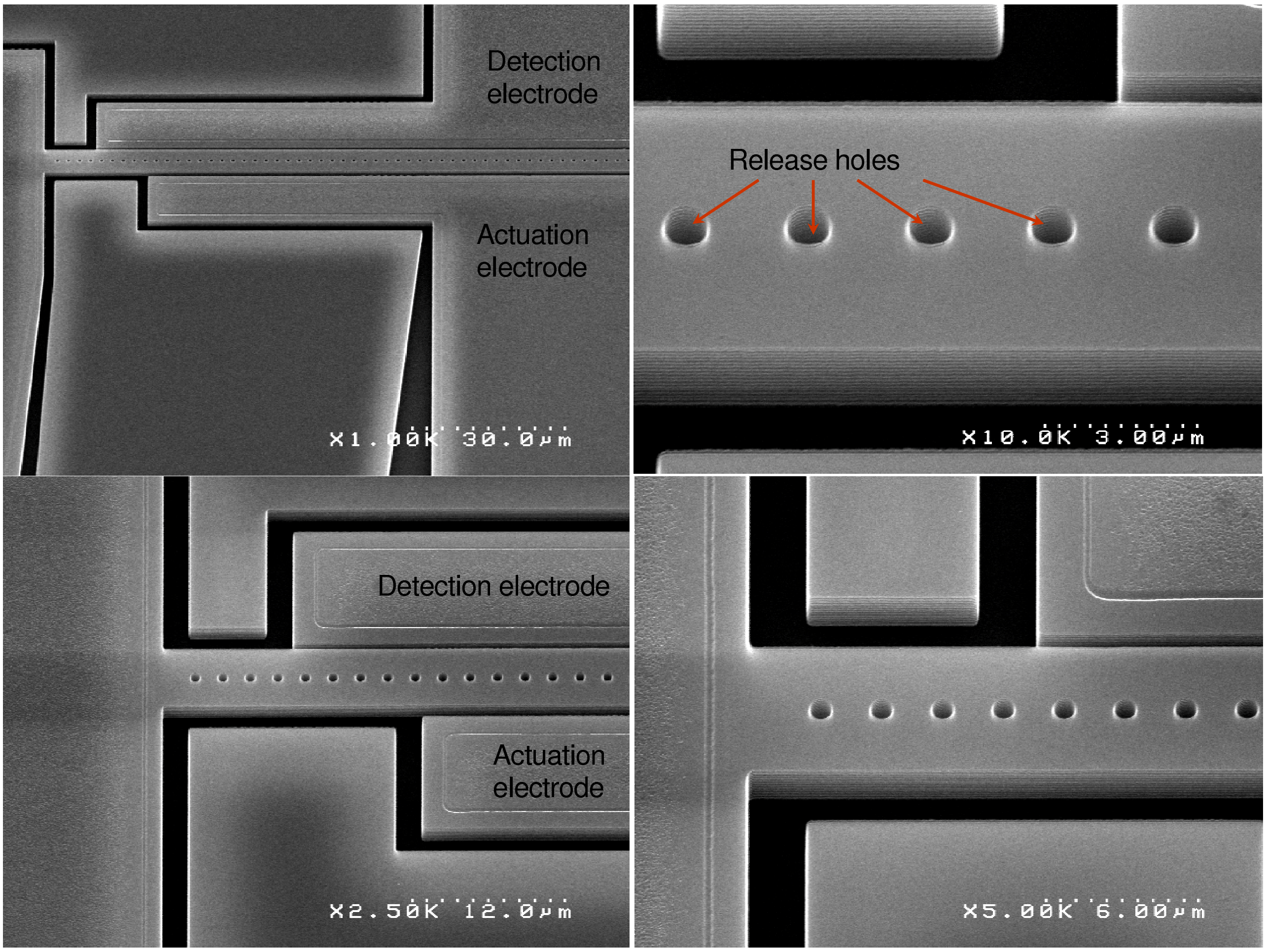

Figure 6.9: SEM images of the resonator RM2.

electric measurements performed using the 2ω mode of a lock-in amplifier. Obviously, the mechanical nonlinearities are very low due to the resonator geometry (high width in the direction of vibration) combined with a low quality factor (between 2000 and 3200). Moreover, the use of high DC voltages increases significantly the electrostatic nonlinear cubic stiffness with respect to the hardening Duffing nonlinearities. Thus, in this configuration the resonator dynamics is dominated by the softening nonlinearities which are not frequently observed in clamped-clamped resonators electrostatically actuated. First, a sweep up frequency is used in order to catch the first bifurcation point. The second bifurcation

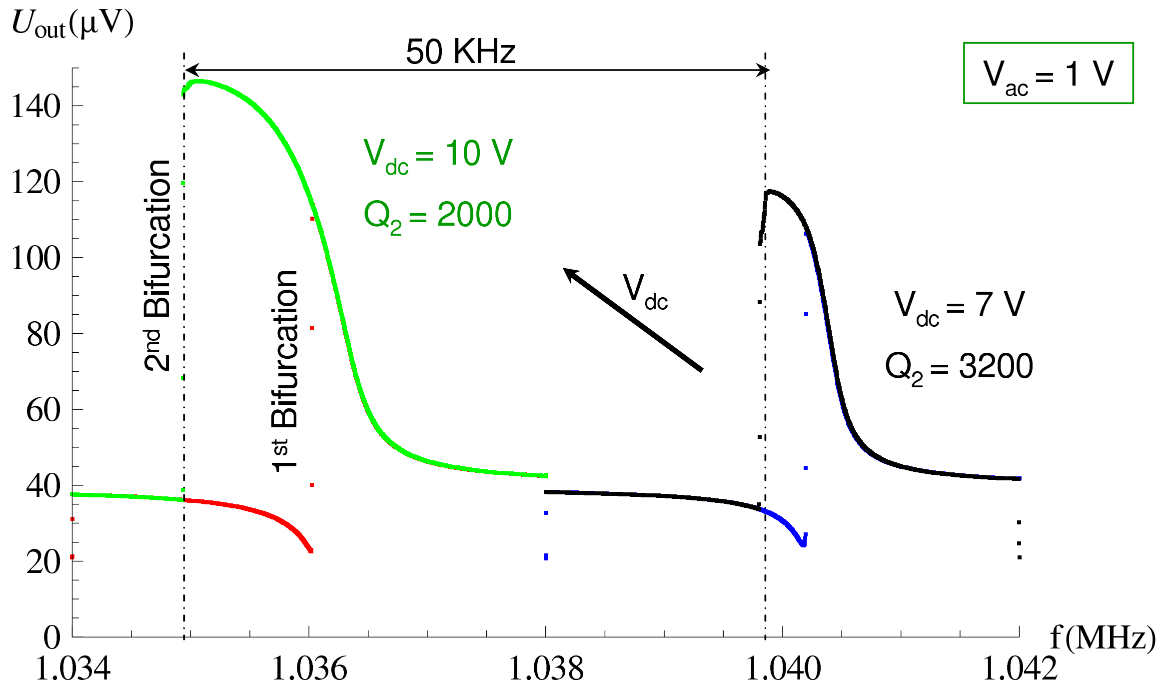

Figure 6.10: Measured softening resonance peaks of resonator RM_2 using 2ω direct characterization.

point in the softening domain is situated by a sweep down frequency. As shown in Figure 6.10, since the negative nonlinear stiffness is proportional to the square of V_{dc} (for $V_{dc} >> V_{ac}$), the second peak (left curve) obtained at a DC voltage of $10V$ is strongly nonlinear with respect to the first one (right curve) obtained at a DC voltage of $7V$. The frequency shift between both curves due to the negative stiffness is about $50KHz$. The critical behavior in this configuration can be computed using Equation (5.10) and it is around $100nm$.

6.3.3.2 Hardening behavior

The resonator RM_2 has also been electrically characterized using a lock-in amplifier in ω mode. We already showed in Figure 6.10, that the design RM_2 could display a softening behavior. Now, as shown in Figure 6.11, a hardening behavior is also possible when the mechanical nonlinearities are much higher than the electrostatic nonlinearities. For a DC voltage of $1V$, the nonlinear negative Duffing nonlinearity is very low. Combined with low ohmic losses, this implies a quality factor much higher than the previous softening resonance curves of Figure 6.10 ($Q \approx 10^4$). Hence, in this configuration, the mechanical critical amplitude is smaller than the electrostatic one ($A_c \approx 80nm$). The hardening peak of Figure 6.11 has been obtained in sweep up and down frequency which displays a critical behavior at an output voltage of $7\mu V$.

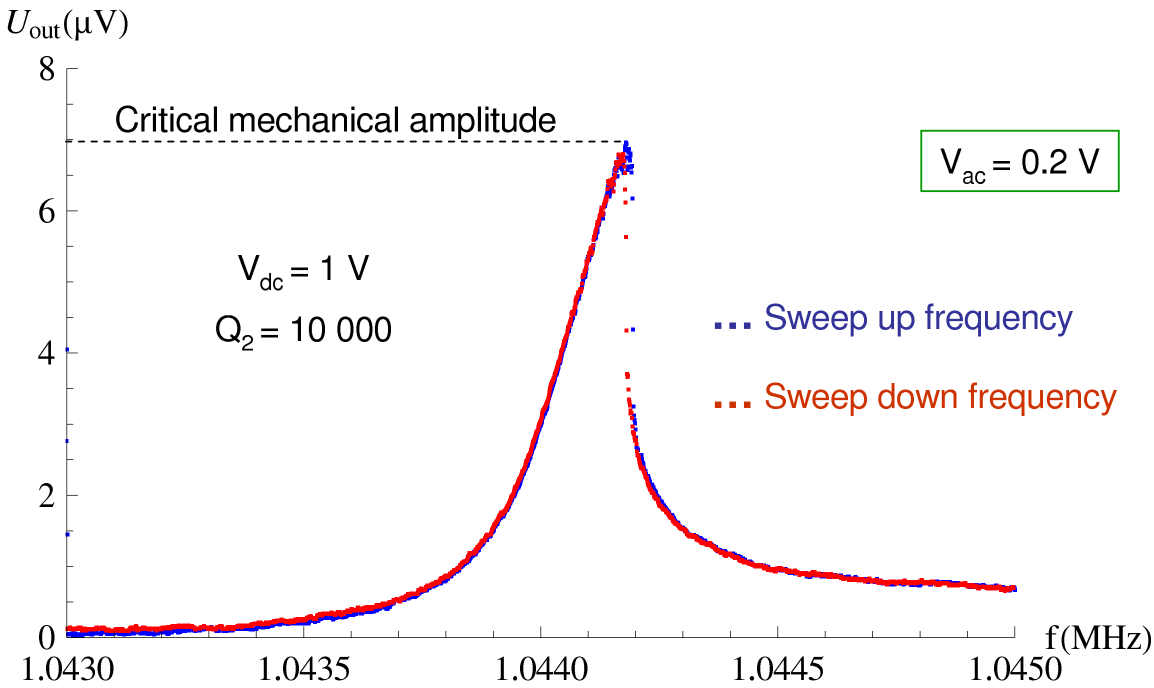

Figure 6.11: Measured critical hardening resonance peak of resonator RM_2 using ω direct characterization.

6.3.3.3 Hysteresis suppression ability

On the same device, both nonlinear dynamics (hardening and softening) have been demonstrated. Consequently, the resonator RM_2 can potentially display a linear compensated behavior when both electrostatic and mechanical nonlinearities are balanced.

In order to approach this operating point (hysteresis suppression) and starting from the previous hardening behavior, the DC voltage has been increased to $3V$ and $5V$ as shown in Figure 6.12 where the resonance curves of RM_2 have been performed in sweep up and down frequency. The first peak measured at $V_{dc} = 3V$ displays a quality factor $Q = 6000$ which has been measured on a linear curve at a low AC voltage and the same DC voltage. The resonance curve, in this case, is strangely nonlinear (hardening behavior). The third bifurcation is the highest one in the hardening domain obtained in sweep up frequency where the red curve displays two regimes: a first fast in amplitude variation and a second slow with a slope approaching zero. The first bifurcation is obtained in sweep down frequency (green curve) and intercepts the red curve in a small part of the slow regime and the entire fast regime of amplitude variation. The strange nonlinear hardening behavior obtained experimentally can be explained by a strong dynamic perturbation due to the increase of the softening nonlinearities (increase in the DC voltage and decrease of the quality factor Q).

6.3.3.4 Sensitivity of the compensation to the mixed behavior

In Figure 6.12 (on the left), the resonance curve measured at $V_{dc} = 5V$ displays a quality factor $Q = 4000$. Using the analytical model of a 2 ports nonlinear resonator (see section 4.5), for these parameters, the resonator should display a linear resonance peak obtained by the compensation of the mechanical and the electrostatic nonlinearities. Unlike the mixed behavior (hardening-softening) discussed in section 5.4, the experimental peak of Figure 6.12 measured at $V_{dc} = 5V$ displays clearly

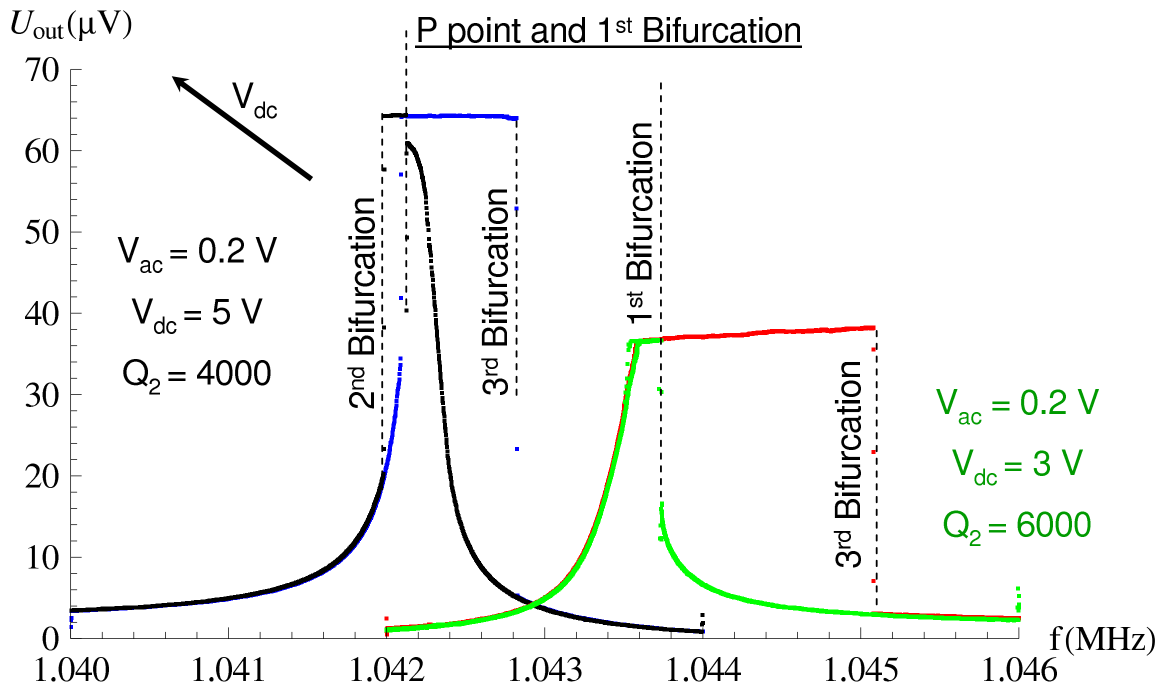

Figure 6.12: Measured strange hardening and mixed resonance peaks of resonator RM_2 using ω direct characterization. P is the mixed behavior initiation point and the third bifurcation is the highest bifurcation in the hardening domain.

a mixed behavior starting by a softening behavior and ending by a hardening one where the peak amplitude is around three times the critical amplitude displayed in Figure 6.11. Particularly, in this mixed behavior, the P point and the first bifurcation have the same frequency and the hardening domain is reduced in comparison with the first resonance curve of Figure 6.12.

Actually, for the resonator RM_2, the fifth order nonlinear terms are no more negligible when it is used to operate close to the hysteresis suppression point. Indeed, the compensation of the nonlinearities is sensitive to the highly unstable mixed behavior.

6.3.3.5 Mixed behavior retarding by simultaneous resonance

In order to retard the onset of the mixed behavior, the resonator RM_2 has been actuated at its primary and secondary resonances simultaneously (see section 5.6). In practice, the use of the 2ω mode of a lock-in amplifier leads to an actuation under superharmonic resonance of order half the fundamental frequency combined with the primary resonance. The resonator is polarized with a DC voltage of $3V$, combined with an AC voltage of $1V$, this should ensure a compensated linear behavior predicted using the analytical model described in section 5.6. Figure 6.13 shows a linear peak obtained by nonlinearity cancellation for $V_{dc} = 3V$, $V_{ac} = 1V$ and $Q = 6000$. No bistability has been detected which is confirmed by the superposition of the frequency curves obtained in sweep up and down frequency. The ratio between the critical amplitude and the peak amplitude is around 5.7 which corresponds to the resolution enhancement rate of the resonant accelerometer.

Remarkably, the compensated linear resonance curve of Figure 6.13 has the particularity to display a clipped peak at a relatively high amplitude with respect to the detection gap (around 250 nm). The peak clipping can be explained by a possible slight variation of the quality factor with respect to the

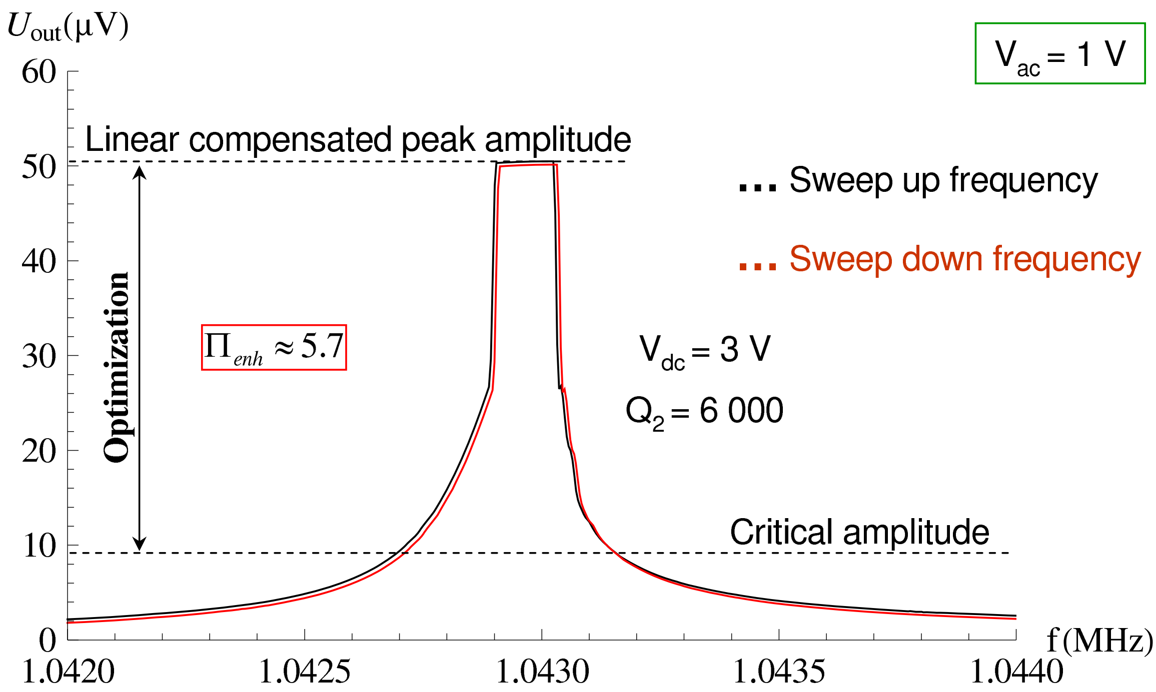

Figure 6.13: Measured linear compensated resonance peak of resonator RM_2 using 2ω direct characterization.

frequency at large amplitudes.

6.3.4 Strange attraction and transition to the softening behavior

Here, the ω mode of a lock-in amplifier is used again for a purely primary resonance excitation. Once the mixed behavior was reached, we continue the increase of the DC voltage in order to track the transition from a mixed to a softening behavior. The first curve of Figure 6.14 has been measured using a lock-in amplifier in ω mode at a DC voltage of $7.5V$ which decreases the quality factor due to the ohmic losses (Q=3000). The black part of the curve is obtained in sweep down frequency enabling the capture of the P point which is the initiation of the mixed behavior bifurcation point and then the second bifurcation point (the highest bifurcation point in the softening domain). Now, in sweep up frequency, the output voltage V_{out} follows the blue curve. When the frequency of the first bifurcation point is reached, the amplitude jumps strangely to the upper branch in the hardening domain instead of following the black curve (jump to the downer branch) which should be physically easier where the basins of attraction are quite larger. Indeed, a strange attractor brings the resonator oscillation to the upper branch of the hardening domain till the third bifurcation point (jump down) where the solution follows the black curve. Unlike the mixed hardening-softening behavior, where no strange attractor has been observed (see section 5.4), the mixed softening-hardening behavior could display a mechanical strange attraction which makes complicated the bifurcation control in such configurations. This is another reason behind the use of simultaneous resonances instead of primary resonance (retard the mixed behavior *i.e.* its strange attractions).

In order to suppress the mixed behavior, the effect of the hardening nonlinearities is reduced in the second peak of Figure 6.14 for $V_{dc} = 10V$ and an estimated quality factor $Q = 2000$. The electrostatic nonlinearities are amplified with respect to the mechanical nonlinearities which brings

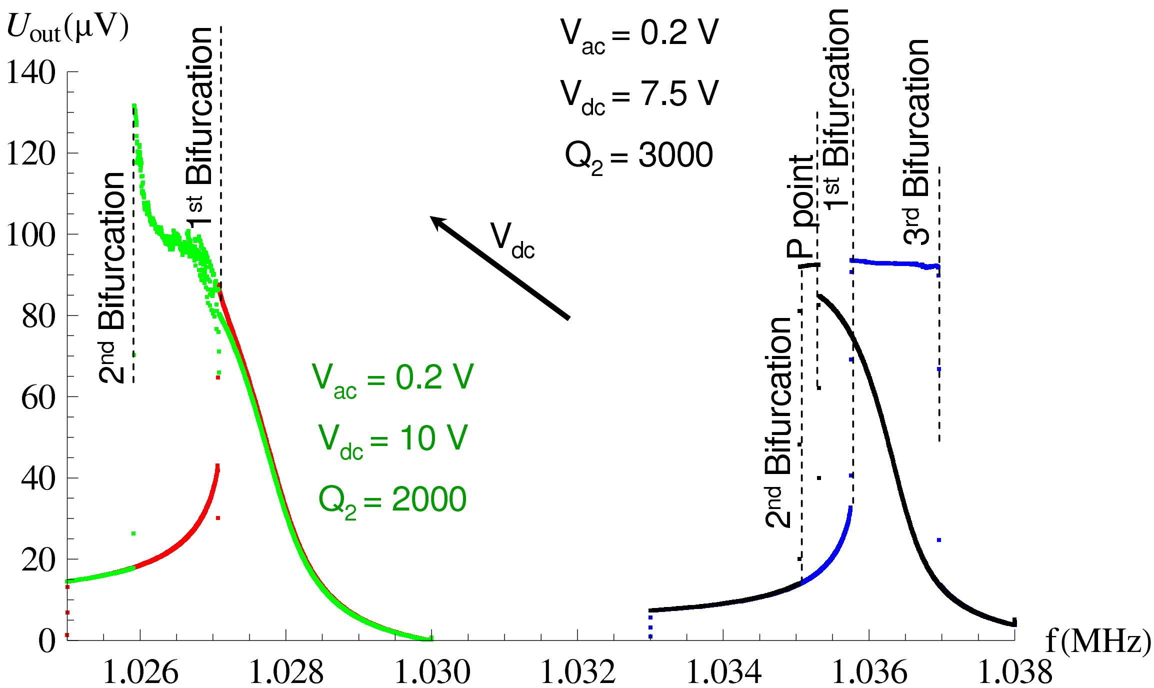

Figure 6.14: Measured mixed and softening resonance peaks of resonator RM_2 using ω direct characterization. The mixed behavior displays a strange mechanical attraction.

the third bifurcation point at the same frequency as the first bifurcation point.

6.4 Summary

In this chapter, high frequency M&NEMS resonators have been designed, fabricated and electrically characterized using a very sensitive capacitive down-mixing set-up allowing the detection of resonator motions below $5nm$. All dynamic behaviors captured by the model have been found experimentally (hardening, softening, mixed and linear compensated). A strange mechanical attraction has been also demonstrated in a mixed softening-hardening behavior. The sensitivity of the compensation to the mixed behavior has been presented. Finally, a superharmonic resonance superposed to the primary one permitted to obtain a linear compensated resonance peak by retarding the mixed behavior which can enhance the resonant accelerometer resolution by a factor 5.7. Thus, the main design rules presented in chapter 5 have been experimentally validated.

Finally, concerning future work, a principal step consists on the confirmation of the detection limit enhancement by measuring Allan variance in open-loop as well as in closed loop for linear, nonlinear and compensated behaviors.

Part III

Extension to other resonant sensors: gyroscopes and mass/gas sensors

Chapter 7

Resonant gyroscope

Contents

7.1 Introduction **156**

7.2 The Resonant Gyroscope **157**

7.3 Device Analysis **158**

7.3.1 Actuation part 160

7.3.2 Lever mechanism 161

7.3.3 Sensing part 163

7.4 Model **163**

7.4.1 Normalization 165

7.4.2 Solving 165

7.5 Analytical results and device specifications **167**

7.5.1 Proof mass frequency effect 167

7.5.2 Resonant gyroscope scale factor 170

7.5.3 Resonant gyroscope resolution 172

7.5.4 Scale factor sensitivity to environmental variables 174

7.5.5 Quadrature error 174

7.5.6 Bias stability 174

7.5.7 Common mode acceleration 174

7.5.8 Decoupled resonant gyroscope 175

7.6 Electronics and Signal Processing **176**

7.7 Designs **177**

7.8 Fabrication **180**

7.9 Experimental validation **180**

7.9.1 Low axial load frequency 180

7.9.2 High axial load frequency 183

7.10 Summary **185**

7.1 Introduction

Gyroscopes are expected to become the next "killer" application for the MEMS industry in the coming years. A multitude of applications already have been developed for consumer and automotive markets. Some of the more well known automotive applications such as vehicle stability control, navigation assist, roll over detection are only used in high-end cars, where cost is not a major factor. Examples of consumer applications are 3D input devices, robotics, platform stability, camcorder stabilization, virtual reality, and more. Primarily due to cost and the size most of these applications have not reached any significant volume. MEMS gyroscope industry plans a high growth potential of the defense and low end automotive applications. The MEMS gyroscope market is expected to generate in the range of 800M\$ value in 2010. The operation principle of the vast majority of all existing micromachined vibratory gyroscopes relies on the generation of a sinusoidal Coriolis force due to the combination of vibration of a proof-mass and an orthogonal angular-rate input. The proof mass is generally suspended above the substrate by a suspension system consisting of flexible beams. The overall dynamical system is typically a two degrees-of-freedom (2-DOF) mass-spring-damper system, where the rotation-induced Coriolis force causes energy transfer to the sense-mode proportional to the angular rate input. In most of the reported micromachined vibratory rate gyroscopes, the proof mass is driven into resonance in the drive direction by an external sinusoidal electrostatic or electromagnetic force. As shown in Figure 7.1, when the gyroscope is subjected to an angular rotation, a sinusoidal Coriolis force is induced in the direction orthogonal to the drive-mode oscillation at the driving frequency.

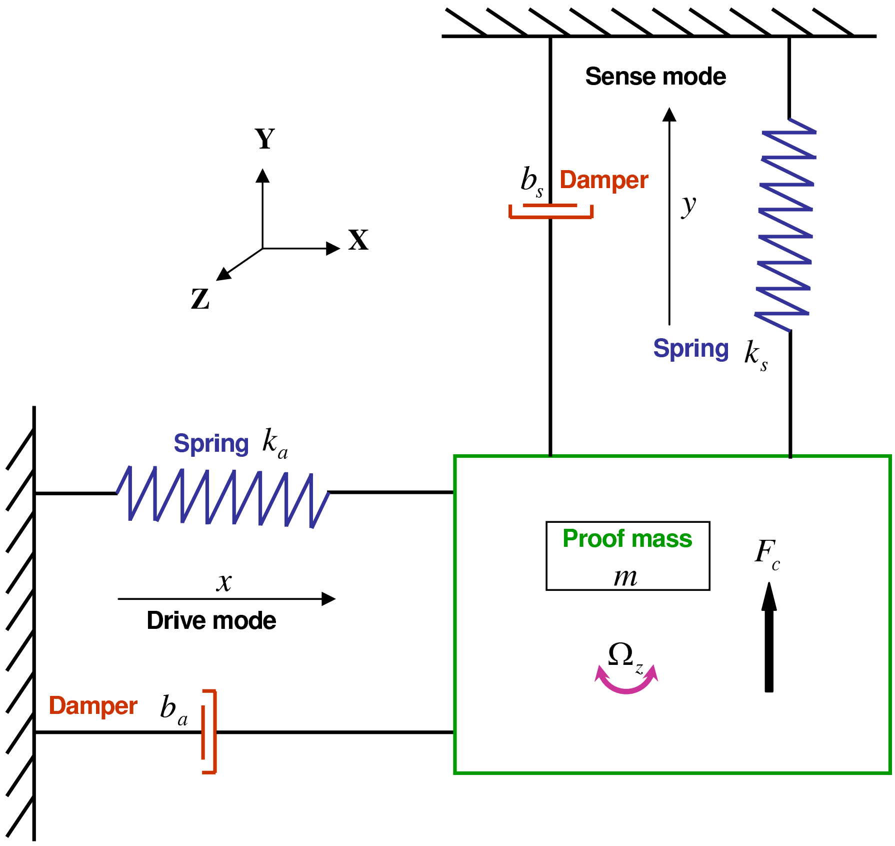

Figure 7.1: Lumped parameter model of a vibratory gyroscope.

To achieve high sensitivity in conventional micro rate gyroscopes based on harmonic oscillators, the drive and the sense resonant frequencies are typically designed and tuned to match, and the device is controlled to operate at or near the peak of the response curve (where amplitude is defined by the Q-factor) [Clark 1997]. However, current micro fabrication processes produce asymmetries causing frequency mismatching between modes, translating to drastic loss of sensitivity [Yazdi 1998]. Although solutions to overcome frequency mismatching have been pursued [Park 2003, Shkel 1999], many of them involve adding complexity to the system by including additional controllers, additional degrees of freedom [Acar 2003] or utilizing multiple drive mode oscillators [Acar 2005]. Besides, the requirement for closed loop control is driven by several considerations:

- Identification and control of the magnitude and the phase of the displacement of the device along the drive and sense directions.
- Calibration of the device requires identification of system parameters such as the natural frequencies along drive and sense directions. In the case of a device operating under the condition of perfectly matched modes, the quality factor of the system in the sense mode must be identified as well.
- Actuator and sensor linearity and stability have to be maintained. This may be achieved by preventing the proof mass from displacing along the sense direction using force feedback.
- It is important to accurately measure the phase of the output relative to the drive, as mismatches in the phase could lead to significant driven motion being coupled to the output.
- Compensation of defects: Mismatches in suspension and proof mass dimensions, electrode gaps, asymmetries in fluidic damping can all result in significant variations in both scale factor and output offset, result in feedthrough of the driven motion onto the sense axis and might also result in instability of the system for the desired operating voltages.

The complexity of closed loop control is evident from the number of variables that need to be simultaneously controlled and identified to ensure device operation. In this case, we are dealing with multi-dimensional dynamics in a poorly identified environment. Hence the control scheme must not only compensate for defects and maintain the evolution of the proof mass motion but also identify system parameters and drive them to desired values. We can identify the control complexity in terms of a combination of the number of states that must be simultaneously identified and controlled and the parameters that need to be identified for system definition (see table 7.1).

In view of the complexity of the proposed control schemes [Park 2003, Shkel 1999], alternate approaches were considered that would minimize the requirement for control and at the same time allow for accurate measurement of the rotation rate. One proposed approach to achieve this goal is to use resonant sensing [Seshia 2002a] of the Coriolis force instead of displacement sensing, which has been employed in most conventional microgyroscopes. Profiting from the high sensitivity of the resonant detection, the matching of the drive and the sense frequencies is not mandatory to achieve a high resolution. Consequently, the number of states that have to be simultaneously controlled and the number of variables that require identification are much smaller and the dynamics is simplified from a minimally two-dimensional system to a series of coupled one-dimensional mass-spring-damper systems.

7.2 The Resonant Gyroscope

The resonant gyroscope, as its name implies, utilizes resonant sensing as the basis for Coriolis force detection. In its simplest form, the device consists of three resonating elements, a proof mass vibrating

Parameter (Identification/Control)	Requirement
Driven mode displacement (x)	❑ Control for constant scale factor and stability.
Sense mode displacement (y)	❑ Identification alone for open-loop sensing; Control allows for extension of bandwidth and overall system stability including constancy of scale factor.
Driven mode natural frequency (ω_x)	❑ Identification required for constancy of scale factor and calibration.
Sense mode natural frequency (ω_y)	❑ Identification required for constancy of scale factor and calibration.
Sense mode quality factor (Q_y)	❑ Identification required for operation under perfect or near mode-matched conditions for constancy of scale factor.

Table 7.1: Primary system parameters required to be simultaneously identified and controlled for a modematched gyroscope. In addition to the above, for defects and error compensation due to fabrication tolerances or other asymmetries, additional variables will require to be identified as described in [Shkel 1999].

in the tens of kilohertz and two resonating sense elements, with a designed resonant frequency, generally, an order of magnitude higher than that of the proof mass in order to avoid possible parametric instabilities in detection.

Although the principle is general enough to accommodate devices that sense rotation rate about in-plane axes with minor modifications (such as driving the proof mass perpendicular to the substrate), the focus of this chapter concerns gyroscopes that sense rotation rate about a single axis orthogonal to the plane of the device substrate. In addition, gyroscope topologies for a dual-mass to cancel common-mode acceleration signals and gyroscope suspensions to reduce quadrature error carry over for a resonant gyroscope. A schematic of the z-axis resonant gyroscope is shown in Figure 7.2.

The device consists of a proof mass suspended by flexures attached to lever mechanisms [Roessig 1998] for Coriolis force amplification. The proof mass is driven about the Y axis using embedded lateral comb drive actuators. Specialized combs can be employed for self-test and for quadrature error cancellation [Clark 1996]. If an external rotation is applied to the chip about the z-axis, the Coriolis forces acting on the proof mass is transmitted to the lever mechanisms that amplify these forces prior to its being communicated axially onto two resonators placed on either side of the proof mass for a differential output. The two resonators vibrate anti-phase to each other and parallel to the direction of motion of the proof mass. The periodic compression and tension of the resonators by the Coriolis force at the proof mass drive frequency modulates the resonant frequency of these force sensors. Each force sensor comprises mechanical resonator electrostatically actuated and embedded in the feedback loop of an oscillator circuit. Thus, by demodulating the oscillation frequency, the rotation rate applied to the device can be estimated.

7.3 Device Analysis

The dynamics of the device (Figure 7.2) can be described by a series of coupled differential equations. The proof mass dynamics can be described for most part by a classical spring-mass-damper equation.

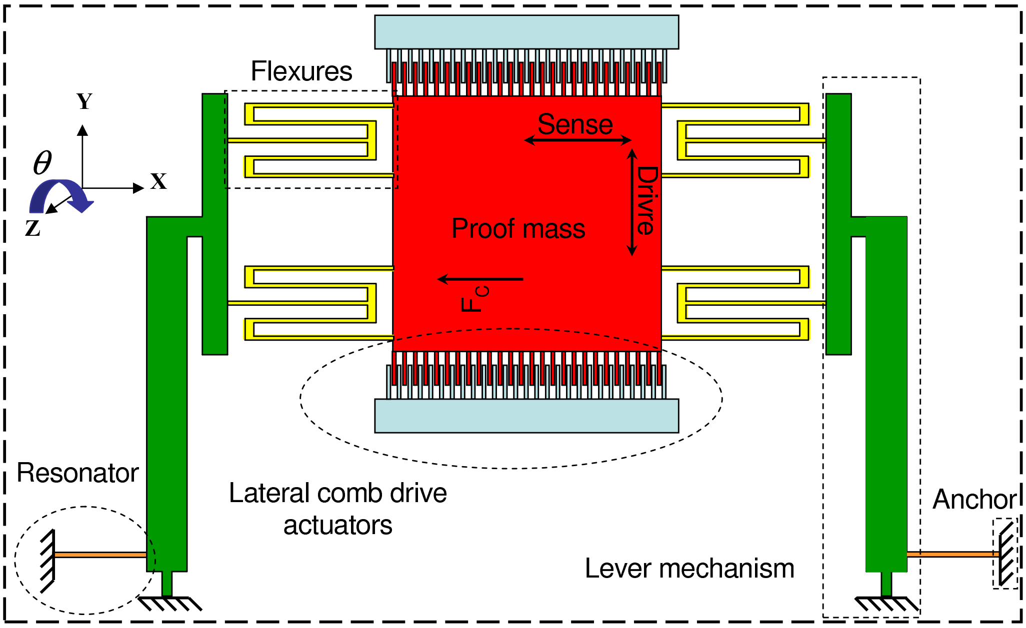

Figure 7.2: Schema of a simple mass resonant gyroscope.

The dynamics of the resonator subjected to an axial time-varying Coriolis force is described by a nonlinear Mathieu partial differential equation. The respective equations can be written as:

$$\frac{d^2Y(\tilde{t})}{d\tilde{t}^2} + \frac{\tilde{\delta}}{Q}\frac{dY(\tilde{t})}{d\tilde{t}} + \tilde{\delta}^2 Y(\tilde{t}) = \frac{F_e}{M}\cos\tilde{\delta}\tilde{t} \tag{7.1}$$

$$EI\frac{\partial^4 \tilde{w}(\tilde{x},\tilde{t})}{\partial \tilde{x}^4} + \rho bh\frac{\partial^2 \tilde{w}(\tilde{x},\tilde{t})}{\partial \tilde{t}^2} + \tilde{c}\frac{\partial \tilde{w}(\tilde{x},\tilde{t})}{\partial \tilde{t}} - \frac{1}{2}\varepsilon_0\frac{bC_n\left[Vdc + Vac\cos(\tilde{\Omega}\tilde{t})\right]^2}{(g-\tilde{w}(\tilde{x},\tilde{t}))^2} = \left[\tilde{N} + A_l\tilde{F}_c\cos\tilde{\delta}\tilde{t} + \frac{Ebh}{2l}\int_0^l\left[\frac{\partial \tilde{w}(\tilde{x},\tilde{t})}{\partial \tilde{x}}\right]^2 d\tilde{x}\right]\frac{\partial^2 \tilde{w}(\tilde{x},\tilde{t})}{\partial \tilde{x}^2} \tag{7.2}$$

$$\tilde{F}_c = 2M\theta\frac{dY(\tilde{t})}{d\tilde{t}} \tag{7.3}$$

where $\tilde{x}$ is the position along the resonator length, E and I are the Young's modulus and moment of inertia of the cross section. $\tilde{N}$ is the applied tensile axial force due to the residual stress on the silicon, $\tilde{t}$ is time, ρ is the material density, h is the microbeam thickness, g is the capacitor gap width, and ε_0 is the dielectric constant of the gap medium. The last term on the left-hand side of Equation (7.2) represents an approximation of the electric force assuming a complete overlap of the area of the microbeam and the stationary electrode including the edge effects by the coefficient C_n [Nishiyama 1990].

Furthermore, $\tilde{Y}$ is the mass displacement along the vertical axis, M is the mass of the drive part of the resonant gyroscope, δ is its resonance frequency, Q the drive quality factor, F_e is the electrostatic force induced by the lateral comb drive actuators, A_l is the amplification coefficient of the Coriolis F_c force due to the lever mechanism. The perturbation term $A_l\tilde{F}_c\cos\tilde{\delta}\tilde{t}$, which represents a modulation of the spring constant of the resonant sensor at the gyroscope drive frequency $(\frac{\tilde{\delta}}{2\pi})$, is directly contributed by the amplified Coriolis force impinging axially on the resonator. Thus, the Coriolis force $(\tilde{F}_c)$ modulates the spring constant of the resonator system.

Clearly, the Equation (7.2) governing the resonator dynamics is similar to the equation of motion (4.8) in the case of the resonant accelerometer. The only difference is the time-varying term proportional to the Coriolis force that modulates the spring constant of the resonator. Obviously, for a very low actuation frequency $\tilde{\delta}$ with respect to the resonator natural frequency, the Coriolis force is quasi-static and then equations (7.2) and (4.8) become equivalent.

Note that the two resonators placed on each side of the structure experience an equal and opposite axial force. The output of the device is the resonant frequency shift difference ($\Delta f = \Delta f_1 - \Delta f_2$) between the two resonators, measured at the gyroscope proof mass drive frequency.

7.3.1 Actuation part

The details about the dimensions (proof mass+spring) are described in Figure 7.3.

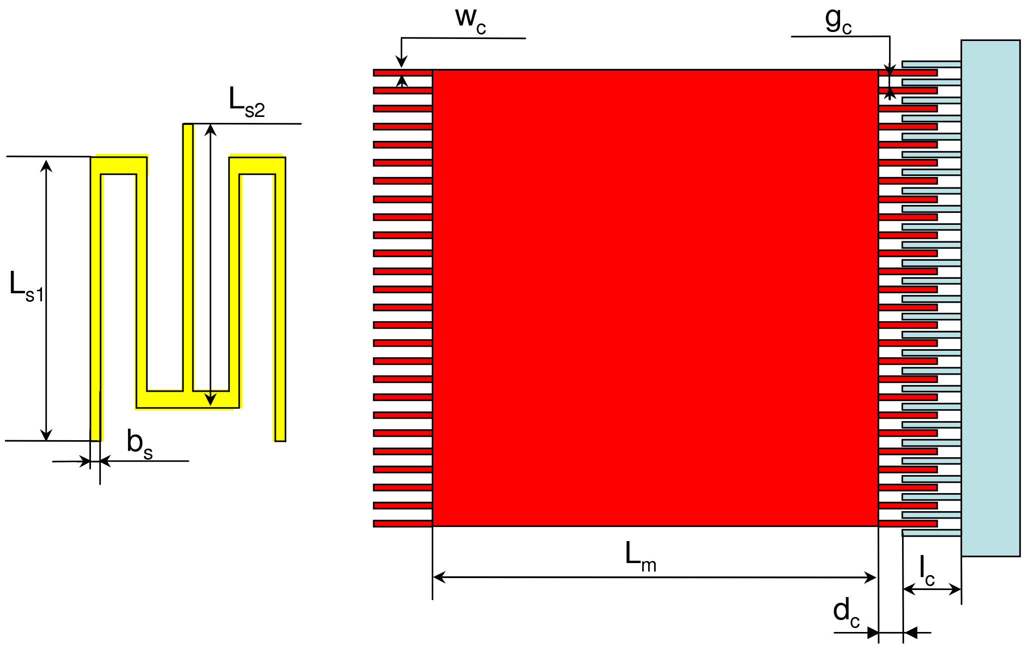

Figure 7.3: Proof mass and spring designs for a resonant gyroscope.

An equivalent mechanical model was used in order to compute analytically the stiffness K_m of the spring-mass-damper system as follow:

$$K_m = \frac{8 E e_M b_s}{3L_{s1} + L_{s2}} \tag{7.4}$$

where e_M is the MEMS level thickness (the resonator thickness could be smaller than the proof mass, springs and lever mechanisms thickness which is the case of a M&NEMS gyroscope). The natural frequency of the actuation system is then:

$$\tilde{\delta} = \sqrt{\frac{8 E b_s}{\rho L_m^2 \left(3L_{s1}^3 + L_{s2}^3\right)}} \tag{7.5}$$

The electrostatic force generated by the comb drive actuators is:

$$F_e = \frac{\partial U}{\partial g_c} = \left\lfloor \frac{2L_m + g_c - W_c}{g_c + W_c} \right\rfloor \frac{\varepsilon_0 e_M \left(V m_{dc} + V m_{ac} \cos \tilde{\delta} \tilde{t}\right)^2}{g_c} \tag{7.6}$$

where $\lfloor\rfloor$ denotes the floor function, U is the energy associated with the applied electric potential (a drive voltage Vm_{ac} and a polarization Vm_{dc}), W_c is the width of a finger, g_c is the gap between two fingers as shown in Figure 7.3.

The quality factor of the mass-spring-damper system being very high ($10^4 < Q_m < 10^6$), the static displacement is negligible with respect to the dynamic displacement and then the proof mass displacement at resonance can be computed as follows:

$$Y_M = \frac{Q_m F_e}{\rho\tilde{\delta}^2 L_m^2 e_M} = \left\lfloor \frac{2L_m + g_c - W_c}{g_c + W_c} \right\rfloor \frac{\varepsilon_0 Q_m V m_{dc} V m_{ac} \left(3L_{s1}^3 + L_{s2}^3\right)}{8Eg_c b_s^3} \tag{7.7}$$

As the proof mass is actuated using a lateral comb drive topology and is allowed to displace along the sense direction as well, then it becomes susceptible to a pull-in like phenomenon since the actuator topology looks more like a parallel-plate capacitor along the sense direction. As a result, motion along the sense direction due to non-idealities or asymmetries in the electromechanical structure place an upper limit on the actuation voltage and the displacement that can be allowed along the sense axis. As it depends on the resonator stiffness along the X axis, this issue is negligible for our designs of resonant gyroscope. If an external rotation $\theta(°/s)$ is applied to the chip about the z-axis, the Coriolis force acting on the proof mass is:

$$\tilde{F}_c = \frac{2\pi}{180} L_m^2 e_M \rho\theta\tilde{\delta} Y_M \tag{7.8}$$

7.3.2 Lever mechanism

Since a high scale factor is required for a low noise sensor, a lever mechanism suitable for surface micromachined technology is used in order to amplify the Coriolis force acting on the proof mass as shown in Figure 7.4. It is made of flexural pivots for leverage and to link to the input (F_c) and output (F_{ca}) forces (true pivots are unavailable in the fabrication processes). As long as the torsional stiffness of the flexures is not too high, the structure will effectively approximate a lever, magnifying the input force and increasing the scale factor of the sensor by applying the magnified force to the resonators.

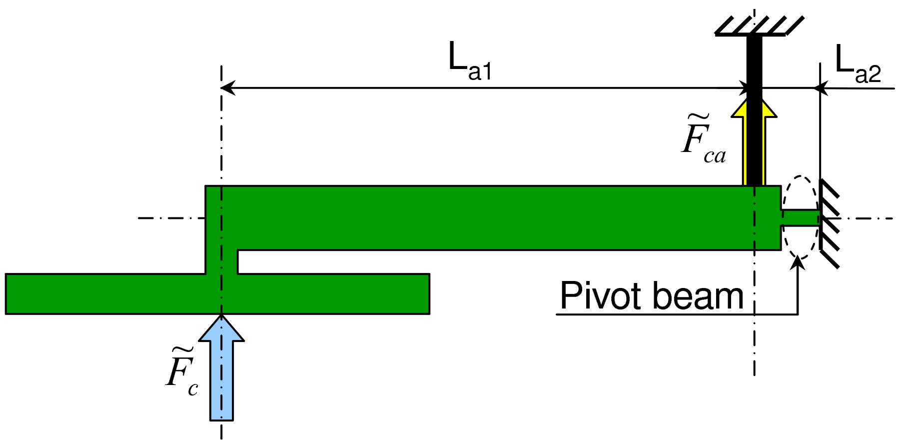

Figure 7.4: Lever mechanism.

The model for determining the actual amount of magnification provided by the lever is shown in Figure 7.5. The behavior of the system must be solved by simultaneously solving for the vertical

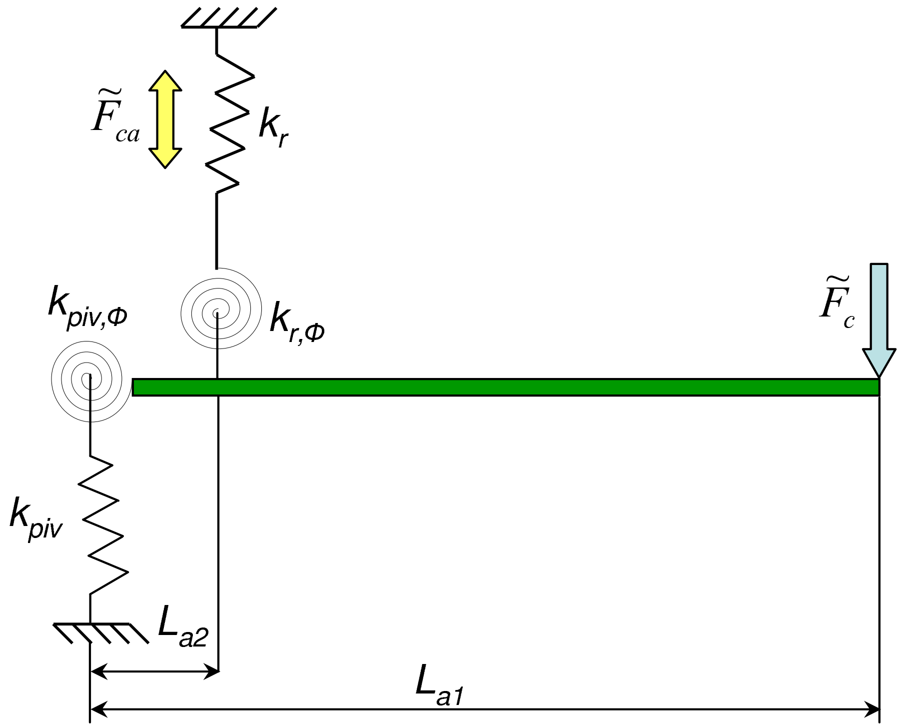

Figure 7.5: Model used to predict leverage force magnification.

deflection and rotation of the system which gives the following equations:

$$X = \frac{1}{k_{piv}}\left(1 - \frac{k_r L_{a1} L_{a2}}{k_\Phi + k_r L_{a2}^2}\right)\tilde{F}_c \tag{7.9}$$

$$\Phi = \frac{L_{a1}}{k_\Phi + k_r L_{a2}^2}\tilde{F}_c \tag{7.10}$$

$$\tilde{F_{ca}} = \frac{k_r L_{a1} L_{a2}}{k_\Phi + k_r L_{a2}^2}\tilde{F}_c \tag{7.11}$$

where X is the deflection of the structure, Φ is the rotation of the structure, $\tilde{F_{ca}}$ is the output force (the amplified Coriolis force), k_{piv} is the vertical stiffness of the pivot beam, k_r is the stiffness of the output structure (the resonator), k_Φ is the sum of the link rotational stiffnesses $k_{r,\Phi}$ and $k_{piv,\Phi}$, L_{a2} is the distance from the pivot to the output, L_{a1} is the distance from the pivot to the input and $\tilde{F}_c$ is the input force (the Coriolis force acting on the proof mass).

In the ideal case, the torsional stiffness of the flexures is zero and the vertical stiffness of the pivot is infinite, and above equations to:

$$X = 0 \tag{7.12}$$

$$\Phi = \frac{L_{a1}}{k_r L_{a2}^2}\tilde{F}_c \tag{7.13}$$

$$\tilde{F_{ca}} = \frac{L_{a1}}{L_{a2}}\tilde{F}_c \tag{7.14}$$

In order to obtain the maximum possible amplification, the position of the resonator with respect to the lever mechanism structure has been optimized by FE simulations.

7.3.3 Sensing part

Several 2-port resonators (see Figure 7.6) have been designed as sensitive parts of our M&NEMS resonant gyroscopes in order to decouple the actuation and the detection which makes easier the characterization of such force sensors. Moreover, since the stiffness of these sensing parts is modulated periodically by a time-varying Coriolis force at the proof mass frequency $\tilde{\delta}$, we are dealing with 2-port Mathieu resonator.

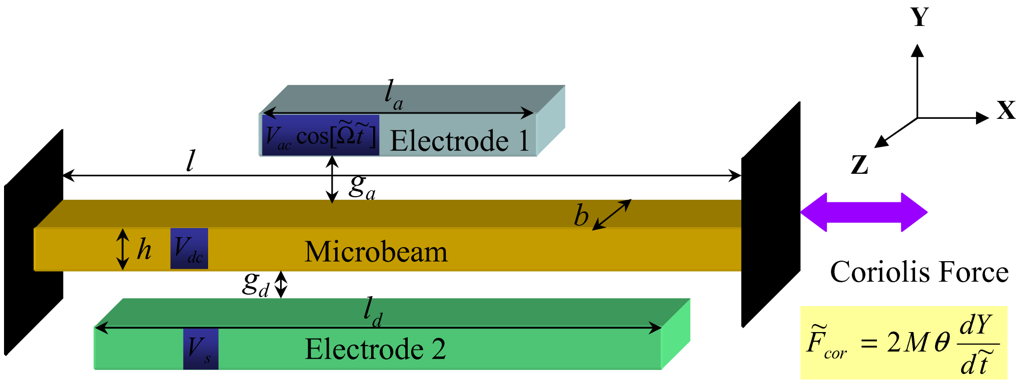

Figure 7.6: Schema of a 2-port Mathieu resonator.

7.4 Model

For simplicity, as a first step, only the 1-port Mathieu resonator dynamics is investigated. Thus, the nonlinear partial differential equation (7.2) is considered with the following boundary conditions:

$$\tilde{w}(0,\tilde{t}) = \tilde{w}(l,\tilde{t}) = \frac{\partial \tilde{w}}{\partial \tilde{x}}(0,\tilde{t}) = \frac{\partial \tilde{w}}{\partial \tilde{x}}(l,\tilde{t}) = 0 \tag{7.15}$$

The Mathieu equation has been widely studied in the context of parametric resonance. Newman et al [Newman 1999] investigated the dynamics of a parametrically excited partial differential equation and particularly the dependence of the steady state behavior on parameter values and initial conditions. In [Abraham 2003], a new technique derived from [Chatterjee 2003] based on an approximate realization of the method of averaging has been used to tackle weakly nonlinear Mathieu equations whose unperturbed dynamics is close to points corresponding to simple resonances between response and parametric forcing. Rand et al [Rand 2003] constructed analytical expressions for the transition curves of the quasiperiodic Mathieu equation in the vicinity of the resonance $2:2:1$ using a double-perturbation procedure. In [Zounes 2002], the interaction of subharmonic resonances in the nonlinear quasiperiodic Mathieu equation has been investigated. Belhaq and fahsi [Belhaq 2007] showed that in the vicinity of the $2:1$ and $1:1$ resonances in a fast harmonically excited Van Der Pol-Mathieu-Duffing oscillator, fast harmonic excitation can change the nonlinear characteristic spring behavior from softening to hardening and causes the entrainment regions to shift. In [Michon 2008], the motion of a sample automotive belt-pulley system subjected to tension fluctuations governed by a Mathieu-Duffing equation was theoretically and experimentally investigated.

Note that the transition curves of a linear Mathieu equation (Figure 7.7) can be approximately plotted using a perturbation technique. The number of tongues of instability corresponds to the truncation order of the asymptotic expansion. Figure 7.7 displays three instability tongues that correspond to a third order expansion of the perturbation technique. The curves are determined analytically using the Floquet theory for small Coriolis forces. Here, Δ is the ratio between the proof mass frequency and the resonator frequency and F_{ca} is the dimensionless input time-varying force axially applied to the resonator. These instability tongues emanate from the points $\frac{1}{\Delta} = \frac{n}{2}$ on the $\frac{1}{\Delta}$ axis. Dufour and Berlioz [Dufour 1998] showed that the dynamic stability of parametrically exited beams depends on the type of parametric excitation, the forcing frequencies and the boundary conditions and demonstrated that the existence of the instability zone is in relationship with the topology of the modal geometric stiffness matrices due to axial force and torque.

Figure 7.7 shows that inside the tongue, the resonator displacement grows exponentially in time. Outside the tongue, the displacement becomes the sum of terms each of which is the product of two periodic (sinusoidal) functions with generally incommensurate frequencies, that is, the displacement is a quasiperiodic function of time. Also, the resonator is very weakly damped (high quality factors)

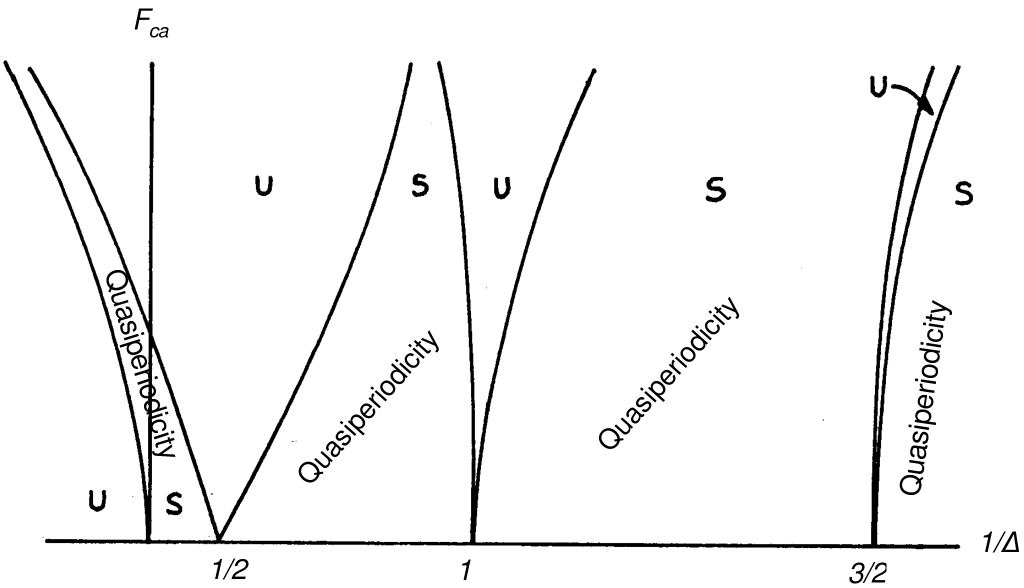

Figure 7.7: Transition curves in a linear autonomous Mathieu equation. S denotes stable quasiperiodic domains and U denotes the unstable domains.

which makes these transition curves approximately valid for a damped linear Mathieu equation. Figure 7.7 shows unbounded solutions to Mathieus equation which can result from resonances between the forcing frequency and the oscillators unforced natural frequency. However, real physical systems do not exhibit unbounded behavior.

The difference lies in the fact that the Mathieu equation is linear. The effects of nonlinearity can be explained as follows: as the resonance causes the amplitude of the motion to increase, the relation between period and amplitude (which is a characteristic effect of nonlinearity) causes the resonance to detune, decreasing its tendency to produce large motions.

The equation that governs the Mathieu resonator is a nonlinear partial differential equation under parametric and external excitation and consequently, further complicated than those already studied in literature. In addition, the structure of the stability regions of the quasiperiodic Mathieu equation is much more complicated than for the Mathieu equation.

Belhaq et al. [Belhaq 2002] and Guennoun et al. [Guennoun 2002] consider a homogeneous Mathieu equation with quasiperiodic linear coefficients and a constant nonlinear coefficient. The small parameter technique of multiple scales is applied twice to the system to obtain an approximate time-invariant system. In another study (see Belhaq and Houssni, [Belhaq 1999] the system under investigation contains quadratic and cubic nonlinearities as well as parametric (linear terms) and external excitations of incommensurate frequencies. The small parameter techniques of generalized averaging and multiple-scale perturbation are employed to obtain a solution. Rand and his associates [Rand 2005, Zounes 2002, Zounes 1998] analyze a linear homogeneous quasiperiodic Mathieu equation via several methods such as numerical integration, Lyapunov exponents, regular perturbation, Lie transform perturbation and harmonic balance.

Note that the aim of this work is to provide practical rules for MEMS designers in order to enhance the performances of resonant microgyroscopes rather than developing complex models or tracking the quasiperiodicity in MEMS and NEMS Mathieu resonators.

For all these reasons, we restrict our studies to the periodic motions of the forced nonlinear Mathieu equation. Following Rand and Morrison [Rand 2005], in our case for an external excitation tuned around the resonator primary resonance and by analogy, the Mathieu equation is quasiperiodic when $\Delta \neq \frac{2-m}{n}$ for $\Delta \in [0, 1]$, $m \in \mathbb{Z}$ and $n \in \mathbb{N}$.

Consequently, the quasiperiodic domains in the (Δ, F_{ca}) plan are very limited for low frequencies actuation ($\tilde{\delta}$) with respect to the periodic motions. This ensures the generality of our parametric analysis of the gyroscope sensitivity out of quasiperiodicity. However, a first order averaging method is valid only for low Coriolis forces which ensure a negligible effect of the superharmonic resonances at each $\Delta < 1$. Otherwise, high order averaging is required. For simplicity, all these conditions are assumed to be satisfied.

7.4.1 Normalization

For convenience and equations simplicity, the following nondimensional variables are introduced:

$$w = \frac{\tilde{w}}{g}, \quad x = \frac{\tilde{x}}{l}, \quad t = \frac{\tilde{t}}{\tau} \tag{7.16}$$

where $\tau = \frac{2l^2}{h}\sqrt{\frac{3\rho}{E}}$. Substituting Equation (7.16) into equations (7.2) and (7.15), yields:

$$\frac{\partial^4 w}{\partial x^4} + \frac{\partial^2 w}{\partial t^2} + c\frac{\partial w}{\partial t} - \left[N + F_c \cos \delta t + \alpha_1 \int_0^1 \left[\frac{\partial w}{\partial x}\right]^2 dx\right] \frac{\partial^2 w}{\partial x^2} = \alpha_2 \frac{[Vdc + Vac\cos(\Omega t)]^2}{(1-w)^2} \tag{7.17}$$

$$w(0,t) = w(1,t) = \frac{\partial w}{\partial x}(0,t) = \frac{\partial w}{\partial x}(1,t) = 0 \tag{7.18}$$

The parameters appearing in Equation (7.17) are:

$$\begin{gathered} c = \frac{\tilde{c}l^4}{EI\tau}, \quad N = \frac{\tilde{N}l^2}{EI}, \quad F_c = A_l\frac{\tilde{F}_c l^2}{EI}, \quad \delta = \tilde{\delta}\tau \\ \alpha_1 = 6\left[\frac{g}{h}\right]^2, \quad \alpha_2 = 6C_n\frac{\varepsilon_0 l^4}{Eh^3g^3}, \quad \Omega = \tilde{\Omega}\tau \end{gathered} \tag{7.19}$$

7.4.2 Solving

The quality factors Q of the designed resonators are in the range of $10^3 - 5.10^4$ which makes the static displacement negligible with respect to the dynamic displacement of the microbeam. A reduced-order model is generated by modal decomposition transforming equations (7.2) into a finite-degree-of-freedom system consisting of nonlinear Mathieu ordinary differential equations in time. The undamped linear mode shapes of the straight microbeam are used as basis functions in the Galerkin procedure. To this end, the deflection is expressed as:

$$w(x,t) = \sum_{k=1}^{n} a_k(t)\phi_k(x) \tag{7.20}$$

where $a_k(t)$ is the k^{th} generalized coordinate and $\phi_k(x)$ is the k^{th} linear undamped mode shape of the straight microbeam, normalized such that $\int_0^1 \phi_k\phi_j = \delta_{kj}$ where $\delta_{kj} = 0$ if $k \neq j$ and $\delta_{kj} = 1$ if $k = j$. The linear undamped mode shapes $\phi_k(x)$ are governed by:

$$\frac{d^4\phi_k(x)}{dx^4} = \lambda_k^2\phi_k(x) \tag{7.21}$$

$$\phi_k(0) = \phi_k'(0) = \phi_k'(1) = \phi_k''(1) \tag{7.22}$$

Here, λ_k is the k^{th} natural frequency of the resonator. The electrostatic force in Equation (7.17) is expanded in a fifth order Taylor series to enable the capture of 5 possible amplitudes for a given frequency in the mixed behavior [Kacem 2009a]. Then, Equation (7.20) is substituted into the resulting equation, Equation (7.21) is used to eliminate $\frac{d^4\phi_k(x)}{dx^4}$, and the outcome is integrated from $x = 0$ to 1. Thus, a system of coupled nonlinear Mathieu ordinary differential equations in time is obtained. The DC voltage, which is generally at least ten times higher than the AC voltage, makes the second harmonic negligible. Also, the first mode should be the dominant mode of the system. According to this assumption, the study can be restricted to the case $n = 1$. then, it gives:

$$\begin{aligned}\ddot{a}_1 + c\dot{a}_1 + (500.564 - 2\alpha_2\xi_0 + 12.3(N + F_c\cos\delta t))\,a_1 + (151.354\alpha_1 - 7.403\alpha_2\xi_0)\,a_1^3 \\ +\alpha_2\xi_0\left(0.831 + 4{a_1}^2 + 13.255{a_1}^4 - 23.17{a_1}^5\right) = 0\end{aligned} \tag{7.23}$$

where $\xi_0 = V_{dc}^2 + V_{ac}\cos\Omega t$. To analyse the equation of motion (7.23), it proves convenient to invoke perturbation techniques which work well with the assumptions of "small" excitation and damping, typically valid in MEMS resonators. Nevertheless, in order to avoid quasiperiodicity, we chose $\frac{\delta}{\omega_n} \in \mathbb{Q} \cap [0,1]$ and we assume that the Coriolis forces are weak enough to make the possible superharmonic resonances negligible with respect to the fundamental primary resonance. To facilitate the perturbation approach, in this case the method of averaging [Nayfeh 1981], a standard constrained coordinate transformation is introduced, as given by:

$$\begin{cases} a_1 = A(t)\cos\left[\Omega t + \beta(t)\right] \\ \dot{a}_1 = -A(t)\Omega\sin\left[\Omega t + \beta(t)\right] \\ \ddot{a}_1 = -A(t)\Omega^2\cos\left[\Omega t + \beta(t)\right] \end{cases} \tag{7.24}$$

In addition, since near-resonant behavior is the principal operating regime of the proposed system, a detuning parameter, σ is introduced, as given by:

$$\Omega = \omega_n + \varepsilon\sigma \tag{7.25}$$

where $\omega_n = \sqrt{500.564 + 12.3N - 2V_{dc}^2\alpha_2}$. Separating the resulting equations and averaging them over the period $\frac{2\pi}{\Omega}$ in the t-domain results in the system's averaged equations, in terms of amplitude and phase, which are given by:

$$\dot{A} = \varepsilon \frac{c}{2} A - \varepsilon \frac{A F_c}{\omega_n} \left(\frac{\sin[\pi\Delta]\sin[\pi\Delta - 2\beta]}{(\Delta - 2)} - \frac{\sin[\pi\Delta]\sin[\pi\Delta + 2\beta]}{(2+\Delta)} \right)$$
$$+\varepsilon \left(0.831 + A^2 + 1.657A^4\right) \frac{\alpha_2 \xi_1}{\omega_n} \sin\beta + O\left(\varepsilon^2\right) \tag{7.26}$$

$$\dot{\beta} = \varepsilon\sigma + \varepsilon \frac{\alpha_2 A^2 V_{dc}^2}{\omega_n}\left(2.776 + 7.241A^2\right) - \varepsilon \frac{\alpha_2 \xi_1}{\omega_n} \left(\frac{0.831}{A} + 3A + 8.285A^3 \right) \cos\beta$$
$$-\varepsilon \frac{F_c}{\omega_n} \left(\frac{\cos[\pi\Delta - 2\beta]\sin[\pi\Delta]}{(\Delta - 2)} + \frac{\cos[\pi\Delta + 2\beta]\sin[\pi\Delta]}{(2+\Delta)} + \frac{\sin[2\pi\Delta]}{\Delta} \right)$$
$$-\varepsilon \frac{56.757A^2\alpha_1}{\omega_n} + O\left(\varepsilon^2\right) \tag{7.27}$$

where $\xi_1 = V_{dc}V_{ac}$ and $\Delta = \frac{\delta}{\omega_n}$. The steady-state motions occur when $\dot{A} = \dot{\beta} = 0$, which corresponds to the singular points of Equations (7.26) and (7.27). Thus, the frequency-response can be written in its parametric form for $\beta \in [0, \pi]$ and $\Delta \in \mathbb{Q} \cap [0, 1]$.

$$\Omega = f_1(\beta, \Delta) \tag{7.28}$$
$$A = f_2(\beta, \Delta) \tag{7.29}$$

This analytic expression (set of two equations) makes the model suitable for MEMS and NEMS designers as a fast and efficient tool for resonant gyroscope performances optimisation.

7.5 Analytical results and device specifications

All the numerical simulations were carried out with the following set of parameters:

- Proof mass: $L_m = 100\,\mu m$, $e_M = 2\,\mu m$, $l_c = 6\,\mu m$, $g_c = 2\,\mu m$, $d_c = 4\,\mu m$ and $W_c = 1\mu m$.
- Resonator: $l = 100\,\mu m$, $b = 2\,\mu m$, $h = 5\,\mu m$, $g = 300\,nm$, $Q = 1000$.

The quality factor of the system mass-spring damper is assumed to be $Q = 10^5$. The proof mass displacement at resonance is assumed to be $2.5\mu m$. The proof mass frequency (via Δ) as well as V_{ac} and V_{dc} were used for parametric studies.

7.5.1 Proof mass frequency effect

Figure 7.8 shows four nonlinear hardening frequency responses at a proof mass frequency ten times smaller than the resonator frequency ($\Delta = 0.1$) and for several angular rates $0 - 900°/s$. The DC polarization of the resonator is low enough ($V_{dc} = 1V$) to keep the global nonlinear stiffness dominated by the mechanical nonlinearities. Hence, the predicted hardening behavior. In this configuration, the Coriolis force that modulates the resonator stiffness at the proof mass frequency represents a slow dynamic with respect to the resonator dynamic ten times faster. Therefore, the frequency effect is negligible and only the resulting stress is considered which implies a positive frequency shift proportional to the external rotation rate θ. Then, for $\Delta = 0.1$ and for several angular rates going from $0°/s$ up to $900°/s$, the DC voltage applied to the resonator is increased from $1V$ up to $9V$ while decreasing the AC voltage from $0.2V$ down to $30mV$ (see Figure 7.9). This increases significantly the negative nonlinear stiffness due to the electrostatic force that dominates in this case the global stiffness of the resonator. Hence, the predicted softening behavior.

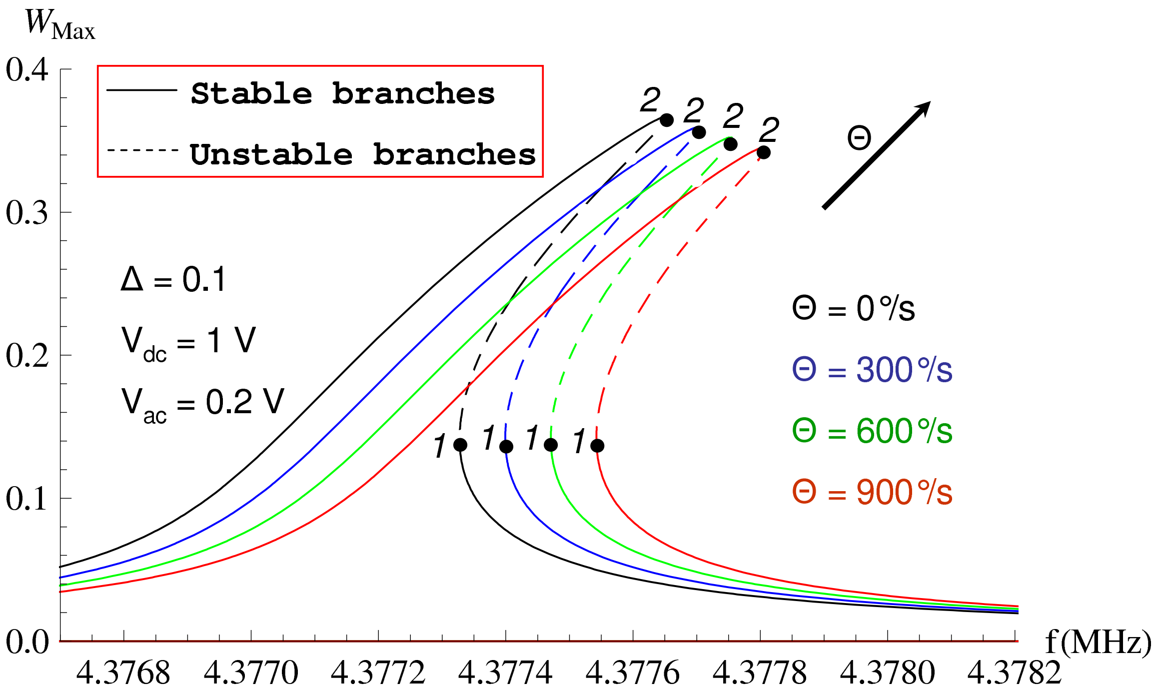

Figure 7.8: Predicted forced frequency responses displaying a hardening behavior for $\Delta = 0.1$. W_{max} is the displacement of the beam normalized by the gap g at its middle point $\frac{l}{2}$, $\{1, 2\}$ are the bifurcation points. The frequency shift is due to the variation of the external angular rate θ.

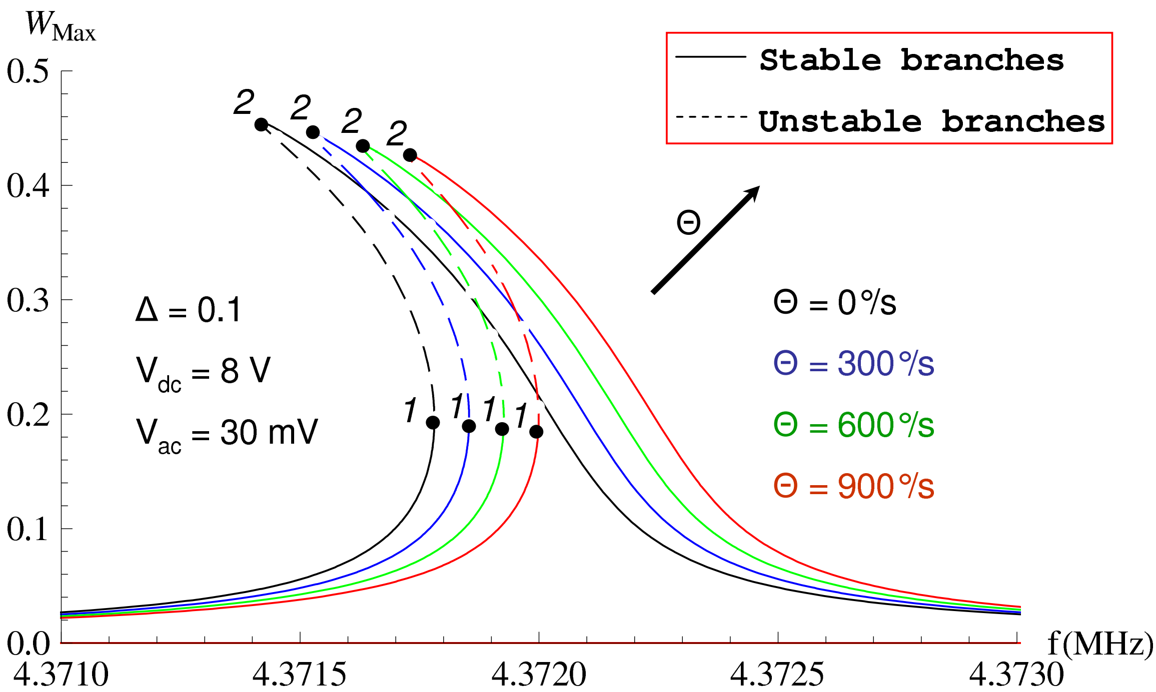

Figure 7.9: Predicted forced frequency responses displaying a softening behavior for $\Delta = 0.1$. W_{max} is the displacement of the beam normalized by the gap g at its middle point $\frac{l}{2}$, $\{1, 2\}$ are the bifurcation points. The frequency shift is due to the variation of the external angular rate θ.

For low actuation frequency with respect to the sensing frequency, the microgyroscope behaves as a resonant accelerometer. Indeed, the Coriolis force is seen by the resonator as a quasi-static force. Consequently, the close-form solutions of the critical amplitude and the mixed behavior initiation amplitude established in chapter 5 can be used here in order to improve the performances of the resonant gyroscope. Particularly, the compensation of the nonlinearities is possible when the mechanical and electrostatic critical amplitudes are equilibrated. This results on an optimal DC voltage for which the obtained frequency resonance peak is linear beyond the critical amplitude.

Afterwards, the frequency of the proof mass in increased up to a quarter the resonator frequency. In the same way, for this configuration, figures 7.10 and 7.11 show respectively several nonlinear hardening and softening forced frequency curves for several rotation rates. Thus, the compensation for the nonlinearities is possible for specific DC voltage. However, the apparition of additional bifurcation points $\{3, 4\}$ is notable and for rotation rates (θ) beyond $600°/s$. The maximum is close to the bifurcation point 4 and no more situated at $\beta = \frac{\pi}{2}$. This strange behavior can be explained by an important contribution of the superharmonic resonance of order quarter the resonator primary resonance for θ beyond $600°/s$. Therefore, even out of quasiperiodicity, the averaging method is not valid except at a higher order defined by the transition curve at the corresponding superharmonic resonance. Indeed, at this level the full scale here is limited by the proof mass frequency (for a valid first order averaging).

Referring to Table 2.3, the classical specifications of current MEMS gyroscopes include a dynamic range at best around $100°/s$ which ensures the validity of the first averaging.

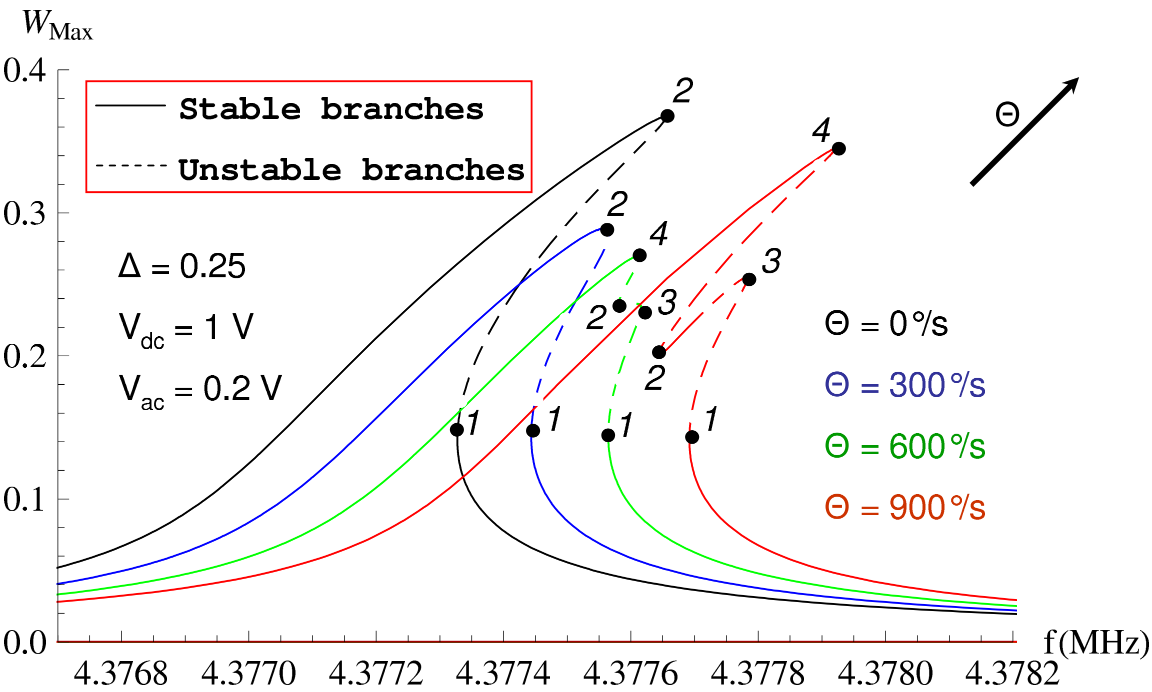

Figure 7.10: Predicted forced frequency responses displaying a hardening behavior for $\Delta = 0.25$. W_{max} is the displacement of the beam normalized by the gap g at its middle point $\frac{l}{2}$, $\{1, 2, 3, 4\}$ are the bifurcation points. The frequency shift is due to the variation of the external angular rate θ.

The curves in Figure 7.12 display the variation of the Mathieu resonator displacement at its middle point and at resonance when the phase $\beta = \frac{\pi}{2}$ for several values of angular rates θ. Remarkably, it

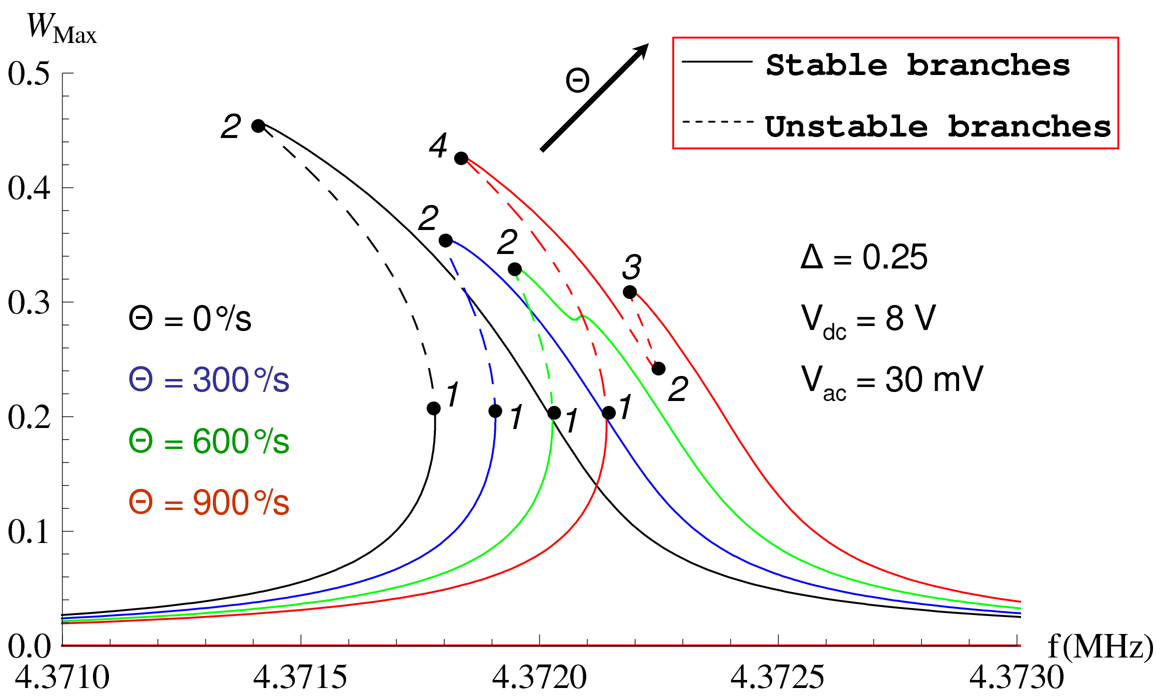

Figure 7.11: Predicted forced frequency responses displaying a softening behavior for $\Delta = 0.25$. W_{max} is the displacement of the beam normalized by the gap g at its middle point $\frac{l}{2}$, $\{1, 2, 3, 4\}$ are the bifurcation points. The frequency shift is due to the variation of the external angular rate θ.

appears that the symmetry can be broken between negative and positive Coriolis stress effect when the resonator dynamic becomes strongly nonlinear for high angular rates and high frequencies. This corresponds to a strong nonlinear parametric spring softening effect for which the resonator displacement averaged over the period $\frac{2\pi}{\omega_n}$ is amplified (parametric perturbation) and then a high instability such as the pull-in could be suddenly reached. Since the sensitivity of the resonant gyroscope could be extremely reduced for a large dynamic range, working at $\Delta < 0.25$ is essential for high grade resonant gyroscopes.

7.5.2 Resonant gyroscope scale factor

The scale factor of the sensor, S_F that relates the output frequency shift difference (δf) between the two resonators to the external input rotation rate (θ) is given by:

$$S_F = \frac{df}{d\theta}\left[\frac{\Pi}{2}, \theta \in DR\right] \tag{7.30}$$

Note that the scale factor corresponds to the derivate of equation (7.28) at the phase $\beta = \frac{\pi}{2}$ with respect to the rotation rate θ for a dynamic range (DR) that ensures stable motions out of quasiperiodicity and negligible superharmonic resonances effects. The expression can be also written in terms of a ratio of some drive and sense parameters multiplied by a lever gain and a constant dependent on the mode shape of the resonating element. The scale factor is only dependent on material and geometrical parameters and the displacement of the gyroscope proof mass at resonance (Y_M). Consequently and unlike classical gyroscopes, the goal of the control scheme is now simplified to the requirement

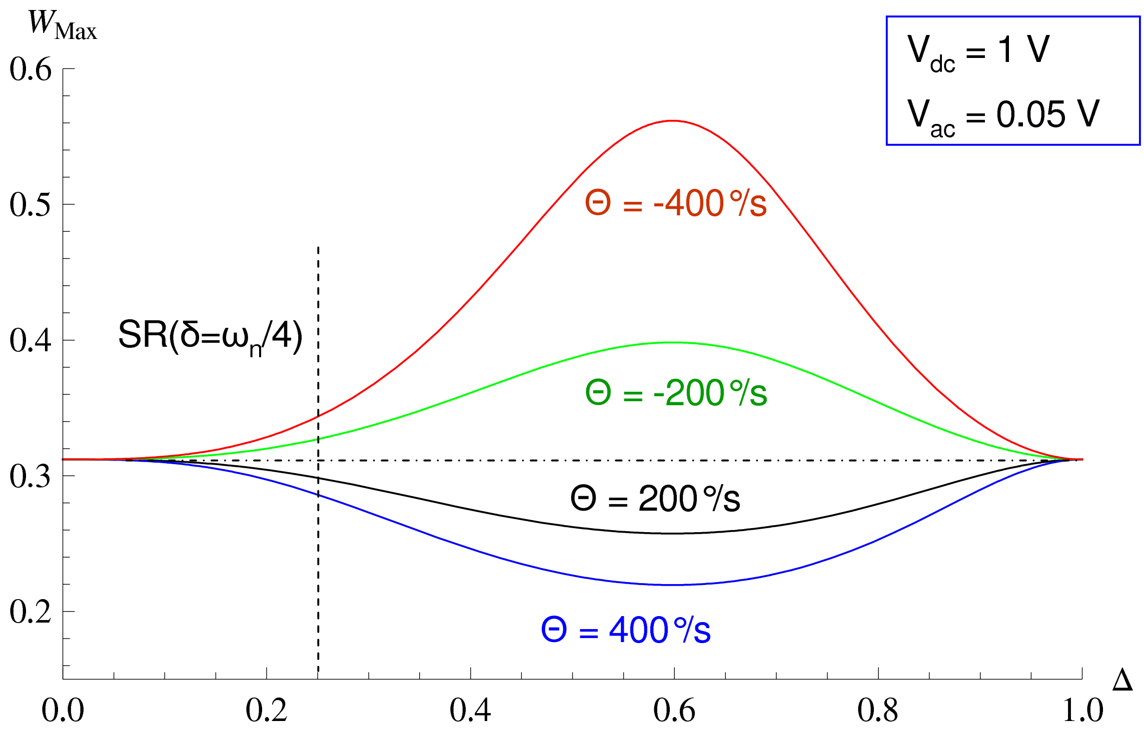

Figure 7.12: Variation of the Mathieu resonator displacement at its middle point and at resonance when the phase $\beta = \frac{\pi}{2}$ for several values of angular rates θ.

of maintaining constant amplitude motion for the gyroscope proof mass and the resonator-sensing elements at their respective resonant frequencies.

Figure 7.13 shows the variation of the resonant gyroscope scale factor with respect to the frequency ratio between the actuation and the sensing parts (Δ) for a resonator driven in the linear regime. Obviously, to use this curve, one should exclude the non-rational values of Δ (quasiperiodic regime). Remarkably, the maximum of sensitivity is located at $\Delta = 0.25$ which corresponds to a superharmonic resonance in the nonlinear regime as shown in Figures 7.10 and 7.11. Moreover the scale factor is approaching zero for 3 cases:

- $\Delta = 0$ which is obvious since the Coriolis force is proportional to the proof mass frequency.
- $\Delta = 0.5$. It corresponds to a simultaneous superharmonic and primary resonances in the nonlinear regime. In this configuration, the performances of the Mathieu resonator are drastically reduced in the linear regime and furthermore, in the nonlinear regime, the secular terms coming from the secondary resonance should be taken into account for analytical investigation in a large dynamic range.
- $\Delta = 1$. It corresponds to a simultaneous parametric and primary resonance in the nonlinear regime. We arrive to the same conclusions as the case $\Delta = 0.5$.

When the resonator is driven beyond its critical amplitude (in the nonlinear regime), unlike the linear case where the scale factor is constant for a given Δ and θ inside the dynamic range, the resonant gyroscope sensitivity highly depends on the external rotation rates for a frequency ratio $\delta > 0.1$. Remarkably, the scale factor is drastically reduced if we assume a negligible secondary resonance effect

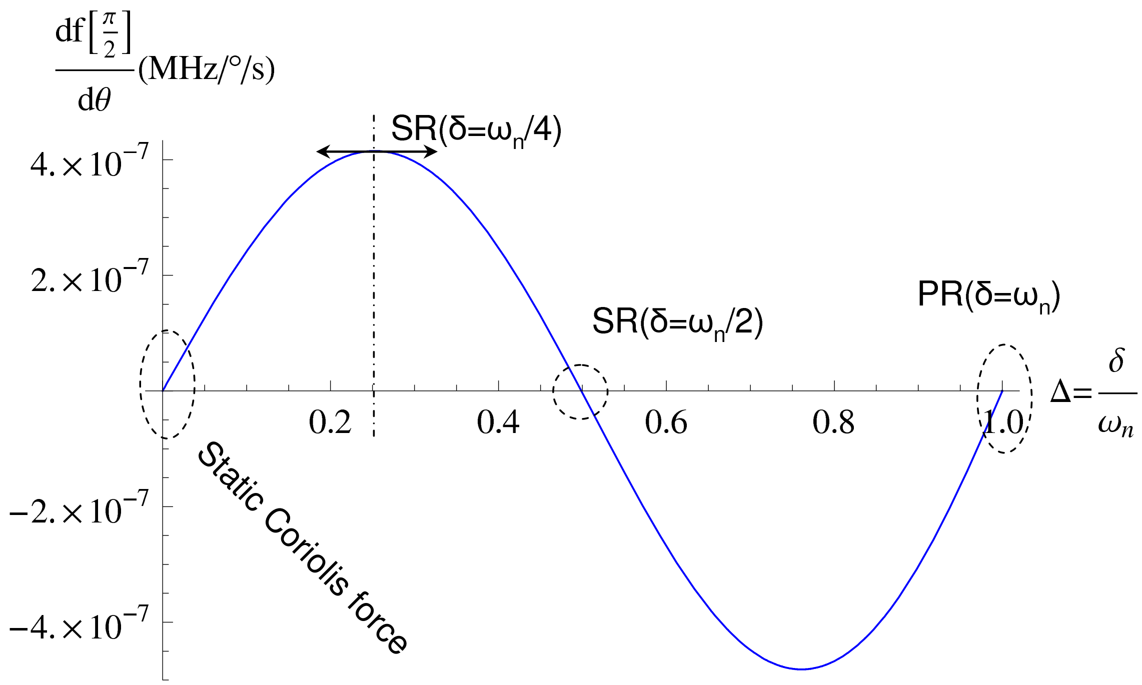

Figure 7.13: Scale factor variation with respect to the proof mass frequency in the resonator linear regime and inside the dynamic range of the resonant gyroscope. SR and PR are superharmonic and parametric resonances.

which is valid up to $\Delta = 0.25$ as shown in Figure 7.13. Furthermore, for an admissible scale factor nonlinearity when the Mathieu resonator is driven in the nonlinear regime, the resonant gyroscope must be designed with $\Delta < 0.05$.

This drastic limit could be avoided by the compensation of the nonlinearities out of quasiperiodicity for $\Delta = 0.25$ which gives the maximum of sensitivity.

7.5.3 Resonant gyroscope resolution

To evaluate the minimum acceleration detectable by the sensor, all noise sources have to be taken into account. The resonator frequency shift is assumed to be measured via a PLL based technique, with the use of a readout amplifier. The noise sources are:

- Thermomechanical fluctuations of the proof mass
- Thermomechanical fluctuations of the resonator
- Readout amplifier's noise

Here, temperature fluctuation, adsorption-desorption as well as defect motion noises are neglected, which is a fair approximation at our scales [Postma 2005]. Also, the Brownian noise of the proof mass is negligible with respect to the thermomechanical fluctuations of the resonator. Therefore, one can restrict the resolution analysis to the resonator and electronic noises.

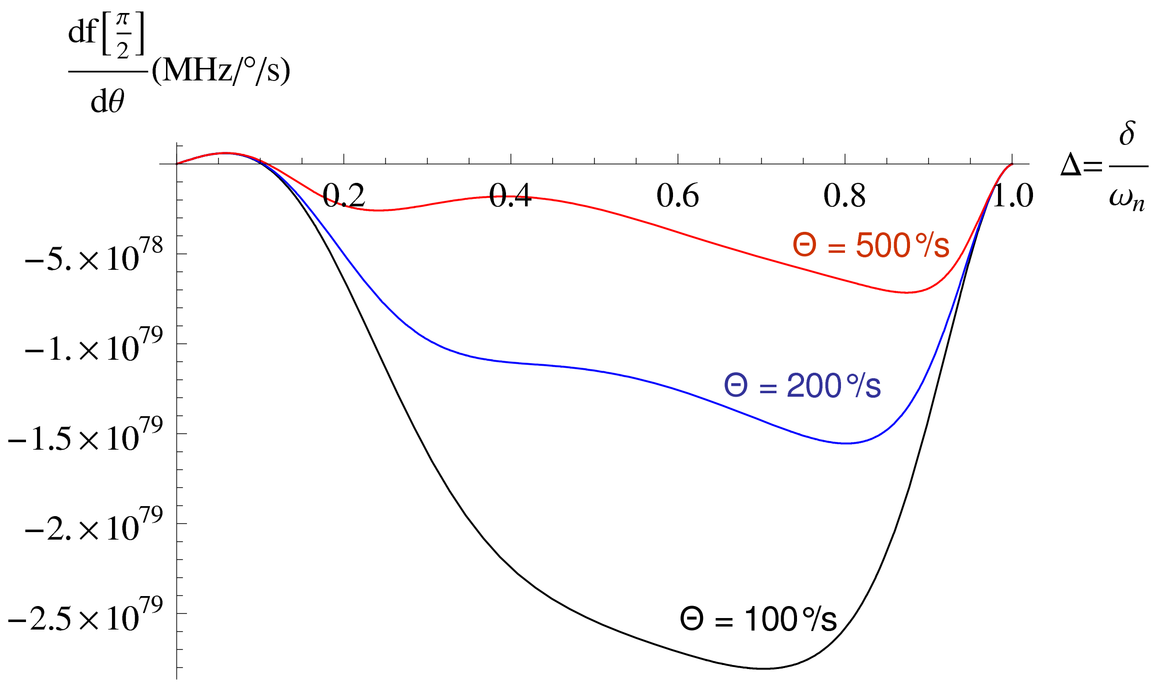

Figure 7.14: Scale factor variation curves with respect to the proof mass frequency for a nonlinear resonator and several rotation rates.

7.5.3.1 Resonator thermomechanical fluctuations

Referring to [Robins 1984], for a PLL-based readout technique, the frequency noise spectral density is:

$$S_\omega^r(\omega) = \left(\frac{\omega_0}{2Q}\right)^2 \frac{S_x(\omega_0)}{P_0} \tag{7.31}$$

where P_0 is the displacement carrier power ($P_0 = \frac{1}{2}W_{max}^2 g^2$), *i.e.* the RMS drive amplitude of the resonator. The latter is classically driven below the hysteretic limit due to the mechanical nonlinearity.

7.5.3.2 Readout amplifier noise

In a very general way, the readout amplifiers noise referred to its input will be evaluated thanks to its noise figure NF. By definition,

$$NF = 10\log\frac{SNR\,at\,input}{SNR\,at\,output} = 10\log\frac{output\,noise\,power\,referred\,to\,its\,input}{noise\,power\,at\,input} \tag{7.32}$$

The displacement noise spectral density brought by the amplifier is then:

$$S_x^a(\omega) = \left(10^{\frac{NF}{10}} - 1\right) S_x^r(\omega) \tag{7.33}$$

and written in frequency noise spectral density:

$$S_\omega^a(\omega) = \left(\frac{\omega_n}{2Q}\right)^2 \frac{S_x^a(\omega_n)}{P_0} = \left(\frac{\omega_n}{2Q}\right)^2 \frac{2S_x^a(\omega_n)}{W_{max}^2 g^2} \tag{7.34}$$

Then, an image of the resonant gyroscope resolution may be chosen as:

$$\theta_{min} = 3\frac{\sqrt{\int_0^{BW} \left[S_\omega^r(\omega) + S_\omega^a(\omega)\right] d\omega}}{S_F} \tag{7.35}$$

where S_F is the resonant gyroscope scale factor and BW is the sensor bandwidth.

7.5.4 Scale factor sensitivity to environmental variables

As previously established, the scale factor S_F is dependent only on geometrical design parameters and material constants. However, the scale factor could vary with respect to the fabrication tolerances as well as temperature, this dependence is much smaller as compared to variations of parameters such as the Young's modulus and quality factor that are typically an order of magnitude or more higher. The smaller variation could be further compensated by an amplitude gain control strategy applied to the gyroscope proof mass motion.

7.5.5 Quadrature error

The quadrature error comes from a coupling of the comb actuated drive mode into the sense signal even if no angular rate is applied to the sensor. There are various sources of quadrature like comb levitation forces, surface curvature and asymmetric side wall angles in the proof mass suspensions. This would result in a displacement along the sense direction whose amplitude is not directly correlated to the Coriolis force. Specialized combs can be employed for self-test and for quadrature error cancellation.

7.5.6 Bias stability

Long-term random drift has a number of potential sources. One source is low frequency noise such as $1/f$ noise, that is coupled to the frequency modulated input by a combination of transduction coefficients due to nonlinearities in the system. Hence, the idea of designing resonant gyroscopes including actuation parts at relatively high frequencies in comparison with the classical commercial devices. A mismatch in the resonators resonant frequencies due to lithographic errors can cause a second-order effect that can degrade the rejection of the effects of environmental parameters. Fabrication tolerances associated with electrode and suspension geometries such as line widths, line spacing, and lithographic alignment could result in portions of the proof mass actuation force and/or displacement coupling along the sense direction, resulting in quadrature error or Coriolis offset. Further investigation into these potential coupling mechanisms is required, but it is possible to conjecture that these coupling mechanisms might result in an offset or quadrature output that might vary as a function of time and environmental parameters.

7.5.7 Common mode acceleration

Cancellation of effects such as common mode acceleration can be achieved through two mechanically coupled masses vibrating anti-phase to each other. The Coriolis force acts along opposite directions for each of the two masses, however the effect of an external acceleration is the same, enabling first-order cancellation of the acceleration and other common mode effects. A fully symmetric dual mass resonant gyroscope that can potentially suppress undesirable acceleration effect is shown in Figure 7.15.

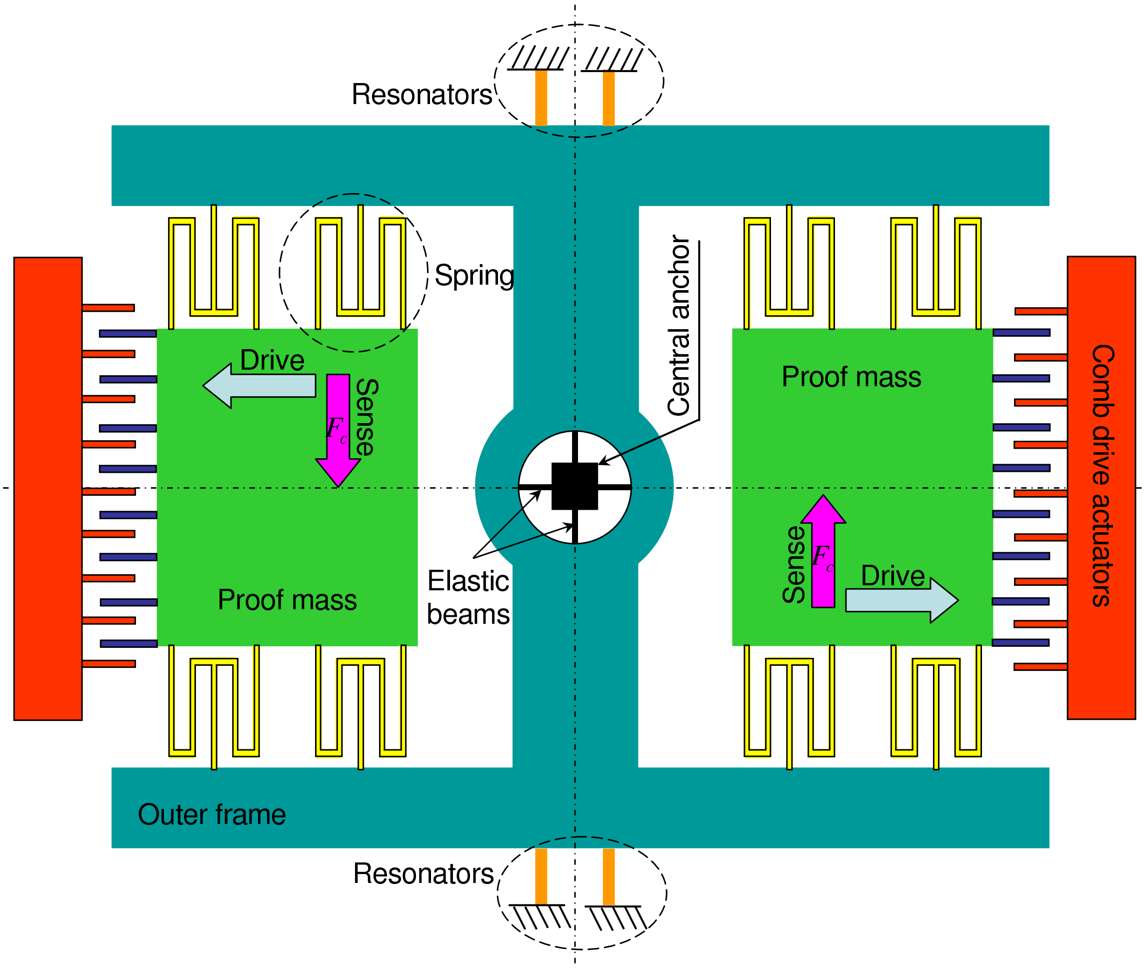

Figure 7.15: Fully symmetric dual mass resonant gyroscope.

7.5.8 Decoupled resonant gyroscope

Furthermore, in order to minimize the mechanical crosstalk, the resonant gyroscope can be designed with a complete decoupling between drive and sense modes thanks to an intermediate mass (inner frame). For a dual-mass decoupled resonant gyroscope, the fully symmetric structure helps to lower the bias of the sensor.

A schematic of a decoupled z-axis resonant gyroscope is shown in Figure 7.16. The device consists of an inner frame suspended by flexures attached to an outer frame and a sense frame which includes a lever mechanism. The outer frame is driven relative to the sense frame using embedded lateral comb drive actuators. If an external rotation is applied to the chip about the Z-axis, the Coriolis force acting on the inner and outer frames is transmitted to the sense frame. Unlike the first structure described in Figure 7.2, the drive part oscillates only in the Y direction and the inner frame is used here to transmit the Coriolis force to the sense frame. This ensures a perfect decoupling between the drive and the sense modes. A lever mechanism amplifies this force prior to its being communicated axially onto two resonators placed on either side of the sense frame for a differential output. The periodic compression and tension of resonators by the Coriolis force at the drive part frequency modulates the resonant frequency of these force sensors. Each force sensor comprises of the tuning fork mechanical structure embedded in the feedback loop of an oscillator circuit. Thus, by demodulating the oscillation

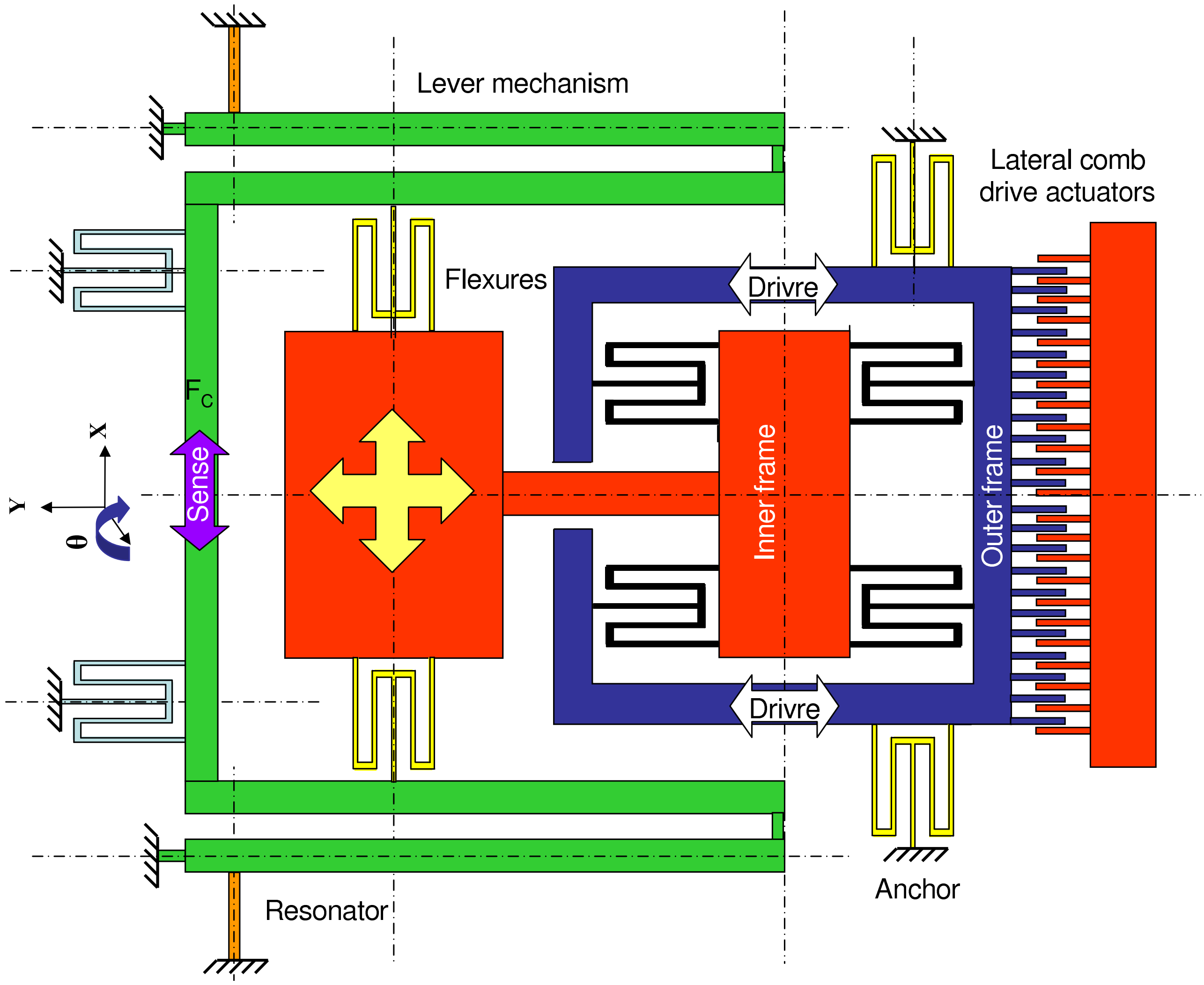

Figure 7.16: Decoupled z-axis resonant gyroscope.

frequency, the rotation rate applied to the device can be estimated.

7.6 Electronics and Signal Processing

Control, detection and signal conditioning electronics are essential for gyroscope operation. The goal of the control electronics is to maintain constant amplitude resonant oscillation in the resonators and the gyroscope proof mass. In the case of the resonant gyroscope, the detection and control electronics are coupled as the frequency output differential between the two output oscillators, measured at the gyroscope drive frequency, serves as the device output. The task of the signal processing electronics is the frequency demodulation of the respective sensing oscillator outputs followed by an amplitude demodulation with the proof mass oscillator output. To obtain a voltage output proportional to rotation rate, a low pass filter is added after the amplitude demodulation.

The above signal processing strategy could be implemented in either the analogical or digital domains. A functional schematic of the gyroscope electronics is shown in Figure 7.17.

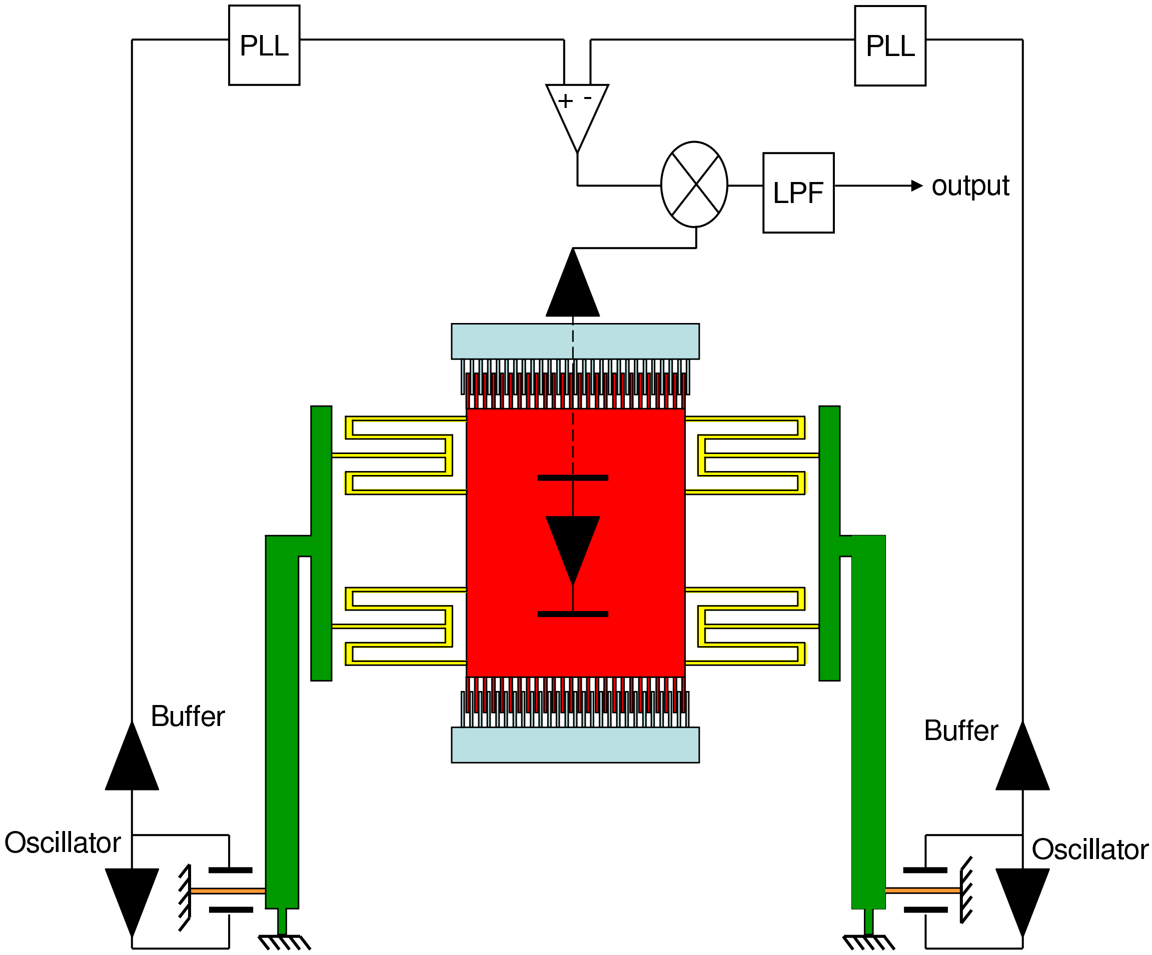

Figure 7.17: Functional block diagram schematic of the resonant gyroscope electronics.

7.7 Designs

Within the framework of the European M&NEMS project, several resonant gyroscopes have been designed and fabricated. The devices involve proof masses with relatively high frequencies compared to the state of art of resonant gyroscopes ($\tilde{\delta} \in$[90 KHz, 190 KHz]). The designed devices can be classified into the following categories:

- MEMS gyroscope: all the parts of the structure including the resonators have the same thickness corresponding to the MEMS level ($2\,\mu m$) on the M&NEMS mask as shown in Figure 7.18.

- M&NEMS gyroscope: the device includes MEMS parts (proof mass, comb drives, lever, springs. . .) and NEMS parts (resonators, electrodes) which potentially increase the gyroscope sensitivity and so enhances its resolution.

- Simple mass gyroscope: it corresponds to the simplest form of the resonant gyroscope. Fully MEMS or M&NEMS, these devices are limited by the common mode acceleration. Nevertheless, they can be simply used for testing important specifications such as the sensitivity and the resolution.

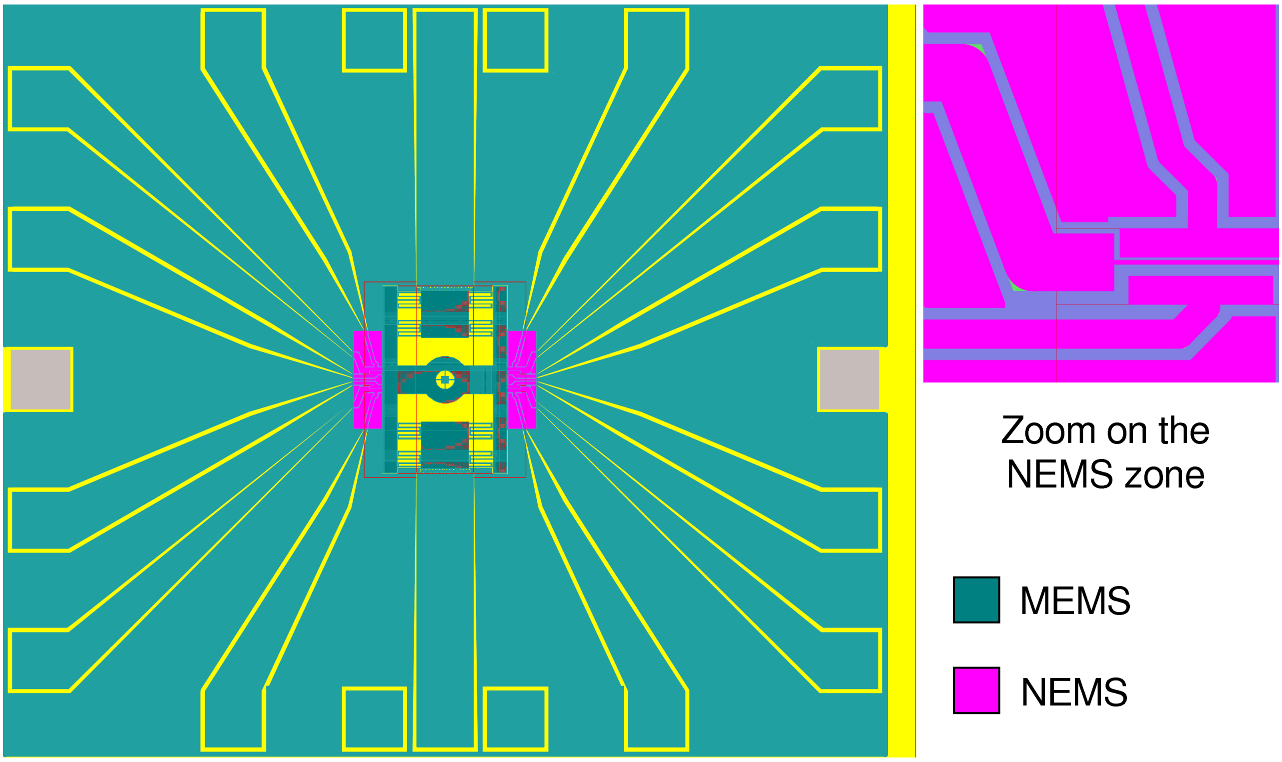

Figure 7.18: M&NEMS mask showing the MEMS ($2\mu m$) and NEMS ($500nm$) levels on a dual-mass resonant gyroscope structure. On the right a zoom on the NEMS protected zone.

- Dual mass gyroscope: these devices permit to overcome the common mode acceleration issue. As opposed to a simple mass structure, a dual mass gyroscope benefits from a differential read-out and then the output due to an acceleration applied to the chip about the sense axis can be suppressed

- Coupled gyroscope: the proof mass undergoes both drive and sense motions. This implies a quadrature error which can be significantly large and alters the device performances.

- Decoupled gyroscope: the device is detailed in subsection 7.5.8.

- Gyroscope with mismatched frequencies: The drive and sense modes are not matched in frequency. Consequently, the device does not benefit from an additional quality factor in the sensing mode.

- Gyroscope with matched frequencies: Under an external angular rate, the proof mass oscillates at resonance in the drive as well as the sense directions. The sensitivity of such devices can potentially be increased due to the amplification of the Coriolis force by the sensing mode quality factor. Nevertheless, the frequency matching often leads to a complex closed loop control.

Furthermore, the sensing parts of the designed gyroscopes were chosen among the several resonators experimentally tested in chapter 6. This ensures different case studies going from a very low frequency ratio (Δ) to a Δ approaching unity. Consequently, parametric instabilities and the sensitivity variation of the device with respect to Δ can be experimentally investigated. Moreover, the designed resonators have not the same dynamic behavior as explained in chapter 6 which can permit the evaluation of the hysteresis suppression potential on a Mathieu resonator. Besides, not all the devices were designed to exhibit high performances. Many structures concern the only analytical model validation.

The resonant gyroscopes were designed analytically in order to evaluate the sensor performances and investigate the nonlinear dynamics of the resonators, as well as using ANSYS finite elements simulations in order to check the frequency matching and the robustness of the devices to undergo high out of plane accelerations.

Figure 7.19 shows a particular design of a dual mass resonant gyroscope in which the frequencies in the actuation and sensing axis have been matched around 90 KHz using FE simulations. The resonator frequency is very high ($10MHz$) compared to the proof mass frequency ($\Delta > 11$) which ensure the stability of the periodic Mathieu resonator for a dynamic range $DR = \pm 200\,°/s$. The predicted resolution of the device is about $6.10^{-4}\,°/s$ when the resonators are driven at their critical amplitude ($A_c = 6\,nm$) which demonstrate the high sensitivity of the resonant sensing. Note that the whole device here is supposed to be at the same thickness ($2\,\mu m$). Then, further optimization can be done using the M&NEMS concept including resonators much thinner than the other parts of the resonant gyroscope.

Ultimate improvements could be reached by driving the resonators beyond their critical amplitudes while keeping a linear behaviour. Hence, the importance of designing resonant gyroscope for which the nonlinearities can be balanced via an electrostatic mechanism (Optimal polarization voltage).

Power consumption	
Actuation	4 V dc and 0.2 V ac
Sensing	1 V dc and 10 mV ac

Temperature	
Range	- 40 °C --- 85 °C
Thermal sensitivity	10^{-2} Hz/K

Fabrication tolerances	
Fabrication tolerances (resonators)	10 ppm
Differential bias	5.10^{-2} °/s

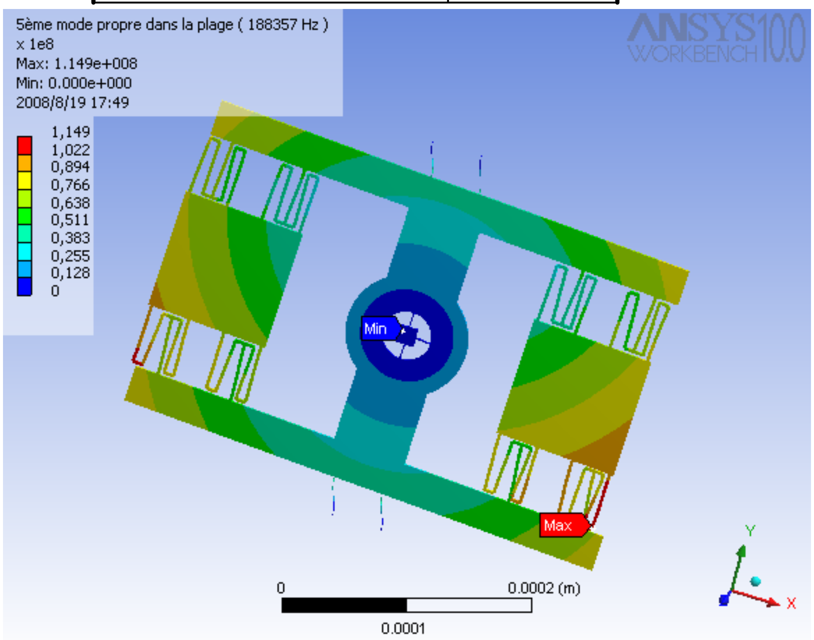

Actuation	
Frequency	90 KHz
Quality factor	10^4
Displacement at resonance	1 µm
Velocity at resonance	0.6 m.s^{-1}
Electrostatic force	2 nN
Proof mass noise	4.10^{-20} Hz²/Hz

Sensing	
Frequency	10 MHz
Quality factor	5200
Critical amplitude	6 nm
Displacement at resonance	4.5 nm
Quality factor in sensing mode	250
Lever mechanism gain	50
Coriolis Force at resonance	2.5 µN
ΔC	7.5 aF
Overall frequency noise	$2.9.10^{-24}$ Hz²/Hz
Band width	100 Hz
Scale factor	4 KHz/°/s
Resolution	6.10^{-4} °/s
Dynamic range	±200 °/s
Resolution class	10^{-5}
Nonlinearity	1 %

Figure 7.19: Design and specifications of a dual mass resonant gyroscope.

The analytical studies performed to design the resonant gyroscope described in Figure 7.15 showed that the sensor can reach an impressive resolution about $2.10^{-5}\,°/s < 0.1\,°/hr$ when its sensing parts (the resonators) are thinner than the drive parts (proof masses, comb drive actuators, springs...) combined with a possible hysteresis suppression allowing the resonators to vibrate linearly at large amplitudes. This can potentially unlock some limitations with current technology in micro gyroscope for typical high performance applications such as tactical weapon guidance as shown in table 7.2.

Applications	Resolution required (°/hr)	Current capability of MEMS technology to provide this resolution
Inertial navigation	0.01 – 0.001	Impossible
Tactical weapon guidance	0.1 – 1	Impossible
Heading and altitude reference	0.1 - 10	Challenging

Table 7.2: Resolution requirement of gyroscope for typical high performance application [Giessibl 2003].

7.8 Fabrication

The M&NEMS process flow with the 6 mask levels (see subsection 4.2.3 for details) was used in the 8 silicon platform of the LETI in order to fabricate several resonant gyroscope structures including simple mass, dual-mass and decoupled gyroscopes. For that proof of concept device, the resonator was limited to $0.25 \times 0.5\,\mu m^2$ section, and the MEMS thickness was reduced to $2\,\mu m$ thick. The total area of the dual-mass gyroscope is less than $0.15\,mm^2$. SEM images of z-axis M&NEMS resonant gyroscopes are shown in figures 7.20 and 7.21.

Some fabricated resonant gyroscope involve self-test comb drive actuators in order to simulate a Coriolis force which can be used also for electrostatic trimming in order to control the frequency matching between the drive and the sense mode. Dual mass resonant gyroscopes fully symmetric were fabricated for testing the cancellation of the common mode acceleration. For these structures, the flexural pivot is located at the center in order to reduce the sensor bias.

7.9 Experimental validation

7.9.1 Low axial load frequency

The ratio between the actuation and the sensing frequencies is assumed to be $\Delta < 0.25$. In this configuration, the resonant gyroscope behaves as a resonant accelerometer, since the periodic axial load due to the Coriolis force can be considered quasi-static with respect to the resonator dynamic.

The resonators described in tables 6.1 and 6.2 are then used for the qualitative as well as quantitative validation of the model. Indeed, a 2-port Mathieu resonator in this case is equivalent to a 2-port normal resonator. Therefore, the model expanded in the previous chapter (see section 4.5) still valid for a resonant gyroscope when $\Delta < 0.25$ and out of quasiperiodicity.

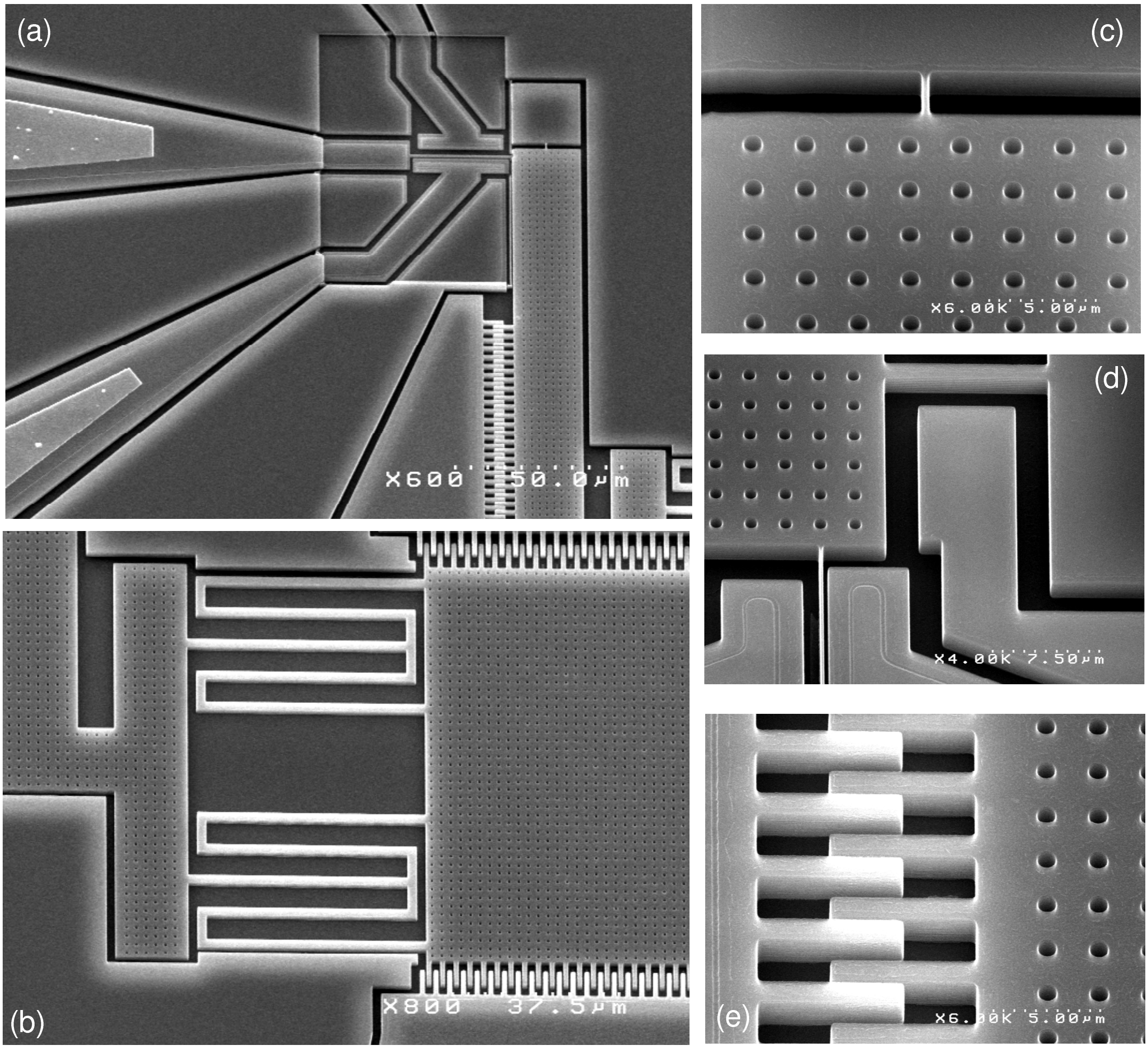

Figure 7.20: SEM images of a M&NEMS simple mass resonant gyroscope. In (a), the lever mechanism and self-test comb drive actuators to simulate a Coriolis force which can be used also for electrostatic trimming in order to control the frequency matching between the drive and the sense mode. In (b) MEMS level: actuation part (proof mass + flexures). (c): Flexural pivot of the lever mechanism. (d) NEMS level: resonator. (e). Self-test comb drive actuators.

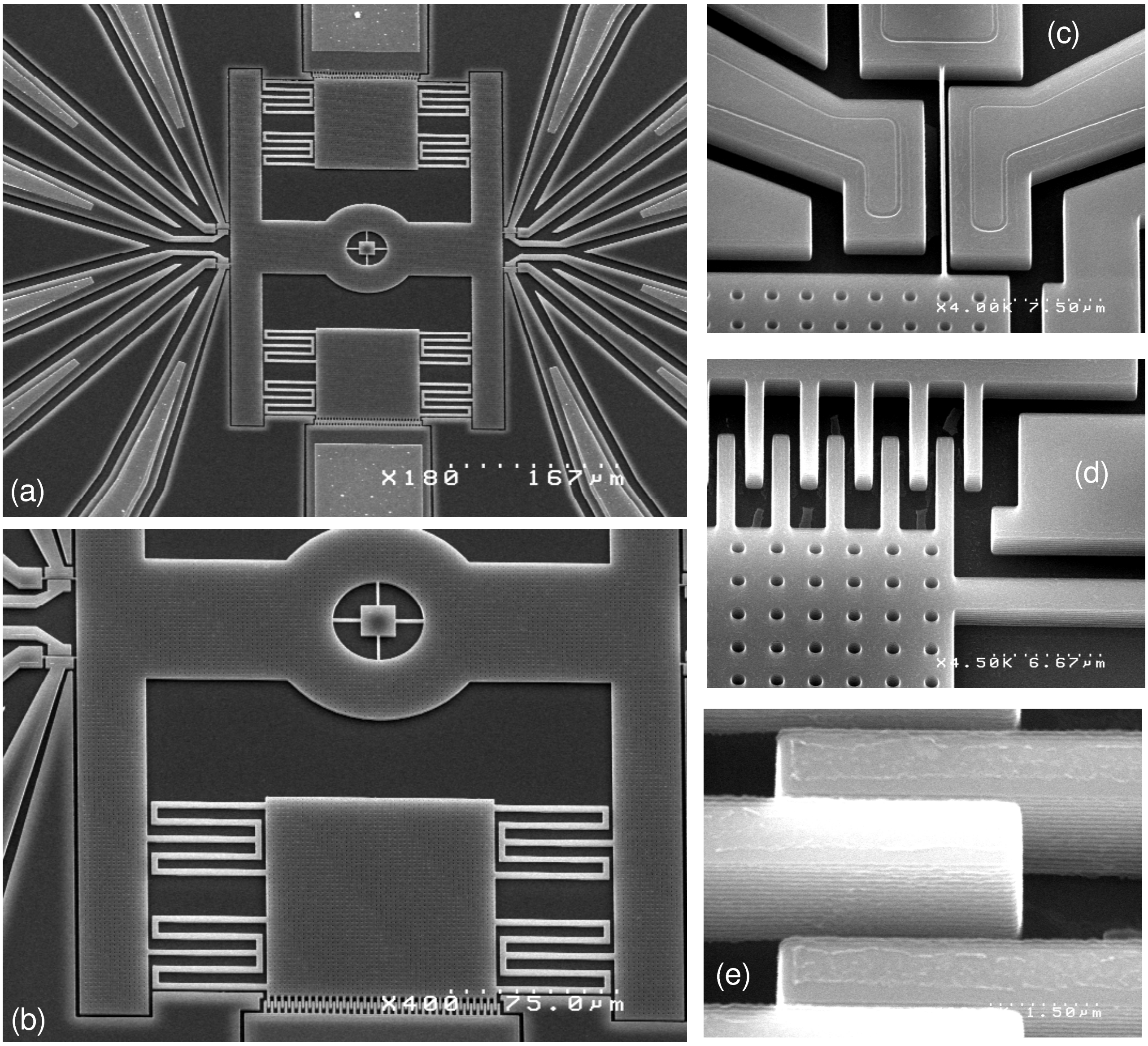

Figure 7.21: SEM images of a M&NEMS dual mass resonant gyroscope. (a): The dual mass fully symmetric structure (the flexural pivot is located at the center of the gyroscope in order to reduce the sensor bias). The two masses are actuated anti-phase to each others for the cancellation of the common mode acceleration. (b): Zoom on the actuation part (proof mass + flexures). (c): Zoom on the sensing part (the resonator). (d): Comb drive actuators for the proof mass actuation. (e): Zoom on the comb drive actuators showing a $0.5\mu m$ gap between the fingers.

7.9.2 High axial load frequency

Now, we consider the case for which the frequency ratio $\Delta > 0.25$. In this configuration, although the stiffness of the resonator is varying slowly with respect to the global dynamic due to the time varying axial load, the Coriolis force can not be considered as quasi-static. Indeed, the natural frequency of the Mathieu resonator can be modulated by an axial load at a comparable frequency which can significantly limit the dynamic range of the resonant gyroscope.

For experimental investigations of gyroscope performances, the device must be tested on a rate table in a portable vacuum chamber. Nevertheless, one can use the test self electrodes (see Figure 7.20) to simulate a Coriolis force and its equivalent in rotation rate for the considered device. This implies the use of a vacuum chamber containing at least six probes.

For simplicity and as a first we chose the use of the superharmonic excitation of order half the natural frequency of the sensing part to simulate Mathieu resonator for which $\Delta = 0.5$. This implies the use of a $2f$ measurement set-up. Moreover, the sensitive parts of the different fabricated gyroscopes correspond to the resonators of table 6.1 and 6.2. Their natural frequency, being very high, down-mixing technique has been then used in order to avoid the parasitic impedance issue. Note that the multiple time scales method has been used in order to incorporate the superharmonic resonance effect in the fast dynamics, since the Mathieu resonator is actuated simultaneously under primary and secondary resonances.

Unlike the 2ω down-mixing set-up that has been used in the previous experiments (see section 6.2), here, the actuation voltage of the resonator includes a polarization voltage in order to generate a parametric excitation at the frequency $\frac{\omega_n}{2}$. A schematic of the downmixing setup used for the electrical characterization is described in Figure 7.22.

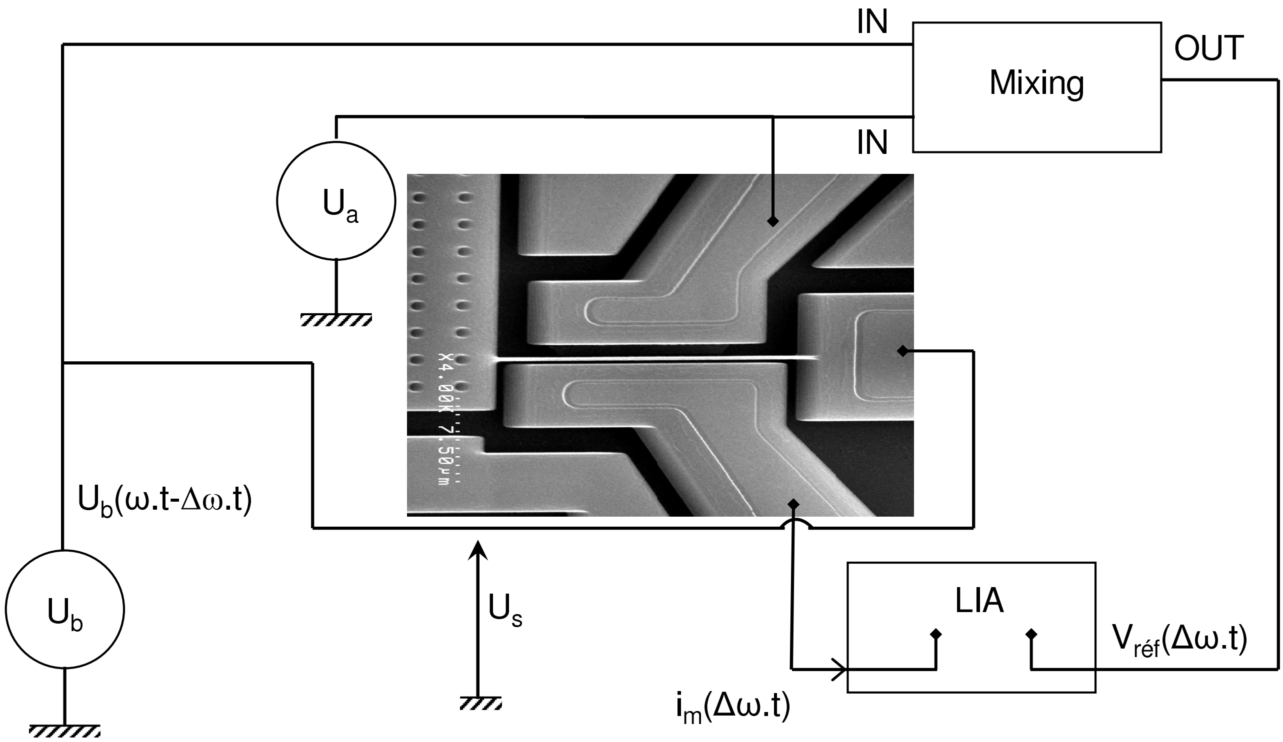

Figure 7.22: Schematic of a downmixing setup.

The resonator RN_5 was placed in a vacuum chamber and the experiments were at room temperature. The bias voltage is fixed around $500mV$, then we vary the DC voltage while keeping $V_{ac} = V_{dc}$. This ensures a parametric stiffness much higher than the negative linear stiffness and then the effect a time-varying load is not covered by the static spring softening effect.

Figure 7.23 shows the variation of the resonator (RN_5) frequency response with respect to the DC voltage. Remarkably, the resonator displays a hardening behavior which corresponds to the predicted dynamics using the analytical model. More specifically, when the DC voltage is increased for an equivalent AC voltage, the parametric linear negative stiffness due to the electrostatic nonlinearities becomes higher.

Furthermore, the quality factor decreases due to the ohmic losses [Sazonova 2006]. Therefore, one waits a relaxation of the hardening behavior as the nonlinear negative stiffness increases and the quality factor too (referring to the critical amplitude close-form solution in Equation (5.10)) which is not the case. This can be explained by the fact that the static negative stiffness is always less important than the time-varying one for the chosen configuration. The parametric perturbation is strong enough and equivalent to a negative rotation rate which amplifies significantly the amplitude. Indeed, the symmetry between negative and positive stress due to the Coriolis load is certainly broken for $V_{dc} = 5V$ (see Figure 7.12) as the corresponding Coriolis force is about $-1\mu N$ equivalent to $\theta = -400°/s$ for the simple mass resonant gyroscope with the parameters that have been used for the analytical analysis.

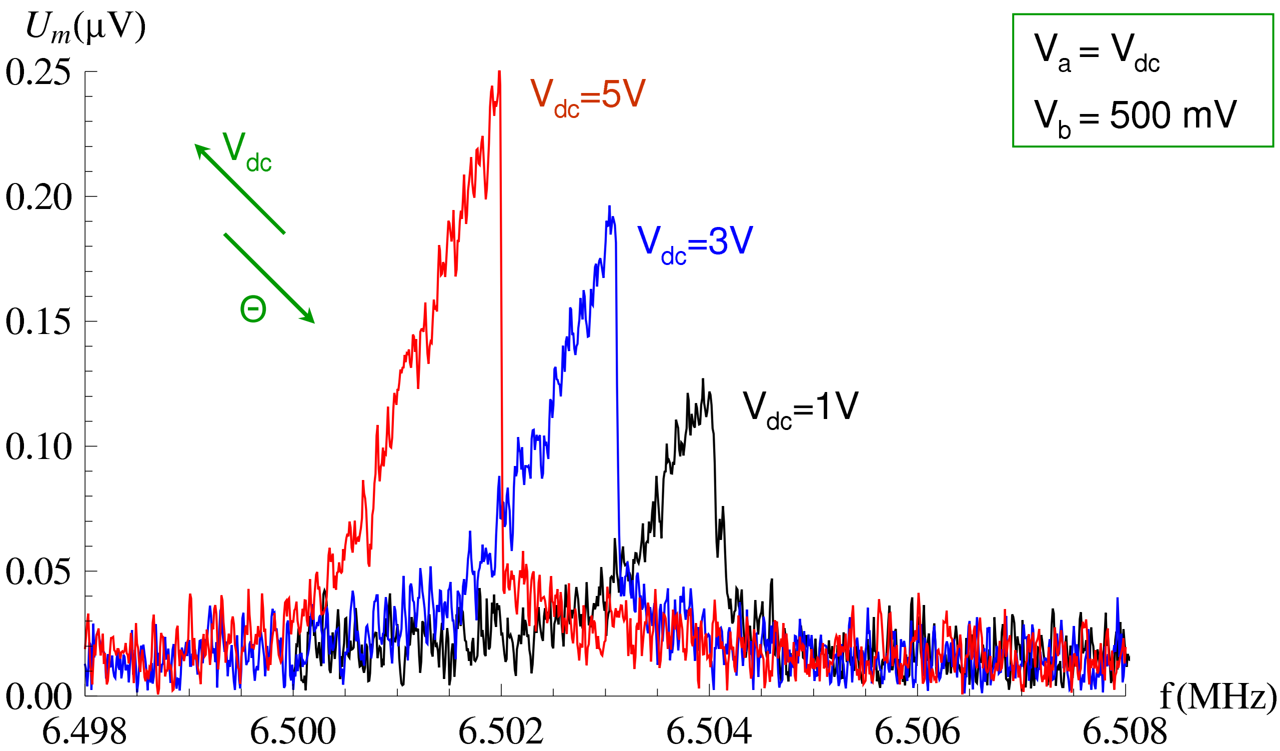

Figure 7.23: Measured hardening nonlinear resonance peaks of resonator RN_5 using 2ω downmixing characterization for several actuation voltages.

7.10 Summary

An implementation of a microelectromechanical resonant gyroscope has been described. Particularly, the nonlinear dynamics of the sensitive part (Mathieu resonator) has been modeled using the Galerkin method coupled with a perturbation technique and under few assumptions that lead to steady-state periodic motions. The relatively simple dynamic model of the nonlinear Mathieu resonator utilized here, is able to predict the measured resonator response for various parameter settings qualitatively and in many cases even quantitatively. Characteristic nonlinear dynamic steady-state behavior is very well predicted by the model. Therefore, it represents a good first step in the modeling process and a suitable starting point for understanding and predicting the dynamic behavior of resonant M&NEMS gyroscopes. The resulting benefits include nonlinear dynamics control, improved scale factor stability over micromechanical gyroscopes utilizing open-loop displacement sensing, large dynamic range and high resolution.

In order to provide some design rules, the variation of the gyroscope sensitivity with respect to the ratio between the proof mass and the resonator frequencies was investigated. The analytical parametric studies showed that in the resonator linear or slightly nonlinear regimes, a frequency ratio $\Delta = 0.25$ provides the greatest scale factor. However, once the resonator dynamics becomes strongly nonlinear (large oscillations beyond the critical amplitude), the sensitivity is significantly reduced if the resonator frequency is not at least an order of magnitude higher than that of the proof mass ($\Delta \leq 0.1$).

Moreover, The M&NEMS technology showed a great potential of performance optimization for angular rate sensors due to the maximization of the resonator sensitivity when it is scaled down to NEMS size while the drive parts of the sensor are set at the MEMS level in order to conserve large Coriolis forces. Besides, several resonant M&NEMS gyroscope were designed and fabricated in order to validate the analytical model as well as the technological choices. An impressive resolution $< 0.1\,^{\circ}/hr$ analytically predicted for a particular dual mass M&NEMS gyroscope fully symmetric with its sensing resonators driven linearly at large amplitudes beyond their open-loop stability limit. If reached experimentally, such a performance could break down the limitation of the current conventional MEMS gyroscopes for typical high performances applications such as tactical weapon guidance. Nevertheless, this demands that all the other parameters (temperature, frequencies, pressure…) are well controlled when the resonators are embedded in the feedback loops of oscillator circuits which can potentially complexify the sensor electronics.

Due to the unavailability of specific test equipments at LETI for a complete gyroscope characterization which is quite complex, further experimental measurements have not been performed. This will be the goal of future work which will also incorporate improvement and extension of the numerical model in order to obtain better predictions. Furthermore, oscillator design aspects and the effect of different resonator layouts will be addressed, since the long-term goal of these investigations is to derive guidelines for optimal resonator layout and to predict the performance of Mathieu resonators in oscillator circuits, based on more enhanced analytical or numerical models.

Chapter 8

Resonant gas and mass sensors

Contents

8.1 Introduction **187**

8.2 Resonant nanocantilever based on electrostatic detection **188**

8.2.1 Equation of motion 189

8.2.2 Normalization 190

8.2.3 Solving 190

8.2.4 Critical amplitude 192

8.2.5 Fabrication: Monolithic integration of nanocantilevers with CMOS 195

8.2.6 Electrical characterization of nanocantilever beams 197

8.3 Resonant nanocantilever based on piezoresistive detection **201**

8.3.1 Device description 201

8.3.2 Transduction 202

8.3.3 Equation of motion 203

8.3.4 Normalization 203

8.3.5 Solving 204

8.3.6 The critical amplitude 208

8.3.7 Fabrication 209

8.3.8 Electrical characterization 210

8.3.9 Mass resolution enhancement 217

8.4 Summary **219**

8.1 Introduction

Mass and gas sensors employing micro/nanoscale cantilevers have been studied for applications in various research fields such as biochemistry, environment, and biomedicine due to their extreme sensitivity [Gupta 2004, Battiston 2001, Ilic 2001a, Jensenius 2000, Lavrik 2003, Ono 2003, Ekinci 2004a, Forsen 2005, Yang 2006]. In a simple harmonic resonance mode, these sensors operate on the basis of the fundamental resonance frequency shifts in response to mass changes. A strong motivation for scaling down cantilevers is to reduce the effect of thermomechanical noise [Rugar 1991], thereby improving the resolution of resonant sensors and also enhancing their response time. This development has increased the sensitivity limit up to the extent that researchers can now visualize the counting of molecules [Feng 2008, Jensen 2008]. With the ability of high throughput analysis of analytes and ultra sensitive detection, NEMS cantilevers potentially hold tremendous promise for the next generation of miniaturized and highly sensitive sensors. Recent accomplishments obtained by these mass sensors are that femtogram order mass detection has been achieved under ambient pressure and temperature using a bimetal silicon cantilever [Lavrik 2003] and higher mass resolutions of $10^{-18} - 10^{-21}\, g$ have been achieved in vacuum and in ultrahigh-vacuum pressure at cryogenic temperature [Ono 2003, Ekinci 2004a, Yang 2006].

However scaling the dimensions of a resonator down to the NEMS range makes nonlinearities quickly reachable and consequently the linear dynamic range is extremely reduced [Postma 2005]. In chapter 5, we demonstrate the drastic fundamental limit of the dynamic range due to the mechanical nonlinearities in clamped-clamped NEMS resonators and we provided a way to enhance the dynamic range of these resonators by hysteresis.

NEMS cantilevers are promising candidates for the new generation of physical, chemical and biological sensing. One reason for this is that they are commonly said to have a very large linear dynamic range compared to clamped-clamped nanoresonators, without any formal proof, quantitative comparison, or thorough study. Models previously used in chapter 4 for doubly clamped beams cannot be easily adapted to cantilevers: indeed, their real specificity comes from their complex nonlinear dynamics including geometric and inertial nonlinearities. This partly explains why so little has been done about nonlinear dynamics of electrostatically actuated cantilevers.

In the past, the non linear dynamics of cantilevers was analytically modelled [Mahmoodi 2007, Alhazza 2008] using perturbation techniques and numerically simulated using nonlinear shooting method [Banerjee 2008] for a piezoelectric actuation. Chowdhury et al [Chowdhury 2005] provided a close-form model for the static pull-in voltage of electrostatically actuated cantilevers without including the geometric nonlinearities. Ahmadian et al [Ahmadian 2009] employed a finite element formulation for the dynamic analysis of nonlinear Euler cantilevers electrostatically actuated including main sources of nonlinearities, but the resonant case has not been considered. Liu et al [Liu 2004] simulated an electrostatically controlled cantilever microbeam and qualitatively showed period-doubling bifurcation, chaos, Hopf bifurcation and strange attractors using the Poincaré map method which are hardly exploitable by MEMS and NEMS designers.

In this chapter, the nonlinear dynamics of nanocantilever beams is modeled including both geometric nonlinearities and nonlinear electrostatic terms up to the fifth order enabling the capture of the mixed behavior (see section 5.4). Close-form solutions of the critical amplitude, respectively under mechanical nonlinearities and electrostatic nonlinearities are deduced in order to compare the dynamic ranges of nanocantilevers and clamped-clamped nanobeams. Moreover, the optimal DC driving voltage expression in function of the design parameters, is provided. It is a quick tool for NEMS designers that can be used for the enhancement of resonant sensors performances based on the compensation of nonlinearities.

The model is purely analytical based on the Galerkin discretization method coupled with a perturbation technique; the resonant case under primary excitation has been considered. The model is compared with the experimentally measured frequency responses of electrostatically actuated nanocantilevers that were driven beyond their linear dynamic range and they show good agreement.

8.2 Resonant nanocantilever based on electrostatic detection

In order to develop a model for micro/nanocantilever beams, a slender uniform flexible beam is considered as shown in Figure 8.1. The beam is initially straight and it is clamped at one end and free at the other end, subject to viscous damping with a coefficient $\tilde{c}$ per unit length and actuated by an electric load $v(t) = Vdc + Vac\cos(\tilde{\Omega}\tilde{t})$, where Vdc is the DC polarization voltage, Vac is the amplitude of the applied AC voltage, $\tilde{t}$ is time and $\tilde{\Omega}$ is the excitation frequency. In addition, the beam follows the Euler-Bernoulli beam theory, where shear deformation and rotary inertia terms are negligible.

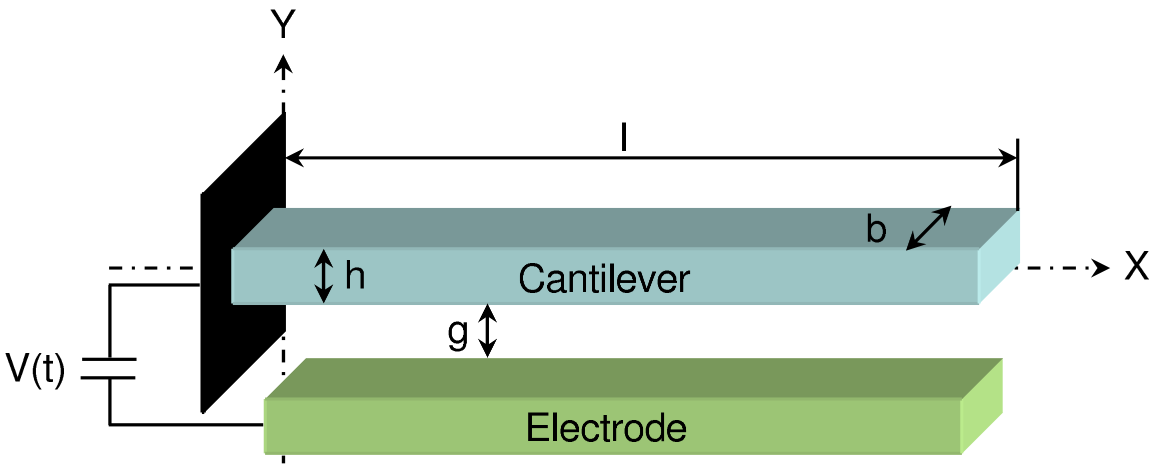

Figure 8.1: Schema of an electrostatically actuated nanocantilever

8.2.1 Equation of motion

We follow a variational approach, based on the extended Hamilton principle and used by Crespo da Silva and Glynn [Silva 1978a, Silva 1978b] and Crespo da Silva [Silva 1988a, Silva 1988b]. In order to derive the nonlinear equation of motion describing the flexural vibration of a cantilever beam electrostatically actuated, Equations (3.9) and (refCSG2) in chapter 3 are reduced to:

$$EI\left\{\tilde{w}'''' + \left[\tilde{w}'\left(\tilde{w}'\tilde{w}''\right)'\right]'\right\} + \rho bh\ddot{\tilde{w}} + \tilde{c}\dot{\tilde{w}} =$$
$$-\frac{1}{2}\rho bh\left\{\tilde{w}'\int_l^s\left[\frac{\partial^2}{\partial\tilde{t}^2}\int_0^{s_1}(\tilde{w}')^2 ds_2\right]ds_1\right\}'$$
$$+\frac{1}{2}\varepsilon\frac{C_n b\left[V_{dc} + V_{ac}\cos(\tilde{\Omega}\tilde{t})\right]^2}{(g-\tilde{w})^2} \tag{8.1}$$

where primes and dots denote respectively the partial differentiation with respect to the arclength s and to the time $\tilde{t}$. $\tilde{w}$ is the beam bending deflection, E and I are the Young's modulus and geometrical moment of inertia of the cross section. l and b are the length and width of the nanobeam, ρ is the material density, h is the nanobeam thickness in the direction of vibration, g is the capacitor gap width, and ε is the dielectric constant of the gap medium.

The first term in the left-hand side of Equation (8.1) is due to the nonlinear expression for the curvature of the beam, while the first term in the right-hand side, which involves a double time derivative, is the nonlinear inertial term. The last term in Equation (8.1) represents an approximation of the electrostatic force assuming a complete overlap of the area of the nanobeam and the stationary electrode where C_n is the fringing field coefficient computed using an existing analytical model [Nishiyama 1990]. The boundary conditions are:

$$\tilde{w}(0,\tilde{t}) = \tilde{w}'(0,\tilde{t}) = \tilde{w}''(l,\tilde{t}) = \tilde{w}'''(l,\tilde{t}) = 0 \tag{8.2}$$

8.2.2 Normalization

For convenience and equation simplicity, we introduce the nondimensional variables:

$$w = \frac{\tilde{w}}{g}, \ \ x = \frac{s}{l}, \ \ t = \frac{\tilde{t}}{\tau} \tag{8.3}$$

where $\tau = \frac{2l^2}{h}\sqrt{\frac{3\rho}{E}}$. Substituting Equation (8.3) into Equations (8.1) and (8.2), we obtain:

$$\begin{aligned} w^{iv} + \ddot{w} + c\dot{w} + \delta_1 \left[w' \left(w' w'' \right)' \right]' = \\ -\delta_2 \left\{ w' \int_1^x \left[\frac{\partial^2}{\partial t^2} \int_0^{x_1} (w')^2 dx_2 \right] dx_1 \right\}' \\ +\delta_3 \frac{V_{dc}}{V_{ac}} \frac{\left[1 + \frac{V_{ac}}{V_{dc}} \cos(\Omega t) \right]^2}{(1-w)^2} \end{aligned} \tag{8.4}$$

$$w(0,t) = w'(0,t) = w''(1,t) = w'''(1,t) = 0 \tag{8.5}$$

where primes and dots denote respectively the partial differentiation with respect to the dimensionless arclength x and to the dimensionless time t. The parameters appearing in Equations (8.4) are:

$$\begin{aligned} c = \frac{\tilde{c} l^4}{EI\tau}, \ \ \delta_1 = \left[\frac{g}{l} \right]^2, \ \ \delta_2 = \frac{1}{2} \left[\frac{g}{l} \right]^2 \\ \delta_3 = 6 V_{ac} V_{dc} \frac{\varepsilon l^4}{E h^3 g^3}, \ \ \Omega = \tilde{\Omega}\tau \end{aligned} \tag{8.6}$$

8.2.3 Solving

The beam total displacement $w(x,t)$ can be written as a sum of a static dc displacement $w_s(x)$ and a time-varying ac displacement $w_d(x,t)$. However, for our devices and under low pressure, the measured quality factors Q are in the range of $10^3 - 10^4$ which makes the static deflection negligible with respect to the dynamic deflection.

A reduced-order model is generated by modal decomposition transforming Equations (8.4) into a multi-degree-of-freedom system consisting of ordinary differential equations in time. We use the undamped linear mode shapes of the cantilever as basis functions in the Galerkin procedure. To this end, we express the deflection as :

$$w(x,t) = \sum_{k=1}^{n} a_k(t) \phi_k(x) \tag{8.7}$$

where $a_k(t)$ is the k^{th} generalized coordinate and $\phi_k(x)$ is the k^{th} linear undamped mode shape of the straight microbeam, normalized such that $\int_0^1 \phi_k \phi_j = \delta_{kj}$ where $\delta_{kj} = 0$ if $k \neq j$ and $\delta_{kj} = 1$ if $k = j$. The linear undamped mode shapes $\phi_k(x)$ are governed by:

$$\frac{d^4 \phi_k(x)}{dx^4} = \lambda_k^2 \phi_k(x) \tag{8.8}$$

$$\phi_k(0) = \phi_k'(0) = \phi_k''(1) = \phi_k'''(1) \tag{8.9}$$

Here, λ_k is the k^{th} natural frequency of the cantilever. The electrostatic force in Equation (8.4) is expanded in a fifth order Taylor series, again, to capture 5 possible amplitudes for a given frequency in the mixed behavior [Kacem 2009a]. Then, Equation (8.7) is substituted into the resulting equation, Equation (8.8) is used to eliminate $\dfrac{d^4\phi_k(x)}{dx^4}$, and the outcome is multiplied by ϕ_k and integrated from $x = 0$ to 1 for $k \in [1, n] \cap \mathbb{N}$. Thus, a system of coupled ordinary differential equations in time is obtained.

We did not multiply Equation (8.4) by the denominator of the electrostatic force as previously done in the case of clamped-clamped beam resonators (see chapter 4) for the following reasons:

- A nonlinear operator such as $w^2 \frac{\partial^4 w}{\partial x^4}$ is not artificially created and consequently the orthogonally with respect to the linear undamped mode shapes is not lost. Moreover, this ensures a low nonlinear coupling between the different modes.

- The mixed behavior is less pronounced in resonant cantilevers compared to clamped-clamped resonators since its initiation amplitude is relatively high and close to pull-in. Consequently, the nonlinearities higher than the fifth order are not physically interesting in the case of electrostatically actuated cantilevers.

The DC voltage, which is generally at least ten times higher than the AC voltage, makes the second harmonic $\cos(2\Omega t)$ negligible with respect to the first harmonic $\cos(\Omega t)$. Also, assuming that the first mode is the dominant mode of the system, the study can be restricted to the case $n = 1$. Then, we obtain:

$$\begin{aligned}
40.44\delta_1 a_1^3 + 0.39\frac{V_{ac}}{V_{dc}}\delta_3 + 0.78\frac{V_{dc}}{V_{ac}}\delta_3 - \frac{V_{ac}}{V_{dc}}\delta_3 a_1 - 2\frac{V_{dc}}{V_{ac}}\delta_3 a_1 \\
+2.22\frac{V_{ac}}{V_{dc}}\delta_3 a_1^2 + 4.43\frac{V_{dc}}{V_{ac}}\delta_3 a_1^2 - 4.7\frac{V_{ac}}{V_{dc}}\delta_3 a_1^3 - 9.4\frac{V_{dc}}{V_{ac}}2\delta_3 a_1^3 \\
+9.75\frac{V_{ac}}{V_{dc}}\delta_3 a_1^4 + 19.5\frac{V_{dc}}{V_{ac}}\delta_3 a_1^4 - 20\frac{V_{ac}}{V_{dc}}\delta_3 a_1^5 - 40\frac{V_{dc}}{V_{ac}}\delta_3 a_1^5 \\
+a_1\lambda_1^2 + c\dot{a}_1 + 9.2\delta_2 a_1 \dot{a}_1^2 + \ddot{a}_1 + 9.2a_1^2\delta_2\ddot{a}_1 \\
+1.56\delta_3\cos(\Omega t) - 4\delta_3 a_1\cos(\Omega t) \\
+9\delta_3 a_1^2\cos(\Omega t) - 19\delta_3 a_1^3\cos(\Omega t) \\
+39\delta_3 a_1^4\cos(\Omega t) - 80\delta_3 a_1^5\cos(\Omega t) = 0
\end{aligned} \tag{8.10}$$

We recognize in the Equation (8.10) some canonical nonlinear terms such as the Duffing nonlinearity as well as the parametric excitation (Mathieu term). However, the presence of other high order nonlinearities makes the described system in Figure 8.1 as a forced nonlinear cantilever under multifrequency parametric excitation. This kind of equation is not so frequently treated in the literature: it includes terms coming from mechanical and electrostatic nonlinearities.

To analyse the equation of motion (8.10), it is convenient to invoke perturbation techniques which work well with the assumptions of "small" excitation and damping, typically valid in NEMS resonators. To simplify the perturbation approach, in this case the averaging method, a standard constrained coordinate transformation is introduced, as given by:

$$a_1 = A(t)\cos[\Omega t + \beta(t)] \tag{8.11}$$

$$\dot{a}_1 = -A(t)\Omega\sin[\Omega t + \beta(t)] \tag{8.12}$$

$$\ddot{a}_1 = -A(t)\Omega^2\cos[\Omega t + \beta(t)] \tag{8.13}$$

$A(t)$ and $\beta(t)$ are slowly time-varying functions. In addition, since near-resonant behavior is the principal operating regime of the proposed system, a detuning parameter σ is introduced, as given by:

$$\Omega = \omega_1 + \xi\sigma \tag{8.14}$$

where $\omega_1 = \sqrt{\lambda_1^2 - \frac{V_{ac}}{V_{dc}}\delta_3 - 2\frac{V_{dc}}{V_{ac}}\delta_3}$ and ξ is the small nondimensional bookkeeping parameter. Separating the resulting equations and averaging them over the period $\frac{2\pi}{\Omega}$ in the t-domain results in the system's averaged equations in terms of amplitude A and phase β given by:

$$\dot{A} = \frac{\xi\delta_3 \sin\beta}{\omega_1}\left(0.78 + 1.11A^2 + 2.44A^4\right) - \frac{\xi c}{2}A + O(\xi^2) \tag{8.15}$$

$$\begin{aligned}\dot{\beta} &= \sigma\xi - \xi\frac{\delta_3\cos\beta}{\omega_1}\left(\frac{0.78}{A} + 3.32A + 12.19A^3\right)\\ &+\xi\frac{A^4\delta_3}{\omega_1}\left(12.51\frac{V_{dc}}{V_{ac}} - 6.25\frac{V_{ac}}{V_{dc}}\right) - \xi\frac{15.16A^2\delta_1}{\omega_1}\\ &+\frac{\xi\delta_3 A^2}{\omega_1}\left(1.76\frac{V_{ac}}{V_{dc}} + 3.52\frac{V_{dc}}{V_{ac}}\right) + 2.3\xi A^2\delta_2\omega_1 + O(\xi^2)\end{aligned} \tag{8.16}$$

The steady-state motions occur when $\dot{A} = \dot{\beta} = 0$, which corresponds to the singular points of Equations (8.15) and (8.16).Thus, the frequency response equation can be written in its parametric form $A = K_1(\beta), \Omega = K_2(\beta)$ as a function of the phase β. This set of two equations is easily implementable in Matlab or Mathematica. This ability makes the model suitable for NEMS designers as a quick tool to optimize the resonant sensors performance.

For a sake of clarity, using Equations (8.15) and (8.16), the frequency response equation can be written in its implicit form as

$$1 - \frac{\left\{15.2A^3\delta_1 + \Lambda_1(A) + \Lambda_2(A,\Omega)\right\}^2}{\left(0.78 + 1.11A^2 + 2.44A^4\right)^2 {\delta_3}^2} = \frac{(c\omega_1 A)^2}{4\left(0.78 + 1.11A^2 + 2.44A^4\right)^2 {\delta_3}^2} \tag{8.17}$$

where $\Lambda_1(A)$ and $\Lambda_2(A,\Omega)$ are given by:

$$\Lambda_1(A) = \left(-1.8 - 6.2A^2\right)\frac{V_{ac}}{V_{dc}}\delta_3 A^3 + \left(-3.5 - 12.5A^2\right)\frac{V_{dc}}{V_{ac}}\delta_3 A^3 \tag{8.18}$$

$$\Lambda_2(A,\Omega) = A\omega_1\left(-\Omega + \left(1 - 2.3A^2\delta_2\right)\omega_1\right) \tag{8.19}$$

The plots of Figure 8.2 were carried out with the following set of parameters: $l = 12.5\mu m$, $h = 300nm$, $b = 500nm$ and $V_{dc} = 50V_{ac}$. g and V_{ac} were used for parametric studies. This analytical model enables the capture of all the nonlinear regimes in the resonator dynamics and describes the competition between the mechanical hardening and the electrostatic softening behaviors. In addition, the model permits the optimization of the resonator design by tuning the geometrical parameters in order to cancel out nonlinearities as shown in Figure 8.2 for $g = 1.8\mu m$, $V_{dc} = 5V$ and $Q = \rho bhl\frac{\omega_1}{\tau\tilde{c}} = 10^4$ (black curve). The obtained linear behavior enhances the detection limit of NEMS resonant sensors.

8.2.4 Critical amplitude

The critical amplitude is the oscillation amplitude A_c above which bistability occurs. Thus, A_c is the transition amplitude from the linear to the nonlinear behavior.

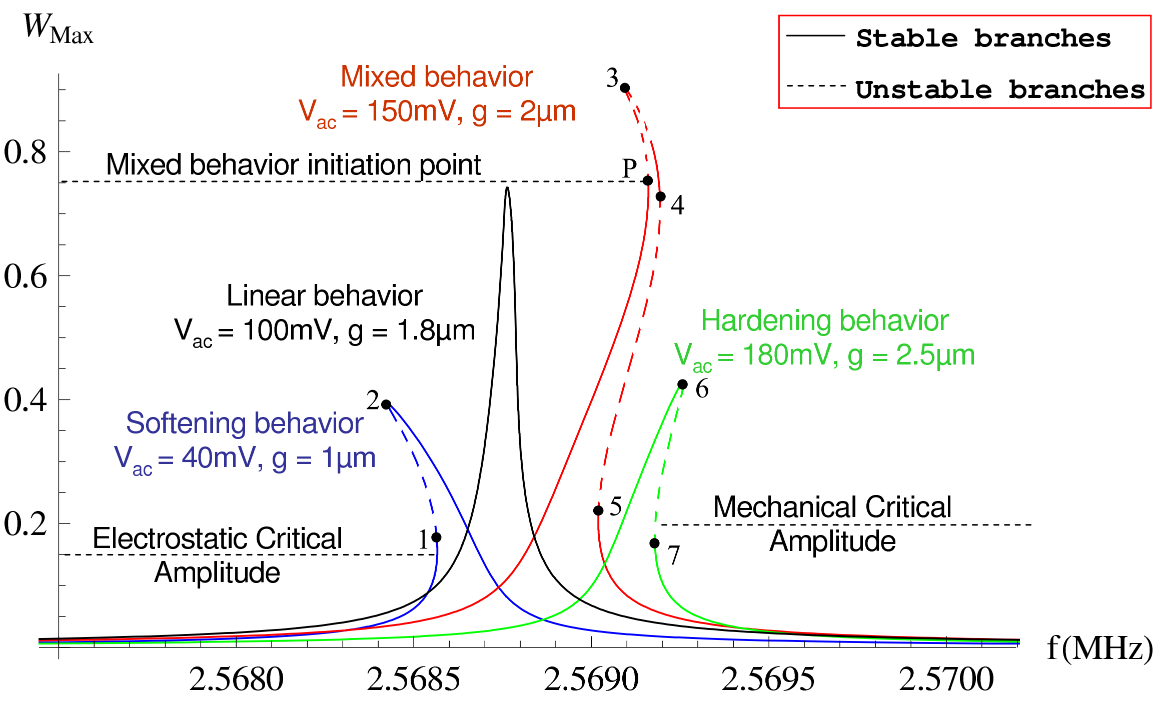

Figure 8.2: Analytical forced frequency responses for $Q = 10^4$ and several values of g and V_{ac}. W_{max} is the beam displacement at its free end normalized by the gap g, A_c is the critical amplitude above which bistability occurs, the different bifurcation points are $\{1, 2, 3, 4, 5, 6, 7, P\}$, the P point characterizes the initiation of the mixed behavior.

8.2.4.1 The mechanical critical amplitude

By using Equations (8.15) and (8.16) when the mechanical nonlinearities (terms proportional to δ_1 or δ_2) are dominating the cantilever dynamics, the parametric form of the frequency response can be written as:

$$\Omega = 1 + \zeta_0 \cot\beta + 0.077\delta_1\zeta_1^2 \sin^2\beta \tag{8.20}$$

$$A = 2\zeta_1 \sin\beta \tag{8.21}$$

where $\zeta_0 = 0.142206c$ and $\zeta_1 = \dfrac{0.445\delta_3}{c}$

Mathematically, A_{cm} is defined as the oscillation amplitude for which the equation $\dfrac{d\Omega}{d\beta} = 0$ (infinite slope) has a unique solution $\beta_{cm} = \dfrac{\pi}{3}$.Thus, the critical electrostatic force is deduced as $\zeta_{1c} = \dfrac{4.456\sqrt{\zeta_0}}{\sqrt{\delta_1}}$.

The critical amplitude A_{cm} is obtained by substituting the critical electrostatic force into Equation (8.21) at the point $\beta = \dfrac{\pi}{2}$ and multiplying by the gap g and the value of the first linear undamped mode shape function ϕ_1 at the free point of the beam. Finally, we obtain the following close-form solution:

$$A_{cm} = 6.3\frac{l}{\sqrt{Q}} \tag{8.22}$$

Remarkably, the mechanical critical amplitude of a resonant cantilever depends only on its length and its quality factor. However, for a clamped-clamped resonator, the mechanical critical amplitude is $A_{cm} = 1.68\dfrac{h}{\sqrt{Q}}$ (details are in chapter 5); it depends only on the resonator width in the direction of vibration and its quality factor. For a given quality factor, the ratio between both critical amplitudes is $R_c = \dfrac{A_{cm}^{c-f}}{A_{cm}^{c-c}} = 3.75\dfrac{l}{h} = 3.75\lambda_e$, where λ_e is the slenderness ratio of the beam. While the resonator is sufficiently slender to validate the Euler-Bernoulli theory, the dynamic range ratio between cantilevers and clamped-clamped beams is very high (> 20) which makes nanocantilevers an advantageous candidate for NEMS resonators-based applications.

8.2.4.2 The electrostatic critical amplitude

In this case, the electrostatic nonlinearities in Equations (8.15) and (8.16) are supposed to be dominating the cantilever dynamics. Considering only nonlinear terms up to the third order, while neglecting the parametric terms and the terms proportional to V_{ac}^2, the form of the frequency response can be written as:

$$\Omega = \frac{c}{2}\cot\beta - \frac{8.64\frac{V_{dc}}{V_{ac}}\delta_3^3}{c^2\omega_1^3}\sin\beta^2 + \frac{6.2}{\omega_1} - \frac{V_{dc}^2\delta_3}{\omega_1} + \frac{\omega_1}{2} \tag{8.23}$$

$$A = \frac{3.13\delta_3}{c\omega_1}\sin\beta \tag{8.24}$$

Mathematically, A_{ce} is defined as the oscillation amplitude for which the equation $\dfrac{d\Omega}{d\beta} = 0$ has a unique solution $\beta_{ce} = -\dfrac{\pi}{3}$.Thus, the critical electrostatic AC voltage is deduced as:

$$V_{ac_c} = 11.2V_{dc}\frac{\delta_3^3}{c^3\omega_1^3} \tag{8.25}$$

The electrostatic critical amplitude A_{ce} is obtained by substituting Equation (8.25) into Equation (8.24) at the point $\beta = \dfrac{\pi}{2}$ and multiplying by the gap g and the value of the first linear undamped mode shape function ϕ_1 at the free point of the beam.

$$A_{ce} = 2 * 10^9 g^{\frac{5}{2}}\frac{h}{l\sqrt{Q}V_{dc}}\left(\frac{7.5 * 10^7 h^2}{l^4} - \frac{3.8 * 10^{-15}V_{dc}^2}{g^3 h}\right)^{\frac{1}{4}} \tag{8.26}$$

Unlike the mechanical critical amplitude (Equation (8.22)), the electrostatic critical amplitude of a resonant cantilever depends on its length l, its width in the direction of vibration h, the gap g, the DC voltage as well as the quality factor Q.

8.2.4.3 Engineering optimization:

It is the first time that close-form expressions of the mechanical and electrostatic critical amplitudes are provided in the case of electrostatically actuated cantilevers. Hence, it constitutes an interesting tool to set the optimal DC drive voltage in order to keep a linear behavior up to and beyond the critical amplitude. The hysteresis suppression is based on the counterbalance between hardening geometric nonlinearities and softening electrostatic nonlinearities.

The mixed behaviour, captured by including the fifth order nonlinear electrostatic terms, is less pronounced than in electrostatically driven clamped-clamped beams. Therefore, while neglecting the fifth order terms, the compensation of cantilevers nonlinearities based on the critical amplitude expressions can be written as

$$A_{c_m} = A_{c_e} \tag{8.27}$$

Thus, assuming a constant quality factor Q, the optimal DC drive voltage is

$$V_{dc_{OP}} = \sqrt{\frac{1}{2}\sqrt{\frac{1.65 * 10^{39} g^{14} h^6}{l^{16}} + \frac{3.2 * 10^{42} g^{10} h^6}{l^{12}}} - \frac{8.1 * 10^{19} g^7 h^3}{l^8}} \tag{8.28}$$

In reality, the overall quality factor may decrease when V_{dc} increases because of the ohmic losses from the electrons moving on and off the resonator due to capacitive coupling to a nearby electrode [Sazonova 2006]. This ohmic contribution adds up to the other sources of dissipation (thermomechanical, anchor losses, adsorption/desorption ...) like $Q^{-1}_{total} = Q^{-1}_{thermo} + Q^{-1}_{anchor} + ... + Q^{-1}_{ohmic}$ and may be expressed as $\left(Q^{-1}_{ohmic} = \frac{1}{\pi\omega}\frac{R(C'V_{dc})^2}{m_{eff}}\right)$ [Sazonova 2006] where C' is the gradient of the capacitance, R is the output resistor and m_{eff} is the effective mass of the considered mode.

Then, the quality factor should be changed to $\frac{1}{Q^{-1}+Q^{-1}_{ohmic}}$, for the electrostatic critical amplitude and thus, the optimal DC drive voltage can be deduced using the same Equation (8.27).

In the particular case of Figure 8.2, the mechanical critical amplitude is $A_{c_m} = 0.2g$. When $g = 1.8\mu m$ and for a quality factor of $Q = 10^4$, the optimal DC drive voltage taking into account the ohmic losses, is around $5V$. At this voltage, as shown by the black curve of Figure 8.2, the peak amplitude is linear and beyond the critical amplitude ($A_{peak} = 0.8g$). Therefore, the enhancement rate of the sensor performance $\left(\frac{A_{peak}}{A_c}\right)$ is around 4.

Remarkably, the electrostatic critical amplitude is independent on the AC voltage. This is due to the use of a low AC voltage compared to the DC voltage for the cantilever actuation which makes the contribution of V_{ac} in the electrostatic Duffing term negligible. Hence, in this configuration, the compensation of the nonlinearities is independent on the AC voltage. This interesting result makes possible the enhancement of the nanocantilever performances up to very high displacements comparable to the gap in the case of an electrostatic actuation by increasing the AC voltage, and limited by an upper bound instability such as the pull-in [Nayfeh 2007].

The aim of this model is to provide practical analytical rules for MEMS and NEMS designers in order to optimize resonant sensor performances. Hence, it is important to check its validity experimentally on nanocantilever electrostatically actuated.

8.2.5 Fabrication: Monolithic integration of nanocantilevers with CMOS

Practical applications of nanocantilever beams benefit much from on-chip signal processing, whereby optimal performance is achieved in case of monolithic integration with CMOS [Verd 2006, Verd 2008, Arcamone 2008, Arcamone 2007]. Such NEMS/CMOS made of silicon combine unique sensing attributes, thanks to the high resonance frequency mobile mechanical part, with the possibility to electrically detect the output signal in enhanced conditions. For those reasons, the nanobeams that are experimentally studied in this work have been monolithically integrated with a dedicated CMOS circuit to enhance the capacitive readout of their resonance ('motional') current. This heterogeneous integration has required a very specific fabrication process described hereafter. More details about the process and the functionality of this NEMS/CMOS system can be found in [Arcamone 2008] and [Arcamone 2007].

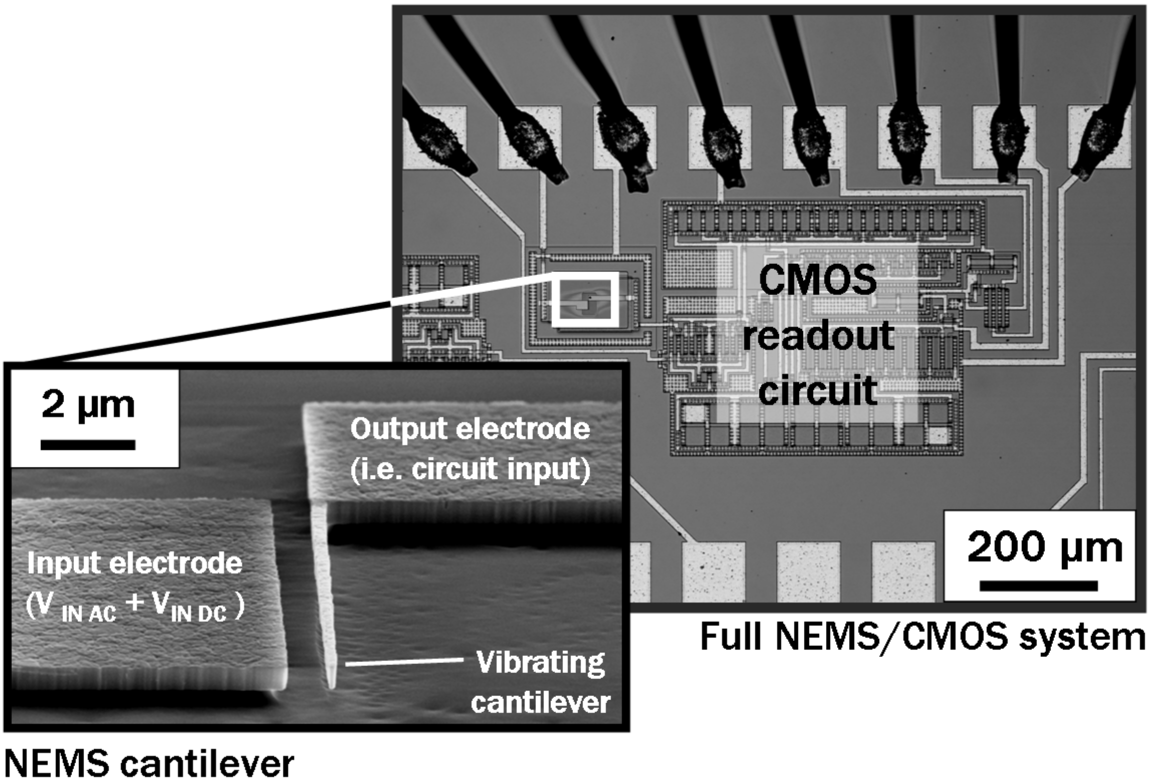

Figure 8.3: Optical picture of the [NEMS resonator / CMOS readout circuit] system. The scanning electron micrograph zooms the cantilever beam itself and its driving electrode.

The cantilevers fabrication process used here has been performed at CNM-IMB (CSIC) in Barcelona (Spain) and at EPFL in Lausanne (Switzerland). It is based on a post-processing approach in which CMOS circuits are first fabricated according to a standard CMOS technology, then NEMS resonators are subsequently patterned by nanostencil lithography (nSL) [van den Boogaart 2004] and fully fabricated. nSL is a shadow-mask based, full-wafer and parallel nanopatterning technique providing a resolution down to 200nm and a high fabrication throughput.

After concluding the fabrication of the CMOS circuits, dedicated areas (located close to each circuit, 1 per circuit) are selectively patterned with an 80nm thick aluminum layer by nSL. The following step is a reactive ion etching (RIE) of silicon that transfers the aluminum patterns to the polysilicon structural layer of the resonators. The last step consists in releasing the resonators and removing the Al mask by a local wet etching based on HF acid. The circuit is robustly protected during this etching by an adequately annealed photoresist layer. This entire process is described in [Arcamone 2008].

CMOS wafers containing each 2000 fully fabricated nanomechanical devices of diverse types have been obtained with that process; all connected to dedicated CMOS circuits for signal interfacing and amplification. Figure 8.3 depicts a fully fabricated nanocantilever beam (optimized for in-plane motion) which is monolithically integrated with its dedicated CMOS readout circuit.

8.2.6 Electrical characterization of nanocantilever beams

Electrostatic actuation and capacitive detection are used for detecting in-plane oscillations (in the MHz range) of those Si nanocantilever resonators. When the resonator is electrostatically driven by a $DC + AC$ voltage, the readout electrode (i.e. the cantilever itself in our case, see Figure 8.3), electrically connected to the closely located CMOS circuit input, collects a capacitive current in enhanced conditions since parasitic capacitances at the NEMS output are drastically reduced to the few fF range. The motional current I_M, which is a fraction of the total NEMS output current I_{MEMS}, is specifically generated by the variation of electrode/resonator capacitance due to the mechanical motion itself. The other part, the background current I_{BG}, is related to the capacitive feedthrough between the NEMS input and output electrodes, one part of it being the 'static' capacitance between the cantilever and the in-front electrode, the other part being the parasitic fringing capacitance between both.

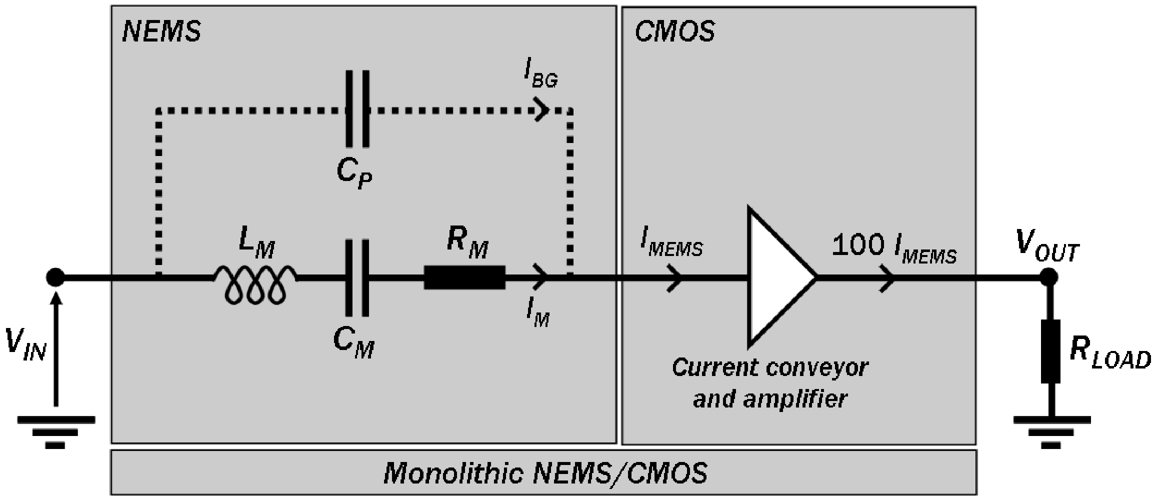

Figure 8.4: Electrical scheme of the monolithic NEMS/CMOS system.

The dedicated CMOS readout circuit ensures a constant voltage biasing at the resonator output, while it amplifies the readout current by a factor 100 and converts it to an output voltage according to an external load resistor R_{LOAD} (see Figure 8.4). The articles [Arcamone 2008, Arcamone 2007] give more details on the circuitry and the readout scheme.

The mechanical frequency response of those nanocantilevers has been electrically characterized with a network analyzer (AGILENT E5100A) in air (with a probe station) and vacuum (with wire-bonded samples). In both configurations, the capacitive detection scheme including the CMOS circuit successfully transduced into an electrical signal the mechanical motion corresponding to the fundamental in-plane flexural resonance mode of vibrating cantilevers. The data collected by the network analyzer, in terms of magnitude and phase, are under the form:

$$R_{NA}(f) = 20 \log \frac{V_{OUTAC}}{V_{INAC}} \tag{8.29}$$

The NEMS resonator total current (at the cantilever output, not at the circuit output) being:

$$I_{BG} + I_M = I_{MEMS} = \frac{V_{INAC}}{100 R_{LOAD}} 10^{\frac{R_{NA}}{20}} \tag{8.30}$$

The modulus and argument of the NEMS resonator electrical admittance Y can be calculated based on the circuit characteristics and the network analyzer response as follows:

$$|Y| \approx \frac{I_{MEMS}}{V_{INAC}} = \frac{10^{\frac{R_{NA}}{20}}}{100R_{LOAD}} \tag{8.31}$$

$$\arg(Y) = P - \Delta\varphi \tag{8.32}$$

where P is the phase signal as measured by the network analyzer and $\Delta\varphi$ is the phase delay introduced by the circuit; in our case $\Delta\varphi \approx \frac{\pi}{4}$. In the 2-port configuration of these measurements, a NEMS cantilever can be modeled as two parallel branches (see Figure 8.4):

- a capacitive branch (of capacitance C_P), of admittance Y_{BG}, corresponding to the background signal, in which I_{BG} flows. Y_{BG} is given by: $Y_{BG} = sC_P$ with $s = j\omega$.
- an RLC branch of admittance Y_M, corresponding to the resonating part, in which I_M flows. Y_M is given by: $Y_M = \frac{Cs}{LCs^2+RCs+1}$

The total admittance is then $Y = Y_{BG}+Y_M$. The theoretical model described in this paper is expressed in terms of Y_M only, i.e. the term describing the oscillations. Therefore it is required to apply a simple data treatment to extract the motional admittance Y_M from the measured admittance Y, Y_M being given by: $Y_M = Y - Y_{BG} = Y - sC_P$. Hence, its modulus is given by:

$$|Y_M| = \sqrt{[|Y|\cos(\arg(Y))]^2 + [|Y|\sin(\arg(Y)) - \omega C_P]^2} \tag{8.33}$$

C_P can be estimated by considering the electrical response R_{NA-OOR} at a given frequency f_{OOR} that is out of resonance, then C_P is given by:

$$C_P = \frac{1}{2\pi f_{OOR}} \frac{10^{\frac{R_{NA-OOR}}{20}}}{100R_{LOAD}} \tag{8.34}$$

Figure 8.5(a) shows the raw electrical response R_{NA} around the mechanical resonance of cantilever A ($l = 14.5\mu m$, $b = 460nm$, $h = 400nm$, $g = 600nm$) as directly measured by the network analyzer. Figure 8.5(b) shows the motional admittance Y_M extracted from the data of Figure 8.5(a) according to Equation (8.33). Using the developed model, the motional admittance can be computed as follows:

$$I_M = Y_M V_{ac} = \frac{dC_{res}}{dt} V_{dc} \tag{8.35}$$

$$\frac{dC_{res}}{dt} = \int_0^1 \frac{bC_n\varepsilon_0\phi_1(x)\dot{a}_1(t)}{(1 - a_1(t)\phi_1(x))^{\,2}}\, dx \tag{8.36}$$

The derivative of the resonator capacitance with respect to the dimensionless time t has been expanded in a fifth order Taylor series which enables the analytical computation of the integral in Equation (8.36). Then, Equation (8.11) and (8.12) are substituted into the outcome equation and the trigonometric functions are linearized. Since the electrical measurement filters out all frequency components of the readout signal except which of the drive frequency, the first harmonic of the Fourier transform of Equation (8.35) gives the motional current frequency response including the coupling between the dynamics of the resonator and the read-out voltage (Equation (8.36)). Although this coupling brings extra nonlinear terms, their contribution happens to be negligible and the read-out voltage is proportional to the dynamic deflection.

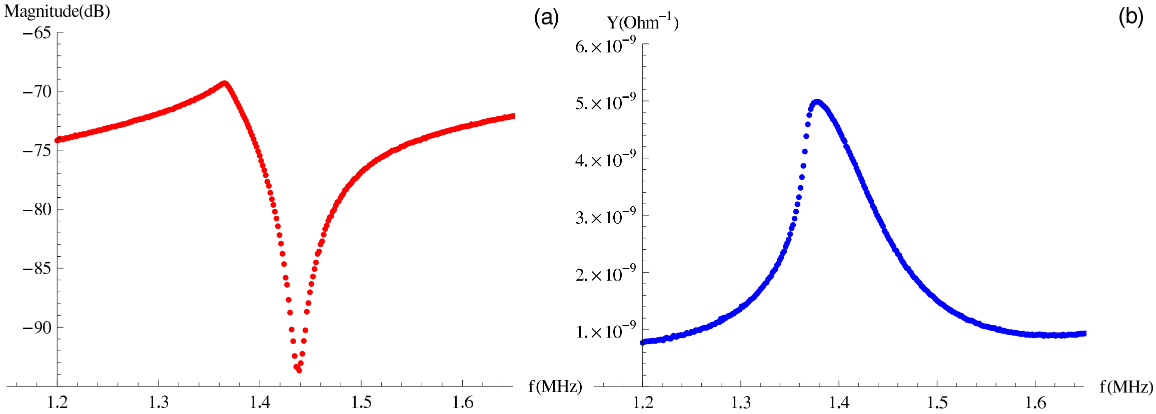

Figure 8.5: (a): Raw electrical response R_{NA} around the mechanical resonance of a nanocantilever. This is the response as measured by the NA of the full NEMS-CMOS system. (b): Motional admittance frequency response extracted from the data of Figure 8.5(a) according to Equation (8.33)

8.2.6.1 Measurements in air

It is important to underline that all the inputs of the model are known physical parameters including the fringing field coefficients computed using the analytical formulae [Nishiyama 1990], except the measured quality factor Q and the parasitic capacitance C_P. So as to evaluate the model, Q has been fitted using linear curves. For a fully analytical prediction, the quality factor may be computed using existing models taking into account the thermoelastic damping [Lifshitz 2000], the support loss [Hao 2003] and the surface loss [Yang 2002]. Such a computation gives results in good agreement with experimental measurements.

Figure 8.6 shows the characteristic responses analytically computed and electrically measured of cantilever A ($l = 14.5\mu m$, $b = 460nm$, $h = 400nm$, $g = 600nm$) operated in air for several DC voltages. Due to some mass that has been deposited at the free end of the cantilever, its resonance frequency was shifted from $2\,MHz$ down to $1.5\,MHz$. The first linear curve ($V_{dc} = 16V$) is fitted by adjusting the parasitic capacitance C_P and the quality factor Q. Then, the same value of C_P has been used for the three other curves while adjusting the Q factor for each one.

Figure 8.6 shows that the resonance frequency of the cantilever can be tuned by varying the applied DC voltage and a clear spring-softening effect is seen with increasing V_{dc}. The analytical curves are in good agreement with experimental results and the critical amplitude predicted analytically for a $21V\ DC$ voltage has been experimentally confirmed as shown in Figure 8.6 which demonstrates the accuracy and performance of the model. Out of resonance, the experimental curves slightly increase which is due to the variation of $\Delta\varphi$ during the measurements.

When experiments are performed in air, in order to reach detectable signals, the applied DC voltage has to be high ($V_{dc} > 10V$). As the quality factor is low ($15 < Q < 20$), the dynamic behavior of the nanocantilever is dominated by the nonlinear softening electrostatic forces which significantly increases the critical amplitude (Equation 8.26).

8.2.6.2 Measurements in vacuum

The chip containing cantilever B ($l = 14.5\mu m$, $b = 570nm$, $h = 260nm$, $g = 820nm$) has been wire bonded and it has been measured in a vacuum chamber under a pressure of $10^{-2}\,mBar$. The fits have

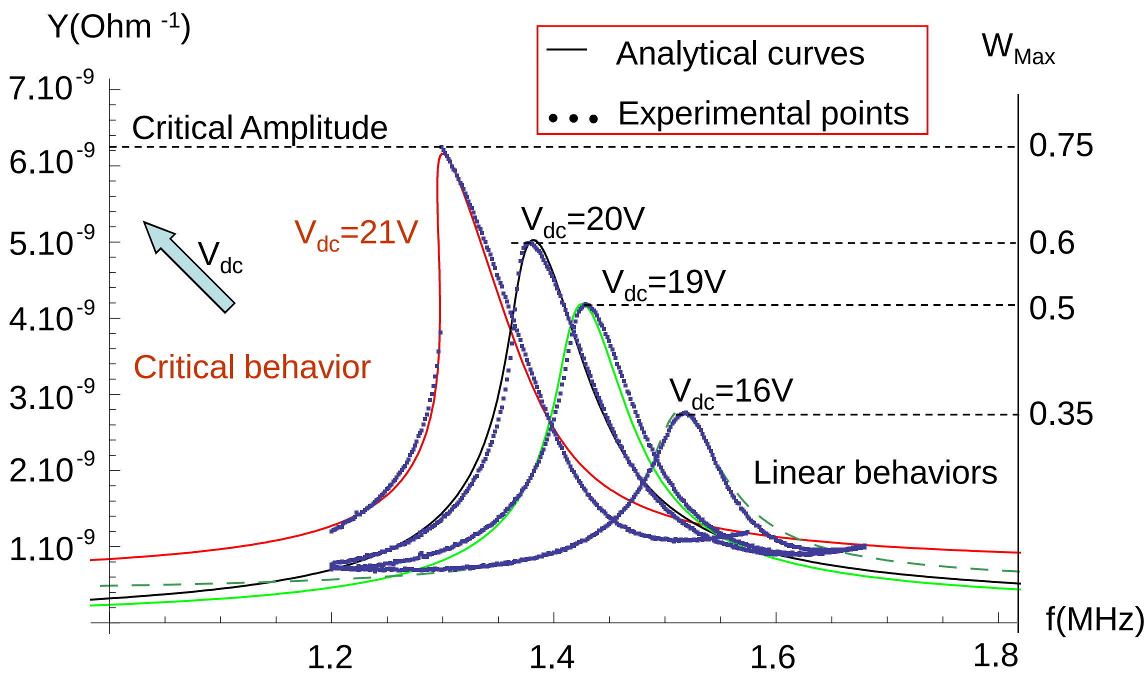

Figure 8.6: Analytical and measured motional admittance frequency curves (in air) of cantilever A. W_{max} is the cantilever displacement at the its free end normalized by the gap.

been made in the same way as for the experimental curves measured in air. Figure 8.7 shows two measured frequency responses and their predicted analytical curves.

Due to the high quality factors obtained in vacuum, low drive voltages are enough to polarize the device: 1 or $2\,V\ \ DC$ added to a $0.092\,V\ AC$. A $2\,V\ \ DC$ polarization is sufficient to provoke a nonlinear behavior yielding almost vertical slopes both in magnitude and in phase. The extracted Q factor decreases from 9150 down to 6650 for 1 and $2\,V\ \ DC$ polarization due to the ohmic losses [Sazonova 2006].

The high quality factors reduce the critical amplitude A_c as shown in Figure 8.7 which confirms the accuracy of the model beyond the critical amplitude (second curve with $2VDC$). The effect of the spring softening is also present due to the electrostatic negative stiffness. Even with high quality factors, the cantilever B displays a softening behavior. This can be explained by the fact that the nonlinearities coming from the electrostatic force are stronger than the mechanical hardening nonlinearities due to the length of the beam and the small gap thickness.

In air, NEMS cantilever have a large critical amplitude (75% of the gap as shown in Figure 8.6 for cantilever A) which implies a large dynamic range compared to clamped-clamped NEMS resonators (their critical amplitude could be lower than 1% of the gap). In addition, even in vacuum with high quality factors, the critical amplitude of nanocantilevers still interestingly large (50% of the gap as shown in Figure 8.7 for cantilever B). This important property makes cantilevers the best candidates for resonant mass and gas sensing devices.

The electric characterization of the NEMS/CMOS devices earlier described was an important step towards the validation of the nonlinear model for NEMS cantilevers. As previously shown, the competition between both behaviors (softening and hardening) is controlled by the design parameters, the quality factor as well as the DC voltage. The model shows that for appropriate values of those parameters, it is possible to suppress the hysteresis and to obtain an optimal design for which the

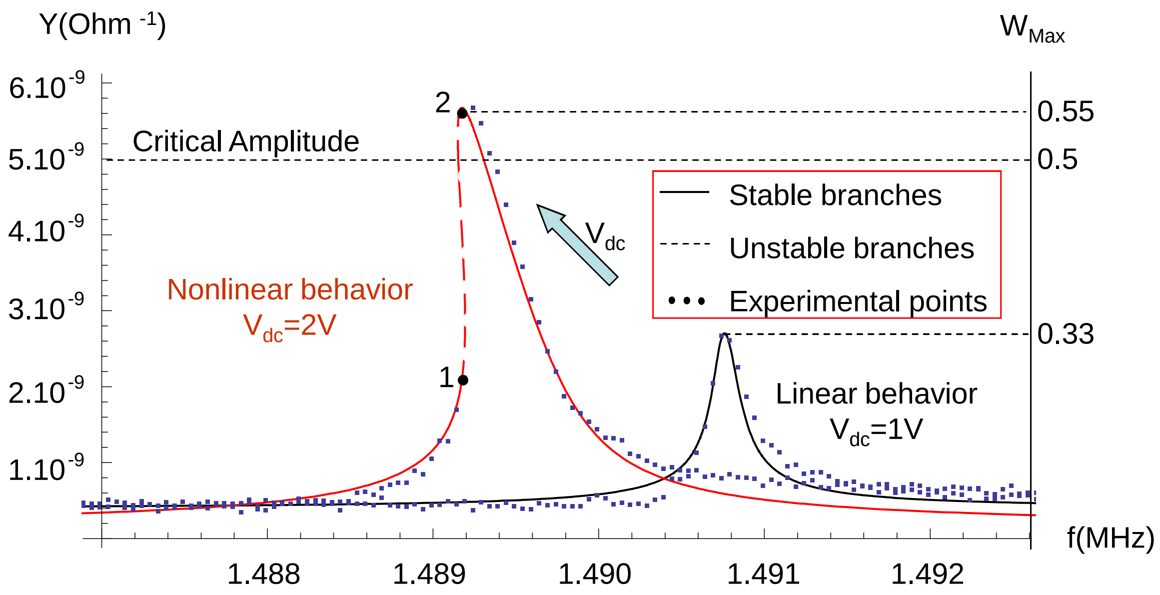

Figure 8.7: Analytical and measured motional admittance frequency curves (in vacuum) of cantilever B. W_{max} is the cantilever displacement at the its free end normalized by the gap.

mechanical and the electrostatic nonlinearities would be equilibrated. The next step is the complete validation of the model through the compensation of the nonlinearities which is the subject of the next section.

8.3 Resonant nanocantilever based on piezoresistive detection

Within the framework of the project CARNOT NEMS financed by the CARNOT institute, resonant NEMS gas and mass sensors have been designed by PhD student Sébastien Labarthe. The process flow was developed by Carine Marcoux and the fabrication was done in the clean rooms of LETI. Among these fabricated devices, a particular resonant nanocantilever based on piezoresistive detection is the scope of this section.

8.3.1 Device description

The device is composed of a fixed-free lever beam and two piezoresistive gauges connected to the cantilever at a distance $d = 0.15l$ from its fixed end. This value was chosen to maximize the stress inside the gauges due to the cantilever motion (Figure 8.8). The gauges have been etched along the $< 110 >$ direction in order to benefit from the high gauge factor associated with p^{++} doped silicon. A driving electrode was patterned along one side of the resonant cantilever for electrostatic actuation. The NEMS cantilever is actuated electrostatically at the primary resonance of its first linear undamped mode shape. The cantilever oscillation induces stress inside the piezoresistive gauges and the collected strain is transduced into a resistance variation due to the piezoresistive effect. Thus, the sensor frequency response is obtained via a piezoresistive read-out perfectly decoupled from the capacitive actuation of the resonator. The amount of molecules absorbed by the functionalized surface of the cantilever changes its effective mass which lowers its frequency resonance. By evaluating the frequency shift, the mass of the added species can be estimated. Thus, the studied device can be used either as a mass or a gas sensor.

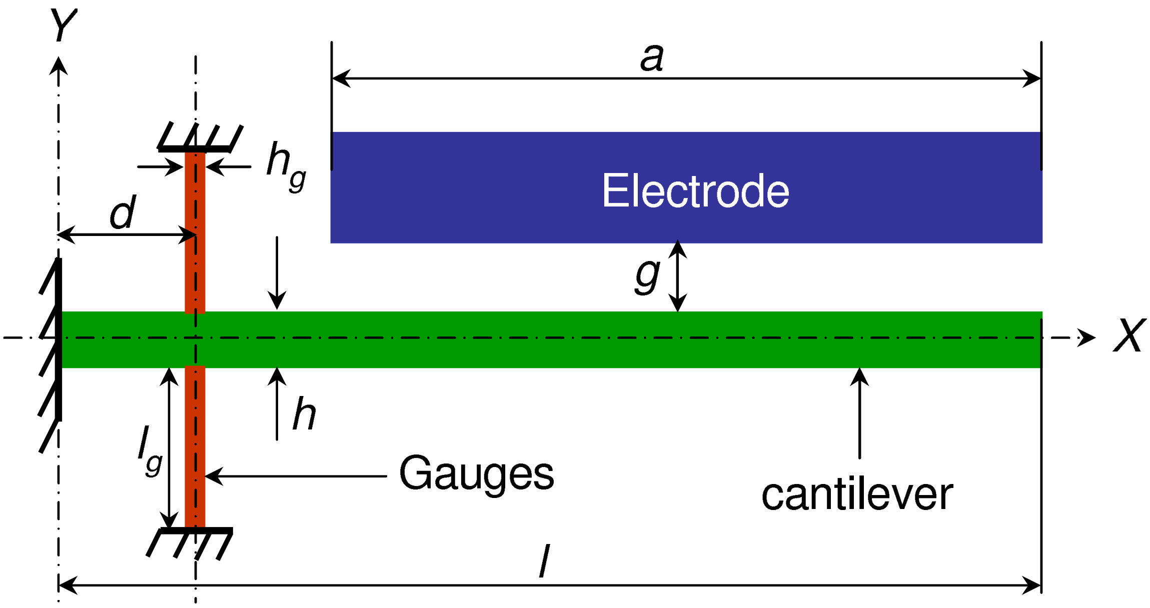

Figure 8.8: Resonant nanocantilever based on piezoresistive detection.

8.3.2 Transduction

The cantilever motion is detected by using the piezoresistive transduction principle [Mo 2007]. The piezoresistive transducers consist on semiconducting silicon $p{+}{+}$ (boron) doped suspended nanogauges. The rationale for using piezoresistive doped silicon nanogauges is related to the giant piezoresistance effect of these materials appearing for sub-100nm dimensions [He 2006]. They are suitable for integrated transducers and for self-sensing devices [L 2006]. The figure of merit characterising these materials is the piezoresistive gauge factor γ defined as:

$$\gamma = (1+\nu) + \frac{1}{\varepsilon_l}\frac{\Delta\rho}{\rho} \tag{8.37}$$

where ρ is the resistivity, ε_l the gauge elongation and ν the Poisson ratio. The gauge factor relates the mechanical strain applied on the gauges to its relative resistance change. The resistance change depends on two effects. The first term in Equation (8.37) is a geometrical consequence and is associated with elastic deformation, while the latter is related to the modification of the energy bands inside a crystal and thus altering its resistivity. In metals only the first term participates which ranges from 1-2 and is the way chosen by Roukes et al [Yang 2006]. In semiconductors, the second term provides a significant contribution which was shown to be more than 3 orders of magnitude higher [He 2006]. The force applied to the lever is amplified by the appropriate design and transferred to the gauges. This design makes possible to exploit a first order piezoresistance effect with the suspended gauges acting as strain collectors instead of second order one [He 2008]. We should notice that there is no need for further metallization layers which lead to additional damping and energy dissipation. The strain collected by the gauges is transduced into a resistance variation due to the piezoresistance effect proportional to:

$$\frac{\Delta R(\Omega)}{R} = \gamma\varepsilon_l(\Omega) \tag{8.38}$$

8.3.3 Equation of motion

We follow a variational approach, based on the extended Hamilton principle [Silva 1978a, Silva 1978b, Silva 1988a, Silva 1988b] in order to derive the nonlinear equations of motion describing the flexural vibration of the device described in Figure 8.8. The cantilever bending deflection $\tilde{w_j}$ is decomposed into $\tilde{w_0}$ for $\tilde{s} \in [0, d]$ and $\tilde{w_1}$ for $\tilde{s} \in [d, l]$.

$$E_c I_c \left\{ \tilde{w_j}'''' + \left[\tilde{w_j}' \left(\tilde{w_j}' \tilde{w_j}'' \right)' \right]' \right\} + \rho b h \ddot{\tilde{w_j}} + \tilde{c} \dot{\tilde{w_j}} =$$
$$-\frac{1}{2} \rho b h \left\{ \tilde{w_j}' \int_{(1-j)d+jl}^{s} \left[\frac{\partial^2}{\partial \tilde{t}^2} \int_{jd}^{s_1} (\tilde{w_j}')^2 ds_2 \right] ds_1 \right\}'$$
$$+\frac{j}{2} \varepsilon \frac{C_n b \left[Vdc + Vac \cos(\tilde{\Omega} \tilde{t}) \right]^2}{(g - \tilde{w_j})^2} H(s + a - l) \tag{8.39}$$

where s is the arclength, E_c and I_c are the Young's modulus and moment of inertia of the nanocantilever cross section. l and h are the length and width of the nanobeam. b is the device thickness, ρ is the material density, g is the capacitor gap width, and ε is the dielectric constant of the gap medium. The last term in Equation (8.39) represents an approximation of the electrostatic force assuming a partial distribution along the nanobeam length. H is a Heaviside function and C_n is the fringing field coefficient. The boundary conditions are:

$$\tilde{w_0}(0, \tilde{t}) = \tilde{w_0}'(0, \tilde{t}) = \tilde{w_1}''(l, \tilde{t}) = \tilde{w_1}'''(l, \tilde{t}) = 0 \tag{8.40}$$
$$\tilde{w_0}(d, \tilde{t}) - \tilde{w_1}(d, \tilde{t}) = \tilde{w_0}'(d, \tilde{t}) - \tilde{w_1}'(d, \tilde{t}) = 0 \tag{8.41}$$
$$\tilde{w_0}''(d, \tilde{t}) - \tilde{w_1}''(d, \tilde{t}) = -\frac{I_g}{I_c l_g} \tilde{w_0}'(d, \tilde{t}) \tag{8.42}$$
$$\tilde{w_0}'''(d, \tilde{t}) - \tilde{w_1}'''(d, \tilde{t}) = -\frac{2 h_g b}{I_c l_g} \tilde{w_0}(d, \tilde{t}) \tag{8.43}$$

where $\tilde{t}$ is time, h_g and I_g are the width and the moment of inertia of the gauge cross section. Equations (8.42) and (8.43) are obtained by writing the force and torque moment equilibrium equations at the point $s = d$.

$$T_{sc}|_d + 2T_{ag}|_d = -\frac{\partial M_{bc}}{\partial s}|_d + 2Ebh_g \varepsilon_g|_d = EI_c \left[\tilde{w_0}'''(d, \tilde{t}) - \tilde{w_1}'''(d, \tilde{t}) \right]$$
$$+2Ebh_g \frac{\tilde{w_0}(d, \tilde{t})}{l_g} = 0 \tag{8.44}$$
$$M_{bc}|_d + M_g|_d = EI_c \left[\tilde{w_0}''(d, \tilde{t}) - \tilde{w_1}''(d, \tilde{t}) \right] - EI_g \frac{\tilde{w_0}'(d, \tilde{t})}{l_g} = 0 \tag{8.45}$$

where T_{sc} is the shear force applied to the cantilever, M_{bc} is its bending moment, T_{ag} is the axial force applied to the gauges and M_g is its corresponding torque moment.

8.3.4 Normalization

We introduce the nondimensional variables:

$$w_j = \frac{\tilde{w_j}}{g}, \quad x = \frac{s}{l}, \quad t = \frac{\tilde{t}}{\tau} \tag{8.46}$$

where $\tau = \frac{2l^2}{h}\sqrt{\frac{3\rho}{E_c}}$. Substituting Equation (8.46) into Equations (8.39-8.43), gives:

$$\begin{aligned}
w_j^{iv} + \ddot{w}_j + c\dot{w}_j + \delta_1 \left[w_j^{'} \left(w_j^{'} w_j^{''} \right)^{'} \right]^{'} = \\
-\delta_2 \left\{ w_j^{'} \int_{(1-j)\frac{d}{l}+j}^{x} \left[\frac{\partial^2}{\partial t^2} \int_{j\frac{d}{l}}^{x_1} (w_j^{'})^2 dx_2 \right] dx_1 \right\}^{'} \\
+ j\delta_3 \frac{V_{dc}}{V_{ac}} \frac{\left[1 + \frac{V_{ac}}{V_{dc}} \cos(\Omega t) \right]^2}{(1-w_j)^2} H(x + \frac{a}{l} - 1)
\end{aligned} \tag{8.47}$$

$$w_0(0,t) = w_0^{'}(0,t) = w_1^{''}(1,t) = w_1^{'''}(1,t) = 0 \tag{8.48}$$

$$w_0(\frac{d}{l},t) - w_1(\frac{d}{l},t) = w_0^{'}(\frac{d}{l},t) - w_1^{'}(\frac{d}{l},t) = 0 \tag{8.49}$$

$$w_0^{''}(\frac{d}{l},t) - w_1^{''}(\frac{d}{l},t) = -\frac{I_g l}{I_c l_g} w_0^{'}(\frac{d}{l},t) \tag{8.50}$$

$$w_0^{'''}(\frac{d}{l},t) - w_1^{'''}(\frac{d}{l},t) = -\frac{2h_g b l^3}{I_c l_g} w_0(\frac{d}{l},t) \tag{8.51}$$

The parameters appearing in Equation (8.47) are:

$$\begin{aligned}
c = \frac{\tilde{c} l^4}{E_c I_c \tau}, \ \ \delta_1 = \left[\frac{g}{l}\right]^2, \ \ \delta_2 = \frac{1}{2}\left[\frac{g}{l}\right]^2 \\
\delta_3 = 6 V_{ac} V_{dc} \frac{\varepsilon l^4}{E_c h^3 g^3}, \ \ \Omega = \tilde{\Omega}\tau
\end{aligned} \tag{8.52}$$

8.3.5 Solving

Similarly to the cantilever model presented in section 8.2, the static deflection is negligible with respect to the dynamic deflection. Then, a reduced-order model is generated by modal decomposition (Equation (8.7)) transforming Equation (8.47) into a multi-degree-of-freedom system consisting in ordinary differential equations in time. We use the undamped linear mode shapes of the device described in Figure 8.9 as basis functions in the Galerkin procedure.

To do so, first we determine the linear bending modes ϕ_k of the mechanical structure. By analogy to the cantilever deflection, the linear undamped bending modes of the device ϕ_k are defined as piecewise functions:

$$x \in \left[0, \frac{d}{l}\right] \quad \phi_{0k}(x) = A_{0k}\cos\sqrt{\lambda_k}x + B_{0k}\sin\sqrt{\lambda_k}x + C_{0k}\cosh\sqrt{\lambda_k}x + D_{0k}\sinh\sqrt{\lambda_k}x \tag{8.53}$$

$$x \in \left[\frac{d}{l}, 1\right] \quad \phi_{1k}(x) = A_{1k}\cos\sqrt{\lambda_k}x + B_{1k}\sin\sqrt{\lambda_k}x + C_{1k}\cosh\sqrt{\lambda_k}x + D_{1k}\sinh\sqrt{\lambda_k}x \tag{8.54}$$

Here, λ_k is the k^{th} natural frequency of the mechanical structure. $\phi_0 k$ and $\phi_1 k$ satisfy the boundary conditions defined in Equations (8.48-8.51). Thus, the constants A_{jk}, B_{jk}, C_{jk} and D_{jk} are solutions of the following algebraic system $\{S\}$:

$$A_{0k} + C_{0k} = 0 \tag{8.55}$$

$$B_{0k} + D_{0k} = 0 \tag{8.56}$$

$$A_{1k}\cos\left(\sqrt{\lambda_k}\right) + B_{1k}\sin\left(\sqrt{\lambda_k}\right) - C_{1k}\cosh\left(\sqrt{\lambda_k}\right) - D_{1k}\sinh\left(\sqrt{\lambda_k}\right) = 0 \tag{8.57}$$

$$A_{1k}\sin\left(\sqrt{\lambda_k}\right) - B_{1k}\cos\left(\sqrt{\lambda_k}\right) + C_{1k}\sinh\left(\sqrt{\lambda_k}\right) + D_{1k}\cosh\left(\sqrt{\lambda_k}\right) = 0 \tag{8.58}$$

$$\begin{aligned}(A_{0k} - A_{1k})\cos\left(\frac{d}{l}\sqrt{\lambda_k}\right) + (B_{0k} - B_{1k})\sin\left(\frac{d}{l}\sqrt{\lambda_k}\right) + (C_{0k} - C_{1k})\cosh\left(\frac{d}{l}\sqrt{\lambda_k}\right)\\ + (D_{0k} - D_{1k})\sinh\left(\frac{d}{l}\sqrt{\lambda_k}\right) = 0\end{aligned} \tag{8.59}$$

$$\begin{aligned}(A_{1k} - A_{0k})\sin\left(\frac{d}{l}\sqrt{\lambda_k}\right) + (B_{0k} - B_{1k})\cos\left(\frac{d}{l}\sqrt{\lambda_k}\right) + (C_{0k} - C_{1k})\sinh\left(\frac{d}{l}\sqrt{\lambda_k}\right)\\ + (D_{0k} - D_{1k})\cosh\left(\frac{d}{l}\sqrt{\lambda_k}\right) = 0\end{aligned} \tag{8.60}$$

$$\begin{aligned}(A_{0k} - A_{1k})\sin\left(\frac{d}{l}\sqrt{\lambda_k}\right) + (B_{1k} - B_{0k})\cos\left(\frac{d}{l}\sqrt{\lambda_k}\right) + (C_{0k} - C_{1k})\sinh\left(\frac{d}{l}\sqrt{\lambda_k}\right)\\ + \frac{24l^3h_g}{h^3l_g\lambda_k^{\frac{3}{2}}}\left(A_{0k}\cos\left(\frac{d}{l}\sqrt{\lambda_k}\right) + B_{0k}\sin\left(\frac{d}{l}\sqrt{\lambda_k}\right) + C_{0k}\cosh\left(\frac{d}{l}\sqrt{\lambda_k}\right)\right)\\ + (D_{0k} - D_{1k})\cosh\left(\frac{d}{l}\sqrt{\lambda_k}\right) + D_{0k}\frac{24l^3h_g}{h^3l_g\lambda_k^{\frac{3}{2}}}\sinh\left(\frac{d}{l}\sqrt{\lambda_k}\right) = 0\end{aligned} \tag{8.61}$$

$$\begin{aligned}(A_{1k} - A_{0k})\cos\left(\frac{d}{l}\sqrt{\lambda_k}\right) + (B_{1k} - B_{0k})\sin\left(\frac{d}{l}\sqrt{\lambda_k}\right) + (C_{0k} - C_{1k})\cosh\left(\frac{d}{l}\sqrt{\lambda_k}\right)\\ + \frac{lh_g^3}{h^3l_g\lambda_k^{\frac{1}{2}}}\left(-A_{0k}\sin\left(\frac{d}{l}\sqrt{\lambda_k}\right) + B_{0k}\cos\left(\frac{d}{l}\sqrt{\lambda_k}\right) + C_{0k}\sinh\left(\frac{d}{l}\sqrt{\lambda_k}\right)\right)\\ + (D_{0k} - D_{1k})\sinh\left(\frac{d}{l}\sqrt{\lambda_k}\right) + D_{0k}\frac{lh_g^3}{h^3l_g\lambda_k^{\frac{1}{2}}}\cosh\left(\frac{d}{l}\sqrt{\lambda_k}\right) = 0\end{aligned} \tag{8.62}$$

The non trivial solution of the algebraic system $\{S\}$ is:

$$det\,[S] = 0 \tag{8.63}$$

The λ_k which are solutions of the transcendental Equation (8.63) are listed in table 8.1.

Mode k	λ_k
1	4.866
2	30.496
3	85.389
4	167.328

Table 8.1: Approximate solutions of $det\,\{S\} = 0$

Then, seven equations from the algebraic system $\{S\}$ are used in order to determine the seven constants $(A_{1k}, B_{0k}, C_{0k}, D_{0k}, B_{1k}, C_{1k}, D_{1k})$ in function of A_{0k}. Thus, the mathematical form of the eigenvectors is given by:

$$\phi_{0k}(x) = A_{0k}\cos\sqrt{\lambda_k}x + f_1(A_{0k})\sin\sqrt{\lambda_k}x + f_2(A_{0k})\cosh\sqrt{\lambda_k}x + f_3(A_{0k})\sinh\sqrt{\lambda_k}x \quad (8.64)$$
$$\phi_{1k}(x) = f_4(A_{0k})\cos\sqrt{\lambda_k}x + f_5(A_{0k})\sin\sqrt{\lambda_k}x + f_6(A_{0k})\cosh\sqrt{\lambda_k}x + f_1(A_{7k})\sinh\sqrt{\lambda_k}x \quad (8.65)$$

These functions are a modal basis for the scalar product:

$$\langle u, v\rangle = \int_0^1 u(x)v(x)dx \quad (8.66)$$

In order to normalize this basis, A_{0k} is computed as follows:

$$A_{0k} = \left[\int_0^{\frac{d}{l}}\left[\frac{\phi_{0k}(x)}{A_{0k}}\right]^2 dx + \int_{\frac{d}{l}}^1\left[\frac{\phi_{1k}(x)}{A_{0k}}\right]^2 dx\right]^{-\frac{1}{2}} \quad (8.67)$$

For the studied mechanical structure, the first mode is then:

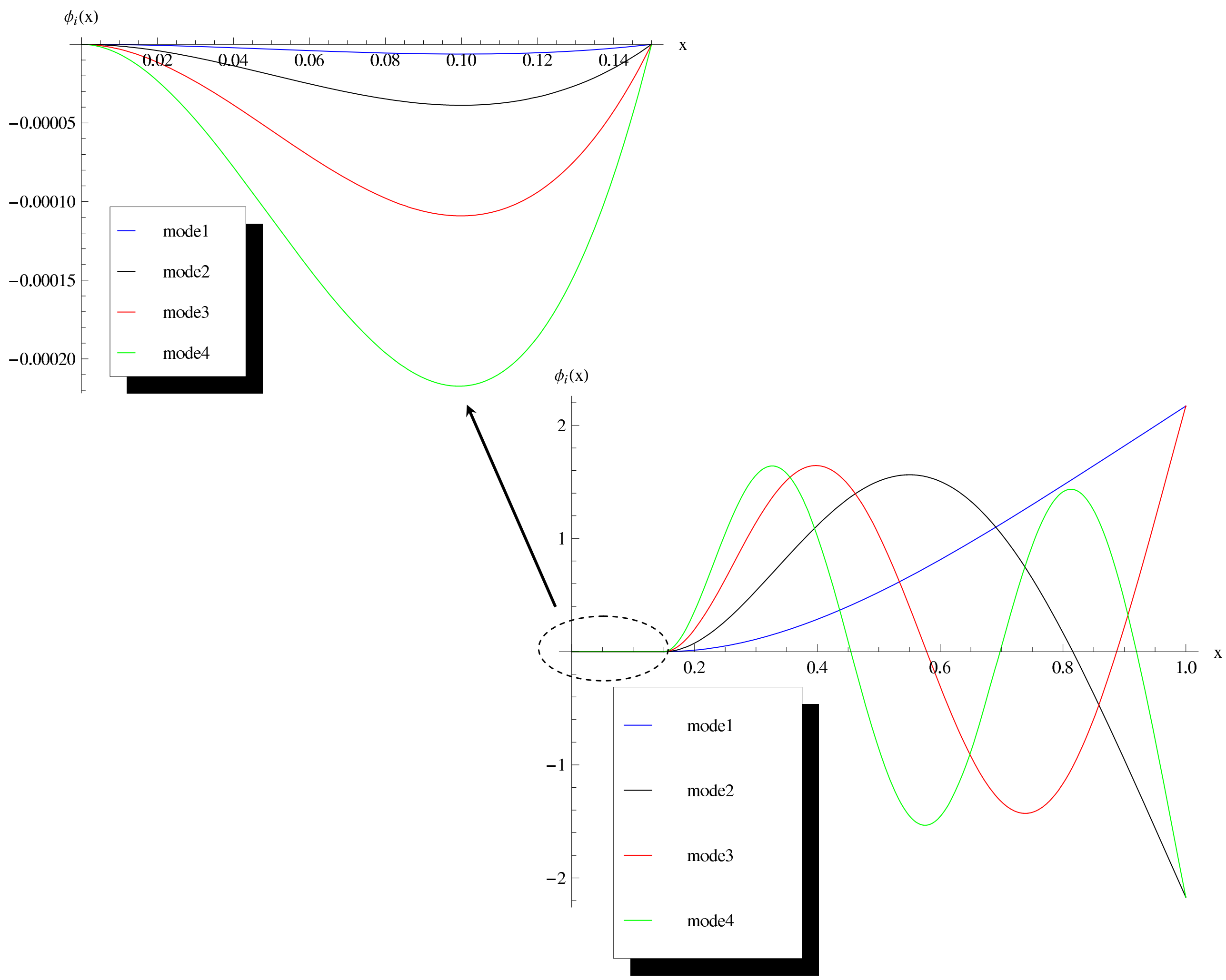

Figure 8.9: The first four linear undamped mode shapes of the device described in Figure 8.8.

$$\phi_{01}(x) = 0.00038\cos(2.21x) - 0.0035\sin(2.21x) - 0.00038\cosh(2.21x) + 0.0035\sinh(2.21x) \quad (8.68)$$
$$\phi_{11}(x) = -1.284\cos(2.21x) + 0.401\sin(2.21x) + 1.413\cosh(2.21x) - 1.206\sinh(2.21x) \quad (8.69)$$

The electrostatic force in Equation (8.47) is expanded in a fifth order Taylor series, and Equation (8.7) is substituted into the resulting equation. Then, Equation (8.8) is used to eliminate $\dfrac{d^4\phi_k(x)}{dx^4}$, and the outcome is multiplied by ϕ_k and integrated from $x = 0$ to 1 for $k \in [1, n] \cap \mathbb{N}$. Thus, a system of coupled ordinary differential equations in time is obtained.

Figure 8.9 shows that between the clamped end of the cantilever and the gauges, the vibrations of the sensor are relatively negligible with respect to its dynamics between the gauges and the free end of the cantilever for the first four modes. Consequently, the nonlinear coupling between the mode shapes is negligible for $x \in [0, d]$ and when the sensor is actuated on its first mode, its dynamics can be approximated by the dynamics of a cantilever of length $l-d$. Hence, the expansion of the electrostatic force in a fifth order Taylor series as previously explained in section 8.2.

Assuming that the first mode is the dominant mode of the system, the study can be restricted to the case $n = 1$. Then, we obtain:

$$\begin{aligned}
126.12\delta_1 a_1^3 + c a_1' + a_1\left(23.68 + 14.97\delta_2 a_1'^2\right) + a_1'' + 14.97\delta_2 a_1^2 a_1'' - \delta_3\left(0.36\frac{V_{ac}}{V_{dc}} + 0.72\frac{V_{dc}}{V_{ac}}\right)& \\
-\delta_3\left[1.43\cos(\Omega t) + \left(\frac{V_{ac}}{V_{dc}} + 2\frac{V_{dc}}{V_{ac}} + 4\cos(\Omega t) + \frac{V_{ac}}{V_{dc}}\cos(2\Omega t)\right)a_1\right]& \\
-\delta_3\left[0.36\frac{V_{ac}}{V_{dc}}\cos(2\Omega t) + \left(2.4\frac{V_{ac}}{V_{dc}} + 4.81\frac{V_{dc}}{V_{ac}} + 9.62\cos(\Omega t) + 2.4\frac{V_{ac}}{V_{dc}}\cos(2\Omega t)\right)a_1^2\right]& \\
-\delta_3\left[5.53\frac{V_{ac}}{V_{dc}} + 11.05\frac{V_{dc}}{V_{ac}} + 22.1\cos(\Omega t) + 5.53\frac{V_{ac}}{V_{dc}}\cos(2\Omega t)\right]a_1^3& \\
-\delta_3\left[12.44\frac{V_{ac}}{V_{dc}} + 24.89\frac{V_{dc}}{V_{ac}} + 49.77\cos(\Omega t) + 12.44\frac{V_{ac}}{V_{dc}}\cos(2\Omega t)\right]a_1^4& \\
-\delta_3\left[27.7\frac{V_{ac}}{V_{dc}} + 55.4\frac{V_{dc}}{V_{ac}} + 110.82\cos(\Omega t) + 27.7\frac{V_{ac}}{V_{dc}}\cos(2\Omega t)\right]a_1^5 = 0& \quad (8.70)
\end{aligned}$$

The averaging method is used in order to solve the nonlinear Mathieu-Duffing Equation (8.70). It permits the transformation of the reduced order nonlinear second order Equation (8.70) into two first order nonlinear ordinary differential equation that describe the amplitude and phase modulation of the system frequency response.

For $V_{ac} << V_{dc}$, the second harmonic terms are neglected. The resulting phase and amplitude averaged equations over the period $\frac{2\pi}{\Omega}$ and around the primary resonance ($\Omega = \lambda_1 + \xi\sigma$) are:

$$\dot{A} = \xi\left[-\frac{c}{2}A - \frac{\delta_3\sin\beta}{\lambda_1}\left(0.716 + 1.2A^2 + 3.11A^4\right)\right] + O(\xi^2) \quad (8.71)$$

$$\begin{aligned}
\dot{\beta} = \xi\left[\frac{11.84}{\lambda_1} + \frac{47.3\delta_1 A^2}{\lambda_1} - \frac{V_{dc}\delta_3}{V_{ac}\lambda_1} - \frac{4.14\delta_3 V_{dc} A^2}{V_{ac}\lambda_1} - \frac{17.32\delta_3 V_{dc} A^4}{V_{ac}\lambda_1} - \frac{\lambda_1}{2} - 3.74\delta_2\lambda_1 A^2\right]& \\
+\varepsilon\left[\frac{\delta_3\cos\beta}{\lambda_1}\left(\frac{0.716}{A} - 3.61A - 15.55A^3\right)\right] + O(\xi^2)& \quad (8.72)
\end{aligned}$$

The steady-state motions occur when $\dot{A} = \dot{\beta} = 0$, which corresponds to the singular points of Equations (8.71) and (8.72). Thus, the frequency-response equation can be written in its implicit form as:

$$\begin{aligned}
\left[\frac{\left(A\left(11.84 + 47.3A^2\delta_1 + \frac{V_{dc}}{V_{ac}}\left(-1 - 4.14A^2 - 17.32A^4\right)\delta_3 - \Omega\lambda_1 + \left(\frac{1}{2} - 3.74A^2\delta_2\right)\lambda_1^2\right)\right)}{\left(\left(0.72 + 3.61A^2 + 15.55A^4\right)\delta_3\right)}\right]^2& \\
+\left[\frac{cA\lambda_1}{2\left(0.72 + 3.61A^2 + 15.55A^4\right)\delta_3}\right]^2 = 1& \quad (8.73)
\end{aligned}$$

The normalized displacement W_{max} with respect to the gap at the middle of the beam and the drive frequency Ω can be expressed in function of the phase β. Thus, the frequency response curve can be plotted parametrically as shown in Figure 8.10 for the following parameters: $l = 5\,\mu m$, $b = 160\,nm$, $h = 300\,nm$, $l_g = 500\,nm$, $h_g = 80\,nm$, $a = 350\,nm$ and $V_{ac} = 0.1V_{dc}$. The gap g and the DC voltage V_{dc} were used for parametric studies.

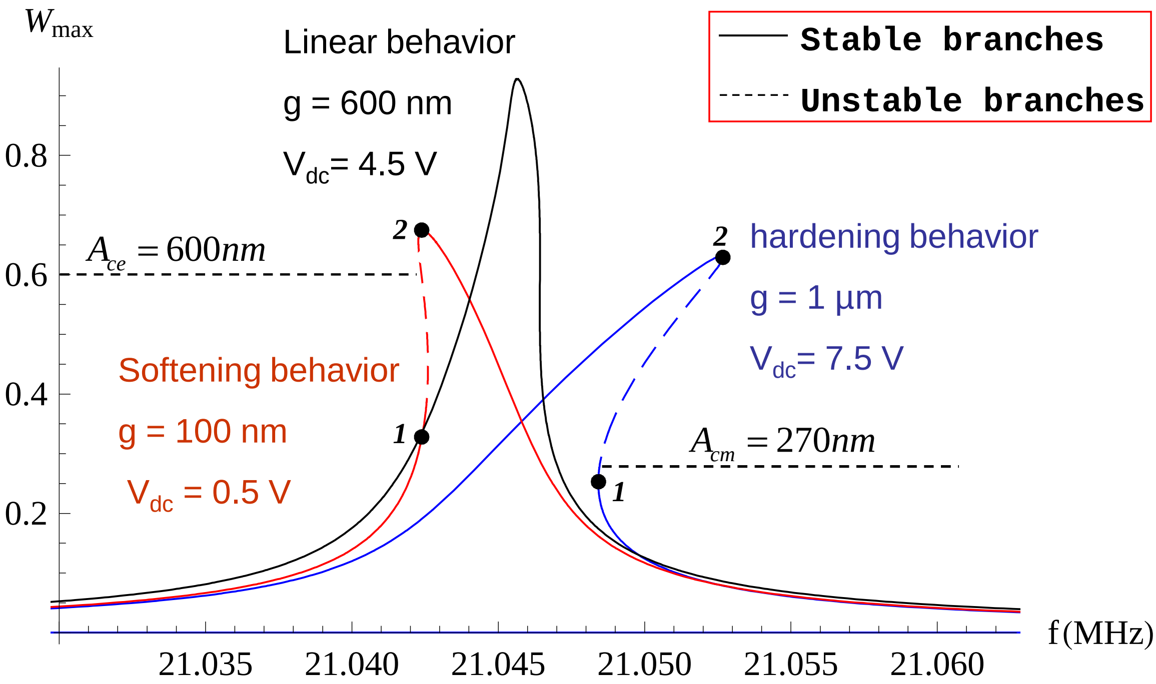

Figure 8.10: Analytical forced frequency responses of the resonant piezoresistive device presented in Figures 8.8 and 8.11 for a quality factor $Q = 10^4$. W_{max} is the displacement of the beam normalized by the gap g at its free end.

8.3.6 The critical amplitude

The critical amplitude is the oscillation amplitude A_c above which bistability occurs. Thus, A_c is the transition amplitude from the linear to the nonlinear behavior.

8.3.6.1 The critical mechanical amplitude

Here, the mechanical nonlinearities are assumed to dominate the NEMS dynamics. Moreover the nonlinearities acting between the fixed end of the cantilever and the nanogauges are negligible since the sensor vibrations in this part are close to zero for the first linear undamped mode shape as shown in Figure 8.9. Therefore, the NEMS dynamics is equivalent to a resonant nanocantilever of length $l - d$. Hence, using Equation (8.22), the critical mechanical amplitude can be written as:

$$A_{cm} = 6.3\frac{l-d}{\sqrt{Q}} \tag{8.74}$$

8.3.6.2 The critical electrostatic amplitude

In this case, the mechanical nonlinearities are neglected. Also, the electrostatic nonlinearities are acting only on the sensor part comprised between the gauges and cantilever the free end. By considering only nonlinear terms up to the third order, while neglecting the parametric terms and the terms proportional to V_{ac}^2, the critical electrostatic amplitude is deduced from Equation (8.26).:

$$A_{ce} = 2 * 10^9 g^{\frac{5}{2}} \frac{h}{(l-d)\sqrt{Q}V_{dc}} \left(\frac{7.5 * 10^7 h^2}{(l-d)^4} - \frac{3.8 * 10^{-15} V_{dc}^2}{g^3 h} \right)^{\frac{1}{4}} \tag{8.75}$$

8.3.6.3 Engineering optimization

As shown in Figure 8.10, when $g << h$, the mechanical nonlinearities are negligible with respect to the electrostatic nonlinearities. Then, The NEMS forced frequency curve displays a softening behavior (red curve of Figure 8.10) and the critical amplitude is given by Equation (8.75) which depends on the quality factor Q, the cantilever width h, the gap g, the DC voltage V_{dc} and the distance between the piezoresistive nanogauges and the cantilever free end $l-d$. In this case, the open-loop stability of the NEMS resonant sensor is limited by an oscillation amplitude around $60\,nm$.

If $g >> h$, the electrostatic nonlinearities are negligible with respect to the mechanical nonlinearities. Then, The NEMS forced frequency curve displays a hardening behavior (blue curve of Figure 8.10) and the critical amplitude is given by Equation (8.74) which only depends on the quality factor Q and the distance between the piezoresistive nanogauges and the cantilever free end $l-d$. In this case, the open-loop stability of the NEMS resonant sensor is limited by an oscillation amplitude around $270\,nm$: more than four times higher than the previous case. Thus the resolution is enhanced by a factor $\Pi_{enh} = 4$ compared to the first case.

Hence, designing NEMS cantilevers displaying softening behaviors is disadvantageous and can significantly alter the sensor resolution especially when this supposes that we are able to fabricate structures with very small gaps which is rather awkward. Indeed, assuming that the upper bound limit which is the pull-in occurs at an amplitude of the gap order, even if the cantilever can vibrate linearly up to very high amplitudes comparable to the gap, the sensor performances can be altered due to its small dimensional amplitude limited by the gap. In other words, enhancing the dimensionless critical amplitude (red curve of Figure 8.10) is not important when the gap is significantly reduced.

The optimal gap is $g_p = 600\,nm$ for which the mechanical and the electrostatic nonlinearities are balanced which permits the linearization of the frequency response as shown in Figure 8.10 (black curve). For this design which is technologically feasible, the resolution is enhanced by a factor $\Pi_{enh} = 9$, compared to first case.

8.3.7 Fabrication

The NEMS device presented in Figure 8.11 was fabricated using CMOS compatible materials with nano-electronics state-of-the-art lithography and etching techniques. We used a $200\,mm$ silicon-on-insulator (SOI) wafer of $< 100 >$ orientation with a $160\,nm$ thick top silicon structural layer (resistivity $\approx 10\,\Omega cm$) and a $400\,nm$ thick sacrificial oxide layer. The top silicon layer was implanted with boron ions (p-type) through a thin layer of thermal oxide. Homogenous doping ($3.10^{19}\,cm^{-3}$) in the whole thickness of the top silicon was obtained through specific annealing step (for material reconstruction and doping activation), resulting in top layer resistivity of approximately $6\,m\Omega cm$. A hybrid e-beam/DUV lithography technique [Colinet 2009] was used to define the nano-resonators and electrode pads, respectively. Top silicon layer was etched by anisotropic reactive ion etching (RIE). In order to decrease the lead resistances, the interconnecting leads have been thickened with a 650 nm thick AlSi layer, a typical metal for CMOS interconnections process. Finally, the nanoresonators have been released using a vapor HF isotropic etching to remove the sacrificial layer oxide beneath the structures. The main process steps are summarized in Figure 8.12.

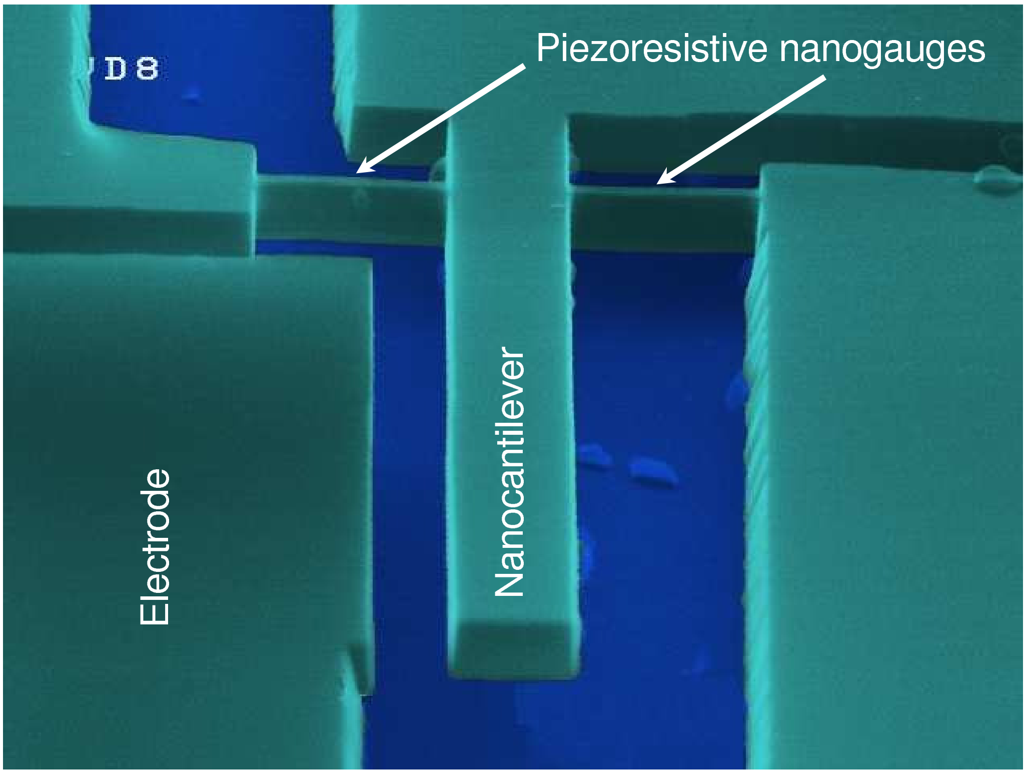

Figure 8.11: SEM image of the in-plane piezoresistive structure.

8.3.8 Electrical characterization

The strain collected by the gauges is transduced into a resistance variation due to the piezoresistance effect proportional to:

$$\frac{\Delta R(\Omega)}{R} = \gamma \varepsilon_l(\Omega) = \gamma \frac{1}{24} l^3 h_g^2 g E \left[\phi_{11}'''(d) - \phi_{01}'''(d)\right] a_1(\Omega) \tag{8.76}$$

where R is the gauge resistance and E the Young's modulus. The displacement frequency response $a_1(\Omega)$ can be written in its parametric form in order to plot parametrically the resistance frequency response with respect to the phase β.

8.3.8.1 ω down-mixing technique

The devices under test were connected to a radio frequency (RF) circuit board through wire bonding and loaded to a RF vacuum chamber for room temperature measurements. The beam is actuated electrostatically through capacitive coupling and detected through piezoresistive displacement transduction. The electrical read-out at high frequency is complicated by parasitic capacitances which change the expected behavior of the electrical circuit. In order to avoid parasitic impedances and to

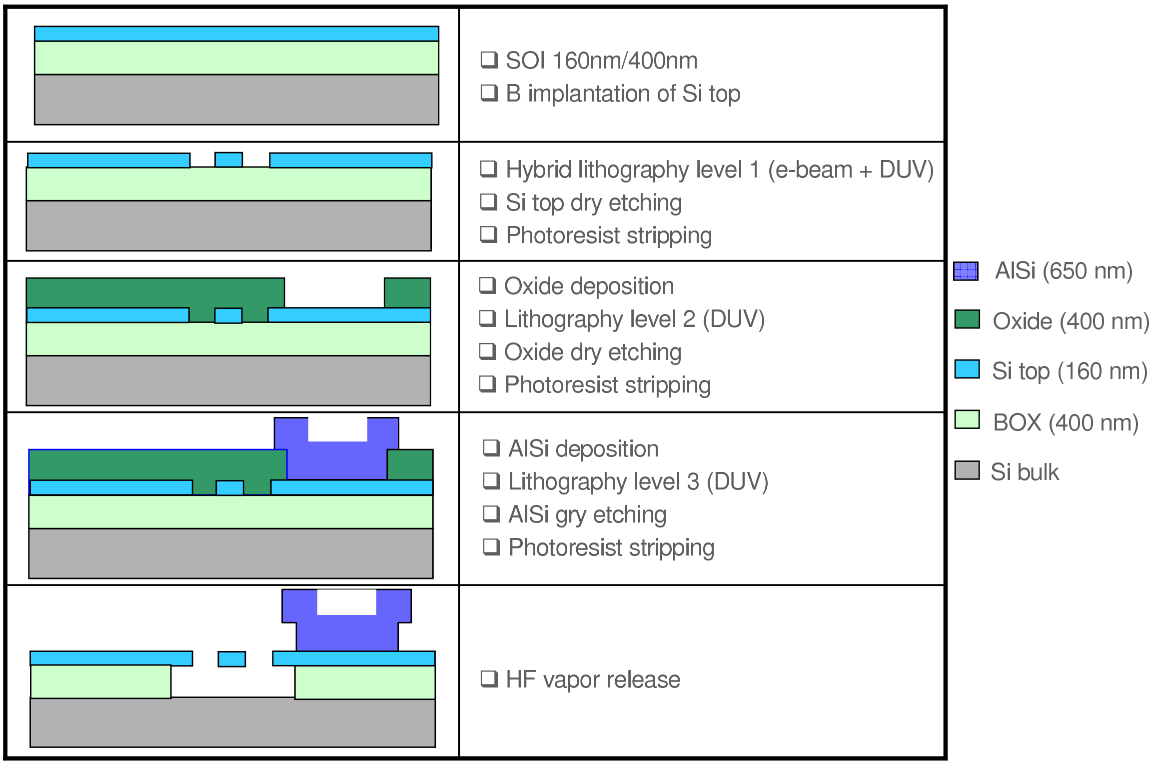

Figure 8.12: In-plane piezoresistive structure process flow

easily reach the nonlinear regime, an ω down-mixing technique has been used to read-out the resistance variation at a lower frequency $\Delta\omega$ [Bargatin 2005] (a schematic of the setup is shown in Figure 8.13). The change in resistance $\Delta R(\omega)$ is read by applying a proper bias $I_b(\omega - \Delta\omega)$ to the gauges which are acting as signal mixers and measuring the potential at the bridge center. The output voltage at low frequency is proportional to:

$$V_{out}(\Delta\omega) \propto \Delta R \cos(\omega t).I_b \cos\left((\omega - \Delta\omega)t\right) = \frac{1}{2} I_b.\Delta R.\cos(\Delta\omega t) \tag{8.77}$$

The two gauges situated on opposite sides of the lever work in tensile and compressive strain alternatively offering a double advantage. Firstly they allow making a differential measurement at the centre, working both at the same time, thus contributing twice on the output signal. Second this flexible design constitutes a balanced bridge configuration which permits suppression of the background at the middle point by applying two 180° out of phase voltage signal to the gauges extremities. The adequate decoupling of actuation and detection by using orthogonal principles as well as separating them in frequency has a direct consequence on the background reduction. As shown in Figure 8.14, a huge signal of the order of $2 - 3mV$ at resonance and a very low background was obtained with these devices giving rise to a signal to background ratio of more than $60\,dB$.

Several measurements were performed on the device for a fixed bias voltage ($V_{bias} = 1.56V$ peak-peak). The cantilever displacement depends on the applied electrostatic force which is proportional to $F = \frac{1}{2}C\left(V_{dc} + Vac\cos(\omega t)\right)^2$. This force will have an AC ($F_{ac}(\omega)$) and a static (F_{dc}) component proportional to V_{dc}^2 for $V_{dc} >> V_{ac}$. The first will have a direct consequence on the displacement amplitude while the latter affects the lever stiffness thus changing the resonance frequency. This is confirmed by the experimental results where the resonance frequency curve shifts to the low frequencies

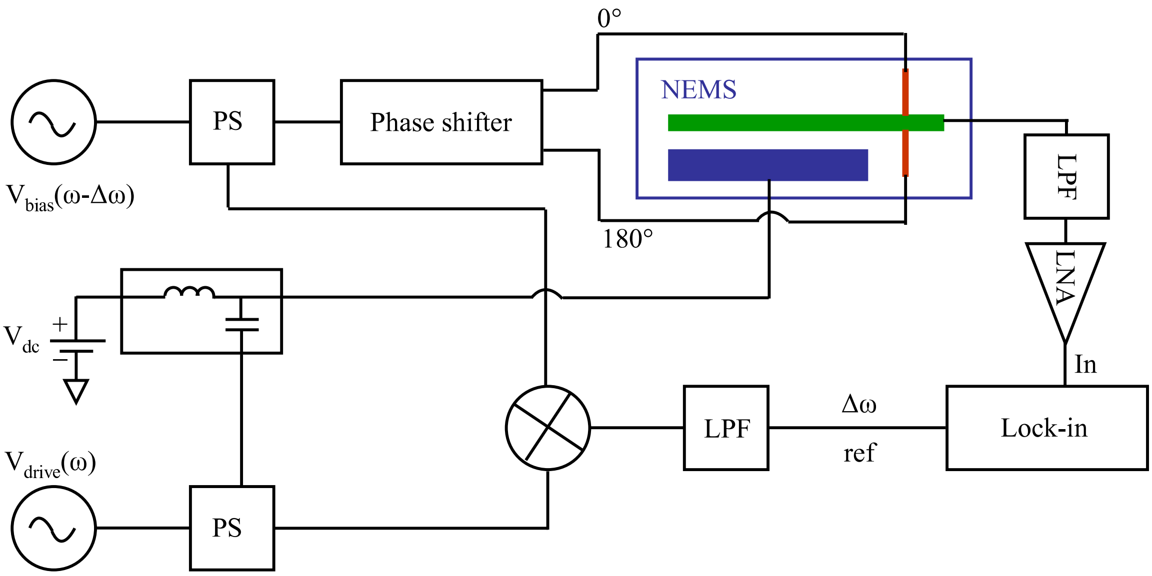

Figure 8.13: Test-bench for motion detection of piezoresistive resonant NEMS based on an ω down-mixing technique. PS, LPF are power splitter and phase shifter, respectively.

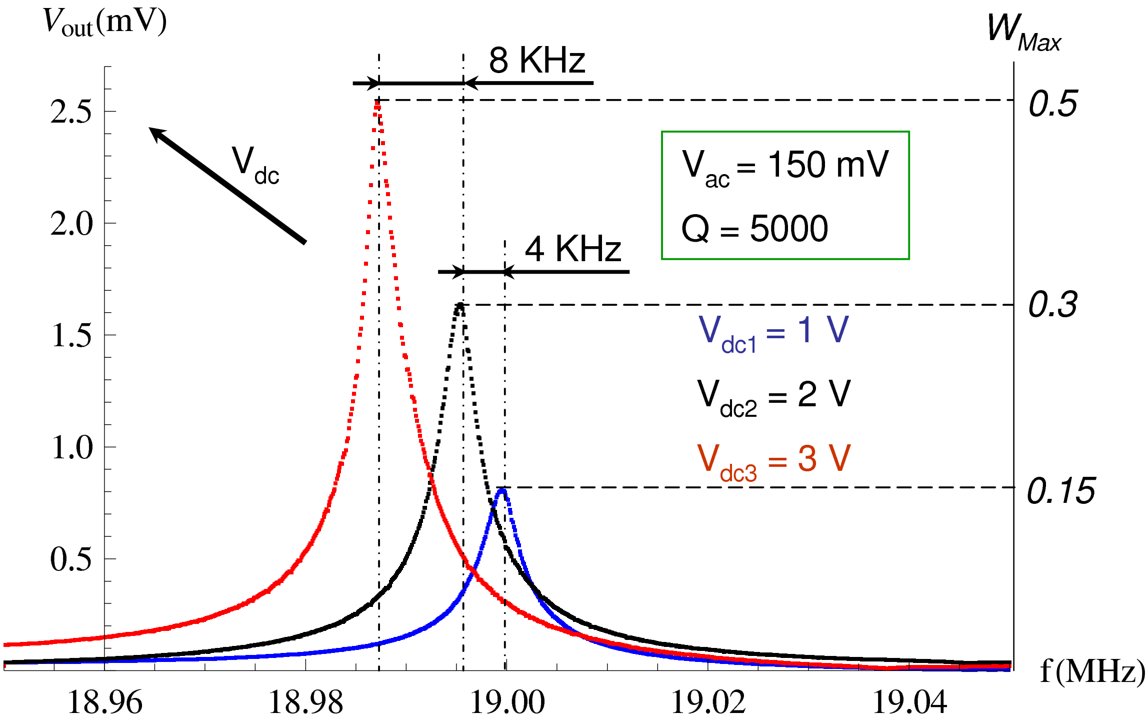

Figure 8.14: Linear resonance frequency responses measured using an ω down-mixing technique. The effect of the DC voltage on the resonance frequency is presented.

due to the electrostatic negative stiffness (Figure 8.14).

Figure 8.14 shows three linear resonance peaks obtained for $V_{ac} = 150mV$ and DC voltages going from $1\,V$ to $3V$. The analytical resonance frequency is around $21MHz$ which is close to the result found by FE analysis made using the software ANSYS. Experimentally, the measured resonance frequency of the device is around $19\,MHz$ which can be due to many factors such as silicon residual stress, size effect on Youngs modulus as well as micro and nanofabrication tolerances. The measured quality factor of the first linear curve ($V_{dc} = 1\,V$) is around 5000. Remarkably, increasing the DC voltage did not degrade the quality factor. In fact, in these devices, since the detection is piezoresistive, there is no correlation between the electrical resistance of the device and the measured quality factor. The expected dissipation from this mechanism (ohmic losses) is thus negligible. The last resonance curve of Figure 8.14 (Red curve) is close to the critical amplitude that has been analytically computed using the nonlinear model (Equation (8.75) for a softening behavior) which gives a value around $90nm$.

Then, in order to reach the nonlinear regime, the cantilever has been actuated using high DC voltages. Moreover, the frequency response has been tracked experimentally using a lock-in amplifier in sweep-up and down frequency in order to obtain a full characterization of the resonator bifurcation topology. No extra-mechanism loss has been observed due to the nonlinear dynamics of the cantilever and therefore the same quality factor has been conserved ($Q = 5000$). Figure 8.15 shows two nonlinear resonance peaks:

- The first resonance curve (in dashed line) was obtained for $V_{ac} = 150\,mV$ and $V_{dc} = 5\,V$. It displays a softening behavior characterized by a jump-up frequency at the bifurcation point B_2 and a jump-down frequency at the bifurcation point B_3 where the cantilever oscillation amplitude is around 75% of the gap ($150\,nm$).

- The second resonance curve was obtained for $V_{ac} = 75\,mV$ and $V_{dc} = 8\,V$. Remarkably, in sweep down frequency, two jumps have been observed: a jump-up at the bifurcation point B_1 and a jump down at the highest bifurcation point in the softening domain B_3 where the cantilever oscillation amplitude is around $150\,nm$. This characterizes a particular mixed hardening-softening behavior (see section 5.4 for more details) which is not the logical expected result since the increase in the DC voltage, amplifies the nonlinear negative stifness due to the electrostatic forces. Combined with an oscillation amplitude below the first softening curve, this should ensure negligible mechanical nonlinearities with respect to the electrostatic nonlinearities. Hence, the dynamic behavior should be purely softening.

  Nevertheless, in sweep up frequency, only a jump-up has been identified at the bifurcation point B_2. Then, the resonance response follows a softening branch. In this configuration, the nonlinear dynamic behavior of the cantilever is uncertain (between a softening and a mixed behavior) which leads to an unpredictability of the frequency response as well as a sensitivity to the initial conditions.

8.3.8.2 Optimal DC voltage

For this piezoresistive resonant NEMS, the quality factor Q is constant with respect to the DC and AC voltage. Then, using equations (8.74) and (8.75), the optimal DC drive voltage is:

$$V_{dc_{OP}} = \sqrt{\frac{1}{2}\sqrt{\frac{1.65*10^{39}g^{14}h^6}{(l-d)^{16}} + \frac{3.2*10^{42}g^{10}h^6}{(l-d)^{12}}} - \frac{8.1*10^{19}g^7h^3}{(l-d)^8}} \tag{8.78}$$

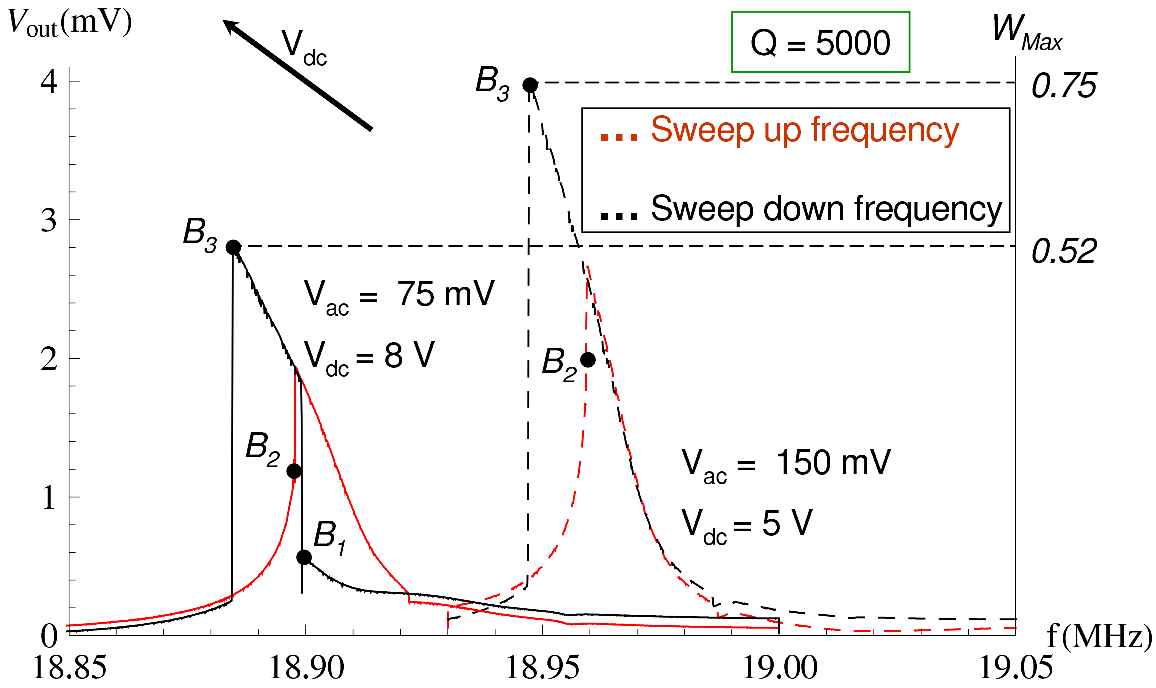

Figure 8.15: Nonlinear resonance frequency responses measured using an ω down-mixing technique and showing the location of the different bifurcation points $\{B_1, B_2$ and $B_3\}$. W_{max} is the cantilever displacement at the its free end normalized by the gap.

The computed DC voltage that permits the compensation of the nonlinearities is then computed using Equation (8.78) which gives a value around $1V$. Hence, a high AC voltage is needed in order to validate the compensation for such a low DC voltage. As shown in Figure 8.14, the AC voltage should be higher than $0.5\,V$. Unfortunately, for $V_{ac} > \frac{Vdc}{2}$, the assumption of neglected second harmonic terms is no more valid and the used model should be corrected by including the missing terms which could not guarantee a simple and quick analytical tool with practical rules of optimization for MEMS and NEMS designers.

Moreover, for the studied device, the optimal DC voltage being low, one can use a 2ω configuration in order to enable the compensation of the nonlinearities as well as to investigate experimentally the effect of the superharmonic resonance on the nonlinear dynamic behavior of a cantilever around the primary resonance. Particularly, as the unpredictability of the sensor behavior is undesirable for MEMS and NEMS designers, the superharmonic resonance could be with a great benefit for retarding dangerous nonlinear behaviors which was demonstrated for clamped-clamped beam resonators (see section 5.6 for more details).

8.3.8.3 2ω down-mixing technique

In order to actuate the cantilever at its primary and super harmonic resonances simultaneously, a 2ω down-mixing technique has been used enabling a read-out of the resistance variation at a lower frequency $\Delta\omega$ (a schematic of the setup is shown in Figure 8.16).

Several measurements were performed on the device for a fixed bias voltage ($V_{bias} = 1.56V$ peak-peak). The cantilever displacement depends on the applied electrostatic force which is proportional to $F = \frac{1}{2}C\left(V_{dc} + Vac\cos(\frac{\omega}{2}t)\right)^2$. This force will have an AC ($F_{ac}(\omega)$) and a static (F_{dc}) component proportional to $V_{dc}^2 + \frac{1}{2}V_{ac}^2$. The first will have a direct consequence on the displacement amplitude while the latter affects the lever stiffness thus changing the resonance frequency.

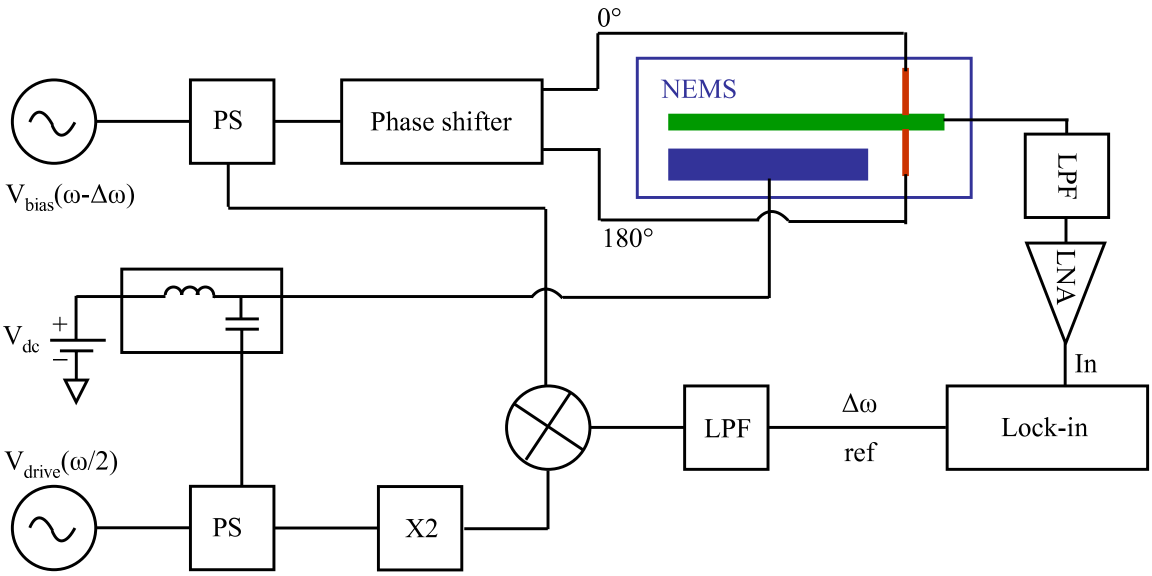

Figure 8.16: Test-bench for motion detection of piezoresistive resonant NEMS based on a 2ω down-mixing technique. PS, LPF are power splitter and phase shifter, respectively. W_{max} is the cantilever displacement at the its free end normalized by the gap.

Figure 8.17 shows two linear peaks obtained using a 2ω down-mixing technique for $V_{ac} = 2V$. The measured quality factor is about 5000 which confirms the independance of Q on the DC and AC voltages. When, the DC voltage has been increased from $0.2V$ up to $0.3V$, the variation of the negative stifness is negligible and consequently, no remarkable frequency shift has been observed. Remarkably, the measured output signal of the second linear peak is close to $3\,mV$ for a low DC voltage which was not reachable linearly in the ω down-mixing configuration.

We previously demonstrated in section 5.6 that the superharmonic resonance has no effect on the critical amplitude of the resonator. By analogy, the mechanical critical amplitude of a cantilever under simultaneous resonance is then $A_{cm} = 6.3\frac{l}{\sqrt{Q}}$. However, in the electrostatic critical amplitude, one must add the contribution of the AC voltage in the nonlinear electrostatic stiffness which changes substantially the close-form solution of the optimal drive DC voltage. The latter has been estimated using the model for $V_{ac} = 2V$ which gives a V_{dc} about $0.5\,V$.

The resonance peak of Figure 8.18 displays a slightly softening behavior close to the critical amplitude. The measured peak has been obtained using a 2ω down-mixing configuration for $V_{ac} = 2V$ and $V_{dc} = 0.5V$. Analytically, for this set of parameters the nonlinear electrostatic and mechanical stifnesses are equilibrated and the oscillation amplitude of the cantilever is close to $200nm$ at its free end. Indeed, the maximum of induced stress into the piezoresistive gauges is reached, as the free end of cantilever touched the electrode without a damageable pull-in for which the cantilever become unstable and collapses. In order to verify that the pull-in amplitude has been reached, the DC voltage has been increased successively from $0.5V$ till $2V$. Consequently, the cantilever nonlinearity becomes potentially softening which should increase the oscillation amplitude of the NEMS sensor.

Figure 8.19 shows a softening resonance curve obtained for $V_{dc} = 2V$. The increase of the electrostatic softening nonlinear stiffness is presented clearly by the distance between the two bifurcation

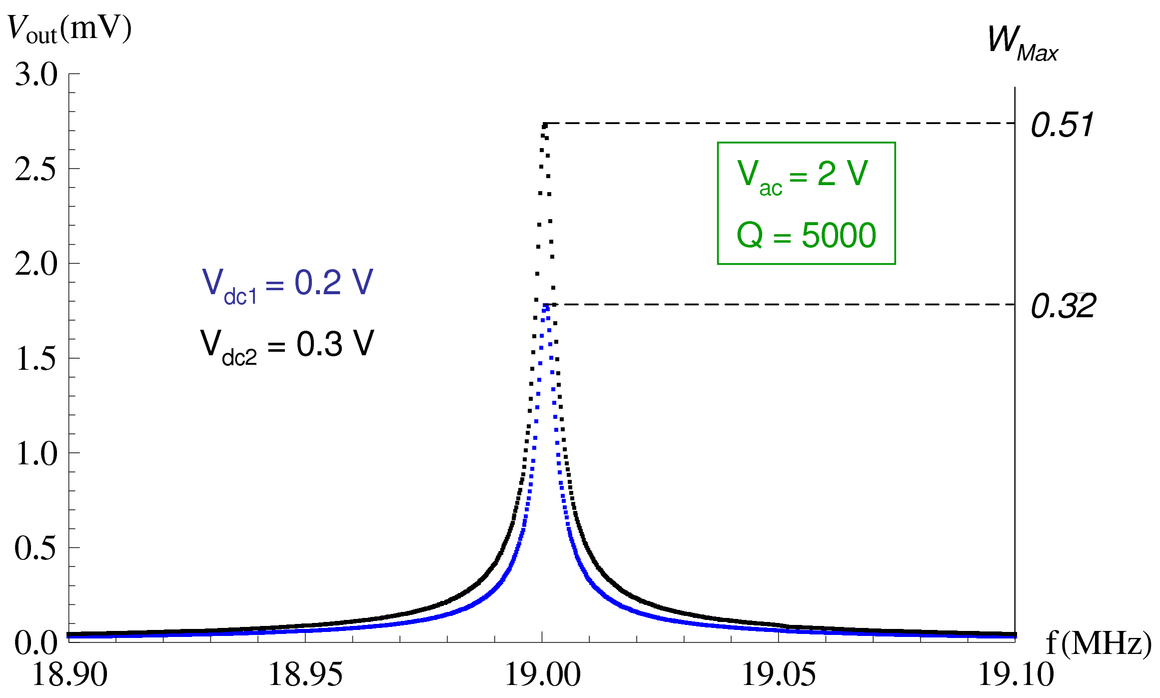

Figure 8.17: Linear resonance frequency responses measured using a 2ω down-mixing technique. The effect of the DC voltage on the resonance frequency is negligeable. W_{max} is the cantilever displacement at its free end normalized by the gap.

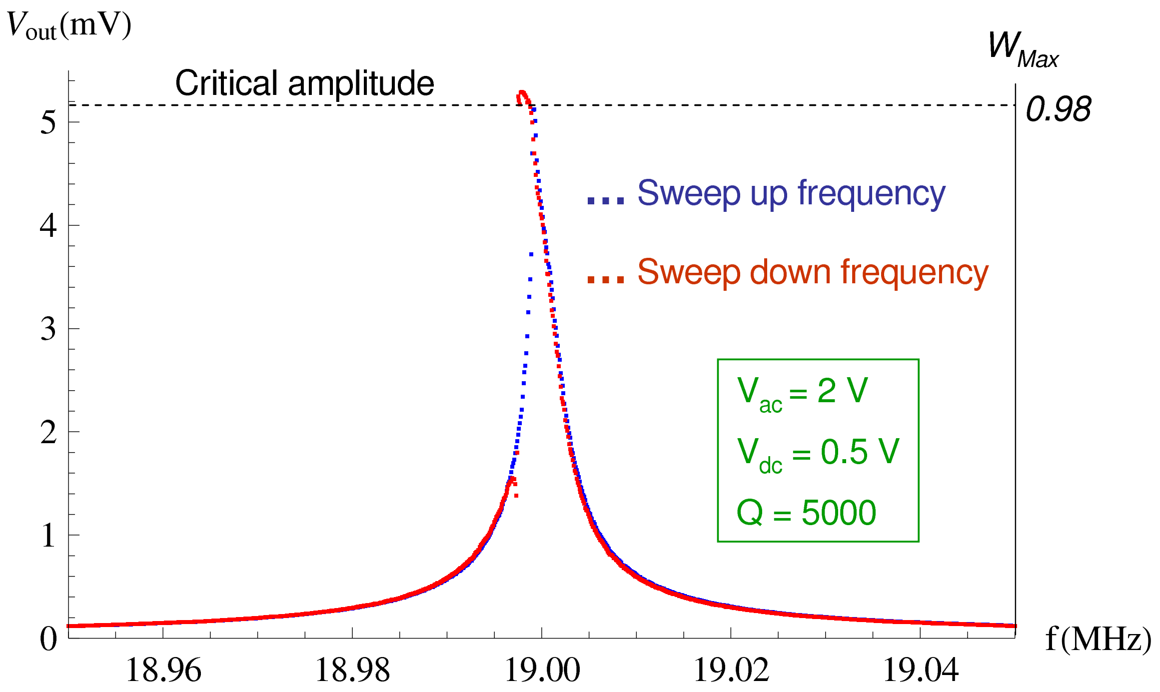

Figure 8.18: Slightly softening resonance frequency response measured using a 2ω down-mixing technique at the optimal DC voltage. The peak is close to the critical amplitude. W_{max} is the cantilever displacement at the its free end normalized by the gap.

points (softening domain) significantly enlarged in comparison with the frequency response in Figure 8.17. Remarkably, the output signal at the peak is around $5.4V$ which is the same value V_{out} at $V_{dc} = 0.5V$. Moreover, the slope of the softening branch between the two bifurcation points is close to zero which confirms that the pull-in amplitude is reached which gives the maximum of stress variation into the piezoresistive gauges.

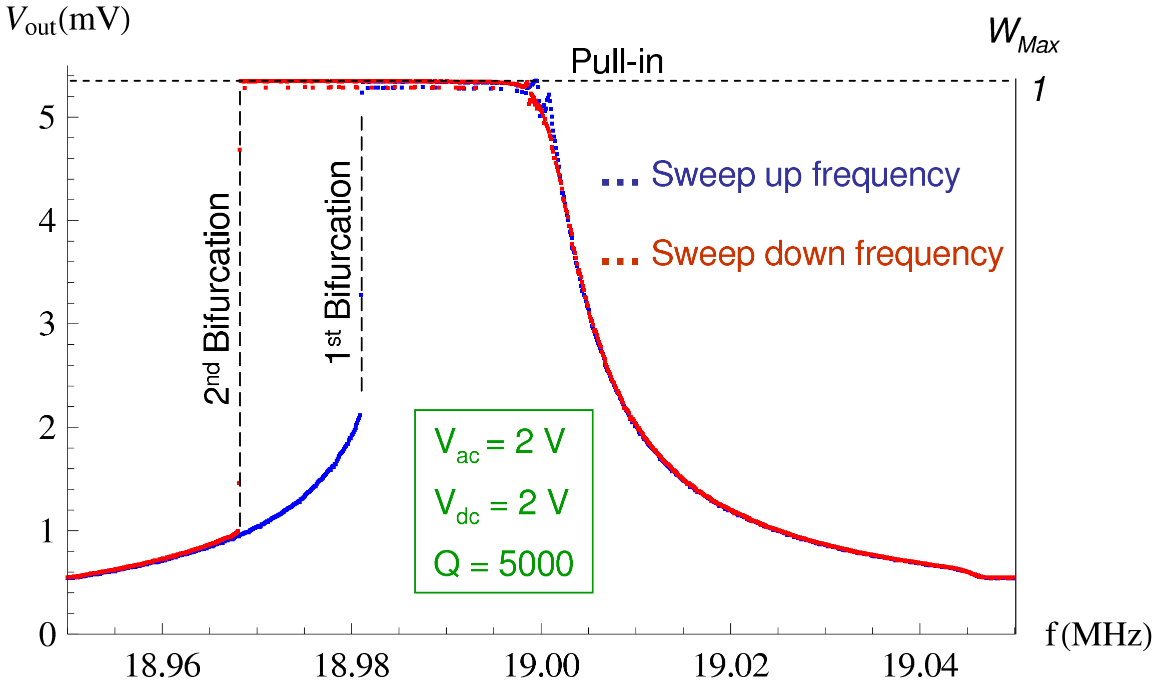

Figure 8.19: Softening frequency response measured using a 2ω down-mixing technique at $V_{dc} = 2V$. The maximal stress on the piezoresistive gauges is reached for the pull-in amplitude. W_{max} is the cantilever displacement at the its free end normalized by the gap.

8.3.9 Mass resolution enhancement

Usually NEMS is embedded in a phase locked loop (PLL) or a self-excited loop in order to monitor time evolution of their resonant frequency. The frequency stability of the overall system (e.g. of the NEMS and the supporting electronics) is characterized by the Allan deviation, defined as [Mo 2007]:

$$\frac{\delta\omega_0}{\omega_0} = \sqrt{\frac{1}{N-1}\sum_{1}^{N}\left(\frac{\bar{\omega}_{i+1}-\bar{\omega}_i}{\omega_0}\right)^2} \tag{8.79}$$

where $\bar{\omega}_i$ is the average angular frequency in the i^{th} time interval, N is the number of independent frequency measurements, which is assumed to be a sufficiently large number. The mass resolution δm is then $\sqrt{2}M_{eff}\frac{\delta\omega_0}{\omega_0}$ for $1\,s$-integration time. At the linear regime and for a cantilever oscillation amplitude around $65nm$, the dynamic range (DR) experimentally measured was about $100\,dB$ [Mile 2010]. This would lead to a theoretical ultimate Allan deviation $\frac{\delta\omega_0}{\omega_0}|_{th} = \frac{10^{-\frac{DR}{20}}}{\sqrt{2Q}}$ of around 10^{-9} [Ekinci 2004b]. For an effective mass of $200\,fg$ and a Q-factor of 6500, this would result in a potential mass resolution of $\delta m = \frac{M_{eff}}{Q}10^{-\frac{DR}{20}} \approx 0.3\,zg$ at room temperature and at relatively low frequency (20 MHz).

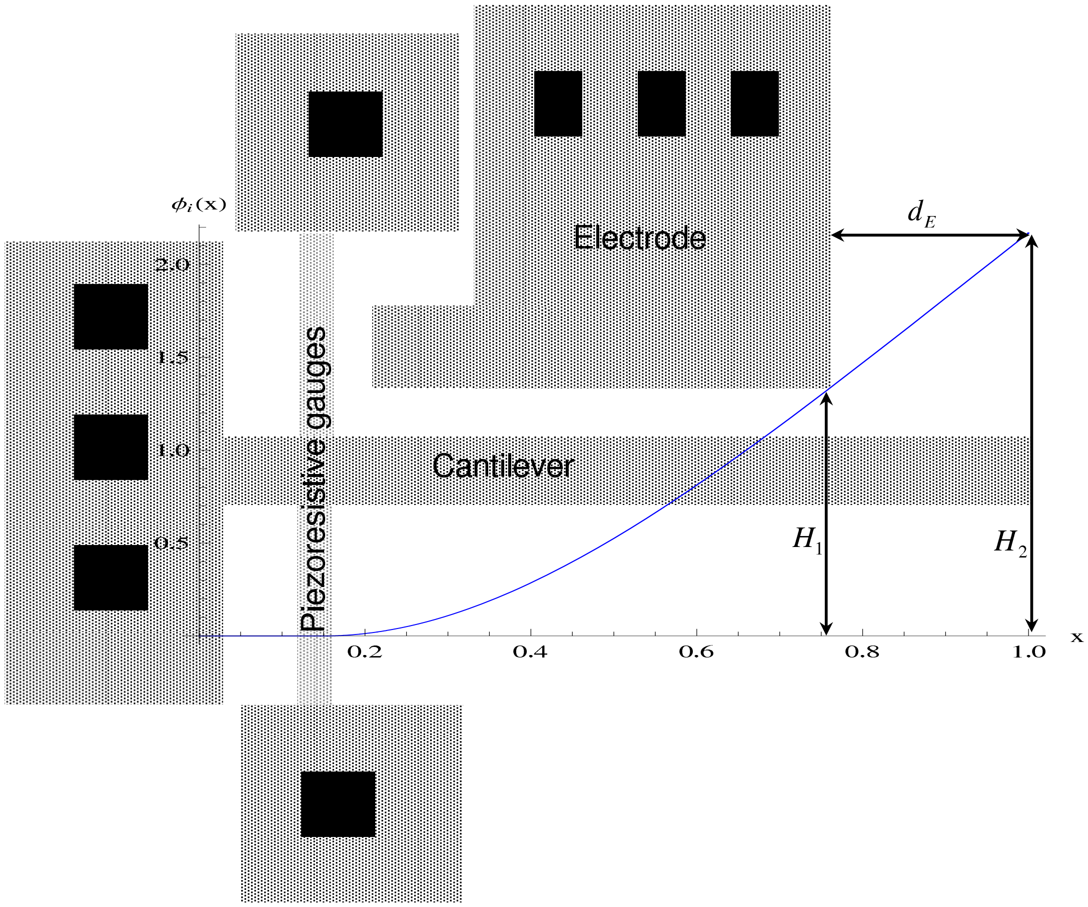

Figure 8.20: The next generation of NEMS resonant mass/gas sensor currently in fabrication in the clean rooms of LETI.

Using the drive conditions of Figure 8.18, at an extremely enhanced critical amplitude of the gap order, the mass sensor dynamic range can be potentially enhanced to reach the level of $110\,dB$. Consequently, a resolution around $100\,Da$ ($0.1\,zg$) is achievable. However, to reach this performance, the temperature fluctuation should be controlled at least below $10^{-2}\,K$ [Giessibl 2003]. Actually, the experimental Allan deviation leads to a mass resolution of approximately $105\,zg$ at room temperature [Mile 2010].

Once the noise contributions from the actuation voltage and the thermal bath issue is solved at low temperature, the ultimate resolution is then 100 . At this level, the cantilever probably touches the electrode as explained in Figure 8.19. Consequently, no further optimizations are possible and one should think about a next generation of the studied device where the gap is quite larger than 200. Nevertheless, the more we enlarge the gap, the more the applied drives voltage must be significantly increased to achieve very high oscillations. Practically, one of the best solutions for the next generation of the NEMS resonant mass sensor is to move the actuation electrode closer to the piezoresistive gauges so that the free end of the cantilever is allowed to oscillate at amplitudes larger than the gap g. As shown in Figure 8.20, the cantilever can potentially undergo oscillations of the order $\frac{H_2}{H_1}g$ at its free end. Combined with the use of an advanced top-down nanowire fabrication techniques [Ernst 2008] with expected giant gauge factors, as well as a possible compensation of nonlinearities, this should greatly decrease the resolution down to one single Dalton.

8.4 Summary

In this chapter, the development of an analytical model and its validation to quantitatively assess the nonlinear dynamics of nanocantilever have been presented. This model includes the main sources of nonlinearities (mechanical and electrostatic) and is based on the modal decomposition using the Galerkin procedure combined with a perturbation technique (the averaging method).

As a first step, the experimental validation of the model has been performed on NEMS cantilevers fabricated using wafer-scale nanostencil lithography (nSL) enabling the definition of very low critical dimension devices. These cantilevers were monolithically integrated with CMOS circuits, which made possible the electrical characterization of their frequency responses. The NEMS devices have been driven in different conditions (in air and in vacuum). All parameters of the model, except the quality factor and the parasitic capacitance, are set prior to the comparison, which shows an excellent agreement in resonance frequency, peak shape and amplitude. Hence, it proves the efficiency of the model as a predictive tool.

The effects of some design parameters on the nonlinear behavior of nanocantilevers have been analytically investigated and close-form solutions of the critical amplitude under dominating mechanical nonlinearities and electrostatic nonlinearities, respectively, have been provided which demonstrates the large dynamic range of NEMS cantilevers compared to doubly clamped nanobeams. The mechanical critical amplitude of a cantilever is then $A_{cm} = 6.3\frac{l}{\sqrt{Q}}$ [Kacem 2010]. More specifically, the analytical expression of the optimal DC drive voltage has been extracted which is an interesting tool for resonant sensors designers. Theoretically, it allows for the cancellation of the nonlinearities in order to drive the NEMS cantilever linearly beyond its critical amplitude. Consequently, this may be a great gain in sensors' sensitivity, as the resonator's carrier power is largely increased while keeping a linear behavior; this may prevent most of noise mixing [Kaajakari 2005a].

In a second step the model has been validated on a high frequency NEMS device electrostatically actuated based on piezoresistive detection ($160nm$ thick) fabricated using a hybrid e-beam/DUV lithography technique. The nanomechanical sensor has been characterized using a down-mixing technique. The ω configuration is first used in order to easily reach the nonlinear regime. Then, the optimal DC voltage being very low, a 2ω down-mixing configuration has been used in order to enable the compensation of the nonlinearities as predicted using the model.

The experimental results show an excellent agreement with the predicted dynamic behaviors. Particularly, the compensation of the nonlinearities has been validated for cantilever displacements up to the gap. Consequently and in a stable linear fashion, the optimal stress variation into the piezoresistive gauges has been reached using the 2ω down-mixing technique. Moreover, in this configuration the mixed behavior has not been observed up to the pull-in amplitude due to the effect of the superharmonic resonance in retarding and suppressing undesirable behaviors. An impressive ultimate resolution about $100\,Da$ is achievable at low temperature and linearly at an oscillation amplitude comparable to the gap for which the maximum of strain collected by the piezoresistive gauges is reached. In order to overcome the gap limitation for the cantilever oscillations, the next generation of the studied device involves an actuation electrode shifted to the gauges side.

Very Large Scale Integration (VLSI) of such devices (Figure 8.20) will potentially enable a wide range of new sensors, such as massive arrays of oscillating NEMS and sensitive multigas sensors. Indeed, the analytical rules provided in this chapter are applicable for resonant chemical and biological nanosensors in order to ensure the optimal mass resolution. Hence, these nonlinear analyses could be very interesting for many nanotechnology challenges such as sub-single-atom resolution in NEMS mass spectrometry [Boisen 2009].

Chapter 9
Conclusions

Contents

9.1 Summary 221
9.2 Future work 223

9.1 Summary

This thesis has detailed the development of several analytical models and their validations to quantitatively assess the nonlinear dynamics of M/NEMS resonators. These models include all sources of nonlinearities, in particular of the electrostatic ones comprising the fringing field effects and are based on the modal decomposition by using the Galerkin procedure combined with perturbation techniques such as the averaging method or the multiple time scales method.

Firstly, this approach has been used to investigate the nonlinear dynamics of clamped-clamped beams for resonant M&NEMS accelerometers. A multimodal approach on a 1-port non linear resonator was performed using the harmonic balance method coupled with a continuation technique (ANM). It has been validated with respect to a reference solution built by shooting. Then, a reduced order model was developed based on the averaging method. This analytical model has been numerically validated by HBM+ANM.

Remarkably, the antisymmetric modes do not change the global dynamics of the resonator and the first mode was enough in order to capture all possible behaviors including the mixed one. Once it was numerically validated, the analytical model has been extended to the 2-port resonators. Also, experimental validation has been performed thanks to the fabrication and electrical measurements of M/NEMS resonators, driven at different (linear and nonlinear) operating conditions.

The shape of the model output (two parametric equations) has the advantage to be simple and easy to implement for M/NEMS designers. The study has notably provided close-form solutions of the critical amplitude including full orders of nonlinearities, as well as the mixed behavior initiation amplitude. It has also shown how it is possible to tune some design parameters (like the ratio between the beam thickness in the direction of vibration h and the detection gap g_d) to keep a linear behavior up to the pull-in point. The consequence of this may be a great gain in sensors' resolution, as the resonator's carrier power is largely increased while keeping a linear behavior may prevent most of noise mixing [Kaajakari 2005a].

Moreover, the importance of the fifth order nonlinearities has been demonstrated through the analytical as well as experimental identification of the mixed behavior. Then, since the hysteresis suppression by nonlinearity cancellation can potentially be sensitive to the fifth order nonlinearities, analytical and experimental investigations were performed to track the onset of the mixed behavior as well as the evolution of its bifurcation topology [Kacem 2009a]. It has been demonstrated that the initiation amplitude of the mixed behavior can be set by design. However, this implies another constraint on the resonator geometry which is not always compatible with sensitivity enhancement (resonator with small length and thickness) as well as with hysteresis suppression (particular ratio between the width and the gap).

In order to overcome in another way the sensitivity of the hysteresis suppression to the mixed behavior issue, the excitation of the resonator at its superharmonic resonance of order-two was analytically investigated. As opposed to the primary resonance case, no mixed behavior has captured and a mechanism to shift up the pull-in has been demonstrated. The principal disadvantage of such excitation is the high polarization voltages that should be applied to the resonator in order to retard the pull-in and conserve a high sensitivity. That is why the next step was the combination of both excitations in simultaneous resonances (primary+superharmonic) and without adding any complexity to the system, since such operation is intrinsic to the electrostatic forces ($2f$ mode of a lock-in amplifier). In this configuration, the analytical results supported by the experimental investigations showed a very interesting mechanism of mixed behavior retarding by superharmonic resonance.

The complete validation of the model was achieved thanks to the fabrication and electrical characterization of several M&NEMS resonators. In particular, a very sensitive capacitive down-mixing set-up allowing the detection of resonator motions bellow $5nm$ was developed. All dynamic behaviors captured by the model have been found experimentally (hardening, softening, mixed and linear compensated). The sensitivity of the compensation to the mixed behavior has been demonstrated as well as the optimization potential of the simultaneous resonances leading to a linear compensated frequency curve by retarding the mixed behavior which can enhance the resonant accelerometer resolution by a factor 5.7.

Secondly, the developed nonlinear modeling approach was extended to the resonant gyroscope. Compared to the resonant accelerometer case, the main change in the equation of motion is the added parametric term due to the time-varying Coriolis force that modulates the resonator stiffness at the proof mass frequency. Nevertheless, this makes the nonlinear partial differential equation quite complex to solve without losing the generality due to possible quasiperiodic motions. Indeed, the developed model was restricted to periodic nonlinear Mathieu resonators and partially validated experimentally. This relatively simple dynamic model is able to predict the measured resonator response for various parameter settings qualitatively and in many cases even quantitatively. A complete parametric study was performed in order to investigate the effect of the proof mass frequency on the resonant gyroscope sensitivity. It has been shown that the maximum of sensitivity is reached when the resonator is driven in the linear regime for a ratio of 25% between the proof mass and the resonator frequencies. Moreover, at a drive frequency higher than 10% the resonator frequency, the angular rate sensor sensitivity decreases significantly in the nonlinear regime. Consequently, the nonlinearity cancellation is needed for ultrasensitive resonant gyroscopes

Besides, a resolution $< 0.1\,°/hr$ was analytically predicted for a particular dual mass M&NEMS gyroscope fully symmetric with its sensing resonators driven linearly beyond their critical amplitude (hysteresis suppression). Such device could overcome the limitations of MEMS vibratory gyroscopes for typical high performances applications such as tactical weapon guidance. Nevertheless, this could potentially imply the use of drastic controllers *i.e.* complexify the sensor electronics.

Finally, the same analytical approach (Galerkin+perturbation technique) used for resonant inertial sensors has been extended to the nonlinear modelling of nanocantilevers for NEMS gas and mass resonant sensors. Unlike the clamped-clamped beam resonators case, the equation of motion of cantilevers is more complicated and includes nonlinear geometric as well as inertial terms. The large dynamic range of cantilevers was demonstrated via the close form expressions of the critical amplitudes. Also, the potential of nonlinearity cancellation was analytically investigated and a close form expression of the optimal DC drive voltage has been extracted which is an interesting tool of optimization for resonant sensors designers. A first validation of the model has been performed on NEMS cantilevers coupled with CMOS circuits, fabricated using wafer-scale nanostencil lithography (nSL) and electrically characterized in different conditions (in air and in vacuum)

The complete validation of the model was achieved on a high frequency NEMS device electrostatically actuated based on piezoresistive detection ($160nm$ thick), fabricated in the LETI clean rooms using a hybrid e-beam/DUV lithography technique and electrically characterized by a piezoresisitive down-mixing technique. Indeed, the model was adapted to the mechanical structure of the sensor in order to extract the close form solutions of the mechanical and electrostatic critical amplitudes as well as the optimal polarization voltage expression.

Particularly, the cancellation of the nonlinearities has been validated for cantilever displacements up to the gap and under simultaneous resonances. An impressive ultimate resolution about $100\,Da$ is achievable at low temperature and linearly at an oscillation amplitude comparable to the gap for which the maximum of strain collected by the piezoresistive gauges was reached.

9.2 Future work

In this thesis, it has been shown that nonlinear design is crucial at the nanoscale, but one still must face all the considerations inherent in device design, such as fabrication tolerances, robustness and reliability.

Anyway, the potential of enhancing the performances of several resonant MEMS and NEMS sensors when the resonators are operating in open-loop was demonstrated. The confirmation by measuring Allan variance in open-loop as well as in closed loop for linear, nonlinear and compensated behaviors will be the next step. Indeed, this can show the influence of noise mixing in the sensor device and evaluate the possible level of enhancement by nonlinear design. Moreover, there are many other steps to accomplish concerning the resonant gyroscope such as the complete numerical and experimental validation of the nonlinear Mathieu resonator model and its extension to quasiperiodic motions as well as the complete characterization of the sensor under angular rate.

Concerning the gas and mass sensors, the next generation of the piezoresistive resonant device has been designed to enable the compensation of nonlinearities at very high oscillations and frequencies in order to exhibit ultrasensitive performances. Indeed, these sensors are good challengers for the single Dalton mass spectroscopy application. Nevertheless, in order to avoid most of temperature fluctuation noise, these devices could ideally operate at low temperature ($> 10\,mK$) which can limit the classical mechanics used for modeling by the quantum effects [Naik 2006, Schwab 2005].

Furthermore, many other applications of the nonlinear dynamics in NEMS are conceivable for our designs. Among these applications, the parametric resonance [Turner 1998, Rugar 1991, Carr 2000, Alhazza 2008] has been widely used in micro and nanotechnology for signal amplification and noise squeezing [Rugar 1991]. Since a resonator electrostatically actuated is intrinsically a parametrically excited nonlinear system, the combination of many resonances could be used to control undesirable behaviors while amplifying the output signal. Also, the high gain achieved when operating close to a bifurcation can also be used in the so called "bifurcation amplifier" applications [Siddiqi 2004].

Appendix A
Appendices

A.1 The fringing field effect

To compute the actuation and detection capacitances, it has been taken into account the fact that the geometry is far from semi-infinite plate capacitors. For weak ratios $\frac{g}{b}$, the fringing field effects are negligible. In our typical cases of ratios $\frac{g}{b}$, higher than 0.05, they can significantly increase the value of the capacitance compared to that of the parallel plates model.

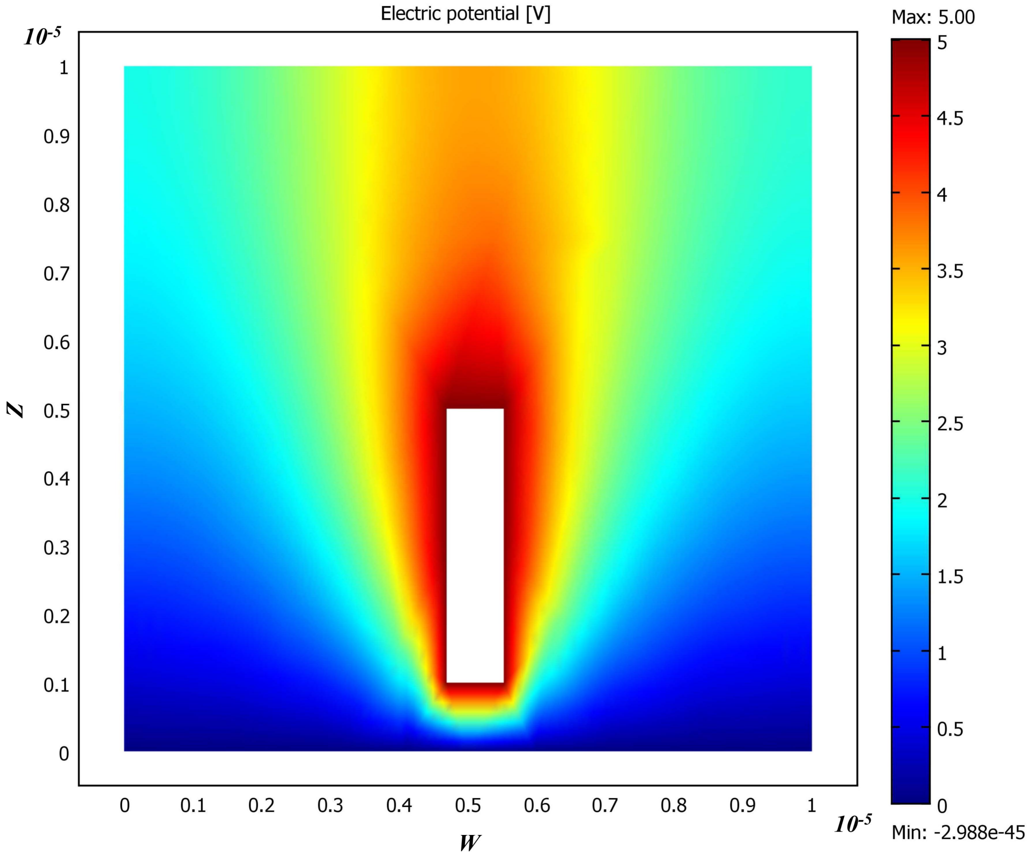

Figure A.1: Fringing field effect: distribution of the electric potential in a cross section of the resonator in the plane (W, Z) under $5V$ of DC voltage.

The fringing field coefficients C_{n1} and $Cn2$ values have been calculated using an analytical model $\left(C_n = 1 + 1.9861 \left(\frac{g}{b}\right)^{0.8258}\right)$ [Nishiyama 1990]. In our case, $C_{n1} = 1.6$ and $C_{n2} = 1.5$. These values have been validated using a 3D COMSOL MULTIPHYSICS FE simulations. Figure A.1 shows the electric potential in a cross section of the resonator described in Figure 4.22 parallel to the beam motion where the inner white rectangle represents the beam and the coloured part represents the air box and the silicon bulk box respectively placed up and down from the mid-plane of the beam. In addition, the silicon oxide between the electrodes and the silicon bulk was incorporated in the 3D FE model. The quantities of electric charges Q_1 and Q_2 have been integrated numerically at each electrode in order to estimate the real capacitances C_1 and C_2 and thus, the fringing field coefficients are directly deduced $C_{ni} = \dfrac{C_i}{C_0 i} = \dfrac{2Q_i g_i^2}{\varepsilon_0 b l V^3}$ where g_i is the gap thickness and V is the DC voltage applied to the beam as a boundary condition in the 3D FE simulations.

A.2 The integration parameters of Equation (4.62)

$$\forall k \in \mathbb{N} \qquad \int_0^1 \left[\Phi_k'\right]^2 dx \simeq \frac{\pi(2k+1)[(2k+1)\pi - 4]}{4}$$

$$\forall i \in \mathbb{N}^* \qquad \int_0^1 \Phi_{2i-1} dx \simeq \frac{8}{\pi\,[1-4i]}$$

$$\forall i \in \mathbb{N}^* \qquad \int_0^1 \Phi_{2i-1}^3 dx \simeq \frac{64}{5\pi(1-4i)}$$

$$\forall i \in \mathbb{N}^* \qquad \int_0^1 \Phi_{2i-1}'' \Phi_{2i-1}^2 dx \simeq \frac{32\pi(4i-1)}{15}$$

$$\forall k \in \mathbb{N}^* \qquad \int_0^1 \Phi_k^4 dx \simeq 3\left\{\frac{1}{\pi[2k+1]} + \frac{1}{2}\right\}$$

$$\forall k \in \mathbb{N}^* \qquad \int_0^1 \Phi_k'' \Phi_k^3 dx \simeq \left[\frac{\pi}{2} + k\pi\right]\left\{0.9 - 1.5\left[\frac{\pi}{2} + k\pi\right]\right\}$$

$$\forall (i,k) \in \mathbb{N}^* \times \mathbb{N}^* \quad and \quad \forall i \neq k$$

$$\int_0^1 \Phi_i' \Phi_k' dx = -\int_0^1 \Phi_i \Phi_k'' dx \simeq \frac{4\pi(i-k)\left[\left(\frac{1}{2}+i\right)+\left(\frac{1}{2}+k\right)\right]^2\left\{1+[-1]^{i+k}\right\}}{k(k+1)\left\{\frac{1}{2}+k(k+1)\right\} - i(i+1)\left\{\frac{1}{2}+i(i+1)\right\}}$$

$$\forall (i,k) \in \mathbb{N}^* \times \mathbb{N}^*$$

$$\int_0^1 \Phi_i \Phi_k^2 dx \simeq \frac{16\left\{1-[-1]^i\right\}\left\{8\left(\frac{\pi}{2}+k\pi\right)^4 - 3\left(\frac{\pi}{2}+i\pi\right)^4 + 10\left(\frac{\pi}{2}+i\pi\right)^3\left(\frac{\pi}{2}+k\pi\right)\right\}}{\left(\frac{\pi}{2}+i\pi\right)\left(\frac{\pi}{2}+k\pi\right)^{-4}\left\{\left(\frac{\pi}{2}+i\pi\right)^8 - 12\left(\frac{\pi}{2}+i\pi\right)^4\left(\frac{\pi}{2}+k\pi\right)^4 - 64\left(\frac{\pi}{2}+k\pi\right)^8\right\}}$$

$$\forall n \in \mathbb{N}^* \qquad \int_0^1 \Phi_{2n-1}^3 dx \simeq \frac{64}{5\pi(1-4n)}$$

$$\forall (i,k) \in \mathbb{N}^* \times \mathbb{N}^* \qquad \int_0^1 \Phi_i \Phi_k \Phi_k'' dx \simeq \frac{32\left([-1]^i - 1\right)\left(\frac{\pi}{2}+k\pi\right)^6}{\left(\frac{\pi}{2}+i\pi\right)\left\{\left(\frac{\pi}{2}+i\pi\right)^4 - 16\left(\frac{\pi}{2}+k\pi\right)^4\right\}}$$

$$\forall n \in \mathbb{N}^* \qquad \int_0^1 \Phi_{2n-1}'' \Phi_{2n-1}^2 dx \simeq \frac{32\pi(4n-1)}{15}$$

$\forall(i,k)\in\mathbb{N}^*\times\mathbb{N}^* \quad and \quad \forall i\neq k$

$$\int_0^1 \Phi_i\Phi_k^3dx \simeq \frac{1}{\pi}\left\{\begin{array}{c}
\frac{3\left(1+[-1]^{i+k}\right)}{1+i+k}+\frac{1+[-1]^{i+3k}}{2+i+3k}+\frac{6\left(1+[-1]^{i+k}\right)(i-k)}{1+2i+2i^2+2k+2k^2}-\frac{3\left(1+[-1]^{i+k}\right)(1+2k)}{2+2i+i^2+6k+2ik+5k^2}\\
+\frac{4-2i+10k+3(1-i+3k)[-1]^{i+k}+(1+i+k)[-1]^{i+3k}}{2(-1+i-3k)(1+i+k)}-\frac{6\left(1+[-1]^{i+3k}\right)(1+i+k)}{5+6i+2i^2+14k+8ik+10k^2}\\
-\frac{6\left(1+[-1]^{i+3k}\right)(1+2k)\left(-1+4i+2i^2-8k+4ik-10k^2\right)}{(1-2i+2i^2+6k-8ik+10k^2)(5+6i+2i^2+14k+8ik+10k^2)}+\frac{2\left(1+[-1]^{i+3k}\right)(-1+i-3k)}{5+2i+2i^2+18k+18k^2}\\
-\frac{2\left(1+[-1]^{i+k}\right)\left(-1+5i+2i^3-11k+20ik-6i^2k-32k^2+26ik^2-30k^3\right)}{(1+2i+2i^2+2k+2k^2)(5+2i+2i^2+18k+18k^2)}\\
-\frac{3\left(1+[-1]^{i+3k}\right)\left(-1-i+i^3-5k-4ik-3i^2k-8k^2-ik^2-5k^3\right)}{(1+i^2+4k-2ik+5k^2)(2+2i+i^2+6k+2ik+5k^2)}
\end{array}\right\}$$

$\forall(i,k)\in\mathbb{N}^*\times\mathbb{N}^* \quad and \quad \forall i\neq k$

$$\int_0^1 \Phi_i\Phi_k^2\Phi_k''dx \simeq \frac{\pi(1+2k)^2}{4}\left\{\begin{array}{c}
\frac{1+[-1]^{i+3k}}{2+i+3k}-\frac{2\left(1+[-1]^{i+k}\right)(i-k)}{1+2i+2i^2+2k+2k^2}+\frac{2\left(1+[-1]^{i+3k}\right)(-1+i-3k)}{5+2i+2i^2+18k+18k^2}\\
-\frac{(1+i+k)[-1]^{i+3k}-3(-1+i-3k)[-1]^{i+k}-2(-2+i-5k)}{2(-1+i-3k)(1+i+k)}-\frac{1+[-1]^{i+k}}{1+i+k}\\
+\frac{\left(1+[-1]^{i+k}\right)(1+2k)}{2+2i+i^2+6k+2ik+5k^2}-\frac{2\left(1+[-1]^{i+3k}\right)(1+i+k)}{5+6i+2i^2+14k+8ik+10k^2}\\
+\frac{2\left(1+[-1]^{i+3k}\right)(1+2k)\left(-1+4i+2i^2-8k+4ik-10k^2\right)}{(1-2i+2i^2+6k-8ik+10k^2)(5+6i+2i^2+14k+8ik+10k^2)}\\
+\frac{2\left(1+[-1]^{i+k}\right)\left(-1+5i+2i^3-11k+20ik-6i^2k-32k^2+26ik^2-30k^3\right)}{(1+2i+2i^2+2k+2k^2)(5+2i+2i^2+18k+18k^2)}\\
-\frac{\left(1+[-1]^{i+3k}\right)\left(-1-i+i^3-5k-4ik-3i^2k-8k^2-ik^2-5k^3\right)}{(1+i^2+4k-2ik+5k^2)(2+2i+i^2+6k+2ik+5k^2)}
\end{array}\right\}$$

A.3 Approximate integrals

$$\omega_n^2=-2\left(Vs^2+V_{dc}^2\right)\frac{C_{n2}\alpha_2}{R_g}\int_{\frac{l-l_d}{2l}}^{\frac{l+l_d}{2l}}{\phi_1}^2\,dx+C_{n1}\alpha_2\frac{2V_{dc}^2+V_{ac}^2}{R_g^2}\int_{\frac{l-l_a}{2l}}^{\frac{l+l_a}{2l}}{\phi_1}^2\,dx$$

$$+4V_{dc}Vs\frac{C_{n2}\alpha_2}{R_g}\int_{\frac{l-l_d}{2l}}^{\frac{l+l_d}{2l}}{\phi_1}^2\,dx+\lambda_1^4-N\int_0^1\phi_1\phi_1''dx$$

$$\mu_1=-2\int_0^1{\phi_1}^3dx\frac{(1+R_g)}{R_g}$$

$$\mu_2=\frac{1+4R_g+R_g^2}{R_g^2}\int_0^1{\phi_1}^4\,dx$$

$$\mu_3=-\frac{2\left(1+R_g\right)}{R_g^2}\int_0^1{\phi_1}^5\,dx$$

$$\mu_4=-\frac{2\left(1+R_g\right)}{R_g^2}\int_0^1{\phi_1}^6\,dx$$

$$\chi_2 = \left(-2\lambda_1^4\frac{(1+2R_g)}{R_g} - \frac{C_{n1}\alpha_2 V_{ac}^2}{{R_g}^2}\right)\int_0^1 {\phi_1}^3\,dx + C_{n2}\alpha_2\frac{\left(V_{dc}^2 - 2V_{dc}Vs + Vs^2\right)}{{R_g}^2}\int_{\frac{l-l_d}{2l}}^{\frac{l+l_d}{2l}} {\phi_1}^3\,dx$$

$$-\frac{V_{dc}^2 C_{n1}\alpha_2}{{R_g}^2}\int_{\frac{l-l_a}{2l}}^{\frac{l+l_a}{2l}} {\phi_1}^3\,dx + 2N\frac{(1+2R_g)}{R_g}\int_0^1 {\phi_1}^2\phi_1''dx$$

$$\chi_3 = -N\frac{1+4R_g+R_g^2}{R_g^2}\int_0^1 {\phi_1}^3\phi_1''dx + \lambda_1^4\frac{1+4R_g+R_g^2}{R_g^2}\int_0^1 {\phi_1}^4\,dx - \alpha_1\int_0^1\left(\int_0^1 {\phi_1'}^2\,dx\right)\phi_1\phi_1''dx$$

$$\chi_4 = 2\alpha_1\frac{1+R_g}{R_g}\int_0^1\left(\int_0^1 {\phi_1'}^2\,dx\right){\phi_1}^2\phi_1''dx + 2N\frac{1+R_g}{R_g^2}\int_0^1 {\phi_1}^4\phi_1''dx - 2\lambda_1^4\frac{1+R_g}{R_g^2}\int_0^1 {\phi_1}^5\,dx$$

$$\chi_5 = \frac{\lambda_1^4}{R_g^2}\int_0^1 {\phi_1}^6\,dx - \frac{N}{R_g^2}\int_0^1 {\phi_1}^5\phi_1''dx - \alpha_1\frac{1+4R_g+R_g^2}{R_g^2}\int_0^1\left(\int_0^1 {\phi_1'}^2dx\right)R_g^2\alpha_1{\phi_1}^3\phi_1''dx$$

$$\chi_6 = 2\alpha_1\frac{1+R_g}{R_g^2}\int_0^1\left(\int_0^1 {\phi_1'}^2dx\right){\phi_1}^4\phi_1''dx$$

$$\chi_7 = -\frac{\alpha_1}{R_g^2}\int_0^1\left(\int_0^1 {\phi_1'}^2dx\right){\phi_1}^5\phi_1''dx$$

$$\nu = -\frac{1}{2}\left(C_{n1}\alpha_2\left(V_{ac}^2 + 2V_{dc}^2\right)\int_{\frac{l-l_a}{2l}}^{\frac{l+l_a}{2l}}\phi_1\,dx\right) + C_{n2}R_g^2\alpha_2\left(V_{dc}^2 - 2V_{dc}Vs + Vs^2\right)\int_{\frac{l-l_d}{2l}}^{\frac{l+l_d}{2l}}\phi_1\,dx$$

$$\zeta_0 = 4V_{ac}V_{dc}C_{n1}\alpha_2\int_{\frac{l-l_a}{2l}}^{\frac{l+l_a}{2l}}\phi_1\,dx$$

$$\zeta_1 = -4V_{ac}V_{dc}C_{n1}\alpha_2\int_{\frac{l-l_a}{2l}}^{\frac{l+l_a}{2l}}\phi_1^2\,dx$$

$$\zeta_2 = 2V_{ac}V_{dc}C_{n1}\alpha_2\int_{\frac{l-l_a}{2l}}^{\frac{l+l_a}{2l}}\phi_1^3\,dx$$

$$\zeta_3 = -V_{ac}^2C_{n1}\alpha_2\int_{\frac{l-l_a}{2l}}^{\frac{l+l_a}{2l}}\phi_1\,dx$$

$$\zeta_4 = V_{ac}^2C_{n1}\alpha_2\int_{\frac{l-l_a}{2l}}^{\frac{l+l_a}{2l}}\phi_1^2\,dx$$

$$\zeta_5 = -\frac{1}{2}V_{ac}^2C_{n1}\alpha_2\int_{\frac{l-l_a}{2l}}^{\frac{l+l_a}{2l}}\phi_1^3\,dx$$

Bibliography

[Abad 2007] Estefania Abad, Stefano Zampolli, Santiago Marco, Andrea Scorzoni, Barbara Mazzolai, Aritz Juarros, David Gómez, Ivan Elmi, Gian Carlo Cardinali, José M. Gómez, Francisco Palacio, Michelle Cicioni, Alessio Mondini, Thomas Becker and Ilker Sayhan. *Flexible tag microlab development: Gas sensors integration in RFID flexible tags for food logistic*. Sensors and Actuators B: Chemical, vol. 127, no. 1, pages 2 – 7, 2007. Special Issue: Eurosensors XX The 20th European Conference on Solid-State Transducers, the 20th European conference on Solid-State Transducers. 25

[Abbaspour-Sani 1994] E. Abbaspour-Sani, R. S. Huang and C. Y. Kwok. *A linear electromagnetic accelerometer*. Sensors Actuators A, vol. 44, no. 2, page 103109, 1994. 19

[Abdel-Rahman 2002] Eihab M Abdel-Rahman, Mohamed I Younis and Ali H Nayfeh. *Characterization of the mechanical behavior of an electrically actuated microbeam*. Journal of Micromechanics and Microengineering, vol. 12, no. 6, page 759, 2002. 88

[Abdel-Rahman 2003] Eihab M Abdel-Rahman and Ali H Nayfeh. *Secondary resonances of electrically actuated resonant microsensors*. Journal of Micromechanics and Microengineering, vol. 13, no. 3, pages 491–501, 2003. 124

[Abraham 2003] Glomin Thomas Abraham and Anindya Chatterjee. *Approximate Asymptotics for a Nonlinear Mathieu Equation Using Harmonic Balance Based Averaging*. Nonlinear Dynamics, vol. 31, no. 4, page 347365, 2003. 163

[Acar 2003] C. Acar and A.M. Shkel. *Nonresonant micromachined gyroscopes with structural mode-decoupling*. Sensors Journal, IEEE, vol. 3, no. 4, pages 497–506, Aug. 2003. 157

[Acar 2005] C. Acar and A.M. Shkel. *An approach for increasing drive-mode bandwidth of MEMS vibratory gyroscopes*. Microelectromechanical Systems, Journal of, vol. 14, no. 3, pages 520–528, June 2005. 157

[Ahmadian 2009] M.T. Ahmadian, H. Borhan and E. Esmailzadeh. *Dynamic analysis of geometrically nonlinear and electrostatically actuated micro-beams*. Communications in Nonlinear Science and Numerical Simulation, vol. 14, no. 4, pages 1627 – 1645, 2009. 188

[Albrecht 1991] T. R. Albrecht, P. Grütter, D. Horne and D. Rugar. *Frequency modulation detection using high-Q cantilevers for enhanced force microscope sensitivity*. Journal of Applied Physics, vol. 69, no. 2, pages 668–673, 1991. 32

[Alhazza 2008] Khaled A. Alhazza, Mohammed F. Daqaq, Ali H. Nayfeh and Daniel J. Inman. *Non-linear vibrations of parametrically excited cantilever beams subjected to non-linear delayed-feedback control*. International Journal of Non-Linear Mechanics, vol. 43, no. 8, pages 801 – 812, 2008. 188, 223

[Allen 1989a] H. V. Allen, S. C. Terry and D. W. DeBruin. *Accelerometer Systems with Self-Testable Features*. Sensors and Actuators, vol. 20, pages 153–161, 1989. 17

[Allen 1989b] H. V. Allen, S. C. Terry and W. Knutti. *Understanding Silicon Accelerometers*. Sensors, pages 1–6, 1989. 18

[Amanda 2001] A. Amanda and S.K. Mallapragada. *Comparison of protein fouling on heat-treated poly(vinyl alcohol), poly(ether sulfone) and regenerated cellulose membranes using diffuse reflectance infrared fourier transform spectroscopy.* Biotechnol. Prog., vol. 17, no. 5, page 917923, 2001. 30

[Arcamone 2007] J. Arcamone, B. Misischi, F. Serra-Graells, M. A. F. van den Boogaart, J. Brugger, F. Torres, G. Abadal, N. Barniol and F. Perez-Murano. *A Compact and Low-Power CMOS Circuit for Fully Integrated NEMS Resonators.* Circuits and Systems II: Express Briefs, IEEE Transactions on, vol. 54, no. 5, pages 377–381, May 2007. 195, 197

[Arcamone 2008] J Arcamone, M A F van den Boogaart, F Serra-Graells, J Fraxedas, J Brugger and F PÃ©rez-Murano. *Full-wafer fabrication by nanostencil lithography of micro/nanomechanical mass sensors monolithically integrated with CMOS.* Nanotechnology, vol. 19, no. 30, page 305302, 2008. 195, 196, 197

[Arntz 2003] Y Arntz, J D Seelig, H P Lang, J Zhang, P Hunziker, J P Ramseyer, E Meyer, M Hegner and Ch Gerber. *Label-free protein assay based on a nanomechanical cantilever array.* Nanotechnology, vol. 14, no. 1, page 86, 2003. 30

[Azrar 1993] L Azrar, B Cochelin, D Damil and M Potier-Ferry. *An asymptotic-numerical method to compute the post-buckling behaviour of elastic plates and shells.* International Journal for Numerical Methods in Engineering, vol. 36, pages 1251–1277, 1993. 75

[Baguet 2003] S Baguet and B Cochelin. *On the behaviour of the ANM in the presence of bifurcations.* Communications in Numerical Methods in Engineering, vol. 19, pages 459–471, 2003. 75, 76

[Ballantine 1989] D.S. Ballantine and H. Wohltjen. *Surface acoustic wave devices for chemical analysis.* Anal. Chem., vol. 61, no. 11, page 704715, 1989. 27

[Ballantine 1996] D.S. Ballantine, R.M. White, S.J. Martin, A.J. Ricco, E.T. Zellers and G.C. Frye et al. Acoustic wave sensors: Theory, design, physico-chemical applications (applications of modern acoustics). Academic Press, 1996. 27, 28

[Ballantine 1997] D. S. Ballantine, R. M. White, S. J. Martin, A. J. Ricco, G. C. Frye, E. T. Zellers and H. Wohltjen. Acoustic wave sensors: Theory, design, and physico-chemical applications. Academic Press., 1997. 30

[Banerjee 2008] A. Banerjee, B. Bhattacharya and A.K. Mallik. *Large deflection of cantilever beams with geometric non-linearity: Analytical and numerical approaches.* International Journal of Non-Linear Mechanics, vol. 43, no. 5, pages 366 – 376, 2008. 188

[Bargatin 2005] I. Bargatin, E. B. Myers, J. Arlett, B. Gudlewski and M. L. Roukes. *Sensitive detection of nanomechanical motion using piezoresistive signal downmixing.* Applied Physics Letters, vol. 86, no. 13, page 133109, 2005. 138, 211

[Barth 1988] P.W. Barth, F. Pourahmadi, R. Mayer, J. Poydock and K. Petersen. *A monolithic silicon accelerometer with integral air damping and overrange protection.* In Solid-State Sensor and Actuator Workshop, 1988. Technical Digest., IEEE, pages 35–38, Jun 1988. 17

[Battiston 2001] F. M. Battiston, J. P. Ramseyer, H. P. Lang, M. K. Baller, Ch. Gerber, J. K. Gimzewski, E. Meyer and H. J. Güntherodt. *A chemical sensor based on a microfabricated* *cantilever array with simultaneous resonance-frequency and bending readout.* Sensors and Actuators B: Chemical, vol. 77, no. 1-2, pages 122 – 131, 2001. 187

[Belhaq 1999] Mohamed Belhaq and Mohamed Houssni. *Quasi-Periodic Oscillations, Chaos and Suppression of Chaos in a Nonlinear Oscillator Driven by Parametric and External Excitations.* Nonlinear Dynamics, vol. 18, pages 1–24(24), January 1999. 165

[Belhaq 2002] Mohamed Belhaq, Kamar Guennoun and Mohamed Houssni. *Asymptotic solutions for a damped non-linear quasi-periodic Mathieu equation.* International Journal of Non-Linear Mechanics, vol. 37, no. 3, pages 445 – 460, 2002. 164

[Belhaq 2007] Mohamed Belhaq and Abdelhak Fahsi. *2:1 and 1:1 frequency-locking in fast excited van der PolMathieuDuffing oscillator.* Nonlinear Dynamics, vol. 53, no. 1-2, pages 139–152, 2007. 163

[Berger 1997] R Berger, E Delamarche, H P Lang, C Gerber, J K Gimzewski, E Meyer and H J Guntherodt. *Surface Stress in the Self-Assembly of Alkanethiols on Gold.* Science, vol. 276, no. 5321, pages 2021–2024, 1997. 28

[Bodenhöfer 1996] K Bodenhöfer, A Hierlemann, G Noetzel, U Weimar and W Göpel. *Performances of mass-sensitive devices for gas sensing: thickness shear mode and surface acoustic wave transducers.* Anal. Chem., vol. 68, pages 2210–2218, 1996. 29

[Boisen 2009] Anja Boisen. *Nanoelectromechanical systems: Mass spec goes nanomechanical.* Nature Nanotechnology, vol. 4, pages 404–405, 2009. 219

[Boltshauser 1992] T Boltshauser, M Schonholzer, O Brand and H Baltes. *Resonant humidity sensors using industrial CMOS-technology combined with postprocessing.* Journal of Micromechanics and Microengineering, vol. 2, no. 3, page 205, 1992. 32

[Brand 1998] Oliver Brand and Henry Baltes. *Micromachined Resonant Sensors - an Overview.* Sensors Update, vol. 4, no. 1, pages 3 – 51, 1998. 33

[Burns 1996a] D. W. Burns, R. D. Horning, W. R. Herb, J. D. Zook and H. Guckel. *Sealed-cavity resonant microbeam accelerometer.* Sensors and Actuators A: Physical, vol. 53, no. 1-3, pages 249 – 255, 1996. Proceedings of The 8th International Conference on Solid-State Sensors and Actuators. 32, 82

[Burns 1996b] D.W. Burns, W. R. Herb, J. D. Zook and M. L. Wilson. *Optically driven resonant microbeam temperature sensors for fiber optical networks.* page 294298, 1996. 32

[Burrer 1995] C. Burrer and J. Esteve. *A novel resonant silicon accelerometer in bulk-micromachining technology.* Sensors and Actuators A: Physical, vol. 46, pages 185–189(5), January 1995. 19

[Campbell 1998] C.K. Campbell. Surface acoustic wave devices for mobile and wireless communications. Academic Press, 1998. 26

[Carr 1999] Dustin W. Carr, S. Evoy, L. Sekaric, H. G. Craighead and J. M. Parpia. *Measurement of mechanical resonance and losses in nanometer scale silicon wires.* Applied Physics Letters, vol. 75, no. 7, pages 920–922, 1999. 124

[Carr 2000] Dustin W. Carr, Stephane Evoy, Lidija Sekaric, H. G. Craighead and J. M. Parpia. *Parametric amplification in a torsional microresonator.* Applied Physics Letters, vol. 77, no. 10, pages 1545–1547, 2000. 124, 223

[Chatterjee 2003] A. Chatterjee. *Harmonic Balance Based Averaging: Approximate Realizations of an Asymptotic Technique.* Nonlinear Dynamics, vol. 32, no. 4, pages 323–343, 2003. 163

[Cho 2003] A Cho. *Physics - researchers race to put the quantum into mechanics.* Science, vol. 299, no. 5603, pages 36–37, 2003. 1

[Chowdhury 2005] S Chowdhury, M Ahmadi and W C Miller. *A closed-form model for the pull-in voltage of electrostatically actuated cantilever beams.* Journal of Micromechanics and Microengineering, vol. 15, no. 4, page 756, 2005. 188

[Clark 1996] W. A. Clark, R. T. Howe and R. Horowitz. *Surface micromachined Z-axis vibratory rate gyroscope.* pages 283–287, 1996. 21, 158

[Clark 1997] W. Clark. *Micromachined vibratory rate gyroscopes.* PhD thesis, University of California, Berkeley, 1997. 157

[Cleland 2002] A. N. Cleland and M. L. Roukes. *Noise processes in nanomechanical resonators.* Journal of Applied Physics, vol. 92, no. 5, pages 2758–2769, 2002. 30, 40, 41, 44

[Cleland 2003] A. Cleland. Foundations of nanomechanics. Springer, 2003. 41

[Cochelin 1994] B Cochelin. *A path-following technique via an asymptotic-numerical method.* Computers and Structures, vol. 53, pages 1181–1192, 1994. 75, 76

[Cochelin 2007] B Cochelin, D Damil and M Potier-Ferry. Méthode asymptotique numérique, collection méthodes numériques. Hermes Sciences Lavoisier (2007) (in French), 2007. 75, 76

[Cochelin 2009] B Cochelin and C Vergez. *A high order purely frequency-based harmonic balance formulation for continuation of periodic solutions.* Journal of Sound and Vibration, vol. 324, pages 243–262, 2009. 75, 76, 77

[Colinet 2009] E. Colinet, C. Durand, L. Duraffourg, P. Audebert, G. Dumas, F. Casset, E. Ollier, P. Ancey, J.-F. Carpentier, L. Buchaillot and A.M. Ionescu. *Ultra-Sensitive Capacitive Detection Based on SGMOSFET Compatible With Front-End CMOS Process.* Solid-State Circuits, IEEE Journal of, vol. 44, no. 1, pages 247–257, Jan. 2009. 209

[Copson 1965] E. T. Copson. Asymptotic expansions. Cambridge University Press, 1965. 53

[Cunningham 2001] B Cunningham, M Weinberg, J Pepper, C Clapp, R Bousquet, B Hugh, R Kant, C Daly and E Hauser. *Design, fabrication and vapor characterization of a microfabricated flexural plate resonator sensor and application to integrated sensor arrays.* Sens Actuators B., vol. 73, pages 112–123, 2001. 29

[Despont 2000] M Despont, J Brugger, U Drechsler, U Durig, W Haberle, M Lutwyche, H Rothuizen, R Stutz, R Widmer, G Binnig, H Rohrer and P Vettiger. *VLSI-NEMS chip for parallel AFM data storage.* Sensors and Actuators A: Physical, vol. 80, pages 100–107(8), 2000. 11

[DeVoe 1997] D.L. DeVoe and A.P. Pisano. *A fully surface-micromachined piezoelectric accelerometer.* In Solid State Sensors and Actuators, 1997. TRANSDUCERS '97 Chicago., 1997 International Conference on, volume 2, pages 1205–1208 vol.2, Jun 1997. 19

[Dufour 1998] R Dufour and A. Berlioz. *Parametric Instability of a Beam Due to Axial Excitations and to Boundary Conditions.* Journal of Vibration and Acoustics, vol. 120, pages 461–467, 1998. 164

[Ekinci 2004a] K L Ekinci, X M H Huang and M L Roukes. *Ultrasensitive nanoelectromechanical mass detection.* Appl. Phys. Lett., vol. 84, page 446971, 2004. 1, 29, 187, 188

[Ekinci 2004b] K. L. Ekinci, Y. T. Yang and M. L. Roukes. *Ultimate limits to inertial mass sensing based upon nanoelectromechanical systems.* Journal of Applied Physics, vol. 95, no. 5, pages 2682–2689, 2004. 41, 217

[Ekinci 2005] K. L. Ekinci and M. L. Roukes. *Nanoelectromechanical systems.* Review of Scientific Instruments, vol. 76, no. 6, page 061101, 2005. 1, 38

[Enoksson 1997] P. Enoksson, G. Stemme and E. Stemme. *A silicon resonant sensor structure for Coriolis mass-flow measurements.* Microelectromechanical Systems, Journal of, vol. 6, no. 2, pages 119–125, Jun 1997. 32

[Ernst 2008] T Ernst, L Duraffourg, C Dupre, E Bernard, P Andreucci, S Becu, E Ollier, A Hubert, C Halte, J Buckley, O Thomas, G Delapierre, S Deleonibus, B de Salvo, P Robert and O Faynot. In Electron Devices Meeting IEDM 2008-IEEE, 2008. 218

[Esashi 1996] M. Esashi. *Resonant sensors by silicon micromachining.* In Frequency Control Symposium, 1996. 50th., Proceedings of the 1996 IEEE International., pages 609–614, Jun 1996. 32

[Fargas-Marques 2007] A. Fargas-Marques, J. Casals-Terre and A.M. Shkel. *Resonant Pull-In Condition in Parallel-Plate Electrostatic Actuators.* Microelectromechanical Systems, Journal of, vol. 16, no. 5, pages 1044–1053, Oct. 2007. 118

[Feng 2007] X L Feng. *Phase noise and frequency stability of very-high frequency silicon nanowire nanomechanical resonators.* In 14th International Conference on Solid-State Sensors, Actuators and Microsystems, pages 327–30, 2007. 1

[Feng 2008] X L Feng, C J White, A Hajimiri and M L Roukes. *A self-sustaining ultrahigh-frequency nanoelectromechanical oscillator.* Nature Nanotechnology, vol. 3, pages 342–346, 2008. 187

[Florin 1995] E. L. Florin, M. Rief, H. Lehmann, M. Ludwig, C. Dornmair, V. T. Moy and H. E. Gaub. *Sensing specific molecular interactions with the atomic force microscope.* Biosensors and Bioelectronics, vol. 10, pages 895–901(7), 1995. 32

[Forsen 2005] et al. Forsen E. *Ultrasensitive mass sensor fully integrated with complementary metal-oxide-semiconductor circuitry.* Appl. Phys. Lett., vol. 87, page 043507, 2005. 187

[Fritz 2000] J Fritz, M K Baller, H P Lang, H Rothuizen, P Vettiger, E Meyer, H J Guntherodt, C Gerber and K J Gimzewski. *Translating Biomolecular Recognition into Nanomechanics.* Science, vol. 288, no. 5464, pages 316–318, 2000. 28

[Gardner 1999] J.W. Gardner and P.N. Bartlett. Electronic noses: principles and application. Oxford University Press, 1999. 25

[Gardner 2004] J. W. Gardner and J. Yinon. Electronic noses and sensors for the detection of explosives, volume 159. Springer, 2004. 25

[Geiger 1999] W. Geiger, B. Folkmer, J. Merz, H. Sandmaier and W. Lang. *A new silicon rate gyroscope*. Sensors and Actuators A: Physical, vol. 73, pages 45–51(7), 9 March 1999. 21

[Geiger 2000] Wolfram Geiger, Jürgen Merz, Thomas Fischer, Bernd Folkmer, Hermann Sandmaier and Walter Lang. *The silicon angular rate sensor system DAVED®*. Sensors and Actuators A: Physical, vol. 84, no. 3, pages 280 – 284, 2000. ix, 21, 22

[Geiger 2002] W. Geiger, W. U. Butt, A. Gaißer, J. Frech, M. Braxmaier, T. Link, A. Kohne, P. Nommensen, H. Sandmaier, W. Lang and H. Sandmaier. *Decoupled microgyros and the design principle DAVED*. Sensors and Actuators A: Physical, vol. 95, no. 2-3, pages 239 – 249, 2002. ix, 21, 22

[Geller 2005] Michael R. Geller and Joel B. Varley. *Friction in nanoelectromechanical systems: Clamping loss in the GHz regime*, 2005. 39

[Giessibl 2003] Franz J. Giessibl. *Advances in atomic force microscopy*. Rev. Mod. Phys., vol. 75, no. 3, pages 949–983, Jul 2003. xv, 180, 218

[Gizeli 2002] E. Gizeli and C. R. Lowe. Biomolecular sensors. Taylor and Frances, 2002. 31

[Guennoun 2002] Kamar Guennoun, Mohamed Houssni and Mohamed Belhaq. *Quasi-Periodic Solutions and Stability for a Weakly Damped Nonlinear Quasi-Periodic Mathieu Equation*. Nonlinear Dynamics, vol. 27, pages 211–236(26), February 2002. 164

[Gui 1995] Chengqun Gui, R. Legtenberg, H.A.C. Tilmans, J.H.J. Fluitman and M. Elwenspoek. *Nonlinearity and hysteresis of resonant strain gauges*. In Micro Electro Mechanical Systems, 1995, MEMS '95, Proceedings. IEEE, pages 157–, Jan-2 Feb 1995. 87, 112, 118

[Gupta 2004] D Akin Gupta A and R Bashir. *Single virus particle mass detection using microresonators with nanoscale thickness*. Appl. Phys. Lett., vol. 84, pages 1976–8, 2004. 29, 187

[Hagleitner 2001] C. Hagleitner, A. Hierlemann, D. Lange, A. Kummer, N. Kerness, O. Brand and H. Baltes. *Smart single-chip gas sensor microsystem*. Nature, vol. 414, pages 293–296, 2001. 31

[Hagleitner 2002] C. Hagleitner, D. Lange, N. Kerness, A. Hierlemann, O. Brand and H. Baltes. *A gas detection system on a single CMOS chip comprising capacitive, calorimetric, and mass-sensitive microsensors*. In Solid-State Circuits Conference, 2002. Digest of Technical Papers. ISSCC. 2002 IEEE International, volume 1, pages 430–479 vol.1, 2002. 32

[Handley 2001] J Handley. *Quartz crystal microbalances*. Anal. Chem., vol. 73, no. 7, page 225229, 2001. 31

[Hao 2003] Zhili Hao, Ahmet Erbil and Farrokh Ayazi. *An analytical model for support loss in micromachined beam resonators with in-plane flexural vibrations*. Sensors and Actuators A: Physical, vol. 109, no. 1-2, pages 156 – 164, 2003. 108, 199

[Hardy 1949] G. H. Hardy. Divergent series. Clarendon Press, 1949. 53

[Harsányi 2000] G Harsányi. *Polymer films in sensor applications: a review of present uses and future possibilities*. Sensor Review, vol. 20, no. 2, pages 98–105, 2000. 26

[He 2002] Ji-Huan He. *Modified Lindstedt-Poincare methods for some strongly non-linear oscillations: Part I: expansion of a constant*. International Journal of Non-Linear Mechanics, vol. 37, no. 2, pages 309 – 314, 2002. 69

[He 2006] Rongrui He and Peidong Yang. *Giant piezoresistance effect in silicon nanowires*. Nature Nanotechnology, vol. 1, pages 42–46, 2006. 202

[He 2008] Rongrui He, X. L. Feng, M. L. Roukes and Peidong Yang. *Self-Transducing Silicon Nanowire Electromechanical Systems at Room Temperature*. Nano Letters, vol. 8, no. 6, pages 1756–1761, 2008. 202

[Holland 1998] N. B. Holland, Y. Qiu, M. Ruegsegger and R. E. Marchant. *Biomimetic engineering of non-adhesive glycocalyx-like surfaces using oligosaccharide surfactant polymers*. Nature, vol. 392, pages 799–801, 1998. 30

[Hu 1999] W Hu, Y Liu, Y Xu, S Liu, S Zhou, P Zeng and D B Zhu. *The gas sensitivity of Langmuir-Blodgett films of a new asymmetrically substituted phthalocyanine*. Sensors and Actuators B, vol. 56, no. 3, pages 228–233, 1999. 26

[Hu 2004] H. Hu and Z. G. Xiong. *Comparison of two Lindstedt-Poincaré-type perturbation methods*. Journal of Sound and Vibration, vol. 278, no. 1-2, pages 437 – 444, 2004. 54

[Husain 2003] A. Husain, J. Hone, Henk W. Ch. Postma, X. M. H. Huang, T. Drake, M. Barbic, A. Scherer and M. L. Roukes. *Nanowire-based very-high-frequency electromechanical resonator*. Applied Physics Letters, vol. 83, no. 6, pages 1240–1242, 2003. 103

[IEE 2001] IEEE, New York. *Gyro and Accelerometer Panel, IEEE Aerospace and Electronic Systems Technology, IEEE standard for inertial sensor terminology*, November 2001. 12

[Ilic 2001a] B Ilic, D Czaplewski, M Zalalutdinov, H G Craighead, P Neuzil, C Campagnolo and C Batt. *Single cell detection with micromechanical oscillators*. J. Vac. Sci. Technol. B, vol. 19, pages 2825–8, 2001. 29, 187

[Ilic 2001b] B. Ilic, D. Czaplewski, M. Zalalutdinov, H. G. Craighead, P. Neuzil, C. Campagnolo and C. Batt. *Single cell detection with micromechanical oscillators*. volume 19, pages 2825–2828. AVS, 2001. 32

[Janata 1989] J Janata. Priniples of chemical sensors. Plenum Press, 1989. 29

[Janshoff 2000] A. Janshoff, H. J. Galla and C. Steinem. *Piezoelectric mass-sensing devices as biosensors an alternative to optical biosensors?* Angewandte Chemie, vol. 39, no. 22, page 40044032, 2000. 27

[Jensen 2006] K. Jensen, Ç. Girit, W. Mickelson and A. Zettl. *Tunable Nanoresonators Constructed from Telescoping Nanotubes*. Physical Review Letters, vol. 96, no. 21, page 215503, 2006. 38

[Jensen 2008] K Kim Jensen K and A Zettl. *An atomic-resolution nanomechanical mass sensor*. Nature Nanotechnology, vol. 3, pages 533–537, 2008. 1, 187

[Jensenius 2000] Henriette Jensenius, Jacob Thaysen, Anette A. Rasmussen, Lars H. Veje, Ole Hansen and Anja Boisen. *A microcantilever-based alcohol vapor sensor-application and response model.* Applied Physics Letters, vol. 76, no. 18, pages 2615–2617, 2000. 28, 187

[Jin 1998] Zhonghe Jin and Yuelin Wang. *Electrostatic resonator with second superharmonic resonance.* Sensors and Actuators A: Physical, vol. 64, no. 3, pages 273 – 279, 1998. 124

[Juillard 2008] J. Juillard, A. Bonnoit, E. Avignon, S. Hentz, N. Kacem and E. Colinet. *From MEMS to NEMS: Closed-loop actuation of resonant beams beyond the critical Duffing amplitude.* In Sensors, 2008 IEEE, pages 510–513, Oct. 2008. 45, 87

[Juneau 1997] T. Juneau, A.P. Pisano and J.H. Smith. *Dual axis operation of a micromachined rate gyroscope.* In Solid State Sensors and Actuators, 1997. TRANSDUCERS '97 Chicago., 1997 International Conference on, volume 2, pages 883–886 vol.2, Jun 1997. ix, 23, 24

[Kaajakari 2005a] V. Kaajakari, J.K. Koskinen and T. Mattila. *Phase noise in capacitively coupled micromechanical oscillators.* Ultrasonics, Ferroelectrics and Frequency Control, IEEE Transactions on, vol. 52, no. 12, pages 2322–2331, Dec. 2005. x, 2, 45, 46, 87, 135, 219, 221

[Kaajakari 2005b] Ville Kaajakari, Tomi Mattila, Antti Lipsanen and Aarne Oja. *Nonlinear mechanical effects in silicon longitudinal mode beam resonators.* Sensors and Actuators A: Physical, vol. 120, no. 1, pages 64 – 70, 2005. 112, 115

[Kacem 2008] N Kacem, S Hentz, H Fontaine, V Nguyen, P Robert, B Legrand and L Buchaillot. *From MEMS to NEMS: Modelling and characterization of the non linear dynamics of resonators, a way to enhance the dynamic range.* In Int. Conf. Nanotech, (Boston : Massachusetts, U.S.A), Juin 2008. 119

[Kacem 2009a] N. Kacem and S. Hentz. *Bifurcation topology tuning of a mixed behavior in nonlinear micromechanical resonators.* Applied Physics Letters, vol. 95, no. 18, page 183104, 2009. 166, 191, 221

[Kacem 2009b] N Kacem, S Hentz, D Pinto, B Reig and V Nguyen. *Nonlinear dynamics of nanomechanical beam resonators: improving the performance of NEMS-based sensors.* Nanotechnology, vol. 20, no. 27, page 275501, 2009. 120

[Kacem 2010] N Kacem, J Arcamone, F Perez-Murano and S Hentz. *Dynamic range enhancement of nonlinear nanomechanical resonant cantilevers for high sensitive NEMS gas/mass sensors applications.* Journal of Micromechanics and Microengineering, vol. 20, no. 4, page 045023, 2010. 219

[Kallergis 2001] K.M. Kallergis. *New fire/smoke detection and fire extinguishing systems for aircraft applications.* Air Space Europe, vol. 3, pages 197–200(4), May 2001. 25

[Kádár 1998] Zs. Kádár, A. Bossche, P.M. Sarro and J.R. Mollinger. *Magnetic-field measurements using an integrated resonant magnetic-field sensor.* Sensors and Actuators A: Physical, vol. 70, no. 3, pages 225 – 232, 1998. 32

[Keller 1977] H.B. Keller. Numerical solution of bifurcation and nonlinear eigenvalue problems. Academic Press, 1977. 72

[Kenig 2009a] Eyal Kenig, Ron Lifshitz and M. C. Cross. *Pattern selection in parametrically driven arrays of nonlinear resonators.* Phys. Rev. E, vol. 79, no. 2, page 026203, Feb 2009. 124

[Kenig 2009b] Eyal Kenig, Boris A. Malomed, M. C. Cross and Ron Lifshitz. *Intrinsic localized modes in parametrically driven arrays of nonlinear resonators.* Phys. Rev. E, vol. 80, no. 4, page 046202, Oct 2009. 124

[Kenny 1992] T.W. Kenny, W.J. Kaiser, J.A. Podosek, H.K. Rockstad and J.K. Reynolds. *Micromachined electron tunneling infrared sensors.* In Solid-State Sensor and Actuator Workshop, 1992. 5th Technical Digest., IEEE, pages 174–177, Jun 1992. 18

[Kim 1997] J Go Kim S and Y Cho. *Fabrication and Static Test of a Resonant Accelerometer.* In the ASME Symposium on Microelectromechanical Systems, pages 21–26, 1997. 82

[Kirianaki 2002] N Kirianaki, S Yurish, N Shpak and V Deynega. Data acquisition and signal processing for smart sensors. John Wiley Sons, 2002. 34

[Kohl 2001] D. Kohl, J. Kelleter and H. Petig. *Detection of fires by gas sensors.* Sens Update., vol. 9, no. 1, page 161223, 2001. 25

[Kozinsky 2006] I. Kozinsky, H. W. Ch. Postma, I. Bargatin and M. L. Roukes. *Tuning nonlinearity, dynamic range, and frequency of nanomechanical resonators.* Applied Physics Letters, vol. 88, no. 25, page 253101, 2006. 87

[L 2006] Arlett J L, J R Maloney, B Gudlewski, M Muluneh and M L Roukes. *Self-Sensing Micro- and Nanocantilevers with Attonewton-Scale Force Resolution.* Nano Letters, vol. 6, no. 5, pages 1000–1006, 2006. 202

[LaHaye 2004] M D LaHaye, O Buu, B Camarota and K C Schwab. *Approaching the quantum limit of a nanomechanical resonator.* Science, vol. 304, pages 74–77, 2004. 1

[Landau 1986] L. D. Landau and E. M. Lifshitz. Theory of elasticity. Butterworth-Heinemann, 1986. 49

[Lau 1981] S L Lau and Y K Cheung. *Amplitude incremental variational principle for nonlinear vibration of elastic systems.* ASME Journal of Applied Mechanics, vol. 28, pages 959–964, 1981. 75

[Lavrik 2003] Nickolay V. Lavrik and Panos G. Datskos. *Femtogram mass detection using photothermally actuated nanomechanical resonators.* Applied Physics Letters, vol. 82, no. 16, pages 2697–2699, 2003. 187, 188

[Leung 1998] A.M. Leung, J. Jones, E. Czyzewska, J. Chen and B. Woods. *Micromachined accelerometer based on convection heat transfer.* In Micro Electro Mechanical Systems, 1998. MEMS 98. Proceedings., The Eleventh Annual International Workshop on, pages 627–630, Jan 1998. 19

[Lifshitz 2000] Ron Lifshitz and M. L. Roukes. *Thermoelastic damping in micro- and nanomechanical systems.* Phys. Rev. B, vol. 61, no. 8, pages 5600–5609, Feb 2000. 39, 108, 120, 199

[Lifshitz 2003] Ron Lifshitz and M. C. Cross. *Response of parametrically driven nonlinear coupled oscillators with application to micromechanical and nanomechanical resonator arrays.* Phys. Rev. B, vol. 67, no. 13, page 134302, Apr 2003. 124

[Lifshitz 2008] Ron Lifshitz and M. C. Cross. *Nonlinear dynamics of nanomechanical and micromechanical resonators.* In Review of Nonlinear Dynamics and Complexity, H. G. Schuster, ed., vol. 1, pages 1–52, 2008. 46

[Liu 2003] Tao Liu, Ji'an Tang, Meimei Han and Long Jiang. *A novel microgravimetric DNA sensor with high sensitivity.* Biochemical and Biophysical Research Communications, vol. 304, no. 1, pages 98 – 100, 2003. 30

[Liu 2004] S Liu, A Davidson and Q Lin. *Simulation studies on nonlinear dynamics and chaos in a MEMS cantilever control system.* Journal of Micromechanics and Microengineering, vol. 14, no. 7, page 1064, 2004. 188

[Lundström 1996] I Lundström. *Approaches and mechanisms to solid state based sensing.* Sensors and Actuators B, vol. 35, no. 1–3, pages 11–19, 1996. 25

[Madou 1989] M J Madou and S R Morrison. Chemical sensing with solid state devices. Academic Press, 1989. 25

[Mahmoodi 2007] S. Nima Mahmoodi and Nader Jalili. *Non-linear vibrations and frequency response analysis of piezoelectrically driven microcantilevers.* International Journal of Non-Linear Mechanics, vol. 42, no. 4, pages 577 – 587, 2007. Special Issue Micro-and Nanoscale Beam Dynamics. 188

[Mandelis 1993] A Mandelis and C Christofides. Physics, chemistry and technology of solid state gas sensor devices. Wiley, 1993. 25

[Martin 1997] G. E. Martin. Geometric constructions. Springer, 1997. 115

[Masson 2005] J. F. Masson, T. M. Battaglia, M. J. Davidson, Y. C. Kim and A. M. C. Prakash. *Biocompatible polymers for antibody support on gold surfaces.* Talanta, vol. 67, no. 5, page 918925, 2005. 30

[Maute 1999] M. Maute, S. Raible, F. E. Prins, D. P. Kern, H. Ulmer, U. Weimar and W. Göpel. *Detection of volatile organic compounds (VOCs) with polymer-coated cantilevers.* Sensors and Actuators B: Chemical, vol. 58, no. 1-3, pages 505 – 511, 1999. 28

[McGeehin 2000] P. McGeehin. *Gas sensors for improved air quality in transportation.* Sensor Rev., vol. 20, no. 2, page 106112, 2000. 25

[Meixner 1996] H Meixner and U Lampe. *Metal oxide sensors.* Sensors and Actuators B, vol. 33, no. 1–3, pages 198–202, 1996. 26

[Mestrom 2008] R.M.C. Mestrom, R.H.B. Fey, J.T.M. van Beek, K.L. Phan and H. Nijmeijer. *Modelling the dynamics of a MEMS resonator: Simulations and experiments.* Sensors and Actuators A: Physical, vol. 142, no. 1, pages 306 – 315, 2008. Special Issue: Eurosensors XX The 20th European conference on Solid-State Transducers - Eurosensors 2006, Eurosensors 20th Edition. 48

[Michon 2008] G Michon, L Manin, R G Parker and R Dufour. *Duffing Oscillator With Parametric Excitation: Analytical and Experimental Investigation on a Belt-Pulley System.* Journal of Computational and Nonlinear Dynamics, vol. 3, page 031001, 2008. 48, 163

[Mielle 2000] F Marquis Mielle P and C Latrasse. *Electronic noses: specify or disappear.* Sensor and Actuators B, vol. 69, no. 3, pages 287–294, 2000. 25

[Mile 2010] E Mile, G Jourdan, I Bargatin, S Labarthe, C Marcoux, P Andreucci, S Hentz, C Kharrat, E Colinet and L Duraffourg. *In-plane nanoelectromechanical resonators based on silicon nanowire piezoresistive detection.* Nanotechnology, vol. 21, no. 16, page 165504, 2010. 217, 218

[Minorsky 1947] N. Minorsky. Introduction to nonlinear mechanics: topological methods, analytical methods, nonlinear resonance, relaxation oscillations. John Wiley Sons, 1947. 52

[Mo 2007] Li Mo, H. X. Tang and M. L. Roukes. *Ultra-sensitive NEMS-based cantilevers for sensing, scanned probe and very high-frequency applications.* Nature Nanotechnology, vol. 2, pages 114–120, 2007. 30, 202, 217

[Mohanty 2002] P. Mohanty, D. A. Harrington, K. L. Ekinci, Y. T. Yang, M. J. Murphy and M. L. Roukes. *Intrinsic dissipation in high-frequency micromechanical resonators.* Phys. Rev. B, vol. 66, no. 8, page 085416, Aug 2002. 40

[Moos 2002] R. Moos, R. Muller, C. Plog, A. Knezevic, H. Leye, E. Irion, T. Braun, K. J. Marquardt and K. Binder. *Selective ammonia exhaust gas sensor for automotive applications.* Sensors and Actuators B: Chemical, vol. 83, pages 181–189(9), 15 March 2002. 25

[Moseley 1987] P. T. Moseley and B. C. Tofield. Solid state gas sensors (adam hilger series on sensors). Taylor Francis, 1987. 25

[Moseley 1997] P T Moseley. *Solid state gas sensors.* Meas. Sci. Technol., vol. 8, no. 3, page 223, 1997. 25

[Murdock 1991] J. A. Murdock. Perturbations: Theory and methods. John Wiley Sons, 1991. 51, 53

[Nacivet 2003] S Nacivet, C Pierre, F Thouverez and L Jezequel. *A dynamic Lagrangian frequency-time method for the vibration of dry-friction-damped systems.* Journal of Sound and Vibration, vol. 265, pages 201–219, 2003. 75

[Naik 2006] A Naik, O Buu, M D LaHaye, A D Armour, A A Clerk, M P Blencowe and K C Schwab. *Cooling a nanomechanical resonator with quantum back-action.* Nature, vol. 443, pages 193–196, 2006. 223

[Najar 2006] F Najar, S Choura, E M Abdel-Rahman, S El-Borgi and A Nayfeh. *Dynamic analysis of variable-geometry electrostatic microactuators.* Journal of Micromechanics and Microengineering, vol. 16, no. 11, page 2449, 2006. 88, 101

[Nayfeh 1979] A. H. Nayfeh and D. T. Mook. Nonlinear oscillations, physics and applied mathematics. Wiley, 1979. 112

[Nayfeh 1981] A. H. Nayfeh. Introduction to perturbation techniques. Wiley, 1981. 95, 124, 166

[Nayfeh 1995] A. M. Nayfeh and B. Balachandran. Applied nonlinear dynamics: Analytical, computational, and experimental methods. Wiley, 1995. 72

[Nayfeh 2005a] Ali Nayfeh. *Resolving Controversies in the Application of the Method of Multiple Scales and the Generalized Method of Averaging.* Nonlinear Dynamics, vol. 40, pages 61–102(42), April 2005. 64

[Nayfeh 2005b] Ali H Nayfeh and Mohammad I Younis. *Dynamics of MEMS resonators under superharmonic and subharmonic excitations.* Journal of Micromechanics and Microengineering, vol. 15, no. 10, pages 1840–1847, 2005. 124, 126

[Nayfeh 2007] A. H. Nayfeh, M. I. Younis and E. M. Abdel-Rahman. *Dynamic pull-in phenomenon in MEMS resonators.* Nonlinear Dynamics, vol. 48, pages 153–163, 2007. 88, 101, 102, 118, 195

[Newman 1999] W. I. Newman, R. H. Rand and A. L. Newman. *Dynamics of a nonlinear parametrically excited partial differential equation.* Chaos: An Interdisciplinary Journal of Nonlinear Science, vol. 9, no. 1, pages 242–253, 1999. 163

[Nguyen 1999a] A C Wong Nguyen C T and D Hao. *Tunable, switchable, high-q vhf microelectromechanical bandpass filters.* In In IEEE International Solid-State Circuits Conference, volume 448, page 78, 1999. 1

[Nguyen 1999b] C T Nguyen. *Micromechanical components for miniaturized low-power communications.* In In 1999 IEEE MTT-S international Microwave Symposium FR MEMS Workshop, pages 48–77, 1999. 1

[Nishiyama 1990] H. Nishiyama and M. Nakamura. *Capacitance of a strip capacitor.* Components, Hybrids, and Manufacturing Technology, IEEE Transactions on, vol. 13, no. 2, pages 417–423, Jun 1990. 89, 101, 108, 133, 159, 189, 199, 225

[OMalley 1991] R. E. OMalley. Singular perturbation methods for ordinary differential equations. Springer-Verlag, 1991. 53

[Ono 2003] T Ono, X X Li, H Miyashita and M Esashi. *Mass sensing of adsorbed molecules in sub-picogram sample with ultrathin silicon resonator.* Rev. Sci. Instrum., vol. 74, pages 1240–3, 2003. 29, 187, 188

[Osterberg 1997] P.M. Osterberg and S.D. Senturia. *M-TEST: A test chip for MEMS material property measurement using electrostatically actuated test structures.* Microelectromechanical Systems, Journal of, vol. 6, no. 2, pages 107–118, Jun 1997. 88, 116, 118

[Ouakad 2008] H M Ouakad and M I Younis. *Nonlinear Dynamics of Electrically-Actuated Carbon Nanotube Resonator.* In Int. Mechanical Engineering Congress and Exposition, (Boston : Massachusetts, U.S.A), 2008. 118

[Palasantzas 2008] G. Palasantzas. *Limit to mass sensitivity of nanoresonators with random rough surfaces due to intrinsic sources and interactions with the surrounding gas.* Journal of Applied Physics, vol. 104, no. 1, page 016107, 2008. 41

[Park 2000] S. Park, J. P. Bearinger, E. P. Lautenschlager, D. G. Castner and K. E. Healy. *Surface modification of poly(ethylene terephthalate) angioplasty balloons with a hydrophilic poly(acrylamide-co-ethylene glycol) interpenetrating polymer network coating.* J. Biomed. Mater. Res., vol. 53, no. 5, pages 568–576, 2000. 30

[Park 2003] Sungsu Park and R. Horowitz. *Adaptive control for the conventional mode of operation of MEMS gyroscopes.* Microelectromechanical Systems, Journal of, vol. 12, no. 1, pages 101–108, Feb 2003. 157

[Postma 2005] H. W. Ch. Postma, I. Kozinsky, A. Husain and M. L. Roukes. *Dynamic range of nanotube- and nanowire-based electromechanical systems.* Applied Physics Letters, vol. 86, no. 22, page 223105, 2005. 40, 87, 172, 188

[Powell 2006] D. A. Powell, K. Kalantar-zadeh, W. Wlodarski and S. J. Ippolito. Layered surface acoustic wave chemical and bio-sensors. American Scientific Publishers, Stevenson Ranch, 2006. 28

[Prak 1993] A. Prak. *Silicon Resonant Sensors: Operation and Response.* PhD thesis, University of Twente, The Netherlands, 1993. 33

[Putty 1994] M. W. Putty and K. Najafi. *A micromachined vibrating ring gyroscope.* page 213220, 1994. 22

[Ramis 1991] J. P. Ramis. Séries divergentes et théories asymptotiques. Université Louis Pasteur, 1991. 53

[Rand 2003] R. Rand, K. Guennoun and M. Belhaq. *2:2:1 Resonance in the Quasiperiodic Mathieu Equation.* Nonlinear Dynamics, vol. 31, pages 367–374(8), March 2003. 163

[Rand 2005] Richard Rand and Tina Morrison. *2:1:1 Resonance in the Quasi-Periodic Mathieu Equation.* Nonlinear Dynamics, vol. 40, pages 195–203(9), April 2005. 165

[Ricco 1991] Antonio J. Ricco and Stephen J. Martin. *Thin metal film characterization and chemical sensors: monitoring electronic conductivity, mass loading and mechanical properties with surface acoustic wave devices.* Thin Solid Films, vol. 206, no. 1-2, pages 94 – 101, 1991. 28

[Robins 1984] W. P. Robins. Phase noise in signal sources. Institution of Engineering and Technology, 1984. 1, 40, 87, 173

[Rockstad 1996] H. K. Rockstad, T. K. Tang, J. K. Reynolds, T. W. Kenny, W. J. Kaiser and T. B. Gabrielson. *A miniature, high-sensitivity, electron tunneling accelerometer.* Sensors and Actuators A: Physical, vol. 53, pages 227–231(5), May 1996. ix, 18

[Roessig 1997a] R T Howe Roessig T A and A P Pisano. *Nonlinear mixing in surface-micromachined tuning fork oscillators.* In Frequency Control Symposium, 1997., Proceedings of the 1997 IEEE International, pages 778–782, May 1997. 2, 45, 87, 135

[Roessig 1997b] T.A. Roessig, R.T. Howe, A.P. Pisano and J.H. Smith. *Surface-micromachined resonant accelerometer.* In Solid State Sensors and Actuators, 1997. TRANSDUCERS '97 Chicago., 1997 International Conference on, volume 2, pages 859–862 vol.2, Jun 1997. ix, 18, 19, 82

[Roessig 1998] T.A. Roessig. *Integrated MEMS Tuning Fork Oscillators for Sensor Applications.* PhD thesis, University of California, Berkeley, 1998. 36, 158

[Roszhart 1995] T.V. Roszhart, H. Jerman, J. Drake and C. de Cotiis. *An Inertial-Grade, Micromachined Vibrating Beam Accelerometer.* In Solid-State Sensors and Actuators, 1995 and Eurosensors IX.. Transducers '95. The 8th International Conference on, volume 2, pages 656–658, Jun 1995. 19, 82

[Roylance 1979] L.M. Roylance and J.B. Angell. *A batch-fabricated silicon accelerometer.* Electron Devices, IEEE Transactions on, vol. 26, no. 12, pages 1911–1917, Dec 1979. 17

[Rugar 1991] D. Rugar and P. Grütter. *Mechanical parametric amplification and thermomechanical noise squeezing*. Phys. Rev. Lett., vol. 67, no. 6, pages 699–702, Aug 1991. 124, 187, 223

[Sanchez 1996] Nestor E. Sanchez. *The Method of Multiple Scales: Asymptotic Solutions and Normal Forms for Nonlinear Oscillatory Problems*. Journal of Symbolic Computation, vol. 21, no. 2, pages 245 – 252, 1996. 57

[Sazonova 2006] Vera A. Sazonova. *A Tunable Carbon Nanotube Resonator*. PhD thesis, Cornell University, 2006. 39, 108, 120, 133, 138, 184, 195, 200

[Schwab 2005] Keith C. Schwab and Michael L. Roukes. *Putting Mechanics into Quantum Mechanics*. Physics Today, vol. 58, no. 7, pages 36–42, 2005. 223

[Seeger 1981] A. Seeger. *THE KINK PICTURE OF DISLOCATION MOBILITY AND DISLOCATION-POINT-DEFECT INTERACTIONS*. J. Phys. Colloques, vol. 42, pages C5–201–C5–228, oct 1981. 40

[Seidel 1995] H. Seidel, U. Fritsch, R. Gottinger, J. Schalk, J. Walter and K. Ambaum. *A Piezoresistive Silicon Accelerometer With Monolithically Integrated CMOS-circuitry*. In Solid-State Sensors and Actuators, 1995 and Eurosensors IX.. Transducers '95. The 8th International Conference on, volume 1, pages 597–600, Jun 1995. ix, 17

[Seshia 2002a] A.A. Seshia, R.T. Howe and S. Montague. *An integrated microelectromechanical resonant output gyroscope*. In Micro Electro Mechanical Systems, 2002. The Fifteenth IEEE International Conference on, pages 722–726, 2002. ix, 24, 25, 32, 157

[Seshia 2002b] A.A. Seshia, M. Palaniapan, T.A. Roessig, R.T. Howe, R.W. Gooch, T.R. Schimert and S. Montague. *A vacuum packaged surface micromachined resonant accelerometer*. Microelectromechanical Systems, Journal of, vol. 11, no. 6, pages 784–793, Dec 2002. 32

[Shao 2008a] L C Shao, M Palaniapan and W W Tan. *The nonlinearity cancellation phenomenon in micromechanical resonators*. Journal of Micromechanics and Microengineering, vol. 18, no. 6, page 065014, 2008. 112, 115, 116, 118

[Shao 2008b] L C Shao, M Palaniapan, W W Tan and L Khine. *Nonlinearity in micromechanical free-free beam resonators: modeling and experimental verification*. Journal of Micromechanics and Microengineering, vol. 18, no. 2, page 025017, 2008. 49

[Shkel 1999] A.M. Shkel, R. Horowitz, A.A. Seshia, Sungsu Park and R.T. Howe. *Dynamics and control of micromachined gyroscopes*. In American Control Conference, 1999. Proceedings of the 1999, volume 3, pages 2119–2124 vol.3, 1999. xv, 157, 158

[Siddiqi 2004] I. Siddiqi, R. Vijay, F. Pierre, C. M. Wilson, M. Metcalfe, C. Rigetti, L. Frunzio and M. H. Devoret. *RF-Driven Josephson Bifurcation Amplifier for Quantum Measurement*. Phys. Rev. Lett., vol. 93, no. 20, page 207002, Nov 2004. 223

[Silva 1978a] M. R. M. Crespo Da Silva and C. C. Glynn. *Nonlinear flexural-flexural-torsional dynamics of inextensional beams. I: Equations of motion*. Journal of Structural Mechanics, vol. 6, page 437448, 1978. 50, 77, 189, 203

[Silva 1978b] M. R. M. Crespo Da Silva and C. C. Glynn. *Nonlinear flexural-flexural-torsional dynamics of inextensional beams. II: Forced motions*. Journal of Structural Mechanics, vol. 6, page 449461, 1978. 50, 77, 189, 203

[Silva 1988a] M. R. M. Crespo Da Silva. *Non-linear flexural-flexural-torsional-extensional dynamics of beams. I: Formulation.* International Journal of Solids and Structures, vol. 24, page 12251234, 1988. 50, 189, 203

[Silva 1988b] M. R. M. Crespo Da Silva. *Non-linear flexural-flexural-torsional-extensional dynamics of beams. II: Response analysis.* International Journal of Solids and Structures, vol. 24, page 12351242, 1988. 50, 189, 203

[Smith 1985] D. R. Smith. Singular-perturbation theory. Cambridge University Press, 1985. 53

[Smith 1995a] J Smith, S Montague, J J Sniegowski, J R Murray and P J McWhorter. *Embedded micromechanical devices for the monolithic integration of MEMS with CMOS.* In In Technical Digest IEDM, pages 609–612, 1995. 87

[Smith 1995b] J.H. Smith and S.D. Senturia. *Self-consistent Temperature Compensation For Resonant Sensors With Application To Quartz Bulk Acoustic Wave Chemical Sensors.* In Solid-State Sensors and Actuators, 1995 and Eurosensors IX.. Transducers '95. The 8th International Conference on, volume 2, pages 724–727, Jun 1995. 31

[Sparks 1999] D. Sparks, D. Slaughter, R. Beni, L. Jordan, M. Chia, D. Rich, J. Johnson and T. Vas. *Chip-scale packaging of a gyroscope using wafer bonding.* Sensors and materials, vol. 11, no. 4, pages 197–207, 1999. ix, 22, 23

[Stephens 2002] D R Stephens. Phase-locked loops for wireless communications: Digital, analog and optical implementations. Kluwer Academic Publishers, 2002. 35

[Struble 1964] Raimond A. Struble. *A note on periodic solutions of the Duffing equation.* Journal of Mathematical Analysis and Applications, vol. 9, page 498501, 1964. 53

[Su 2003] Ming Su, Shuyou Li and Vinayak P. Dravid. *Microcantilever resonance-based DNA detection with nanoparticle probes.* Applied Physics Letters, vol. 82, no. 20, pages 3562–3564, 2003. 30

[Subramanian 2002] A. Subramanian, P. I. Oden, S. J. Kennel, K. B. Jacobson, R. J. Warmack, T. Thundat and M. J. Doktycz. *Glucose biosensing using an enzyme-coated microcantilever.* Applied Physics Letters, vol. 81, no. 2, pages 385–387, 2002. 30

[Tabata 1999] Osamu Tabata and Takeshi Yamamoto. *Two-axis detection resonant accelerometer based on rigidity change.* Sensors and Actuators A: Physical, vol. 75, no. 1, pages 53 – 59, 1999. 33

[Tamayo 2003] Javier Tamayo, Mar Alvarez and Laura M. Lechuga. *Digital tuning of the quality factor of micromechanical resonant biological detectors.* Sensors and Actuators B: Chemical, vol. 89, no. 1-2, pages 33 – 39, 2003. 30

[Thompson 2001] J. M. T. Thompson and H. B. Stewart. Nonlinear dynamics and chaos. Wiley, 2001. 118

[Thundat 1995a] T Thundat, G Y Chen, R J Warmack, D P Allison and E A Wachter. *Vapor Detection Using Resonating Microcantilevers.* Anal. Chem., vol. 67, no. 3, pages 519–521, 1995. 28

[Thundat 1995b] T Thundat, E A Wachter, S L Sharp and R J Warmack. *Detection of mercury vapor using resonating microcantilevers.* Appl. Phys. Letters, vol. 66, pages 1695–7, 1995. 29

[Tilmans 1994] Harrie A.C. Tilmans and Rob Legtenberg. *Electrostatically driven vacuum-encapsulated polysilicon resonators: Part II. Theory and performance.* Sensors and Actuators A: Physical, vol. 45, no. 1, pages 67 – 84, 1994. 87

[Turner 1998] K.L. Turner, S.A. Miller, P.G. Hartwell, N.C. MacDonald, H.S. Strogatz and S.G. Adams. *Five parametric resonances in a microelectromechanical system.* Nature, vol. 396, pages 149–152, 1998. 124, 223

[Uttamchandani 1992] D. Uttamchandani, D. Liang and B. Culshaw. *A micromachined silicon accelerometer with fiber optic integration.* page 2733, 1992. 19

[van den Boogaart 2004] M. A. F. van den Boogaart, G. M. Kim, R. Pellens, J.-P. van den Heuvel and J. Brugger. *Deep-ultraviolet–microelectromechanical systems stencils for high-throughput resistless patterning of mesoscopic structures.* volume 22, pages 3174–3177. AVS, 2004. 196

[Verd 2006] J. Verd, A. Uranga, J. Teva, J.L. Lopez, F. Torres, J. Esteve, G. Abadal, F. Perez-Murano and N. Barniol. *Integrated CMOS-MEMS with on-chip readout electronics for high-frequency applications.* Electron Device Letters, IEEE, vol. 27, no. 6, pages 495–497, June 2006. 195

[Verd 2008] J. Verd, A. Uranga, G. Abadal, J.L. Teva, F. Torres, J.L. Lopez, E. Perez-Murano, J. Esteve and N. Barniol. *Monolithic CMOS MEMS Oscillator Circuit for Sensing in the Attogram Range.* Electron Device Letters, IEEE, vol. 29, no. 2, pages 146–148, Feb. 2008. 195

[Wang 2000] Kun Wang, Ark-Chew Wong and C.T.-C. Nguyen. *VHF free-free beam high-Q micromechanical resonators.* Microelectromechanical Systems, Journal of, vol. 9, no. 3, pages 347–360, Sep 2000. 39

[Wohltjen 1979] H. Wohltjen and R. Dessy. *Surface acoustic-wave probe for chemical-analysis .I. Introduction and Instrument Description.* Anal Chem., vol. 51, no. 9, page 14581464, 1979. 27

[Wolaver 1991] D H Wolaver. Phase-locked loop circuit design. Englewood Cliffs, NJ: Prentice Hall, 1991. 35

[Xie 2003] W C Xie, H P Lee and S P Lim. *Nonlinear dynamic Analysis of MEMS Switches by Nonlinear Modal Analysis.* Nonlinear Dynamics, vol. 31, pages 243–256, 2003. 91

[Yang 2002] Jinling Yang, T. Ono and M. Esashi. *Energy dissipation in submicrometer thick single-crystal silicon cantilevers.* Microelectromechanical Systems, Journal of, vol. 11, no. 6, pages 775–783, Dec 2002. 108, 199

[Yang 2003] Y. Yang, H. F. Ji and T. Thundat. *Nerve agents detection using a Cu2+/L-cysteine bilayer-coated microcantilever.* J. Am. Chem. Soc., vol. 125, no. 5, pages 1124–1125, 2003. 30

[Yang 2004] C. H. Yang, S. M. Zhu and S. H. Chen. *A modified elliptic Lindstedt-Poincaré method for certain strongly non-linear oscillators.* Journal of Sound and Vibration, vol. 273, no. 4-5, pages 921 – 932, 2004. 69

[Yang 2006] Y T Yang, C Callegari, X L Feng, K L Ekinci and M L Roukes. *Zeptogram-Scale Nanomechanical Mass Sensing.* Nano Letters, vol. 6, no. 4, pages 583–586, 2006. 187, 188, 202

[Yazdi 1998] N. Yazdi, F. Ayazi and K. Najafi. *Micromachined inertial sensors.* Proceedings of the IEEE, vol. 86, no. 8, pages 1640–1659, Aug 1998. 157

[Yazdi 2000] N. Yazdi and K. Najafi. *An all-silicon single-wafer micro-g accelerometer with a combined surface and bulk micromachining process.* Microelectromechanical Systems, Journal of, vol. 9, no. 4, pages 544–550, Dec 2000. ix, 15, 16

[Yong 1989] Y.K. Yong and J.R. Vig. *Resonator surface contamination-a cause of frequency fluctuations?* Ultrasonics, Ferroelectrics and Frequency Control, IEEE Transactions on, vol. 36, no. 4, pages 452–458, Jul 1989. 41

[Yong 1990] YK Yong and JR Vig. *Modeling resonator frequency fluctuations induced by adsorbing and desorbing surface molecules.* IEEE Trans Ultrason Ferroelectr Freq Control, vol. 37, no. 6, pages 543–50, 1990. 41

[Younis 2003a] M.I. Younis, E.M. Abdel-Rahman and A. Nayfeh. *A reduced-order model for electrically actuated microbeam-based MEMS.* Microelectromechanical Systems, Journal of, vol. 12, no. 5, pages 672–680, Oct. 2003. 88, 91

[Younis 2003b] M.I. Younis and A. H. Nayfeh. *A Study of the Nonlinear Response of a Resonant Microbeam to an Electric Actuation.* Nonlinear Dynamics, vol. 31, no. 1, pages 91–117, 2003. 124

[Younis 2004] M.I. Younis, E. M. Abdel-Rahman and A. H. Nayfeh. *Global dynamics of MEMS resonators under superharmonic excitation.* In the International Conference on MEMS, NANO, and Smart Systems, Banff, Canada (ICMENS), page 694699, August 2004. 124

[Yurke 1995] B. Yurke, D. S. Greywall, A. N. Pargellis and P. A. Busch. *Theory of amplifier-noise evasion in an oscillator employing a nonlinear resonator.* Phys. Rev. A, vol. 51, no. 5, pages 4211–4229, May 1995. 45

[Yuste 1992] S. Bravo Yuste. *Quasi-pure-cubic oscillators studied using a krylov-Bogoliubov method.* Journal of Sound and Vibration, vol. 158, no. 2, pages 267 – 275, 1992. 67

[Zener 1938] Clarence Zener. *Internal Friction in Solids II. General Theory of Thermoelastic Internal Friction.* Phys. Rev., vol. 53, no. 1, pages 90–99, Jan 1938. 39

[Zounes 1998] Randolph S. Zounes and Richard H. Rand. *Transition curves for the quasi-periodic Mathieu equation.* SIAM J. Appl. Math., vol. 58, no. 4, pages 1094–1115, 1998. 165

[Zounes 2002] R.S. Zounes and R.H. Rand. *Global Behavior of a Nonlinear Quasiperiodic Mathieu Equation.* Nonlinear Dynamics, vol. 27, pages 87–105(19), January 2002. 163, 165

Abstract

Nanoelectromechanical systems (NEMS) have been the focus of recent applied and fundamental research. With critical dimensions down to a few tens of nm, most NEMS are used working in resonance. In this size regime, they display high fundamental resonance frequencies, diminished active masses, tolerable force constants and relatively high quality factors in the range of $10^2 - 10^4$. These attributes collectively make NEMS suitable for a multitude of technological applications such as ultrasensitive force and mass sensing, narrow band filtering, and time keeping. So as to fulfill their full promises, that is, to begin to come out of industrial foundries, a certain number of challenges are yet to be addressed: in particular, their frequency stability, *i.e.* their output carrier power has to be improved. Mechanical transduction gain of the devices has been thoroughly studied, but the drive power has always been a priori limited to the onset of nonlinearities. Besides, the smaller the structures, the sooner nonlinearities occur, reducing their dynamic range and even making extremely difficult to detect their oscillation, as the abundant literature about characterization techniques proves.

In this thesis, this limitation is reconsidered, *i.e.* the behavior of NEMS at large amplitude through the nonlinear dynamics of NEMS-based resonant sensors is investigated. A review of inertial, mass and gas sensors is carried out. Particularly, the design issues of resonant sensors are addressed and the sources of nonlinearities in clamped-clamped resonators and cantilevers are exposed. A review of nonlinear methods is also presented in order to define a modeling strategy for the dynamics of resonant accelerometers, gyroscopes and mass/gas sensors. Close-form solutions of the critical amplitudes were provided for several devices and the importance of the fifth order nonlinearities has been demonstrated through the mixed behavior identification. Several analytical design rules are provided in order to enhance the dynamic range of NEMS resonators and the detection limit of NEMS-based resonant sensors. These rules essentially include hysteresis suppression by nonlinearity cancellation as well as mixed behavior and pull-in retarding under superharmonic resonance and simultaneous resonances leading to the possibility of driving the resonator linearly at high oscillations compared to the critical amplitude. The experimental validation of the model has been performed in the case of resonant capacitive ($4\,\mu m$ SOI) MEMS and ($2\,\mu m$ MEMS level/$500\,nm$ NEMS level) SOI M&NEMS accelerometers and gyroscopes as well as capacitive (fabricated using nanostencil lithography) and piezoresistive ($160\,nm$ SOI NEMS) gas/mass sensors.

Keywords

Nonlinear dynamics, resonator, MEMS and NEMS, dynamics range, detection limit, resonant sensors, accelerometer, gyroscope, gas and mass sensors, design rules, superharmonic resonance, simultaneous resonances, mixed behavior, pull-in, critical amplitude